Dynamics of self-propelled particles: inertial effects, orientation-dependent motilities, and complex environments

Inaugural-Dissertation

zur Erlangung des Doktorgrades
der Mathematisch-Naturwissenschaftlichen Fakultät
der Heinrich-Heine-Universität Düsseldorf

vorgelegt von

Alexander Ralf Sprenger
aus Düsseldorf, Deutschland

Düsseldorf, April 2023

aus dem Institut für Theoretische Physik II: Weiche Materie
der Heinrich-Heine-Universität Düsseldorf

Gedruckt mit der Genehmigung der
Mathematisch-Naturwissenschaftlichen Fakultät der
Heinrich-Heine-Universität Düsseldorf

Referent: Prof. Dr. Hartmut Löwen

Korreferent: Prof. Dr. Raphael Wittkowski

Tag der mündlichen Prüfung: 21. Juli 2023

Kurzfassung

Das Studium der aktiven Materie offenbart bedeutende Einblicke in die Physik beweglicher lebender Organismen und motiviert die Entwicklung synthetischer Mikroroboter, welche Anwendungen in Bereichen wie dem Gesundheitswesen und den Materialwissenschaften versprechen. Beispiele für aktive Materie lassen sich überall um uns herum finden - von der mikroskopischen bis zur makroskopischen Skala - einschließlich molekularer Motoren, Bakterien, Algen, Insekten wie Ameisen oder Heuschrecken und sogar größerer Tiere wie Vögel und Fische. Diese Wesen operieren unter Nichtgleichgewichtsbedingungen, indem sie die verfügbare Energie ihrer Umgebung nutzen, um sich persistent zu bewegen oder Kräfte auf das umgebende Medium auszuüben. In dieser Arbeit untersuchen wir den Einfluss der Trägheit des Teilchens, einer anisotropen oder viskoelastischen Umgebung und möglicher geometrischer Begrenzungen auf die Dynamik eines einzelnen aktiven Teilchens. Das Verständnis der zugrunde liegenden Physik für ein einzelnes Teilchen stellt den entscheidenden ersten Schritt dar, bevor man sich komplizierteren Vielteilchensystemen zuwendet.

Der Großteil dieser Arbeit basiert auf dem wegweisenden Active Brownian Particle (ABP) Modells und diskutiert mehrere Verallgemeinerungen. Zunächst untersuchen wir die überdämpfte Dynamik von Teilchen, die sich mit orientierungsabhängiger Motilität bewegen, unter Verwendung von Experimenten an kontrollierten aktiven Kolloiden und der Theorie der aktiven Brownschen Bewegung. Die Studie liefert eine Methode zur Konstruktion komplexer anisotroper Motilitäten mit potenziellen Anwendungen in der Navigation von Mikroschwimmern und bietet gleichzeitig einen theoretischen Rahmen für selbstangetriebene Teilchen in anisotropen Umgebungen. Während viele Experimente an aktiven Teilchen mit einem newtonschen Hintergrundfluid durchgeführt werden, bewegen sich Mikroorganismen in vivo durch komplexere Umgebungen. Um dies zu berücksichtigen, schaffen wir einen theoretischen Rahmen für ABPs in einer viskoelastischen Umgebung. Wir verwenden zeitabhängige Reibungskerne, um die verzögerte Reaktion des Mediums zu beschreiben, und finden eine gedächtnisinduzierte Verzögerung zwischen der effektiven Selbstantriebskraft und der Partikelorientierung. Ähnliche Gedächtniseffekte treten bei selbstangetriebenen Objekten auf, die groß genug sind, um Trägheitseffekte zu zeigen. Wir diskutieren explizit zeitabhängige Massen und Trägheitsmomente und schlagen spezifische Bewegungsgleichungen in Abhängigkeit vom physikalischen Ursprung der Trägheitsänderung vor. Diese Situation ist in verschiedenen Systemen relevant, von Miniaturraketen über Staubpartikel

in Plasma bis hin zu Walkern mit begrenzter Aktivität. Wir analysieren ebenfalls verschiedene Massenausstoßstrategien um die Reichweite einer Langevin-Rakete zu maximieren, die wir definieren, indem wir Orientierungsfluktuationen in die traditionelle Tsiolkovsky-Raketengleichung miteinbeziehen. Als nächstes betrachten wir die kombinierte Wirkung von Teilchenträgheit und orientierungsabhängiger Motilität in einem System aktiver Vibrobots auf einem gestreiften Substrat. Die Auswertung zeigt anisotrope Bewegung auf verschiedenen Zeitskalen, die durch eine Erweiterung des ABP-Modells erklärt wird das orientierungsabhängige Motilität und Trägheitseffekte umfasst. Das Modell kann auf n-fache rotationssymmetrische Anisotropie angewendet werden und zur Vorhersage der Dynamik aktiver Materie in komplexen Umgebungen verwendet werden. Der quantitative Vergleich zwischen experimentellen Daten und theoretischen Vorhersagen beruht auf der korrekten Bestimmung der Modellparameter. In einer technischen Studie diskutieren wir mehrere Fitting-Methoden für die mittlere quadratische Verschiebung eines ABPs mit verbesserter Parameterbestimmung.

Obwohl das ABP-Modell zweifellos das bekannteste ist, teilt es beträchtliche Ähnlichkeiten mit dem mathematisch zugänglicheren Active Ornstein-Uhlenbeck Particle (AOUP) Modell. Wir verdeutlichen die Gemeinsamkeiten und Unterschiede, indem wir ein Parental Active Modell (PAM) einführen, dass diese beiden Paradigmen als Spezialfälle berücksichtigt. Als nächstes wenden wir den vorteilhaften Ornstein-Uhlenbeck-Ansatz auf die Modellierung von trägheitsbehafteten selbstangetriebenen Teilchen an. Wir stellen daher ein trägheitsbehaftetes AOUP-Modell vor, das sowohl die Translations- als auch die Rotationsträgheit berücksichtigt. Dieses neue Modell erfasst die wichtigsten Merkmale des etablierten trägheitsbehafteten ABP-Modells. Die beiden Modelle sagen im Allgemeinen ähnliche Dynamiken bis hin zu moderatem Trägheitsmoment voraus.

Im letzten Abschnitt dieser Arbeit untersuchen wir die hydrodynamischen Strömungsfelder in unmittelbarer Nähe zu Grenzflächen und die daraus resultierende hydrodynamische Wechselwirkung an aktiven und passiven Teilchen. Unsere Arbeit bietet einen theoretischen Rahmen für das Verständnis der Bewegung aktiver Teilchen in viskosen Tropfen, mit oder ohne Tenside. Diese Erkenntnisse haben potenzielle Anwendungen bei der Kontrolle von Systemen aktiver Materie und der Verwendung synthetischer Mikroschwimmer für zielgerichtete Arzneifreisetzung. Darüber hinaus untersuchen wir die Stokes-Strömung zwischen zwei starren Scheiben, die durch einen Stokeslet oder Rotlet erzeugt wird, und den daraus resultierenden Effekt der Scheiben auf die Teilchenmobilität. Diese Systeme können potenzielle Anwendungen beim Mikromischen und der Herstellung von mikropartikelbasierten Sensoren haben.

Abstract

The study of active matter reveals significant insight into the physics of motile living organisms and motivates the engineering of synthetic micro-robots, which hold promising applications in areas like health care and material science. Examples of active matter can be found all around us - from the microscopic up to the macroscopic scale - including molecular motors, bacteria, algae, insects like ants or locusts, and even larger animals such as birds and fish. Those entities operate under non-equilibrium conditions by using the available energy of their environment to move persistently or exert forces on the surrounding medium. In this dissertation, we study the influence of the particle's inertia, an anisotropic or viscoelastic environment, and possible geometric confinement on the dynamics of a single active particle. Understanding the underlying physics at a single-particle level constitutes the crucial first step before advancing to more complicated many-particle systems.

The bulk of this dissertation is based on the seminal active Brownian particle (ABP) model and discusses several generalizations. We first examine the overdamped dynamics of particles that move with orientation-dependent motility, using experiments on controlled active colloids and the theory of active Brownian motion. The study yields a method for engineering complex anisotropic motilities with potential applications in microswimmer navigation and provides a theoretical framework for self-propelled particles in anisotropic environments. While many experiments on active particles are performed with a Newtonian background fluid, in many in-vivo situations, microorganisms move through more complex environments. To account for this, we create a theoretical framework for ABPs in a viscoelastic environment. We use time-dependent friction kernels to represent the delayed response of the medium and find a memory-induced delay between the effective self-propulsion force and particle orientation. Similar memory effects occur for self-propelled objects large enough to exhibit inertial effects. We explicitly discuss time-dependent mass and moment of inertia and propose specific equations of motion depending on the physical origin of the change in inertia. This situation is relevant in various systems, from mini-rockets to dust particles in plasma and walkers with limited activity. We also analyze different mass ejection strategies to maximize the reach of the Langevin rocket, which we define by including orientational fluctuations in the traditional Tsiolkovsky rocket equation. Next, the work examines the combined effect of particle inertia and orientation-dependent motility in a system of active vibrobots on a striated substrate. The results show anisotropic movement at different time scales, explained by an extension of the ABP model

that includes orientation-dependent motility and inertial effects. The model can be applied to n-fold symmetric anisotropy and used to predict the dynamics of active matter in complex environments. The quantitative comparison between experimental data and theoretical predictions relies on the correct determination of input parameters. In a technical study, we discuss several fitting schemes for an ABP's mean-squared displacement with improved parameter estimation.

Whilst the ABP model is arguably the most prominent one, it shares considerable similarities with the mathematically more accessible active Ornstein-Uhlenbeck particle (AOUP) model. We elucidate the similarities and differences by introducing a parental active model (PAM) which accommodates these two paradigms as decedents. Next, we apply the advantageous Ornstein-Uhlenbeck approach to the modeling of inertial self-propelled particles. Thus, we introduce an inertial AOUP model which accounts for both translational and rotational inertia. This new model captures the key features of the established inertial ABP model. The two models generally predict similar dynamics up to moderate moment of inertia.

In the final section of this dissertation, we investigate hydrodynamic flow fields in close proximity to boundaries and the resulting hydrodynamic interaction on both active and passive particles. Our work provides a theoretical framework for understanding the motion of active particles in viscous drops, with or without surfactants. These findings have potential applications in the control of active matter systems and the use of synthetic microswimmers for targeted drug delivery. Moreover, we investigate the Stokes flow between two rigid disks generated by a Stokeslet or rotlet and the consequent effect of the disks on particle mobility. These systems may have potential applications in micromixing and the creation of microparticle-based sensors.

Preface

The content of this dissertation is based on articles that I co-authored, and that have been published in / submitted to peer-reviewed scientific journals. These articles are reproduced in Chapter 3 and are listed in the following (in topical order):

- **P1** A. R. Sprenger, M. A. Fernandez-Rodriguez, L. Alvarez, L. Isa, R. Wittkowski, and H. Löwen, *Active Brownian Motion with Orientation-Dependent Motility: Theory and Experiments*, Langmuir **36**, 7066-7073 (2020).
- **P2** A. R. Sprenger, C. Bair, and H. Löwen, *Active Brownian motion with memory delay induced by a viscoelastic medium*, Phys. Rev. E **105**, 044610 (2022).
- **P3** A. R. Sprenger, S. Jahanshahi, A. V. Ivlev, and H. Löwen, *Time-dependent inertia of self-propelled particles: The Langevin rocket*, Phys. Rev. E **103**, 042601 (2021).
- **P4** A. R. Sprenger, C. Scholz, A. Ldov, R. Wittkowski, and H. Löwen, *Inertial self-propelled particles in anisotropic environments*, (under review) (2022).
- **P5** M. R. Bailey, A. R. Sprenger, F. Grillo, H. Löwenand L. Isa, *Fitting an active Brownian particle's mean-squared displacement with improved parameter estimation*, Phys. Rev. E **106**, L052602 (2022).
- **P6** L. Caprini, A. R. Sprenger, H. Löwen, and R. Wittmann, *The Parental Active Model: a unifying stochastic description of self-propulsion*, J. Chem. Phys. **156**, 071102 (2022).
- **P7** A. R. Sprenger, L. Caprini, H. Löwen, and R. Wittmann, *Dynamics of active particles with translational and rotational inertia*, (under review) (2023).
- **P8** A. R. Sprenger, V. A. Shaik, A. M. Ardekani, M. Lisicki, A. J. T. M. Mathijssen, F. Guzmán-Lastra, H. Löwen, A. M. Menzel, and A. Daddi-Moussa-Ider, *Towards an analytical description of active microswimmers in clean and in surfactant-covered drops*, Eur. Phys. J. E **43**, 58 (2020).
- **P9** A. Daddi-Moussa-Ider, A. R. Sprenger, Y. Amarouchene, T. Salez, C. Schönecker, T. Richter, H. Löwen, and A. M. Menzel, *Axisymmetric Stokes flow due to a point-force singularity acting between two coaxially positioned rigid no-slip disks*, J. Fluid Mech. **904**, A34 (2020).

- **P10** A. Daddi-Moussa-Ider, A. R. Sprenger, T. Richter, H. Löwen, and A. M. Menzel, *Steady azimuthal flow field induced by a rotating sphere near a rigid disk or inside a gap between two coaxially positioned rigid disks*, Phys. Fluids **33**, 082011 (2021).

My contributions to these scientific articles are specified in Chapter 3.

Acknowledgments

I would like to take this opportunity to express my heartfelt gratitude and appreciation to the many individuals who have supported and encouraged me throughout my Ph.D. journey and even before during my time as a Bachelor's and Master's student:

Firstly, I thank my advisor, Prof. Dr. Hartmut Löwen, for his exceptional guidance, encouragement, and support. His passion, creativity, and dedication to physics have been truly inspiring for me. I am grateful for all the experience I gained and all the opportunities that came my way under his mentorship.

My work would not have been possible without the many collaborators who offered valuable insights, discussions, and guidance. I extend my thanks, in particular, to Dr. Lorenzo Caprini, Dr. Abdallah Daddi-Moussa-Ider, Prof. Dr. Lucio Isa, Prof. Dr. Benno Liebchen, Prof. Dr. Andreas Menzel, Dr. Christian Scholz, Prof. Dr. Raphael Wittkowski, and Dr. René Wittmann. I learned a lot from working with you on various physics problems.

Special thanks go to my TP2 mates, including Davide Breoni, Jens Grauer, Jannis Kolker, Paul Monderkamp, and Fabian Schwarzendahl, as well as all the former and current members of the institute. Their camaraderie created a stimulating environment for research to flourish. I enjoyed all the lunch (and extended coffee) breaks, shared evening dinners, and improvised adventures. Next, I offer thanks to Lukas Fischer, who proofread various versions of this dissertation. Claudia and Jo also deserve special recognition for their help at the institute.

Next, I would also like to express my gratitude to the friends I met and kept during my years at Heinrich-Heine University, including Alexandra, Dominik, Jonathan, Lars, Marc, Mu, Sebastian, Shiwi, Tabea, and Thomas. Your friendship and support were invaluable and made my academic journey more fulfilling. In particular, I owe my warmest thanks and gratitude to my close friend, Simon, for our unforgettable library sessions till midnight, chess matches in the afternoon, and all the club-mate breaks – let's praise the sun.

Lastly, I would like to thank my family for their unwavering support and encouragement throughout this journey. Mama, thank you for your love, which I am forever grateful for, and Papa, thank you for your trust and encouragement. Sabrina, I am so glad about our ever-thriving siblingship *big hugs*. To my grandparents, both present and past, thank you for your unconditional love and support.

– My deepest thanks to all of you!

Contents

Chapter 1

Introduction

The natural world is a continuously evolving and dynamic place filled with living organisms going about in a state of constant movement and adaptation to their environment – from the microscopic motion of cells in the human body up to the giant swarming behavior of birds in the sky – understanding the principles that govern these movements has given rise to a most fascinating field of study known as active matter.

Located at the intersection of physics, chemistry, biology, and engineering, the field of active matter offers a vast range of problems to tackle. By delving into questions such as how animals like birds or fish move together in swarms, what interaction rules drive penguins to organize in huddles, or how bacteria navigate towards nutrients, we can gain insights into the remarkable strategies living matter have developed to optimize evolutionary benefit.

As a theoretical field, active matter research makes for a rewarding experience as models and theories find applications in a wide range of systems. Moreover, the autonomous navigation of living organisms has inspired the engineering of artificial active swimmers. These micro-sized particles can convert the energy from their environment to self-propel in fluids at short-length scales, thus holding promising applications in health care to perform medical drug delivery.

From a physical standpoint, moving objects at this length scale face various problems starting with fluctuations due to the many collisions with fluid molecules or how to overcome the viscous nature of microscopic hydrodynamics. To accurately describe the stochastic active motion of these particles, theoretical descriptions often rely on a mixed approach of non-equilibrium statistical physics and hydrodynamic field theories.

In this dissertation, we seek to contribute to the growing field of active matter by exploring the influence of the particle's inertia, an anisotropic or viscoelastic environment, and possible geometric confinement on the dynamics of a single active particle. By developing theoretical models and analyzing experimental data, we aim to deepen our understanding at a single-particle level and build a physical intuition for their dynamics. The description of more complicated many-particle systems can build upon our work in the future.

This dissertation is written as a cumulative thesis that theoretically examines active matter physics and covers a wide range of topics. The content of this thesis is organized in the following way. Chapter 2 provides an exposition of various modeling approaches in active matter, highlighting the contextual links between the various publications constituting this dissertation. This chapter begins by discussing different statistical descriptions of self-propelled particles, with the active Brownian particle (ABP) model being the most prominent example. Standard analytical methods for studying stochastic dynamics are introduced, along with a brief discussion of the properties of the ABP. Generalizations of this model and the phenomenology in many-particle systems of active particles are also presented. Additionally, the active Ornstein-Uhlenbeck particle (AOUP) model is introduced and compared to the ABP model. The second part of Chapter 2 starts discussing classical hydrodynamic descriptions and low Reynolds number hydrodynamics, with a focus on how to describe flow near boundaries. Next, a simplified description of a self-propelled microswimmer in an unbounded bulk fluid is introduced in terms of a superposition of Stokes singularities. The use of Faxén's law to determine hydrodynamic interactions with boundaries and other microswimmers is also explained. Chapter 3 lists the scientific publications, with the first five focused on the ABP model, and the sixth and seventh on the AOUP model (and its relation to the ABP model), while the last three explore hydrodynamics near boundaries. Finally, Chapter 4 provides a conclusion and outlook for the thesis.

Chapter 2

Exposition: Theoretical Models of Active Matter

This chapter aims to glue the individual contributions of this thesis together. The field of active matter spans across a vast array of systems [1–3]. One usually distinguishes between dry and wet active matter based on whether the system conserves or dissipates momentum. In that sense, we categorize the contributions of this thesis. The first seven publications use dry stochastic approaches, while the last three employ wet hydrodynamic descriptions.

Dry models consist of equations of motion only for the particles, without explicitly including the liquid solvent [4, 5]. Thus, they are naturally used to describe active systems such as granular particles on vibrating plates [6, 7], robots [8], insects like ants [9], locusts [10] and beetles [11] or various animals [12–15].

In contrast, wet models allow for the study of the interaction between microswimmers and the surrounding solvent, as well as the cross interactions among different microswimmers and confining boundaries [16–19]. Examples include microswimmers such as synthetic active colloids [20–24], droplet swimmers [25–27], and biological microorganisms like bacteria [28, 29], algae [30], or sperm cells [31]. Generally, wet models are more difficult to study. Therefore, dry models are also commonly used as simplified descriptions of active matter systems that involve a solvent, where the solvent is only effectively represented and acts as a thermal bath that induces fluctuations in the equations of motion of individual particles.

In Sec. 2.1 we will discuss concepts of dry active matter. Starting by giving a brief outline of the historical development of the first statistical theories in soft condensed matter up to contemporary models in active matter. We then introduce two commonly used paradigm in active matter: the active Brownian particle model (ABP) and the Ornstein-Uhlenbeck particle model (AOUP). Further, we comment on their single particle statistics and collective phenomena.

In Sec. 2.2. we introduce a general framework for describing hydrodynamic flow fields, with an emphasis on the flow patterns of motile swimming particles including puller, pusher and squirmer-type microswimmer. Additionally, we will discuss hydrodynamic interactions induced by boundaries as well as other particles.

2.1 Statistical description of active particles

The origins of stochastic models can be traced back to Einstein's pioneering work on Brownian motion in 1905 [32, 33], which refers to the erratic movement of small pollen grains in a water solution [34, 35]. Einstein's approach in terms of positional probability distributions was soon followed by similar works by Smoluchowski [36,37], Fokker [38, 39], and Planck [40]. Langevin then formulated the first stochastic equation based on Newton's second law, which recovered Einstein's result [41]. Since then, Brownian motion and stochastic concepts have played a significant role in soft matter physics due to their sensitivity to thermal fluctuations.

When botanist Brown first observed the erratic motion of small pollen grains in a liquid, his initial impression was that they were living entities. It is noteworthy that as early as 1913, Przibram highlighted this natural intuition and proposed that the mathematical description of Brownian motion could be indeed used to explain the erratic motion of self-propelled living organisms [42, 43]. However, he noted that the diffusion for microorganisms is generally much larger than that set by the thermal temperature. Subsequently, Fürth demonstrated that persistent random walks provide a better description for self-propelled particles [44]. Interestingly, his theoretical results were formally equivalent to the considerations made by Ornstein and Uhlenbeck, who studied inertial passive Brownian particles [45, 46].

Next, the run-and-tumble particle was a pioneering concept that since then has been studied extensively. It refers to the motion of an organism, such as the E. coli bacterium, that moves in a straight line for a period of time, and then changes direction by tumbling. In 1972, his type of motion was first reported by Berg and Brown [47]. They found that E. coli tunes its tumbling rate in response to nutrient concentration to migrate to favorable regions. This phenomenon is known as chemotaxis, and many mathematical models have been developed to describe the run-and-tumble motion of particles [48–53].

The birth of active matter can be attributed to the groundbreaking works by Vicsek and Tonner and Tu in 1995 [54–56]. These physicists studied the collective motion of self-propelled particles and developed a simple understanding of the seemingly complicated behavior of active entities by assuming some sort of local interaction. These models showed non-trivial self-organization leading to complex global behavior fundamentally different from equilibrium model approaches. In the last 20 years, active matter physics has undergone rapid development and become a booming discipline.

After the turn of the 21st century, there was a growing interest in manufacturing artificial active swimmers. This interest was motivated by microorganisms' ability to autonomously navigate complex environments. Various methods for designing artificial microswimmers have been developed, such as autochemotactic Janus particles, which feature two differently coated hemispheres, and can swim in self-produced phoretic gradients of electrophoretic, thermophoretic, or diffusiophoretic origin [57, 58]. Other methods include propulsion through ultrasound [59, 60], quincke rollers [61–63], active droplets [25–27], or actuation via magnetic or electric fields [64,65]. In contrast to run-and-tumble particles, these active colloids randomize their orientation continuously due to rotational diffusion. From the theoretical side, these experimental advances were answered by an intuitive model coupling active propulsion with rotational diffusivity – namely the Active Brownian particle model.

2.1.1 Active Brownian particle model

Although theoretical models of persistent random walks have been around since the early 20th century, the notion of an active Brownian particle (ABP) emerged with the manufacturing of artificial microswimmers. One of the first experimental realizations of an artificial microswimmer was reported by Paxton et al. who observed the autonomous motion of platinum-gold nanorods [66]. Later, Howse et al. studied self-motile Janus spheres which move by a process of self-diffusiophoresis [67]. They were also one of the first to give analytic expressions for the mean-square displacement of an ABP. Soon after the model was generalized to account for an effective torque acting on the particle thereby presenting the first Langevin equations for a Brownian circle swimmer [68]. Later, a rigorous analysis of the stochastic dynamics of a single ABP was given by ten Hagen and coworkers [69, 70]. With the success of describing non-equilibrium phenomena like motility-induced phase separation [71–74], the ABP model is nowadays an established framework to study self-propelled particles. To elucidate its fundamental properties, we shall now introduce the model in its most rudimentary form.

Fitting the scope of this thesis, we consider only a single particle at the position $\mathbf{r}(t)$ and propelling with constant speed v_0 along the body-fixed orientation $\hat{\mathbf{n}}(t)$. We consider the dynamics in two dimensions, thus, the orientation can analogously be described by the angle $\phi(t)$ between the x-axis and the orientation $\hat{\mathbf{n}}(t) = (\cos\phi(t), \sin\phi(t))^T$. In addition, to its activity, there is translational $\boldsymbol{\xi}(t)$ and rotational noise $\eta(t)$ with respective diffusivity D_t and D_r. The noise is specified as zero-mean unit-variance white noise, i.e., $\langle\boldsymbol{\xi}(t)\rangle = \mathbf{0}$, $\langle\eta(t)\rangle = 0$ and $\langle\xi_i(t)\xi_j(t')\rangle = \delta_{ij}\,\delta(t-t')$, $\langle\eta(t)\eta(t')\rangle = \delta(t-t')$. Accounting for previous considerations the overdamped dynamics are given by the following coupled Langevin equations

$$\dot{\mathbf{r}}(t) = v_0\hat{\mathbf{n}}(t) + \sqrt{2D_t}\boldsymbol{\xi}(t), \tag{2.1a}$$

$$\dot{\phi}(t) = \sqrt{2D_r}\eta(t). \tag{2.1b}$$

Here, we assumed that the particle's motion is overdamped, i.e., the inertia of the particle is negligible. In this form, the ABP model is often used to describe the stochastic motion of artificial and living microswimmers. Although the description does not include the dynamics in the surrounding fluid, the fluid is effectively represented in the dissipation and fluctuations. In that case, a fluctuation-dissipation relation is often assumed which is also reflected in the Einstein–Smoluchowski relation $D_t = k_B T/\gamma_t$ (analogously $D_r = k_B T/\gamma_r$), which relates the translational diffusivity D_t (or rotational diffusivity D_r) with the thermal energy of the fluid $k_B T$ and the translational frictions coefficient γ_t (or rotational friction coefficient γ_r) [75, 76]. Further, in the ABP model, the origin of the motility is not specified, rather effective forces and torques are used to model the self-propulsion of microswimmers (thus, not in contradiction to the fact that a swimmer at low-Reynolds number is force-free and torque-free [77]). We note that Eqs. (2.1) only describe the dynamics of an active particle in the most basic form. Generalizations will be discussed in Chapter **2.1.3**.

In contrast to deterministic differential equations that always have a unique solution for a given initial condition, the stochastic differential Eqs. (2.1) does not produce repeatable solutions. Instead, each solution represents a realization of a random trajectory, and the ensemble behavior of numerous sample paths becomes a significant deterministic characteristic. Therefore, one usually characterizes the stochastic nature of self-propelled particles in terms of correlation functions and low-order moments for the displacement. Analogously to Eqs. (2.1), the dynamics can also be described in terms of a probability density function $\mathrm{P}(\mathbf{r}, \phi, t)$, which gives the probability, at time t, of finding a particle at position $\mathbf{r}$ and with orientation ϕ. This probability distribution obeys the following Fokker-Planck equation

$$\partial_t \mathrm{P}(\mathbf{r}, \phi, t) = \boldsymbol{\nabla} \cdot \left(D_t \boldsymbol{\nabla} - v_0 \hat{\mathbf{n}}\right) \mathrm{P}(\mathbf{r}, \phi, t) + D_r \partial_\phi^2 \mathrm{P}(\mathbf{r}, \phi, t). \tag{2.2}$$

The stochastic description via the Langevin equations (2.1) and the Fokker-Planck equation (2.2) is formally equivalent [76, 78]. However, the Langevin approach is often preferred since it is analytically more accessible when compared to the Fokker-Planck approach. As a result, stochastic analysis is usually limited to investigating the noise-averaged trajectory and mean-square displacement, which still offer valuable insight into stochastic motion and can be measured in experiments. On the other hand, the Fokker-Planck equation is commonly used as a starting point for simplified field theories [79, 80].

Next, we will first discuss the single-particle statistics of active Brownian particles followed up by a brief review of collective phenomena and their theoretical description.

Single particle statistics

In the absence of fluctuations ($D_t = D_r = 0$), the particle moves on trivial linear trajectories $\mathbf{r}(t) = \mathbf{r}(0) + v_0 t\, \hat{\mathbf{n}}(0)$. However, when noise is present, the trajectory of an ABP goes through a period of directed motion before the self-propulsion direction becomes randomized due to rotational diffusion. This decorrelation is characterized by the exponential decay of the orientational correlation function

$$\langle \hat{\mathbf{n}}(t) \cdot \hat{\mathbf{n}}(0) \rangle = e^{-D_r t}, \tag{2.3}$$

from which the persistence time of an active particle is deduced

$$\tau_p = \int_0^\infty \langle \hat{\mathbf{n}}(t) \cdot \hat{\mathbf{n}}(0) \rangle \, dt = \frac{1}{D_r}, \tag{2.4}$$

which represents the average time that an ABP retains its orientation.

Next, we discuss the positional correlation functions – the mean and mean square displacement. The time-averaged mean displacement vanishes due to uniformity in all orientations. To get a meaningful result, we consider the conditional mean displacement for a given initial orientation $\hat{\mathbf{n}}(0)$,

$$\langle \mathbf{r}(t) - \mathbf{r}(0) \rangle = \frac{v_0}{D_r}\left(1 - e^{-D_r t}\right)\hat{\mathbf{n}}(0). \tag{2.5}$$

For short times, the particle moves ballistic in time with $\langle \mathbf{r}(t) - \mathbf{r}(0) \rangle = v_0 t \, \hat{\mathbf{n}}(0) + \mathcal{O}\left(t^2\right)$, while over intermediate times, the orientation of the particle begins to decorrelate and then eventually the mean displacement saturates to the persistence length

$$\mathbf{L}_p = \lim_{t \to \infty} \langle \mathbf{r}(t) - \mathbf{r}(0) \rangle = \frac{v_0}{D_r}\hat{\mathbf{n}}(0), \tag{2.6}$$

for long times. The mean-square displacement (MSD) can be expressed as

$$\left\langle \left(\mathbf{r}(t) - \mathbf{r}(0)\right)^2 \right\rangle = 4D_t t + 2\frac{v_0^2}{D_r^2}\left(D_r t - 1 + e^{-D_r t}\right), \tag{2.7}$$

The temporal scaling behavior of the MSD can be studied to classify the dynamics of ABPs into different temporal regimes, $\langle (\mathbf{r}(t) - \mathbf{r}(0))^2 \rangle \propto t^\alpha$, with scaling exponent α. By expanding the analytic result for the mean-square displacement in time, we obtain $\langle (\mathbf{r}(t) - \mathbf{r}(0))^2 \rangle = 4D_t t + v_0^2 t^2 + \mathcal{O}\left(t^3\right)$. Therefore the mean-square displacement starts in a short-time diffusion regime ($\alpha = 1$), increasing linearly in time with the short-time diffusion coefficient $D_S = D_t$. If the deterministic swimming motion dominates translational diffusion, a transition from the short-time diffusive regime to a ballistic regime occurs ($\alpha = 2$). Ultimately, the particle enters a long-time diffusive regime for times greater than the persistence time $\tau_p = 1/D_r$ ($\alpha = 1$). This diffusive regime is characterized by an enhanced long-time diffusion coefficient

$$D_L = \lim_{t \to \infty} \frac{\left\langle \left(\mathbf{r}(t) - \mathbf{r}(0)\right)^2 \right\rangle}{4t} = D_t + \frac{v_0^2}{2D_r}. \tag{2.8}$$

Understanding the averaged dynamics of a single particle provides a useful intuition when studying more complicated systems. In this context, the persistence time τ_p and length $\mathbf{L}_p$ and long-time diffusion coefficient D_L are useful quantities.

In **P1** to **P4**, we will provide analytic expressions for the here-introduced observables for different physical settings. Especially, the MSD is frequently measured in soft matter physics as it characterizes the dynamics of the observed particle as well as the surrounding fluid. In active matter, experimental investigation often involves measuring physical properties such as the self-propulsion velocity or the rotational diffusion coefficient. In **P5**, we compare different fitting methods for extracting these parameters using the theoretical expression for the MSD of an ABP. We also address issues such as heteroscedasticity and the effect of hidden correlations when using overlapping displacements.

Collective phenomena

When many self-propelled particles interact with one another, large-scale patterns and complex dynamics can emerge. Although collective effects exceed the scope of the thesis, we want to briefly touch upon some of the most notable phenomena in active matter. However, it is important to note that we tackle only a fraction of the collective phenomena and instead we refer to Refs. [1–4].

As we already mentioned, one of the first studied collective effects is the formation of swarms or flocks, in which individual particles self-organize to create large-scale structures [54–56, 81]. Another important collective effect in active matter is the emergence of active turbulence, a type of fluid-like motion that arises when the self-propulsion of individual particles creates large-scale flow patterns [82–84].

Collective effects are not limited to biological systems, but can also be observed in synthetic materials, such as colloidal suspensions. In stark contrast to passive colloidal particles, self-propelled particles with purely repulsive interactions can undergo a liquid-gas phase transition known as motility-induced phase separation (MIPS) [71–73, 85]. This clustering occurs because the effective motility of an active particle in a many-body system depends on the local particle density due to steric repulsion, which leads to the accumulation of particles in regions of low motility. This positive feedback loop can cause nucleation when the effective motility decreases as the local density increases. Also, clogging and jamming are common phenomena in active matter with important implications for the transport properties of self-propelled particles [86–89].

When examining suspensions of self-propelled particles, an interesting question naturally arises: Can the principles of equilibrium statistical mechanics be employed to describe the macroscopic characteristics of active matter in terms of thermodynamic properties, such as pressure and temperature? To address this question, researchers have gained a deeper understanding of the departure of active systems from equilibrium by examining the entropy production due to time irreversibility [90–94]. Furthermore, non-equilibrium definitions for effective temperature and pressure have been proposed [95, 96].

2.1.2 Active Ornstein-Uhlenbeck particle model

Recently, a new model called the active Ornstein-Uhlenbeck particles (AOUP) model has been proposed as an alternative to the traditional active Brownian particle (ABP) model [97, 98]. The AOUP model was initially introduced to describe the motion of a passive colloid in a bath formed by active bacteria [99–102]. In the ABP model, the activity term $v_0\hat{\mathbf{n}}(t)$ introduces a non-linear combination of Gaussian variables which leads to non-Gaussian behavior for intermediate times [103]. This non-Gaussian nature of the ABP model generally complicates analytic calculations. To tackle this issue, the AOUP model replaces the non-Gaussian orientation vector $\hat{\mathbf{n}}(t) = (\cos\phi(t), \sin\phi(t))^T$ in the ABP model with an Ornstein-Uhlenbeck process $\mathbf{n}(t)$, while ensuring that the steady-state temporal correlations of both models are equal. The corresponding equations of motion can be written in the following way

$$\dot{\mathbf{r}}(t) = v_0\mathbf{n}(t) + \sqrt{2D_t}\,\boldsymbol{\xi}(t), \tag{2.9a}$$

$$\dot{\mathbf{n}}(t) = -\frac{\mathbf{n}(t)}{\tau} + \frac{1}{\sqrt{\tau}}\boldsymbol{\chi}(t). \tag{2.9b}$$

The equations of motion for the AOUP model involve zero-mean unit-variance white noise $\boldsymbol{\chi}(t)$ and the persistence time τ. The ABP and AOUP models share the same autocorrelation function for the self-propulsion vector $\langle \mathbf{n}(t)\cdot\mathbf{n}(0)\rangle = e^{-t/\tau}$, when implying that $\tau = 1/D_r$ (compare with Eq. (2.3)). The AOUP model provides a great starting point for analytic studies [104–108]. We remark, that usually the AOUP model is introduced in terms of an equation for the self-propulsion $\mathbf{u}(t) = v_0\mathbf{n}(t)$ (or effective force $\mathbf{f}_a(t) = v_0\gamma_t\mathbf{n}(t)$) with $\tau\dot{\mathbf{u}}(t) = -\mathbf{u}(t) + \sqrt{2D_a}\boldsymbol{\chi}(t)$, where the active diffusivity D_a serves as an additional free parameter connecting the AOUP to the ABP model via the mapping $2D_a/\tau = v_0$.

With this mapping, the AOUP model can correctly reproduce the single-particle statics of ABPs up to the mean-square displacement (Eqs. (2.3)-(2.8)). Moreso, AOUPs shows similar accumulation behavior near walls and obstacle [109, 110], the famous motility-induced clustering [111, 112], spontaneous velocity alignment in MIPS [113, 114] and active glassy dynamics [115, 116].

Per definition, the ABP and AOUP models differ in their descriptions of self-propulsion. In ABPs, the direction is described by a steady-state distribution with a uniformly distributed orientational angle and a fixed modulus. In contrast, in AOUPs, the distribution is a two-dimensional Gaussian, with each component fluctuating around a vanishing mean value with unitary variance. This fundamental difference is why AOUPs fail to reproduce the bimodal spatial distribution in a harmonic potential [97, 117].

In **P6**, we define the parental active model (PAM) which allows for a more general distribution of the fluctuating self-propulsion vector $\mathbf{n}$. The distribution is given by $P(\mathbf{n}) \sim \exp\big(-(|\mathbf{n}|-\mu)^2/(2\alpha^2(\mu))\big)$, where μ is a single free parameter that determines the most likely value of the modulus $|\mathbf{n}|$, and $\alpha^2(\mu)$ is a quantity that constrains the width of the distribution such that $\langle \mathbf{n}^2 \rangle = 1$. In that way, the PAM includes both ABPs ($\mu = 1$) and AOUPs ($\mu = 0$) as limiting cases while providing a better description for active particles which exhibit natural speed fluctuations.

In **P7**, we introduce a generalized AOUP model that accounts for inertial effects in mesoscopic self-propelled particles [118, 119]. In inertial ABPs, rotational inertia introduces memory into the angular velocity, leading to a double exponential decorrelation in the orientational correlation function [7]. To approximate the non-Gaussian rotational dynamics of inertial ABPs, we replace the white noise term $\boldsymbol{\chi}(t)$ with another Ornstein-Uhlenbeck process. Consequently, the inertial AOUP model is characterized not only by a typical timescale τ (which coincides with the persistence time in overdamped systems) but also by an additional timescale and diffusivity. These two free parameters are determined by ensuring that the orientation correlations are normalized $\langle \mathbf{n}^2 \rangle = 1$ and that the inertial AOUP model has the same persistence time τ_p as the inertial ABP model. We benchmark the inertial AOUP model against the inertial ABP model and thus provide a Gaussian alternative for future studies on inertial active matter.

2.1.3 Beyond active Brownian motion

The basic ABP model and its alternatives have been successfully generalized to account for various specific particle properties or to include effective interactions with the environment. Hereunder, we shall provide an overview of a few generalizations and outline the contribution of this thesis.

Particle shape and chirality

Additional effective torques and translation-rotation coupling can arise from anisotropy in shape or propulsion mechanism. Wittkowski et al. have provided a rigorous theoretical framework for active Brownian particles with arbitrary shapes [120, 121], and several theoretical studies have inferred their statistical properties [68, 122, 123]. Circle swimmers have been experimentally realized as active L-shaped particles [124, 125], and many motile microorganisms exhibit circular motion near surfaces and substrates [126, 127]. In dense suspensions, collective effects can result in the formation of circling clusters [128, 129]. In macroscopic active chiral fluids, spinners rotating clockwise and anti-clockwise can separate into distinct phases [130], but the addition of active surfactants can prevent this phenomenon [131].

In **P2** and **P3**, we explore how memory - be it caused by its particle inertia or by fluid-viscoelasticity - affects the dynamics of circle swimmers. The ABP model predicts that a combination of circle swimming and rotational noise leads to a spira mirabilis for the mean trajectory. For once, the perfect spira mirabilis gets distorted in the presence of memory. Further, we discuss the non-monotonic behavior long-time diffusion coefficient of circle swimmer as a function of memory. Predicting optimal memory (or more precisely an optimal particle inertia or fluid-viscoelasticity, respectively) for optimal diffusivity.

External potentials

Applying external potentials to active particles, such as simple harmonic traps [117, 132, 133] or complex potential landscapes [134, 135], can result in different statistical behavior. Optical tweezers, acoustic traps, and parabolic dishes are used to apply external potentials to active colloids [136–139]. Numerous theoretical studies have explored the movement of self-propelled particles in external harmonic traps and have revealed that self-propulsion induces greater delocalization within the trap [117, 132, 133]. In addition, active particles can also show non-equilibrium phenomena such as ratchet effects where they exhibit directed motion in the presence of a spatially varying potential, even in the absence of an external driving force [140–142].

In **P6**, we explore the behavior of ABPs and AOUPs in a harmonic potential. Our approach involves developing a unified, parental active model (PAM) that allows for continuous interpolation between the ABP and AOUP models. The key distinction between the two models is the distribution of the self-propulsion velocity modulus, which can range from a Gaussian form (AOUP) to a sharp peak (ABP). Further, we conducted a benchmark study of the stationary distribution in a harmonic potential. Our findings revealed a transition from unimodal to bimodal distributions, which signifies the failure of AOUPs to replicate the behavior of ABPs in the large-persistence regime.

State-dependent motility

A rich phenomenology is found for active particles with state-dependent motility (i.e., dependency on position, orientation, and/or time). The motility of active matter can be tuned externally via several means, such as the variation of illumination, which can increase or decrease the swim velocity leading to complex self-assembly [111, 143–145]. This experimental advance provides intriguing possibilities for active matter research and offers exciting applications, from micro-motors [146, 147] and rectification devices [148, 149] to motility-ratchets [150]. Researchers have also employed spatial motility landscapes to trap Janus particles [151] and investigate polarization patterns induced by motility gradients [152]. Among the most fascinating applications based on light-sensitive active particles is the painting with bacteria, which was experimentally realized by Arlt et al. [28]. Theoretical studies include [153–156]. Further, the basic model of an ABP can be generalized to situations where the self-propulsion velocity is time-dependent, such as in the run-and-tumble motion of many bacteria [157]. State-dependent motilities are relevant steering methods in the context of optimized navigation of active agents [158–162].

In **P1** and **P4**, we study the orientational analog to a position-dependent motility landscape namely an orientation-dependent motility. In **P1**, we implemented a feedback scheme to program the propulsion velocity of magnetic dumbbells as a function of the particles' orientation. While in **P4**, we introduced orientation-dependent motility to macroscopic granular walkers by utilizing an anisotropic substrate. Accompanying, we developed a theoretical framework that explains the dynamic features of the particles moving with arbitrary orientation-dependent motility. Thus, our description can be used for all sorts of different experimental realizations – for example, anisotropic illuminated Janus particles or triangular microparticles in traveling ultrasound [163–165]. Most recently, complicated anisotropic clusters have been formed with particles moving with orientation-dependent motility [166].

Memory effects

Self-propelled or swimming particles often encounter environments that deviate from Newtonian fluids [167–171]. For instance, they may navigate through polymer solutions [172–175], micelles [176,177], crystalline [178,179] or liquid crystalline [180, 181] environments, or even biologically relevant substrates such as the cytoplasm [182–184]. The simplest generalization is introduced for the Maxwell fluid for passive [185,186] and active [187,188] particles. There are several memory effects for active particles in non-Newtonian media: first, the noise which perturbs the swimming motion is temporally correlated, and second dissipation involves non-instantaneous but with time delay. Recently, Narinder et al. proposed a model for self-propelled Janus particles in a viscoelastic fluid [189], which contains an additional torque proportional to the swim force, explaining an increase of rotational diffusion [190] and the onset of circular trajectories [189].

In **P2**, we decouple the swim torque from the swim force, allowing us to solve the stochastic Langevin equations for arbitrary memory delay in an analytical manner. We applied our general results to the Maxwell fluid, which introduces exponentially decaying memory to the standard instantaneous Stokes friction. Our analysis revealed a double-exponential pattern in the orientational correlation function, featuring partial decorrelation in the short term and persistent plateaus in the intermediate term. We also discussed how memory affects the mean and mean-square displacement of the particle at intermediate and long timescales. Finally, we established the memory delay function quantifying the mismatch between the effective self-propulsion force and the particle orientation.

Auto-chemotactic Janus particles [191], swimming oil droplets [192], and crawling microorganisms [193] are also affected by memory effects. As these particles move, they leave diffusing substances in their wake that impact their own dynamics [194]. The diffusing substances exhibit independent dynamics, resulting in interactions that are non-local in time. This gives rise to intriguing collective phenomena such as Keller-Segel clustering, traveling patterns, and more [195–200].

Inertial effects

Even macroscopic active matter that exhibits inertial effects can still suffer from environmental fluctuations [118,119]. Prominent examples include granular particles on vibrating plates [6, 7], robots [8], inertial dust particles in complex plasma [201–205], insects like ants [9], locusts [10], and beetles [11], and various larger animals [13, 15]. On a single particle level, inertial particle show enhanced orientational correlation, non-trivial inertial scaling behavior, and an inertia-induced delay between velocity and orientation [206–208]. Moreover, these theoretical models have been employed to evaluate the effect of inertia on the collective phenomena typical of active matter [209–215], revealing that translational inertia reduces MIPS [216, 217].

In **P3**, we accounted for the case of time-dependent inertia and discussed various specific setups - including a Langevin-rocket model. Describing the dynamic in the case of time-dependent inertia is not a straightforward task as the underlying equations of motion will depend on the precise mechanism behind the change of inertia [218–220]. To do this systematically, we discuss the idealized cases of directed mass ejection, isotropic mass evaporation, and isotropic shape change. For those systems, we compare several dynamic correlation functions for an exponential mass/moment of inertia loss. Further, we provide an adiabatic approximation for the long-time diffusivity in the case of slow temporal variation [221]. For a simplified model of directed mass ejection, which we refer to as the Langevin rocket, we provide analytic results for the mean reach. Interestingly, the optimal strategy of a Langevin rocket for achieving maximal reach undergoes a discontinuous change from a complete, extended mass ejection over time to an instantaneous ejection of a mass fraction as rotational noise increases.

In general, the mass and the moment of inertia have different effects on the dynamics of active particles. For increasing mass, the dynamics of the particle involve stronger delay effects smoothing the trajectory. On the other hand, increasing the moment of inertia leads to more resistance to reorientation and subsequently to higher persistence. In **P4**, we explore the combined effect of orientation-dependent motility and inertia on the dynamics of self-propelled particles. Interestingly, the anisotropy on short, intermediate, and long times is not only set by the anisotropic propulsion but depends on the particle inertia.

In **P7**, we propose an inertial AOUP model that includes both translational and rotational inertia. We validate the inertial AOUP model by comparing the analytic correlations for appropriate parameters to those of the inertial ABP. This Gaussian model of inertial active matter offers a platform for future studies and a potential starting point to understand interactions between inertial self-propelled particles.

2.2 Hydrodynamic description of microswimmer

Microswimmers are able to propel in self-generated flow fields by exerting forces on the surrounding fluid. The flows can be reflected by nearby solid obstacles, boundaries, or other active particles and, in turn, affect the orientation and translation of the microswimmer itself. In this section, we will introduce a general framework for describing hydrodynamic flow fields, with an emphasis on the flow patterns of motile swimming particles. Additionally, we will discuss hydrodynamic interactions induced by both boundaries and other particles.

2.2.1 Hydrodynamics

The Navier-Stokes equation together with the continuity equation provides a classical continuum theory describing the motion of fluids [222]. Euler initially presented the continuity equation in 1757 [223], and the Navier-Stokes equation was first proposed by Navier in 1822 [224], and later refined by Stokes in 1845 [225]. We describe the dynamical state of the fluid in terms of fields, namely the density field $\rho(\mathbf{r}, t)$ and flow field $\mathbf{v}(\mathbf{r}, t)$. Note, we now employ an Eulerian point of view, i.e., the position vector $\mathbf{r}$ is now a variable of the field and not the location of a particle. The Navier-Stokes equation reads as

$$\rho(\mathbf{r}, t)\Big(\partial_t \mathbf{v}(\mathbf{r}, t) + \mathbf{v}(\mathbf{r}, t) \cdot \boldsymbol{\nabla}\mathbf{v}(\mathbf{r}, t)\Big) = \boldsymbol{\nabla} \cdot \underline{\boldsymbol{\sigma}}(\mathbf{r}, t) + \mathbf{f}_b(\mathbf{r}, t), \tag{2.10}$$

The left hand side denotes the change of momentum per volume $\rho\,\mathrm{D}\mathbf{v}/\mathrm{D}t$, where $\mathrm{D}/\mathrm{D}t = \partial_t + \mathbf{v} \cdot \boldsymbol{\nabla}$ denotes the material derivative which guarantees that we correctly consider the temporal change in the velocity of the fluid element (at position $\mathbf{r}$) in analogy to Newton's law for a single particle. The right hand side gives the sum of the bulk force density $\mathbf{f}_b$ and surface force density $\mathbf{f}_s = \hat{\mathbf{n}} \cdot \underline{\boldsymbol{\sigma}}$, where the latter is expressed in terms of the stress tensor

$$\underline{\boldsymbol{\sigma}}(\mathbf{r}, t) = -p(\mathbf{r}, t)\,\underline{\mathbb{I}} + \underline{\boldsymbol{\sigma}}'(\mathbf{r}, t). \tag{2.11}$$

The first term in Eq. (2.11), is given by the local pressure field $p(\mathbf{r}, t)$ describing acceleration of fluid elements in pressure gradients from areas of high pressure towards areas of low pressure. The second term involves the viscous stress tensor

$$\underline{\boldsymbol{\sigma}}'(\mathbf{r}, t) = \eta\bigg(\boldsymbol{\nabla}\mathbf{v}(\mathbf{r}, t) + \big(\boldsymbol{\nabla}\mathbf{v}(\mathbf{r}, t)\big)^T - \frac{2}{3}\boldsymbol{\nabla} \cdot \mathbf{v}(\mathbf{r}, t)\,\underline{\mathbb{I}}\bigg) + \zeta\boldsymbol{\nabla} \cdot \mathbf{v}(\mathbf{r}, t)\,\underline{\mathbb{I}}, \tag{2.12}$$

which describes frictional forces due to internal shearing and compression. These contribution depend on the specific fluid under study and are characterized in terms of the shear viscosity η and the compressive viscosity ζ. Following from the conservation of mass, the continuity equation governs the temporal change of the density field

$$\partial_t \rho(\mathbf{r}, t) + \nabla \cdot (\rho(\mathbf{r}, t)\, \mathbf{v}(\mathbf{r}, t)) = 0. \tag{2.13}$$

To solve for the flow and density field for a given bulk force density, an additional equation is necessary to close our system of equations and specify the pressure field. Depending on the specific fluid under observation additional laws can be applied. Common examples involve the equation of state for an ideal gas or the Bernoulli equation for ideal and incompressible fluids [222].

A frequently used approximation assumes incompressibility for the fluids (meaning $\rho = \text{const}$). From Eq. (2.13) follows in that case, that the flow field is source free and the Navier-Stokes equation for incompressible fluids reads as

$$\rho \Big(\partial_t \mathbf{v}(\mathbf{r}, t) + \mathbf{v}(\mathbf{r}, t) \cdot \boldsymbol{\nabla} \mathbf{v}(\mathbf{r}, t) \Big) = -\boldsymbol{\nabla} p(\mathbf{r}, t) + \eta \triangle \mathbf{v}(\mathbf{r}, t) + \mathbf{f}_b(\mathbf{r}, t), \tag{2.14a}$$

$$\boldsymbol{\nabla} \cdot \mathbf{v}(\mathbf{r}, t) = 0 \tag{2.14b}$$

Note that the pressure is not an independent field for incompressible fluids. It must guarantee that $\boldsymbol{\nabla} \cdot \mathbf{v}$ holds at all time.

Interestingly, the whole dynamics of incompressible fluids only depend on a single dimensionless number, namely the Reynolds number [226]

$$\mathrm{Re} = \frac{LV\rho}{\eta}, \tag{2.15}$$

where L is the typical length scale and V typical speed of the system. For $\mathrm{Re} \gg 1$, the momentum part (l.h.s. of Eq. (2.14a)) dominates the viscous part ($\eta \triangle \mathbf{v}$) and turbulence may arise. In that case analytic solutions are hard to derive due to the non-linear character of the equations of motion. For $\mathrm{Re} \ll 1$, the viscous part dominates the momentum one. This case is particular relevant for active matter since lots of microorganism operate at small enough length and velocity scales and thus produce flows of small Reynolds number.

Low Reynolds number Hydrodynamics

At the short length and velocity scales of propelling microorganisms, the generated fluid flow field is mainly dominated by viscous dissipation ($\mathrm{Re} \ll 1$). In that case the Navier-Stokes equation for incompressible fluids simplifies to the Stokes equation

$$-\boldsymbol{\nabla} p(\mathbf{r}) + \eta \triangle \mathbf{v}(\mathbf{r}) + \mathbf{f}_b(\mathbf{r}) = \mathbf{0}, \tag{2.16a}$$

$$\boldsymbol{\nabla} \cdot \mathbf{v}(\mathbf{r}) = 0. \tag{2.16b}$$

Stokes flows evolve instantaneous and are fully reversible. There are no time-delay effects and the flow is solely due to momentary pressure gradients and bulk force densities. When one reverses $p(t)$ and $\mathbf{f}(t)$ in time the flow reverses accordingly in time. Further Eq. (2.16a) describes a linear differential equation and a fundamental solution in terms of a Green's function can be derived as

$$\mathbf{v}(\mathbf{r}) = \int_{\mathbb{R}^3} \underline{\mathbf{G}}(\mathbf{r}-\mathbf{r}') \cdot \mathbf{f}_b(\mathbf{r}')\, d^3r' \tag{2.17}$$

with the Oseen tensor [227]

$$\underline{\mathbf{G}}(\mathbf{r}) = \frac{1}{8\pi\eta r}\Big(\underline{\mathbb{I}} + \hat{\mathbf{r}}\hat{\mathbf{r}}\Big). \tag{2.18}$$

It's worth noting that the pressure field does not factor into the ultimate solution for the velocity field. Rather, it is the pressure that guarantees that $\boldsymbol{\nabla}\cdot\mathbf{v} = 0$ to begin with. If there were a net inflow of fluid into a volume element, it would violate $\boldsymbol{\nabla}\cdot\mathbf{v} = 0$. Nevertheless, the pressure would increase locally and counterbalance the net inflow (in the case of an incompressible fluid, this happens instantaneously). The pressure field is given as

$$p(\mathbf{r}) = \int_{\mathbb{R}^3} \boldsymbol{\Phi}(\mathbf{r}-\mathbf{r}') \cdot \mathbf{f}_b(\mathbf{r}')\, d^3r'. \tag{2.19}$$

with the respective Green's function

$$\boldsymbol{\Phi}(\mathbf{r}) = \frac{\mathbf{r}}{4\pi r^3}. \tag{2.20}$$

Boundary conditions

In the following we comment on the most common types of boundary conditions used to model fluid flow near surfaces and interfaces. Up to now, we only considered the unhindered fluid flow in the bulk without any boundary conditions at walls, obstacles or other objects. However, close to a boundary the confinement affects the flow field as it introduces extra boundary conditions to the solutions of the Stokes equations. The two most common boundary conditions are no-slip and free-slip boundary conditions.

Dirichlet-type no-slip condition assumes that the fluid in contact with the solid boundary is at rest relative to the boundary ∂S, i.e., its velocity is zero,

$$\mathbf{v}(\mathbf{r}, t) = \mathbf{0}, \quad \text{for } \mathbf{r} \in \partial S. \tag{2.21}$$

This condition implies that there is no slip between the fluid and the boundary, and that the fluid velocity smoothly transitions from a non-zero value in the bulk to zero at the boundary. The no-slip condition is often used to model flows over rough surfaces.

In contrast, a free-slip boundary condition assumes that the flow velocity in the normal direction of the boundary is zero, i.e., impermeable boundary and the tangential stress of fluid at the boundary is zero, i.e., no shear force is exerted from the fluid to the boundary

$$\mathbf{v}(\mathbf{r},t)\cdot\hat{\mathbf{s}} = 0, \quad \text{for } \mathbf{r}\in\partial S, \tag{2.22a}$$

$$\big(\underline{\boldsymbol{\sigma}}(\mathbf{r},t)\cdot\hat{\mathbf{s}}\big)\times\hat{\mathbf{s}} = \mathbf{0}, \quad \text{for } \mathbf{r}\in\partial S, \tag{2.22b}$$

with the unit normal vector $\hat{\mathbf{s}}$ of the boundary ∂S at position $\mathbf{r}$. This condition implies that the fluid slips freely over the surface without any frictional drag. The free-slip condition is often used to model flows over smooth surfaces or liquid-air interfaces.

Other types of boundary conditions may be used depending on the specific problem being studied including inlet/outlet boundary condition, constant pressure boundary condition, slip boundary condition (introducing a slip length L_s), symmetric, and periodic boundary conditions [228]. In the context of this thesis we want to highlight the surface tension boundary condition used to model surfactants at an interface. The presence of surfactants can affect the surface tension of the fluid interface. This effect can be modeled using a surface tension boundary condition that depends on the concentration of the surfactant at the interface [229–231].

There are several analytic and numerical methods that can be used to solve hydrodynamic problems with boundary conditions. For specific geometries, analytic solutions can be found using integral-transformations, perturbation approaches and the method of images [232]. Solutions for fluid flows near various types of geometries can be found in Ref. [233]. As an example, similar to electrostatic boundary value problems, the methods of images can be used to satisfy free-slip conditions at an infinite flat wall. For an infinite flat no-slip wall the solution is more complicated and the corresponding Green's function is given in terms of the Blake tensor [234].

In **P8**, we derive the Stokes flow for a point force and dipole singularities within a spherical drop, with both clean and surfactant-covered surfaces. Our derivation is similar to the method initially introduced by Fuentes et al. [235, 236], who derived the solution for a point force acting outside a clean viscous drop. An analogous approaches report the Stokeslet solution outside [237, 238] or inside [239, 240] a spherical elastic object, and outside a surfactant-covered drop [241].

In **P9** and **P10**, we solve for the Stokes flow of an axisymmetric Stokeslet and rotlet singularity between two equal-radius circular disks, respectively. In both cases, we transformed the solution of the flow field into integral equations and used standard numerical approaches to solve them. The approach is similar the approach by Kim who studied the Stokes flow near a single disk [242]. Recently the method has been applied to derive the flow field of a parallel Stokeslet between two coaxially positioned rigid no-slip disk [243].

2.2.2 Self-propelled microswimmer

This section explores various swimming mechanisms used by microswimmers and how to describe the flow fields they produce. Microwsimmer including artificially engineered particles as well as microorganism like Escherichia coli (bacteria) or Chlamydomonas reinhardtii (alga) operate usually under low-Reynolds number conditions. Typical dimensions are $L \sim 10$ μm, $V \sim 10$ μm/s, $\rho \sim 10^3$ kg/m^3 and $\eta \sim 10^{-3}$ Pas which results in a low Reynolds number of $\mathrm{Re} \sim 10^{-4} \ll 1$. When it comes to self-propulsion at low Reynolds numbers, a different swimming mechanism is needed than what we experience with our own swimming. Our inertia-based swimming doesn't work due to the reversibility of the Stokes flow, which means that reciprocal deformations of swimmers won't result in net migration, as the Scallop theorem states [49]. Bacteria solve this problem by using a complicated rotary motor [244], while sperm cells make their reciprocal beating of the flagellum non-reciprocal through elasticity [245]. Similarly, Chlamydomonas can move despite its nearly reciprocal breaststrokes [246]. In contrast, artificial microswimmers either mimic the non-reciprocal shape change of self-propelled microorganisms [247], or swim in self-generated phoretic fields [58]. In the latter case, swimming requires breaking symmetry in the design, which is often accomplished by combining two half-spheres with different physical properties, creating what is known as Janus spheres [57].

In the following, we outline the general procedure of how to hydrodynamically describe a microswimmer. In essence, the specific swimming mechanism is incorporated with appropriate boundary conditions for the flow field over the surface of the swimmer. Living active particles, which swim by changing their shape, are described using sticky boundary conditions (swimmers). Janus particles or ciliated organisms, on the other hand, are well-described using slip velocity boundary conditions tangential to the particle's surface (squirmers). With these boundary conditions, the swimming problem is completely defined and is typically studied in three steps. First, the Stokes equation with boundary conditions is solved to obtain the flow field. Second, the total force $\mathbf{F} = \int_S \underline{\boldsymbol{\sigma}}(\mathbf{r}, t) \cdot \hat{\mathbf{n}}\, dS$ and total torque $\mathbf{T} = \int_S \mathbf{r} \times (\underline{\boldsymbol{\sigma}}(\mathbf{r}, t) \cdot \hat{\mathbf{n}})\, dS$ acting on the microswimmer are calculated, where S and $\mathrm{d}S$ denote the surface of the microswimmer and a differential element of it, respectively. Finally, employing the force-free condition ($\mathbf{F} = 0$ and $\mathbf{T} = 0$), the translational self-propulsion velocity $\mathbf{v}_0$ and angular velocity $\boldsymbol{\omega}_0$ can be determined. We would like to mention two minimal microswimmer models for the swimmer case [248] and the squirmer case [249, 250].

The detailed description of the hydrodynamic interactions of microswimmers has the disadvantage of being too complicated for analytic treatment and numerically costly. To simplify matters, a common approach is to perform a multipole expansion of the swimmer's velocity field. Such an approach allows for the creation of theoretical models of microswimmers that can reproduce certain physical features in a simplified but analytically tractable way. Each term in the multipole expansion can be associated with a physical property of the swimmer. It should be noted that a multipole description has its limitations and falls short in the near vicinity of boundaries or other particles. The agents are effectively treated as point-like unless steric or other interactions are included. In the following section, we will introduce the multipole description of a microswimmer.

Multipole representation of a mircoswimmer

In the following, we will describe the state of the microswimmer by its position vector $\mathbf{r}_0$ and orientation $\hat{\mathbf{n}}_0$. Analogously, we denote the self-propulsion velocity as $\mathbf{v}_0$ and the angular velocity as $\boldsymbol{\omega}_0$. Every bulk flow field generated by a uniaxial microswimmer can be expanded as [16, 251],

$$\mathbf{v}_b(\mathbf{r}) = \mathbf{v}_{\mathrm{FD}}(\mathbf{r}) + \mathbf{v}_{\mathrm{SD}}(\mathbf{r}) + \mathbf{v}_{\mathrm{FQ}}(\mathbf{r}) + \mathbf{v}_{\mathrm{RD}}(\mathbf{r}) + \mathcal{O}\big(|\mathbf{r}-\mathbf{r}_0|^{-4}\big), \tag{2.23}$$

where the terms correspond to contributions of a force dipole $\mathbf{v}_{\mathrm{FD}}(\mathbf{r})$, source dipole $\mathbf{v}_{\mathrm{SD}}(\mathbf{r})$, force quadrupole $\mathbf{v}_{\mathrm{FQ}}(\mathbf{r})$, and rotlet dipole $\mathbf{v}_{\mathrm{RD}}(\mathbf{r})$. Next, we will systematically discuss these terms step by step.

For a general bulk force density $\mathbf{f}_b(\mathbf{r})$, the first contribution is given by the so called 'Stokeslet' which is defined as a single point force of stength f at position $\mathbf{r}_0$ oriented along $\hat{\mathbf{n}}_0$, i.e., $\mathbf{f}_b(\mathbf{r}) = f\hat{\mathbf{n}}_0\,\delta\,(\mathbf{r}-\mathbf{r}_0)$, and produces the following flow field

$$\mathbf{v}_{\mathrm{S}}(\mathbf{r}) = \Lambda_{\mathrm{S}}\mathbf{G}_{\mathrm{S}}(\mathbf{r}-\mathbf{r}_0;\hat{\mathbf{n}}_0) \tag{2.24}$$

with $\Lambda_{\mathrm{S}} = f/(8\pi\eta)$ and where we defined the Green's function associated with the $\hat{\mathbf{n}}_0$-directed Stokeslet acting at the position $\mathbf{r}_0$ of an unbounded fluid medium as

$$\mathbf{G}_{\mathrm{S}}(\mathbf{r};\hat{\mathbf{n}}) = \frac{1}{|\mathbf{r}|}\left(\hat{\mathbf{n}} + \frac{(\hat{\mathbf{n}}\cdot\mathbf{r})\mathbf{r}}{|\mathbf{r}|^2}\right). \tag{2.25}$$

However, for microswimmer, this first contribution vanishes $\Lambda_{\mathrm{S}} = 0$ since microswimmer propel under force-free conditions.

The leading-order flow field for microswimmer is generated by the force dipole, which consists out of two opposing $\hat{\mathbf{n}}_0$-directed Stokeslets separated by a distance ℓ along the direction $\hat{\mathbf{n}}_0$ [252, 253],

$$\begin{aligned}\mathbf{v}_{\mathrm{FD}}(\mathbf{r}) &= \frac{f}{8\pi\eta}\Big(\mathbf{G}_{\mathrm{S}}(\mathbf{r}-(\mathbf{r}_0+\ell\hat{\mathbf{n}}_0/2);\hat{\mathbf{n}}_0) - \mathbf{G}_{\mathrm{S}}(\mathbf{r}-(\mathbf{r}_0-\ell\hat{\mathbf{n}}_0/2);\hat{\mathbf{n}}_0)\Big)\\ &\simeq -\Lambda_{\mathrm{FD}}\,\hat{\mathbf{n}}_0\cdot\boldsymbol{\nabla}\mathbf{G}_{\mathrm{S}}(\mathbf{r}-\mathbf{r}_0;\hat{\mathbf{n}}_0),\end{aligned} \tag{2.26}$$

where Eq. (2.26) remains valid for small ℓ and we have introduced the strength of the force dipole $\Lambda_{\mathrm{FD}} = f\ell/(8\pi\eta)$. This allows us to introduce the force-dipolar singularity solution as

$$\mathbf{G}_{\mathrm{FD}}(\mathbf{r};\hat{\mathbf{n}}_1,\hat{\mathbf{n}}_2) = -\hat{\mathbf{n}}_2\cdot\boldsymbol{\nabla}\mathbf{G}_{\mathrm{S}}(\mathbf{r};\hat{\mathbf{n}}_1). \tag{2.27}$$

This flow is generated by two equal and opposite forces that represent balanced propulsion and drag (force-free in total). A "pusher" swimmer has a positive dipole moment ($\Lambda_{\mathrm{FD}} > 0$), with forces pointing away from each other, while a "puller" has a negative dipole moment ($\Lambda_{\mathrm{FD}} < 0$), with forces pointing towards each other. Pushers push liquid forward with their head and backward with their tail, while pullers pull liquid in towards their body with their flagella. This creates an extensile flow for pushers and a contractile flow for pullers. For example, Escherichia coli bacteria generates an extensile flow [254, 255], while Chlamydomonas reinhardtii algae generates on average a contractile flow [256, 257].

Similar relations hold for the higher-order singularities. Neutral swimmers are characterized by a balanced spread of propulsion and drag forces over their surface, resulting in $\Lambda_{\mathrm{FD}} \approx 0$, and a predominantly quadrupolar flow field. Examples of neutral swimmers include ciliated organisms [256] and active droplets [25–27].

In particular, the source dipole flow field describes the far-field hydrodynamics induced by the finite size of the swimmer

$$\mathbf{v}_{\mathrm{SD}}(\mathbf{r}) = \Lambda_{\mathrm{SD}} \mathbf{G}_{\mathrm{SD}}(\mathbf{r} - \mathbf{r}_0; \hat{\mathbf{n}}), \tag{2.28}$$

where the source-dipolar singularity solution can be expressed in terms of the Stokeslet solution via

$$\mathbf{G}_{\mathrm{SD}}(\mathbf{r}; \hat{\mathbf{n}}_1) = -\frac{1}{2} \boldsymbol{\nabla}^2 \mathbf{G}_{\mathrm{S}}(\mathbf{r}; \hat{\mathbf{n}}_1), \tag{2.29}$$

and Λ_{SD} denotes the strength of the source dipole. Ciliated organisms like Volvox carteri, with a slip velocity at their surface, have a positive value ($\Lambda_{\mathrm{FD}} > 0$), while flagellated organisms have a negative value ($\Lambda_{\mathrm{FD}} < 0$) [256].

We can use the force quadrupole to describe the shape-asymmetry of a swimmer

$$\mathbf{v}_{\mathrm{FQ}}(\mathbf{r}) = \Lambda_{\mathrm{FQ}} \mathbf{G}_{\mathrm{FQ}}(\mathbf{r} - \mathbf{r}_0; \hat{\mathbf{n}}, \hat{\mathbf{n}}, \hat{\mathbf{n}}), \tag{2.30}$$

with

$$\mathbf{G}_{\mathrm{FQ}}(\mathbf{r}; \hat{\mathbf{n}}_1, \hat{\mathbf{n}}_2, \hat{\mathbf{n}}_3) = -\hat{\mathbf{n}}_3 \cdot \boldsymbol{\nabla} \mathbf{G}_{\mathrm{FD}}(\mathbf{r}; \hat{\mathbf{n}}_1, \hat{\mathbf{n}}_2) \tag{2.31}$$

A positive force-quadrupolar strength $\Lambda_{\mathrm{FQ}} > 0$ ($\Lambda_{\mathrm{FQ}} < 0$) corresponds to swimmers with long (short) flagella compared to its body size [251].

Additionally, the rotlet-dipolar flow field is given by

$$\mathbf{v}_{\mathrm{RD}}(\mathbf{r}) = \Lambda_{\mathrm{RD}} \mathbf{G}_{\mathrm{RD}}(\hat{\mathbf{n}}, \hat{\mathbf{n}}) \tag{2.32}$$

with the rotlet dipole strength Λ_{RD} and its corresponding singularity solution

$$\mathbf{G}_{\mathrm{RD}}(\mathbf{r}; \hat{\mathbf{n}}_1, \hat{\mathbf{n}}_2) = -\hat{\mathbf{n}}_2 \cdot \boldsymbol{\nabla} \mathbf{G}_{\mathrm{R}}(\mathbf{r}; \hat{\mathbf{n}}_1). \tag{2.33}$$

obtained from the singularity solution of a rotlet$\mathbf{G}_{\mathrm{R}}(\mathbf{r}; \hat{\mathbf{n}}) = \big[\mathbf{G}_{\mathrm{FD}}(\hat{\mathbf{n}}_{\perp\perp}, \hat{\mathbf{n}}_{\perp}) - \mathbf{G}_{\mathrm{FD}}(\hat{\mathbf{n}}_{\perp}, \hat{\mathbf{n}}_{\perp\perp})\big]/2$ with unit vectors $\hat{\mathbf{n}}_{\perp}$ and $\hat{\mathbf{n}}_{\perp\perp}$ obeying $\hat{\mathbf{n}}_{\perp} \times \hat{\mathbf{n}}_{\perp\perp} = \hat{\mathbf{n}}$ [251]. The rotlet dipole can be used to describe the flow field produced by the rotation of the flagellum and counter-rotation of the cell body.

2.2.3 Hydrodynamic interactions

In the following we introduce Faxen's law which we consequently use to determine hydrodynamic interactions with solid objects (boundaries and other particles). First, we consider the fluid flow around a sphere of radius a at position $\mathbf{r}_0$ being dragged with velocity $\mathbf{v}_0$. Assuming stick boundary conditions on the surface of the particle (or equivalently no-slip conditions in the rest frame of the particle) the flow field can be derived as [222],

$$\mathbf{v}(\mathbf{r}) = 6\pi\eta a\Big(1 + \frac{a^2}{6}\boldsymbol{\nabla}^2\Big)\underline{\mathbf{G}}(\mathbf{r} - \mathbf{r}_0) \cdot \mathbf{v}_0. \tag{2.34}$$

Integrating the stress over the surface of the particle gives the Stokes' friction law $\mathbf{F} = 6\pi\eta a\mathbf{v}_0$, relating the force $\mathbf{F}$ needed to drag the particle with the velocity $\mathbf{v}_0$ in terms of the Stokesian friction coefficient $\gamma_t = 6\pi\eta a$. Analogously, the relation between a torque $\mathbf{T}$ needed to rotate a sphere with an angular velocity $\boldsymbol{\omega}_0$ is given as $\mathbf{T} = 8\pi\eta a^3\boldsymbol{\omega}_0$, with the rotational friction coefficient $\gamma_r = 8\pi\eta a^3$. Reversing the point of view, Faxen's first and second law consider the force $\mathbf{F}$ and torque $\mathbf{T}$ exerted by the fluid onto the sphere

$$\mathbf{F} = 6\pi\eta a\left[\Big(1 + \frac{a^2}{6}\boldsymbol{\nabla}^2\Big)\mathbf{v}(\mathbf{r})\Big|_{\mathbf{r}=\mathbf{r}_0} - \mathbf{v}_0\right], \tag{2.35a}$$

$$\mathbf{T} = 8\pi\eta a^3\left[\frac{1}{2}\boldsymbol{\nabla} \times \mathbf{v}(\mathbf{r})\Big|_{\mathbf{r}=\mathbf{r}_0} - \boldsymbol{\omega}_0\right], \tag{2.35b}$$

in the presence of an advective flow field $\mathbf{v}(\mathbf{r})$. In the overdamped limit at low-Reynolds number, it readily follows for the translational $\mathbf{v}_0$ and angular velocity $\boldsymbol{\omega}_0$ of the sphere that

$$\mathbf{v}_0 = \Big(1 + \frac{a^2}{6}\boldsymbol{\nabla}^2\Big)\mathbf{v}(\mathbf{r})\Big|_{\mathbf{r}=\mathbf{r}_0}, \tag{2.36a}$$

$$\boldsymbol{\omega}_0 = \frac{1}{2}\boldsymbol{\nabla} \times \mathbf{v}(\mathbf{r})\Big|_{\mathbf{r}=\mathbf{r}_0}. \tag{2.36b}$$

Particle-boundary interactions

To determine the hydrodynamic interactions between a boundary and both passive or active particles, one first needs to solve the Stokes equations with corresponding boundary conditions.The solution for the fluid flow is then split into two contributions $\mathbf{v}(\mathbf{r}) = \mathbf{v}_b(\mathbf{r}) + \mathbf{v}^*(\mathbf{r})$, wherein $\mathbf{v}_b(\mathbf{r})$ denotes the bulk flow field solution (if boundaries were absent), and $\mathbf{v}^*(\mathbf{r})$ is the image flow field that is required to satisfy the boundary conditions.

The boundary effect on passive particles is usually described in terms of the corrections factor of the hydrodynamic mobility function $\Delta\mu/\mu$ [233, 258, 259].

Hydrodynamic mobility is a measure of how easily a particle or object moves through a fluid under the influence of drag forces $\mathbf{F}_{\text{drag}}$ (and torques $\mathbf{T}_{\text{drag}}$). Specifically, it is defined as the ratio of the velocity $\mathbf{v}_0$ (and rotation $\boldsymbol{\omega}_0$) of the particle to the magnitude of the force acting on it

$$\mu_t \left(1 + \frac{\Delta\mu_t}{\mu_t}\right) \mathbf{F}_{\text{drag}} = \mathbf{v}_0, \tag{2.37a}$$

$$\mu_r \left(1 + \frac{\Delta\mu_r}{\mu_r}\right) \mathbf{T}_{\text{drag}} = \boldsymbol{\omega}_0, \tag{2.37b}$$

where $\mu_t = 1/(6\pi\eta a)$ (and $\mu_r = 1/(8\pi\eta a^3)$) corresponds to the bulk mobility function of a spherical particle of radius a [260]. In the presence of boundary, the leading-order correction to the particle mobility $\Delta\mu$ is obtained by evaluating the image flow field $\mathbf{v}^*(\mathbf{r})$ at the particle position as

$$\Delta\mu_t \, \mathbf{F}_{\text{drag}} = \mathbf{v}^*(\mathbf{r})\Big|_{\mathbf{r}=\mathbf{r}_0}, \tag{2.38a}$$

$$\Delta\mu_r \, \mathbf{T}_{\text{drag}} = \frac{1}{2} \boldsymbol{\nabla} \times \mathbf{v}^*(\mathbf{r})\Big|_{\mathbf{r}=\mathbf{r}_0}. \tag{2.38b}$$

In the case of more than one boundary, the hydrodynamic correction is often approximated by superimposing the effects induced by the individual boundaries [261].

In **P9** and **P10**, we study the hydrodynamic effect of two equal-radius circular disks on a small particle axially moving or rotating between the plates. We derive the correction for the translational and rotational mobility. We further test the superposition approximation using the solution for a single disk against the mobility correction for two disk.

For active particles, Faxen's law (see Eqs. (2.36)) relates the flow field induced by the mirror images of the swimmer to the corresponding corrections to the translational $\mathbf{v}_{\text{HI}}$ and rotational velocity $\boldsymbol{\omega}_{\text{HI}}$,

$$\mathbf{v}_{\text{HI}} = \left(1 + \frac{a^2}{6} \boldsymbol{\nabla}^2\right) \mathbf{v}^*(\mathbf{r})\Big|_{\mathbf{r}=\mathbf{r}_0}, \tag{2.39a}$$

$$\boldsymbol{\omega}_{\text{HI}} = \frac{1}{2} \boldsymbol{\nabla} \times \mathbf{v}^*(\mathbf{r})\Big|_{\mathbf{r}=\mathbf{r}_0}. \tag{2.39b}$$

here $\mathbf{v}^*(\mathbf{r})$ denotes the image flow field to the far-field flow of the microswimmer as specified in Eq. (2.23). Thus the hydrodynamic effect of each multipole contribution can be calculated. By including the boundary-induced corrections in particle-based descriptions like the active Brownian particle model (see Eqs. (2.1)), one can study the dynamics of a microswimmer near boundaries.

For instance, motile microorganisms exhibit circular motion near surfaces and substrates [126, 127, 262–264]. Further, confined microswimmers in a microchannel with two interfaces or immersed in a thin liquid film exhibit a wide range of complex trajectories [265–269]. Microswimmer can be trapped at round obstacles [270,271] or in wedge confinements [265, 272]. Additionally, curved boundaries can significantly affect the stability and topology of active suspensions under confinement [273–277].

In **P8**, the translational and rotational velocities of a microswimmer in a viscous drop were analyzed by developing analytical expressions for the hydrodynamic correction. The analysis included drops with and without homogeneously distributed surfactant on their surface, and was based on a description of the swimmer in terms of a force dipole. Our findings serve as a starting point for an analytical description of active microswimmers in clean and surfactant-covered drops, and our framework can be expanded to include higher multipole terms and study swimmer dynamics inside the drop. This study may prove to be helpful in describing bacteria-driven droplets, which have been realized recently [278, 279].

Particle-particle interactions

In this final section, we will briefly discuss the hydrodynamic interactions among microswimmers. For Stokes flows, hydrodynamic interactions between particles are described in terms of the mobility matrix - a linear relation between the individual forces or torques and the resulting translational or rotational velocities of the particles [280]. Unfortunately, there is no exact analytical solution for this problem when dealing with many interacting suspended particles of finite size. However, several approximation methods have been established for suspensions of both passive and active colloidal particles including the method of reflections or the method of induced force multipoles [280–282]. For dilute suspensions, these approximation methods provide reliable results for the interaction between active particles [252,253]. In denser suspensions, one usually recourses by simulating finite-sized microswimmer [283–286] using squirmer-type swimmer or sorts. Hydrodynamic interactions are essential for understanding the fundamental physics of active matter suspensions as they influence their collective behavior. Further, they play an important role in efficient nutrition and maintaining biofunctionality in active carpets of bacteria or self-propelled colloids [287, 288].

Chapter 3

Scientific publications

In the following, Publications **P1**–**P10** that form the basis of this dissertation are reproduced. For each publication, I present a summary of my contributions and a notice on copyright and licensing.

P1 Active Brownian Motion with Orientation - Dependent Motility: Theory and Experiments

Reproduced from

A. R. Sprenger, M. A. Fernandez-Rodriguez, L. Alvarez,
L. Isa, R. Wittkowski, and H. Löwen,
Active Brownian Motion with Orientation-Dependent Motility: Theory and Experiments,
Langmuir **36**, 7066-7073 (2020),
published by *American Chemical Society* [289].

Digital Object Identifier (DOI): doi.org/10.1021/acs.langmuir.9b03617

Statement of contribution

L.I., R.W., and H.L. planned the research. M.A.F.R. carried out the experiments. A.R.S. analyzed the experimental data. A.R.S. performed the analytic calculations. A.R.S. and L.A. prepared the figures. A.R.S., M.A.F.R., and L.A. wrote the manuscript. All authors discussed and interpreted the results, edited the text, and finalized the manuscript.

Copyright and license notice

©American Chemical Society.
Authors may reuse all or part of the Submitted, Accepted or Published Work in a thesis or dissertation that the author writes and is required to submit to satisfy the criteria of degree-granting institutions. Reprinted with permission from Langmuir **36**, 7066-7073. Copyright 2020 American Chemical Society.

LANGMUIR

pubs.acs.org/Langmuir Article

Active Brownian Motion with Orientation-Dependent Motility: Theory and Experiments

Alexander R. Sprenger, Miguel Angel Fernandez-Rodriguez, Laura Alvarez, Lucio Isa,*
Raphael Wittkowski,* and Hartmut Löwen

Cite This: *Langmuir* 2020, 36, 7066–7073 Read Online

ACCESS | Metrics & More | Article Recommendations | Supporting Information

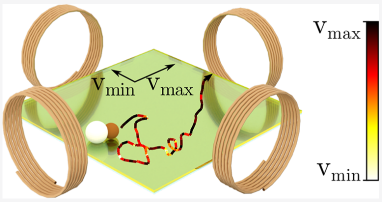

ABSTRACT: Combining experiments on active colloids, whose propulsion velocity can be controlled via a feedback loop, and the theory of active Brownian motion, we explore the dynamics of an overdamped active particle with a motility that depends explicitly on the particle orientation. In this case, the active particle moves faster when oriented along one direction and slower when oriented along another, leading to anisotropic translational dynamics which is coupled to the particle's rotational diffusion. We propose a basic model of active Brownian motion for orientation-dependent motility. On the basis of this model, we obtain analytical results for the mean trajectories, averaged over the Brownian noise for various initial configurations, and for the mean-square displacements including their non-Gaussian behavior. The theoretical results are found to be in good agreement with the experimental data. Orientation-dependent motility is found to induce significant anisotropy in the particle displacement, mean-square displacement, and non-Gaussian parameter even in the long-time limit. Our findings establish a methodology for engineering complex anisotropic motilities of active Brownian particles, with a potential impact in the study of the swimming behavior of microorganisms subjected to anisotropic driving fields.

INTRODUCTION

Active Brownian particles, the synthetic analogues of biological microswimmers such as bacteria and protozoa, have the ability to self-propel at low Reynolds numbers via the conversion of energy available in their surroundings into directed motion by exploiting intrinsic asymmetries in their shape and material properties.[1,2] Their motion arises from the interplay between thermal fluctuations and propulsion, which renders active colloids an excellent model system for studying far-from-equilibrium physical phenomena,[3−5] also featured in their biological counterparts. The basic model for describing the trajectories of a self-propelling colloid, called active Brownian motion, couples a constant velocity v along the particle's asymmetry direction with its rotational diffusivity D_R, which constantly randomizes the propulsion direction with a characteristic time scale $\tau_R = 1/D_R$. In this model, the particle displacements result from propulsion combined with stochastic translational and rotational noise. The propensity for straight paths is defined by the persistence length of the trajectory, $L_P = v/D_R$. To date, various propulsion mechanisms have been realized for active colloids. Among them are self-propulsion induced by chemical reactions,[6−8] illumination,[9−14] or ultrasound[15] and actuation by magnetic[16−19] or electric[20,21] fields. Regardless of the origin of propulsion, the scenario defined by active Brownian motion[1] was verified in experiments for a range of artificial microswimmers.[22−24]

Despite the success of ordinary active Brownian motion, the complexity of some behaviors found in biological and artificial microswimmers implies the urge to extend our experimental and theoretical models, in particular, to include complex spatiotemporal dependencies of propulsion velocity as well as translational and rotational noise. These situations are frequently encountered for systems where the external stimulus governing the motility is inhomogeneous.[25−32] Recently, motility landscapes, where the particle propulsion speed depends on spatial coordinates, time, or a combination of both,[33−36] have been experimentally realized[25,31,37−41] and numerically modeled.[31,42−49] However, with rare recent exceptions aside,[50] the orientational analogue to a position-dependent motility landscape, which is an orientation-dependent motility, remains unexplored for systems of noninteracting anisotropic active particles.

In this article, we experimentally and theoretically study active dumbbells with an orientation-dependent motility. This system offers a basic setup for anisotropic actuation in which the particle's propulsion speed is modulated according to its orientation, which is constantly randomized by rotational

Special Issue: Advances in Active Materials

Received: November 22, 2019
Revised: January 21, 2020
Published: January 24, 2020

Downloaded via DUESSELDORF LIBRARIES on March 9, 2022 at 15:25:30 (UTC).
See https://pubs.acs.org/sharingguidelines for options on how to legitimately share published articles.

diffusion, thus introducing anisotropy into the particle dynamics. In our experiments, we use active dumbbell-shaped colloids composed of a polystyrene and a magnetic silica particle assembled via sequential capillary assembly[51] and self-propelling on a planar substrate via alternating electric fields.[52,53] The particle's position and orientation are tracked in real time and used as the input for a feedback loop that updates the particle velocity with full programmability.[54] These results are used to verify the basic theoretical model for active Brownian motion with an orientation-dependent velocity, which we propose and establish here. We obtain analytical results for mean trajectories averaged over the Brownian noise for various initial configurations and arbitrary angular dependencies of the velocity. We further calculate the corresponding mean-square displacements, including their anisotropic non-Gaussian behavior, and characterize the anisotropy as a function of time. We find that the theoretical calculations are in good agreement with the experimental data. The results of this work shed new light on anisotropically active Brownian particles, inspiring both a better understanding of the behavior exhibited by motile microorganisms when subjected to inhomogeneous or anisotropic driving fields[55] and new design ideas for smarter synthetic microswimmers.

■ MATERIALS AND METHODS

Theoretical Description. In our theoretical model, we consider a single overdamped active Brownian particle in two spatial dimensions. The state of this particle is fully described by the center-of-mass position $\mathbf{r}(t)$ and the angle of orientation $\phi(t)$, which denotes the angle between the orientation vector $\hat{\mathbf{u}} = (\cos\phi, \sin\phi)$ and the positive x axis, at the corresponding time t. The centerpiece of our model is an arbitrary orientation-dependent motility $\mathbf{v}(\phi)$. Without a loss of generality, we represent the propulsion velocity $\mathbf{v}(\phi)$ as a Fourier series

$$\mathbf{v}(\phi) = \overline{v} \sum_{k=-\infty}^{\infty} \mathbf{c}_k \exp(\mathrm{i}k\phi) \tag{1}$$

where $\overline{v}$ denotes a reference velocity, $\mathbf{c}_k$ is the Fourier coefficient vector of mode k, and i denotes the imaginary number. For a given propulsion velocity $\mathbf{v}(\phi)$, these Fourier coefficients can be calculated as $\mathbf{c}_k = \int_{-\pi}^{\pi}(\mathbf{v}(\phi)/(2\pi\overline{v}))\, \exp(-\mathrm{i}k\phi)\, \mathrm{d}\phi$. The overdamped Brownian dynamics of the particle is described by the coupled Langevin equations for orientation-dependent motility

$$\dot{\mathbf{r}}(t) = \mathbf{v}(\phi(t)) + \sqrt{2D_\mathrm{T}}\,\boldsymbol{\xi}(t) \tag{2}$$

$$\dot{\phi}(t) = \sqrt{2D_\mathrm{R}}\,\eta(t) \tag{3}$$

where D_T and D_R are the translational and rotational short-time diffusion coefficients of the particle, respectively. To take translational and rotational diffusion into account, the Langevin equations contain independent Gaussian white noise terms $\boldsymbol{\xi}(t)$ and $\eta(t)$, with zero means, $\langle\boldsymbol{\xi}(t)\rangle = 0$ and $\langle\eta(t)\rangle = 0$, and delta-correlated variances, $\langle\xi_i(t_1)\xi_j(t_2)\rangle = \delta_{ij}\delta(t_1 - t_2)$ and $\langle\eta(t_1)\eta(t_2)\rangle = \delta(t_1 - t_2)$, where $i, j \in \{x, y\}$. The brackets $\langle\cdots\rangle$ denote the noise average, and δ_{ij} is the Kronecker delta.

To keep the model initially as general as possible, we prescribe the self-propulsion by a vector function $\mathbf{v}(\phi)$. Later, we will focus on special motility scenarios and proceed to the less general factorization $v_0(\phi)\,\hat{\mathbf{u}}(\phi)$ that is typically assumed in the literature.[1] The special case of isotropic self-propulsion corresponds to the form $v_0\hat{\mathbf{u}}(\phi)$ with a constant speed v_0. It is associated with the only nonzero Fourier coefficient vectors $\mathbf{c}_1 = (1, -\mathrm{i})/2$ and $\mathbf{c}_{-1} = (1, \mathrm{i})/2$. In the following sections, we neglect mode $k = 0$ in eq 1, which would describe a trivial constant drift.

Fabrication of Active Magnetic Dumbbells. Active magnetic dumbbells composed of a 2.0-μm-diameter polysterene (PS) and a 1.7-μm-diameter magnetic silica (SiO_2-mag) particle (Microparticles GmbH) were fabricated using the sequential capillarity-assisted particle assembly (sCAPA) technique as described in previous work.[51] First, a 40 μL water droplet (Milli-Q) with 0.1 mM sodium dodecyl sulfate (SDS, 99.0%, Sigma-Aldrich), 0.01 wt % of surfactant Triton X-45 (Sigma), and 0.5 wt % PS particles was deposited and dragged at a controlled speed over a polydimethylsiloxane (PDMS) template with rectangular traps of 2.2 μm × 1.1 μm lateral dimensions and 0.5 μm depth, fabricated by conventional photolithography. This deposition step resulted in one PS particle deposited per trap, leaving space for a second particle. The process was then repeated with a dispersion of SiO_2-mag particles. Individual SiO_2-mag particles were deposited inside the traps in close contact with the PS particles forming dumbbells. Next, the dumbbells were sintered in the traps by heating the template to 85 °C for 25 min. Finally, the dumbbells were harvested by freezing a droplet of a 10 μM KCl (Fluka) aqueous solution over the traps and lifting it from the template. The thawed droplet containing the dumbbells was used to fill the experimental cell as described below.

Cell Preparation and Active Motion Control. Transparent electrodes were fabricated from 22 mm × 22 mm glass slides (85−115 μm thick, Menzel Gläser, Germany) coated via e-beam metal evaporation with 3 nm of Cr and 10 nm of Au (Evatec BAK501 LL, Switzerland), followed by a top layer of 10 nm of SiO_2 (STS Multiplex CVD, U.K.) deposited by plasma-enhanced chemical vapor deposition. A 7.4 μL droplet of the dumbbell suspension was placed on the bottom electrode inside a 0.12-mm-thick sealing spacer with a 9 mm circular opening (Grace Bio-Laboratories SecureSeal, U.S.).

After sealing the cell with the top electrode, both electrodes were connected to a signal generator (National Instruments Agilent 3352X, U.S.) to apply an ac electric field with a fixed frequency of 1 kHz and varying peak-to-peak voltage $V_\mathrm{PP}(t)$ of between 1 and 10 V, depending on the dumbbell orientation. The particles are propelled thanks to unbalanced electrohydrodynamic (EHD) flows on each side of the dumbbell, with the SiO_2-mag lobe leading the motion. The propulsion velocity is proportional to V_PP^2.[52,53]

We furthermore imposed a fixed rotational diffusivity $D_\mathrm{R} = 0.25$ rad^2/s for the dumbbells in all experiments, as described in a previous work.[54] In brief, we applied external magnetic fields via two pairs of independent Helmholtz coils to align the magnetic moment of the SiO_2-mag particle. The angle $\phi(t)$ of the applied magnetic field is randomly varied in time according to the relation $\phi(t + \Delta t) = \phi(t) + \sqrt{2D_\mathrm{R}\Delta t}\,\eta(t)$, where in the experiments $\Delta t = 1$ ms and $\eta(t)$ is defined as above.

Imaging and Feedback Loop. The dumbbells were imaged in transmission mode with a home-built bright-field microscope. Image sequences were taken with a sCMOS camera (Andor Zyla) with a 1024 pixels × 1024 pixels field of view and a 50× objective (Thorlabs). The center of mass $\mathbf{r}(t)$ and the angle $\phi(t)$ of the dumbbells with respect to the x axis were tracked in real time using customized software written in Labview and Matlab. The detected orientation of the dumbbell is symmetric with respect to π, being 0 or π when it is perfectly aligned with the x axis. After the experiments, we postprocessed the acquired images to identify both lobes of the dumbbell and convert the angles to the interval from 0 to 2π. The velocity of the dumbbell was varied as a function of its orientation by changing the applied peak-to-peak voltage V_PP according to

$$V_\mathrm{PP}(t) = (V_\mathrm{PP}^\mathrm{max} - V_\mathrm{PP}^\mathrm{min})\sin^2(n\phi(t)) + V_\mathrm{PP}^\mathrm{min} \tag{4}$$

where $V_\mathrm{PP}^\mathrm{max}$ and $V_\mathrm{PP}^\mathrm{min}$ are the maximum and minimum values of the applied peak-to-peak voltage and $n = 1, 2$ is the number of symmetric lobes in $\mathbf{v}(\phi)$. For $n = 1$, the dumbbell velocity is maximal when the particle is aligned with the y axis and minimal when it is aligned with the x axis. In the case of $n = 2$, the dumbbell velocity is maximal for an orientation angle $\pi/4$ and minimal when the particle is aligned with the x or y axis.

There is an inherent delay in capturing an image, extracting the dumbbell angle, and updating the voltage according to it. In our experimental setup, a full cycle takes 400 ms, leading to an update frequency of the particle velocity of 2.5 Hz. This frequency is much lower than the one used to randomize the dumbbell orientation (1

https://dx.doi.org/10.1021/acs.langmuir.9b03617
Langmuir 2020, 36, 7066−7073

kHz) so that there is a clear separation of time scales between the two types of updates, and the dumbbell undergoes standard rotational diffusion at an imposed rate.

■ RESULTS AND DISCUSSION

Orientation-Dependent Motility. Our active colloidal dumbbells are produced by sequential capillary assembly,[51] as represented in Figure 1a in Materials and Methods, and self-

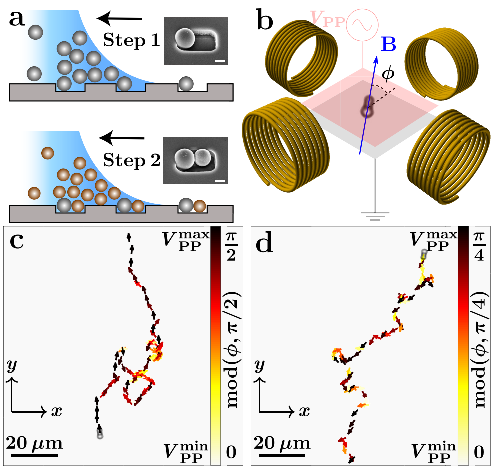

Figure 1. (a) Side-view representation of the sCAPA fabrication of active magnetic dumbbells. The PS particles (gray spheres) are deposited first, followed by the SiO_2-mag particles (brown spheres). The black arrows indicate the deposition direction. The insets show SEM images of the particles in the traps after each deposition step (2 μm scale bar). (b) Scheme of the experimental setup. Four magnetic coils impose a randomly oriented magnetic field **B** (blue arrow) to set the rotational diffusivity of the dumbbells to D_R = 0.25 rad^2/s. An ac electric field applied between two transparent electrodes is used to actuate the dumbbell with velocity $v \propto V_{PP}^2(t)$. A feedback loop updates the applied voltage as a function of the dumbbell orientation angle $\phi(t)$ to achieve an orientation-dependent propulsion velocity. (c, d) Trajectories of active magnetic dumbbells with a motility with 2-fold (c) and 4-fold (d) rotational symmetry. The particle positions at discrete times are represented by arrows indicating the dumbbell orientation and are color coded according to the applied voltage in the range from V_{PP}^{min} to V_{PP}^{max}, which corresponds to $\mathrm{mod}(\phi(t), \pi/2)$ (c) and $\mathrm{mod}(\phi(t), \pi/4)$ (d). See the corresponding Supporting Information Movies.

propel under an ac electric fields thanks to induced-charge electrophoresis.[56−58] The compositional asymmetry of the dumbbell results in local unbalanced EHD flows producing a net force that generates propulsion along the long axis of the dumbbell.[52,53] In order to achieve robust experimental control of orientational dynamics, we decouple it from the thermal bath by randomizing the dumbbell orientation using an external magnetic field (Figure 1b) to set a constant rotational diffusivity of D_R = 0.25 rad^2/s.[54] We furthermore include a feedback loop to update the dumbbell's propulsion velocity according to its orientation, as described in Materials and Methods and sketched in Figure S1 in the Supporting Information, to experimentally realize active Brownian particles with orientation-dependent motility.

In this work, we study two representative orientation-dependent motilities. In the first case, the particle's motility has a 2-fold rotational symmetry, with the lowest velocity occurring when the particle is oriented along the x axis and the highest when it is oriented along the y axis (Figure 1c and Supporting Information Movie 1). We incorporate this motility effectively in leading order as

$$\mathbf{v}_1(\phi) = 2\overline{v}_1 \sin^2 \phi \, \hat{\mathbf{u}}(\phi) \tag{5}$$

where $\overline{v}_1$ denotes the orientationally averaged speed of the particle. In the second case, the velocity has 4-fold symmetry, where the dumbbell achieves the highest velocity when it is aligned along the diagonal corresponding to an orientation angle $\pi/4$ and the lowest when it is aligned with the x or y axis (Figure 1d and Supporting Information Movie 2). This case is analogously described as

$$\mathbf{v}_2(\phi) = 2\overline{v}_2 \sin^2 (2\phi) \, \hat{\mathbf{u}}(\phi) \tag{6}$$

Figure 2 shows that the prescribed motility scenarios are experimentally realized. In Figure 2a,b, we fit eqs 5 and 6 to the

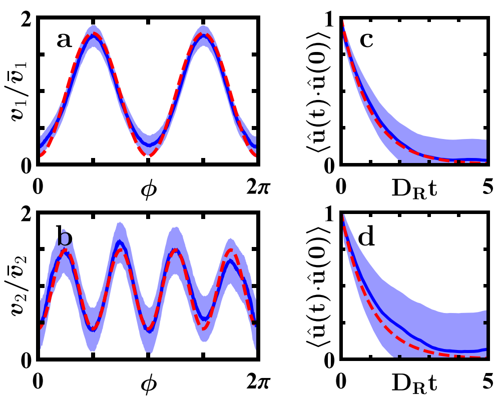

Figure 2. (a, b) Orientation-dependent motility with 2-fold rotational symmetry $v_1(\phi)/\overline{v}_1$ = 2 $\sin^2 \phi$ and 4-fold rotational symmetry $v_2(\phi)/\overline{v}_2$ = 2 $\sin^2 (2\phi)$. Solid dark-blue and dashed red curves show the experimental data and a trigonometric fit, respectively. The fits yield $\overline{v}_1$ = 1.4 μm/s and $\overline{v}_2$ = 1.1 μm/s. Light-blue areas express the standard error of the mean. (c, d) Orientation-correlation function $\langle \hat{\mathbf{u}}(t) \cdot \hat{\mathbf{u}}(0) \rangle$ for the two experiments and the expected function $\langle \hat{\mathbf{u}}(t) \cdot \hat{\mathbf{u}}(0) \rangle$ = $\exp(-D_R t)$ for comparison, validating the imposed rotational diffusivity D_R = 0.25 rad^2/s.

data for the orientation-dependent velocity observed in the experiments corresponding to the first and second scenario, respectively. We find good agreement of the fit curves and experimental data and determine orientationally averaged speeds $\overline{v}_1$ = 1.4 μm/s and $\overline{v}_2$ = 1.1 μm/s. The orientational decorrelation of the velocity vector obeys a simple exponential decay with a rate corresponding to the imposed rotational diffusivity D_R = 0.25 rad^2/s (Figure 2c,d). In the following sections, we will denote all lengths in units of the orientationally averaged persistence length $L = \overline{v}/D_R$ (i.e., $\mathbf{r} \to \mathbf{r}/L$) and time in units of the persistence time $\tau_R = 1/D_R$ (i.e., $t \to D_R t$). The importance of translational noise relative to the imposed speed $\overline{v}$ and rotational diffusion can be defined by the dimensionless Péclet number, $Pe = \overline{v}/\sqrt{D_R D_T}$, where the thermal transla-

https://dx.doi.org/10.1021/acs.langmuir.9b03617
Langmuir 2020, 36, 7066−7073

Langmuir pubs.acs.org/Langmuir Article

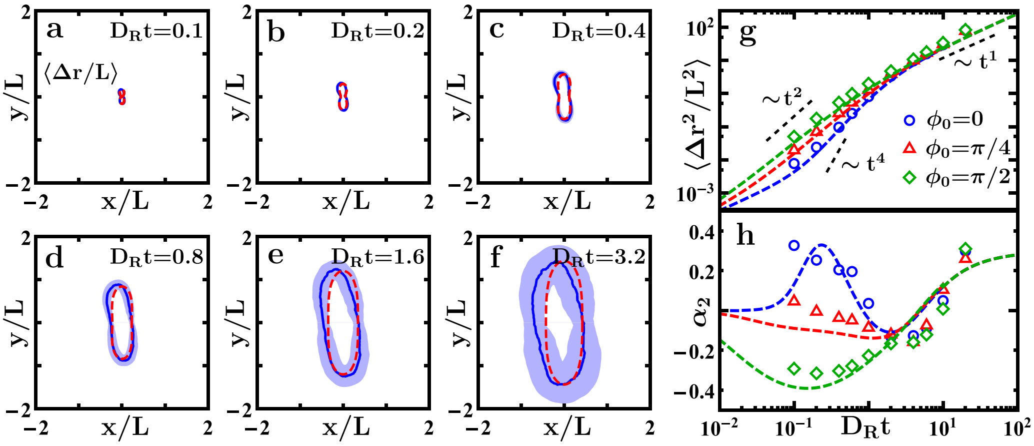

Figure 3. Comparison between theoretical and experimental results for a propulsion velocity with 2-fold symmetry. (a−f) The anisotropic motion of the particle is visualized by plotting the mean displacement $\langle\Delta\mathbf{r}(\phi_0)\rangle$ as a function of the initial orientation ϕ_0 for fixed times (a) $D_Rt = 0.1$, (b) $D_Rt = 0.2$, (c) $D_Rt = 0.4$, (d) $D_Rt = 0.8$, (e) $D_Rt = 1.6$, and (f) $D_Rt = 3.2$. Solid dark-blue and dashed red curves show the experimental data and analytical results, respectively. Light-blue areas express the standard error of the mean. (g) Mean-square displacement $\langle\Delta\mathbf{r}^2(t)\rangle$ for initial orientations $\phi_0 = 0$ (blue), $\phi_0 = \pi/4$ (red), and $\phi_0 = \pi/2$ (green). Symbols and dashed curves show the experimental data and analytical results, respectively. In addition, reference slopes are included for diffusive ($\nu = 1$), ballistic ($\nu = 2$), and quartic ($\nu = 4$) temporal behavior. (h) Non-Gaussian parameter $\alpha_2(t)$ for the same initial orientations. Lengths are given in units of $L = 5.6\ \mu$m and time in units of $1/D_R = 0.4$ s, and the Péclet number is set to $Pe = 12$.

tional diffusion coefficient of the dumbbells was experimentally determined to be $D_T = 0.055\ \mu\text{m}^2/\text{s}$.

Mean Displacement. To characterize the effect of orientation-dependent motility on the Brownian dynamics, we first discuss the mean displacement $\langle\Delta\mathbf{r}(t)\rangle$ of the particle. In Figures 3a−f and 4a−f, the experimentally determined mean displacement is compared with that resulting from our theoretical model, where we emphasize the anisotropic motion of the particle by plotting the mean displacement as a function of the initial orientation $\phi_0 = \phi(0)$ after fixed times t. The theoretical result for the mean displacement is given for a general orientation-dependent motility as

$$\frac{\langle\Delta\mathbf{r}(t)\rangle}{L} = \sum_{\substack{k_1=-\infty\\ k_1\neq 0}}^{\infty} \mathbf{c}_{k_1} C_{k_1}(D_Rt)\,\mathrm{e}^{\mathrm{i}k_1\phi_0} \tag{7}$$

with

$$C_{k_1}(t) = \frac{1}{k_1^2}\left(1 - \mathrm{e}^{-k_1^2 t}\right) \tag{8}$$

where the Fourier-coefficient vectors $\mathbf{c}_k$ are determined by the motility $\mathbf{v}(\phi)$. Here, $\mathbf{c}_k = \int_{-\pi}^{\pi}(\mathbf{v}_n(\phi)/(2\pi\bar{v}_n))\exp(-\mathrm{i}k\phi)\,\mathrm{d}\phi$ for $n = 1, 2$. (All analytical results for the two studied scenarios are listed explicitly in the Supporting Information.) For short times $t \lesssim \tau_R$, the particle moves linearly in time with $\langle\Delta\mathbf{r}(t)\rangle = \mathbf{v}(\phi_0)t + O(t^2)$, and the anisotropy with respect to the initial orientation, as is visible in Figures 3a and 4a, is a deterministic consequence of the anisotropic propulsion of the particle. For intermediate times $t \approx \tau_R$, the orientation of the particle starts to decorrelate, which directly affects the anisotropic shape of the mean displacement (Figures 3b−e and 4b−e). Finally, for long times $t \gtrsim \tau_R$, the mean displacement saturates to an anisotropic persistence length $\lim_{t\to\infty}\langle\Delta\mathbf{r}(t)\rangle = L\sum_{k=-\infty,k\neq0}^{\infty}\mathbf{c}_k\mathrm{e}^{\mathrm{i}k\phi_0}/k^2$ (Figures 3f and 4f). The faster varying contributions (i.e., the higher Fourier modes) of the propulsion velocity saturate faster and have a smaller impact on the mean motion of the particle, resulting in a more isotropic final shape (cf. Figures 3f and 4).

Mean-Square Displacement. The dynamics of active Brownian motion can be further classified in temporal regimes by investigating the scaling behavior of the mean-square displacement (i.e., $\langle\Delta\mathbf{r}^2(t)\rangle \propto t^\nu$). For $\nu = 1$, the particle shows ordinary diffusive behavior. If $\nu < 1$ or $\nu > 1$, then the particle undergoes subdiffusion or superdiffusion, respectively. The mean-square displacement for a general orientation-dependent motility is given by

$$\frac{\langle\Delta\mathbf{r}^2(t)\rangle}{L^2} = \frac{4D_Rt}{Pe^2} + \sum_{\substack{k_1=-\infty\\ k_1\neq 0}}^{\infty}\sum_{\substack{k_2=-\infty\\ k_2\neq 0}}^{\infty} \mathbf{c}_{k_1}\cdot\mathbf{c}_{k_2}\big(C_{k_1k_2}(D_Rt) + C_{k_2k_1}(D_Rt)\big)\mathrm{e}^{\mathrm{i}(k_1+k_2)\phi_0} \tag{9}$$

with

$$C_{k_1k_2}(t) = \begin{cases} \frac{1}{k_2^4}\left(k_2^2 t - \left(1 - e^{-k_2^2 t}\right)\right), & \text{for } k_1 = -k_2,\\ \frac{1}{k_2^4}\left(1 - \left(1 + k_2^2 t\right)e^{-k_2^2 t}\right), & \text{for } k_1 = -2k_2,\\ \frac{1}{k_1(k_1+2k_2)}\left(\frac{1}{k_2^2}\left(1 - e^{-k_1^2 t}\right) - \frac{1}{(k_1+k_2)^2}\left(1 - e^{-(k_1+k_2)^2 t}\right)\right), & \text{else} \end{cases} \tag{10}$$

In Figures 3h and 4h, we compare the experimentally determined mean-square displacement with the corresponding theoretical result. We observe three temporal regimes, characterized by two crossover times. By expanding the

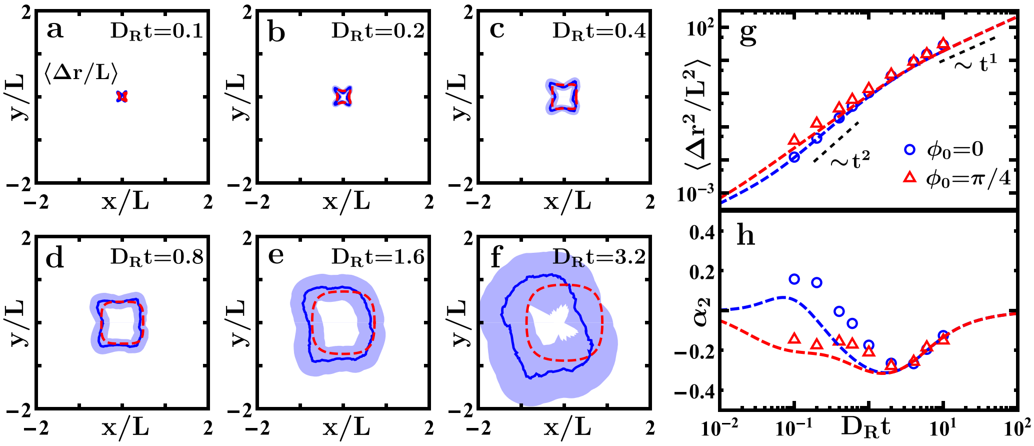

Figure 4. The same as in Figure 3 for a propulsion velocity with 4-fold symmetry. Lengths are given in units of $L = 4.4\ \mu$m and time in units of $1/D_R = 0.4$ s, and the Péclet number is $Pe = 9$.

analytical result for the mean-square displacement in time, we obtain

$$\langle \mathbf{r}^2(t)\rangle = 4D_T t + \mathbf{v}^2(\phi_0)t^2 + D_R(3\partial^2_{\phi_0}\mathbf{v}^2(\phi_0) - 2(\partial_{\phi_0}\mathbf{v}(\phi_0))^2)\frac{t^3}{6} + O(t^4) \tag{11}$$

where ∂_{ϕ_0} denotes the partial derivative with respect to the initial orientation ϕ_0. Thus, the mean-square displacement starts in a short-time diffusion regime ($\nu = 1$), increasing linearly in time with the short-time diffusion coefficient $D_S = D_T$. A transition from the short-time diffusive regime to a superdiffusive regime ($\nu > 1$) occurs if the deterministic swimming motion dominates translational diffusion. This condition is fulfilled for times t greater than the translational diffusion time $\tau_D = D_T/\mathbf{v}^2(\phi_0)$. As shown in Figure 3h, the transition to an intermediate superdiffusive regime is sensitive with respect to the initial velocity. If the particle is oriented initially along directions of high motility (see Figure 3h for $\phi_0 = \pi/2$), then the mean-square displacement displays a crossover to the ballistic regime ($\nu = 2$). However, if the initial velocity of the particle is not large enough to dominate translational diffusion or even vanishes (eq 11), then we observe a delayed crossover (see Figure 3h for $\phi_0 = 0$). In that case, the particle has to undergo an angular displacement first such that its propulsion grows until it overcomes translational diffusion. Due to this multiplicative coupling of diffusive and ballistic behavior for the angular and positional displacements, respectively, the mean-square displacement shows a superballistic power-law behavior ($\nu > 2$), which is masked by finite translational diffusion (eq 11). For the specific initial orientation $\phi_0 = 0$, the second- and even third-order terms in eq 11 vanish such that the next leading order after normal diffusion scales even quartically ($\nu = 4$), which is more visible for a higher Péclet number Pe. (See Figure S2 in the Supporting Information for the emergence of this scaling regime.) For times t greater than the rotational diffusion time $\tau_R = 1/D_R$, the mean-square displacement evolves toward the diffusive limit ($\nu = 1$) again, and it is described by a long-time diffusion coefficient

$$D_L = \lim_{t\to\infty}\frac{\langle \Delta\mathbf{r}^2(t)\rangle}{4t} = D_T + \frac{\overline{v}^2}{D_R}\sum_{k_1=1}^{\infty}\frac{|\mathbf{c}_{k_1}|^2}{k_1^2} \tag{12}$$

In the two experimental scenarios, the long-time diffusion coefficients are $D_{L,1} = 5.1\ \mu\text{m}^2/\text{s}$ and $D_{L,2} = 2.6\ \mu\text{m}^2/\text{s}$, respectively.

Non-Gaussian Parameter. Finally, we study the non-Gaussian features of our active dynamics in more detail. Hence, we introduce the non-Gaussian parameter, which is defined in two spatial dimensions as[59]

$$\alpha_2(t) = \frac{1}{2}\frac{\langle \Delta\mathbf{r}^4(t)\rangle}{\langle \Delta\mathbf{r}^2(t)\rangle^2} - 1 \tag{13}$$

The non-Gaussian parameter quantifies how far the distribution of displacements deviates from a Gaussian (i.e., $\alpha_2(t) = 0$ for an isotropic Gaussian distribution). For $\alpha_2(t) < 0$ or $\alpha_2(t) > 0$, the underlying distribution has less- or more-pronounced tails, respectively. Interesting for active Brownian motion is the case of deterministic motion (no tails), for which the non-Gaussian parameter is $\alpha_2(t) = -1/2$. To derive the analytical expression for the non-Gaussian parameter from our theoretical model, in addition to the mean-square displacement $\langle \Delta\mathbf{r}^2(t)\rangle$ the mean-quartic displacement $\langle \Delta\mathbf{r}^4(t)\rangle$ is also required, which is explicitly calculated in the Supporting Information. In Figures 3h and 4h, the anisotropy of the non-Gaussian behavior is visualized. For very small times $t \ll \tau_D$, the displacements are simply diffusive (i.e., Gaussian), thus the non-Gaussian parameter $\alpha_2(t)$ is zero. For intermediate times $\tau_D < t < \tau_R$, the non-Gaussian parameter behaves anisotropically with respect to the initial orientation ϕ_0. For a sufficiently high initial velocity, $\alpha_2(t)$ becomes negative, which is characteristic of persistently swimming Brownian particles (see Figure 3h for $\phi_0 = \pi/2$). When the initial velocity vanishes (i.e., $\mathbf{v}(\phi_0) = 0$; see Figure 3h for $\phi_0 = 0$), we observe a positive non-Gaussian parameter. In this case, the particle moves mostly diffusively even for intermediate times, except for rare events where a fluctuation rotates the particle sufficiently such that it experiences a large ballistic step. The underlying distribution of displacements is thus Gaussian with pronounced tails which

https://dx.doi.org/10.1021/acs.langmuir.9b03617
Langmuir 2020, 36, 7066−7073

dominate the fourth moment over the second and lead to positive non-Gaussian character. Finally, for long times $t > \tau_R$, we observe long-lived non-Gaussian behavior in the case of 2-fold symmetry and Gaussian behavior in the case of 4-fold symmetry. To explain this observation, we consider the covariance matrix of the displacement distribution, and we define the long-time diffusion matrix

$$\begin{aligned}(\mathbf{D}_L)_{ij} &= \lim_{t\to\infty} \frac{\langle \Delta r_i(t)\, \Delta r_j(t)\rangle}{2t} \\ &= D_T\delta_{ij} + \frac{\bar{v}^2}{D_R}\sum_{k_1=1}^{\infty}\frac{1}{k_1^2}(c_{k_1,i}c_{-k_1,j} + c_{-k_1,i}c_{k_1,j})\end{aligned} \quad (14)$$

for $i, j \in \{x, y\}$. The eigenvalues of this matrix are given as $D_\pm = D_L \pm \Delta D_L$, where ΔD_L denotes the long-time anisotropy

$$\Delta D_L = \frac{\bar{v}^2}{D_R}\sqrt{\sum_{k_1=1}^{\infty}\sum_{k_2=1}^{\infty}\frac{1}{k_1^2k_2^2}(|\mathbf{c}_{k_1}\cdot\mathbf{c}_{k_2}|^2 + |\mathbf{c}_{k_1}\cdot\mathbf{c}_{-k_2}|^2 - |\mathbf{c}_{k_1}|^2|\mathbf{c}_{k_2}|^2)} \quad (15)$$

which describes the long-time diffusion along the principal axes of maximal and minimal diffusion, respectively. In the two experimental scenarios, the long-time anisotropy yields $\Delta D_{L,1} = 4.0\ \mu m^2/s$ and $\Delta D_{L,2} = 0\ \mu m^2/s$, respectively. Using the introduced notation, the long-time behavior of the non-Gaussian parameter can be expressed as

$$\lim_{t\to\infty} \alpha_2(t) = \frac{1}{2}\left(\frac{\Delta D_L}{D_L}\right)^2 \quad (16)$$

which coincides with the non-Gaussian character of an anisotropic Gaussian distribution with covariance matrix $2\mathbf{D}_L t$. Thus, the long-time behavior of the non-Gaussian parameter quantifies the anisotropy of the long-time diffusion. For the motility with 2-fold symmetry, we have enhanced long-time diffusion along the y axis and decreased long-time diffusion along the x axis leading to non-Gaussian character for long times (Figure 3h). In the second scenario, the long-time behavior can be described with solely one long-time diffusion coefficient, thus the non-Gaussian parameter vanishes (Figure 4h).

■ CONCLUSIONS

In this work, we reported on a new methodology to impose complex anisotropic motility behavior on active Brownian particles. We engineered the orientation-dependent motility of active dumbbells whose rotational diffusivity is externally controlled by randomized magnetic fields and whose propulsion velocity is prescribed using a feedback scheme, which updates the velocity based on the particles' orientation. To describe the dynamic features of the particles, we developed a theoretical framework that proved to be in good agreement with the corresponding experimental data. In particular, a particle's mean displacement shows deterministic active motion at very short times, decorrelation at intermediate times, and saturation to anisotropic persistence trajectories at long times. The mean-square displacement is also characterized by different temporal regimes. We found that the transition from isotropic diffusion at short times to a superdiffusive intermediate regime is very sensitive to the initial velocity of the particle such that the coupling of diffusive-rotational and ballistic-translational motion can result in superballistic motion. Moreover, the motion is characterized by anisotropic diffusion at long times, as described by the long-time diffusion coefficient and the long-time anisotropy. Finally, we have investigated the deviation from a standard Gaussian distribution by calculating the non-Gaussian parameter as a function of time. It becomes nonzero for intermediate times: negative when there is persistent swimming and positive during reorientation events from an initial orientation with low velocity to orientations with high velocity. Furthermore, the long-time behavior quantifies the anisotropy of the long-time diffusion, being nonzero for the 2-fold-symmetric motility and zero for the 4-fold-symmetric motility.

The basic model we proposed here is applicable to a broad range of systems with anisotropic external propulsion mechanisms and relevant in the context of the orientational dependence of the propulsion speed, which can intrinsically emerge for both artificial and biological microswimmers.[50,55] In the future, intricate combinations of spatial, orientational, and temporal modulations of motility could be considered. One could also proceed to particles with a complex shape, which have more involved trajectories.[60,61] Finally, although in our current experiments one particle at a time is controlled, we envision possible experimental realizations to control many particles to explore emerging collective effects.[62]

■ ASSOCIATED CONTENT

Supporting Information

The Supporting Information is available free of charge at https://pubs.acs.org/doi/10.1021/acs.langmuir.9b03617.

Real-time feedback applied in the experiments; details of the postprocessing and data analysis; expressions for the nth moment of the translational displacement $\langle \Delta \mathbf{r}^n(t)\rangle$ for active Brownian motion with a general orientation-dependent motility; expressions for the low-order moments corresponding to the two studied motility scenarios; the emergence of the quartic intermediate regime for a propulsion velocity with 2-fold symmetry and a large Péclet number (PDF)

Representative trajectory of a dumbbell with a motility with 2-fold symmetry (AVI)

Representative trajectory of a dumbbell with a motility with 4-fold symmetry (AVI)

■ AUTHOR INFORMATION

Corresponding Authors

Lucio Isa − *Laboratory for Soft Materials and Interfaces, Department of Materials, ETH Zürich, 8093 Zürich, Switzerland;* orcid.org/0000-0001-6731-9620; Email: lucio.isa@mat.ethz.ch

Raphael Wittkowski − *Institut für Theoretische Physik, Center for Soft Nanoscience, Westfälische Wilhelms-Universität Münster, D-48149 Münster, Germany;* orcid.org/0000-0003-4881-9173; Email: raphael.wittkowski@uni-muenster.de

Authors

Alexander R. Sprenger − *Institut für Theoretische Physik II: Weiche Materie, Heinrich-Heine-Universität Düsseldorf, D-40225 Düsseldorf, Germany*

Miguel Angel Fernandez-Rodriguez − *Laboratory for Soft Materials and Interfaces, Department of Materials, ETH Zürich, 8093 Zürich, Switzerland*

Laura Alvarez − *Laboratory for Soft Materials and Interfaces, Department of Materials, ETH Zürich, 8093 Zürich, Switzerland;* orcid.org/0000-0001-7018-7817

Hartmut Löwen − *Institut für Theoretische Physik II: Weiche Materie, Heinrich-Heine-Universität Düsseldorf, D-40225 Düsseldorf, Germany*

Complete contact information is available at:
https://pubs.acs.org/10.1021/acs.langmuir.9b03617

Notes

The authors declare no competing financial interest.

■ ACKNOWLEDGMENTS

R.W. and H.L. are funded by the Deutsche Forschungsgemeinschaft (DFG, German Research Foundation; WI 4170/3-1 and LO 418/23-1). M.A.F-R., L.A., and L.I. acknowledge financial support from the Swiss National Science Foundation (grant PP00P2-172913/1) and fruitful discussions with Dr. Heiko Wolf.

■ REFERENCES

(1) Bechinger, C.; Di Leonardo, R.; Löwen, H.; Reichhardt, C.; Volpe, G.; Volpe, G. Active particles in complex and crowded environments. *Rev. Mod. Phys.* **2016**, *88*, No. 045006.
(2) Ebbens, S. J.; Howse, J. R. In pursuit of propulsion at the nanoscale. *Soft Matter* **2010**, *6*, 726−738.
(3) Romanczuk, P.; Bär, M.; Ebeling, W.; Lindner, B.; Schimansky-Geier, L. Active Brownian particles. From individual to collective stochastic dynamics. *Eur. Phys. J.: Spec. Top.* **2012**, *202*, 1−162.
(4) Elgeti, J.; Winkler, R. G.; Gompper, G. Physics of microswimmers−single particle motion and collective behavior: a review. *Rep. Prog. Phys.* **2015**, *78*, No. 056601.
(5) Zöttl, A.; Stark, H. Emergent behavior in active colloids. *J. Phys.: Condens. Matter* **2016**, *28*, No. 253001.
(6) Paxton, W. F.; Kistler, K. C.; Olmeda, C. C.; Sen, A.; St. Angelo, S. K.; Cao, Y.; Mallouk, T. E.; Lammert, P. E.; Crespi, V. H. Catalytic nanomotors: autonomous movement of striped nanorods. *J. Am. Chem. Soc.* **2004**, *126*, 13424−13431.
(7) Palacci, J.; Cottin-Bizonne, C.; Ybert, C.; Bocquet, L. Sedimentation and effective temperature of active colloidal suspensions. *Phys. Rev. Lett.* **2010**, *105*, No. 088304.
(8) Dietrich, K.; Renggli, D.; Zanini, M.; Volpe, G.; Buttinoni, I.; Isa, L. Two-dimensional nature of the active Brownian motion of catalytic microswimmers at solid and liquid interfaces. *New J. Phys.* **2017**, *19*, No. 065008.
(9) Volpe, G.; Buttinoni, I.; Vogt, D.; Kümmerer, H.-J.; Bechinger, C. Microswimmers in patterned environments. *Soft Matter* **2011**, *7*, 8810−8815.
(10) Buttinoni, I.; Volpe, G.; Kümmel, F.; Volpe, G.; Bechinger, C. Active Brownian motion tunable by light. *J. Phys.: Condens. Matter* **2012**, *24*, No. 284129.
(11) Palacci, J.; Sacanna, S.; Steinberg, A.; Pine, D.; Chaikin, P. Living crystals of lightactivated colloidal surfers. *Science* **2013**, *339*, 936−940.
(12) Palacci, J.; Sacanna, S.; Vatchinsky, A.; Chaikin, P. M.; Pine, D. J. Photoactivated colloidal dockers for cargo transportation. *J. Am. Chem. Soc.* **2013**, *135*, 15978−15981.
(13) Palacci, J.; Sacanna, S.; Kim, S.-H.; Yi, G.-R.; Pine, D. J.; Chaikin, P. M. Lightactivated self-propelled colloids. *Philos. Trans. R. Soc., A* **2014**, *372*, No. 20130372.
(14) Moyses, H.; Palacci, J.; Sacanna, S.; Grier, D. G. Trochoidal trajectories of self-propelled Janus particles in a diverging laser beam. *Soft Matter* **2016**, *12*, 6357−6364.
(15) Wang, W.; Castro, L. A.; Hoyos, M.; Mallouk, T. E. Autonomous motion of metallic microrods propelled by ultrasound. *ACS Nano* **2012**, *6*, 6122−6132.
(16) Dreyfus, R.; Baudry, J.; Roper, M. L.; Fermigier, M.; Stone, H. A.; Bibette, J. Microscopic artificial swimmers. *Nature* **2005**, *437*, 862−865.
(17) Grosjean, G.; Lagubeau, G.; Darras, A.; Hubert, M.; Lumay, G.; Vandewalle, N. Remote control of self-assembled microswimmers. *Sci. Rep.* **2015**, *5*, No. 16035.
(18) Steinbach, G.; Gemming, S.; Erbe, A. Non-equilibrium dynamics of magnetically anisotropic particles under oscillating fields. *Eur. Phys. J. E: Soft Matter Biol. Phys.* **2016**, *39*, No. 69.
(19) Kaiser, A.; Snezhko, A.; Aranson, I. S. Flocking ferromagnetic colloids. *Science Advances* **2017**, *3*, No. e1601469.
(20) Bricard, A.; Caussin, J. B.; Desreumaux, N.; Dauchot, O.; Bartolo, D. Emergence of macroscopic directed motion in populations of motile colloids. *Nature* **2013**, *503*, 95−98.
(21) Morin, A.; Desreumaux, N.; Caussin, J.-B.; Bartolo, D. Distortion and destruction of colloidal flocks in disordered environments. *Nat. Phys.* **2017**, *13*, 63−67.
(22) Kümmel, F.; ten Hagen, B.; Wittkowski, R.; Buttinoni, I.; Eichhorn, R.; Volpe, G.; Löwen, H.; Bechinger, C. Circular motion of asymmetric self-propelling particles. *Phys. Rev. Lett.* **2013**, *110*, No. 198302.
(23) Kümmel, F.; ten Hagen, B.; Wittkowski, R.; Takagi, D.; Buttinoni, I.; Eichhorn, R.; Volpe, G.; Löwen, H.; Bechinger, C. Reply to "Comment on 'Circular motion of asymmetric self-propelling particles'. *Phys. Rev. Lett.* **2014**, *113*, No. 029802.
(24) Zheng, X.; ten Hagen, B.; Kaiser, A.; Wu, M.; Cui, H.; Silber-Li, Z.; Löwen, H. Non-Gaussian statistics for the motion of self-propelled Janus particles: experiment versus theory. *Phys. Rev. E* **2013**, *88*, No. 032304.
(25) Hong, Y.; Blackman, N. M.; Kopp, N. D.; Sen, A.; Velegol, D. Chemotaxis of nonbiological colloidal rods. *Phys. Rev. Lett.* **2007**, *99*, No. 178103.
(26) Pohl, O.; Stark, H. Dynamic clustering and chemotactic collapse of self-phoretic active particles. *Phys. Rev. Lett.* **2014**, *112*, No. 238303.
(27) Saha, S.; Golestanian, R.; Ramaswamy, S. Clusters, asters, and collective oscillations in chemotactic colloids. *Phys. Rev. E* **2014**, *89*, No. 062316.
(28) Liebchen, B.; Marenduzzo, D.; Pagonabarraga, I.; Cates, M. E. Clustering and pattern formation in chemorepulsive active colloids. *Phys. Rev. Lett.* **2015**, *115*, No. 258301.
(29) Liebchen, B.; Marenduzzo, D.; Cates, M. E. Phoretic interactions generically induce dynamic clusters and wave patterns in active colloids. *Phys. Rev. Lett.* **2017**, *118*, No. 268001.
(30) Jin, C.; Krüger, C.; Maass, C. C. Chemotaxis and autochemotaxis of self-propelling droplet swimmers. *Proc. Natl. Acad. Sci. U. S. A.* **2017**, *114*, 5089−5094.
(31) Lozano, C.; ten Hagen, B.; Löwen, H.; Bechinger, C. Phototaxis of synthetic microswimmers in optical landscapes. *Nat. Commun.* **2016**, *7*, No.12828.
(32) Garcia, X.; Rafaï, S.; Peyla, P. Light control of the flow of phototactic microswimmer suspensions. *Phys. Rev. Lett.* **2013**, *110*, No. 138106.
(33) Geiseler, A.; Hänggi, P.; Marchesoni, F.; Mulhern, C.; Savel'ev, S. Chemotaxis of artificial microswimmers in active density waves. *Phys. Rev. E: Stat. Phys., Plasmas, Fluids, Relat. Interdiscip. Top.* **2016**, *94*, No. 012613.
(34) Geiseler, A.; Hänggi, P.; Marchesoni, F. Self-polarizing microswimmers in active density waves. *Sci. Rep.* **2017**, *7*, No. 41884.
(35) Geiseler, A.; Hänggi, P.; Marchesoni, F. Taxis of artificial swimmers in a spatiotemporally modulated activation medium. *Entropy* **2017**, *19*, No. 97.
(36) Sharma, A.; Brader, J. M. Brownian systems with spatially inhomogeneous activity. *Phys. Rev. E: Stat. Phys., Plasmas, Fluids, Relat. Interdiscip. Top.* **2017**, *96*, No. 032604.
(37) Dai, B.; Wang, J.; Xiong, Z.; Zhan, X.; Dai, W.; Li, C.-C.; Feng, S.-P.; Tang, J. Programmable artificial phototactic microswimmer. *Nat. Nanotechnol.* **2016**, *11*, 1087−1092.
(38) Li, W.; Wu, X.; Qin, H.; Zhao, Z.; Liu, H. Light-driven and light-guided microswimmers. *Adv. Funct. Mater.* **2016**, *26*, 3164−3171.
(39) Lozano, C.; Bechinger, C. Diffusing wave paradox of phototactic particles in traveling light pulses. *Nat. Commun.* **2019**, *10*, No. 2495.

(40) Lozano, C.; Liebchen, B.; ten Hagen, B.; Bechinger, C.; Löwen, H. Propagating density spikes in light-powered motility-ratchets. *Soft Matter* **2019**, *15*, 5185−5192.
(41) Palagi, S.; Singh, D. P.; Fischer, P. Light-controlled micromotors and soft microrobots. *Adv. Opt. Mater.* **2019**, *7*, No. 1900370.
(42) Ghosh, P. K.; Li, Y.; Marchesoni, F.; Nori, F. Pseudochemotactic drifts of artificial microswimmers. *Phys. Rev. E* **2015**, *92*, No. 012114.
(43) Magiera, M. P.; Brendel, L. Trapping of interacting propelled colloidal particles in inhomogeneous media. *Phys. Rev. E* **2015**, *92*, No. 012304.
(44) Grauer, J.; Löwen, H.; Janssen, L. M. C. Spontaneous membrane formation and self-encapsulation of active rods in an inhomogeneous motility field. *Phys. Rev. E: Stat. Phys., Plasmas, Fluids, Relat. Interdiscip. Top.* **2018**, *97*, No. 022608.
(45) Scacchi, A.; Brader, J. M.; Sharma, A. Escape rate of transiently active Brownian particle in one dimension. *Phys. Rev. E: Stat. Phys., Plasmas, Fluids, Relat. Interdiscip. Top.* **2019**, *100*, No. 012601.
(46) Vuijk, H. D.; Brader, J. M.; Sharma, A. Anomalous fluxes in overdamped Brownian dynamics with Lorentz force. *J. Stat. Mech.: Theory Exp.* **2019**, *2019*, No. 063203.
(47) Merlitz, H.; Vuijk, H. D.; Brader, J.; Sharma, A.; Sommer, J.-U. Linear response approach to active Brownian particles in time-varying activity fields. *J. Chem. Phys.* **2018**, *148*, No. 194116.
(48) Liebchen, B.; Löwen, H. Optimal navigation strategies for active particles. *EPL* **2019**, *127*, No.34003.
(49) Maggi, C.; Angelani, L.; Frangipane, G.; Di Leonardo, R. Currents and flux-inversion in photokinetic active particles. *Soft Matter* **2018**, *14*, 4958−4962.
(50) Uspal, W. E. Theory of light-activated catalytic Janus particles. *J. Chem. Phys.* **2019**, *150*, No. 114903.
(51) Ni, S.; Leemann, J.; Buttinoni, I.; Isa, L.; Wolf, H. Programmable colloidal molecules from sequential capillarity-assisted particle assembly. *Science Advances* **2016**, *2*, No. e1501779.
(52) Ma, F.; Yang, X.; Zhao, H.; Wu, N. Inducing propulsion of colloidal dimers by breaking the symmetry in electrohydrodynamic flow. *Phys. Rev. Lett.* **2015**, *115*, No. 208302.
(53) Ni, S.; Marini, E.; Buttinoni, I.; Wolf, H.; Isa, L. Hybrid colloidal microswimmers through sequential capillary assembly. *Soft Matter* **2017**, *13*, 4252−4259.
(54) Fernandez-Rodriguez, M. A.; Grillo, F.; Alvarez, L.; Rathlef, M.; Buttinoni, I.; Volpe, G.; Isa, L. Active colloids with position-dependent rotational diffusivity. *arXiv:1911.02291*, 2019.
(55) Hu, J.; Wysocki, A.; Winkler, R. G.; Gompper, G. Physical sensing of surface properties by microswimmers − directing bacterial motion via wall slip. *Sci. Rep.* **2015**, *5*, No. 9586.
(56) Squires, T. M.; Bazant, M. Z. Breaking symmetries in induced-charge electro-osmosis and electrophoresis. *J. Fluid Mech.* **2006**, *560*, 65−101.
(57) Gangwal, S.; Cayre, O. J.; Bazant, M. Z.; Velev, O. D. Induced-Charge Electrophoresis of Metallodielectric Particles. *Phys. Rev. Lett.* **2008**, *100*, No. 058302.
(58) Yan, J.; Han, M.; Zhang, J.; Xu, C.; Luijten, E.; Granick, S. Reconfiguring active particles by electrostatic imbalance. *Nat. Mater.* **2016**, *15*, 1095−1099.
(59) Kurzthaler, C.; Franosch, T. Intermediate scattering function of an anisotropic Brownian circle swimmer. *Soft Matter* **2017**, *13*, 6396−6406.
(60) Wittkowski, R.; Löwen, H. Self-propelled Brownian spinning top: dynamics of a biaxial swimmer at low Reynolds numbers. *Phys. Rev. E* **2012**, *85*, No. 021406.
(61) Voß, J.; Wittkowski, R. Hydrodynamic resistance matrices of colloidal particles with various shapes. *arXiv:1811.01269*, 2018.
(62) Cohen, J. A.; Golestanian, R. Emergent cometlike swarming of optically driven thermally active colloids. *Phys. Rev. Lett.* **2014**, *112*, No. 068302.

■ NOTE ADDED AFTER ASAP PUBLICATION

Due to a production oversight, this article was published February 12, 2020 with several formatting issues. The corrected article was published February 17, 2020.

https://dx.doi.org/10.1021/acs.langmuir.9b03617
Langmuir 2020, 36, 7066−7073

Supporting Information: Active Brownian motion with orientation-dependent motility: theory and experiments

Alexander R. Sprenger,† Miguel Angel Fernandez-Rodriguez,‡ Laura Alvarez,‡ Lucio Isa,*,‡ Raphael Wittkowski,*,¶ and Hartmut Löwen†

†*Institut für Theoretische Physik II: Weiche Materie, Heinrich-Heine-Universität Düsseldorf, D-40225 Düsseldorf, Germany*

‡*Laboratory for Soft Materials and Interfaces, Department of Materials, ETH Zürich, 8093 Zürich, Switzerland*

¶*Institut für Theoretische Physik, Center for Soft Nanoscience, Westfälische Wilhelms-Universität Münster, D-48149 Münster, Germany*

E-mail: lucio.isa@mat.ethz.ch; raphael.wittkowski@uni-muenster.de

Real-time feedback

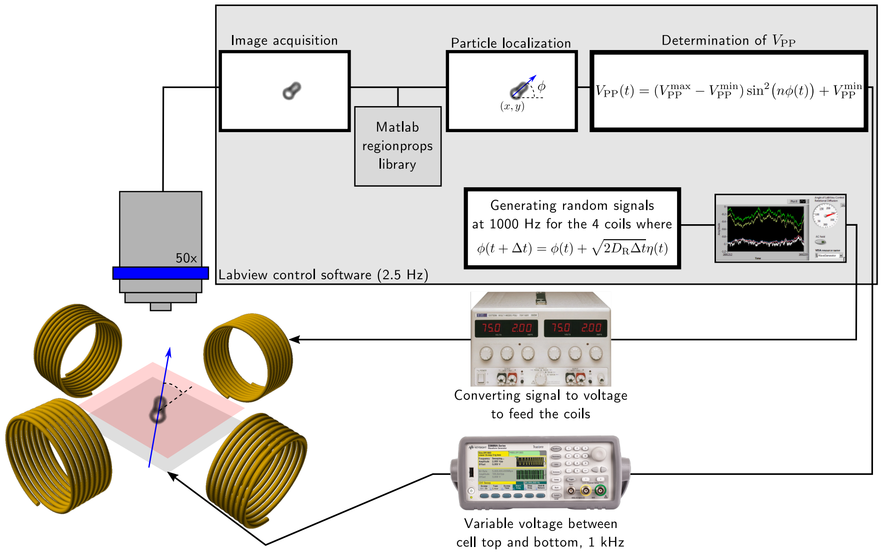

Figure S1: Scheme of the real-time feedback applied in the experiments.

Post-processing and data analysis

We collected 45 trajectories (86 min recording time in total) with a propulsion velocity with two-fold symmetry and 15 trajectories (28 min recording time in total) with a propulsion velocity with four-fold symmetry. Their lengths were limited by the time after which the particles left the field of view of the microscope. The position $\mathbf{r}$ and the orientation ϕ were recorded at 2.5 fps and the velocity was calculated from the displacement of successive positions of the particle as $\mathbf{v}(t) = (\mathbf{r}(t + \Delta t) - \mathbf{r}(t))/\Delta t$, where $\Delta t = 0.4\,\mathrm{s}$ is the time between two frames. The time steps are not fully equidistant, therefore the experimental data were linearly interpolated to obtain equidistant points. Initially, we did not distinguish each lobe of the dumbbell and thus we measured its orientation modulo π. From the direction of the velocity we could post-process the trajectory to reconstruct the angles in the interval $[0, 2\pi)$. Finally, we rescaled all displacements with a characteristic length $L = \overline{v}/D_{\mathrm{R}}$ and all times with the inverse rotational diffusion coefficient $1/D_{\mathrm{R}}$, where $\overline{v}$ is the orientationally averaged speed for a trajectory. Experimental means with respect to a specific initial orientation ϕ_0 were calculated by averaging in the interval $[\phi_0 - \delta\phi, \phi_0 + \delta\phi]$. We chose $\delta\phi = 25°$ and modified the theoretical results accordingly by $\exp(\mathrm{i}k\phi) \to \exp(\mathrm{i}k\phi)\sin(k\delta\phi)/(k\delta\phi)$. In Figs. 3g-h and 4g-h, we took advantage of the rotational and inflection symmetries of the experiment to increase the statistics.

General theoretical result

In this section, we calculate the n-th moment of the translational displacement $\langle \Delta\mathbf{r}^n(t)\rangle = \langle(\mathbf{r}(t)-\mathbf{r}_0)^n\rangle$ for active Brownian motion with a general orientation-dependent motility. With respect to initial conditions $\mathbf{r}(0)=\mathbf{r}_0$ and $\phi(0)=\phi_0$, solutions to the Langevin equations (2) and (3) are obtained via simple integration as

$$\mathbf{r}(t) = \mathbf{r}_0 + \int_0^t \Big(\mathbf{v}\big(\phi(t')\big) + \sqrt{2D_\mathrm{T}}\boldsymbol{\xi}(t')\Big)\,dt', \tag{S1}$$

$$\phi(t) = \phi_0 + \sqrt{2D_\mathrm{R}}\int_0^t \eta(t')\,dt'. \tag{S2}$$

Since $\phi(t)$ is a linear combination of Gaussian variables, the corresponding probability distribution is Gaussian as well and the conditional probability density $\mathrm{P}(\phi_2,t_2|\phi_1,t_1)$ is given by

$$\mathrm{P}(\phi_2,t_2|\phi_1,t_1) = \frac{1}{\sqrt{4\pi D_\mathrm{R}(t_2-t_1)}}\exp\left(-\frac{(\phi_2-\phi_1)^2}{4D_\mathrm{R}(t_2-t_1)}\right). \tag{S3}$$

The conditional probability density $\mathrm{P}(\phi_2,t_2|\phi_1,t_1)$ embodies the probability of finding the particle with orientation ϕ_2 at time t_2 under the condition that the particle was oriented at an angle ϕ_1 at former time t_1. Next, we construct the joint probability density of finding the particle at an angle ϕ_1 at time t_1, at an angle ϕ_2 at time t_2, ..., and at an angle ϕ_n at time t_n as $\mathrm{P}(\phi_n,t_n;\dots;\phi_1,t_1) = \prod_{j=1}^n \mathrm{P}(\phi_j,t_j|\phi_{j-1},t_{j-1})$ using the Markovian property of the Gaussian white noise. The knowledge of the joint probability density $\mathrm{P}(\phi_n,t_n;\dots;\phi_1,t_1)$ allows for an analytic calculation of the n-th moment of the translational displacement $\langle\Delta\mathbf{r}^n(t)\rangle$. The translational displacement $\Delta\mathbf{r}(t) = \Delta\mathbf{r}_\mathrm{A}(t)+\Delta\mathbf{r}_\mathrm{D}(t)$ can be split into an active contribution $\Delta\mathbf{r}_\mathrm{A}(t) = \int_0^t \mathbf{v}\big(\phi(t_1)\big)\,dt_1$ and a diffusive contribution $\Delta\mathbf{r}_\mathrm{D}(t) = \sqrt{2D_\mathrm{T}}\int_0^t \boldsymbol{\xi}(t_1)\,dt_1$. These two parts are stochastically independent and therefore the n-th moment of the total displacement can be represented as

$$\left\langle \Delta\mathbf{r}^{2n}(t)\right\rangle = \sum_{n_1+2n_2+n_3=n} \frac{n!}{n_1!n_2!n_2!n_3!}\left\langle \Delta\mathbf{r}_\mathrm{A}^{2(n_1+n_2)}(t)\right\rangle\left\langle \Delta\mathbf{r}_\mathrm{D}^{2(n_2+n_3)}(t)\right\rangle, \tag{S4}$$

$$\begin{aligned}\left\langle \Delta\mathbf{r}^{2n+1}(t)\right\rangle = &\sum_{n_1+2n_2+n_3=n} \frac{n!}{n_1!n_2!n_2!n_3!}\left\langle \Delta\mathbf{r}_\mathrm{A}^{2(n_1+n_2)+1}(t)\right\rangle\left\langle \Delta\mathbf{r}_\mathrm{D}^{2(n_2+n_3)}(t)\right\rangle \\ &+ \sum_{n_1+2n_2+n_3=n-1} \frac{n!}{n_1!n_2!(n_2+1)!n_3!}\left\langle \Delta\mathbf{r}_\mathrm{A}^{2(n_1+n_2)+1}(t)\right\rangle\left\langle \Delta\mathbf{r}_\mathrm{D}^{2(n_2+n_3+1)}(t)\right\rangle.\end{aligned} \tag{S5}$$

Like the orientation angle, also the diffusive displacement $\Delta\mathbf{r}_\mathrm{D}(t)$ is a sum of Gaussian variables and hence it follows a Gaussian distribution. The corresponding moments are calculated as

$$\left\langle \Delta\mathbf{r}_\mathrm{D}^{2n}(t)\right\rangle = n!\,(4D_\mathrm{T}t)^n, \tag{S6}$$

$$\left\langle \Delta\mathbf{r}_\mathrm{D}^{2n+1}(t)\right\rangle = \mathbf{0}. \tag{S7}$$

In contrast to the diffusive displacement, the active displacement $\Delta\mathbf{r}_{\mathrm{A}}(t)$ is a nonlinear combination of Gaussian variables. Here, the joint probability density $\mathrm{P}(\phi_n, t_n; \ldots; \phi_1, t_1)$ is used to calculate the n-th moment as

$$\langle \Delta\mathbf{r}_{\mathrm{A}}^n(t)\rangle = L^n \sum_{\substack{k_1=-\infty \\ k_1\neq 0}}^{\infty} \cdots \sum_{\substack{k_n=-\infty \\ k_n\neq 0}}^{\infty} \mathbf{c}_{k_1} \cdot \cdots \cdot \mathbf{c}_{k_n} e^{\mathrm{i}\left(\sum_{j=1}^{n} k_j\right)\phi_0} \sum_{\sigma\in S_n} \mathrm{C}_{k_{\sigma(1)}\cdots k_{\sigma(n)}}(D_{\mathrm{R}}t), \tag{S8}$$

where the sum has to be performed over the $n!$ permutations of the symmetric group S_n and

$$\mathrm{C}_{k_1\cdots k_n}(t) = \int_0^t dt_n \int_0^{t_n} dt_{n-1} \cdots \int_0^{t_2} dt_1 \prod_{j=1}^{n} e^{-\left(\sum_{l=j}^{n} k_l\right)^2 (t_j - t_{j-1})}. \tag{S9}$$

Low-order moments

The low-order moments for Brownian motion with an orientation-dependent motility are

$$\frac{\langle \Delta\mathbf{r}(t)\rangle}{L} = \frac{\langle \Delta\mathbf{r}_{\mathrm{A}}(t)\rangle}{L}, \tag{S10}$$

$$\frac{\langle \Delta\mathbf{r}^2(t)\rangle}{L^2} = \frac{4D_{\mathrm{R}}t}{\mathrm{Pe}^2} + \frac{\langle \Delta\mathbf{r}_{\mathrm{A}}^2(t)\rangle}{L^2}, \tag{S11}$$

$$\frac{\langle \Delta\mathbf{r}^4(t)\rangle}{L^4} = \frac{32(D_{\mathrm{R}}t)^2}{\mathrm{Pe}^4} + \frac{16D_{\mathrm{R}}t}{\mathrm{Pe}^2}\frac{\langle \Delta\mathbf{r}_{\mathrm{A}}^2(t)\rangle}{L^2} + \frac{\langle \Delta\mathbf{r}_{\mathrm{A}}^4(t)\rangle}{L^4}. \tag{S12}$$

For a propulsion velocity with two-fold symmetry $\mathbf{v}_1(\phi) = 2\overline{v}_1 \sin^2(\phi)\,\hat{\mathbf{u}}(\phi)$, with non-zero Fourier-coefficient vectors $\mathbf{c}_{-3} = -(1,\mathrm{i})/4$, $\mathbf{c}_{-1} = (1, 3\mathrm{i})/4$, $\mathbf{c}_1 = (1, -3\mathrm{i})/4$, and $\mathbf{c}_3 = (-1, \mathrm{i})/4$, one obtains

$$\frac{\langle \Delta\mathbf{r}_{\mathrm{A}}(t)\rangle}{L} = \frac{1}{2}\left(1 - e^{-\tau}\right)\begin{pmatrix}\cos(\phi_0)\\ 3\sin(\phi_0)\end{pmatrix} - \frac{1}{18}\left(1 - e^{-9\tau}\right)\begin{pmatrix}\cos(3\phi_0)\\ \sin(3\phi_0)\end{pmatrix}, \tag{S13}$$

$$\begin{aligned}\frac{\langle \Delta\mathbf{r}_{\mathrm{A}}^2(t)\rangle}{L^2} &= \frac{1}{162}\left(414\tau - 406 + 405e^{-\tau} + e^{-9\tau}\right) - \frac{\cos(2\phi_0)}{45}\left(35 - 45e^{-\tau} + 9e^{-4\tau} + e^{-9\tau}\right) \\ &\quad + \frac{\cos(4\phi_0)}{5040}\left(175 - 168e^{-\tau} - 40e^{-9\tau} + 33e^{-16\tau}\right),\end{aligned} \tag{S14}$$

$$\begin{aligned}\frac{\langle \Delta\mathbf{r}_{\mathrm{A}}^4(t)\rangle}{L^4} &= \frac{1}{185177664}\Big(6615\left(477619.2\tau^2 - 1646424\tau + 2289911.3\right) - 2057529.6(2025\tau \\ &\quad + 7376)e^{-\tau} + 27905245.2e^{-4\tau} - 6.4(84105\tau - 92242)e^{-9\tau} + 79388.1e^{-16\tau} + 98e^{-36\tau}\Big) \\ &- \frac{\cos(2\phi_0)}{28291032}\Big(14553(21396\tau - 41812.87) + 314344.8(854\tau + 1986.9)e^{-\tau} - 80.19(221648\tau \\ &+ 203425.3)e^{-4\tau} - 8.8(37724.4\tau - 24587.89)e^{-9\tau} + 25776.63e^{-16\tau} + 1422.36e^{-25\tau} + 116.375e^{-36\tau}\Big) \\ &+ \frac{\cos(4\phi_0)}{1287241956}\Big(27027(30135\tau - 50390.53) + 119189.07(4296\tau + 1143.67)e^{-\tau} + 4580265.69e^{-4\tau} \\ &+ 7.15(999432\tau - 779845.1)e^{-9\tau} - 21.06(128898\tau + 27634.9)e^{-16\tau} + 340798.185e^{-25\tau}\end{aligned}$$

$$+ 10718.75e^{-36\tau} + 1318.275e^{-49\tau}\Big)$$
$$- \frac{\cos(6\phi_0)}{3895779888}\Big(122694(196\tau - 70.67) + 1082161.08e^{-\tau} + 8541342.81e^{-4\tau} + 8179.6(112\tau$$
$$- 130.1)e^{-9\tau} + 563165.46e^{-16\tau} - 565994.52e^{-25\tau} - 49(1144\tau - 1918.79)e^{-36\tau} + 20255.4e^{-49\tau}\Big)$$
$$+ \frac{\cos(8\phi_0)}{217945728}\Big(24277.11 - 31231.2e^{-\tau} + 7207.2e^{-4\tau} - 2955.68e^{-9\tau} + 4204.2e^{-16\tau}$$
$$- 1515.36e^{-25\tau} + 308e^{-36\tau} - 491.04e^{-49\tau} + 196.77e^{-64\tau}\Big) \tag{S15}$$

with $L = \overline{v}_1/D_\mathrm{R}$ and $\tau = D_\mathrm{R}t$. In the case of a propulsion velocity with four-fold symmetry $\mathbf{v}_2(\phi) = 2\overline{v}_2 \sin^2(2\phi)\,\hat{\mathbf{u}}(\phi)$, with non-zero Fourier-coefficient vectors $\mathbf{c}_{-5} = -(1,\mathrm{i})/4$, $\mathbf{c}_{-3} = (-1,\mathrm{i})/4$, $\mathbf{c}_{-1} = (-1,\mathrm{i})/2$, $\mathbf{c}_1 = (1,-\mathrm{i})/2$, $\mathbf{c}_3 = -(1,\mathrm{i})/4$, and $\mathbf{c}_5 = (-1,\mathrm{i})/4$, one finds

$$\frac{\langle \Delta\mathbf{r}_\mathrm{A}(t)\rangle}{L} = \left(1 - e^{-\tau}\right)\begin{pmatrix}\cos(\phi_0)\\ \sin(\phi_0)\end{pmatrix} - \frac{1}{18}\left(1 - e^{-9\tau}\right)\begin{pmatrix}\cos(3\phi_0)\\ -\sin(3\phi_0)\end{pmatrix} - \frac{1}{50}\left(1 - e^{-25\tau}\right)\begin{pmatrix}\cos(5\phi_0)\\ \sin(5\phi_0)\end{pmatrix}, \tag{S16}$$

$$\frac{\langle \Delta\mathbf{r}^2_\mathrm{A}(t)\rangle}{L^2} = \frac{1}{101250}\left(210150\tau - 203206 + 202500e^{-\tau} + 625e^{-9\tau} + 81e^{-25\tau}\right)$$
$$- \frac{\cos(4\phi_0)}{6300}\left(847 - 840e^{-\tau} - 100e^{-9\tau} + 65e^{-16\tau} + 28e^{-25\tau}\right)$$
$$+ \frac{\cos(8\phi_0)}{2059200}\left(2431 - 2080e^{-9\tau} - 1056e^{-25\tau} + 705e^{-64\tau}\right), \tag{S17}$$

$$\frac{\langle \Delta\mathbf{r}^4_\mathrm{A}(t)\rangle}{L^4} = \frac{1}{473337256392}\Big(2705.4027\big(1507431168\tau^2 - 5233851943.2\tau + 7368029142.0341\big)$$
$$- 858661689.6(6657\tau + 23236)e^{-\tau} + 18488059504.2e^{-4\tau} - 135.2(12871089\tau + 1792537.7)e^{-9\tau}$$
$$+ 100773489.96e^{-16\tau} - 3.73248(17191424.25\tau - 5307384.493)e^{-25\tau} + 10678232.89e^{-36\tau}$$
$$+ 110963.93765625e^{-64\tau} + 4207.44227904e^{-100\tau}\Big)$$
$$- \frac{\cos(4\phi_0)}{29728209352842}\Big(20805.83505(1594853568\tau - 2813134015.1) + 898812074.16(26628\tau$$
$$+ 65452.9)e^{-\tau} - 2689320626.8929e^{-4\tau} + 10917.4(25742178\tau + 588955.9)e^{-9\tau}$$
$$- 302.328(353017665\tau + 138167563)e^{-16\tau} - 65.1168(343828485\tau - 31369636.51)e^{-25\tau}$$
$$+ 1905187479.104e^{-36\tau} + 32724549.585e^{-49\tau} + 21910524.654375e^{-64\tau} + 13975832.871e^{-81\tau}$$
$$+ 3112728.130512e^{-100\tau}\Big)$$
$$+ \frac{\cos(8\phi_0)}{22558338586688831441}\Big(154412.13645(143187946902\tau - 107200347827.9)$$
$$+ 14390958251825349.48e^{-\tau} + 1820467586121508.467e^{-4\tau} + 6589810.87375(205937424\tau$$
$$+ 56996291.3)e^{-9\tau} + 13520156814211.905e^{-16\tau} + 712671.399(275062788\tau - 12848345.233)e^{-25\tau}$$
$$- 25027863332221.3925e^{-36\tau} - 10926088510221.027e^{-49\tau} - 2.32875(15961369498074\tau$$
$$+ 4924072925496.7)e^{-64\tau} + 8109806453743.995e^{-81\tau} + 874623947689.664172e^{-100\tau}$$

$$+ 72681246322.059375e^{-121\tau} + 14384547897.773625e^{-169\tau}\Big)$$
$$- \frac{\cos(12\phi_0)}{781427217274704}\Big(57715889002.165 - 64186495813.44e^{-\tau} + 4134535541.136e^{-4\tau}$$
$$- 1797741837.892e^{-9\tau} + 2877730703.3475e^{-16\tau} + 706117054.5e^{-25\tau} + 1193818065.44e^{-36\tau}$$
$$- 298802203.128e^{-49\tau} + 128580438.987e^{-64\tau} - 379027122.76e^{-81\tau} - 90311261.04e^{-100\tau}$$
$$- 124790292.9e^{-121\tau} + 78641802.3677e^{-144\tau} + 41855923.2168e^{-169\tau}\Big)$$
$$+ \frac{\cos(16\phi_0)}{3836848982174208}\Big(459813765.7869 - 523542493.76e^{-9\tau} - 178637472.4992e^{-25\tau}$$
$$+ 105544799.36e^{-36\tau} + 185188888.17e^{-64\tau} + 23763464.5248e^{-100\tau} - 52195257.92e^{-121\tau}$$
$$- 29527988.16e^{-169\tau} + 9592294.4975e^{-256\tau}\Big) \qquad \text{(S18)}$$

with $L = \overline{v}_2/D_\mathrm{R}$ and $\tau = D_\mathrm{R}t$.

Emergence of the quartic intermediate regime

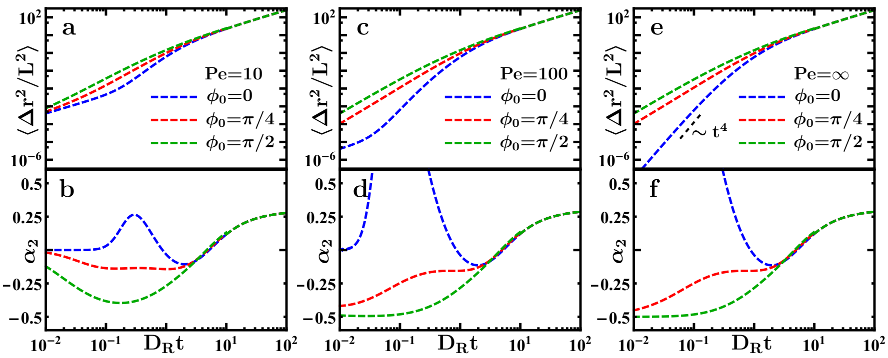

Figure S2: Theoretical results for a propulsion velocity with two-fold symmetry. **a-f** The mean-square displacement $\langle\Delta\mathbf{r}^2(t)\rangle$ as well as the non-Gaussian parameter $\alpha_2(t)$ are shown for initial orientations $\phi_0 = 0$ (blue), $\phi_0 = \pi/4$ (red), and $\phi_0 = \pi/2$ (green) and for different Péclet numbers Pe = 10, Pe = 100, and Pe = ∞. A reference slope indicates the quartic ($\nu = 4$) temporal behavior.

P2 Active Brownian motion with memory delay induced by a viscoelastic medium

Reproduced from

A. R. Sprenger, C. Bair, and H. Löwen,
Active Brownian motion with memory delay induced by a viscoelastic medium,
Phys. Rev. E **105**, 044610 (2022),
published by *American Physical Society* [290].

Digital Object Identifier (DOI): doi.org/10.1103/PhysRevE.105.044610

Statement of contribution

A.R.S. and H.L. designed the research. A.R.S. and C.B. developed the theoretical and numerical results. A.R.S. prepared the figures. A.R.S. and H.L. wrote the manuscript. All authors discussed the results.

Copyright and license notice

©American Physical Society.
The American Physical Society (APS) grants any co-author the right to use the article or a portion of the article in a thesis or dissertation without requesting permission from APS, provided the bibliographic citation and the APS copyright credit line are given.

PHYSICAL REVIEW E **105**, 044610 (2022)

Active Brownian motion with memory delay induced by a viscoelastic medium

Alexander R. Sprenger,* Christian Bair, and Hartmut Löwen
Institut für Theoretische Physik II: Weiche Materie, Heinrich-Heine-Universität Düsseldorf, 40225 Düsseldorf, Germany

(Received 9 February 2022; accepted 11 April 2022; published 28 April 2022)

By now active Brownian motion is a well-established model to describe the motion of mesoscopic self-propelled particles in a Newtonian fluid. On the basis of the generalized Langevin equation, we present an analytic framework for active Brownian motion with memory delay assuming time-dependent friction kernels for both translational and orientational degrees of freedom to account for the time-delayed response of a viscoelastic medium. Analytical results are obtained for the orientational correlation function, mean displacement, and mean-square displacement which we evaluate in particular for a Maxwell fluid characterized by a kernel which decays exponentially in time. Further, we identify a memory-induced delay between the effective self-propulsion force and the particle orientation which we quantify in terms of a special dynamical correlation function. In principle, our predictions can be verified for an active colloidal particle in various viscoelastic environments such as a polymer solution.

DOI: 10.1103/PhysRevE.105.044610

I. INTRODUCTION

The physics of active matter is a booming research area exploring nonequilibrium phenomena of self-propelled particles [1,2]. Apart from viscous damping in a fluid medium, fluctuations become important if the particle size is on the mesoscopic colloidal scale. A by now well-established model to describe the persistent random dynamics of a single self-propelled particle is so-called active Brownian motion [1–7]. Here the translational coordinate of the particle is coupled to its self-propulsion direction, which is the orientational degree of freedom establishing basically a persistent random walk. Active Brownian motion assumes an instantaneous friction which is a well-justified assumption for a Newtonian background fluid, or in other terms, there is no memory effect of the medium. However, in many situations, self-propelled or swimming particles are exposed to environments different from a Newtonian fluid [8–19]. Important examples for non-Newtonian backgrounds offered to self-propelled particles are polymer solutions [20–24] and crystalline [25–27] or liquid crystalline [28–36] environments or even biologically relevant backgrounds such as mucus [37,38], dense tissues, [39] or soil [40].

In this paper we use an extended model for active Brownian motion in a viscoelastic medium. In doing so we assume memory effects of the solvent via a friction kernel for both translational and orientational degrees of freedom besides fluctuations. In fact, there are different models for active Brownian motion with memory effects induced by the surrounding medium [41–53] and for passive Brownian motion in a viscoelastic medium [54–59]. Here we include activity explicitly. In contrast to Ref. [46] where an active Ornstein-Uhlenbeck approach was chosen and to Ref. [52] where negative friction was used to achieve activity, we choose our model to recover the established active Brownian motion case for a Newtonian medium as a clear reference state. In particular, the model used here is a special case of that recently proposed by Narinder *et al.* [45], which contains an additional term of translation-rotation coupling between the swim force and the swim torque. We consider here the special case of decoupled effective swim force and swim torque with the benefit that we can solve the stochastic Langevin equations analytically. We evaluate the solution in particular for a Maxwell fluid which is characterized by a kernel that decays exponentially in time and obtain analytical results for the mean displacement, the mean-square displacements, and the orientational correlation function. Further we define a memory delay function which measures the memory-induced delay between the effective driving force and particle orientation. In principle, our predictions can be verified for an active colloidal particle in various viscoelastic environments such as a polymer solution.

The paper is organized as follows. The model is introduced and discussed in Sec. II. In Sec. III general results are listed. The solution is evaluated further for a generalized Maxwell (or Jeffrey) kernel with a memory exponentially decaying in time in Sec. IV. We summarize in Sec. V.

II. MODEL

In our model we consider a colloidal self-propelled particle in two spatial dimensions moving at a constant speed v_0 along its orientation $\hat{\mathbf{n}}(t)$ through a fluid with memory properties. We describe the state of the particle by its position $\mathbf{r}(t)$ and its angle of orientation $\phi(t)$, which denotes the angle between the orientation vector $\hat{\mathbf{n}}(t) = (\cos\phi, \sin\phi)$ and the positive x axis, at the corresponding time t. The time-delayed response of the fluid is incorporated in the model in terms of a translational memory kernel $\Gamma_T(t)$ and a rotational memory kernel

*sprenger@thphy.uni-duesseldorf.de

 ©2022 American Physical Society

$\Gamma_R(t)$ which directly couple to the translation and rotation of the particle, respectively. To further model circle swimming, we also include an effective swim torque which acts on the particle and leads to a circling frequency ω_0. On the basis of the generalized Langevin equation, the overdamped Brownian dynamics of the particle is described by the coupled non-Markovian Langevin equations

$$\int_{-\infty}^{t} \Gamma_T(t-t')[\dot{\mathbf{r}}(t') - v_0\hat{\mathbf{n}}(t')]dt' = \boldsymbol{\xi}(t), \tag{1a}$$

$$\int_{-\infty}^{t} \Gamma_R(t-t')[\dot{\phi}(t') - \omega_0]dt' = \eta(t), \tag{1b}$$

where $\boldsymbol{\xi}(t)$ and $\eta(t)$ denote zero-mean Gaussian colored noise

$$\langle \boldsymbol{\xi}(t)\rangle = 0, \quad \langle \boldsymbol{\xi}(t)\otimes\boldsymbol{\xi}(t')\rangle = \mathbb{I}k_BT\gamma_T(t-t'), \tag{2a}$$

$$\langle \eta(t)\rangle = 0, \quad \langle \eta(t)\eta(t')\rangle = k_BT\gamma_R(t-t'), \tag{2b}$$

with the translational noise correlator $\gamma_T(t)$ and the rotational noise correlator $\gamma_R(t)$. Here $\otimes$ is the dyadic product, $\mathbb{I}$ is the identity matrix, k_BT is the thermal energy, and $\langle\cdots\rangle$ denotes the noise average.

In discussing Eqs. (1a) and (1b), we first suppose we are at zero temperature $T=0$ (no noise). In this case, the velocity is identical to the active propulsion and the particle performs either linear or circular swimming motion. Now we introduce fluctuations or noise in the system that kick the particle out of that particular situation. Then there are two effects: first temporally correlated noise which perturbs the swimming motion and second dissipation incorporated in the memory kernels which lead to a relaxation back to the steady state.

For reasons of generality, we first do not imply any relation between the dissipation and the fluctuations in the system. However, in the case of internal noise, the memory kernels are related to the correlation function of the noise via the second fluctuation-dissipation theorem, i.e., $\Gamma_T(t)=\gamma_T(t)$ and $\Gamma_R(t)=\gamma_R(t)$ [60]. On the other hand, when fluctuation and dissipation come from different sources, the memory kernel and the noise correlator are independent [61,62]. This was explicitly realized in a recent experiment on magnetic active dumbbells where the rotational diffusivity was artificially enhanced with magnetic fields and therefore decoupled from the thermal bath [63].

The memory kernels $\Gamma_T(t)$ and $\Gamma_R(t)$ describe the viscoelastic response of the fluid and can be determined experimentally. Probably most commonly used are microrheological measurements on passive probe particles to extract the functional form of the memory kernel by tracking the particles mean-square displacement [64,65]. Alternatively, the memory kernel can be approximately linked to the shear relaxation modulus of the medium which can be measured with oscillatory shear experiments [66]. Further, we point out that the stochastic process given by Eqs. (1a) and (1b) is defined as stationary by setting the lower limit of the integral equal to $-\infty$ (see Ref. [54] for a detailed discussion on the choice of the lower limit in the memory term).

In Eq. (1a), the effective self-propulsion force is of the form $\mathbf{F}_v(t) = v_0\int_{-\infty}^{t}\Gamma_T(t-t')\hat{\mathbf{n}}(t')dt'$. This choice is not unique but could in principle vary for different systems (for instance, externally actuated or mesoscopic swimmers). In our model, we describe the force-free propulsion of a colloidal microswimmer which sets the fluid around itself in motion and translates in the resulting flow field. As a consequence, the propulsion force is linked to the viscoelastic response of the fluid and the internal active force $\mathbf{F}_v(t)$ lags generally behind the orientation $\hat{\mathbf{n}}(t)$ [45].

Importantly, we remark that Eqs. (1a) and (1b) mark a special case of the model recently proposed by Narinder *et al.* [45] which contains an additional torque proportional to the swim force, proportional to $\hat{\mathbf{n}}(t)\times\mathbf{F}_v(t)$, explaining an increase of rotational diffusion [47] and the onset of circular trajectories [45] for self-propelled Janus particles in a viscoelastic fluid. Here we decouple the swim torque from the swim force with the benefit that we can solve the stochastic Langevin equations analytically.

Finally, the special case of active Brownian motion [67–69] is recovered for instantaneous friction and zero-mean Gaussian white noise

$$\Gamma_T(t) = \gamma_T(t) = 2\gamma_t\delta(t), \tag{3a}$$

$$\Gamma_R(t) = \gamma_R(t) = 2\gamma_r\delta(t), \tag{3b}$$

where γ_t and γ_r are translational and rotational friction coefficients, respectively.

III. GENERAL RESULTS

In this section we present analytic results for the arbitrary memory kernel and noise correlator. By calculating the Fourier transform of Eqs. (1a) and (1b), a solution for the position $\mathbf{r}(t)$ and the orientation angle $\phi(t)$ can be derived as

$$\mathbf{r}(t) = \mathbf{r}(t_0) + v_0\int_{t_0}^{t}\hat{\mathbf{n}}(t')dt' + \int_{-\infty}^{\infty}[\chi_T(t-t') - \chi_T(t_0-t')]\boldsymbol{\xi}(t')dt', \tag{4a}$$

$$\phi(t) = \phi(t_0) + \omega_0(t-t_0) + \int_{-\infty}^{\infty}[\chi_R(t-t') - \chi_R(t_0-t')]\eta(t')dt', \tag{4b}$$

with the inverse Fourier transform of

$$\tilde{\chi}_T(\omega) = [i\omega\tilde{\Gamma}_T^+(\omega)]^{-1}, \quad \Gamma_T^+(t) = \Gamma_T(t)\Theta(t), \tag{5a}$$

$$\tilde{\chi}_R(\omega) = [i\omega\tilde{\Gamma}_R^+(\omega)]^{-1}, \quad \Gamma_R^+(t) = \Gamma_R(t)\Theta(t), \tag{5b}$$

where we used the convention $\tilde{f}(\omega) = \int_{-\infty}^{\infty} f(t)e^{-i\omega t}dt$ for the Fourier transform of a function $f(t)$ and, multiplied with the Heaviside function $f(t)\Theta(t)$, $\tilde{f}^+(\omega)$ yields the one-sided Fourier transform $\int_0^{\infty} f(t)e^{-i\omega t}dt$.

The deterministic solution of Eqs. (1) (at zero temperature $T=0$) is independent of the specific form of the memory kernel and the particle moves on either linear or circular trajectories

$$\mathbf{r}(t) = \begin{cases} \mathbf{r}(0) + v_0 t\,\hat{\mathbf{n}}(0), & \omega_0 = 0 \\ \mathbf{r}(0) + \frac{v_0}{\omega_0}[\hat{\mathbf{n}}_\perp(0) - \hat{\mathbf{n}}_\perp(t)], & \omega_0 \neq 0, \end{cases} \tag{6}$$

with $\hat{\mathbf{n}}_\perp(t) = (-\sin[\phi(0)+\omega_0 t], \cos[\phi(0)+\omega_0 t])^T$. In the presence of noise, the motion of the particle can be characterized in terms of the low-order moments of the stochastic process. Although Eq. (1b) is nonlocal in time (and thus non-Markovian), the transitional probability for an angular displacements $\Delta\phi$ after a time t is still Gaussian and specified by the mean $\mu(t) = \langle \Delta\phi(t)\rangle$ and the variance of the angular displacement $\sigma(t) = \langle \Delta\phi^2(t)\rangle - \langle \Delta\phi(t)\rangle^2$, which are given by

$$\mu(t) = \omega_0 t, \tag{7}$$

$$\sigma(t) = \frac{k_B T}{\pi} \int_{-\infty}^{\infty} (1 - e^{i\omega t})\tilde{\gamma}_R(\omega)\tilde{\chi}_R(\omega)\tilde{\chi}_R(-\omega)d\omega. \tag{8}$$

From that the orientation correlation function $C(t) = \langle \hat{\mathbf{n}}(t) \cdot \hat{\mathbf{n}}(0)\rangle$ can be readily derived and follows from

$$\langle \hat{\mathbf{n}}(t_2) \cdot \hat{\mathbf{n}}(t_1)\rangle = \cos[\mu(|t_2 - t_1|)]e^{-\sigma(|t_2-t_1|)/2}. \tag{9}$$

Due to the stationarity of the underlying stochastic process, the two-time orientational correlation function only depends on the time difference.

The general result for the mean displacement $\langle \Delta\mathbf{r}(t)\rangle = \langle \mathbf{r}(t) - \mathbf{r}(0)\rangle$ is

$$\langle \Delta\mathbf{r}(t)\rangle = v_0 \int_0^t \langle \hat{\mathbf{n}}(t')|\hat{\mathbf{n}}(0)\rangle dt', \tag{10}$$

where the conditional average

$$\langle \hat{\mathbf{n}}(t_2)|\hat{\mathbf{n}}(t_1)\rangle = \hat{\mathbf{P}}[e^{-\sigma(t_2-t_1)/2+i[\phi(t_1)+\mu(t_2-t_1)]}] \tag{11}$$

is the mean orientation at time t_2 under the condition that the particle had the angle $\phi(t_1)$ at previous time t_1 and $\hat{\mathbf{P}}[z] = (\mathrm{Re}(z), \mathrm{Im}(z))^T$ transforms a complex number z into its two-dimensional vector. We remark that the mean displacement is in general independent of the specific choice of the translational memory kernel $\Gamma_T(t)$ and only involves the coupling to the rotational dynamics of the particle.

Next the mean-square displacement is given by

$$\langle \Delta\mathbf{r}^2(t)\rangle = v_0^2 \int_0^t \int_0^t \langle \hat{\mathbf{n}}(t') \cdot \hat{\mathbf{n}}(t'')\rangle dt'' dt' + \frac{2k_B T}{\pi} \int_{-\infty}^{\infty} (1 - e^{i\omega t})\tilde{\gamma}_T(\omega)\tilde{\chi}_T(\omega)\tilde{\chi}_T(-\omega)d\omega. \tag{12}$$

The first term describes the active contribution to mean-square displacement, while the second term contains information on the passive translation caused by the noise [via $\gamma_T(t)$] and influenced by dissipation [via $\Gamma_T(t)$].

The effective self-propulsion force $\mathbf{F}_v(t)$ does not follow instantaneously the orientation of the particle. It rather contains integrated information of past orientations and therefore lags behind $\hat{\mathbf{n}}(t)$. To quantify the delay between the effective self-propulsion force and the particle orientation, we define the memory delay function

$$d(t) = \langle \mathbf{F}_v(t) \cdot \hat{\mathbf{n}}(0)\rangle - \langle \mathbf{F}_v(0) \cdot \hat{\mathbf{n}}(t)\rangle \tag{13}$$

as the average difference between the projection of the active force $\mathbf{F}_v(t)$ on the initial orientation $\hat{\mathbf{n}}(0)$ and the projection of the orientation $\hat{\mathbf{n}}(t)$ and the initial active force $\mathbf{F}_v(0)$. In Newtonian fluids, the effective self-propulsion force is proportional and instantaneous in the orientation, and thus the delay function equates to zero for all time. In a similar manner, the inertial delay function was previously defined for macroscopic active particles which measured the mismatch between the particle velocity $\dot{\mathbf{r}}(t)$ and the particle orientation $\hat{\mathbf{n}}(t)$ [5,70,71]. In our overdamped system, this inertial delay function is always zero since the average velocity is aligned with the orientation. Conversely, for inertial particles subject to instantaneous friction, the memory delay function vanishes.

In the following section we explicitly evaluate the introduced quantities for an exponential memory kernel and discuss the effect of memory on the dynamics of active Brownian particles.

IV. MAXWELL KERNEL

Arguably, the most prominently used memory kernel is given by the generalized Maxwell model (also know as Jeffrey's model) which adds additional exponential memory to the instantaneous friction [72]. For simplicity, we assume internal noise such that the memory kernels are related to the correlation functions of the noise via the second fluctuation-dissipation theorem. Further, the same temporal dependence is adopted for the translation and the rotation, respectively,

$$\Gamma_T(t) = \gamma_T(t) = \gamma_t\left(2\delta(t) + \frac{\Delta}{\tau}e^{-|t|/\tau}\right), \tag{14a}$$

$$\Gamma_R(t) = \gamma_R(t) = \gamma_r\left(2\delta(t) + \frac{\Delta}{\tau}e^{-|t|/\tau}\right). \tag{14b}$$

Here γ_t and γ_r denote reference translational and rotational friction coefficients, respectively. The first term in Eqs. (14a) and (14b) accounts for the instantaneous relaxation, whereas the second term introduces the time-delayed response of the viscoelastic fluid with the relaxation time τ and the memory strength Δ. We remark that for $\Delta = 0$, $\tau \to 0$, or $\tau \to \infty$ the translation and rotational memory kernels become solely instantaneous and we recover the Markovian (no-memory) active Brownian particle model [67–69].

Numerous rheological measurements have shown this Maxwell-like behavior in fluids including polymer solutions [73,74], micelles [75,76], and cytoplasm [77,78]. From the theoretical side, there exist several works which considered the effects of exponential memory on the Brownian motion of passive [56,57] and active colloids [44–46,52].

A. Orientation correlation function

The dynamical orientation correlation function $C(t) = \langle \hat{\mathbf{n}}(t) \cdot \hat{\mathbf{n}}(0)\rangle$ has a double-exponential structure

$$C(t) = \cos(\omega_0 t) \times \exp\left[-\frac{D_r}{1+\Delta}\left(t + \frac{\tau\Delta}{1+\Delta}(1 - e^{-(1+\Delta)t/\tau})\right)\right], \tag{15}$$

with the short-time rotational diffusion coefficient $D_r = k_B T/\gamma_r$. Equation (15) simplifies to a single-exponential decay for either short relaxation times τ or long ones

$$C(t) \sim \begin{cases} \cos(\omega_0 t)\, e^{-D_r t}, & D_r\tau \gg 1+\Delta \\ \cos(\omega_0 t)\, e^{-[D_r/(1+\Delta)]t}, & D_r\tau \ll 1+\Delta. \end{cases} \tag{16}$$

These Markovian (no-memory) extreme cases are shown in orange ($\tau \to 0$) and black ($\tau \to \infty$) in Fig. 1, where we plot-

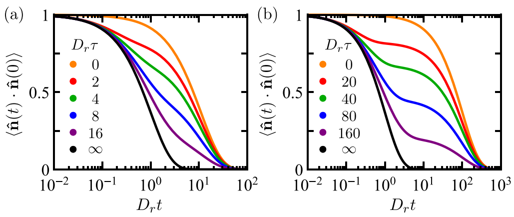

FIG. 1. Orientation correlation $\langle \hat{\mathbf{n}}(t) \cdot \hat{\mathbf{n}}(0) \rangle$ as a function of $D_r t$ for different reduced relaxation times $D_r\tau$, obtained with $\omega_0 = 0$ and (a) $\Delta = 10$ and (b) $\Delta = 100$. For $D_r\tau \to 0$ and $D_r\tau \to \infty$, the orientation decorrelates single exponentially. For in-between values, we find partial decorrelations at separated timescales.

ted the orientation correlation for sufficiently high memory strength Δ and various values of $D_r\tau$. We note that memory effects only occur when

$$D_r\tau \simeq 1 + \Delta. \tag{17}$$

In this case, we first see a partial decorrelation at time $1/D_r$ and a final decorrelation at a later time $(1 + \Delta)/D_r$ (see Fig. 1).

A double-exponential structure for the orientation correlation was previously reported by Ghosch *et al.* [44] and for inertial active particles [70,79]. Compared to these systems, we find different behavior for short times where the exponent is linear in time

$$C(t) = \cos(\omega_0 t)\, e^{-D_r[t-(\Delta/2\tau)t^2 + O(t^3)]}. \tag{18}$$

One characterizing quantity of active particles is the persistence time $\tau_p = \int_0^\infty C(t)dt$, which is the average time the particle holds its orientation. Here the persistence time is evaluated as

$$\tau_p = \frac{\tau}{1+\Delta}\,\mathrm{Re}[S^{-\Omega} e^S \Gamma(\Omega, 0, S)], \tag{19}$$

with

$$S = \frac{-\Delta\tau D_r}{(1+\Delta)^2}, \quad \Omega = \frac{\tau}{1+\Delta}\left(\frac{D_r}{1+\Delta} - i\omega_0\right), \tag{20}$$

and the incomplete Gamma function $\Gamma(x, z_0, z_1) = \int_{z_0}^{z_1} t^{x-1} e^{-t} dt$. Obvious from Eq. (16), the persistence time simplifies for short or long relaxation times τ to

$$\tau_p \sim \begin{cases} \frac{D_r}{D_r^2+\omega_0^2}, & D_r\tau \gg 1+\Delta \\ \frac{D_r(1+\Delta)}{D_r^2+\omega_0^2(1+\Delta)^2}, & D_r\tau \ll 1+\Delta, \end{cases} \tag{21}$$

representing the known result for active Brownian particles in simple Newtonian fluids [68,69,80].

B. Mean displacement

Next we address the mean displacement $\langle \Delta\mathbf{r}(t) \rangle$ for a given initial orientation $\phi(0)$ at $t = 0$,

$$\langle \Delta\mathbf{r}(t) \rangle = \frac{v_0\tau}{1+\Delta}\hat{\mathbf{P}}[S^{-\Omega} e^S \Gamma(\Omega, Se^{-(1+\Delta)t/\tau}, S) e^{i\phi(0)}], \tag{22}$$

with the operator $\hat{\mathbf{P}}[z] = (\mathrm{Re}(z), \mathrm{Im}(z))^T$. The mean displacement increases linearly for short times $\langle \Delta\mathbf{r}(t) \rangle = v_0 t \hat{\mathbf{n}}(0) + O(t^2)$ and saturates to a finite persistence length

$$\lim_{t\to\infty} \langle \Delta\mathbf{r}(t) \rangle = \frac{v_0\tau}{1+\Delta}\hat{\mathbf{P}}[S^{-\Omega} e^S \Gamma(\Omega, 0, S) e^{i\phi_0}]. \tag{23}$$

We again mention that the mean trajectory is independent of the translational memory kernel noise [see Eq. (14a)] and only involves the coupling to the rotational dynamics of the particle [see Eq. (10)].

In Fig. 2 we show the mean trajectory of a circle swimmer ($\omega_0 \neq 0$) for different values of $D_r\tau$. For very long relaxation times, the particle decorrelates before additional memory can prolong the persistence. Consequently, the mean trajectory displays a *spira mirabilis* known for active particles in Newtonian fluids (see the black curve in Fig. 2). When the relaxation time τ becomes comparable to $(1 + \Delta)/D_r$, the rotational friction gets enhanced at later times and circular motion gets more stable against noise perturbation (see the purple and blue curves in Fig. 2). Upon further decreasing the relaxation time (see the green and red curves in Fig. 2) the mean displacement approaches again the form of a *spira mirabilis* with a decreased rotational diffusion coefficient $D_r/(1 + \Delta)$ (see the orange curve in Fig. 2).

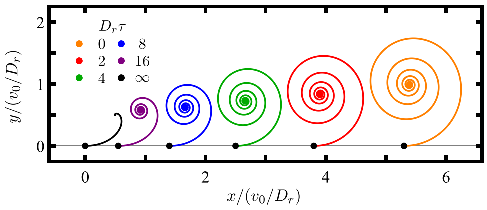

FIG. 2. Mean displacement $\langle \Delta\mathbf{r}(t) \rangle$ in the xy plane for $\Delta = 10$, $\omega_0 = D_r$, and several values of $D_r\tau$. The initial orientation is set along the x axis and the starting point at $t = 0$ is denoted by a black dot. For $D_r\tau \to 0$ and $D_r\tau \to \infty$, the trajectory displays a perfect *spira mirabilis*.

C. Mean-square displacement

The mean-square displacement can be calculated as

$$\langle \Delta\mathbf{r}^2(t) \rangle = 4D_L t + \frac{4\Delta\tau D_t}{(1+\Delta)^2}(1 - e^{-(1+\Delta)t/\tau}) - \frac{2v_0^2\tau^2}{(1+\Delta)^2}[F(0) - F(t)], \tag{24}$$

with the long-time diffusion coefficient

$$D_L = \frac{D_t}{1+\Delta} + \frac{v_0^2\,\tau}{2(1+\Delta)}\,\mathrm{Re}[S^{-\Omega} e^S \Gamma(\Omega, 0, S)] \tag{25}$$

and

$$F(t) = \mathrm{Re}\left\{\frac{e^S}{\Omega^2}\,{}_2F_2\left[\begin{matrix}\Omega,\ \Omega \\ \Omega+1,\ \Omega+1\end{matrix}\ ; -Se^{-(1+\Delta)t/\tau}\right] \times e^{-(1+\Delta)\Omega t/\tau}\right\}, \tag{26}$$

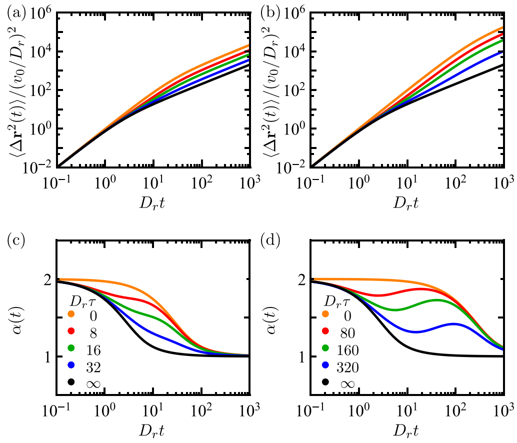

FIG. 3. Mean-square displacement $\langle \Delta \mathbf{r}^2(t) \rangle$ and the corresponding dynamic exponent $\alpha(t)$ as a function of time t for several values of $D_r\tau$, obtained with $\omega_0 = 0$ and (a) and (c) $\Delta = 10$ and (b) and (d) $\Delta = 100$.

where ${}_qF_p$ represents the generalized hypergeometric function. In the passive case ($v_0 = 0$), the particle starts in a diffusive regime $\langle \Delta \mathbf{r}^2(t) \rangle = 4D_t t + O(t^2)$, characterized by the short-time translational diffusion coefficient $D_t = k_B T/\gamma_t$, and then enters a subdiffusive regime which leads to long-time diffusion with a reduced translational diffusivity $D_t/(1 + \Delta)$. Considering the active contribution ($D_t = 0$), the particle moves ballistic for short times $\sim v_0^2 t^2$ and then undergoes a superdiffusive (or subballistic) transition towards a long-time diffusive regime proportional to the speed squared and the persistence time $\sim v_0^2 \tau_p t/2$. In Fig. 3 we plot the active contribution of the mean-square displacement ($D_t = 0$) for two values of the memory strength Δ over the range of relevant values of $D_r\tau$ and also show the corresponding dynamic exponent given by the logarithmic derivative

$$\alpha(t) = \frac{d \log[\langle \Delta \mathbf{r}^2(t) \rangle]}{d \log(t)}. \tag{27}$$

The dynamic exponent $\alpha(t)$ is able to resolve the relevant timescales of the system more clearly: If, for example, the mean-square displacement follows a power law $\langle \Delta \mathbf{r}^2(t) \rangle \sim t^\alpha$, $\alpha(t)$ is equal to the power-law exponent α. For the Markovian extreme cases ($\tau \to 0$ and $\tau \to \infty$), we find a clean transition from a ballistic regime ($\alpha = 2$) to a diffusive one ($\alpha = 1$). For in-between values of $D_r\tau$, the dynamic exponent $\alpha(t)$ starts decreasing when the first decorrelation happens at times $t \gtrsim 1/D_r$. If the memory strength Δ is sufficiently high [see Fig. 3(d)], the dynamic exponent is increasing again at times $t \gtrsim \tau/(1 + \Delta)$. This event coincides with the persistent plateau in the orientation correlation function [see Fig. 1(d)]. Finally, the particle transitions to a diffusive regime ($\alpha = 1$) for times $t \gtrsim (1 + \Delta)/D_r$.

The long-time diffusion coefficient D_L [see Eq. (25)] depends nontrivially on the parameter of the model. In Fig. 4 we show the long-time diffusion coefficient as a function of the memory strength Δ and various values of $D_r\tau$. For a vanishing circling frequency ($\omega_0 = 0$), the long-time diffusion coefficient is monotonically increasing as a function of the memory strength Δ and monotonically decreasing as a function of the relaxation time τ [see Fig. 4(a)]. However, for a finite relaxation time, the asymptotic behavior of the long-time diffusion coefficient for high Δ is given by $D_L \sim v_0^2 \Delta / 2D_r$. For low circling frequency [see Fig. 4(b)], the long-time diffusion behaves nonmonotonically in Δ. The optimal memory Δ_{opt} is increasing as a function of relaxation time τ, while the corresponding maximal value $D_L(\Delta_{\mathrm{opt}})$ is decreasing. At higher circling frequency [see Fig. 4(c)], the long-time diffusion decreases immediately as a function of Δ, $D_L \sim v_0^2 D_r / 2\Delta\omega_0^2$.

D. Delay function

In Eq. (13) we defined the memory delay function $d(t)$ to quantify the memory-induced mismatch between the effective self-propulsion force $\mathbf{F}_v(t)$ and the particle orientation $\hat{\mathbf{n}}(t)$. Evaluated for the Maxwell kernel, we find

$$\begin{aligned} d(t) = \gamma_t v_0 \frac{\Delta e^S}{1 + \Delta} \mathrm{Re}\{ & S^{-\Omega_+} [\Gamma(\Omega_+, 0, S) e^{-t/\tau} \\ & - \Gamma(\Omega_+, 0, S e^{-(1+\Delta)t/\tau}) e^{t/\tau}] \\ & + S^{-\Omega_-} \Gamma(\Omega_-, S e^{-(1+\Delta)t/\tau}, S) e^{-t/\tau} \}, \end{aligned} \tag{28}$$

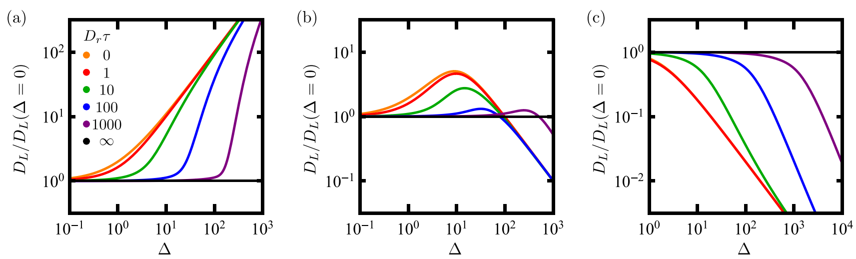

FIG. 4. Long-time diffusion coefficient D_L as a function of the memory strength Δ for several values of $D_r\tau$ and different circling frequencies (a) $\omega_0 = 0$, (b) $\omega_0 = 0.1D_r$, and (c) $\omega_0 = D_r$. The translational diffusion coefficient was set to zero, $D_t = 0$.

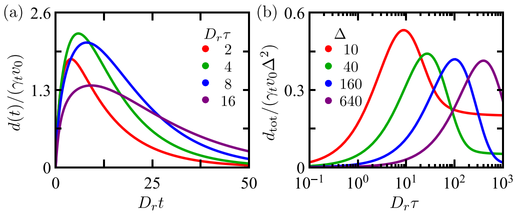

FIG. 5. (a) Memory delay function $d(t)$ as a function of $D_r t$ for different reduced relaxation times $D_r\tau$, $\Delta = 10$, and $\omega_0 = 0$. (b) Total delay $d_{\rm tot}$ weighted with Δ^2 as a function of the reduced relaxation time $D_r\tau$ for different values of the memory strength Δ and $\omega_0 = 0$.

with

$$\Omega_\pm = \frac{\tau}{1+\Delta}\left(\frac{D_r}{1+\Delta} \pm \frac{1}{\tau} - i\omega_0\right). \qquad (29)$$

The memory delay function is constructed such that it vanishes when the translational memory function responds instantaneously [meaning $\Gamma_T(t) = 2\gamma_t\delta(t)$]. Thus, consistent with previous considerations, $d(t)$ vanishes for the Markovian limits of the model $\Delta = 0$, $\tau \to 0$, and $\tau \to \infty$. In Fig. 5(a) we show the delay function $d(t)$ as a function of time for in-between values of $D_r\tau$. The delay function is always positive for a linear swimmer ($\omega_0 = 0$), starts at zero, has a positive peak $d(t_{\rm opt})$ after a typical delay time $t_{\rm opt}$, and decorrelates to zero for long times. Both the peak value and the typical delay time depend nonmonotonically on the relaxation time τ and show a single maximum around $D_r\tau \simeq 1 + \Delta$ [recalling the condition for memory effects (17)].

We define the total delay of the particle as $d_{\rm tot} = \int_0^\infty d(t)dt$, which yields

$$d_{\rm tot} = \gamma_t v_0 \tau \frac{2\Delta e^S}{1+\Delta} \mathrm{Re}[S^{-\Omega_+}\Gamma(\Omega_+, 0, S)] \qquad (30)$$

and is shown in Fig. 5(b) as a function of the reduced relaxation time $D_r\tau$. Similar to the peak value $d(t_{\rm opt})$, the total delay becomes maximal around $D_r\tau \simeq 1 + \Delta$. For representative reasons, we decided to weight the total memory by the memory strength square, i.e., $d_{\rm tot}/\gamma_t v_0 \Delta^2$ in Fig. 5(b). In that way, we find that $d_{\rm tot} \sim \Delta^2$ around the relevant values of $D_r\tau$ [see Eq. (17)]. Although $d(t) \to 0$ for $\tau \to \infty$, the total memory saturates to the nonzero value $d_{\rm tot} \sim 2\Delta\gamma_t v_0$ for $\tau \to \infty$ (the limit and integral do not commute in this case).

V. CONCLUSION

In this work we studied a self-propelled colloid in a viscoelastic medium. The particle itself was modeled in terms of non-Markovian Langevin equations which included memory effects in the particle friction to account for the viscoelastic background. Analytical solutions were presented. This model may serve as a benchmark and simple framework to evaluate and interpret experimental or simulation data for particle trajectories obtained in realistic and more complex environments [50]. In particular, the nature of the memory kernel can in principle be determined by fitting the experimental correlations to the solutions of our model corresponding to microrheology [81–85].

We evaluated our general results explicitly for the Maxwell kernel, which adds exponentially decaying memory to the standard instantaneous Stokes friction. In particular, we found a double-exponential structure for the orientational correlation function exhibiting partial decorrelation at short times and the existence of persistent plateaus for intermediate times. In order for memory effects to occur, we identified a relation between the short-time rotational diffusion coefficient, the memory strength, and the corresponding relaxation time [see Eq. (17)] and discussed the influence of memory at intermediate and long timescales for the mean and mean-square displacement of the particle. Finally, we quantified the delay between effective self-propulsion force and the particle orientation in terms of a defined memory delay function.

Our model can be extended to higher spatial dimensions [69], to harmonic confinement [86–89], to external fields [90,91], and to include inertia [5,70,71,92–95] where an analytical solution seems to be in reach as well. Moreover, different combinations of friction and memory kernel as well as colored noise can be considered for future work [96–100], for instance, Mittag-Leffler noise [101,102] or power-law memory [103,104]. Finally, the collective behavior of many interacting active particles in a viscoelastic medium [105–111] needs to be explored more and will be an important area of future research.

ACKNOWLEDGMENTS

This work was supported by the SPP 2265 within Project No. LO 418/25-1.

[1] C. Bechinger, R. Di Leonardo, H. Löwen, C. Reichhardt, G. Volpe, and G. Volpe, Rev. Mod. Phys. **88**, 045006 (2016).
[2] G. Gompper, R. G. Winkler, T. Speck, A. Solon, C. Nardini, F. Peruani, H. Löwen, R. Golestanian, U. B. Kaupp, L. Alvarez, T. Kiorboe, E. Lauga, W. C. K. Poon, A. DeSimone, S. Muiños-Landin, A. Fischer, N. A. Söker, F. Cichos, K. Raymond, P. Gaspard *et al.*, J. Phys.: Condens. Matter **32**, 193001 (2020).
[3] P. Romanczuk, M. Bär, W. Ebeling, B. Lindner, and L. Schimansky-Geier, Eur. Phys. J. Spec. Top. **202**, 1 (2012).
[4] A. Callegari and G. Volpe, in *Flowing Matter*, edited by F. Toschi and M. Sega (Springer, Cham, 2019), pp. 211–238.
[5] H. Löwen, J. Chem. Phys. **152**, 040901 (2020).
[6] L. Hecht, J. C. Ureña, and B. Liebchen, An introduction to modeling approaches of active matter,arXiv:2102.13007.
[7] B. Liebchen and A. K. Mukhopadhyay, Interactions in active colloids, J. Phys.: Condens. Matter **34**, 083002 (2022).
[8] T. Qiu, T.-C. Lee, A. G. Mark, K. I. Morozov, R. Münster, O. Mierka, S. Turek, A. M. Leshansky, and P. Fischer, Nat. Commun. **5**, 5119 (2014).

[9] H. C. Fu, T. R. Powers, and C. W. Wolgemuth, Phys. Rev. Lett. **99**, 258101 (2007).
[10] X. N. Shen and P. E. Arratia, Phys. Rev. Lett. **106**, 208101 (2011).
[11] B. Jakobsen, K. Niss, C. Maggi, N. B. Olsen, T. Christensen, and J. C. Dyre, J. Non-Cryst. Solids **357**, 267 (2011).
[12] D. A. Gagnon, N. C. Keim, and P. E. Arratia, J. Fluid Mech. **758**, R3 (2014).
[13] B. Liu, T. R. Powers, and K. S. Breuer, Proc. Natl. Acad. Sci. USA **108**, 19516 (2011).
[14] J. Schwarz-Linek, C. Valeriani, A. Cacciuto, M. E. Cates, D. Marenduzzo, A. N. Morozov, and W. C. K. Poon, Proc. Natl. Acad. Sci. USA **109**, 4052 (2012).
[15] L. Zhu, E. Lauga, and L. Brandt, J. Fluid Mech. **726**, 285 (2013).
[16] E. E. Riley and E. Lauga, Europhys. Lett. **108**, 34003 (2014).
[17] G. J. Elfring and E. Lauga, in *Complex Fluids in Biological Systems: Experiment, Theory, and Computation*, edited by S. E. Spagnolie (Springer, New York, 2015), pp. 283–317.
[18] C. Datt, G. Natale, S. G. Hatzikiriakos, and G. J. Elfring, J. Fluid Mech. **823**, 675 (2017).
[19] G. Li, E. Lauga, and A. M. Ardekani, J. Non-Newtonian Fluid Mech. **297**, 104655 (2021).
[20] V. A. Martinez, J. Schwarz-Linek, M. Reufer, L. G. Wilson, A. N. Morozov, and W. C. K. Poon, Proc. Natl. Acad. Sci. USA **111**, 17771 (2014).
[21] A. E. Patteson, A. Gopinath, M. Goulian, and P. E. Arratia, Sci. Rep. **5**, 15761 (2015).
[22] A. Zöttl and J. M. Yeomans, Nat. Phys. **15**, 554 (2019).
[23] K. Qi, E. Westphal, G. Gompper, and R. G. Winkler, Phys. Rev. Lett. **124**, 068001 (2020).
[24] S. Liu, S. Shankar, M. C. Marchetti, and Y. Wu, Nature (London) **590**, 80 (2021).
[25] M. S. Krieger, S. E. Spagnolie, and T. R. Powers, Phys. Rev. E **90**, 052503 (2014).
[26] B. van der Meer, L. Filion, and M. Dijkstra, Soft Matter **12**, 3406 (2016).
[27] A. T. Brown, I. D. Vladescu, A. Dawson, T. Vissers, J. Schwarz-Linek, J. S. Lintuvuori, and W. C. K. Poon, Soft Matter **12**, 131 (2016).
[28] S. Zhou, A. Sokolov, O. D. Lavrentovich, and I. S. Aranson, Proc. Natl. Acad. Sci. USA **111**, 1265 (2014).
[29] O. D. Lavrentovich, Curr. Opin. Colloid Interface Sci. **21**, 97 (2016).
[30] P. C. Mushenheim, R. R. Trivedi, H. H. Tuson, D. B. Weibel, and N. L. Abbott, Soft Matter **10**, 88 (2014).
[31] S. Hernàndez-Navarro, P. Tierno, J. Ignés-Mullol, and F. Sagués, IEEE Trans. NanoBiosci. **14**, 267 (2015).
[32] M. S. Krieger, M. A. Dias, and T. R. Powers, Eur. Phys. J. E **38**, 94 (2015).
[33] M. S. Krieger, S. E. Spagnolie, and T. Powers, Soft Matter **11**, 9115 (2015).
[34] R. R. Trivedi, R. Maeda, N. L. Abbott, S. E. Spagnolie, and D. B. Weibel, Soft Matter **11**, 8404 (2015).
[35] J. Toner, H. Löwen, and H. H. Wensink, Phys. Rev. E **93**, 062610 (2016).
[36] C. Ferreiro-Córdova, J. Toner, H. Löwen, and H. H. Wensink, Phys. Rev. E **97**, 062606 (2018).
[37] M. A. Sleigh, J. R. Blake, and N. Liron, Am. Rev. Resp. Dis. **137**, 726 (1988).
[38] S. Suarez and A. A. Pacey, Hum. Reprod. Update **12**, 23 (2006).
[39] C. Josenhans and S. Suerbaum, Int. J. Med. Microbiol. **291**, 605 (2002).
[40] H. R. Wallace, Annu. Rev. Phytopathol. **6**, 91 (1968).
[41] C.-T. Hu, J.-C. Wu, and B.-Q. Ai, J. Stat. Mech. (2017) 053206.
[42] F. Peruani and L. G. Morelli, Phys. Rev. Lett. **99**, 010602 (2007).
[43] D. Debnath, P. K. Ghosh, Y. Li, F. Marchesoni, and B. Li, Soft Matter **12**, 2017 (2016).
[44] P. K. Ghosh, Y. Li, G. Marchegiani, and F. Marchesoni, J. Chem. Phys. **143**, 211101 (2015).
[45] N. Narinder, C. Bechinger, and J. R. Gomez-Solano, Phys. Rev. Lett. **121**, 078003 (2018).
[46] F. J. Sevilla, R. F. Rodríguez, and J. R. Gomez-Solano, Phys. Rev. E **100**, 032123 (2019).
[47] J. R. Gomez-Solano, A. Blokhuis, and C. Bechinger, Phys. Rev. Lett. **116**, 138301 (2016).
[48] C. Lozano, J. R. Gomez-Solano, and C. Bechinger, New J. Phys. **20**, 015008 (2018).
[49] C. Lozano, J. R. Gomez-Solano, and C. Bechinger, Nat. Mater. **18**, 1118 (2019).
[50] S. Saad and G. Natale, Soft Matter **15**, 9909 (2019).
[51] N. Narinder, J. R. Gomez-Solano, and C. Bechinger, New J. Phys. **21**, 093058 (2019).
[52] B. G. Mitterwallner, L. Lavacchi, and R. R. Netz, Eur. Phys. J. E **43**, 67 (2020).
[53] M. Muhsin, M. Sahoo, and A. Saha, Phys. Rev. E **104**, 034613 (2021).
[54] T. Indei, J. D. Schieber, A. Córdoba, and E. Pilyugina, Phys. Rev. E **85**, 021504 (2012).
[55] J. M. Brader, J. Phys.: Condens. Matter **22**, 363101 (2010).
[56] M. Grimm, S. Jeney, and T. Franosch, Soft Matter **7**, 2076 (2011).
[57] Y. L. Raikher, V. V. Rusakov, and R. Perzynski, Soft Matter **9**, 10857 (2013).
[58] J. Berner, B. Müller, J. R. Gomez-Solano, M. Krüger, and C. Bechinger, Nat. Commun. **9**, 999 (2018).
[59] T. J. Doerries, S. A. M. Loos, and S. H. L. Klapp, J. Stat. Mech. (2021) 033202.
[60] R. Kubo, M. Toda, and N. Hashitsume, in *Statistical Physics II: Nonequilibrium Statistical Mechanics*, edited by P. Fulde, Springer Series in Solid-State Sciences Vol. 31 (Springer, Berlin, 1985), pp. 146–202.
[61] K. G. Wang and M. Tokuyama, Physica A **265**, 341 (1999).
[62] M. A. Despósito and A. D. Viñales, Phys. Rev. E **77**, 031123 (2008).
[63] A. R. Sprenger, M. A. Fernandez-Rodriguez, L. Alvarez, L. Isa, R. Wittkowski, and H. Löwen, Langmuir **36**, 7066 (2020).
[64] J. H. van Zanten and K. P. Rufener, Phys. Rev. E **62**, 5389 (2000).
[65] J. van der Gucht, N. A. M. Besseling, W. Knoben, L. Bouteiller, and M. A. Cohen Stuart, Phys. Rev. E **67**, 051106 (2003).
[66] T. G. Mason and D. A. Weitz, Phys. Rev. Lett. **74**, 1250 (1995).
[67] J. R. Howse, R. A. L. Jones, A. J. Ryan, T. Gough, R. Vafabakhsh, and R. Golestanian, Phys. Rev. Lett. **99**, 048102 (2007).

[68] S. van Teeffelen and H. Löwen, Phys. Rev. E **78**, 020101(R) (2008).
[69] B. ten Hagen, S. van Teeffelen, and H. Löwen, J. Phys.: Condens. Matter **23**, 194119 (2011).
[70] C. Scholz, S. Jahanshahi, A. Ldov, and H. Löwen, Nat. Commun. **9**, 5156 (2018).
[71] A. R. Sprenger, S. Jahanshahi, A. V. Ivlev, and H. Löwen, Phys. Rev. E **103**, 042601 (2021).
[72] S. Paul, B. Roy, and A. Banerjee, J. Phys.: Condens. Matter **30**, 345101 (2018).
[73] T. Annable, R. Buscall, R. Ettelaie, and D. Whittlestone, J. Rheol. **37**, 695 (1993).
[74] J. Sprakel, J. van der Gucht, M. A. Cohen Stuart, and N. A. M. Besseling, Phys. Rev. E **77**, 061502 (2008).
[75] F. Cardinaux, L. Cipelletti, F. Scheffold, and P. Schurtenberger, Europhys. Lett. **57**, 738 (2002).
[76] J. Galvan-Miyoshi, J. Delgado, and R. Castillo, Eur. Phys. J. E **26**, 369 (2008).
[77] C. Wilhelm, F. Gazeau, and J.-C. Bacri, Phys. Rev. E **67**, 061908 (2003).
[78] J. F. Berret, Nat. Commun. **7**, 10134 (2016).
[79] L. Walsh, C. G. Wagner, S. Schlossberg, C. Olson, A. Baskaran, and N. Menon, Soft Matter **13**, 8964 (2017).
[80] C. Kurzthaler and T. Franosch, Soft Matter **13**, 6396 (2017).
[81] T. G. Mason, T. Gisler, K. Kroy, E. Frey, and D. A. Weitz, J. Rheol. **44**, 917 (2000).
[82] I. Gazuz, A. M. Puertas, T. Voigtmann, and M. Fuchs, Phys. Rev. Lett. **102**, 248302 (2009).
[83] S. Heidenreich, S. Hess, and S. H. L. Klapp, Phys. Rev. E **83**, 011907 (2011).
[84] A. M. Puertas and T. Voigtmann, J. Phys.: Condens. Matter **26**, 243101 (2014).
[85] P. Malgaretti, A. M. Puertas, and I. Pagonabarraga, J. Colloid Interface Sci. **608**, 2694 (2022).
[86] M. A. Despósito and A. D. Viñales, Phys. Rev. E **80**, 021111 (2009).
[87] G. Szamel, Phys. Rev. E **90**, 012111 (2014).
[88] S. Jahanshahi, H. Löwen, and B. ten Hagen, Phys. Rev. E **95**, 022606 (2017).
[89] L. Caprini, A. R. Sprenger, H. Löwen, and R. Wittmann, J. Chem. Phys. **156**, 071102 (2022).
[90] B. ten Hagen, F. Kümmel, R. Wittkowski, D. Takagi, H. Löwen, and C. Bechinger, Nat. Commun. **5**, 4829 (2014).
[91] I. Abdoli, H. D. Vuijk, R. Wittmann, J. U. Sommer, J. M. Brader, and A. Sharma, Phys. Rev. Research **2**, 023381 (2020).
[92] H. Löwen, Phys. Rev. E **99**, 062608 (2019).
[93] M. Sandoval, Phys. Rev. E **101**, 012606 (2020).
[94] D. Breoni, M. Schmiedeberg, and H. Löwen, Phys. Rev. E **102**, 062604 (2020).
[95] L. Caprini and U. Marini Bettolo Marconi, J. Chem. Phys. **154**, 024902 (2021).
[96] R. Metzler and J. Klafter, Phys. Rep. **339**, 1 (2000).
[97] I. M. Zaid, J. Dunkel, and J. M. Yeomans, J. R. Soc. Interface **8**, 1314 (2011).
[98] F. Höfling and T. Franosch, Rep. Prog. Phys. **76**, 046602 (2013).
[99] R. Gernert, S. A. M. Loos, K. Lichtner, and S. H. L. Klapp, in *Control of Self-Organizing Nonlinear Systems*, edited by E. Schöll, S. H. L. Klapp, and P. Hövel (Springer, Cham, 2016), pp. 375–392.
[100] S. A. M. Loos, S. M. Hermann, and S. H. L. Klapp, Non-reciprocal hidden degrees of freedom: A unifying perspective on memory, feedback, and activity, arXiv:1910.08372.
[101] A. D. Viñales and M. A. Despósito, Phys. Rev. E **75**, 042102 (2007).
[102] R. Figueiredo Camargo, E. Capelas de Oliveira, and J. Vaz, J. Math. Phys. **50**, 123518 (2009).
[103] W. Min, G. Luo, B. J. Cherayil, S. C. Kou, and X. S. Xie, Phys. Rev. Lett. **94**, 198302 (2005).
[104] J. R. Gomez-Solano and F. J. Sevilla, J. Stat. Mech. (2020) 063213.
[105] Y. Bozorgi and P. T. Underhill, J. Rheol. **57**, 511 (2013).
[106] B. Liebchen and D. Levis, Phys. Rev. Lett. **119**, 058002 (2017).
[107] S. Paliwal, J. Rodenburg, R. van Roij, and M. Dijkstra, New J. Phys. **20**, 015003 (2018).
[108] W. L. Murch and E. S. G. Shaqfeh, Phys. Rev. Fluids **5**, 073301 (2020).
[109] M. te Vrugt, J. Jeggle, and R. Wittkowski, New J. Phys. **23**, 063023 (2021).
[110] V. Holubec, D. Geiss, S. A. M. Loos, K. Kroy, and F. Cichos, Phys. Rev. Lett. **127**, 258001 (2021).
[111] Z. Ma and R. Ni, J. Chem. Phys. **156**, 021102 (2022).

P3 Time-dependent inertia of self-propelled particles: The Langevin rocket

Reproduced from

A. R. Sprenger, S. Jahanshahi, A. V. Ivlev, and H. Löwen,
Time-dependent inertia of self-propelled particles: The Langevin rocket,
Phys. Rev. E **103**, 042601 (2021),
published by *American Physical Society* [291].

Digital Object Identifier (DOI): doi.org/10.1103/PhysRevE.103.042601

Statement of contribution

A.R.S. and S.J. developed the theoretical results. A.R.S. generated the numerical results. A.R.S. prepared the figures. S.J. wrote the initial draft. A.R.S. and H.L. wrote the manuscript. All authors discussed the results.

Copyright and license notice

©American Physical Society.
The American Physical Society (APS) grants any co-author the right to use the article or a portion of the article in a thesis or dissertation without requesting permission from APS, provided the bibliographic citation and the APS copyright credit line are given.

PHYSICAL REVIEW E **103**, 042601 (2021)

Time-dependent inertia of self-propelled particles: The Langevin rocket

Alexander R. Sprenger,[1,*] Soudeh Jahanshahi,[1,*] Alexei V. Ivlev,[2] and Hartmut Löwen[1]
[1]*Institut für Theoretische Physik II: Weiche Materie, Heinrich-Heine-Universität Düsseldorf, D-40225 Düsseldorf, Germany*
[2]*Max-Planck-Institut für Extraterrestrische Physik, 85748 Garching, Germany*

(Received 19 January 2021; accepted 16 March 2021; published 5 April 2021)

Many self-propelled objects are large enough to exhibit inertial effects but still suffer from environmental fluctuations. The corresponding basic equations of motion are governed by active Langevin dynamics, which involve inertia, friction, and stochastic noise for both the translational and orientational degrees of freedom coupled via the self-propulsion along the particle orientation. In this paper, we generalize the active Langevin model to time-dependent parameters and explicitly discuss the effect of time-dependent inertia for achiral and chiral particles. Realizations of this situation are manifold, ranging from minirockets (which are self-propelled by burning their own mass), to dust particles in plasma (which lose mass by evaporating material), to walkers with expiring activity. Here we present analytical solutions for several dynamical correlation functions, such as mean-square displacement and orientational and velocity autocorrelation functions. If the parameters exhibit a slow power law in time, we obtain anomalous superdiffusion with a nontrivial dynamical exponent. Finally, we constitute the "Langevin rocket" model by including orientational fluctuations in the traditional Tsiolkovsky rocket equation. We calculate the mean reach of the Langevin rocket and discuss different mass ejection strategies to maximize it. Our results can be tested in experiments on macroscopic robotic or living particles or in self-propelled mesoscopic objects moving in media of low viscosity, such as complex plasma.

DOI: 10.1103/PhysRevE.103.042601

I. INTRODUCTION

The nonequilibrium dynamics of active Brownian particles—also referred to as microswimmers—are typically described in the overdamped limit, where inertial effects are sufficiently small relative to viscous ones [1–4]. This is an excellent approximation for micron-sized self-propelled particles swimming in a viscous Newtonian liquid such as water [5] at low Reynolds number. The standard model of a single active Brownian particle [1,4,6] involves a translational and an orientational degree of freedom and includes Stokesian friction and fluctuations. These degrees of freedom are coupled via self-propulsion along the particle orientation, which is modeled in a simple averaged way by an internal velocity, sometimes referred to as the particle activity.

However, inertial effects become relevant for larger particle sizes or the motion in gaseous media of lower viscosity. Though highly relevant for swimming and flying organisms as well as for autonomous machines (e.g., flying insect-drones, marine robots, etc.) [7], mesoscale active matter at intermediate Reynolds number has been much less studied. Aiming at a simple description of a single particle first, one basic model is that of *active Langevin motion* [8–11]: it generalizes the common overdamped model of active Brownian motion [1,4,6] toward underdamped dynamics by including the finite particle mass and the moment of inertia in the equations of motion [12–20]. The inertial self-propelled particles may therefore be called "microflyers" (rather than "microswimmers"); sometimes they are also termed "runners," "walkers," or "hoppers" [21–23]. Examples of inanimate inertial self-propelled particles modeled by active Langevin dynamics are manifold. They include a complex plasma consisting of mesoscopic dust particles in a weakly ionized gas [24–29], vibration-driven granular particles [22,30–39], autorotating seeds and fruits [40,41], camphor surfers [42], hexbug crawlers [42], trapped aerosols [43], and minirobots [44–48]. Moreover, there are numerous examples of animals moving at intermediate Reynolds number, such as swimming organisms (nematodes, brine shrimps, whirligig beetles, etc.) [7,49] and flying insects and birds [50–56].

In this paper, we extend the active Langevin model to *time-dependent* parameters such as time-dependent inertia, self-propulsion, and friction. This is a situation frequently encountered in nature and realizable in laboratory experiments on artificial self-propelled objects. Let us mention some examples: scallops move their shells and accelerate by jet propulsion. Therefore, they become smaller in the course of the motion such that their moment of inertia and their friction coefficients become time-dependent. Moving animals typically have a finite energy reservoir [21] implying that their self-propulsion velocity is getting slower as a function of time. The maneuverability of animal motion is provided by changes in the body shape [57,58], which implies a change in the moment of inertia at fixed total mass. Likewise, in the inanimate world, *minirockets*, which are propelled by ejecting mass, are getting lighter as a function of time [59,60]. Similarly, inflated toy balloons [61,62] are self-propelled by jet propulsion and strongly subject to random fluctuations in their orientation; their body size shrinks as a function of time, and so does

[*]A.R.S. and S.J. contributed equally to this work.

 ©2021 American Physical Society

the mass, the moment of inertia, the friction coefficient, and the self-propulsion speed. Granulate hoppers equipped with an internal vibration motor ("hexbugs") [39] will consume energy such that the self-propulsion speed will slowly expire and fade away as a function of time. Robots that pick up or release objects also possess a mass variation [63], and a time-dependent mass can bring about time-dependent friction coefficients [64]. Last but not least, any prescribed time dependence can be programed artificially for man-made robots, artificial walkers, and microswimmers: the self-propulsion speed can be made time-dependent by exposing particles to external optical fields [65], the noise strength can be steered by external fields [66,67], the damping by the solvent viscosity [68,69], or both by the external vibration amplitude and frequency [8,34,70,71].

For the active Langevin model with prescribed time-dependent parameters, we present here analytical solutions for several dynamical correlation functions, such as the orientational and velocity autocorrelation function, the mean displacement, the mean-square displacement, and the delay function. Our results are as follows: First, we constitute a model that we refer to as the *Langevin rocket*. In doing so, we combine orientational fluctuations and mass loss described by the traditional Tsiolkovsky rocket equation [72]. We calculate the mean reach of the Langevin rocket and discuss different mass ejection strategies to maximize it. For increasing rotational noise, the optimal strategy to achieve a maximal reach changes discontinuously from a complete mass ejection extended over a long time to an instantaneous ejection of a mass fraction. Second, we compare different setups of time-dependent inertia, such as directed and isotropic mass ejection and isotropic shape changes with constant mass. Last, we study the case of slow ("adiabatic") variation of system parameters. In particular, for a change in the system parameters described by a power law in time, we predict a superdiffusive *anomalous* diffusion involving a mean-square displacement $\propto t^{\alpha}$ which scales as a power law in time t with a nontrivial exponent α [73–81]. In particular, we discuss chiral particles exposed to a torque that exhibit circling motion. This generalizes earlier work for overdamped systems [82–84]. Our predictions can be tested in various experimental setups ranging from macroscopic vibrated granular matter, robots, or living systems to self-propelled micron particles that are flying in a gaseous medium or in a plasma.

The paper is organized as follows: In Sec. II, we introduce the theoretical model for active Langevin motion describing an inertial particle. In Sec. III, we recapitulate the case of time-independent self-propulsion, inertia, damping, and fluctuations found earlier [8,13], but we include also results such as an analytical expression for the time-resolved mean trajectory and mean-square displacement. In Sec. IV, we demonstrate how time-dependent parameters change the dynamics of the system: in particular, we introduce the Langevin rocket model and study slow temporal variations. Finally, we conclude in Sec. V.

II. BASIC MODEL AND DIFFERENT SETUPS

In this section, we define the basic model of underdamped Langevin motion for a self-propelled particle with time-dependent inertia. We consider a self-propelled inertial particle with a center-of-mass coordinate $\mathbf{R}(t)$ at time t moving with its center in the two-dimensional xy-plane, see Fig. 1 for a sketch. The particle is polar such that it possesses an orientational degree of freedom characterized by a unit vector $\hat{\mathbf{n}}(t) = (\cos\phi(t), \sin\phi(t))$, where $\phi(t)$ is the angle relative to the x-axis. The particle self-propels along its orientation with the self-propulsion velocity $v_0\hat{\mathbf{n}}$, also indicated in Fig. 1. It may also additionally be exposed to an external or internal torque M along the z-axis leading to an angular velocity as shown by the blue arrow in Fig. 1. As the particle has inertia in both translation and rotation, its configuration is fully specified by its center-of-mass coordinate $\mathbf{R}(t)$, its center-of-mass velocity $\dot{\mathbf{R}}(t) = d\mathbf{R}(t)/dt$, its orientational angle $\phi(t)$, and its angular velocity $\dot{\phi}(t)$.

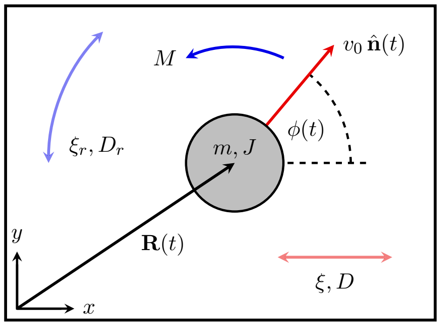

FIG. 1. Self-propelled inertial particle with center position $\mathbf{R}(t)$ at time t moving with its center in the two-dimensional xy plane. The particle position is indicated as $\mathbf{R}(t)$ (black arrow). Moreover, the particle possesses an orientational degree of freedom that is characterized by a unit vector $\hat{\mathbf{n}} = (\cos\phi, \sin\phi)$ with ϕ denoting the angle relative to the x-axis. The particle self-propels along its orientation with the velocity $v_0\hat{\mathbf{n}}$ (red arrow). It may also experience a torque M along the z-axis leading to rotational motion as indicated by the blue arrow. The translational motion is further influenced by a translational friction ξ and the noise strength D (as indicated by the light red horizontal double arrow) while the rotational motion is influenced by a rotational friction ξ_r and the orientational noise strength D_r (as indicated by the light blue curved double arrow).

While previous work [8,11,19] has considered constant particle mass and moment of inertia, here we generalize the model toward time-dependent parameters with a particular focus on a time-dependent particle mass $m(t)$ and a time-dependent moment of inertia $J(t)$, which we define with respect to the center-of-mass to describe the rotation around the z-axis. It turns out that the corresponding equations of motion need to be discussed with care as they depend on the physical origin of the change in inertia. To do this systematically step by step, we first consider four different setups, which are outlined in Fig. 2 and which are actually realizable in nature. We then give the most general model equation, which accommodates all these setups as special cases.

A. Time-independent inertia

First of all, as a reference, the special case of time-independent inertia is considered. This setup is sketched in

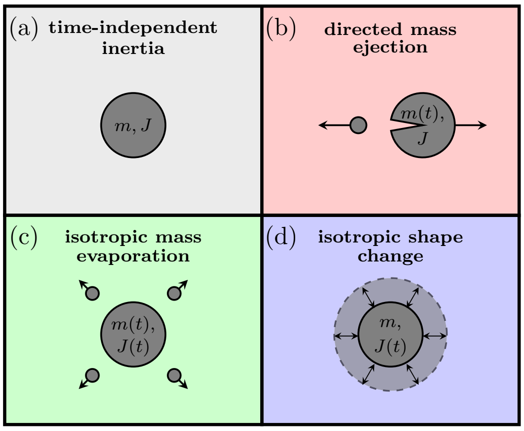

FIG. 2. Schematic illustration of the different special setups for an active inertial particle. The particle is shown as a dark-gray sphere and its inertia is characterized by the particle mass m and its moment of inertia J. (a) Time-independent inertia with constant m and J as a reference situation (gray background). (b) Directed mass ejection: Per unit time, the mass $\dot{m}(t)$ is ejected centrally with a velocity $-u\hat{\mathbf{n}}(t)$ along the particle orientation $\hat{\mathbf{n}}(t)$ which leads to a change $-u\hat{\mathbf{n}}\dot{m}(t)$ in the translational momentum of the particle and a time-dependent particle mass $m(t)$ but a constant moment of inertia J (red background). (c) Isotropic mass evaporation. Here the translational and the angular momentum of the particle are both conserved, but the particle mass $m(t)$ and moment of inertia $J(t)$ are time-dependent (green background). (d) Isotropic change in the particle shape. Here again the linear and the angular momentum of the particle are both conserved, the particle mass m is constant, but the moment of inertia $J(t)$ is time-dependent (blue background).

Fig. 2(a) (gray background). The particle has a constant mass m and a constant moment of inertia J. In this case, the Langevin equation of motion reads

$$m\,\ddot{\mathbf{R}}(t) = \xi\, v_0\, \hat{\mathbf{n}}(t) - \xi\, \dot{\mathbf{R}}(t) + \xi\sqrt{2D}\,\mathbf{f}_{\mathrm{st}}(t), \tag{1}$$

$$J\,\ddot{\phi}(t) = M - \xi_r\,\dot{\phi}(t) + \xi_r\sqrt{2D_r}\,\tau_{\mathrm{st}}(t). \tag{2}$$

As far as the translational dynamics is concerned, there is a frictional damping force $-\xi\,\dot{\mathbf{R}}(t)$ and a self-propelling effective force along the particle orientation $\xi\, v_0\,\hat{\mathbf{n}}(t)$, which gives rise to the particle self-propulsion velocity v_0 [85]. The latter does not stem from mass ejection but is of another origin, such as diffusiophoresis or photophoresis. This self-propulsion force couples the orientational and translational degrees of freedom. Furthermore, there is a stochastic force ("noise") $\xi\sqrt{2D}\,\mathbf{f}_{\mathrm{st}}(t)$, where the effective translational diffusion coefficient D quantifies the noise strength. We describe the stochastic term $\mathbf{f}_{\mathrm{st}}(t)$ as zero-mean Gaussian white noise with unit variance,

$$\overline{\mathbf{f}_{\mathrm{st}}(t)\otimes\mathbf{f}_{\mathrm{st}}(t')} = \delta(t-t')\mathbb{I}, \tag{3}$$

where $\overline{\cdots}$ indicates a noise average and $\mathbb{I}$ is the unit matrix. Likewise, the rotational dynamics in Eq. (2) involves a frictional torque $-\xi_r\,\dot{\phi}$ and an imposed torque M plus the stochastic torque $\xi_r\sqrt{2D_r}\,\tau_{\mathrm{st}}(t)$, where the effective rotational diffusion coefficient D_r now quantifies the rotational noise strength, and the Gaussian noise $\tau_{\mathrm{st}}(t)$ has zero-mean and unit variance

$$\overline{\tau_{\mathrm{st}}(t)\tau_{\mathrm{st}}(t')} = \delta(t-t'). \tag{4}$$

One of the best experimental realizations of active Langevin motion [see Eqs. (1) and (2)] can be found in self-propelled granular particles. These particles are capable of transferring the energy of a vibrating surface or an internal motor to translational or rotational motion. Asymmetry in the particle design causes them to jump forward or to rotate when lifted from the ground. From a recent experiment on these active granular particles [8], we list exemplary orders of magnitude for our model parameters $m = 1$ g, $J = 10$ g mm^2, $\xi = 10$ g/s, $\xi_r = 100$ g mm^2/s, $D = 100$ mm^2/s, $D_r = 1/s$, $v_0 = 10$–100 mm/s, and $M = 10^{-7}$ N m.

We shall revisit this standard situation again in Sec. III. In the absence of any inertial effects, i.e., when $m = J = 0$, the equations of motion are overdamped and lead to the standard picture of active Brownian motion [1,4,6].

B. Directed mass ejection

A rocket is self-propelled by directed mass ejection, so it establishes a fundamental setup of time-dependent inertia. In the typical geometry assumed here and shown in Fig. 2(b) (red background), the direction of the mass ejection is centrally outward opposite to the particle orientation. For simplicity, the mass ejection occurs with a constant velocity u relative to the moving rocket ($u > 0$) and the outlet coincides with the center of mass as indicated by a wedge in Fig. 2(b). The general case in which the ejection occurs not from the center but from a point distant to the center leads to additional terms that complicate the analysis, thus it is left for future studies.

We assume, however, for more generality here that the rocket also has an internal motor, which leads to an additional self-propulsion of velocity v_0. In typical descriptions of macroscopic rockets, translational and rotational fluctuations are ignored. While this is a reasonable assumption for macroscopic rockets, it breaks down for minirockets. The characteristic equations of motion for a self-propelled particle with directed mass ejection are

$$\begin{aligned}\frac{d}{dt}(m(t)\,\dot{\mathbf{R}}(t)) &= \xi\, v_0\,\hat{\mathbf{n}}(t) - \xi\,\dot{\mathbf{R}}(t) + \xi\sqrt{2D}\,\mathbf{f}_{\mathrm{st}}(t)\\ &\quad - \dot{m}(t)(u\,\hat{\mathbf{n}}(t) - \dot{\mathbf{R}}(t)),\end{aligned} \tag{5}$$

and the orientational equation of motion is given by (2).

In discussing the basic physics of Eq. (5), we use Newton's second postulate, which states that the total change in translational momentum is the total force, which is in this case the sum of friction, translational stochastic, and self-propulsion forces. But even in the force-free case, the ejected mass carries away the momentum $\dot{m}(t)(u\,\hat{\mathbf{n}}(t) - \dot{\mathbf{R}}(t))$ per unit time, which needs to be included in the balance of (5) with a minus sign due to the conservation of total momentum; see also [86–88]. This constitutes in fact the thrust force which accelerates the rocket. It is important to note here that the special case of the traditional Tsiolkovsky rocket equation is obtained as a special limit of no fluctuations, no frictions, no additional self-propulsion, no external torque, and a vanishing initial angular velocity, i.e., for $D = D_r = \xi = \xi_r = v_0 = M = \dot{\phi}(t = 0) = 0$ [72].

Since we assume that the outlet/tank of the particle coincides with the center-of-mass, the moment of inertia is not affected by the mass ejection and remains constant. Hence the orientational motion is identical to the case of time-independent inertia. Clearly, via the mass ejection, the two equations (5) and (2) are coupled.

Realizations of the rocketlike self-propelled objects can in principle be found for self-propelled Janus particles in a complex plasma, which are laser-heated such that they evaporate mass in a certain direction [29,59,60], or even for inflated toy balloons [61,62] or active granular particles equipped with compressed air tanks. For the latter, we would expect the particle loss mass at a rate of approximately $\dot{m} = -1$ g/s by exhausting air at a velocity $u = 100$ mm/s. The initial mass and moment of inertia are $m_0 = 10$ g and $J = 100\ \mathrm{g\,mm}^2$. The remaining parameters are of the order of $\xi = 10$ g/s, $\xi_r = 100\ \mathrm{g\,mm}^2/\mathrm{s}$, $D = 100\ \mathrm{mm}^2/\mathrm{s}$, $D_r = 1/s$, $v_0 = 10$–100 mm/s, and $M = 10^{-7}$ N m. We finally remark that there is some overdamped counterpart of rocketlike motion in the osmotophoresis of semipermeable vesicles [89] where the ejection of molecules out of the vesicle body leads to self-propulsion driven by the osmotic pressure difference [90] and for Janus-particles and nanorockets driven by reactive momentum transfer [91,92].

C. Isotropic mass evaporation

A different situation occurs if the mass ejection is not directed but isotropic as sketched in Fig. 2(c) (green background). Imagine a particle coated with an isotropic layer that evaporates likewise in all directions, as realizable in dusty plasmas [29,59,60]. In this case, the ejected mass only carries away the translational momentum given by $-\dot{m}(t)\,\dot{\mathbf{R}}(t)$ such that the translational equations of motion for this case coincide with Eq. (5) for $u = 0$. However, the mass ejection is radial only in the body frame, but for a rotating particle the angular momentum $\dot{J}(t)\,\dot{\phi}(t)$ is taken away in the laboratory frame even in the absence of any torque. Therefore, the orientational equation of motion reads as (2) with J replaced by $J(t)$, as follows:

$$J(t)\,\ddot{\phi}(t) = M - \xi_r\,\dot{\phi}(t) + \xi_r\sqrt{2D_r}\,\tau_{\mathrm{st}}(t). \tag{6}$$

This setup could be realized in experiments by placing a leaking water tank or evaporating material on an active granular particle. The order of magnitude of the parameters might be $m_0 = 10$ g, $\dot{m} = -1$ g/s, $J_0 = 100\ \mathrm{g\,mm}^2$, $\xi = 10$ g/s, $\xi_r = 100\ \mathrm{g\,mm}^2/\mathrm{s}$, $D = 100\ \mathrm{mm}^2/\mathrm{s}$, $D_r = 1/s$, $v_0 = 10$–100 mm/s, and $M = 10^{-7}$ N m.

Finally, we remark that the inverse situation of mass adsorption can be treated in a similar way with a positive sign of $\dot{m}(t)$.

D. Isotropic shape change

The pirouette in figure skating is an example of a fourth situation in which the total mass m of the body is time-independent but the moment of inertia does change due to a shape change of the body. In this special case, sketched in Fig. 2(d) (blue background), the shape change does not carry away angular momentum but the total angular momentum is conserved. Consequently, while the translational equation of motion is identical with Eq. (1), the orientational equation of motion is given by

$$\frac{d}{dt}(J(t)\,\dot{\phi}(t)) = M - \xi_r\,\dot{\phi}(t) + \xi_r\sqrt{2D_r}\,\tau_{\mathrm{st}}(t). \tag{7}$$

Lastly, this model could describe an active granular particle with a stretched elastic material attached to it. In that way, the initial moment of inertia could be increased by an order of magnitude $J_0 = 100\ \mathrm{g\,mm}^2$, relaxing over a few seconds to its equilibrium shape with $\dot{J} = -1\ \mathrm{g\,mm}^2/\mathrm{s}$. The order of magnitude of the other parameters might be $m = 1$ g, $\xi = 10$ g/s, $\xi_r = 100\ \mathrm{g\,mm}^2/\mathrm{s}$, $D = 100\ \mathrm{mm}^2/\mathrm{s}$, $D_r = 1/s$, $v_0 = 10 - 100$ mm/s, and $M = 10^{-7}$ N m.

E. General model

The lesson to be learned from the previous examples is that the equations of motion depend on the imposed setup of mass change. To proceed in a general way, we now present a general framework of equations of motion that accommodates all previous special cases. To define this model as generally as possible, we also assume an effective time-dependent self-propulsion speed $v_0(t)$, a time-dependent internal torque $M(t)$, a time-dependent translational $\xi(t)$ and rotational friction coefficient $\xi_r(t)$, as well as a time-dependent translational $D(t)$ and rotational diffusion coefficient $D_r(t)$ and a time-dependent mass ejection velocity $u(t)$.

We now consider the following general Langevin equations governing the translational and the rotational motion for a self-propelled particle:

$$\begin{aligned}\frac{d}{dt}(m(t)\,\dot{\mathbf{R}}(t)) &= \xi(t)(v_0(t)\,\hat{\mathbf{n}}(t) - \dot{\mathbf{R}}(t) + \sqrt{2D(t)}\,\mathbf{f}_{\mathrm{st}}(t)) \\ &\quad - \dot{m}(t)(u(t)\,\hat{\mathbf{n}}(t) - \dot{\mathbf{R}}(t)),\end{aligned} \tag{8}$$

$$\begin{aligned}\frac{d}{dt}(J(t)\,\dot{\phi}(t)) &= M(t) - \xi_r(t)\,\dot{\phi}(t) + \xi_r(t)\sqrt{2D_r(t)}\,\tau_{\mathrm{st}}(t) \\ &\quad + \nu\,\dot{J}(t)\,\dot{\phi}(t).\end{aligned} \tag{9}$$

Clearly, all situations discussed so far and shown in Fig. 2 are obtained from these equations as special cases: of course, Fig. 2(a) is the special limit where the parameters m, J, ξ, ξ_r, D, D_r, v_0, and M are constant. The rocket setup in Fig. 2(b) coincides with the general equations (8) and (9) when the parameters J, ξ, ξ_r, D, D_r, v_0, M, and the relative velocity u are constant. The isotropic mass evaporation [Fig. 2(c)] is contained in (8) and (9) when the parameters ξ, ξ_r, D, D_r, v_0, and M are constant, the relative velocity vanishes, $u = 0$, and $\nu = 1$. Finally, the equations for an isotropic shape change [Fig. 2(d)] follow when in (8) and (9) the parameters m, ξ, ξ_r, D, D_r, v_0, and M are constant and $\nu = 0$.

At this stage, we remark that more realistic situations can also be accommodated in the general equations (8) and (9). These include, for example, a rocket where the outlet of the mass ejection does not coincide with the center-of-mass or where the ejection direction is not parallel to the particle orientation [93].

From a mathematical point of view, the equations of motion (8) and (9) are stochastic differential equations with Gaussian noise. The rotational equation (9) is linear so that the distribution of the angle and angular velocity is Gaussian for any time. We give the corresponding general solutions of (8) and (9) in Appendix A.

III. TIME-INDEPENDENT INERTIA

We now turn to the special case of time-independent parameters defined by Eqs. (1) and (2). These equations of motion were studied before in Refs. [8,11,19]. Here we summarize essential known results, but we also provide additional analytical results for the full time-resolved mean displacement, velocity correlation function, and mean-square displacement. In doing so, we first consider the noise-free case and then we include the effects of noise.

A. Results for vanishing noise

For given initial orientations $\phi_0 = \phi(0)$ and angular velocities $\dot{\phi}_0 = \dot{\phi}(0)$ at time $t = 0$, the deterministic solution of the general orientational equation of motion (2) in the absence of noise is

$$\phi(t) = \phi_0 + \omega t + \frac{\dot{\phi}_0 - \omega}{\gamma_r}(1 - e^{-\gamma_r t}) \tag{10}$$

with the spinning frequency $\omega = M/\xi_r$ and rotational damping rate $\gamma_r = \xi_r/J$. Plugging this solution into the noise-free translational equation (1), we obtain for given initial positions $\mathbf{R}_0 = \mathbf{R}(0)$ and velocities $\dot{\mathbf{R}}_0 = \dot{\mathbf{R}}(0)$ at time $t = 0$ the particle velocity

$$\begin{aligned}\dot{\mathbf{R}}(t) = {} & \dot{\mathbf{R}}_0 e^{-\gamma t} + v_0 \hat{\mathbf{P}}[\tilde{\gamma}\,(i\theta)^{\tilde{\gamma}+i\tilde{\omega}} e^{i(\phi_0+\theta)} \\ & \times \Gamma(-(\tilde{\gamma}+i\tilde{\omega}), i\theta e^{-\gamma_r t}, i\theta)]e^{-\gamma t},\end{aligned} \tag{11}$$

where we introduced the translational damping rate $\gamma = \xi/m$ and the notations $\tilde{\gamma} = \gamma/\gamma_r$, $\tilde{\omega} = \omega/\gamma_r$, $\theta = (\dot{\phi}_0 - \omega)/\gamma_r$. Moreover, $\Gamma(s, x_1, x_2)$ denotes the generalized Gamma function [94],

$$\Gamma(s, x_1, x_2) = \int_{x_1}^{x_2} dt\, t^{s-1} e^{-t}, \tag{12}$$

and the operator $\hat{\mathbf{P}}$ formally transforms a complex number z into its two-dimensional vector $(\mathrm{Re}\, z, \mathrm{Im}\, z)$ in the complex plane. This results in the particle trajectory

$$\begin{aligned}\mathbf{R}(t) = {} & \mathbf{R}_0 + \frac{\dot{\mathbf{R}}_0}{\gamma}(1 - e^{-\gamma t}) \\ & + \frac{v_0}{\gamma_r}\hat{\mathbf{P}}[(i\theta)^{i\tilde{\omega}} e^{i(\phi_0+\theta)}\Gamma(-i\tilde{\omega}, i\theta e^{-\gamma_r t}, i\theta)] \\ & - \frac{v_0}{\gamma_r}\hat{\mathbf{P}}[(i\theta)^{\tilde{\gamma}+i\tilde{\omega}} e^{i(\phi_0+\theta)}\Gamma(-(\tilde{\gamma}+i\tilde{\omega}), i\theta e^{-\gamma_r t}, i\theta)]e^{-\gamma t}.\end{aligned} \tag{13}$$

In the limit of long times, the angular velocity reaches the spinning frequency, $\lim_{t\to\infty} \dot{\phi}(t) = \omega$, so that the particle is rotating with this frequency around a circle of radius

$$r = \frac{v_0}{\omega}\sqrt{\frac{\gamma^2}{\gamma^2 + \omega^2}}, \tag{14}$$

centered at the position

$$\mathbf{R}_c = \mathbf{R}_0 + \frac{\dot{\mathbf{R}}_0}{\gamma} + \frac{v_0}{\gamma_r}\hat{\mathbf{P}}[(i\theta)^{i\tilde{\omega}} e^{i(\phi_0+\theta)}\Gamma(-i\tilde{\omega}, 0, i\theta)]. \tag{15}$$

Clearly, the spinning frequency ω does not depend on any inertia. However, the circle radius r depends on the mass m via the translational damping rate γ due to the centrifugal force, but it is independent on the moment of inertia J. The center of the circle depends on $\mathbf{R}_0$, $\dot{\mathbf{R}}_0$, ϕ_0, and $\dot{\phi}_0$, demonstrating that for vanishing noise even the long-time limit may depend on the initial conditions. Finally, in the overdamped limit of vanishing inertia, the results reduce to that of Brownian circle swimmers [82,95].

B. Effect of Brownian noise

Subjected to Brownian noise, the particle will relax to a steady state after a long time forgetting about its initial conditions $\mathbf{R}_0$, $\dot{\mathbf{R}}_0$, ϕ_0, and $\dot{\phi}_0$ at time $t = 0$. The static and dynamical correlation in the steady state can be calculated as a time average over a very long time window, which we shall denote with angular brackets $\langle\cdots\rangle$. In the sequel, we shall consider several of such dynamical correlations. In the steady state, one can also calculate conditional averages. For example, one can build dynamical averages in the steady state after a lag time under the condition that the particle's position and orientation are prescribed at an initial time. We shall compile analytical results for the different correlation functions first and show examples for numerical evaluations of the analytical formula.

1. Velocity correlation function

First we introduce the translational velocity correlation function [96],

$$Z(t) = \langle \dot{\mathbf{R}}(t) \cdot \dot{\mathbf{R}}(0)\rangle, \tag{16}$$

where t now denotes a lag time and $\dot{\mathbf{R}}(0)$ is taken from the velocity distribution in the steady state. We remark that the latter was computed recently for small inertia [97] and for the formally equivalent model of an overdamped particle in a harmonic potential [98]. The velocity distribution is non-Gaussian (i.e., non-Maxwellian), and its second moment, $Z(0) = \langle \dot{\mathbf{R}}(0) \cdot \dot{\mathbf{R}}(0)\rangle$, which is proportional to the mean kinetic energy, is known analytically [8] as

$$Z(0) = 2D\gamma + v_0^2\, \mathrm{Re}[\tilde{\gamma} e^{\tilde{D}_r} \tilde{D}_r^{-\Omega_+}\, \Gamma(\Omega_+, 0, \tilde{D}_r)], \tag{17}$$

where we introduced $\tilde{D}_r = D_r/\gamma_r$ and $\Omega_\pm = (D_r \pm (\gamma + i\omega))/\gamma_r$. For an active inertial particle considered here, we have obtained the analytical result

$$Z(t) = 2D\gamma e^{-\gamma t} + \frac{v_0}{2}(\langle \dot{\mathbf{R}}(t) \cdot \hat{\mathbf{n}}(0)\rangle + \langle \dot{\mathbf{R}}(0) \cdot \hat{\mathbf{n}}(t)\rangle) \tag{18}$$

with

$$\begin{aligned}\langle \dot{\mathbf{R}}(t) \cdot \hat{\mathbf{n}}(0)\rangle = {} & v_0\, \mathrm{Re}\big[\tilde{\gamma} e^{\tilde{D}_r}\big(\tilde{D}_r^{-\Omega_-}\Gamma(\Omega_-, \tilde{D}_r e^{-\gamma_r t}, \tilde{D}_r) \\ & + \tilde{D}_r^{-\Omega_+}\Gamma(\Omega_+, 0, \tilde{D}_r)\big)e^{-\gamma t}\big]\end{aligned} \tag{19}$$

and

$$\langle \dot{\mathbf{R}}(0) \cdot \hat{\mathbf{n}}(t)\rangle = v_0\, \mathrm{Re}\big[\tilde{\gamma} e^{\tilde{D}_r} \tilde{D}_r^{-\Omega_+}\Gamma(\Omega_+, 0, \tilde{D}_r e^{-\gamma_r t}) e^{\gamma t}\big], \tag{20}$$

which implies that the long-time behavior of $Z(t)$ is exponential in time.

2. Orientation correlation function

Similarly, the dynamical orientational correlation function $C(t) = \langle \hat{\mathbf{n}}(t) \cdot \hat{\mathbf{n}}(0) \rangle$ in the steady state can be expressed analytically as a double exponential as

$$C(t) = \cos(\omega t) e^{-D_r[t-\gamma_r^{-1}(1-e^{-\gamma_r t})]}, \tag{21}$$

which was found previously in another context by Ghosh and co-workers [13] for $\omega = 0$ and for general ω in Ref. [8]. Again it decays exponentially in time for long times. A characteristic orientational persistence time τ_p can be determined as

$$\tau_p = \int_0^\infty C(t)dt = \frac{1}{D_r} \mathrm{Re}\left[\tilde{D}_r e^{\tilde{D}_r} \tilde{D}_r^{-\Omega}\, \Gamma(\Omega, 0, \tilde{D}_r)\right], \tag{22}$$

with $\Omega = (D_r - i\omega)/\gamma_r$. For vanishing inertia, we recover the known result of the persistence time $\tau_p = D_r/(D_r^2 + \omega^2)$ [82,95], which simplifies further to the standard result $\tau_p = 1/D_r$ for a linear swimmer [1].

3. Mean displacement

Next, we address the mean displacement $\langle \Delta \mathbf{R}(t) \rangle = \langle \mathbf{R}(t) - \mathbf{R}_0 \rangle$ of the particle in the steady state as a function of time t. The average is now taken in the steady state but under the condition that for the initial time $t = 0$, the position $\mathbf{R}(0) = \mathbf{R}_0$ and the orientation $\hat{\mathbf{n}}(0)$ [embodied in $\phi(0) = \phi_0$] are prescribed. Since the particle velocities and the orientations are correlated in the steady state, the average over the translational velocity $\langle \dot{\mathbf{R}}(0) \rangle$ is not vanishing due to the prescribed orientation $\hat{\mathbf{n}}(0)$. This average is given by

$$\langle \dot{\mathbf{R}}(0) \rangle = v_0 \hat{\mathbf{P}}\left[\tilde{\gamma} e^{\tilde{D}_r} \tilde{D}_r^{-\Omega_+} \Gamma(\Omega_+, 0, \tilde{D}_r) e^{i\phi_0}\right]. \tag{23}$$

We obtain for the mean displacement

$$\begin{aligned} \langle \Delta \mathbf{R}(t) \rangle = {} & \frac{\langle \dot{\mathbf{R}}(0) \rangle}{\gamma}(1 - e^{-\gamma t}) \\ & + \frac{v_0}{D_r} \hat{\mathbf{P}}\big[\tilde{D}_r e^{\tilde{D}_r} \big(\tilde{D}_r^{-\Omega} \Gamma(\Omega, \tilde{D}_r e^{-\gamma_r t}, \tilde{D}_r) \\ & + \tilde{D}_r^{-\Omega_-} \Gamma(\Omega_-, \tilde{D}_r e^{-\gamma_r t}, \tilde{D}_r) e^{-\gamma t}\big) e^{i\phi_0}\big]. \end{aligned} \tag{24}$$

For short times t, the particle proceeds on average ballistically (i.e., linearly in time) with

$$\langle \Delta \mathbf{R}(t) \rangle = \langle \dot{\mathbf{R}}(0) \rangle t + O(t^2). \tag{25}$$

Then the rotational noise decorrelates the current orientation from the initial orientation, and the mean displacement saturates to a finite persistence length $\mathbf{L}_p = \lim_{t\to\infty} \langle \Delta \mathbf{R}(t) \rangle$ given as

$$\mathbf{L}_p = \frac{\langle \dot{\mathbf{R}}(0) \rangle}{\gamma} + \frac{v_0}{D_r} \hat{\mathbf{P}}\left[\tilde{D}_r e^{\tilde{D}_r} \tilde{D}_r^{-\Omega}\, \Gamma(\Omega, 0, \tilde{D}_r) e^{i\phi_0}\right]. \tag{26}$$

In the case of a vanishing spinning frequency ($\omega = 0$), the persistence length simplifies to $\mathbf{L}_p = \langle \dot{\mathbf{R}}(0) \rangle/\gamma + v_0 \tau_p \hat{\mathbf{n}}_0$ with τ_p given by (22). In the overdamped limit, we obtain the standard results of the persistence length for linear microswimmers $\mathbf{L}_p = v_0 \hat{\mathbf{n}}_0/D_r$ ($\omega = 0$) [1]. Moreover, for an overdamped circle swimmer, the full time-resolved mean displacement given by (24) simplifies to a *spira mirabilis* [82,99]. The presence of

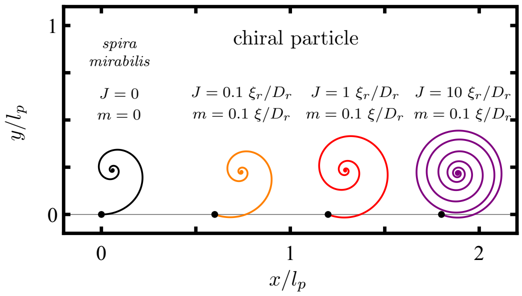

FIG. 3. Mean displacement $\langle \Delta \mathbf{R}(t) \rangle$ in the xy-plane for a chiral particle with initial orientation along the x-axis for different moment of inertia, $J = 0.1\ \xi_r/D_r$ (orange), $J = 1\ \xi_r/D_r$ (red), and $J = 10\, \xi_r/D_r$ (purple). Lengths are given in units of $l_p = v_0/D_r$. The parameters are $\omega = 4\ D_r$, $m = 0.1\ \xi/D_r$. The starting point at $t = 0$ is denoted by a black dot. The *spira mirabilis* of the overdamped limit is plotted on the left (black) for comparison.

inertia will distort the ideal *spira mirabilis* and give rise to a more complex mean trajectory. This is shown in Fig. 3, where three shapes of the mean trajectory for increasing moment of inertia J are compared to the overdamped case. Increasing J reduces effectively the role of fluctuations such that there are more turns until the particle reaches half of the distance to its final fixpoint. Even though $\hat{\mathbf{n}}(0)$ is oriented toward the positive x-axis in all cases, the inertial mean trajectory first “oversteers” the initial orientation due to the velocity average, an effect that we shall elaborate on and quantify further in Sec. III B 5.

4. Mean-square displacement

The full time-resolved mean-square displacement (MSD) can be calculated as

$$\langle \Delta \mathbf{R}^2(t) \rangle = 4 D_L t + \frac{2}{\gamma^2}(Z(t) - Z(0)) + 2\frac{v_0^2}{\gamma_r^2} F(t), \tag{27}$$

with the long-time diffusion coefficient

$$D_L = D + \frac{v_0^2}{2D_r} \mathrm{Re}[\tilde{D}_r e^{\tilde{D}_r} \tilde{D}_r^{-\Omega}\, \Gamma(\Omega, 0, \tilde{D}_r)], \tag{28}$$

and the function

$$\begin{aligned} F(t) = \mathrm{Re}\Bigg\{ \frac{e^{\tilde{D}_r}}{\Omega^2} \Bigg(& {}_2F_2\left[\begin{matrix}\Omega, \Omega \\ \Omega+1, \Omega+1\end{matrix}; -\tilde{D}_r\right] \\ & - {}_2F_2\left[\begin{matrix}\Omega, \Omega \\ \Omega+1, \Omega+1\end{matrix}; -\tilde{D}_r e^{-\gamma_r t}\right] e^{-\gamma_r \Omega t} \Bigg) \Bigg\}, \end{aligned} \tag{29}$$

where ${}_pF_q$ represents the generalized hypergeometric function [100].

Figures 4(a)–4(d) compare the temporal behavior of the mean-square displacement of an achiral particle to that of a chiral particle for different masses and moments of inertia J. All curves exhibit the characteristic crossover from a short-time ballistic behavior

$$\langle \Delta \mathbf{R}^2(t) \rangle = Z(0) t^2 + O(t^3) \tag{30}$$

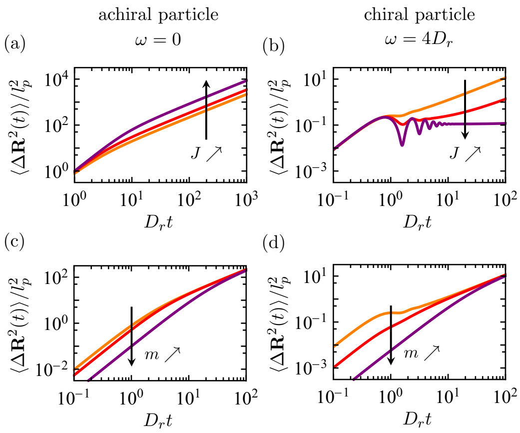

FIG. 4. Mean-square displacement as a function of time on a double-logarithmic plot. (a) For an achiral particle with fixed mass m and varied moment of inertia J. (b) For a chiral particle with fixed mass m and varied moment of inertia J. The fixed parameters are $m = 0.1\,\xi/D_r$, $D = 0$ and the moment of inertia is $J = 0.1\,\xi_r/D_r$ (orange), $J = 1\,\xi_r/D_r$ (red), or $J = 10\,\xi_r/D_r$ (purple). (c) For an achiral particle with varied m and fixed J. (d) For a chiral particle with varied m and fixed J. Here, the fixed parameters are $J = 0.1\,\xi_r/D_r$, $D = 0$ and the mass is $m = 0.1\,\xi/D_r$ (orange), $m = 1\,\xi/D_r$ (red), or $m = 10\,\xi/D_r$ (purple).

to the long-time diffusive behavior governed by

$$\langle \Delta \mathbf{R}^2(t) \rangle \sim 4 D_L t. \tag{31}$$

In the limit of small J, the short-time ballistic dynamics is

$$\lim_{J\to 0} \langle \Delta \mathbf{R}^2(t) \rangle = \left(2D\gamma + v_0^2 \frac{\gamma(\gamma + D_r)}{(\gamma + D_r)^2 + \omega^2} \right) t^2 + O(t^3), \tag{32}$$

while for large J we have

$$\lim_{J\to\infty} \langle \Delta \mathbf{R}^2(t) \rangle = \left(2D\gamma + v_0^2 \frac{\gamma^2}{\gamma^2 + \omega^2} \right) t^2 + O(t^3). \tag{33}$$

In general, the long-time diffusion coefficient D_L [see Eq. (28)] can be represented as

$$D_L = D + \frac{v_0^2}{2} \tau_p, \tag{34}$$

where the first term in Eq. (22) captures the diffusive behavior of a passive particle and the second is consistent with the standard picture of a typical jump length of $v_0 \tau_p$ and a typical jump time of τ_p, similar to the overdamped expression of microswimmers when $\omega = 0$ [1]. It was emphasized in Ref. [8] that D_L depends on the moment of inertia J but not explicitly on the mass m.

In the case of small moments of inertia, the long-time diffusion coefficient of the circle flyer asymptotically goes to [8]

$$D_L = D + \frac{v_0^2}{2} \frac{D_r}{D_r^2 + \omega^2} \left(1 + \frac{D_r}{\xi_r} J \right) + O(J^2), \tag{35}$$

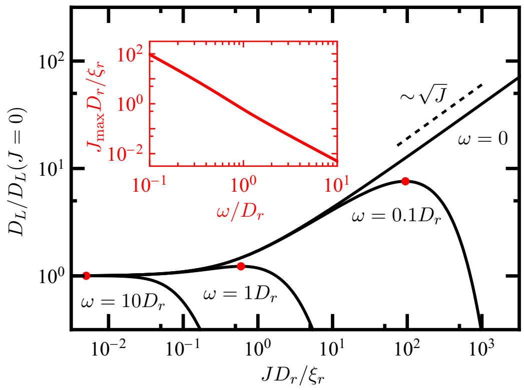

FIG. 5. Long-time diffusion coefficient D_L as a function of the moment of inertia J for different circling frequencies $\omega = 10 D_r$, $\omega = 1 D_r$, $\omega = 0.1 D_r$, and $\omega = 0$. The translational diffusion coefficient was set to zero, $D = 0$. In the inset, the global maximum point $J_{\max}$ for a given circling frequency ω is depicted. The corresponding maximal value $D_L(J_{\max})$ is shown as a red dot in the main figure.

which grows dominantly in proportion to the moment of inertia. The asymptotic behavior of the long-time diffusion coefficient for large moments of inertia is [8]

$$D_L \sim \begin{cases} v_0^2 \sqrt{\frac{\pi}{8 D_r \xi_r}} \sqrt{J} & (\omega = 0), \\ D & (\omega \neq 0). \end{cases} \tag{36}$$

As the moment of inertia grows for $\omega \neq 0$, the activity-induced part of the long-time diffusion coefficient goes asymptotically to zero [see Eq. (36)] since diffusion is hampered by systematic circling motion, i.e., the particle gets trapped in a circular path due to its huge moment of inertia.

Figures 4(a) and 4(c) show data for an achiral swimmer with different moments of inertia J and different masses. The short-time ballistic prefactor is somewhat independent of J but decreases with increasing m. The latter trend follows from the fact that for large m the particle cannot accelerate toward its self-propulsion velocity v_0. Conversely, the long-time diffusivity is also increasing with J according to (35) and (36) as the persistence in orientation increases with J but it is independent of m. For a chiral particle, shown in Figs. 4(b) and 4(d), the MSD exhibits wiggles due to the circling.

An immediate consequence of (35) and (36) is that the long-time diffusivity behaves *nonmonotonically* in J. Explicit data are presented in Fig. 5, which illustrates the nonmonotonic dependence of D_L on the moment of inertia J for different spinning frequencies ω for the special case $D = 0$. There is an intermediate maximum in D_L which is indicated in Fig. 5 by a red point. This peak could be exploited for an optimal exploration of an unknown territory by adapting the moment of inertia accordingly. The associated optimal moment of inertia is plotted as a function of the spinning frequency ω in the inset of Fig. 5.

5. Delay function

Contrary to the overdamped case, the velocity of an inertial particle does not coincide with its self-propulsion direction, and in Ref. [8] a dynamical correlation function, referred to as a delay function $d(t)$, was introduced to quantify the delay between the velocity and orientation dynamics,

$$d(t) = \langle \dot{\mathbf{R}}(t) \cdot \hat{\mathbf{n}}(0) \rangle - \langle \dot{\mathbf{R}}(0) \cdot \hat{\mathbf{n}}(t) \rangle. \tag{37}$$

The "mixed" difference ensures that this function is trivially zero in the overdamped limit, but when nonzero its sign contains valuable information about the delay process between $\hat{\mathbf{n}}(t)$ and $\dot{\mathbf{R}}(t)$. If, for example, $d(t)$ is positive, this means that—on average—first the particle orientation changes and then the velocity will follow that change after a time t. A positive $d(t)$ is the standard behavior exploited by the oversteering of racing cars, which is also expected for achiral particles. The full analytical result for $d(t)$ directly follows from (19) and (20) and was given in Ref. [8]. Most notably, for an achiral particle, $d(t)$ has a positive peak after a typical delay time, while for a chiral particle, $d(t)$ oscillates due to the systematic change in orientation. The latter oscillation was recently observed in macroscopic whirligig beetles swimming at the water surface [49].

Here we also provide analytical limits of small and large moments of inertia J. For small J we get

$$d(t) = 2v_0 A(t)\left(1 + \frac{D_r}{\xi_r} J\right) + O(J^2), \tag{38}$$

with

$$A(t) = \frac{\gamma\, D_r \left(\gamma^2 - D_r^2 - \omega^2\right)[\cos(\omega t)\, e^{-D_r t} - e^{-\gamma t}]}{((\gamma + D_r)^2 + \omega^2)((\gamma - D_r)^2 + \omega^2)} + \frac{\gamma\, \omega \left(\gamma^2 + D_r^2 + \omega^2\right) \sin(\omega t)\, e^{-D_r t}}{((\gamma + D_r)^2 + \omega^2)((\gamma - D_r)^2 + \omega^2)}. \tag{39}$$

Since $A(t)$ is positive for small times t, the delay effect is enhanced for increasing J. Moreover, the oscillatory behavior of a chiral particle can be seen here directly. In the opposite limit of large moment of inertia, the inertial delay approaches

$$\lim_{J \to \infty} d(t) = 2v_0 \frac{\gamma\, \omega}{\gamma^2 + \omega^2} \sin(\omega t), \tag{40}$$

independent of the rotational diffusion coefficient D_r, which documents again the oscillatory behavior for chiral particles.

IV. TIME-DEPENDENT INERTIA

Here we study the effect of time-dependent inertia on the Langevin motion of an underdamped particle. We first introduce a reduced Langevin rocket model in which the mass of the particle gets burned to accelerate the particle giving rise to a time-dependent mass and propulsion speed. Then we compare the four different setups introduced in Sec. II. Last, we consider the limiting case of slowly varying parameters with respect to time.

A. Langevin rocket

We define the "Langevin rocket" model by including orientational fluctuations in the traditional Tsiolkovsky rocket equation [72]. The effect of noise on rocket motion has been considered previously (see, e.g., [101]), but a simple basis reference model for that is missing. We therefore simplify the general Eqs. (5) and (2) for directed mass ejection and assume a vanishing moment of inertia, torque, and translational diffusion ($J = 0$, $M = 0$, and $D = 0$) The Langevin rocket dynamics for a prescribed $m(t)$ is then given by

$$m(t)\, \ddot{\mathbf{R}}(t) + \xi\, \dot{\mathbf{R}}(t) = -u\, \dot{m}(t)\, \mathbf{n}(t), \tag{41}$$

$$\dot{\phi}(t) = \sqrt{2D_r}\, \tau_{\mathrm{st}}(t). \tag{42}$$

This set of equations approaches the ideal Tsiolkovsky rocket equation, $m(t)\, \ddot{\mathbf{R}}(t) = -u\, \dot{m}(t)\, \mathbf{n}_0$, in the limit of vanishing damping ($\xi = 0$) and noise ($D_r = 0$) [72].

For the sake of simplicity, we assume that the rocket is ejecting mass at a constant rate $(m_\infty - m_0)/\Delta t$, where m_0 denotes the initial mass, m_∞ is the final rest mass of the rocket, and Δt is the total burn time. The ejection process happens in the window $0 < t < \Delta t$ such that the time-dependent particle mass is

$$m(t) = m_0 + (m_\infty - m_0) \frac{\min(t, \Delta t)}{\Delta t}. \tag{43}$$

In the following, we discuss the average reach of the rocket (i.e., its mean displacement) as a function time. In particular, we investigate the final reach for long times as a function of the burn time Δt and the propellant mass fraction

$$\zeta = \frac{m_0 - m_\infty}{m_0}. \tag{44}$$

1. Results for vanishing noise

In the absence of rotational noise, the displacement of the rocket for a vanishing initial velocity at $t = 0$ is

$$\Delta\mathbf{R}(t) = u \frac{\min(t, \Delta t)}{S_1 + 1} \hat{\mathbf{n}}_0 - \frac{u}{\gamma_0} \frac{m(t)}{m_0} \frac{1 - \left(\frac{m(t)}{m_0}\right)^{S_1}}{S_1 + 1} \hat{\mathbf{n}}_0 + \frac{u}{\gamma_0} \frac{m(t)}{m_0} \frac{1 - \left(\frac{m(t)}{m_0}\right)^{S_1}}{S_1} (1 - e^{-\gamma_\infty(\max(t, \Delta t) - \Delta t)}) \hat{\mathbf{n}}_0, \tag{45}$$

with the initial damping rate $\gamma_0 = \xi/m_0$, the final damping rate $\gamma_\infty = \xi/m_\infty$, and the reduced burn time $S_1 = \gamma_0 \Delta t/\zeta$.

For short times, the rocket exhibits an acceleration by ejecting mass such that the displacement scales with t^2,

$$\Delta\mathbf{R}(t) = \frac{u\zeta}{2\Delta t} \hat{\mathbf{n}}_0\, t^2 + O(t^3). \tag{46}$$

After the burn time Δt, the rocket reaches its maximal velocity, which is subsequently exponentially damped with the final damping rate γ_∞ until the rocket comes to a standstill. The total long-time displacement $\Delta R_\infty = \lim_{t \to \infty} |\Delta\mathbf{R}(t)|$ is given by

$$\Delta R_\infty = \frac{u \Delta t}{S_1 + 1} + \frac{u}{\gamma_0} \frac{(1 - \zeta)(1 - (1 - \zeta)^{S_1})}{S_1(S_1 + 1)}. \tag{47}$$

In Fig. 6, we show the long-time displacement ΔR_∞ as a function of the propellant mass fraction ζ for different burn times Δt. For long burn times $\Delta t \gg 1/\gamma_0$, the ultimate displacement increases linearly with the propellant mass fraction

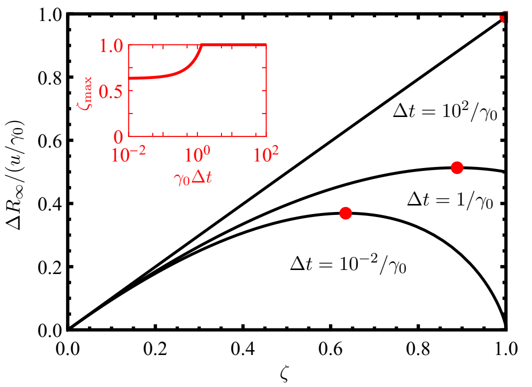

FIG. 6. Maximal reach ΔR_∞ as a function of the propellant mass fraction ζ for several burn times $\Delta t = 10^{-2}/\gamma_0$, $\Delta t = 1/\gamma_0$, and $\Delta t = 10^2/\gamma_0$. The inset depicts the optimal propellant mass fraction $\zeta_{\max}$ for a given burn time Δt. The corresponding maximal value $R_\infty(\zeta_{\max})$ is shown as a red dot in the main figure.

$\Delta R_\infty \sim u\zeta/\gamma_0$. The rocket reaches the longest distance when $\zeta_{\max} \sim 1$, a situation that can be called *complete extended mass ejection*. Interestingly, however, there is a qualitatively different behavior for burn times that are comparable to or smaller than the characteristic damping time $1/\gamma_0$, where the displacements behave nonmonotonically in the mass fraction ζ. This can be intuitively understood as follows: for small mass fractions, more ejection means more propulsion and acceleration such that ΔR_∞ increases with ζ. Conversely for ζ close to 1, the rocket becomes very light after the burn time and therefore very quickly stops within an extremely short damping time $1/\gamma_\infty$, which reduces its reach relative to a situation of smaller ζ. Consequently, the optimal value $\zeta_{\max}$ for the mass ratio for which the reach is maximal is smaller than 1. These corresponding optimal mass ratios are marked by red points in Fig. 6 and plotted as a function of the reduced burn time in the inset. For decreasing burn times the optimal mass ratio $\zeta_{\max}$ exhibits a bifurcation-like behavior from complete mass ejection to a finite fraction with the special limit of $\zeta_{\max} \sim 1 - e^{-1} \approx 0.63$ as Δt approaches zero.

The special limit of $\Delta t \ll 1/\gamma_0$ deserves some more attention. In this case of *fractional instantaneous mass ejection*, the particle ejects only a fraction of its propellant to gain momentum very quickly. But it keeps a rest mass in order to still proceed during the subsequent damping time. In this limit, we obtain

$$\Delta\mathbf{R}(t) = -\frac{u}{\gamma_0}(1-\zeta)\ln(1-\zeta)(1-e^{-\gamma_\infty t})\hat{\mathbf{n}}_0, \tag{48}$$

which scales for $\Delta t \ll t \ll 1/\gamma_0$ linearly in time,

$$\Delta\mathbf{R}(t) = -u\,\ln(1-\zeta)\,\hat{\mathbf{n}}_0\,t + O(t^2). \tag{49}$$

For long times, $t \gg 1/\gamma_0$, we obtain

$$\Delta R_\infty = -\frac{u}{\gamma_0}(1-\zeta)\ln(1-\zeta). \tag{50}$$

We finally remark that one can consider a full *optimization problem* with respect to both burn time Δt and the mass fraction ζ by posing the following question: What is the maximal reach of the rocket if the burn time Δt and the mass fraction ζ can be varied freely and independently? The answer in the fluctuation-free case is simple: the best strategy is to burn all mass $\zeta_{\max} \to 1$ and do this over a very long time $\Delta t \to \infty$. Then one achieves the maximum

$$\max(\Delta R_\infty) = \frac{u}{\gamma_0}, \tag{51}$$

shown in the upper right corner of Fig. 6. In other terms, the strategy of complete extended mass ejection always outperforms that of an fractional instantaneous mass ejection. This simple answer will change if orientational noise is included, a case that we shall address next.

2. Noise-averaged mean reach and noise-induced transition between two mass ejection strategies

In the case of finite rotational noise ($D_r > 0$), we obtain for the noise-averaged displacement of the Langevin rocket the analytical result

$$\begin{aligned}
&\overline{\Delta\mathbf{R}(t)}\\
&= \frac{u}{D_r}\frac{1}{S_1+1}(1-e^{-D_r\min(t,\Delta t)})\hat{\mathbf{n}}_0\\
&\quad + \frac{u}{D_r}\,\mathrm{Re}\left[e^{S_2}(-S_2)^{S_1+1}\Gamma\Big(-S_1, -S_2\big(\tfrac{m(t)}{m_0}\big), -S_2\Big)\right]\hat{\mathbf{n}}_0\\
&\quad \times \left(\frac{\big(\frac{m(t)}{m_0}\big)^{S_1+1}}{S_1+1} - \frac{\big(\frac{m(t)}{m_0}\big)^{S_1+1}}{S_1}(1-e^{-\gamma_\infty(\max(t,\Delta t)-\Delta t)})\right),
\end{aligned} \tag{52}$$

with $S_2 = D_r\Delta t/\zeta$ proportional to the rotational noise. Orientational fluctuations do not contribute to the short-time behavior as witnessed by the fact that in this limit the mean displacement coincides with the noise-free acceleration behavior of Eq. (46). For long times, on the other hand, the mean reach of the Langevin rocket is

$$\begin{aligned}
\overline{\Delta R_\infty} &= \frac{u}{D_r}\frac{1}{S_1+1}(1-e^{-D_r\Delta t}) + \frac{u}{D_r}\frac{(1-\zeta)^{S_1+1}}{S_1(S_1+1)}\\
&\quad \times \mathrm{Re}[e^{S_2}(-S_2)^{S_1+1}\Gamma(-S_1, -S_2(1-\zeta), -S_2)].
\end{aligned} \tag{53}$$

Returning to the previous optimization problem, we now maximize the mean reach as a function of burn time Δt and mass fraction ζ for fixed prescribed noise strength D_r/γ_0. In Fig. 7(a), the resulting maximal reach $\max(\overline{\Delta R_\infty})$ is shown for varied noise strength D_r/γ_0 in units of its universal noise-free limit u/γ_0 of complete extended mass ejection. The associated optimal burn time $\Delta t_{\max}$ and optimal mass fraction $\zeta_{\max}$ are also presented [see Figs. 7(b) and 7(c)]. If rotational noise is increased, the complete extended mass ejection is still the best strategy, but it is optimal to burn the full mass over a finite burn time. This strategy defies best the ultimate orientational decorrelation, which reduces the mean reach. In the opposite limit of very large orientational noise, the best strategy is to get momentum quickly by ejecting part of the

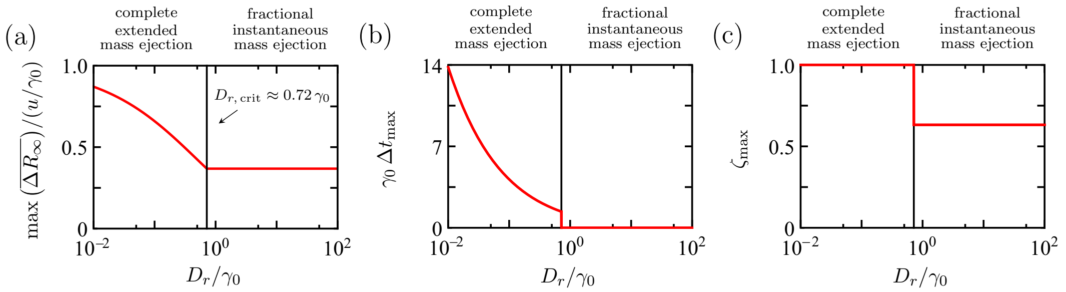

FIG. 7. (a) The optimal mean reach $\max(\overline{\Delta R_\infty})$ maximized with respect to the propellant mass fraction ζ and the burn time Δt as a function of the rotational noise strength D_r/γ_0. (b) Optimal burn time $\Delta t_{\max}$ as a function of the rotational noise strength D_r/γ_0. (c) Optimal propellant mass fraction $\zeta_{\max}$ as a function of the rotational noise strength D_r/γ_0. The transition from the complete extended mass ejection strategy to that of the fractional instantaneous mass ejection is marked by vertical black lines at $D_{r,\,\mathrm{crit}} \approx 0.72\,\gamma_0$ in all three figures.

mass and using it to proceed further within the characteristic damping time. If one were to eject the mass completely, the system would be overdamped after the burn time and would stop immediately, lacking the additional benefit of the inertia. Hence the fractional instantaneous mass ejection is the optimal strategy. Interestingly, there is a sharp noise-induced discontinuous transition between the two strategies for an intermediate finite value

$$D_{r,\mathrm{crit}} \approx 0.72\,\gamma_0 \tag{54}$$

of the orientational noise. The latter is signaled by a sharp jump in the optimal burn time from $1.39\,\gamma_0$ to 0 [see Fig. 7(b)]. The optimal propellant mass fraction jumps from 1 to the universal value of $1 - e^{-1} \approx 0.63$ [see Fig. 7(c)] and can thus be viewed as the "order parameter" of the transition.

B. Comparison between the different setups

We now compare the different setups for time-dependent inertia as discussed in Sec. II in more detail (see again Fig. 2). In the case of directed mass ejection or isotropic mass evaporation [Figs. 2(b) and 2(c)], we assume a mass loss exponentially in time t as

$$m(t) = m_\infty + (m_0 - m_\infty)e^{-\gamma_m t}, \tag{55}$$

where m_0 is the initial mass, m_∞ is the rest mass, which remains after the fuel is burned, and γ_m is the mass decay rate. As outlined in Appendix B, an exponential mass loss occurs in particular for a rocket that ejects gas molecules at constant speed from a tank under isothermal and isochoric conditions. In this case, the exponential mass reduction follows from the reduction of the gas density in the tank. Accordingly, we also assume an exponential decrease in the moment of inertia,

$$J(t) = J_\infty + (J_0 - J_\infty)e^{-\gamma_J t}, \tag{56}$$

where J_0 is the initial and J_∞ the final moment of inertia, and γ_J is the decay rate of the moment of inertia. For the isotropic shape change [Fig. 2(d)], the mass is assumed to be constant, and only an exponential loss in the moment of inertia is prescribed.

The protocol is as follows. At time $t = 0$, we start from a steady state achieved for constant parameters and then initiate the mass loss and moment of inertia change (or in general arbitrary time dependences). For the different dynamical correlation functions, we correlate the system configuration after a time t with the steady-state condition at time $t = 0$ (over which we perform the average). For the different dynamical correlation functions, we correlate the steady-state condition at time $t = 0$ over which we perform the average with the system configuration after a time t. Under these conditions, we obtain general analytical results for arbitrary time dependences. Since the system is relaxing or "aging," the two-point correlation functions now depend explicitly on two times—t_1, t_2—not just on the time difference as in the steady state.

For $t_1 < t_2$, the orientational correlation function $C(t_1, t_2) = \langle \hat{\mathbf{n}}(t_1) \cdot \hat{\mathbf{n}}(t_2) \rangle$ is given by

$$C(t_1, t_2) = \cos(\mu(t_1, t_2))\, e^{-\frac{1}{2}\sigma(t_1, t_2)}, \tag{57}$$

with the mean angle difference

$$\mu(t_1, t_2) = \int_{t_1}^{t_2} dt'' \int_{-\infty}^{t''} dt'\, \frac{\xi_r(t')}{J(t')}\, \omega(t') e^{-\Gamma_r(t', t'')}, \tag{58}$$

the corresponding variance

$$\sigma(t_1, t_2) = 4 \int_{t_1}^{t_2} dt''' \int_{t_1}^{t'''} dt'' \times \left(\int_{-\infty}^{t''} dt' \left(\frac{\xi_r(t')}{J(t')} \right)^2 D_r(t') e^{-2\Gamma_r(t', t'')} \right) e^{-\Gamma_r(t'', t''')}, \tag{59}$$

and the rotational damping function

$$\Gamma_r(t_1, t_2) = \int_{t_1}^{t_2} dt'\, \frac{\xi_r(t')}{J(t')} + (1 - \nu) \ln\left(\frac{J(t_2)}{J(t_1)} \right). \tag{60}$$

Here, $\nu = 0$ in the case of isotropic shape change, and $\nu = 1$ in the case of isotropic mass evaporation.

TABLE I. Simulation parameter for the different setups.

	Time-independent inertia	Directed mass ejection	Isotropic mass ejection	Isotropic shape change
$m(t)$	m_0	$m_\infty + (m_0 - m_\infty)e^{-\gamma_m t}$	$m_\infty + (m_0 - m_\infty)e^{-\gamma_m t}$	m_0
γ_m		$0.1\ D_r$	$0.1\ D_r$	
m_∞/m_0		0.1	0.1	
u		$1\ v_0$		
$J(t)$	J_0	J_0	$J_\infty + (J_0 - J_\infty)e^{-\gamma_J t}$	$J_\infty + (J_0 - J_\infty)e^{-\gamma_J t}$
γ_J			$0.1\ D_r$	$0.1\ D_r$
J_∞/J_0			0.1	0.1

Similarly, the velocity correlation function $Z(t_1,t_2) = \langle \dot{\mathbf{R}}(t_1)\cdot\dot{\mathbf{R}}(t_2)\rangle$ for $t_1 < t_2$ is

$$Z(t_1,t_2) = 4\int_{-\infty}^{t_1} dt' \left(\frac{\xi(t')}{m(t')}\right)^2 D(t')e^{-\Gamma(t',t_1)}e^{-\Gamma(t',t_2)} + \int_{-\infty}^{t_1} dt' \int_{-\infty}^{t_2} dt'' a(t')a(t'')\langle \hat{\mathbf{n}}(t')\cdot\hat{\mathbf{n}}(t'')\rangle e^{-\Gamma(t',t_1)} \times e^{-\Gamma(t'',t_2)}, \tag{61}$$

with the acceleration

$$a(t) = \frac{\xi(t)}{m(t)}v_0(t) - \frac{\dot{m}(t)}{m(t)}u(t) \tag{62}$$

and the translational damping function

$$\Gamma(t_1,t_2) = \int_{t_1}^{t_2} dt' \frac{\xi(t')}{m(t')}. \tag{63}$$

For the delay function $d(t_1,t_2) = \langle \dot{\mathbf{R}}(t_2)\cdot\hat{\mathbf{n}}(t_1)\rangle - \langle \dot{\mathbf{R}}(t_1)\cdot\hat{\mathbf{n}}(t_2)\rangle$, we obtain

$$d(t_1,t_2) = \int_{-\infty}^{t_2} dt' a(t')\, \langle \hat{\mathbf{n}}(t')\cdot\hat{\mathbf{n}}(t_1)\rangle\, e^{-\Gamma(t',t_2)} - \int_{-\infty}^{t_1} dt' a(t')\, \langle \hat{\mathbf{n}}(t')\cdot\hat{\mathbf{n}}(t_2)\rangle\, e^{-\Gamma(t',t_1)}. \tag{64}$$

The general expression for the mean displacement $\langle \Delta\mathbf{R}(t_1,t_2)\rangle = \langle \mathbf{R}(t_2) - \mathbf{R}(t_1)\rangle$ is

$$\langle \Delta\mathbf{R}(t_1,t_2)\rangle = \int_{t_1}^{t_2} dt' \int_{-\infty}^{t'} dt'' a(t'')\, \langle \hat{\mathbf{n}}(t'')|\hat{\mathbf{n}}(t_1)\rangle e^{-\Gamma(t'',t')}, \tag{65}$$

where the conditional average

$$\langle \hat{\mathbf{n}}(t_2)|\hat{\mathbf{n}}(t_1)\rangle = \begin{cases} \hat{\mathbf{P}}\left[e^{-\frac{1}{2}\sigma(t_2,t_1) + i(\phi_1 + \mu(t_2,t_1))}\right] & \text{for } t_2 > t_1, \\ \hat{\mathbf{P}}\left[e^{-\frac{1}{2}\sigma(t_1,t_2) + i(\phi_1 + \mu(t_1,t_2))}\right] & \text{for } t_2 < t_1, \end{cases} \tag{66}$$

denotes the mean orientation under the condition that the particle has the angle $\phi(t_1) = \phi_1$ at time t_1.

Last, the mean-square displacement $\langle \Delta\mathbf{R}^2(t_1,t_2)\rangle = \langle (\mathbf{R}(t_2) - \mathbf{R}(t_1))^2\rangle$ is

$$\langle \Delta\mathbf{R}^2(t_1,t_2)\rangle = \int_{t_1}^{t_2} dt' \int_{t_1}^{t_2} dt'' Z(t',t''). \tag{67}$$

For time-independent parameters, we recover the results discussed in Sec. III. In particular, we have $C(t_1,t_2) = C(|t_1 - t_2|)$ [see Eq. (21)], $Z(t_1,t_2) = Z(|t_1 - t_2|)$ [see Eq. (18)], $d(t_1,t_2) = d(|t_1 - t_2|)$ [see Eq. (37)], $\langle \Delta\mathbf{R}(t_1,t_2)\rangle = \langle \Delta\mathbf{R}(|t_1 - t_2|)\rangle$ [see Eq. (24)], and $\langle \Delta\mathbf{R}^2(t_1,t_2)\rangle = \langle \Delta\mathbf{R}^2(|t_1 - t_2|)\rangle$ [see Eq. (27)].

Numerical data for the special case of an exponential mass loss [see Eq. (55)] and/or an exponential decay of the moment of inertia [see Eq. (56)] as summarized in Table I are presented in Figs. 8 and 9. Figure 8 is for an achiral particle and Fig. 9 for a chiral particle. The case of time-independent inertia (with the parameters at time $t = 0$) is shown as a reference, too. Equations (8) and (9) were discretized to perform Brownian dynamics simulations. For these simulations, we chose the time step $\Delta t = 10^{-2}/D_r$ and we performed 10^6 realizations to calculate the respective ensemble averages.

We first discuss the case of an achiral particle. For isotropic shape change, the orientational correlation function $C(0,t)$ decorrelates faster [see Fig. 8(a)], since the rotational noise is amplified during the decay of the moment of inertia. The velocity autocorrelation $Z(0,t)$ as well as the delay function $d(0,t)$ decorrelate faster if the particle actually loses mass [see Figs. 8(b) and 8(c)]. For the particle with directed mass ejection, we see an increase in the velocity autocorrelation for short times and a more pronounced peak in the delay function due to the additional acceleration, which enhances the particle velocity. The mean displacement along the initial displacement $\langle \Delta\mathbf{R}(0,t)\rangle\cdot\hat{\mathbf{n}}_0$ is displayed in Fig. 8(d). Although the particle with directed mass ejection is the fastest for short times, it gets overtaken for long times by the particle with time-independent inertia. Last, we discuss the mean-square displacement $\langle \Delta\mathbf{R}^2(0,t)\rangle$. Besides the additional acceleration for the particle with directed mass ejection for short times, the long-time diffusivity is identical to the case of time-independent inertia. In contrast, the cases of isotropic mass evaporation and isotropic shape end up with a decreased long-time diffusion coefficient [see Fig. 8(e)] due to a smaller persistence. The differences between the setups become clearer by considering the logarithmic derivative of the mean-square displacement

$$\alpha(t_1,t_2) = \frac{d\ln(\langle \Delta\mathbf{R}^2(t_1,t_2)\rangle)}{d\ln(t_2)}. \tag{68}$$

If the mean-square displacement follows a power law $\langle \Delta\mathbf{R}^2(t_1,t_2)\rangle \sim (t_2 - t_1)^\alpha$, $\alpha(t_1,t_2)$ is equal to the power-law exponent α. This scaling exponent is shown in Fig. 8(f). All setups start in a ballistic regime ($\alpha = 2$) for short times and

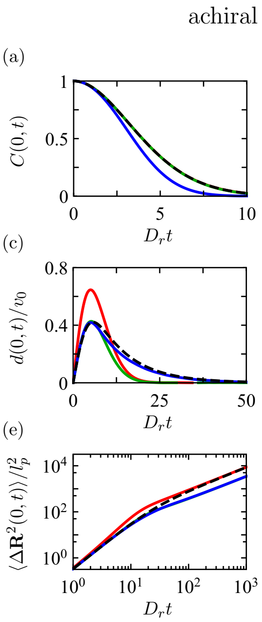

FIG. 8. Comparison of the different special setups for an achiral active particle ($\omega = 0$) with time-dependent inertia: (a) orientation autocorrelation function $C(0, t)$, (b) velocity autocorrelation function $Z(0, t)$, (c) delay function $d(0, t)$, (d) mean displacement along the initial orientation $\langle \Delta \mathbf{R}(0, t) \rangle \cdot \hat{\mathbf{n}}_0$, (e) mean-square displacement $\langle \Delta \mathbf{R}^2(0, t) \rangle$, and (f) the corresponding scaling exponent $\alpha(0, t)$ for time-independent inertia (dashed black), directed mass ejection (red), isotropic mass evaporation (green), and an isotropic change in the particle shape (blue). Velocities are given in units of v_0, times in $1/D_r$, and lengths in $l_p = v_0/D_r$. The time dependencies of the mass $m(t)$ and the moment of inertia $J(t)$ for the different setups are summarized in Table I. The remaining parameters are $D = 0$, $\gamma_0 = \xi/m_0 = 0.1 D_r$, and $\gamma_{r,0} = \xi_r/J_0 = 0.1 D_r$.

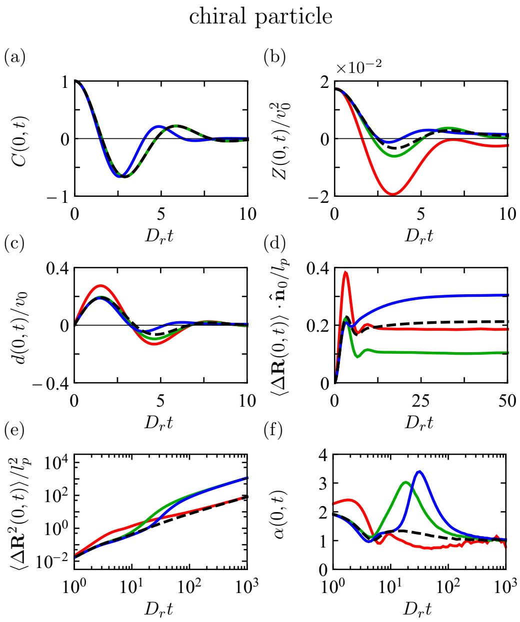

FIG. 9. Same as in Fig. 8 for a chiral particle with a spinning frequency of $\omega = 0.1 D_r$.

end up in a diffusive regime ($\alpha = 1$) for long times. Again for the particle with directed mass ejection we observe faster motion for short times indicated by a superballistic scaling $\alpha > 2$ due to the acceleration. For times greater than the inverse decay rate of the moment of inertia $1/\gamma_J$, the particles with isotropic mass evaporation and an isotropic shape change behave subdiffusively with $\alpha < 1$ since their effective diffusivity decreases.

Now we turn to the case of a chiral particle. First of all, even for constant parameters, the presence of the torque M yields systematic oscillations in the orientation and velocity autocorrelations, and also in the delay function [see Figs. 9(a)–9(c)]. Indeed, such oscillations in the delay function have been found recently in data for whirligig beetles [49]. Turning to the time-dependent cases, similar to the pirouette of figure skating, the particle with an isotropic shape contraction is spinning with a higher frequency during the decay of the moment of inertia. This is visible in the orientational and velocity autocorrelation functions and the delay function [see Figs. 9(a)–9(c)]. Also, when the particle loses mass, the oscillation becomes more pronounced since the particle can adapt more easily to orientation changes. In contrast to the achiral case, the long-time behavior of the mean-square displacement increases for the time-dependent setups when the moment of inertia $J(t)$ decreases [see Fig. 9(e)] in line with the trend discussed previously in Fig. 5. This is marked by a peak in the scaling exponent for times larger than $1/\gamma_J$ [see Fig. 9(f)].

C. Adiabatic approximation for slow variations

When the parameters [such as mass $m(t)$, moment of inertia $J(t)$, friction coefficients $\xi(t)$ and $\xi_r(t)$, noise strengths $D(t)$ and $D_r(t)$, and self-propulsion velocity $v_0(t)$] change very slowly in time, i.e., much slower than any other timescale inherent in the model, the system can be analyzed using the adiabatic approximation. In other words, one can take the expressions for the dynamical correlation function with constant parameters (as discussed in Sec. III) and insert into these expressions the slowly varying time-dependent parameters. This approximation becomes exact if the two time scales (largest system timescale and fastest timescale governing the change of all parameters) are separated completely.

Let us elaborate on the adiabatic approximation for the MSD by considering an achiral active particle. Corresponding analytical expressions for the MSD in the two limits of small and high moments of inertia J are given by (35) and (36), respectively. Using the long-time limit (31), we obtain within the adiabatic approximation for large J,

$$\langle \Delta \mathbf{R}^2(t)\rangle \sim 4\left(D(t) + \frac{v_0^2(t)}{4}\sqrt{\frac{2\pi J(t)}{D_r(t)\,\xi_r(t)}}\right)t, \tag{69}$$

when the moment of inertia J becomes sufficiently large, and

$$\langle \Delta \mathbf{R}^2(t)\rangle \sim 4\left(D(t) + \frac{v_0^2(t)}{2D_r(t)} + \frac{v_0^2(t)J(t)}{2\xi_r(t)}\right)t, \tag{70}$$

in the case of a small moment of inertia J. Let us now assume a slow power law in time for the moment of inertia, the self-propulsion, the rotational friction, and the diffusion coefficients,

$$v_0(t) \sim t^{\beta}, \quad J(t) \sim t^{\delta}, \quad \xi_r(t) \sim t^{\varepsilon}, \quad D_r(t) \sim t^{\eta}, \tag{71}$$

with prescribed dynamical exponents β, δ, ϵ, and η. Plugging this into the expressions (69) and (70), we obtain a power law for the long-time MSD of the active particle,

$$\langle \Delta \mathbf{R}^2(t)\rangle \sim t^{\alpha}, \tag{72}$$

with

$$\alpha = \max(1, 1 + 2\beta - \tfrac{1}{2}(\varepsilon - \delta + \eta)) \tag{73}$$

for large J and

$$\alpha = \max\,(1, 1 + 2\beta - \min(\varepsilon - \delta, \eta)) \tag{74}$$

for small J. If $\alpha > 1$, the adiabatic term is dominated overwhelmingly by the standard diffusion such that the particle exhibits *anomalous superdiffusion*. If $\alpha = 1$, the full MSD is dominated by the translational diffusion. We finally remark that simpler scaling laws were obtained earlier in the overdamped limit [83].

V. CONCLUSIONS

To conclude, we have investigated the dynamics of an inertia-dominated Brownian particle, referred to as active Langevin dynamics. Dynamical correlations within a simple model were calculated for a single "microflyer," which is simultaneously subjected to self-propulsion, inertia, damping, and fluctuations, and analytical results known for the overdamped limit of microswimmers were generalized to the inertial situation. In particular, we considered the case of time-dependent inertia. Furthermore, we identified a basic Langevin model for a rocketlike particle self-propelled by the ejection of mass for which we calculated its mean reach and found a noise-induced discontinuous transition in the optimal propulsion strategy for reaching the furthest distance. The case of chiral particles referred to as circle-flyers was included. One characteristic dynamical correlation absent in the overdamped case concerns the inertial delay between the orientation variations and the subsequent changes in the velocity direction. For achiral particles with vanishing spinning frequency, the inertial delay decays to zero after a profound peak at a typical delay time. Conversely, for chiral particles, the inertial delay correlation may oscillate between positive and negative values. Finally, we have also addressed the limiting "adiabatic" case of very slow inertia variation, and we have highlighted that a microflyer can undergo anomalous diffusion if the parameters are varying as a power law in time.

Future work should generalize the present model to external potentials such as optical fields, disorder, and confinement [39,102–105], and to motion in noninertial rotating frames [106,107]. Furthermore, anisotropic particles that show out-of-plane orientations and positions relevant for active complex plasmas [108] should be considered in the future. In this case, the equations of motion are getting more complex involving friction and inertia tensors significantly more complicated than in the overdamped limit [109,110]. Next, the "rocketlike" particles studied here should be realized in experiments; the most promising way seems to be dust particles in the plasma with evaporating mass. Moreover, it would be interesting to study collective effects of inertia-dominated active particles such as motility-induced phase separation [111–116] or pattern formation in general [117]. Finally, it would be interesting to generalize the more coarse-grained Ornstein-Uhlenbeck model for inertial active particles [118,119] to the situation of time-dependent parameters.

ACKNOWLEDGMENTS

We thank Christian Scholz, Ian Williams, and Anton Ldov for helpful discussions. This work is supported by the German Research Foundation through Grants No. LO 418/23-1 and No. IV 20/3-1.

APPENDIX A: GENERAL SOLUTION

For an analytical solution of the equations of motion, we first consider the rotational part [see Eq. (9)]. For $\phi_0 = \phi(t = 0)$ and $\dot\phi_0 = \dot\phi(t = 0)$, the solution of Eq. (9) is

$$\begin{aligned}\dot\phi(t) = {}& \dot\phi_0\, e^{-\Gamma_r(0,t)} \\ &+ \int_0^t dt' \frac{\xi_r(t')}{J(t')}\,\omega(t')\, e^{-\Gamma_r(t',t)} \\ &+ \int_0^t dt' \frac{\xi_r(t')}{J(t')}\sqrt{2D_r(t')}\tau_{\mathrm{st}}(t')\, e^{-\Gamma_r(t',t)},\end{aligned} \tag{A1}$$

and thus

$$\begin{aligned}\phi(t) = {}& \phi_0 + \int_0^t dt' \dot\phi_0\, e^{-\Gamma_r(0,t')} \\ &+ \int_0^t dt' \int_0^{t'} dt'' \frac{\xi_r(t'')}{J(t'')}\,\omega(t'') e^{-\Gamma_r(t'',t')} \\ &+ \int_0^t dt' \int_0^{t'} dt'' \frac{\xi_r(t'')}{J(t'')}\sqrt{2D_r(t'')}\tau_{\mathrm{st}}(t'') e^{-\Gamma_r(t'',t')},\end{aligned} \tag{A2}$$

where

$$\Gamma_r(t_1, t_2) = \int_{t_1}^{t_2} dt'\, \frac{\xi_r(t')}{J(t')} + (1 - \nu)\ln\left(\frac{J(t_2)}{J(t_1)}\right). \tag{A3}$$

The translational equation of motion yields for the particle velocity

$$\begin{aligned}\dot{\mathbf{R}}(t) = {}& \dot{\mathbf{R}}_0\, e^{-\Gamma(0,t)} + \int_0^t dt' a(t')\,\hat{\mathbf{n}}(t')\, e^{-\Gamma(t',t)} \\ &+ \int_0^t dt' \frac{\xi(t')}{m(t')}\sqrt{2D(t')}\mathbf{f}_{\mathrm{st}}(t')\, e^{-\Gamma(t',t)}.\end{aligned} \tag{A4}$$

Hence, the center-of-mass position is calculated as

$$\mathbf{R}(t) = \mathbf{R}_0 + \int_0^t dt' \dot{\mathbf{R}}_0\, e^{-\Gamma(0,t')} + \int_0^t dt' \int_0^{t'} dt'' a(t'')\, \hat{\mathbf{n}}(t'') e^{-\Gamma(t'',t')} + \int_0^t dt' \int_0^{t'} dt'' \frac{\xi(t'')}{m(t'')} \sqrt{2D(t'')}\mathbf{f}_{\rm st}(t'') e^{-\Gamma(t'',t')}, \tag{A5}$$

where

$$a(t) = \frac{\xi(t)}{m(t)} v_0(t) - \frac{\dot{m}(t)}{m(t)} u(t) \tag{A6}$$

and

$$\Gamma(t_1, t_2) = \int_{t_1}^{t_2} dt' \frac{\xi(t')}{m(t')}. \tag{A7}$$

Here $\mathbf{R}_0$ and $\dot{\mathbf{R}}_0$ are the initial position and velocity at time $t = 0$.

APPENDIX B: EXPONENTIAL MASS LOSS

In an isothermal environment of temperature T, the mass loss through a small leak of cross section S in the rocket tank of volume V in quasiequilibrium is governed by

$$\dot{m}_{\rm fuel}(t) = -\frac{1}{6}\frac{S}{V}\sqrt{\frac{3k_BT}{m_{\rm mol}}}\, m_{\rm fuel}(t) = -\gamma_m\, m_{\rm fuel}(t), \tag{B1}$$

where $m_{\rm mol}$ is the mass of the ejected molecules and k_B is the Boltzmann constant. Equation (B1) implies an exponential decay of the rocket fuel, i.e., $m_{\rm fuel}(t) = m_{\rm fuel}(0)\, e^{-\gamma_m t}$ with the mass decay rate γ_m and thus motivates Eq. (55).

[1] J. R. Howse, R. A. L. Jones, A. J. Ryan, T. Gough, R. Vafabakhsh, and R. Golestanian, Phys. Rev. Lett. **99**, 048102 (2007).
[2] P. Romanczuk, M. Bär, W. Ebeling, B. Lindner, and L. Schimansky-Geier, Eur. Phys. J. Spec. Top. **202**, 1 (2012).
[3] J. Elgeti, R. G. Winkler, and G. Gompper, Rep. Prog. Phys. **78**, 056601 (2015).
[4] C. Bechinger, R. Di Leonardo, H. Löwen, C. Reichhardt, G. Volpe, and G. Volpe, Rev. Mod. Phys. **88**, 045006 (2016).
[5] E. M. Purcell, Am. J. Phys. **45**, 3 (1977).
[6] B. ten Hagen, S. van Teeffelen, and H. Löwen, J. Phys.: Condens. Matter **23**, 194119 (2011).
[7] D. Klotsa, Soft Matter **15**, 8946 (2019).
[8] C. Scholz, S. Jahanshahi, A. Ldov, and H. Löwen, Nat. Commun. **9**, 5156 (2018).
[9] A. Callegari and G. Volpe, *Flowing Matter* (Springer International, Cham, 2019), pp. 211–238.
[10] J. Um, T. Song, and J.-H. Jeon, Front. Phys. **7**, 143 (2019).
[11] H. Löwen, J. Chem. Phys. **152**, 040901 (2020).
[12] M. Enculescu and H. Stark, Phys. Rev. Lett. **107**, 058301 (2011).
[13] P. K. Ghosh, Y. Li, G. Marchegiani, and F. Marchesoni, J. Chem. Phys. **143**, 211101 (2015).
[14] M. Joyeux and E. Bertin, Phys. Rev. E **93**, 032605 (2016).
[15] A. Manacorda and A. Puglisi, Phys. Rev. Lett. **119**, 208003 (2017).
[16] S. C. Takatori and J. F. Brady, Phys. Rev. Fluids **2**, 094305 (2017).
[17] Z. Mokhtari, T. Aspelmeier, and A. Zippelius, Europhys. Lett. **120**, 14001 (2017).
[18] S. Das, G. Gompper, and R. G. Winkler, Sci. Rep. **9**, 6608 (2019).
[19] M. Sandoval, Phys. Rev. E **101**, 012606 (2020).
[20] L. L. Gutierrez-Martinez and M. Sandoval, J. Chem. Phys. **153**, 044906 (2020).
[21] W. Ebeling, F. Schweitzer, and B. Tilch, Bio Systems **49**, 17 (1999).
[22] C. A. Weber, T. Hanke, J. Deseigne, S. Léonard, O. Dauchot, E. Frey, and H. Chaté, Phys. Rev. Lett. **110**, 208001 (2013).
[23] D. R. Parisi, R. Cruz Hidalgo, and I. Zuriguel, Sci. Rep. **8**, 9133 (2018).
[24] G. E. Morfill and A. V. Ivlev, Rev. Mod. Phys. **81**, 1353 (2009).
[25] K. R. Sütterlin, A. Wysocki, A. V. Ivlev, C. Räth, H. M. Thomas, M. Rubin-Zuzic, W. J. Goedheer, V. E. Fortov, A. M. Lipaev, V. I. Molotkov, O. F. Petrov, G. E. Morfill, and H. Löwen, Phys. Rev. Lett. **102**, 085003 (2009).
[26] L. Couëdel, V. Nosenko, A. V. Ivlev, S. K. Zhdanov, H. M. Thomas, and G. E. Morfill, Phys. Rev. Lett. **104**, 195001 (2010).
[27] M. Chaudhuri, A. V. Ivlev, S. A. Khrapak, H. M. Thomas, and G. E. Morfill, Soft Matter **7**, 1287 (2011).
[28] A. V. Ivlev, J. Bartnick, M. Heinen, C.-R. Du, V. Nosenko, and H. Löwen, Phys. Rev. X **5**, 011035 (2015).
[29] V. Nosenko, F. Luoni, A. Kaouk, M. Rubin-Zuzic, and H. Thomas, Phys. Rev. Res. **2**, 033226 (2020).
[30] V. Narayan, S. Ramaswamy, and N. Menon, Science **317**, 105 (2007).
[31] A. Kudrolli, G. Lumay, D. Volfson, and L. S. Tsimring, Phys. Rev. Lett. **100**, 058001 (2008).
[32] J. Deseigne, O. Dauchot, and H. Chaté, Phys. Rev. Lett. **105**, 098001 (2010).
[33] L. Giomi, N. Hawley-Weld, and L. Mahadevan, Proc. R. Soc. A **469**, 20120637 (2013).
[34] D. Klotsa, K. A. Baldwin, R. J. A. Hill, R. M. Bowley, and M. R. Swift, Phys. Rev. Lett. **115**, 248102 (2015).
[35] G. A. Patterson, P. I. Fierens, F. Sangiuliano Jimka, P. G. König, A. Garcimartín, I. Zuriguel, L. A. Pugnaloni, and D. R. Parisi, Phys. Rev. Lett. **119**, 248301 (2017).
[36] G. Junot, G. Briand, R. Ledesma-Alonso, and O. Dauchot, Phys. Rev. Lett. **119**, 028002 (2017).
[37] S. Ramaswamy, J. Stat. Mech. (2017) 054002.
[38] A. Deblais, T. Barois, T. Guerin, P. H. Delville, R. Vaudaine, J. S. Lintuvuori, J. F. Boudet, J. C. Baret, and H. Kellay, Phys. Rev. Lett. **120**, 188002 (2018).
[39] O. Dauchot and V. Démery, Phys. Rev. Lett. **122**, 068002 (2019).
[40] J. Rabault, R. A. Fauli, and A. Carlson, Phys. Rev. Lett. **122**, 024501 (2019).
[41] R. A. Fauli, J. Rabault, and A. Carlson, Phys. Rev. E **100**, 013108 (2019).

[42] M. Leoni, M. Paoluzzi, S. Eldeen, A. Estrada, L. Nguyen, M. Alexandrescu, K. Sherb, and W. W. Ahmed, Phys. Rev. Research **2**, 043299 (2020).
[43] R. Di Leonardo, G. Ruocco, J. Leach, M. J. Padgett, A. J. Wright, J. M. Girkin, D. R. Burnham, and D. McGloin, Phys. Rev. Lett. **99**, 010601 (2007).
[44] M. Rubenstein, A. Cornejo, and R. Nagpal, Science **345**, 795 (2014).
[45] R. Fujiwara, T. Kano, and A. Ishiguro, Adv. Robot. **28**, 639 (2014).
[46] S. Tolba, R. Ammar, and S. Rajasekaran, in *2015 IEEE Symposium on Computers and Communication (ISCC)* (IEEE, Piscataway, 2015), pp. 1007–1013.
[47] Z. Zhakypov, K. Mori, K. Hosoda, and J. Paik, Nature (London) **571**, 381 (2019).
[48] X. Yang, C. Ren, K. Cheng, and H. P. Zhang, Phys. Rev. E **101**, 022603 (2020).
[49] M. Turner (private discussion).
[50] J. Toner and Y. Tu, Phys. Rev. Lett. **75**, 4326 (1995).
[51] J. Toner and Y. Tu, Phys. Rev. E **58**, 4828 (1998).
[52] E. Chiappini, *Encyclopedia of Entomology* (Springer, The Netherlands, 2008), pp. 152–154.
[53] J. Bartussek and F. O. Lehmann, R. Soc. Open Sci. **3**, 150562 (2016).
[54] H. Mukundarajan, T. C. Bardon, D. H. Kim, and M. Prakash, J. Exp. Biol. **219**, 752 (2016).
[55] J. Bartussek and F. O. Lehmann, J. R. Soc. Interface **15**, 20180408 (2018).
[56] A. Attanasi, A. Cavagna, L. Del Castello, I. Giardina, T. S. Grigera, A. Jelic, S. Melillo, L. Parisi, O. Pohl, E. Shen, and M. Viale, Nat. Phys. **10**, 691 (2014).
[57] C. van den Berg and J. M. V. Rayner, J. Exp. Biol. **198**, 1655 (1995).
[58] M. Qiao, B. Brown, and D. L. Jindrich, J. Exp. Biol. **217**, 432 (2014).
[59] S. I. Krasheninnikov, A. Y. Pigarov, R. D. Smirnov, and T. K. Soboleva, Contrib. Plasma Phys. **50**, 410 (2010).
[60] V. Nosenko, A. V. Ivlev, and G. E. Morfill, Phys. Plasmas **17**, 123705 (2010).
[61] I. Müller and P. Strehlow, Physik. Blätter **55**, 37 (1999).
[62] R. Mangan and M. Destrade, Int. J. Non Linear Mech. **68**, 52 (2015).
[63] F. O. Eke and T. C. Mao, IJMEE **30**, 123 (2002).
[64] V. Panchal and R. Jangid, Nucl. Eng. Des. **238**, 1304 (2008).
[65] C. Lozano, B. Liebchen, B. ten Hagen, C. Bechinger, and H. Löwen, Soft Matter **15**, 5185 (2019).
[66] M. A. Fernandez-Rodriguez, F. Grillo, L. Alvarez, M. Rathlef, I. Buttinoni, G. Volpe, and L. Isa, Nat. Commun. **11**, 4223 (2020).
[67] A. R. Sprenger, M. A. Fernandez-Rodriguez, L. Alvarez, L. Isa, R. Wittkowski, and H. Löwen, Langmuir **36**, 7066 (2020).
[68] J. Embs, H. W. Müller, C. Wagner, K. Knorr, and M. Lücke, Phys. Rev. E **61**, R2196(R) (2000).
[69] B. A. Stickler, B. Schrinski, and K. Hornberger, Phys. Rev. Lett. **121**, 040401 (2018).
[70] Y. Couder and E. Fort, Phys. Rev. Lett. **97**, 154101 (2006).
[71] R. N. Valani, A. C. Slim, and T. Simula, Phys. Rev. Lett. **123**, 024503 (2019).
[72] K. E. Tsiolkovsky, *The Exploration of Cosmic Space by Means of Reaction Devices* (The Science Review, 1903), Vol. 5.
[73] R. Metzler, E. Barkai, and J. Klafter, Phys. Rev. Lett. **82**, 3563 (1999).
[74] R. Golestanian, Phys. Rev. Lett. **102**, 188305 (2009).
[75] F. Hoefling and T. Franosch, Rep. Prog. Phys. **76**, 046602 (2013).
[76] J. Bleibel, A. Dominguez, F. Gunther, J. Harting, and M. Oettel, Soft Matter **10**, 2945 (2014).
[77] A. Morin, D. L. Cardozo, V. Chikkadi, and D. Bartolo, Phys. Rev. E **96**, 042611 (2017).
[78] A. Taloni, O. Flomenbom, R. Castaneda-Priego, and F. Marchesoni, Soft Matter **13**, 1096 (2017).
[79] C. Charalambous, M. Á. García-March, G. Muñoz-Gil, P. R. Grzybowski, and M. Lewenstein, Quantum **4**, 232 (2020).
[80] S. Chaki and R. Chakrabarti, J. Chem. Phys. **150**, 094902 (2019).
[81] A. S. Bodrova, A. V. Chechkin, A. G. Cherstvy, H. Safdari, I. M. Sokolov, and R. Metzler, Sci. Rep. **6**, 30520 (2016).
[82] S. van Teeffelen and H. Löwen, Phys. Rev. E **78**, 020101(R) (2008).
[83] S. Babel, B. ten Hagen, and H. Löwen, J. Stat. Mech. (2014) P02011.
[84] K. S. Olsen, arXiv:2012.05415.
[85] B. ten Hagen, R. Wittkowski, D. Takagi, F. Kümmel, C. Bechinger, and H. Löwen, J. Phys. Condens. Matter **27**, 194110 (2015).
[86] A. Sommerfeld, *Mechanics*, Lectures on Theoretical Physics (Academic, New York, 1952), Vol. 1, p. 28.
[87] W. T. Thomson, AIAA J. **4**, 766 (1966).
[88] A. R. Plastino and J. C. Muzzio, Celest. Mech. Dynam. Astron. **53**, 227 (1992).
[89] J. L. Anderson, Phys. Fluids **26**, 2871 (1983).
[90] J. Nardi, R. Bruinsma, and E. Sackmann, Phys. Rev. Lett. **82**, 5168 (1999).
[91] S. Eloul, W. C. K. Poon, O. Farago, and D. Frenkel, Phys. Rev. Lett. **124**, 188001 (2020).
[92] J. Li, I. Rozen, and J. Wang, ACS Nano **10**, 5619 (2016).
[93] R. A. Rankin and L. Rosenhead, Philos. Trans. R. Soc. London Ser. A **241**, 457 (1949).
[94] R. B. Paris, Incomplete gamma function, in *NIST Handbook of Mathematical Functions* (Cambridge University Press, Cambridge, 2010).
[95] C. Kurzthaler and T. Franosch, Soft Matter **13**, 6396 (2017).
[96] J.-P. Hansen and I. R. McDonald, *Theory of Simple Liquids* (Elsevier, Amsterdam, 1990).
[97] P. Herrera and M. Sandoval, Phys. Rev. E **103**, 012601 (2021).
[98] K. Malakar, A. Das, A. Kundu, K. V. Kumar, and A. Dhar, Phys. Rev. E **101**, 022610 (2020).
[99] F. Kümmel, B. ten Hagen, R. Wittkowski, I. Buttinoni, R. Eichhorn, G. Volpe, H. Löwen, and C. Bechinger, Phys. Rev. Lett. **110**, 198302 (2013).
[100] R. A. Askey and A. B. O. Daalhuis, Generalized hypergeometric function, in *NIST Handbook of Mathematical Functions* (Cambridge University Press, Cambridge, 2010).
[101] N. Srivastava, P. T. Tkacik, and R. G. Keanini, Proc. R. Soc. A **468**, 3965 (2012).
[102] S. Bianchi, R. Pruner, G. Vizsnyiczai, C. Maggi, and R. di Leonardo, Sci. Rep. **6**, 27681 (2016).

[103] L. Caprini, U. Marini Bettolo Marconi, A. Puglisi, and A. Vulpiani, J. Chem. Phys. **150**, 024902 (2019).

[104] A. Militaru, M. Innerbichler, M. Frimmer, F. Tebbenjohanns, L. Novotny, and C. Dellago, arXiv:2012.04478.

[105] D. Breoni, M. Schmiedeberg, and H. Löwen, Phys. Rev. E **102**, 062604 (2020).

[106] H. Löwen, Phys. Rev. E **99**, 062608 (2019).

[107] Y. Zheng and H. Löwen, Phys. Rev. Res. **2**, 023079 (2020).

[108] L. D. Landau and E. M. Lifshitz, *Mechanics*, Course of Theoretical Physics (Pergamon, Oxford, 1976), Vol. 1.

[109] R. Wittkowski and H. Löwen, Phys. Rev. E **85**, 021406 (2012).

[110] D. J. Kraft, R. Wittkowski, B. ten Hagen, K. V. Edmond, D. J. Pine, and H. Löwen, Phys. Rev. E **88**, 050301(R) (2013).

[111] A. Suma, G. Gonnella, D. Marenduzzo, and E. Orlandini, Europhys. Lett. **108**, 56004 (2014).

[112] C. Scholz, M. Engel, and T. Pöschel, Nat. Commun. **9**, 931 (2018).

[113] I. Petrelli, P. Digregorio, L. F. Cugliandolo, G. Gonnella, and A. Suma, Eur. Phys. J. E **41**, 128 (2018).

[114] S. Mayya, G. Notomista, D. Shell, S. Hutchinson, and M. Egerstedt, in *2019 IEEE/RSJ International Conference on Intelligent Robots and Systems (IROS)* (IEEE, Piscataway, 2019), pp. 4106–4112.

[115] S. Mandal, B. Liebchen, and H. Löwen, Phys. Rev. Lett. **123**, 228001 (2019).

[116] L. Caprini and U. Marini Bettolo Marconi, Soft Matter (2021), doi: 10.1039/D0SM02273J.

[117] D. Arold and M. Schmiedeberg, J. Phys.: Condens. Matter **32**, 315403 (2020).

[118] L. Caprini and U. Marini Bettolo Marconi, J. Chem. Phys. **154**, 024902 (2021).

[119] P. Nguyen, R. Wittmann, and H. Löwen (unpublished).

P4 Inertial self-propelled particles in anisotropic environments

The following manuscript was submitted to a peer-reviewed scientific journal and is currently under review

A. R. Sprenger, C. Scholz, A. Ldov, R. Wittkowski, and H. Löwen,
Inertial self-propelled particles in anisotropic environments,
(under review) (2022).

Statement of contribution

C.S. and H.L. designed the research. C.S. designed the experimental setup. C.S. and A.L. carried out the experiments. A.R.S. and C.S. analyzed the measurements. A.R.S. developed the theoretical and numerical results. A.R.S. prepared the figures. All authors discussed the results and wrote the manuscript.

Inertial self-propelled particles in anisotropic environments

Alexander R. Sprenger,[1] Christian Scholz,[1] Anton Ldov,[1] Raphael Wittkowski,[2] and Hartmut Löwen[1]
[1] *Institut für Theoretische Physik II: Weiche Materie, Heinrich-Heine-Universität Düsseldorf, D-40225 Düsseldorf, Germany*
[2] *Institut für Theoretische Physik, Center for Soft Nanoscience, Westfälische Wilhelms-Universität Münster, D-48149 Münster, Germany*

Self-propelled particles in anisotropic environments can exhibit a motility that depends on their orientation. This dependence is relevant for a plethora of living organisms but difficult to study in controlled environments. Here, we present a macroscopic system of self-propelled vibrated granular particles on a striated substrate that displays orientation-dependent motility. An extension of the active Brownian motion model involving orientation-dependent motility and inertial effects reproduces and explains our experimental observations. The model can be applied to general n-fold symmetric anisotropy and can be helpful for predictive optimization of the dynamics of active matter in complex environments.

The survival of organisms in complex environments essentially depends on their fitness and strategy to react and adapt to external conditions. In particular, a realistic environment is never isotropic but typically *anisotropic*, i.e., its traversability depends on the direction of motion [1]. Anisotropy can be caused on various scales by many different means: by an external force arising from gravity [2, 3], viscosity [4], light [5], and chemical gradients [6], electromagnetic fields [7], through steric confinement by channels, veins, and anisotropic porous media [8, 9], or by motion in a liquid-crystalline [10–14] or crystalline [15–17] medium. Anisotropic environments can have a pronounced impact on the motion of self-propelled particles. These "active" particles convert energy from their environment into directed motion and comprise both living organisms and artificial inanimate objects, like activated colloids [18–20], granules [21–25], and robots [26–28]. Standard models of self-propelled particles [29] assume that the propulsion force is isotropic in the sense that it always points into the direction of the particle orientation with a constant self-propulsion speed even in an inhomogeneous environment [30–36]. In anisotropic environments, a dependence of the self-propulsion speed of the particle on its orientation is frequently observed. Some biological organisms react to their environment in a sense that the propulsion force depends on their orientation relative to the environment. For instance, microorganisms can move faster towards light sources [37] or in the direction of food sources [38]. Additionally, flying animals such as bees and birds control their flying speed by relative changes of their environment, which in turn leads to anisotropic flying velocities within structured environments [39–41]. Similarly, anisotropic movement is also observed for smaller insects like ants in guiding structures [42, 43]. Those macroscopic self-propelled particles in low-friction environments (e.g., such as flying insects) where the effect of anisotropy is most prominent, are also governed by inertial effects [44]. This poses a challenging problem because inertia introduces correlations that can persist for longer times [45–53].

In this communication, we present an experimental realization of a self-propelled granular particle on an anisotropically structured substrate, which mimics this behavior. For these inanimate self-propelled objects, we find pronounced anisotropy in the motion of the particles, which is well explained by an extension of the active Brownian motion model with inertia and orientation-dependent motility. The orientation-dependence can be written in terms of a Fourier series which allows a general solution for anisotropic motility that can be applied to our experiments. Our findings not only open a new model class of active matter in anisotropic environments but also shed new light on the self-propulsion strategies of organisms in such anisotropies. Our model is particularly relevant for predictive optimization of control parameters of artificial active agents, such as robots [26–28], to better explore anisotropic environments [54].

RESULTS

Experimental observation of anisotropic self-propulsion

Macroscopic active matter with orientation-dependent motility can be realized from self-propelled 3D-printed agents called vibrobots (see Fig. 1a) on structured substrates. These particles are excited by vertical vibrations generated by a rectangular acrylic baseplate attached to an electromagnetic shaker. The particles stand on slightly tilted legs, which causes the particles to hop forward. These legs are all tilted equally along the orientation (or symmetry axis) of the particle. The baseplate is covered with a lenticular plastic sheet on top, which is the source for the anisotropic motility. The experimental setup is depicted in Fig. 1b. An illustration with a side-view of the particle resting on such a grooved surface are shown in Fig. 1c. The vibration frequency is set to $f = 80\,\mathrm{Hz}$, which ensures robust experimental

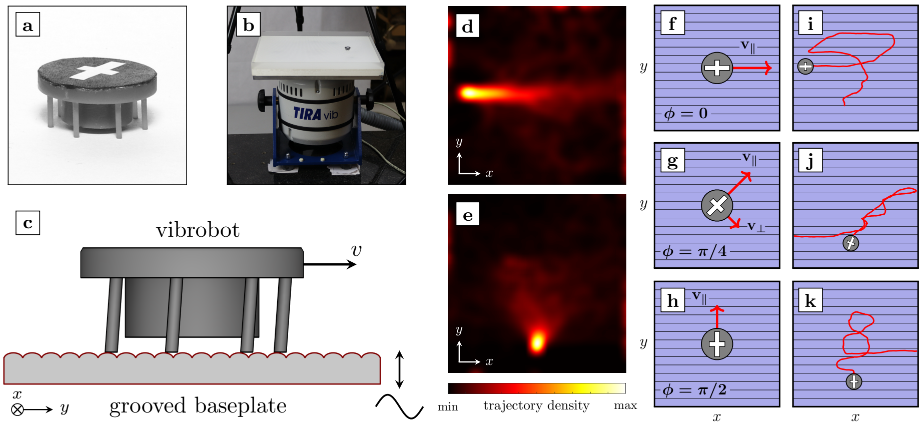

Figure 1. Vibrationally driven self-propelled particle (vibrobot) manufactured by 3D printing (**a**). The white cross indicates the particle orientation. Experimental setup (**b**): Rectangular acrylic baseplate attached to an electromagnetic shaker. Cross-section of the anisotropic substrate (lenticular foil) with particle to scale (**c**). Panels **d**,**e**: Trajectory density for vibrobots starting parallel (**d**) and perpendicular (**e**) to grooves with an excitation amplitude $A = 1.28\,g$. Panels **f**-**h**: Sketch of the two velocity contributions. The particle moves with increased velocity $v_\parallel$ when aligned along the grooves (**f**). When orientated diagonally, the particle moves with average velocity $v_\parallel$ along its orientation while simultaneously experiencing active propulsion $v_\perp$ perpendicular to it (**g**). The particle moves with decreased velocity $v_\parallel$ when perpendicularly aligned to the grooves (**h**). Panels **i**-**k**: Three representative trajectories with an excitation amplitude $A = 1.60\,g$. The persistence length is noticeably shorter for perpendicularly aligned particles than for parallel aligned particles. Length ratios and velocity contributions are not to scale.

conditions [47]. Three different peak acceleration amplitudes $A = 1.28\,g$, $1.44\,g$, and $1.60\,g$ are investigated, which varies the motility and motion properties of the vibrobot.

We find pronounced anisotropy in the motion of the particle and observe a modulation of the velocity parallel but also perpendicular to the orientation of the grooves, as well as an increased activity with increasing excitation amplitude. The motion of the particles is illustrated in Supplementary videos 1 - 6, where we show a montage of all measured trajectories for each excitation amplitude as well as for parallel and perpendicular initial orientation, respectively. From the trajectories, the anisotropy is already visible by the naked eye, in particular when comparing parallel and perpendicular starting orientations.

This anisotropy is best illustrated when displaying all recorded trajectories (integrated and smoothed) and distinguishing parallel and perpendicular initial orientations, as shown in Fig. 1d, e. For particles starting parallel to the grooves, we observe that the peak of the density (which is linked to the starting position of the particles) is broad along and narrow perpendicular to the starting orientation since the particles tend to move faster parallel to the grooves and therefore propagate further before they reorient. In the case of perpendicular starting orientation, the density spreads more around the peak, since particles reorient near to the starting position. Hence the persistence length depends on the orientation of the particle. Surprisingly, from individual particle trajectories, we also identify a driving-force component perpendicular to the orientation, whenever a particle is not moving exactly parallel or perpendicular to the grooves.

The anisotropic self-propulsion is caused by the grooved surface of the vibrating plate. Our conjecture is that this is due to the strong dependence of the particle speed on the relative inclination angle between legs and surface [55]. When resting on the vibrating plate, the legs are bent along the orientation of the particle. This deformation stores elastic energy. Then, after detaching from the base, the energy is released and the vibrobot jumps forward. When the particle is oriented perpendicular to the grooves, the legs face an elliptical half-cylinder and the relative inclination angle of the legs is decreased (see Fig. 1c). As a result, the legs will bend less compared to the case where the particle is oriented along the grooves. If the particle is diagonally aligned with the grooves, the legs will not bend along the orientation and the particle experiences a force perpendicular to its orientation. This in fact results in propulsion perpendicular to the orientation of the particle. In Fig. 1f-h, we illustrate the two velocity contributions for three different orientations of the particle.

As described in the literature, we also observe orientational fluctuations, caused by an instability of the driving mechanism to the microscopic surface roughness, and inertial delay effects due to the mass of the particles [47]. When vibrobots are excited above a certain amplitude threshold, they begin to tumble [56]. As a result, they randomly reorient while moving and eventually change the direction of their path. Figure 1i-k shows three representative trajectories with different initial orientations. Clearly, the particle does not show a deterministic motion, apart from short-time correlations due to initial orientation and inertia. The particle rather undergoes an anisotropic two dimensional random walk with a certain persistence length.

Due to the simplicity of our particles, compared to living active matter, our experiment allows us to investigate kinetic properties of particles with orientation-dependent motility, which can be useful for optimization of motion and search strategies of active matter in general. This requires an analytical description of the motion that captures the essential properties of the particle and must be applicable to general cases of anisotropic motility.

Langevin dynamics model

Finding an analytical description for macroscopic self-propelled systems can be challenging due to the complex interaction of particles and environment. Here, we model those interactions with an effective driving force and thereby introduce a minimal model, where the interplay of orientation-dependent motility, inertia, and fluctuations, is treated in terms of a generalized active Langevin dynamics model. Our model reproduces the experimental observations quantitatively despite its complex anisotropic nature.

We assume that the particle has non-negligible mass M and moment of inertia J. The motion of such an underdamped particle is in general characterized by the translational center-of-mass velocity $\dot{\mathbf{r}}(t)$ with the center-of-mass position $\mathbf{r}(t)$ and the time variable t as well as by the angular velocity $\dot{\phi}(t)$ and the angle of orientation $\phi(t)$, which denotes the angle between the orientation vector $\hat{\mathbf{n}} = (\cos\phi, \sin\phi)$ and the positive x-axis. By taking the above considerations into account, the translational and rotational motion of the particle is governed by the force balance between inertial, frictional, self-propulsive driving, and random forces and torques

$$M\,\ddot{\mathbf{r}}(t) + \gamma_T\,\dot{\mathbf{r}}(t) = \gamma_T\,\mathbf{v}\big(\phi(t)\big) + \sqrt{2D_T}\,\gamma_T\,\boldsymbol{\xi}(t), \quad (1)$$

$$J\,\ddot{\phi}(t) + \gamma_R\,\dot{\phi}(t) = \gamma_R\,\omega + \sqrt{2D_R}\,\gamma_R\,\eta(t). \quad (2)$$

Here, γ_T and γ_R denote the translational and rotational friction coefficients, respectively. To take translational and rotational diffusion into account, the Langevin equations contain independent Gaussian white noise terms $\boldsymbol{\xi}(t)$ and $\eta(t)$, with zero means $\langle\boldsymbol{\xi}(t)\rangle = \mathbf{0}$ and $\langle\eta(t)\rangle = 0$ and delta-correlated variances $\langle\xi_i(t_1)\xi_j(t_2)\rangle = \delta_{ij}\,\delta(t_1 - t_2)$ and $\langle\eta(t_1)\eta(t_2)\rangle = \delta(t_1 - t_2)$, where $i, j \in \{x, y\}$. Therein, D_T and D_R are the translational and rotational short-time diffusion coefficients of the particle, respectively. The brackets $\langle\ldots\rangle$ denote the noise average in the stationary state (meaning after losing correlation with initial conditions [52]) and δ_{ij} is the Kronecker delta.

Most importantly, $\mathbf{v}(\phi)$ denotes an arbitrary orientation-dependent motility which accounts for the interaction between the particle and environment. For mathematical convenience, we represent $\mathbf{v}(\phi)$ as a Fourier series

$$\mathbf{v}(\phi) = \sum_{\substack{k=-\infty \\ k\neq 0}}^{\infty} \mathbf{c}_k \exp(\mathrm{i}k\phi), \quad (3)$$

where $\mathbf{c}_k$ is the Fourier-coefficient vector of the mode k, and i denotes the imaginary unit. This representation lets us solve the model for any type of orientation-dependence and then apply the results to our experimental system. In particular, this description can be used for different experimental realizations ranging from anisotropic illuminated Janus particles, triangular microparticles in traveling ultrasound waves, and the motion of living insects in guiding structures to the specific setup studied in this communication [57, 58]. In general, for a given propulsion velocity $\mathbf{v}(\phi)$, these Fourier coefficients can be calculated as $\mathbf{c}_k = \int_{-\pi}^{\pi}(\mathbf{v}(\phi)/(2\pi))\exp(-\mathrm{i}k\phi)\,\mathrm{d}\phi$ (thus we have after complex conjugation $\mathbf{c}_k^* = \mathbf{c}_{-k}$). The seminal case of isotropic propulsion is recovered for the two non-zero coefficients $\mathbf{c}_{\pm1} = v(1, \mp\mathrm{i})/2$. Note that we exclude the mode $k = 0$ in Eq. (3), which would correspond to a drift velocity induced by a constant external force (e.g., gravity) not measured in the experiment.

Moreover, as typical 3D-printed particles are not perfectly symmetrical, they tend to perform circular motions on long time scales. To capture this behaviour, we assume a systematic torque which acts on the particle and leads to an angular speed ω. In contrast to $\mathbf{v}(\phi)$, we measured no orientational dependency in the angular speed which could in principle be caused by the anisotropic substrate.

Concluding, our theoretical model depends on a number of parameters: the angular velocity ω, the rotational diffusion coefficient D_R, the rotational friction time $\tau_J = J/\gamma_R$, the set of Fourier coefficients $\{\mathbf{c}_k\}$ describing the anisotropic motility, the translational diffusion coefficient D_T and the translational friction time $\tau_M = M/\gamma_T$. In the context of the experimental observations, we assume that the vibrobot is moving with an orientation-dependent velocity

$$\mathbf{v}(\phi) = \big(\mathrm{v}_\parallel + \delta\mathrm{v}_\parallel\cos(2\phi)\big)\,\hat{\mathbf{n}}(\phi) - \delta\mathrm{v}_\perp\sin(2\phi)\hat{\mathbf{n}}_\perp(\phi), \quad (4)$$

where $\hat{\mathbf{n}}(\phi) = (\cos\phi, \sin\phi)$ is pointing parallel and $\hat{\mathbf{n}}_\perp(\phi) = (-\sin\phi, \cos\phi)$ is pointing perpendicular to the particle's orientation. The sine and cosine terms in Eq. (4) reflect the orientation dependence of the particle velocity and the symmetry of the system. This adds the parallel speed $v_\parallel$, the parallel speed anisotropy $\delta v_\parallel$, and the perpendicular speed anisotropy $\delta v_\perp$, leading to a total of 8 independent parameters. The four non-zero Fourier coefficients of Eq. (4) read $\mathbf{c}_{\pm1} = v_\parallel(1, \mp i)/2 + (\delta v_\parallel + \delta v_\perp)(1, \pm i)/4$ and $\mathbf{c}_{\pm3} = (\delta v_\parallel - \delta v_\perp)(1, \mp i)/4$.

These parameters are determined from analytic fits to the experimental results. We use temporal correlation functions, like the orientational correlation function $C(t) = \langle \hat{\mathbf{n}}(t) \cdot \hat{\mathbf{n}}(0) \rangle$ and the velocity correlation function $Z(t) = \langle \dot{\mathbf{r}}(t) \cdot \dot{\mathbf{r}}(0) \rangle$, to determine the relevant timescales and diffusion coefficients. Further stationary observables, like the mean translational velocity $\mathbf{v}_0 = \langle \dot{\mathbf{r}}(0) \rangle$ and the mean angular velocity $\langle \dot{\phi}(0) \rangle$, are used to estimate all motility parameters. More information on the parameter estimation can be found in the Methods section and the parameter values are listed in Tab. I. In the following, we compare the experimental data with analytic predictions derived from the theoretical model and discuss the anisotropy found in several observables.

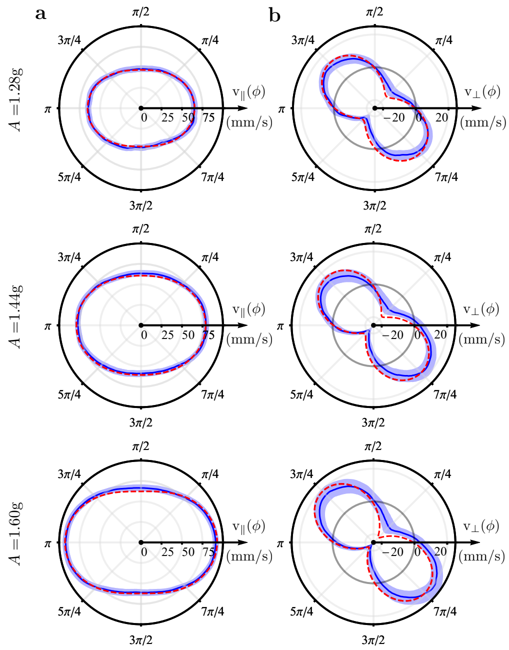

Figure 2. Stationary parallel velocity $v_\parallel$ (**a**) and stationary perpendicular velocity $v_\perp$ (**b**) plotted as a function of the orientation angle ϕ for three different excitation amplitudes A = 1.28 g (upper row), A = 1.44 g (middle row), and 1.60 g (lower row). Solid dark blue and dashed red curves show the experimental data and analytical results, respectively. Blue experimental error intervals represent the standard error of the mean.

Comparison between analytical results and experiment

As described above, the mean self-propulsion strongly depends on the relative orientation of the particle with respect to the groove direction. The model describes this via two orthogonal velocity components. In Fig. 2, we separately show the mean velocity along the body-axis $v_\parallel = \mathbf{v}_0 \cdot \hat{\mathbf{n}}$ and perpendicular to it $v_\perp = \mathbf{v}_0 \cdot \hat{\mathbf{n}}_\perp$ as functions of the orientation ϕ. The parallel contribution $v_\parallel$ in Fig. 2a shows considerably greater propulsion along the grooves than perpendicular to them. For the perpendicular contribution (see Fig. 2b) we find the assumed $\sin(2\phi)$-modulation (see Eq. (4)), which has an alignment effect on the overall velocity direction in favor of the groove direction. Overall, we measure increased activity for larger excitation amplitudes while the degree of anisotropy remains almost the same for all three measurements. From the theoretical side, the mean instantaneous velocity $\mathbf{v}_0 = \langle \dot{\mathbf{r}}(0) \rangle$ at a specific orientation ϕ_0 can be computed in general as instataneous

$$\mathbf{v}_0 = \frac{\tau_J}{\tau_M} \sum_{\substack{k=-\infty \\ k\neq 0}}^{\infty} \mathbf{c}_k e^{S_k} S_k^{-\Omega_k^+} \Gamma(\Omega_k^+, 0, S_k) e^{ik\phi_0}, \qquad (5)$$

with the dimensionless coefficients $S_k = D_R \tau_J k^2$, $\Omega_k^+ = D_R \tau_J k^2 + i\omega\tau_J k + \tau_J/\tau_M$, and the generalized incomplete gamma function $\Gamma(s, x_1, x_2) = \int_{x_1}^{x_2} t^{s-1} e^{-t}\, dt$. The analytic result is plotted in Fig. 2 and yields good agreement with the experimental data. In contrast to overdamped motion, where the particle's mean velocity is simply equal to the internal self-propulsion velocity, here the particle moves on average with a smaller velocity due to inertial delay effects, i.e., $|\mathbf{v}_0(\phi)| \leq |\mathbf{v}(\phi)|$. Further, the faster varying contributions (i.e., the higher Fourier modes) of the propulsion are more affected by these inertial delay effects, resulting in a more isotropic mean velocity for increasing mass M. Conversely, the anisotropy is restored for increasing moment of inertia: $\lim_{J\to\infty} \mathbf{v}_0(\phi) = \mathbf{v}(\phi)$.

A suitable quantifier for the presence of inertial effects is the delay function $d(t) = \langle \dot{\mathbf{r}}(t) \cdot \hat{\mathbf{n}}(0) \rangle - \langle \dot{\mathbf{r}}(0) \cdot \hat{\mathbf{n}}(t) \rangle$ [47, 48, 59]. This function quantifies the average difference between the projection of the initial velocity on the orientation and the projection of the initial orientation on the velocity. In overdamped systems, this function is zero at all times. Here, we find that this function is significantly different from zero in particular for large excitation amplitudes A (see the Methods section). The standard delay function can be generalized to resolve anisotropy in the system by conditioning the average with a specific initial orientation ϕ_0 at time $t = 0$.

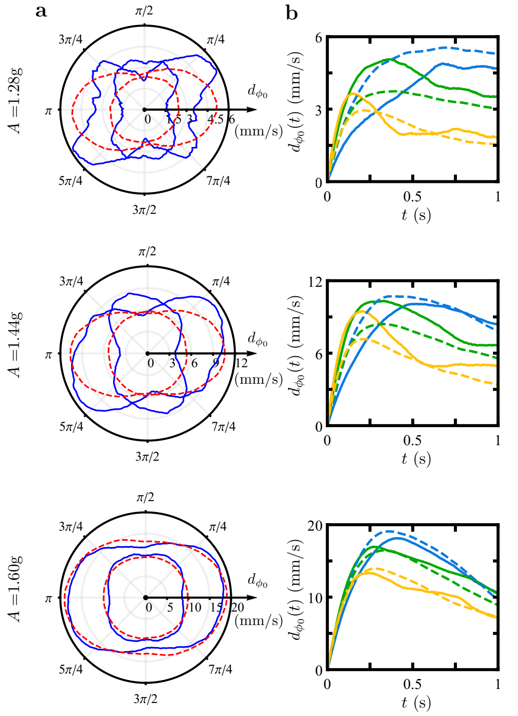

Figure 3. Panels **a**: The anisotropic delay function $d_{\phi_0}(t)$ plotted as function of the initial orientation ϕ_0 after fixed times $t = 0.1\,\mathrm{s}$, $t = 0.4\,\mathrm{s}$. Solid blue and dashed red curves show the experimental data and analytical results, respectively. Panels **b**: The anisotropic delay function $d_{\phi_0}(t)$ plotted as a function time t for parallel $\phi_0 = 0$ (cyan), diagonal $\phi_0 = \pi/4$ (green), and perpendicular $\phi_0 = \pi/2$ (yellow) orientations, each. Both for excitation amplitude $A = 1.28\,\mathrm{g}$ (upper row), $A = 1.44\,\mathrm{g}$ (middle row) and $A = 1.60\,\mathrm{g}$ (lower row). Solid and dashed curves the experimental data and the simulated data (using the parameter values given in Tab. I), respectively.

In Fig. 3 we plot the anisotropic delay function $d_{\phi_0}(t)$ both as a function of ϕ_0 for given t and as a function of t for given ϕ_0. We compare the experimental data with simulations which follow Eqs. (1) and (2) and are initialized similar to the experiments. The delay function is a highly fluctuating quantity making the experimental data difficult to interpret. The simulated data suggests an isotropic delay for short times and a larger delay along the grooves as time proceeds mimicking the modulation of the self-propulsion velocity. The simulated data always fits within the standard error of the experimental data.

For stochastic processes, it is common to analyze the

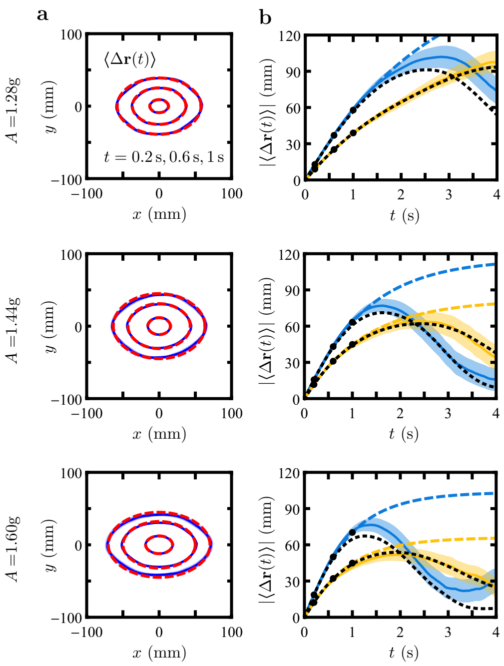

Figure 4. Comparison between model and measurement with excitation amplitude $A = 1.28\,\mathrm{g}$ (upper row), $A = 1.44\,\mathrm{g}$ (middle row), and $A = 1.60\,\mathrm{g}$ (lower row). Panels **a**: The anisotropic motion of the particle is visualized by plotting the mean displacement $\langle \Delta\mathbf{r}(\phi_0) \rangle$ for $\phi_0 \in [0, 2\pi)$ and fixed times $t = 0.2\,\mathrm{s}$, $t = 0.6\,\mathrm{s}$ and $t = 1.0\,\mathrm{s}$. Solid blue and dashed red curves show the experimental data and analytical results, respectively. Light blue area expresses the standard error of the mean. Panels **b**: The absolute mean displacement $|\langle \Delta\mathbf{r}(t) \rangle|$ is plotted as a function of time t for initial orientations $\phi_0 = 0$ (cyan) and $\phi_0 = \pi/2$ (yellow). Solid colored curves represent the experimental data and dashed colored curves the analytic results. In addition, dashed black curves depict simulation data for a particle in confinement. Black dots correspond to the experimental values for the fixed times of Fig. 4a. Theoretical predictions and simulations use the parameters given in Tab. I.

first and seconds moments of the motion, i.e., the mean and mean square displacement. In anisotropic systems, these quantities will strongly depend on the initial orientation of a particle. In Fig. 4, we compare the experimental mean displacement $\langle \Delta\mathbf{r}(t) \rangle$ conditioned at different initial orientations ϕ_0 with that resulting from our theoretical model. To demonstrate the effect of the orientation-dependent motility, we show the mean displacement as a function of the initial orientation ϕ_0 after fixed times t forming elliptic-like shapes in the $xy-$plane (see Fig. 4a). In Fig. 4b, we plot the absolute mean displacement $|\langle \Delta\mathbf{r}(t) \rangle|$ as a function of time t for particles which are initially orientated along the grooves (blue) and for those starting perpendicular to the grooves (red). The experimental data fit within theoretical results for short time, where the particle moves linearly in time with $\langle \Delta\mathbf{r}(t)\rangle = \mathbf{v}_0 t + \mathcal{O}(t^2)$. For longer time, confinement effects play an increasing role. Since recordings are stopped once a particle hits the boundary, events where the particle reorients beforehand dominate the statistic. As a consequence, the measured mean displacement decreases for times larger than the mean first-passage time of hitting the boundary. We perform simulations with absorbing boundaries and find an excellent agreement for all experimental accessible time scales (indicated by the black dashed lines in Fig. 4b). Without confinement, the theoretical mean displacement saturates to an anisotropic persistence length $\mathbf{L}_p = \lim_{t\to\infty}\langle \Delta\mathbf{r}(t)\rangle$ for long times

$$\mathbf{L}_p = \mathbf{v}_0\tau_M + \sum_{\substack{k=-\infty \\ k\neq 0}}^{\infty} \mathbf{c}_k\,\tau_k\,e^{\mathrm{i}k\phi_0}, \tag{6}$$

with the persistence time of mode k

$$\tau_k = \tau_J e^{\mathrm{S}_k}\mathrm{S}_k^{-\Omega_k}\Gamma(\Omega_k, 0, \mathrm{S}_k) \tag{7}$$

and $\Omega_k = D_R\tau_J k^2 + \mathrm{i}\omega\tau_J k$. The persistence length $\mathbf{L}_p$ consists of two contributions: the first term is given by the mean stationary velocity $\mathbf{v}_0$ which is damped over the translational friction time τ_M. The second term in Eq. (6) describes the active propulsion getting decorrelated due to the rotational noise D_R. Again, the degree of anisotropy increases as a function of the moment of inertia J. For vanishing angular speed $\omega = 0$, we find the following asymptotic behavior for small and large J, respectively:

$$\tau_k \sim \begin{cases} \frac{1}{D_R k^2}\left(1 + \frac{D_R k^2}{\gamma_R}J\right), & \text{for } J \to 0, \\ \frac{1}{k}\sqrt{\frac{\pi}{2D_R\gamma_R}}\sqrt{J}, & \text{for } J \to \infty. \end{cases} \tag{8}$$

Note that for large J the contribution of higher modes decays only linearly instead of quadratically, demonstrating the relevance of the moment of inertia as an important control parameter.

Last, we address the mean-square displacement, which is most commonly investigated for passive and active Brownian motion. In Fig. 5, we compare the experimentally determined mean-square displacement with the corresponding theoretical result. For short times, the particle is moving ballistically, as $\langle \Delta\mathbf{r}^2(t)\rangle = \langle \dot{\mathbf{r}}^2(0)\rangle\, t^2 + \mathcal{O}(t^3)$. For larger times, the particle transitions towards a diffusive regime $\langle \Delta\mathbf{r}^2(t)\rangle \sim 4D_L t$, which is characterized by the long-time diffusion coefficient

$$D_L = D_T + \sum_{k=1}^{\infty} |\mathbf{c}_k|^2\,\mathrm{Re}\{\tau_k\}. \tag{9}$$

Similar to the mean displacement, the mean-square displacement is affected by the confinement for long times

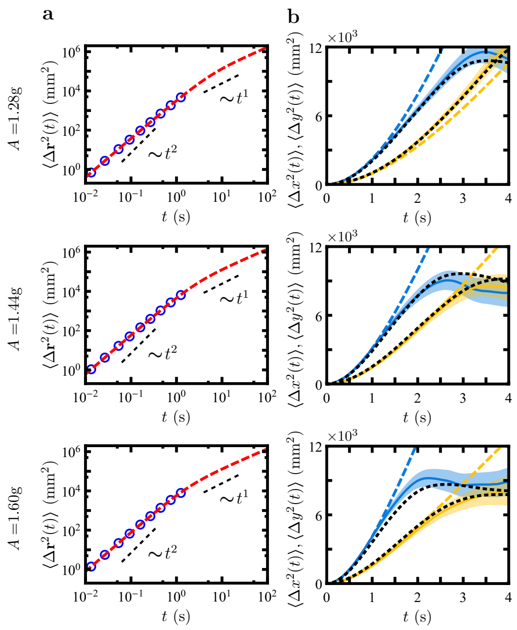

Figure 5. Comparison between model and measurement with excitation amplitude $A = 1.28\,$g (upper row), $A = 1.44\,$g (middle row), and $A = 1.60\,$g (lower row). Panels **a**: The total mean-square displacement as a function of time t (double logarithmic scaling). Open blue circles and dashed red curves show the experimental data and analytical results, respectively. Panels **b**: The mean-square displacement along the x-axis (cyan) and y-axis (yellow) as functions of time t. Solid colored curves and dashed colored curves show the experimental data and analytical results, respectively. Light colored areas represent the standard error of the mean. Dashed black curves show simulation data for a particle in confinement. Theoretical predictions correspond to the parameters given in Tab. I.

which hinders the particle to reach a diffusive state. In Fig. 5b, we show the mean-square displacement parallel and perpendicular to the grooves comparing experiment, theory, and simulation. Interestingly, the mean-square displacement is non-monotonic in time due to the confinement. At longer times, the particle needs to reorient before hitting the wall. The non-monotonic behavior results from the persistency of the particle and therefore is not observed for passive particles. The particle makes larger displacements along the grooves than perpendicular to them. In the absence of confinement, this anisotropy can persist even in the long-time limit characterized by the long-time diffusion matrix

$$\left(\mathbf{D}_L\right)_{ij} = D_T\delta_{ij} + \sum_{k=1}^{\infty} \left(\mathrm{c}_{k,i}\mathrm{c}_{-k,j} + \mathrm{c}_{-k,i}\mathrm{c}_{k,j}\right) \mathrm{Re}\{\tau_k\}, \tag{10}$$

for $i, j \in \{x, y\}$. The eigenvalues of this matrix are given as $D_\pm = D_\mathrm{L} \pm \Delta D_\mathrm{L}$, with the long-time anisotropy

$$\Delta D_L = \Bigg(\sum_{k,l=1}^{\infty} \left(|\mathbf{c}_k \cdot \mathbf{c}_l|^2 + |\mathbf{c}_k \cdot \mathbf{c}_{-l}|^2 - |\mathbf{c}_k|^2|\mathbf{c}_l|^2\right) \times \mathrm{Re}\{\tau_k\}\,\mathrm{Re}\{\tau_l\} \Bigg)^{1/2}, \tag{11}$$

which describes the long-time diffusion along the principal axes of maximal and minimal diffusion, respectively. The existence of a long-time anisotropy $\Delta D_L \neq 0$ will depend in general on the specific form of $\mathbf{v}(\phi)$.

DISCUSSION

Anisotropic motility has a strong impact on the motion of active particles both on short and long time scales. Our experiments demonstrate this explicitly for short and intermediate times and implicitly for long time-scales through simulations. Anisotropy persists for long times in the mean and mean-square displacement. We derived an analytical description that explains this behavior in terms of the Fourier series of the anisotropic driving term. The Fourier modes of the motility are linked to different time scales that add up and have an effect on the stationary mean velocity, persistence length and long-time diffusion. Specifically, these quantities are mostly affected by the low-order Fourier coefficients.

Our theoretical results predict that the degree of anisotropy is not only set by the orientation-dependent motility itself but depends non-trivially on all time scales $1/D_R$, $1/|\omega|$, τ_M, and τ_J of the model. In Fig. 6, we depict the anisotropy of the stationary mean velocity, persistence length, and long-time diffusion for different values of the moment of inertia J and two exemplary orientation-dependent motilities $\mathbf{v}(\phi) = v(1 + \cos(n\phi))\hat{\mathbf{n}}(\phi)$ with 2-fold symmetry ($n = 2$) and 3-fold symmetry ($n = 3$). In general, the mass and the moment of inertia have contrary effects on the anisotropy for short and intermediate times. For increasing mass, the dynamics of the particle involves stronger delay effects, smoothing the trajectories of the particle and effectively decreasing the anisotropy. On the other hand, increasing the moment of inertia leads to more resistance to reorientation and subsequently to higher persistence. The stationary parallel velocity in Fig. 6a,b shows an increasing degree of anisotropy (being the ratio of outermost points to the innermost points on these curves) for increasing moment of inertia J. For the persistence length (see Fig. 6c,d), the degree of anisotropy remains fairly invariant with increasing J but overall we find a large persistence length (recalling Eq. (8)). Note that the mean displacement and thus the persistence length inherit the symmetry of the driving velocity $\mathbf{v}(\phi)$. This symmetry is in general lost for long times, since the long-time diffusion can either follow a 2-fold symmetric modulation or behaves fully isotropic in every direction (see Fig. 6e,f). In fact, for motilities with higher rotational symmetry than two-fold, the long-time diffusion is always isotropic. Thus, we like to stress that even a system showing isotropic diffusion can hide anisotropic dynamics on shorter time scales.

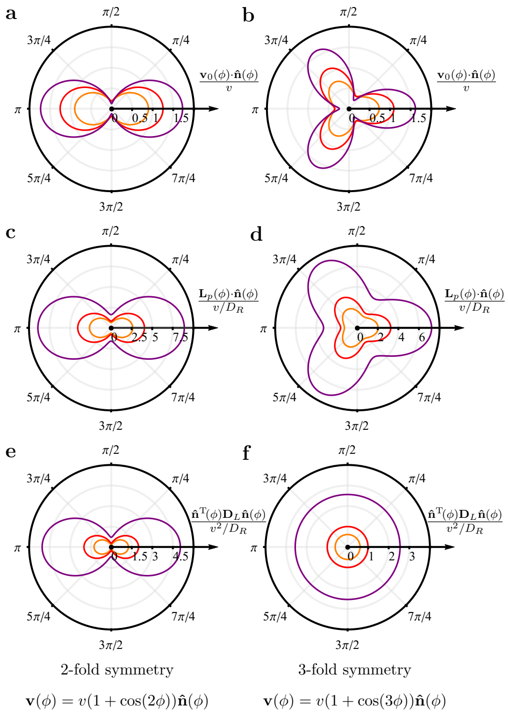

Figure 6. Anisotropy of the stationary mean velocity $\mathbf{v}_0$, persistence length $\mathbf{L}_p$, and long-time diffusion $\mathbf{D}_L$ for various values of the moment of inertia J evaluated for a 2-fold symmetric motility (left column) and a 3-fold symmetric motility (right column). Stationary mean velocity as a function of the current orientation $\mathbf{v}_0(\phi)\cdot\hat{\mathbf{n}}(\phi)$ (**a**, **b**). Persistence length as a function of the initial orientation $\mathbf{L}_p(\phi)\cdot\hat{\mathbf{n}}(\phi)$ (**c**, **d**). Long-time diffusion projected along different directions $\hat{\mathbf{n}}^\mathrm{T}(\phi)\,\mathbf{D}_L\,\hat{\mathbf{n}}(\phi)$ (**e**, **f**). The moment of inertia is set to $J = 0.1\,\gamma_R/D_R$ (orange), $J = \gamma_R/D_R$ (red), and $J = 10\,\gamma_R/D_R$ (purple). The mass is fixed at $M = \gamma_T/D_R$.

Our model can be used to predictively optimize driving parameters for the navigation of active matter in anisotropic environments [60–63], for instance robotic systems. In particular, the persistence length is an important control parameter that strongly impacts collective phenomena, like motility-induced phase separation [64–66]. Swarms of self-propelled particles moving with an orientation-dependent motility would be an interesting topic for future research, for which our model provides a baseline [67–70].

METHODS

Particle fabrication

The particle used in this work has been manufactured by 3D-printing using a stereolithographic acrylic based photopolymer 3D printer (Formlabs Form 2, using Grey V3 material, identical to Ref. [47]). Figure 1a shows an image of the particle. It consists of a cylindrical core (diameter 9 mm, height 4 mm) and a cap (diameter 15 mm, height 2 mm). Seven tilted cylindrical legs (diameter 0.8 mm, inclination angle 4 degrees) are attached to the cap in a regular heptagon around the bottom cylinder. The legs are tilted parallel to each other defining the orientation of the particle. The length of the legs is chosen such that the bottom of the particle is lifted by 1 mm above the surface. The particle is marked with a sticker from which the orientation can be determined using computational image processing. The particle's mass is about $m = 0.76\,\mathrm{g}$. From the particle's mass and shape, its moment of inertia is computed to be $J = 1.64 \times 10^{-8}$ kg m^2, assuming homogeneous density.

Experimental setup and analysis

Particle motion is excited by vertical vibrations of a rectangular acrylic baseplate (side length 300 mm, thickness 15 mm) with a lenticular plastic sheet on top, attached to an electromagnetic shaker (Tira TV 51140). The sheet's surface consists of equally spaced elliptical half-cylinders with a density of 0.787mm^{-1} (20 lines per inch) and a groove depth of 0.315 mm. An illustration and a cross-section of the particle resting on such a grooved surface are shown in Fig. 1c, respectively. Lenticular sheets of this kind are typically used in digital printing or displays to create images with the illusion of depth. Here, we use it to induce an anisotropic driving of the particle parallel and perpendicular to the lines, since the speed of the particle is very sensitive to the contact angle of the legs to the surface. Note that the width and height of the grooves are chosen such that the particle legs cannot be significantly trapped (see Fig. 1c), in order to prevent the particle simply from sliding along grooves.

The tilt of the plate is adjusted with an accuracy of 0.01° to minimize gravitational drift. The vibration frequency is set to $f = 80\,\mathrm{Hz}$ and three different peak acceleration amplitudes $A = 1.28\,g$, $1.44\,g$ and $1.60\,g$ are studied.

A mid-to-high-speed camera system (Allied Vision Mako-U130B) operating at 150 frames per second is used to record the experiment with a spatial resolution of 1024×1024 pixels. The particle location and orientation are determined and tracked using standard image recognition methods (Hough transform and morphological image region analysis) to a spatial accuracy of about $\pm 3 \times 10^{-5}$ m and a orientational accuracy of $\pm 0.74°$ [47]. Multiple single trajectories are recorded for each amplitude, until 20 min of data are acquired per recording. Half of the recorded time the particle starts parallel and the other half of the time it starts perpendicular to the grooves. Events involving particle-border collisions mark a trajectory's termination and are subsequently discarded, resulting in trajectories of various lengths.

The velocity was calculated from the displacement of successive positions of the particle as $\mathbf{v}(t) = (\mathbf{r}(t + \Delta t) - \mathbf{r}(t))/\Delta t$, where $\Delta t = 1/150\,\mathrm{s}$ is the time between two frames. The time steps are not fully equidistant between recorded frames, therefore the experimental data were linearly interpolated to obtain equidistant points. Experimental means with respect to a specific initial orientation ϕ_0 were calculated by averaging in the interval $[\phi_0 - \delta\phi, \phi_0 + \delta\phi]$. We chose $\delta\phi = 10°$ and modified the theoretical results accordingly by $\exp(\mathrm{i}k\phi) \to \exp(\mathrm{i}k\phi)\sin(k\delta\phi)/(k\delta\phi)$. We took advantage of the rotational and inflection symmetries of the experiment (by rotating some trajectories by 180 degrees) to increase the angular statistics for the mean displacement.

Analytic results

Both the translational velocity $\dot{\mathbf{r}}(t)$ and the angular velocity $\dot{\phi}(t)$ undergo a simple stochastic process for which a general solution is easily obtained (see Eqs. (1) and (2)). Several dynamical correlation function as well as low-order moments can be consequently calculated using standard methods of stochastic calculus [71]. The orientational correlation function $C(t) = \langle \hat{\mathbf{n}}(t) \cdot \hat{\mathbf{n}}(0) \rangle$ displays a double exponential decay

$$C(t) = \cos(\omega t) e^{-D_\mathrm{R}\left(t - \tau_J\left(1 - e^{-t/\tau_J}\right)\right)}, \tag{12}$$

(as previously discussed in Ref. [45–47]). The velocity correlation function $Z(t) = \langle \dot{\mathbf{r}}(t) \cdot \dot{\mathbf{r}}(0) \rangle$ is given as

$$Z(t) = 2\frac{D_\mathrm{T}}{\tau_M} e^{-t/\tau_M} + 2\sum_{k=1}^{\infty} |\mathbf{c}_k|^2 \,\mathrm{Re}\{V_k^+(t)\}, \tag{13}$$

where the Fourier-coefficient vectors are determined by the orientation-dependent motility, as $\mathbf{c}_k =$

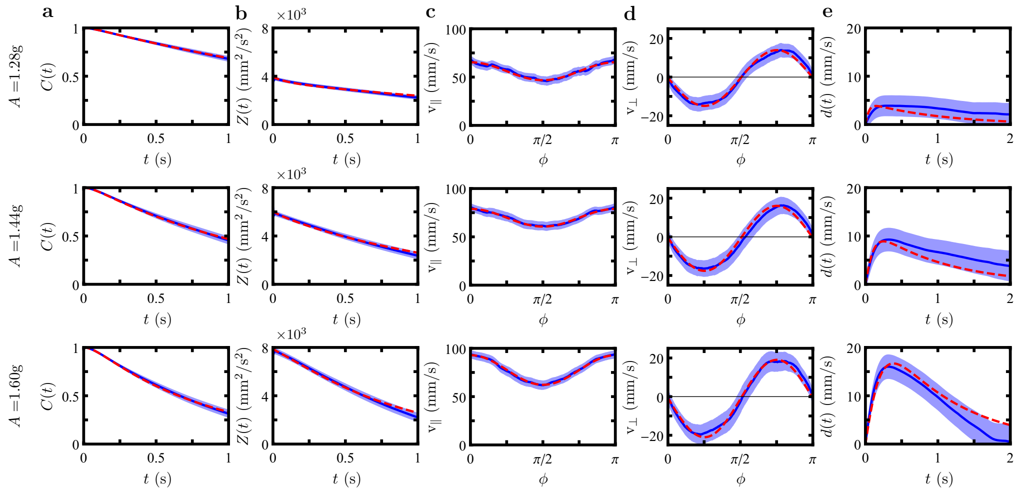

Figure 7. Determination of model parameters for different vibration amplitudes, A = 1.28 g (upper row), A = 1.44 g (middle row) and A = 1.60 g (lower row). Orientational correlation function $C(t)$ (**a**), velocity correlation function $Z(t)$ (**b**), stationary parallel velocity $\mathrm{v}_{\parallel}$ (**c**), stationary perpendicular velocity $\mathrm{v}_{\perp}$ (**d**). Solid dark blue and dashed red curves show the experimental data and analytical results, respectively. Experimental error intervals represent the standard error of the mean. The parameter values are listed in Tab. I.**e** Time-dependence of the delay function $d(t)$ testing the parameters on an independent quantity.

$\int_{-\pi}^{\pi}\mathbf{v}(\phi)\exp(-\mathrm{i}k\phi)/(2\pi)\,\mathrm{d}\phi$ (see Eq. (3)), and

$$V_k^{\pm}(t) = \frac{\tau_J}{\tau_M}\frac{e^{\mathrm{S}_k}}{2}\bigg(\pm\,\mathrm{S}_k^{-\Omega_k^+}\Gamma\left(\Omega_k^+,0,\mathrm{S}_k e^{-t/\tau_J}\right)e^{t/\tau_M} - \mathrm{S}_k^{-\Omega_k^-}\Gamma\left(\Omega_k^-,0,\mathrm{S}_k e^{-t/\tau_J}\right)e^{-t/\tau_M} + \left(\mathrm{S}_k^{-\Omega_k^+}\Gamma\left(\Omega_k^+,0,\mathrm{S}_k\right)+\mathrm{S}_k^{-\Omega_k^-}\Gamma\left(\Omega_k^-,0,\mathrm{S}_k\right)\right)e^{-t/\tau_M}\bigg), \tag{14}$$

with $\Omega_k^{\pm} = D_{\mathrm{R}}\tau_J k^2 \pm (\mathrm{i}\omega\tau_J k + \tau_J/\tau_M)$ and $\mathrm{S}_k = D_{\mathrm{R}}\tau_J k^2$. The real part is denoted by $\mathrm{Re}\{\dots\}$ and the generalized incomplete gamma function is $\Gamma(s,x_1,x_2) = \int_{x_1}^{x_2} t^{s-1}e^{-t}\,\mathrm{d}t$. The delay function measuring the difference between the direction of the velocity and the current orientation, $d(t) = \langle\dot{\mathbf{r}}(t)\cdot\hat{\mathbf{n}}(0)\rangle - \langle\dot{\mathbf{r}}(0)\cdot\hat{\mathbf{n}}(t)\rangle$, is given by

$$d(t) = \mathrm{Re}\{\left(\mathrm{c}_{1,x}+\mathrm{c}_{1,x}^* + \mathrm{i}(\mathrm{c}_{1,y}-\mathrm{c}_{1,y}^*)\right)V_1^-(t)\}, \tag{15}$$

which coincides with the result for isotropic self-propulsion [47] (due to the projection onto the orientation). Next, we give the mean displacement $\langle\Delta\mathbf{r}(t)\rangle = \langle\mathbf{r}(t)-\mathbf{r}_0\rangle$ under the condition that initially the position $\mathbf{r}_0$ and the orientation ϕ_0 are prescribed,

$$\langle\Delta\mathbf{r}(t)\rangle = \mathbf{v}_0\tau_M(1-e^{-t/\tau_M}) + \sum_{\substack{k=-\infty\\k\neq 0}}^{\infty}\mathbf{c}_k R_k(t)e^{\mathrm{i}k\phi_0}, \tag{16}$$

with the stationary velocity $\mathbf{v}_0$ (see Eq. (5)),

$$R_k(t) = \tau_J e^{\mathrm{S}_k}\bigg(\mathrm{S}_k^{-\Omega_k}\Gamma\left(\Omega_k,\mathrm{S}_k e^{-t/\tau_J},\mathrm{S}_k\right) - \mathrm{S}_k^{-\Omega_k^-}\Gamma\left(\Omega_k^-,\mathrm{S}_k e^{-t/\tau_J},\mathrm{S}_k\right)e^{-t/\tau_M}\bigg), \tag{17}$$

and $\Omega_k = D_{\mathrm{R}}\tau_J k^2 + \mathrm{i}\omega\tau_J k$. Lastly, we provide the result for the mean-square displacement $\langle\Delta\mathbf{r}^2(t)\rangle = \langle(\mathbf{r}(t)-\mathbf{r}_0)^2\rangle$ which can be expressed as

$$\langle\Delta\mathbf{r}^2(t)\rangle = 4D_{\mathrm{L}}t + 2\big(Z(t)-Z(0)\big)\tau_M^2 - 4F(t)\tau_J^2 \tag{18}$$

with the long-time diffusion coefficient D_{L} (see Eq. (9)), the velocity correlation function $Z(t)$ (see Eq. (13)) and

$$F(t) = \sum_{k=1}^{\infty}|\mathbf{c}_k|^2\,\mathrm{Re}\left\{\frac{e^{\mathrm{S}_k}}{\Omega_k^2}\left({}_2F_2\left[\begin{matrix}\Omega_k,\ \Omega_k\\ \Omega_k+1,\ \Omega_k+1\end{matrix};-\mathrm{S}_k\right] - {}_2F_2\left[\begin{matrix}\Omega_k,\ \Omega_k\\ \Omega_k+1,\ \Omega_k+1\end{matrix};-\mathrm{S}_k e^{-t/\tau_J}\right]e^{-\Omega_k t/\tau_J}\right)\right\}, \tag{19}$$

where ${}_2F_2$ denotes the generalized hypergeometric function. Last we remark that in the overdamped limit, i.e.$m \to 0$ and $J \to 0$, we recover the results of orientation-dependent motility in underdamped systems [7] and similarly for an isotropic self-propulsion $\mathbf{v}(\phi) = v_0\hat{\mathbf{n}}(\phi)$, we obtain the expressions of Ref. [52].

Parameter estimation

The underdamped active Brownian motion model depends on eight independent parameters. All parameters were obtained using the MatLab standard optimizer `fminsearch` (Nelder-Mead optimization of a function of several variables on an unbounded domain). Our cost function consists of five terms covering different parameters. Each term is constructed as follows: The absolute deviation between the experimental mean and the analytical expectation is weighted with the standard error of the mean and then averaged over time or orientation. This procedure takes into account the experimental uncertainty. At the same time, the value of our cost function quantifies the fit itself. We call a fit sufficiently representative of the experimental mean if the mean deviation between experimental mean and analytical expectation is no greater than one standard error. We use this definition to determine an error interval for our optimal parameters. The orientational correlation function $C(t)$ (see Eq. (12)) is used to determine the rotational diffusion constant D_{R} and the rotational friction time τ_J. In addition, we use the mean stationary angular velocity $\langle\dot{\phi}(0)\rangle = \omega$ to determine the angular speed ω. Further, we use the velocity correlation function $Z(t)$ (see Eq. (13)) to extract values for the translational friction time τ_M and the translational short-time diffusion coefficient D_T. Lastly, we use the mean stationary velocity $\mathbf{v}_0$ (see Eq. (5)), which is projected parallel ($\mathrm{v}_\parallel = \mathbf{v}_0 \cdot \hat{\mathbf{n}}$) and perpendicular ($\mathrm{v}_\perp = \mathbf{v}_0 \cdot \hat{\mathbf{n}}_\perp$) to the body axis, to determine all the motility parameters $\mathrm{v}_\perp$, $\delta\mathrm{v}_\parallel$, and $\delta\mathrm{v}_\perp$. In Fig. 7a-d, the analytic fitting curves to the experimental data are shown and the resulting set of parameter is listed in Tab. I. For vibrobots, the delay function $d(t)$ (see Eq. (15)) proved to be a sensitive measure for the quality of the determined parameter-set [47]. Figure 7e shows good agreement between theory and experiment for all three measurements.

Table I. Model parameters obtained from analytical fits to measurements in Fig. 7. Lower and upper 95% confidence bounds are displayed behind each value.

A	(g)	1.28	1.44	1.60
ω	(1/s)	$0.09\ ^{+0.76}_{-0.76}$	$0.12\ ^{+0.88}_{-0.99}$	$0.11\ ^{+0.89}_{-1.11}$
D_{R}	(1/s)	$0.39\ ^{+0.05}_{-0.04}$	$0.80\ ^{+0.07}_{-0.10}$	$1.18\ ^{+0.11}_{-0.13}$
τ_J	(s)	$0.05\ ^{+0.02}_{-0.02}$	$0.06\ ^{+0.03}_{-0.01}$	$0.07\ ^{+0.03}_{-0.02}$
$\mathrm{v}_\parallel$	(mm/s)	$57.5\ ^{+4.8}_{-4.1}$	$73.2\ ^{+4.9}_{-4.4}$	$85.0\ ^{+5.3}_{-4.8}$
$\delta\mathrm{v}_\parallel$	(mm/s)	$9.2\ ^{+7.0}_{-6.8}$	$8.5\ ^{+7.5}_{-7.3}$	$15.7\ ^{+8.6}_{-8.5}$
$\delta\mathrm{v}_\perp$	(mm/s)	$15.6\ ^{+5.7}_{-5.5}$	$19.3\ ^{+7.1}_{-7.0}$	$23.8\ ^{+9.4}_{-9.1}$
D_{T}	(mm^2/s)	$27.89\ ^{+31.85}_{-27.89}$	$36.23\ ^{+44.38}_{-36.23}$	$59.41\ ^{+40.59}_{-59.41}$
τ_M	(s)	$0.07\ ^{+0.10}_{-0.07}$	$0.10\ ^{+0.09}_{-0.06}$	$0.13\ ^{+0.6}_{-0.6}$

Simulation

Numerical data for a self-propelled particle with orientation-dependent motility enclosed by absorbing boundaries are included in Figs. 3, 4b, and 5b. Equations (1) and (2) were discretized to perform Brownian dynamics simulations using first-order finite difference discretization. For these simulations, we chose the time step size $\Delta t = 10^{-2}s$ and we performed 10^5 realizations in Fig. 4b, and 5b and 2000 realizations in Fig. 3 to calculate the respective ensemble averages. Half of the trajectories started at $x_0 = 0\,\mathrm{mm}$, $y_0 = -100\,\mathrm{mm}$, and $\phi_0 = \pi/2$ and the other half at $x_0 = 100\,\mathrm{mm}$, $y_0 = 0\,\mathrm{mm}$ and $\phi_0 = \pi$ (modelling the initialisation in the experiment). The rectangular absorbing boundary was set at $\{(x, y)|(x = \pm 130\,\mathrm{mm},\, y \in [-130\,\mathrm{mm},\, 130\,\mathrm{mm}]) \vee (x \in [-130\,\mathrm{mm},\, 130\,\mathrm{mm}],\, y = \pm 130\,\mathrm{mm})\}$.

DATA AVAILABILITY

Supplementary data containing the codes and raw data underlying this work are available at https://doi.org/10.5281/zenodo.7220326.

ACKNOWLEDGMENTS

C.S., R.W., and H.L. are funded by the Deutsche Forschungsgemeinschaft (DFG, German Research Foundation) – SCHO 1700/1-1; 283183152 (WI 4170/3-2); LO 418/23-1.

AUTHOR CONTRIBUTIONS

C.S. and H.L. designed the research. C.S. designed the experimental setup. C.S. and A.L. carried out the experiments. A.S. and C.S. analyzed the measurements. A.S. developed the theoretical and numerical results. All authors discussed the results and wrote the manuscript.

COMPETING INTERESTS

The authors declare no competing interests.

ADDITIONAL INFORMATION

Correspondence and requests for materials should be addressed to A.S. (email: sprenger@thphy.uni-duesseldorf.de) or to C.S. (email: christian.scholz@hhu.de).

[1] I. S. Aranson, "Harnessing medium anisotropy to control active matter," Accounts of Chemical Research **51**, 3023–3030 (2018).
[2] M. Enculescu and H. Stark, "Active colloidal suspensions exhibit polar order under gravity," Physical Review Letters **107**, 058301 (2011).
[3] D.-P. Häder and R. Hemmersbach, "Gravitaxis in Euglena," Advances in Experimental Medicine and Biology **979**, 237266 (2017).
[4] B. Liebchen, P. Monderkamp, B. ten Hagen, and H. Löwen, "Viscotaxis: Microswimmer navigation in viscosity gradients," Physical Review Letters **120**, 208002 (2018).
[5] C. Lozano, B. ten Hagen, H. Löwen, and C. Bechinger, "Phototaxis of synthetic microswimmers in optical landscapes," Nature Communications **7**, 12828 (2016).
[6] Y. Hong, N. M. Blackman, N. D. Kopp, A. Sen, and D. Velegol, "Chemotaxis of nonbiological colloidal rods," Physical Review Letters **99**, 178103 (2007).
[7] A. R. Sprenger, M. A. Fernandez-Rodriguez, L. Alvarez, L. Isa, R. Wittkowski, and H. Löwen, "Active Brownian motion with orientation-dependent motility: Theory and experiments," Langmuir **36**, 7066–7073 (2020).
[8] A. Wysocki, J. Elgeti, and G. Gompper, "Giant adsorption of microswimmers: Duality of shape asymmetry and wall curvature," Physical Review E **91**, 050302 (2015).
[9] D. R. Parisi, R. C. Hidalgo, and I. Zuriguel, "Active particles with desired orientation flowing through a bottleneck," Scientific Reports **8**, 9133 (2018).
[10] P. C. Mushenheim, R. R. Trivedi, H. H. Tuson, D. B. Weibel, and N. L. Abbott, "Dynamic self-assembly of motile bacteria in liquid crystals," Soft Matter **10**, 88–95 (2014).
[11] S. Zhou, A. Sokolov, O. D. Lavrentovich, and I. S. Aranson, "Living liquid crystals," Proceedings of the National Academy of Sciences U.S.A. **111**, 1265–1270 (2014).
[12] P. Guillamat, J. Ignés-Mullol, and F. Sagués, "Control of active liquid crystals with a magnetic field," Proceedings of the National Academy of Sciences U.S.A. **113**, 5498–5502 (2016).
[13] J. Toner, H. Löwen, and H. H. Wensink, "Following fluctuating signs: Anomalous active superdiffusion of swimmers in anisotropic media," Physical Review E **93**, 062610 (2016).
[14] C. Peng, T. Turiv, Y. Guo, Q.-H. Wei, and O. D. Lavrentovich, "Command of active matter by topological defects and patterns," Science **354**, 882–885 (2016).
[15] G. Volpe, I. Buttinoni, D. Vogt, H.-J. Kümmerer, and C. Bechinger, "Microswimmers in patterned environments," Soft Matter **7**, 8810–8815 (2011).
[16] A. T. Brown, I. D. Vladescu, A. Dawson, T. Vissers, J. Schwarz-Linek, J. S. Lintuvuori, and W. C. K. Poon, "Swimming in a crystal," Soft Matter **12**, 131–140 (2016).
[17] B. van der Meer, L. Filion, and M. Dijkstra, "Fabricating large two-dimensional single colloidal crystals by doping with active particles," Soft Matter **12**, 3406–3411 (2016).
[18] P. Romanczuk, M. Bär, W. Ebeling, B. Lindner, and L. Schimansky-Geier, "Active Brownian particles. From individual to collective stochastic dynamics," European Physical Journal Special Topics **202**, 1–162 (2012).
[19] J. Elgeti, R. G. Winkler, and G. Gompper, "Physics of microswimmers–single particle motion and collective behavior: a review," Reports on Progress in Physics **78**, 056601 (2015).
[20] A. M. Menzel, "Tuned, driven, and active soft matter," Physics Reports **554**, 1–45 (2015).
[21] H. M. Jaeger, S. R. Nagel, and R. P. Behringer, "Granular solids, liquids, and gases," Reviews of Modern Physics **68**, 1259–1273 (1996).
[22] E. Altshuler, J. M. Pastor, A. Garcimartín, I. Zuriguel, and D. Maza, "Vibrot, a simple device for the conversion of vibration into rotation mediated by friction: Preliminary evaluation," PLoS ONE **8**, e67838 (2013).
[23] O. Dauchot and V. Démery, "Dynamics of a self-propelled particle in a harmonic trap," Physical Review Letters **122**, 068002 (2019).
[24] C. Scholz, A. Ldov, T. Pöschel, M. Engel, and H. Löwen, "Surfactants and rotelles in active chiral fluids," Science Advances **7**, eabf8998 (2021).
[25] H. T. Menéndez, E. Altshuler, N. V. Brilliantov, and T. Pöschel, "Lack of collective motion in granular gases of rotators," New Journal of Physics **24**, 073002 (2022).
[26] M. Leyman, F. Ogemark, J. Wehr, and G. Volpe, "Tuning phototactic robots with sensorial delays," Physical Review E **98**, 052606 (2018).
[27] M. Y. B. Zion, N. Bredeche, and O. Dauchot, "Distributed on-line reinforcement learning in a swarm of sterically interacting robots," (2021), arXiv:2111.06953.
[28] M. J. Falk, V. Alizadehyazdi, H. Jaeger, and A. Murugan, "Learning to control active matter," Phys. Rev. Research **3**, 033291 (2021).
[29] C. Bechinger, R. Di Leonardo, H. Löwen, C. Reichhardt, G. Volpe, and G. Volpe, "Active particles in complex and crowded environments," Reviews of Modern Physics **88**, 045006 (2016).
[30] P. K. Ghosh, Y. Li, F. Marchesoni, and F. Nori, "Pseudochemotactic drifts of artificial microswimmers," Physical Review E **92**, 012114 (2015).
[31] M. P. Magiera and L. Brendel, "Trapping of interacting propelled colloidal particles in inhomogeneous media," Physical Review E **92**, 012304 (2015).
[32] R. Großmann, F. Peruani, and M. Bär, "A geometric approach to self-propelled motion in isotropic & anisotropic environments," The European Physical Journal Special Topics **224**, 1377–1394 (2015).
[33] A. Geiseler, P. Hänggi, F. Marchesoni, C. Mulhern, and S. Savel'ev, "Chemotaxis of artificial microswimmers in active density waves," Physical Review E **94**, 012613 (2016).
[34] A. Geiseler, P. Hänggi, and F. Marchesoni, "Self-polarizing microswimmers in active density waves," Scientific Reports **7**, 41884 (2017).
[35] A. Geiseler, P. Hänggi, and F. Marchesoni, "Taxis of artificial swimmers in a spatio-temporally modulated activation medium," Entropy **19**, 97 (2017).
[36] A. Sharma and J. M. Brader, "Brownian systems with spatially inhomogeneous activity," Physical Review E **96**, 032604 (2017).
[37] R. R. Bennett and R. Golestanian, "A steering mechanism for phototaxis in *Chlamydomonas*," Journal of The Royal Society Interface **12**, 20141164 (2015).
[38] M. E. Cates, "Diffusive transport without detailed balance in motile bacteria: Does microbiology need statistical physics?" Reports on Progress in Physics **75**, 042601

(2012).
[39] E. Baird, E. Kreiss, W. Wcislo, E. Warrant, and M. Dacke, "Nocturnal insects use optic flow for flight control," Biology Letters **7**, 499–501 (2011).
[40] C. Scholtyssek, M. Dacke, R. Kröger, and E. Baird, "Control of self-motion in dynamic fluids: Fish do it differently from bees," Biology Letters **10**, 20140279 (2014).
[41] P. S. Bhagavatula, C. Claudianos, M. R. Ibbotson, and M. V. Srinivasan, "Optic flow cues guide flight in birds," Current Biology **21**, 1794–1799 (2011).
[42] S. Bolek and H. Wolf, "Food searches and guiding structures in North African desert ants, Cataglyphis," Journal of Comparative Physiology A **201**, 631–644 (2015).
[43] O. Feinerman, I. Pinkoviezky, A. Gelblum, E. Fonio, and N. S. Gov, "The physics of cooperative transport in groups of ants," Nature Physics **14**, 683–693 (2018).
[44] H. L. Devereux, C. R. Twomey, M. S. Turner, and S. Thutupalli, "Whirligig beetles as corralled active Brownian particles," Journal of The Royal Society Interface **18**, 20210114 (2021).
[45] P. K. Ghosh, Y. Li, G. Marchegiani, and F. Marchesoni, "Communication: Memory effects and active Brownian diffusion," Journal of Chemical Physics **143**, 211101 (2015).
[46] L. Walsh, C. G. Wagner, S. Schlossberg, C. Olson, A. Baskaran, and N. Menon, "Noise and diffusion of a vibrated self-propelled granular particle," Soft Matter **13**, 8964–8968 (2017).
[47] C. Scholz, S. Jahanshahi, A. Ldov, and H. Löwen, "Inertial delay of self-propelled particles," Nature Communications **9**, 5156 (2018).
[48] H. Löwen, "Inertial effects of self-propelled particles: From active Brownian to active Langevin motion," Journal of Chemical Physics **152**, 040901 (2020).
[49] L. Caprini and U. Marini Bettolo Marconi, "Inertial self-propelled particles," Journal of Chemical Physics **154**, 024902 (2021).
[50] L. L. Gutierrez-Martinez and M. Sandoval, "Inertial effects on trapped active matter," Journal of Chemical Physics **153**, 044906 (2020).
[51] P. Herrera and M. Sandoval, "Maxwell-Boltzmann velocity distribution for noninteracting active matter," Physical Review E **103**, 012601 (2021).
[52] A. R. Sprenger, S. Jahanshahi, A. V. Ivlev, and H. Löwen, "Time-dependent inertia of self-propelled particles: The Langevin rocket," Physical Review E **103**, 042601 (2021).
[53] G. H. P. Nguyen, R. Wittmann, and H. Löwen, "Active Ornstein-Uhlenbeck model for self-propelled particles with inertia," Journal of Physics: Condensed Matter **34**, 035101 (2022).
[54] G. Volpe and G. Volpe, "The topography of the environment alters the optimal search strategy for active particles," Proceedings of the National Academy of Sciences U.S.A. **114**, 11350–11355 (2017).
[55] N. Koumakis, A. Gnoli, C. Maggi, A. Puglisi, and R. D. Leonardo, "Mechanism of self-propulsion in 3D-printed active granular particles," New Journal of Physics **18**, 113046 (2016).
[56] C. Scholz and T. Pöschel, "Actively rotating granular particles manufactured by rapid prototyping," Revista Cubana de Fsica **33**, 37–38 (2016).
[57] W. E. Uspal, "Theory of light-activated catalytic Janus particles," Journal of Chemical Physics **150**, 114903 (2019).
[58] J. Voß and R. Wittkowski, "Orientation-dependent propulsion of triangular nano- and microparticles by a traveling ultrasound wave," ACS Nano **16**, 3604–3612 (2022).
[59] A. R. Sprenger, C. Bair, and H. Löwen, "Active Brownian motion with memory delay induced by a viscoelastic medium," Physical Review E **105**, 044610 (2022).
[60] M. Selmke, U. Khadka, A. P. Bregulla, F. Cichos, and H. Yang, "Theory for controlling individual self-propelled micro-swimmers by photon nudging i: directed transport," Physical Chemistry Chemical Physics **20**, 10502–10520 (2018).
[61] D. Breoni, M. Schmiedeberg, and H. Löwen, "Active Brownian and inertial particles in disordered environments: Short-time expansion of the mean-square displacement," Physical Review E **102**, 062604 (2020).
[62] M. A. Fernandez-Rodriguez, F. Grillo, L. Alvarez, M. Rathlef, I. Buttinoni, G. Volpe, and L. Isa, "Feedback-controlled active Brownian colloids with space-dependent rotational dynamics," Nature Communications **11**, 4223 (2020).
[63] A. Daddi-Moussa-Ider, H. Löwen, and B. Liebchen, "Hydrodynamics can determine the optimal route for microswimmer navigation," Communications Physics **4**, 15 (2021).
[64] I. Buttinoni, J. Bialké, F. Kümmel, H. Löwen, C. Bechinger, and T. Speck, "Dynamical clustering and phase separation in suspensions of self-propelled colloidal particles," Physical Review Letters **110**, 238301 (2013).
[65] M. E. Cates and J. Tailleur, "Motility-induced phase separation," Annual Review of Condensed Matter Physics **6**, 219–244 (2015).
[66] L. Caprini, R. K. Gupta, and H. Löwen, "Role of rotational inertia for collective phenomena in active matter," Physical Chemistry Chemical Physics (2022), 10.1039/D2CP02940E.
[67] J. A. Cohen and R. Golestanian, "Emergent cometlike swarming of optically driven thermally active colloids," Physical Review Letters **112**, 068302 (2014).
[68] F. A. Lavergne, H. Wendehenne, T. Bäuerle, and C. Bechinger, "Group formation and cohesion of active particles with visual perception-dependent motility," Science **364**, 70–74 (2019).
[69] M. Casiulis, M. Tarzia, L. F. Cugliandolo, and O. Dauchot, "Velocity and speed correlations in Hamiltonian flocks," Physical Review Letters **124**, 198001 (2020).
[70] A. Solon, H. Chaté, J. Toner, and J. Tailleur, "Susceptibility of polar flocks to spatial anisotropy," Physical Review Letters **128**, 208004 (2022).
[71] H. Risken, *The Fokker-Planck Equation: Methods of Solution and Applications*, Springer Series in Synergetics (Springer, Berlin Heidelberg, 1996).

P5 Fitting an active Brownian particle's mean-squared displacement with improved parameter estimation

Reproduced from

M. R. Bailey, A. R. Sprenger, F. Grillo, H. Löwen, and L. Isa,
Fitting an active Brownian particle's mean-squared displacement with improved parameter estimation,
Phys. Rev. E **106**, L052602 (2022),
published by *American Physical Society* [292].

Digital Object Identifier (DOI): doi.org/10.1103/PhysRevE.106.L052602

Statement of contribution

F.G., H.L., and L.I. supervised the research. M.R.B. generated the numerical results. M.G.B. and A.R.S. investigated the model and analysed the data. A.R.S performed the analytic results. M.G.B. prepared the figures. M.R.B., A.R.S., and L.I. wrote the manuscript. All authors discussed the results, edited the text, and finalized the manuscript.

Copyright and license notice

©American Physical Society.
The American Physical Society (APS) grants any co-author the right to use the article or a portion of the article in a thesis or dissertation without requesting permission from APS, provided the bibliographic citation and the APS copyright credit line are given.

PHYSICAL REVIEW E **106**, L052602 (2022)

Letter Editors' Suggestion

Fitting an active Brownian particle's mean-squared displacement with improved parameter estimation

Maximilian R. Bailey,[1,*] Alexander R. Sprenger,[2,3] Fabio Grillo,[1] Hartmut Löwen,[2] and Lucio Isa[1,†]

[1]*Laboratory for Soft Materials and Interfaces, Department of Materials, ETH Zürich, Vladimir-Prelog-Weg 5, 8093 Zurich, Switzerland*

[2]*Institut für Theoretische Physik II: Weiche Materie, Heinrich-Heine-Universität Düsseldorf, D-40225 Düsseldorf, Germany*

[3]*Institut für Physik, Otto-von-Guericke-Universität Magdeburg, Universitätsplatz 2, 39106 Magdeburg, Germany*

(Received 3 August 2022; accepted 3 October 2022; published 22 November 2022)

The active Brownian particle (ABP) model is widely used to describe the dynamics of active matter systems, such as Janus microswimmers. In particular, the analytical expression for an ABP's mean-squared displacement (MSD) is useful as it provides a means to describe the essential physics of a self-propelled, spherical Brownian particle. However, the truncated or "short-time" form of the MSD equation is typically fitted, which can lead to significant problems in parameter estimation. Furthermore, heteroscedasticity and the often statistically dependent observations of an ABP's MSD lead to a situation where standard ordinary least-squares regression leads to biased estimates and unreliable confidence intervals. Instead, we propose here to revert to always fitting the full expression of an ABP's MSD at short timescales, using bootstrapping to construct confidence intervals of the fitted parameters. Additionally, after comparison between different fitting strategies, we propose to extract the physical parameters of an ABP using its mean logarithmic squared displacement. These steps improve the estimation of an ABP's physical properties and provide more reliable confidence intervals, which are critical in the context of a growing interest in the interactions of microswimmers with confining boundaries and the influence on their motion.

DOI: 10.1103/PhysRevE.106.L052602

Overdamped active Brownian motion is often invoked to describe the physics of experimental realizations of active matter [1,2]. The "active Brownian particle's" (ABP) motion is described using Langevin dynamics in the overdamped (inertia-free) regime and consists of an object simultaneously subjected to thermal fluctuations and directed self-propulsion. In this model, the particle moves with a constant velocity V_0 in the direction of its internal orientation axis $\hat{\boldsymbol{u}}$, which fluctuates over time due to rotational Brownian motion [3]. Particles therefore travel ballistically over times shorter than the characteristic timescale for rotational diffusion (persistent motion), displaying diffusive motion (with a larger, effective diffusion coefficient) at longer times, as their direction of motion is randomized [4]. This model provides meaningful statistical quantities such as an analytical description for the mean-squared displacement (MSD) of spherical microswimmers, which often shows good agreement with experimental findings [5]. Most analyses in the experimental literature on microswimmers are in fact based on parameters estimated by fitting the sample MSD to the ABP model, extracting particle velocity V_0, translational diffusivity D_T, and rotational diffusivity D_R. In two spatial dimensions, the ABP model prescribes the following expression for the MSD $\langle\Delta\mathbf{r}^2(\tau)\rangle$ as a function of lag time τ [1,6]:

$$\langle\Delta\mathbf{r}^2(\tau)\rangle = 4D_T\tau + \frac{2V_0^2}{D_R^2}\left(D_R\tau - 1 + e^{-D_R\tau}\right). \quad (1)$$

The standard approach to parameter estimation from a defined model is to use ordinary least-squares (OLS) regression [7,8] following

$$\hat{\boldsymbol{\theta}} = \underset{\theta}{\operatorname{argmin}} \sum_{i=1}^{P}(Y_i - f_{i,\theta})^2, \quad (2)$$

where $\hat{\boldsymbol{\theta}}$ is the vector of estimated parameters, Y_i are individual observations from the data set P (here given by the sample's MSD after a given lag time τ), and $f_{i,\theta}$ corresponds to the values of the fitted model [here given by the theoretical prediction; see Eq. (1)]. $\operatorname{argmin}_\theta$ finds the vector $\boldsymbol{\theta}$, which minimizes the objective function. In practice, there are two main strategies to determine the MSD of a population of particles from their coordinates: one can perform either an ensemble average or a time average over the displacements. Ensemble averaging over many particles preserves the statistical independence of the observations and efficiently averages out spurious noise [9], but collecting sufficient statistics in the dilute limit where Eq. (1) holds is experimentally challenging.

Therefore, one often resorts to the calculation of the MSD via time averaging the displacements of a few ABP trajectories followed over time. Moreover, time averaging is advantageous in that it describes the physics of individual microswimmers, whereas studying the EMSD removes information about the heterogeneities present within the system, such as particles displaying atypical motion or changing dynamics within different spatial domains [10]. The time-averaged MSD (TAMSD) of a single particle at a lag time

*maximilian.bailey@mat.ethz.ch
†lucio.isa@mat.ethz.ch

 ©2022 American Physical Society

$n\Delta\tau$ is calculated as

$$\text{TAMSD}\ |_{n\Delta\tau} = \sum_{m=1}^{M-n} \frac{\{\mathbf{r}[(n+m)\Delta\tau] - \mathbf{r}(m\Delta\tau)\}^2}{M-n}, \quad (3)$$

where $\mathbf{r}[(n+m)\Delta\tau]$ is the particle position at lag time $n\Delta\tau$ from its previous (reference) position $\mathbf{r}(m\Delta\tau)$, for a trajectory of length M. By collecting sufficiently long trajectories, there is the implicit assumption that statistically robust averaging is performed, which is required for accurate parameter estimation with OLS.

However, there are several key assumptions that must be satisfied when using least-squares regression: of these, two can be violated when evaluating the MSD of an ABP. The rotational and time symmetry of a theoretical ABP ensures that consecutive *nonoverlapping* squared displacements are statistically independent, but nonidealities in experimental systems can create hidden correlations, thereby violating the assumption of statistically independent measurements [11,12]. Furthermore, to increase the statistics, one typically evaluates *overlapping* squared displacements when investigating ABPs, which are in fact correlated (see below for further discussion). This impacts the reliability of the estimated confidence intervals, which can become unrealistically narrow. In the case of statistically dependent measurements, confidence intervals for estimated parameters can nevertheless be constructed by fitting the model to bootstrapped datasets from experimental values [11,13].

The second violation is the assumption of homoscedasticity in the error terms of the MSD. There are two sources for heteroscedasticity (nonconstant variance) within the error terms of the MSD with lag time. First, as we show later, the theoretical population variance of an ABP's MSD increases with lag time. Furthermore, the number of data points used to estimate the TAMSD decreases with increasing lag time when evaluating single trajectories, further amplifying the sampling error. These factors, coupled with the presence of localization errors at shorter timescales [14], create a situation where there is an optimal lag time over which the TAMSD of a particle should be evaluated to obtain proper fits of its physical properties [15,16].

To this end, weighted least-squares (WLS) regression is often implemented in order to reduce the dependence of the fit on data points with greater variance, following

$$\hat{\boldsymbol{\theta}} = \underset{\theta}{\text{argmin}} \sum_{i=1}^{P} w_{i,\theta}(Y_i - f_{i,\theta})^2, \quad (4)$$

where $\hat{\boldsymbol{\theta}}$ is again the vector of estimated parameters, Y_i are the P data observations, $w_{i,\theta}$ are the weights, and $f_{i,\theta}$ is the model fitted. Here argmin_θ now finds the vector $\boldsymbol{\theta}$, which minimizes the weighted objective function. The objective function can be weighted by the inverse of the analytical expression of the population variance (here the variance of the squared displacements) as an estimation of the sample error of the mean [15,17]. The variance of the mean of a random variable X, i.e., $\text{E}[X] = \sum_{i=1}^{N} X_i/N$, can be obtained using the variance sum law for uncorrelated variables as

$$\text{Var}[\text{E}[X]] = \text{Var}\left[\sum_{i=1}^{N} \frac{X_i}{N}\right] = \frac{1}{N^2}\sum_{i=1}^{N}\text{Var}[X_i] = \frac{\sigma^2}{N}, \quad (5)$$

where N is the sample size, and σ^2 is the variance of the random variable X. Thus, from Eq. (5), we obtain the following expression for the weights $w_{i,\theta}$:

$$w_{i,\theta} = \frac{1}{\text{Var}[\text{E}[X]]} = \frac{N_i}{\sigma_{i,\theta}^2}, \quad (6)$$

where N_i is the number of statistically independent data points contributing to each observation i, and $\sigma_{i,\theta}^2$ is the population variance of each observation i, in terms of the fitted values $\boldsymbol{\theta}$.

Nonetheless, the standard approach in the literature is parameter estimation from TAMSDs using unweighted least-squares regression [18]. Additionally, perhaps the most widespread expression that is fitted is the so-called "short-time" MSD of ABPs [19] (7). First proposed by Howse *et al.* for the analysis of Janus catalytic microswimmers [1], the short-time MSD equation approximates the full MSD [Eq. (1)] at an arbitrarily short time lag, typically defined as 10% of the characteristic persistence or rotational diffusion time $\tau_R = 1/D_R$, using a Maclaurin series expansion assuming $\tau/\tau_R \to 0$ [6]

$$\langle\Delta\mathbf{r}^2(\tau)\rangle \sim 4D_T\tau + V_0^2\tau^2. \quad (7)$$

This simplification provides reasonable fits to the experimental TAMSD of single particles under certain conditions, particularly in relation to the extraction of microswimmer velocities [1,18,20–23]. However, care should be taken when fitting this truncated form of the MSD to short experimental trajectories, as it can lead to the spurious detection of velocity in the presence of experimental artifacts [24]. The problems associated with the standard fitting of the truncated form of the MSD were comprehensively demonstrated by Mestre *et al.* [8]. Interestingly, their proposed solution was to expand the Maclaurin series to higher polynomial orders. Nonetheless, we are interested in evaluating the fitting of the full ABP's MSD to the "short-time" regime, as the approximation is simply that: an approximation of a theoretical model.

In this work, we propose multiple approaches to improve the fitting of the full ABP MSD model. We verify the robustness of our approach by comparing it against the "standard" approach of performing unweighted OLS regression on the truncated form of an ABP's MSD at short lag times. We begin by considering the case where D_T and D_R are coupled by the Einstein relation $D_T = d_p^2 D_R/3$ to avoid the introduction of additional fitting parameters and thus allow a fair comparison between the standard approach and our proposed alternatives. In the final section of this study, we then treat D_R as an additional free fitting parameter, corresponding to experimental situations where D_T and D_R are often decoupled. We evaluate the different fitting procedures against simulated ABP trajectories using input values representative of experiments. Specifically, in the coupled case, our ABPs are simulated via Langevin dynamics [25], with an active velocity of $V_0 = 5\ \mu\text{m s}^{-1}$ and diffusivities $D_T = 0.2\ \mu\text{m}^2\ \text{s}^{-1}$ and $D_R = 0.15\ \text{rad}^2\ \text{s}^{-1}$. The simulations are numerically solved at 1 ms

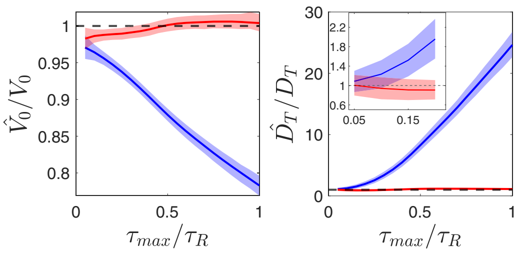

FIG. 1. Parameter estimation from fitting the truncated (blue) and full MSD (red) expression to simulated data (estimates $\hat{V}_0$, $\hat{D}_T$ respectively normalized to the simulation inputs V_0, D_T). The same trajectory is fitted to increasing maximal lag times τ_{max}, up to the persistence time of an ABP (τ_R). We obtain 95% confidence intervals by bootstrapping. Inset (right): Fits of D_T for short τ_{max}, indicating the rapid deviation from the input simulation value when using the truncated expression.

increments and sampled at 20 frames per second (fps) for 60 s to replicate experimental videos.

Properly applied, there are several advantages to the standard approach of fitting the TAMSD at short timescales. Generally, the scatter of the sample MSD will increase with lag time. This increase not only is caused by the decrease in data points for a trajectory of a given length, but also is due to the growing correlation between sequential observations [see Eq. (3)]. Therefore, the fitting of the MSD to unnecessarily long lag times is generally discouraged [17]. By evaluating the TAMSD over a time period during which the variance does not grow significantly, the effects of heteroscedasticity on parameter estimation are reduced [15]. Nonetheless, the term "short lag times," where the simplified expression holds, is flawed since it is often arbitrarily defined and used in the literature. Furthermore, by eliminating the opportunity to fit D_R, the truncated form of Eq. (7) removes characteristic information on the physics of ABPs. Finally, for smaller particles, the characteristic persistence time may be so short that only a few data points can be used to fit the expression, unless experiments are performed at very high frame rates, introducing measurement error and reducing the accuracy of parameter estimation [14].

There are, in fact, further model-specific problems associated with fitting the truncated form of the MSD. As seen in Eq. (2), OLS regression is weighted towards larger values, i.e., MSD values at longer lag times. If left untreated, the fitting of the MSD will therefore be weighted towards the "long-time diffusive" regime of the ABP [4]. Moreover, due to the monotonically growing variance in the error terms of the MSD (discussed below in more detail), this procedure assigns greater importance to more uncertain values, leading to poorer estimates. The effects of these considerations are illustrated by comparing the estimates for D_T and V_0 obtained by fitting the truncated and full form of the MSD equation to simulated trajectories (see Fig. 1).

The problems of using Eq. (7) become quickly apparent as the lag times evaluated increase beyond small fractions of the characteristic relaxation time τ_R. As the estimated velocity decreases, the fitted D_T value rapidly increases to over an order of magnitude greater than the simulation input (see Fig. 1, blue). The inverse relationship between V_0 and D_T can be understood by their respective contributions to the overall MSD of an ABP. The increasingly diffusive nature of an ABP's motion with time [4] results in an overestimated D_T at the expense of a reduction in the fitted V_0. This problem is caused by the absence of the D_R-related terms in Eq. (7), which would otherwise result in the crossover to a long-time diffusive regime (see Eq. (1)). In short, due to the systematic errors associated with using Eq. (7) we strongly advise against its use when fitting the MSD of ABPs. To compare the accuracy of our different fitting methods, we use the median symmetric accuracy metric as described in [26]. By evaluating the point estimates over the range of lag times studied, we obtain errors of 14.5% for $\hat{V}_0$ and 799.2% for $\hat{D}_T$ respectively when using the truncated expression for an ABP's MSD.

In contrast, the bootstrapped confidence intervals of the estimated parameters using Eq. (1) more often include the true simulation input values for different maximal lag times τ_{max} and also converge to reasonable values as the lag time evaluated approaches the characteristic rotational relaxation time τ_R (see Fig. 1, red). Fitting Eq. (1) also carries the advantage of not assuming a limited short-time regime, enabling the fitting to longer lag times and thus providing more data points for better parameter estimation. Errors on the model parameters estimated are improved to 0.6% and 12.1% for $\hat{V}_0$ and $\hat{D}_T$, respectively. We again emphasize that we do not fit D_R as a free parameter here but instead assume that the Einstein relation $D_T = d_p^2 D_R/3$ holds and fit Eq. (1) accordingly. However, decoupling D_T and D_R better approximates experimental situations where the presence of confining boundaries [27], activity [28–30], or external fields [31] can have a different effect on rotation and translation respectively.

Despite the significant improvement in estimating the physical parameters of an ABP by using the full form of its MSD equation, this operation still does not address underlying statistical issues such as heteroscedasticity of the data. The presence of heteroscedasticity can be clearly observed in the residuals of the fitted ABP model (see Fig. 2, top row, red). One of the most frequently used heuristic approach to address heteroscedasticity is to log transform the data and fit the model's log-transformed analog. Log transforms work particularly well for right skew, constantly positive, and increasing data, such as the case for the ABP's MSD. Studying the "mean logarithmic squared displacement" (MLSD) has previously been suggested to improve the estimation of the distribution of anomalous diffusion coefficients in a population of heterogeneous particles [10].

By fitting the log-transformed (cyan) data, we observe a clear reduction of the heteroscedasticity of the residuals. This provides improved estimated fits and confidence intervals obtained from bootstrapping, and we obtain percentage errors of the point estimates of 0.5% and 2.3% for $\hat{V}_0$ and $\hat{D}_T$ respectively. In Fig. 2 (bottom row), we highlight the improvement in fitting after this simple preprocessing step, evaluating the same trajectory as in Fig. 1 but now with the log-transformed, full MSD ABP fit included as a comparison to the full fit without log transformation. We see both a reduction in the width of the confidence intervals and a smaller difference

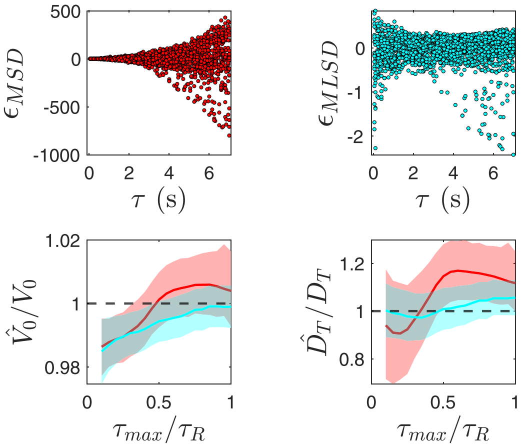

FIG. 2. Top row: Plots of the residuals from the mean squared displacements based on the point estimates in the bottom row for $\tau_{max}/\tau_R = 1$ as a function of lag time τ. Left (red): Residuals of Eq. (1) fitted to unprocessed data (MSD). Right (cyan): Residuals of log[Eq. (1)] fitted to log-transformed data (MLSD). The extent of heteroscedasticity is clearly reduced, as the variance remains relatively constant with τ after log transformation. Bottom row: Parameter estimation without (red) and with (cyan) log transformation of the data and the model.

between the point estimate and the input simulation values. In particular, the estimates for D_T are notably improved.

As a next step, we turn to WLS regression as a tool for determining the parameters of an ABP. As previously alluded to, within the WLS regression approach, one typically relates the weights to the variance of the expectation value [see Eq. (6)]. Under the assumption that all observations are statistically independent, the variance of the expectation value can be obtained from the population variance itself, using the variance sum law as shown in Eq. (5). Where applicable, we will follow this approach and specify the weights in terms of the theoretical result for the variance of the mean-squared displacement [5,32,33]

$$\begin{aligned}\sigma^2(\tau) &= \langle \Delta\mathbf{r}^4(\tau)\rangle - \langle \Delta\mathbf{r}^2(\tau)\rangle^2 \\ &= 16D_T^2\tau^2 + 16D_T\tau\frac{V_0^2}{D_R^2}\left(D_R\tau - 1 + e^{-D_R\tau}\right) \\ &\quad + \frac{V_0^4}{D_R^4}\left(4D_R^2\tau^2 - 22D_R\tau + \frac{79}{2} - \frac{64}{3}D_R\tau e^{-D_R\tau}\right. \\ &\quad \left. - \frac{320}{9}e^{-D_R\tau} - 4e^{-2D_R\tau} + \frac{1}{18}e^{-4D_R\tau}\right). \qquad (8)\end{aligned}$$

We note that this result is an exact representation of the variance of the mean only if nonoverlapping squared displacements are considered. For overlapping displacements, a proper analysis requires additional covariance contributions in Eq. (5), describing the correlation between subsequent displacements. In that case, we will still employ Eq. (8), however, as an approximation, and without the contributing term of

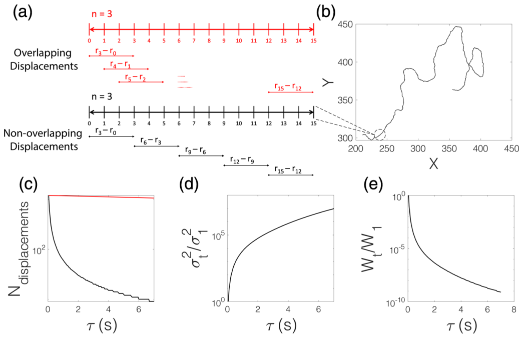

FIG. 3. (a) Definition of overlapping and nonoverlapping displacements from the simulated trajectory shown in (b). (c) Number of displacements as a function of lag time when overlapping (red) and nonoverlapping (black) displacements are evaluated. (d) Normalized variance of the MSD as a function of τ (σ_1 is the variance at the shortest lag time $\tau_1 = 0.05$ s), as derived by Eq. (8). (e) Corresponding normalized weight at time τ (w_1 is the weight at $\tau_1 = 0.05$ s) extracted according to Eq. (4) as a function of τ for the TAMSD of a single particle.

the number of observations. Equipped with this expression, we can now investigate the presence of heteroscedasticity in an ABP's MSD and attempt to minimize its effects on parameter estimation using WLS regression. As discussed before, we stress that in an experimental context, there might be further hidden correlations between square displacements requiring special consideration, whose evaluation lies beyond the aims of this work. As alluded to above, the TAMSD of particles can be evaluated with one of two different approaches: by determining the overlapping or nonoverlapping particle displacements [see Figs. 3(a) and 3(b)]. Evaluating nonoverlapping squared displacements reduces the correlation between subsequent observations of motion in experimental scenarios and removes it entirely within the framework of the ABP model. However, in this case, the decay in the number of displacements is hyperbolic, decreasing much more rapidly than when overlapping displacements are evaluated [see Fig. 3(c)]. Furthermore, using only nonoverlapping displacements leads to a different sampling of points along the trajectory depending on how many prime factors are present in the number of the time step. These factors lead to a situation where using overlapping displacements typically improves fitting performance and is generally preferable [17].

We now discuss the potential benefits of applying the weighting coefficient to minimize the effects of the large and high-variance long lag time values in the objective function [see Eq. (4)]. From Eq. (8), we find that the variance increases with time [see Fig. 3(d)], and combined with the decay in the number of observations [see Fig. 3(c)], we obtain with Eq. (5) a weighting vector that rapidly decays with time [see Fig. 3(e)]. This in turn demonstrates that the low numbers of observations at longer timescales, which inherently have a larger variance due to the nature of the TAMSD, will have a significantly reduced influence on parameter estimation.

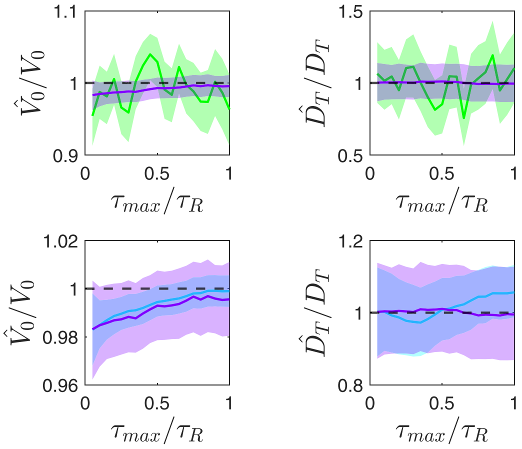

FIG. 4. Top row: Parameter estimation using WLS regression on nonoverlapping (green) and overlapping (purple) displacements. Bottom row: Parameter estimation on overlapping displacements using WLS regression (purple) and the MLSD (cyan).

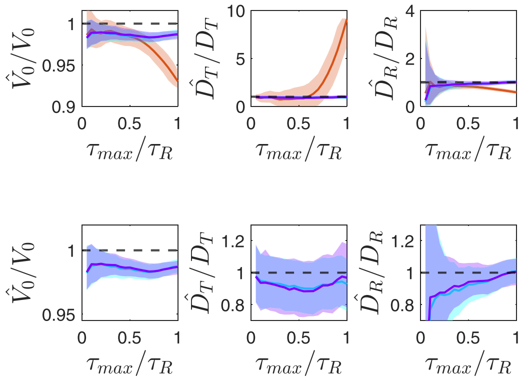

FIG. 5. Parameter estimation of an ABP's MSD where D_T and D_R are uncoupled, using WLS regression (purple), MLSD (cyan), and the third-order truncation of the MSD equation (orange). Top row: Comparison of the three fitting approaches. The truncated expression clearly performs worse, particularly at larger τ_{max} (see the estimates for D_T and D_R). Bottom row: Only the MLSD and WLS regression are represented for better visualization.

We now fit the TAMSD of a single particle using WLS regression, beginning with the analysis of nonoverlapping displacements (see Fig. 4, top row, green). We obtain percentage errors of 2.0% and 5.9% for $\hat{V}_0$ and $\hat{D}_T$, respectively, for the point estimates. We note a significant instability in the point estimates and confidence intervals, particularly for $\hat{D}_T$, in direct comparison to the fits obtained with the MLSD. Therefore, we also evaluate the performance of WLS regression on overlapping displacements, noting that the underlying assumption of statistically independent observations no longer holds (see Fig. 4, top row, purple). We again highlight here that the variance sum law no longer holds, and therefore we weight the objective function for overlapping displacements using only Eq. (8). Comparing the overlapping to the nonoverlapping case, we find that the resulting confidence intervals and point estimates for WLS regression are much narrower and less subject to fluctuations. Under these conditions, we observe percentage errors of 0.7% and 0.5% for $\hat{V}_0$ and $\hat{D}_T$, respectively. We expect this discrepancy arises, in large part, from the statistical issues associated with evaluating nonoverlapping displacements, as described in [17]. Motivated by the improved parameter estimation, we continue to evaluate WLS regression using overlapping displacements for the rest of this work.

We now compare the performance of the MLSD and WLS regression for parameter estimation from overlapping displacements (see Fig. 4, bottom row). Although the resulting confidence intervals are broader for the WLS regression than for the MLSD, we note that in the former case the estimate for D_T is more stable, and the true simulation input parameters are included for all values of τ_{max}. We conclude that for a two-parameter fit, where $D_T = d_p^2 D_R/3$, the estimates obtained from WLS regression and OLS regression of the MLSD are similar.

So far, we have considered only particles satisfying the ideal condition where D_T and D_R are related by the Einstein relationship for freely diffusing spherical particles. However, in many situations, e.g., when in proximity with a solid wall, D_T and D_R are likely to be decoupled [2,27–30], and it is therefore important, in most experimental realizations of ABPs, to fit these parameters separately. We account for these circumstances by modifying the value of D_T, while keeping the same value of D_R in our simulations. In particular, we modify the translational diffusivity by applying Faxen's correction factor to D_T, as if to mimic the presence of a solid wall 250 nm away from the particle surface [34]. This correction approximately reduces the theoretical D_T value we initially used by half.

In Fig. 5 we compare the performance of the MLSD and WLS regression approaches when estimating the parameters V_0, D_T, and D_R (blue and purple, respectively). For the MLSD, we determine percentage errors of 1.5%, 7.8%, and 7.9% for $\hat{V}_0$, $\hat{D}_T$, and $\hat{D}_R$, respectively, for the point estimates across all the lag times evaluated, while for the WLS regression we obtain corresponding errors of 1.4%, 8.7%, and 5.9%. We also study the truncated MSD equation expanded to third order, as outlined in [8] (Fig. 5, top row, orange). This expression is obtained by evaluating the Maclaurin series expansion of Eq. (1) to the third order

$$\langle \Delta \mathbf{r}^2(\tau) \rangle \sim 4D_T\tau + V_0^2\tau^2 - \frac{V_0^2}{3\tau_R}\tau^3. \tag{9}$$

We find that as before, the truncated form of the full MSD equation is not able to satisfactorily capture the input simulation parameters, an effect which is particularly noticeable for D_T as τ_{max} increases, as previously observed in Fig. 1. We determine percentage errors of 1.6%, 32.2%, and 24.4% for $\hat{V}_0$, $\hat{D}_T$, and $\hat{D}_R$ respectively. We note the use of the median function in the median symmetric accuracy metric [26], and the effect this has on the measured accuracy relative to the instability observed in Fig. 5 (top row, orange).

When evaluating overlapping displacements using WLS regression and the MLSD, we note a remarkable overlap in both the point estimates and confidence intervals (see Fig. 5, bottom row). This observation indicates that both the log transformation and weighting of the data have a similar effect on addressing the heteroscedasticity present in an ABP's MSD. In both instances, we also note the instability of the short-time estimates for D_R, which is unsurprising given the independence of the MSD from D_R at short lag times [see Eq. (7)].

In conclusion, the ABP model provides a useful framework to study the motion of microswimmers and extract meaningful physical properties from mean quantities. However, "blind" fitting of MSDs can affect results, as hidden correlations may arise in experimental systems. Therefore, we recommend constructing confidence intervals by bootstrapping in almost all experimental situations. We additionally always advise against the use of the truncated form of the MSD equation. Further steps beyond fitting to short lag times should also be taken to treat the heteroscedasticity of an ABP's MSD. In particular, we find that log transforming the data before fitting the MLSD equation outperforms standard approaches used in literature, and provides similar estimates as WLS regression using the theoretical variance of an ABP's MSD. With this approach, overlapping displacements can be evaluated, significantly increasing the amount of data available. Furthermore, the simplicity of fitting log-transformed data to shorter lag times should assist in its widespread uptake. We nevertheless stress that we have studied simulated data of an ideal, noninteracting ABP model, neglecting, e.g., the presence of torque in the Langevin force balance [28,35], a situation that is often observed in experiments due to nonsymmetric surface modification [36] or shape [37], which can significantly affect the fitting of model parameters. Signatures for an angular propulsion velocity should therefore be additionally investigated when analyzing experimental trajectories, and its effect duly included in the fits. We have also not treated the effect of ABP speed on the coupling between D_T and V_0 [38] and experimental errors from static and dynamic localization errors [10,15,16,39]. These are nevertheless critical factors which should be considered when designing experiments and analyzing data.

The authors thank Dr. S. Ketzetzi and Dr. B. ten Hagen for various insightful discussions.

Author contributions are defined based on the CRediT (Contributor Roles Taxonomy). Conceptualization: M.R.B., F.G. Formal analysis: M.R.B., A.R.S. Funding acquisition: L.I. Investigation: M.R.B., A.R.S. Methodology: M.R.B., F.G. Software: M.R.B. Supervision: F.G., L.I., H.L. Validation: M.R.B., A.R.S. Visualization: M.R.B. Writing: original draft: M.R.B., A.R.S., L.I. Writing: review and editing: M.R.B., A.R.S., H.L, L.I.

[1] J. R. Howse, R. A. Jones, A. J. Ryan, T. Gough, R. Vafabakhsh, and R. Golestanian, Phys. Rev. Lett. **99**, 048102 (2007).
[2] K. Dietrich, D. Renggli, M. Zanini, G. Volpe, I. Buttinoni, and L. Isa, New J. Phys. **19**, 065008 (2017).
[3] B. ten Hagen, S. Van Teeffelen, and H. Löwen, J. Phys.: Condens. Matter **23**, 194119 (2011).
[4] C. Bechinger, R. Di Leonardo, H. Löwen, C. Reichhardt, G. Volpe, and G. Volpe, Rev. Mod. Phys. **88**, 045006 (2016).
[5] X. Zheng, B. ten Hagen, A. Kaiser, M. Wu, H. Cui, Z. Silber-Li, and H. Löwen, Phys. Rev. E **88**, 032304 (2013).
[6] H. Löwen, J. Chem. Phys. **152**, 040901 (2020).
[7] A. van den Bos, *Parameter Estimation for Scientists and Engineers* (John Wiley & Sons, New York, 2007).
[8] R. Mestre, L. S. Palacios, A. Miguel-López, X. Arqué, I. Pagonabarraga, and S. Sánchez, arXiv:2007.15316 (2020)
[9] F. Novotný and M. Pumera, Sci. Rep. **9**, 13222 (2019).
[10] E. Kepten, I. Bronshtein, and Y. Garini, Phys. Rev. E **87**, 052713 (2013).
[11] K. Fogelmark, M. A. Lomholt, A. Irbäck, and T. Ambjörnsson, Sci. Rep. **8**, 6984 (2018).
[12] H. Qian, M. P. Sheetz, and E. L. Elson, Biophys. J. **60**, 910 (1991).
[13] B. Efron and R. J. Tibshirani, *An Introduction to the Bootstrap* (Chapman & Hall/CRC, Philadelphia, 1994).
[14] E. Kepten, A. Weron, G. Sikora, K. Burnecki, and Y. Garini, PLoS ONE **10**, e0117722 (2015).
[15] X. Michalet, Phys. Rev. E **82**, 041914 (2010).
[16] J. Devlin, D. Husmeier, and J. A. Mackenzie, Phys. Rev. E **100**, 022134 (2019).
[17] M. J. Saxton, Biophys. J. **72**, 1744 (1997).
[18] X. Arqué, A. Romero-Rivera, F. Feixas, T. Patiño, S. Osuna, and S. Sánchez, Nat. Commun. **10**, 2826 (2019).
[19] W. Wang and T. E. Mallouk, ACS Nano **15**, 15446 (2021).
[20] A. M. Pourrahimi, K. Villa, C. L. Manzanares Palenzuela, Y. Ying, Z. Sofer, and M. Pumera, Adv. Funct. Mater. **29**, 1808678 (2019).
[21] V. Sridhar, F. Podjaski, J. Kröger, A. Jiménez-Solano, B. W. Park, B. V. Lotsch, and M. Sitti, Proc. Natl. Acad. Sci. U. S. A. **117**, 24748 (2020).
[22] S. Ketzetzi, J. De Graaf, R. P. Doherty, and D. J. Kraft, Phys. Rev. Lett. **124**, 048002(R) (2020).
[23] M. R. Bailey, N. Reichholf, A. Flechsig, F. Grillo, and L. Isa, Part. Part. Syst. Charact. **39**, 2100200 (2021).
[24] G. Dunderdale, S. Ebbens, P. Fairclough, and J. Howse, Langmuir **28**, 10997 (2012).
[25] A. Callegari and G. Volpe, Flowing Matter **1**, 211 (2019).
[26] S. K. Morley, T. V. Brito, and D. T. Welling, Space Weather **16**, 69 (2018).
[27] A. J. Goldman, R. G. Cox, and H. Brenner, Chem. Eng. Sci. **22**, 637 (1967).
[28] S. Ebbens, R. A. L. Jones, A. J. Ryan, R. Golestanian, and J. R. Howse, Phys. Rev. E **82**, 015304(R) (2010).
[29] S. Das, A. Garg, A. I. Campbell, J. Howse, A. Sen, D. Velegol, R. Golestanian, and S. J. Ebbens, Nat. Commun. **6**, 8999 (2015).

[30] J. Simmchen, J. Katuri, W. E. Uspal, M. N. Popescu, M. Tasinkevych, and S. Sánchez, Nat. Commun. **7**, 10598 (2016).

[31] A. R. Sprenger, M. A. Fernandez-Rodriguez, L. Alvarez, L. Isa, R. Wittkowski, and H. Löwen, Langmuir **36**, 7066 (2020).

[32] C. Kurzthaler and T. Franosch, Soft Matter **13**, 6396 (2017).

[33] F. J. Sevilla and P. Castro-Villarreal, Phys. Rev. E **104**, 064601 (2021).

[34] S. Ketzetzi, J. de Graaf, and D. J. Kraft, Phys. Rev. Lett. **125**, 238001 (2020).

[35] S. van Teeffelen and H. Löwen, Phys. Rev. E **78**, 020101(R) (2008).

[36] X. Wang, M. In, C. Blanc, A. Würger, M. Nobili, and A. Stocco, Langmuir **33**, 13766 (2017).

[37] F. Kümmel, B. ten Hagen, R. Wittkowski, I. Buttinoni, R. Eichhorn, G. Volpe, H. Löwen, and C. Bechinger, Phys. Rev. Lett. **110**, 198302 (2013).

[38] E. M. Tang and P. T. Underhill, Langmuir **34**, 10694 (2018).

[39] T. Savin and P. S. Doyle, Biophys. J. **88**, 623 (2005).

P6 The Parental Active Model: a unifying stochastic description of self-propulsion

Reproduced from

L. Caprini, A. R. Sprenger, H. Löwen, and R. Wittmann,
The Parental Active Model: a unifying stochastic description of self-propulsion,
J. Chem. Phys. **156**, 071102 (2022),
with the permission of *AIP Publishing* [293].

Digital Object Identifier (DOI): doi.org/10.1063/5.0084213

Statement of contribution

R.W. came up with the research idea. L.C., A.R.S., and R.W. investigated the model. L.C. developed most of the theoretical and numerical results. L.C. and A.R.S. prepared the figures. L.C. and R.W. wrote the manuscript. All authors discussed and interpreted the results, edited the text, and finalized the manuscript.

Copyright and license notice

©AIP Publishing LLC.
AIP Publishing permits authors to reprint the Version of Record (VOR) in their theses or dissertations. It is understood and agreed that the thesis or dissertation may be made available electronically on the university's site or in its repository and that copies may be offered for sale on demand.

The Journal of Chemical Physics COMMUNICATION scitation.org/journal/jcp

The parental active model: A unifying stochastic description of self-propulsion

Cite as: J. Chem. Phys. **156**, 071102 (2022); doi: 10.1063/5.0084213
Submitted: 4 January 2022 • Accepted: 1 February 2022 •
Published Online: 17 February 2022

View Online Export Citation CrossMark

Lorenzo Caprini,[a] Alexander R. Sprenger, Hartmut Löwen,[b] and René Wittmann[c]

AFFILIATIONS

Institut für Theoretische Physik II: Weiche Materie, Heinrich-Heine-Universität Düsseldorf, 40225 Düsseldorf, Germany

[a]Electronic mail: lorenzo.caprini@gssi.it and lorenzo.caprini@hhu.de
[b]Electronic mail: hlowen@hhu.de
[c]Author to whom correspondence should be addressed: rene.wittmann@hhu.de

ABSTRACT

We propose a new overarching model for self-propelled particles that flexibly generates a full family of "descendants." The general dynamics introduced in this paper, which we denote as the "parental" active model (PAM), unifies two special cases commonly used to describe active matter, namely, active Brownian particles (ABPs) and active Ornstein–Uhlenbeck particles (AOUPs). We thereby document the existence of a deep and close stochastic relationship between them, resulting in the subtle balance between fluctuations in the magnitude and direction of the self-propulsion velocity. Besides illustrating the relation between these two common models, the PAM can generate additional offsprings, interpolating between ABP and AOUP dynamics, that could provide more suitable models for a large class of living and inanimate active matter systems, possessing characteristic distributions of their self-propulsion velocity. Our general model is evaluated in the presence of a harmonic external confinement. For this reference example, we present a two-state phase diagram that sheds light on the transition in the shape of the positional density distribution from a unimodal Gaussian for AOUPs to a Mexican-hat-like profile for ABPs.

Published under an exclusive license by AIP Publishing. https://doi.org/10.1063/5.0084213

INTRODUCTION

Active matter includes a broad variety of biological and physical systems,[1–3] ranging from bacteria,[4,5] colloids,[6–11] more complex organisms, such as sperms and cells,[12] and even animals at the macroscopic scales,[13,14] such as birds[15] and fish.[16] Each of these systems is formed by individual active units that convert energy into motion, a property that allows them to be denoted as active systems.[17] Despite this generic label, the multitude of mechanisms behind active motion results in a large amount of diversity, e.g., giving rise to systems whose typical active velocity is constant or subject to fluctuations.

On the theoretical side, there are two major paradigms for modeling active particles as a diffusive stochastic process:[18,19] active Brownian particles (ABPs),[20–26] introduced to describe the diffusion-driven behavior of active colloids, and active Ornstein–Uhlenbeck particles (AOUPs),[27–34] originally proposed for mathematical convenience[35,36] but also found to be a good approximation for a passive particle in an active bath.[37–40] Both models possess two major common ingredients: the typical self-propulsion velocity induced by the active force (sometimes called the swim velocity), which is constant for ABPs or given by an average value for AOUPs, and the persistence time, indicating the strength of rotational diffusion for ABPs and the characteristic time scale in the autocorrelation of the active noise for AOUPs.

It is well known that ABPs and AOUPs share a similar phenomenology in a large range of fundamental physical problems, e.g., both predict the accumulation near walls and obstacles,[41–43] clustering[44,45] and motility induced phase separation,[20,24,46–51] and spatial velocity correlations in dense systems[26,52–54] and active glasses.[55,56] However, some prominent differences emerge in a few special cases, such as the failure of AOUPs to reproduce the bimodal spatial distribution in a harmonic potential (for instance, see Ref. 36 for AOUPs and Refs. 57 and 58 for ABPs) or the distinct behavior of the density in the bulk of a confined system.[59–61] For this reason, ABPs are usually perceived as the established model to describe active colloids, while AOUPs are considered as a useful but over-simplified approximation for ABPs when the model parameters are appropriately chosen. However, the propitious theoretical possibilities offered by the AOUPs have contributed to establish it as an important model for active matter systems in its own right. This has led to a continuously increasing number of works dedicated to

Published under an exclusive license by AIP Publishing

The Journal of Chemical Physics COMMUNICATION scitation.org/journal/jcp

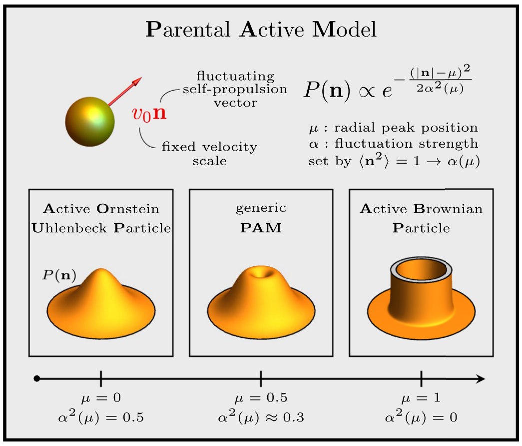

FIG. 1. Illustration of the considered family of active models, uniquely characterized by a velocity scale v_0 and the self-propulsion vector $\mathbf{n}$, determined by a stochastic process of unit variance. The parental active model (PAM) is described by the shown distribution $P(\mathbf{n})$ in the form of a shifted Gaussian [see Eq. (7)] with the single free parameter μ, which identifies the most likely value of the modulus $|\mathbf{n}|$. The width of the distribution, quantified by $\alpha(\mu)$, is constrained by the condition $\langle \mathbf{n}^2 \rangle = 1$ [see Eq. (9)]. The 3d plots at the bottom show $P(\mathbf{n})$ for three specific choices of μ, indicated by the axis below, which are further discussed in the text.

the AOUP model with the aim of deriving exact or approximate analytical results for single-particle[62,63] or interacting systems.[64–68] The recent interest in AOUPs implies the need to reevaluate the unilateral relation to the ABP model by going beyond the standard qualitative way to compare these two fundamental approaches.

In this work, we propose a general model to describe the self-propulsion mechanism of active particles on the microscale, which we call the parental active model (PAM) because it includes both ABPs and AOUPs as two subcases. We thus show that these classical models actually stand on the same hierarchical level as descendants of the PAM; see Fig. 1 for an illustrative picture. Specifically, they differ only by the value of a single parameter, indicating the shape of the probability distribution of the radial component of the active velocity. In other words, the relation between ABPs and AOUPs is that of two sisters rather than two cousins. By considering a whole class of overarching models, we both uncover the deep connection between ABPs and AOUPs going beyond a mutual mapping[64,69] and bridge the gap between these two extreme cases, which may provide a crucial step toward a more realistic description of experimental systems. To explore the whole family of models, we compare the (famously distinct) probability density of ABPs and AOUPs in a harmonic trap to the results for intermediate offspring of the PAM.

GENERIC DYNAMICS OF ACTIVE PARTICLES

The typical overdamped dynamics of a generic active particle is described by the differential equation

$$\gamma\dot{\mathbf{x}} = \gamma v_0 \mathbf{n} + \gamma\sqrt{2D_t}\mathbf{w} + \mathbf{F}(\mathbf{x}) \tag{1}$$

for its position $\mathbf{x}$, where $\mathbf{F}(\mathbf{x})$ is the external force exerted on the particle, $\mathbf{w}$ is a white noise with unit variance and zero average, and γ and D_t are the friction coefficient and the translational diffusion coefficient, respectively, related to the temperature of the bath through the Einstein relation. The term $v_0\gamma\mathbf{n}$ is called the active force and $v_0\mathbf{n}$ is the resulting self-propulsion velocity, where the constant v_0 provides a velocity scale. The self-propulsion vector $\mathbf{n}$ is a general stochastic process with unit variance whose specific dynamics determine the active model under consideration. For simplicity, we restrict ourselves to two spatial dimensions.

ACTIVE BROWNIAN PARTICLES (ABPs)

In the case of ABPs, $\mathbf{n}$ represents a unit vector, which denotes the fluctuating particle orientation. In other words, the direction of $\mathbf{n} = (\cos\theta, \sin\theta)$ is described by the steady-state distribution

$$P_{\mathrm{ABP}}(n,\theta) \sim \frac{1}{2\pi} n\delta(n-1) \tag{2}$$

with a uniformly distributed orientational angle θ and fluctuation-free modulus $n = |\mathbf{n}|$ that is always fixed to the average value $\langle n \rangle = 1$. As known, the ABP dynamics in polar coordinates is simply a diffusive process,

$$\dot{\theta} = \sqrt{\frac{2}{\tau}}\,\xi \tag{3}$$

for θ, where ξ is a white noise with unit variance and zero average, and the time scale $\tau = 1/D_r$ represents the persistence time induced by the rotational diffusion coefficient D_r.

ACTIVE ORNSTEIN–UHLENBECK PARTICLES (AOUPs)

In the case of AOUPs, $\mathbf{n}$ is represented by a two-dimensional Ornstein–Uhlenbeck process that allows both the modulus n and the orientation θ to fluctuate with related amplitudes. The AOUP distribution is a two-dimensional Gaussian such that each component fluctuates around a vanishing mean value with unitary variance. In polar coordinates, the probability distribution of the AOUP self-propulsion reads

$$P_{\mathrm{AOUP}}(n,\theta) \sim \frac{1}{2\pi} n \exp\left(-n^2\right). \tag{4}$$

The dynamics $\dot{\mathbf{n}} = -\frac{\mathbf{n}}{\tau} + \sqrt{\frac{1}{\tau}}\boldsymbol{\chi}$ generating the process is usually written in Cartesian coordinates, where $\boldsymbol{\chi}$ is a two-dimensional vector of white noises with uncorrelated components having unitary variance and zero average. To shed light on the relation with the ABP, it is convenient to express the dynamics of AOUP in polar coordinates, which gives (Itô integration)

$$\dot{n} = -\frac{n}{\tau} + \sqrt{\frac{1}{\tau}}\chi_n + \frac{1}{2\tau n}, \tag{5a}$$

$$\dot{\theta} = \sqrt{\frac{1}{\tau}}\frac{\chi_\theta}{n}, \tag{5b}$$

Published under an exclusive license by AIP Publishing

The Journal of Chemical Physics COMMUNICATION scitation.org/journal/jcp

where χ_n and χ_θ are white noises with unit variance and zero average. While still being coupled to the dynamics of n, the angular equation for θ is quite similar to that describing the ABP dynamics in Eq. (3).

MAPPING BETWEEN ABPs AND AOUPs

Usually, the connection between ABPs and AOUPs is established by demanding that the steady-state temporal correlations of the self-propulsion velocity $v_0\mathbf{n}$ of ABPs and AOUPs are equal. Note that by introducing this generic form of the active force in Eq. (1), we have already included in the dynamics the mapping $2D_a/\tau = v_0^2$ through which we have eliminated the active diffusivity D_a from the conventional notation for the AOUP dynamics. Likewise, the second relation $D_r = 1/\tau$ is implied in Eq. (3). As a result, both models share the same autocorrelation function

$$\langle \mathbf{n}(t)\cdot\mathbf{n}(0)\rangle = \exp\left(-\frac{t}{\tau}\right) \tag{6}$$

of the self-propulsion vector $\mathbf{n}$, despite possessing different distribution $P_{\mathrm{ABP}}(n,\theta) \neq P_{\mathrm{AOUP}}(n,\theta)$. Apart from this mapping, there is currently no apparent deeper relation between the stochastic processes Eq. (3) and Eq. (5b), underlying the dynamics of ABP and AOUP, respectively. As a next step, we establish such a connection by introducing a more general model.

UNIFICATION IN THE PARENTAL ACTIVE MODEL (PAM)

Now, we are ready to define a "parental" active model (PAM) from which one can recover both ABPs and AOUPs as limiting cases. The most natural steady-state distribution for a PAM accounting for these features simply introduces Gaussian fluctuations and reads

$$P(n,\theta) \sim \frac{n}{2\pi}\exp\left(-\frac{(n-\mu)^2}{2\alpha^2}\right). \tag{7}$$

This is one of the most simple distributions that allow the modulus to fluctuate around a nonzero peak of the distribution, μ, with modulus fluctuations, α^2, which are independent of those of the active force direction θ. Note that $P(n,\theta)$ is constant in θ so that $P(n,\theta)\sim\bar{P}(n)$, where $\bar{P} = \int_0^{2\pi} d\theta P$ is the reduced distribution of the self-propulsion velocity modulus (cf. Fig. 2).

The dynamics of the PAM, i.e., the dynamics that generate the steady-state distribution (7) in polar coordinates are (Itô integration)

$$\dot{n} = -\frac{(n-\mu)}{\tau} + \sqrt{\frac{2\alpha^2}{\tau}}\chi_n + \frac{\alpha^2}{\tau n}, \tag{8a}$$

$$\dot{\theta} = \sqrt{\frac{2f(\alpha)}{\tau}}\frac{\chi_\theta}{n}, \tag{8b}$$

where $f(\alpha) = 1-\alpha^2$ and $\alpha \in [0, 1/\sqrt{2}]$. The representation of Eq. (8) in Cartesian coordinates is discussed in Appendix A. The form of $f(\alpha)$ guarantees that the total noise strength remains constant

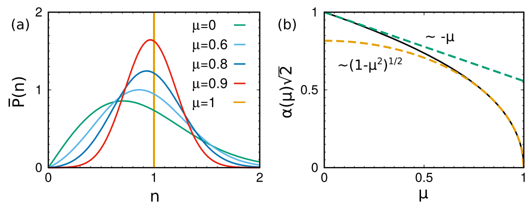

FIG. 2. Stationary solution for the self-propulsion vector $\mathbf{n}$ in the PAM. Panel (a): distribution $\bar{P}(n) = \int_0^{2\pi} d\theta P(n,\theta)$, given by Eq. (7), of the radial component $n = |\mathbf{n}|$ for different values of μ, interpolating between AOUP ($\mu = 0$) and ABP ($\mu = 1$). Panel (b): relation between the parameters α and μ, which guarantees that $\langle n^2\rangle = 1$, leaving the velocity scale v_0 invariant. Red and yellow dashed curves indicate the asymptotic solutions for $\mu \to 0$ and $\mu \to 1$, respectively, given by Eq. (9).

throughout all offsprings of the PAM, namely, $\alpha^2 + f(\alpha) = 1$. Fixing $\alpha = 1/\sqrt{2}$ and $\mu = 0$, the dynamics coincides with that of an AOUP [cf. Equation (5)]. For $\alpha = 0$ and $\mu = 1$, we obtain the ABP dynamics because the deterministic time evolution of n, Eq. (8a), admits the general solution $n(t) = 1 + (n(0)-1)\exp(-t/\tau)$ for $n(0) \neq 1$ and the special solution $n(t) \equiv 1$ for $n(0) = 1$. In fact, the latter initial condition, $n(0) = 1$, is the only physical choice (consistent with the requirement $\langle n^2\rangle = 1$ stated below). This implies that the normalized self-propulsion vector $\mathbf{n} = (\cos\theta, \sin\theta)$ of an ABP is recovered for every time t. Moreover, the dynamics, Eq. (8b), for the angle θ then reverts to Eq. (3).

While our general PAM contains the two parameters α and μ, it is sufficient to restrict the offspring to those models that give rise to the typical speed v_0 as a common scale of the self-propulsion velocity. To see this, we note that any process $\mathbf{n}$ with $\langle n^2\rangle = a$ can be rewritten as $\sqrt{a}\tilde{\mathbf{n}}$, where $\tilde{\mathbf{n}}$ has unit standard deviation, such that the case $a \neq 1$ would merely correspond to renormalizing v_0 in Eq. (1). Therefore, we can simply relate the modulus fluctuations α to the peak position μ by requiring $\langle n^2\rangle = 1$. The resulting relation $\alpha(\mu)$ (see Appendix B) leaves μ as the only free parameter of the PAM (at fixed v_0). Near the two limiting cases of the AOUP ($\mu \to 0$) and ABP ($\mu \to 1$), the relation $\alpha(\mu)$ simplifies and reads

$$\alpha \approx \begin{cases} \dfrac{1}{\sqrt{2}}\left(1-\dfrac{\sqrt{\pi}}{4}\mu\right), & \mu \to 0, \\ \sqrt{\dfrac{1-\mu^2}{3}}, & \mu \to 1. \end{cases} \tag{9}$$

In Fig. 2(b), we compare these simple representations to $\alpha(\mu)$, obtained by solving numerically $\langle n^2\rangle = 1$, and we find good agreement in the regimes $0 \le \mu \lesssim 0.3$ and $0.7 \lesssim \mu \le 1$. The resulting steady-state distributions are shown in Fig. 2(a) for different μ, interpolating between AOUPs (green curve) and ABPs (yellow curve); see also Fig. 1 for the representation in Cartesian coordinates.

Apart from the free parameter μ, which uniquely characterizes each descendant of the PAM for a given scale v_0 of the self-propulsion velocity, the whole family of models shares a common persistence time τ of the active motion and an equal dynamical

Published under an exclusive license by AIP Publishing

The Journal of Chemical Physics COMMUNICATION scitation.org/journal/jcp

correlation, given by Eq. (6). As a result, some basic dynamical properties for a potential-free particle are the same for each value of μ, such as the velocity autocorrelation function and the mean and mean-squared displacements, in accordance with the well-known results in the limiting cases of ABPs[70,71] and AOUPs.[18]

PAM IN HARMONIC CONFINEMENT

The main difference between ABPs and AOUPs occurs in the dynamics of the radial component of the active force. The consequences of that become highly relevant if the particle is subject to an additional, external potential. As a reference study, we confine the system via a harmonic trap so that the external force $\mathbf{F}(\mathbf{x}) = -k\mathbf{x}$ is exerted on the active particle. The curvature of the potential k introduces an additional time scale that is recast onto a dimensionless parameter $k\tau$ controlling the dynamics. In Fig. 3, we study the radial probability distribution, $\rho(r)$, and the reduced distribution in Cartesian coordinates, $p(x)$, projected onto the x axis for different values of μ and $k\tau$.

Before discussing the behavior of the generic PAM in detail, we provide further analytic insight into the extreme cases (calculations are reported in Appendixes C and D). As a Gaussian process, the AOUP gives rise to the exact solution,[42,69,72]

$$\rho(r) \sim \exp\left(-\frac{k\Gamma}{\left(D\Gamma + \frac{v_0^2\tau}{2}\right)}\frac{r^2}{2}\right), \tag{10}$$

where as usual, in AOUP systems, $\Gamma = 1 + k\tau$ plays the role of an effective friction coefficient.[73] Assuming large persistence, $k\tau \gg 1$, we further develop the analytical prediction

$$\rho(r) \sim r^{1/2} \exp\left(-\left(k + \frac{1}{2\tau}\right)\frac{1}{2D}\left(r - \frac{v_0}{k + \frac{1}{2\tau}}\right)^2\right) \tag{11}$$

for the ABP, which reflects the bimodality of the density distribution[58,74–78] (see also Refs. 57 and 79 for experimental studies) as a distinct feature compared to the Gaussian shape of the AOUP solution.

When the active force relaxes faster than the particle position such that $k\tau \ll 1$, the dynamical details of the active force in the generic PAM cannot affect the distribution, which is thus independent of μ, as shown in Figs. 3(a) and 3(d). In this regime, the

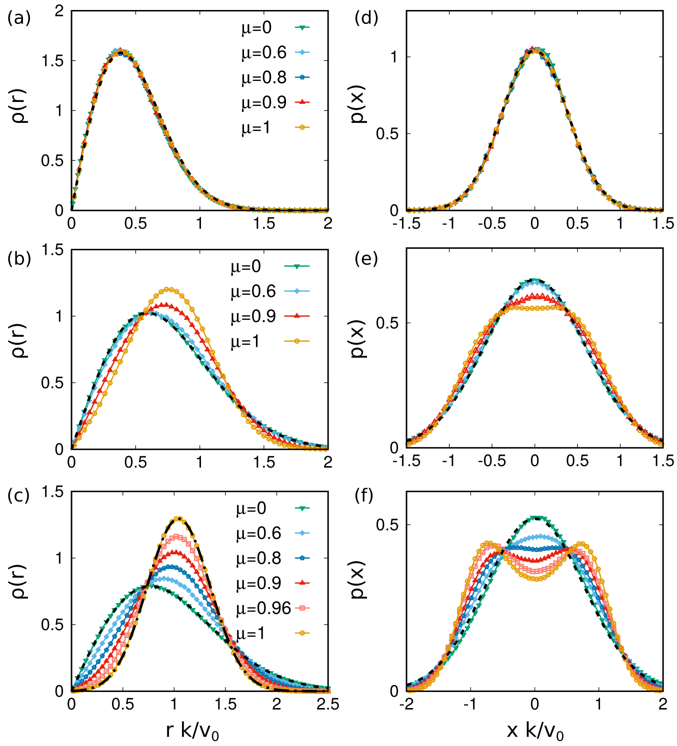

FIG. 3. Probability distribution of the active particle position in a harmonic external potential. Panels (a)–(c) show the radial density distribution $\rho(r)$ as a function of rk/v_0, while panels (d)–(f) plot the distribution (projected onto one axis) $p(x)$ as a function of xk/v_0. Panels (a) and (d) are obtained with $k\tau = 10^{-1}$, panels (b) and (e) with $k\tau = 1$, and finally, panels (c) and (f) with $k\tau = 10^2$. The black dashed lines in all the panels are obtained by Eq. (10), while the black dashed–dotted line in panel (c) by Eq. (11). Panels (a) and (d), (b) and (e), and (c) and (f) share the same legend.

The Journal of Chemical Physics COMMUNICATION scitation.org/journal/jcp

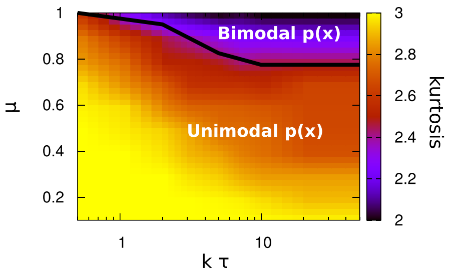

FIG. 4. Two-states phase diagram of the active harmonic oscillator by varying $k\tau$ and μ [and, thus, $\alpha(\mu)$ accordingly] distinguishing between the regions where the spatial distribution, $p(x)$, is unimodal and bimodal, as explicitly indicated in the graph. The two regions are separated by a black solid line, $\mu_c(\tau_c)$, tracked in correspondence with the first value of $k\tau$ such that $p(x)$ shows a bimodality: in practice, we fit the exponential of a fourth order polynomial $\exp(-ax^4 + bx^2 + c)$, identifying a point on the critical line $\mu_c(\tau_c)$ as the smaller value of μ (for each $k\tau$) such that $b < 0$. In addition, we plot the kurtosis of $p(x)$, namely, $\langle x^4\rangle/\langle x^2\rangle^2$, as a color gradient. We remark that the typical values of the kurtosis in correspondence with the transition line are between 2.3 and 2.5.

shape of $\rho(r)$ [or equivalently $p(x)$] coincides with the analytical AOUP result, Eq. (10) with $\Gamma \to 1$, for every μ. This approximation can be explicitly derived also in the opposite extreme case of ABPs (see Appendix D). This occurs because the active force behaves as a noise term, and thus, it only modifies the variance of $\rho(r)$ with respect to the passive case in the spirit of an effective temperature. In the intermediate persistence regime, $k\tau \sim 1$, Figs. 3(b) and 3(e) indicate that the density gradually departs from its Gaussian form, given by Eq. (10), when μ is increased: the position of the main peak of $\rho(r)$ shifts toward larger values of r while the shape $p(x)$ displays the onset of bimodality. These differences become most significant in the large persistence regime, $k\tau \gg 1$, where the ABP solution is well-represented by Eq. (11), roughly centered around $v_0/[k + 1/(2\tau)] \to v_0/k$ (for $k\tau \gg 1$). In addition, for smaller μ, the radial density $\rho(r)$ has a strongly non-Gaussian shape [see Fig. 3(c)]. We further show in Fig. 3(f) that for a large persistence, even a small increase of μ induces drastic changes in the shape of $p(x)$, eventually inducing a unimodal $\to$ bimodal transition.

In Fig. 4, such a transition is depicted through a phase diagram as a function of μ and $k\tau$, distinguishing between unimodal and bimodal configurations and showing the kurtosis of $p(x)$ as a color gradient. For small values of μ, the distribution $p(x)$ is unimodal (region 1) independently of $k\tau$. Starting from $\mu = 0$ (AOUP model), which is Gaussian, the increase of μ induces non-Gaussianity in the shape of $p(x)$, which reflects onto the decrease in the kurtosis to values smaller than 3. However, while for small values of $k\tau$, $p(x)$ still remains unimodal upon increasing μ [compare Fig. 3(d)], a transition toward a bimodal distribution, which is characterized by kurtosis values ~2, takes place (region 2) as soon as $k\tau \sim 1$. The corresponding critical curve $\mu_c(\tau_c)$ (black line in Fig. 4) decreases when $k\tau$ is increased until reaching a plateau for $k\tau \gg 1$. This is consistent with Eq. (10) and Eq. (11) in which $\rho(r)$ does not depend on $k\tau$ for $k\tau \gg 1$. In general, the fluctuation of the modulus n of the self-propulsion vector inhibits the ability of the active particle to stay far from the potential minimum, even in the harmonic oscillator case.

CONCLUSIONS

We developed a unifying parental active model (PAM) for the stochastic dynamics of active particles. This PAM shows that the established ABPs and AOUPs descriptions stand on an equal level as being sisters rather than cousins. The family of explored models shares defining properties of active matter, such as the exponential dynamical correlations on the scale of the persistence time τ and the common velocity scale v_0. The only differences lie in the modulus distributions of the self-propulsion velocity, which can be continuously transferred from a Gaussian form (AOUP) to a sharp peak (ABP) by sweeping a single parameter. As a benchmark study, we examined the stationary distribution in a harmonic potential and mapped out the transition between unimodal and bimodal, which marks the classical "failure" of AOUPs to reproduce the behavior of ABPs in the large-persistence regime.

For the purpose of realistic modeling, however, both AOUPs and ABPs are idealized. This is because a perfectly constant modulus of the self-propulsion velocity is highly unlikely due to the individual nature of biological agents and various types of fluctuations. Bacteria, for example, can display fairly broad[80,81] or even bimodal[82,83] speed distributions. In addition, macroscopic agents, such as locusts,[84] whirligig beetles,[85] or zebrafish,[14,86,87] exhibit natural speed fluctuations. To realistically describe these systems, a theoretical approach should incorporate both fluctuations of the modulus and the direction of the self-propulsion velocity.[86–92] For this purpose, our description within the PAM is particularly convenient because it is based on a single stochastic process $\mathbf{n}$ of unit standard deviation (i.e., v_0 is treated as a velocity scale and does not fluctuate itself) such that all descendant models with an intermediate value of the parameter μ can be evaluated with the same numerical effort as ABPs and AOUPs.

The family of models can be systematically extended by realizing that the PAM merely gives rise to more diversity in the stationary properties of the underlying stochastic process, while the autocorrelation (6) of the self-propulsion velocity remains equal for all offsprings. Another common model of active particles involves the run and tumble motion[93–96] where the autocorrelation is a step function because after running for a straight path, the particle instantaneously changes the direction of its active velocity after a typical tumbling rate. In our line of reasoning, this particular shape (at the same persistence time scale τ related to the inverse of the tumbling rate) of the dynamical autocorrelation function could be viewed as, say, a different gender. In practice, the notion of run-and-tumble-like dynamics can be easily combined with our PAM by drawing after each tumbling event the new direction and modulus of the self-propulsion vector according to the stationary distribution in Eq. (7).

In conclusion, the PAM both unifies ABPs and AOUPs and provides a crucial step toward more realistic modeling of overdamped (dry) active motion, in general, which should in future work be employed to provide an improved fit of experimental swim-velocity distributions. Investigating the effect of the swim-velocity fluctuations could represent an interesting perspective for circle swimming,[97–102] systems with spatial-dependent swim

Published under an exclusive license by AIP Publishing

The Journal of Chemical Physics COMMUNICATION scitation.org/journal/jcp

velocity,[103–108] and inertial dynamics[109–113] even affecting the orientational degrees of freedom.[114,115] The generalization of PAM to these cases could be responsible for new intriguing phenomena, which will be investigated in future works.

ACKNOWLEDGMENTS

We thank Alexandra Zampetaki for helpful discussions. L.C. acknowledges support from the Alexander von Humboldt Foundation. H.L. and R.W. acknowledge support from the Deutsche Forschungsgemeinschaft (DFG) through SPP 2265 under Grant Nos. LO 418/25-1 (H.L.) and WI5527/1-1 (R.W.).

AUTHOR DECLARATIONS

Conflict of Interest

The authors have no conflicts of interest to disclose.

DATA AVAILABILITY

The data that support the findings of this study are available from the corresponding author upon reasonable request.

APPENDIX A: PAM DYNAMICS IN CARTESIAN COORDINATES

In this appendix, we report the expression for the PAM dynamics in Cartesian coordinates. Applying Itô calculus, we obtain

$$\begin{aligned}\dot{\mathbf{n}} = &-\frac{1}{\tau}\left(\mathbf{n}-\mu\frac{\mathbf{n}}{n}\right)+\frac{\mathbf{n}}{n^2}\frac{1}{\tau}\left(\alpha^2-f(\alpha)\right)\\ &+\sqrt{\frac{2\alpha^2}{\tau}}\frac{\mathbf{n}}{n}\chi_n+\sqrt{\frac{2f(\alpha)}{\tau}}\boldsymbol{R}\cdot\frac{\mathbf{n}}{n}\chi_\theta\end{aligned} \tag{A1}$$

with $\boldsymbol{R}$ denoting the rotational matrix of 90°. Alternatively, the last term can be expressed in a more familiar form

$$\boldsymbol{R}\cdot\frac{\mathbf{n}}{n}\chi_\theta=\frac{\mathbf{n}}{n}\times\hat{z}\chi_\theta \tag{A2}$$

in terms of the cross product. By setting $\mu = 0$ and $\alpha = 1/\sqrt{2}$ in Eq. (A1), we recover the AOUP model. Indeed, only the term $-\mathbf{n}/\tau$ survives on the first line, while the noise terms in the second line reduce to a vector of white noise because any orthogonal transformation applied on a vector of white noises is still a vector of white noise. Instead, by setting $\mu = 1$ and $\alpha = 0$ in Eq. (A1), only the term $-\mathbf{n}/\tau$ survives on the first line because $n^2 = n = 1$ and only the second noise survives on the second line so that we obtain the ABP equation (Itô integration)

$$\dot{\mathbf{n}} = -D_r\mathbf{n}+\sqrt{2D_r}\mathbf{n}\times\mathbf{z}\,\xi \tag{A3}$$

in Cartesian coordinates, where $\mathbf{z} = (0, 0, 1)$.

APPENDIX B: OBEYING THE UNIT-VARIANCE CONDITION

In this appendix, we give the analytic expression of the second moment $\langle n^2\rangle$ of the PAM distribution [see Eq. (7)] needed to impose the constraint $\langle n^2\rangle = 1$ dictated by the given velocity scale v_0. After algebraic manipulations, we get

$$\langle n^2\rangle = 3\alpha^2+\mu^2-\mathcal{N}\alpha^4 e^{-\frac{\mu^2}{2\alpha^2}}, \tag{B1}$$

where $\mathcal{N}$ is the normalization constant of the distribution (7), which explicitly reads

$$\mathcal{N}^{-1} = \frac{\alpha^2}{2}\frac{\mu}{\sqrt{2}\alpha}\left(4\sqrt{\pi}+\Gamma\left(-\frac{1}{2},\frac{\mu^2}{2\alpha^2}\right)\right). \tag{B2}$$

Here, $\Gamma(s, x)$ denotes the upper incomplete gamma function. The condition requiring $\langle n^2\rangle = 1$ follows as

$$3\alpha^2+\mu^2-\mathcal{N}\alpha^4 e^{-\frac{\mu^2}{2\alpha^2}} = 1, \tag{B3}$$

which is solved for $\alpha(\mu)$ in Fig. 2 and yields the asymptotic solutions near the two limiting cases of the AOUP ($\mu \to 0$) and ABP ($\mu \to 1$) models, given by Eq. (9).

APPENDIX C: AOUP IN A HARMONIC POTENTIAL

Here, we provide the solution of Eq. (1) with the external force $\mathbf{F}(\mathbf{x}) = -k\mathbf{x}$. In the AOUP case (or the PAM with $\mu = 0$ and thus $\alpha = 1/\sqrt{2}$), the dynamics can be solved exactly because of its linearity. The whole solution for the probability distribution $\mathcal{P}(\mathbf{x},\mathbf{n})$ reads

$$\begin{aligned}\mathcal{P}(\mathbf{x},\mathbf{n}) = &\,\mathcal{N}\exp\left(-\frac{\Gamma k}{\Gamma D+\frac{v_0^2\tau}{2}}\frac{r^2}{2}\right)\\ &\times\exp\left(-\frac{\Gamma}{v_0^2}\left(\mathbf{n}-\frac{k}{2}\frac{\Gamma v_0^2\tau}{\left(\frac{v_0^2\tau}{2}+D\right)}\mathbf{x}\right)\right),\end{aligned} \tag{C1}$$

where $r^2 = x^2 + y^2$ in two spatial dimensions. By integrating out the self-propulsion vector $\mathbf{n}$ and switching to polar coordinates, we easily obtain the expression for the radial probability distribution, $\rho(r)$, which reads

$$\rho(r) = \mathcal{N}\exp\left(-\frac{k\Gamma}{\left(D\Gamma+\frac{v_0^2\tau}{2}\right)}\frac{r^2}{2}\right), \tag{C2}$$

where Γ plays the role of an effective friction coefficient and reads

$$\Gamma = 1 + k\tau, \tag{C3}$$

as stated in Eq. (10) of the main text. From Eq. (C2), we can identify an effective temperature, say the variance of the distribution, as

$$T_{\text{eff}} = \left(D+\frac{v_0^2\tau}{2\Gamma}\right). \tag{C4}$$

APPENDIX D: ABP IN A HARMONIC POTENTIAL

To get analytical results in the case of an ABP (or the PAM with $\mu = 1$ and thus $\alpha = 0$) in a harmonic trap, it is convenient to express the positional dynamics (1) in polar coordinates, $(x, y) \to (r, \phi)$, such that $r = \sqrt{x^2+y^2}$ and $\phi = \operatorname{atan}\frac{y}{x}$. Applying Itô calculus to the

Published under an exclusive license by AIP Publishing

The Journal of Chemical Physics COMMUNICATION scitation.org/journal/jcp

dynamics (1) of the main text to perform the change in variables, we get

$$\dot{r} = -k\,r + \frac{D}{r} + v_0\,\cos(\theta - \phi) + \sqrt{2D}w_r, \tag{D1a}$$

$$\dot{\phi} = v_0\frac{\sin(\theta - \phi)}{r} + \frac{\sqrt{2D}}{r}\sqrt{2D}w_\phi, \tag{D1b}$$

where the orientation θ of the (normalized) self-propulsion vector $\mathbf{n}$ evolves according to Eq. (3). From here, the Fokker–Planck equation for the probability distribution, $p = p(r, \phi, \theta)$, reads

$$\begin{aligned}\partial_t p = \partial_r\left[k\,r - \frac{D}{r} - v_0\,\cos(\theta - \phi) + D\partial_r\right]p \\ + \partial_\phi\left[\frac{D}{r^2}\partial_\phi - \frac{v_0}{r}\sin(\theta - \phi)\right]p + \frac{1}{\tau}\partial_\theta^2 p.\end{aligned} \tag{D2}$$

Separating angular and radial currents in Eq. (D2) allows us to find approximated solutions for the conditional angular probability distribution $f(\theta - \phi|r)$ (i.e., the angular probability distribution at the fixed radial position r), which we will use later to estimate the radial density distribution $\rho(r)$. In other words, by setting the second line in Eq. (D2) equal to zero, we obtain

$$f(\theta - \phi|r) = \mathcal{N}e^{a\,\cos(\theta-\phi)}, \tag{D3}$$

where a reads

$$a = \frac{v_0}{D}\frac{r}{\left(1 + \frac{r^2}{D\tau}\right)}. \tag{D4}$$

In the small persistence regime, $k\tau \ll 1$, this distribution converges to a flat profile because $a \to 0$ vanishes. This reflects the fact that both θ and ϕ are uniformly distributed and, thus, also their difference. Instead, in the large persistence regime, Eq. (D3) is peaked around $\phi \sim \theta$ and its variance becomes smaller as $k\tau$ is increased.

As a first step to finding an approximation for $\rho(r)$, we now calculate the average

$$\langle\cos(\theta - \phi)\rangle = \frac{I_1(a)}{I_0(a)} \tag{D5}$$

with respect to the conditional angular distribution, Eq. (D3), where $I_0(a)$ and $I_1(a)$ are the modified Bessel functions of the first kind of order 0 and 1, respectively. With this result, we can achieve the derivation starting directly from Eq. (D2). First, we assume the zero-current condition for the radial current, namely, we set to zero the first line in Eq. (D2). Then, we replace $\cos(\theta - \phi) \to \langle\cos(\theta - \phi)\rangle$, where we approximate the result from Eq. (D5) in two different regimes.

Small-persistence regime

In the small persistence regime such that $k\tau \ll 1$, we have $a \ll 1$ and we can approximate

$$\langle\cos(\theta - \phi)\rangle = \frac{I_1(a)}{I_0(a)} \approx \frac{a}{2} = \frac{1}{2}\frac{v_0}{D}\frac{r}{\left(1 + \frac{r^2}{D\tau}\right)}. \tag{D6}$$

The small persistence time regime further allows us to replace $r^2 \to \langle r^2\rangle = \frac{1}{k}\left(D + \frac{v_0^2\tau}{2}\right)$ in Eq. (D6). The expression for $\langle r^2\rangle$ is achieved by recalling that the active particle in the small persistence regime is subject to the effective temperature $D + v_0^2\tau/2$, a result holding for a general potential. From here, the zero-current condition in Eq. (D2) leads to the equation

$$\left[k^* r - \frac{D}{r} + D\frac{\partial}{\partial r}\right]\rho(r) = 0 \tag{D7}$$

for $\rho(r)$, where

$$k^* = k + \frac{v_0^2}{D + \frac{1}{k\tau}\left(D + \frac{v_0^2\tau}{2}\right)}. \tag{D8}$$

This equation can be easily solved to obtain an expression for $\rho(r)$ that after algebraic manipulation reads

$$\rho(r) = \mathcal{N}\exp\left(-\frac{k\Gamma}{\left(D\Gamma + \frac{v_0^2\tau}{2}\right)}\frac{r^2}{2}\right), \tag{D9}$$

where $\Gamma = 1 + k\tau \to 1$ is defined according to Eq. (C3). This distribution coincides with the AOUP one (C2).

We observe that in the limit of very small τ, the above result (D9) coincides with that obtained in the passive limit, which can be achieved by setting $v_0 \to 0$. In this case, we have $a \to 0$ and thus $\langle\cos(\theta - \phi)\rangle = 0$ in Eq. (D2) (and the same for the sinus) because θ is uniformly distributed between 0 and 2π. Therefore, Eq. (D1) simply converges onto the equation of a passive particle holding for $v_0^2\tau \ll D$. We further remark that our result is consistent with that obtained by the hydrodynamic approach holding in the case of ABP in the regime of small τ, which allows us to recover Eq. (D9) with $\Gamma \to 1$.

Large-persistence regime

In the large persistence case, $k\tau \gg 1$, the self-propulsion relaxes much slower than the position distribution. In addition, in this case, we can adopt the same strategy used in the small persistence regime with the crucial difference that now we have $a \gg 1$ so that we can approximate Eq. (D5) as

$$\langle\cos(\theta - \phi)\rangle = \frac{I_1(a)}{I_0(a)} \approx 1 - \frac{1}{2a} = 1 - \frac{1}{2}\frac{r}{v_0}\left(\frac{D}{r^2} + \frac{1}{\tau}\right). \tag{D10}$$

Plugging this result into Eq. (D2) and using the zero-current condition allow us to find the equation for the radial density, $\rho(r)$, which reads

$$\left[r\left(k + \frac{1}{2\tau}\right) - \frac{D}{r^{1/2}} - v_0 + D\frac{\partial}{\partial r}\right]\rho(r) = 0 \tag{D11}$$

and whose solution can be explicitly obtained,

$$\rho(r) = \mathcal{N}r^{1/2}\exp\left(-\left(k + \frac{1}{2\tau}\right)\frac{1}{2D}\left(r - \frac{v_0}{k + \frac{1}{2\tau}}\right)^2\right). \tag{D12}$$

Here, the result is fairly different from the Gaussian distribution (C2) obtained in the case of AOUP dynamics. The profile (D12) is

Published under an exclusive license by AIP Publishing

The Journal of Chemical Physics COMMUNICATION scitation.org/journal/jcp

well-approximated by a Gaussian centered at $r = v_0/(k + 1/2\tau)$ with variance $D/(k + 1/2\tau)$.

Note that the result (D12) is almost consistent with that obtained in Ref. 69 in the limit $\tau \to \infty$. However, with respect to Ref. 69, here, we improve the approximation for the angular distribution that leads to a prefactor $r^{1/2}$ (instead of simply r), which is in better agreement with the data. To establish a closer relation to this result, we remark that in the large persistence regime, the angular distribution (D3) derived here can be further approximated by a Gaussian

$$f(\theta - \phi|r) = \mathcal{N}e^{-\frac{a}{2}(\theta-\phi)^2} \tag{D13}$$

after expanding the cosine around $\theta \sim \phi$. The expression for $\rho(r)$ resulting from this approximation is then consistent with the previous prediction[69] in the large persistence regime.

REFERENCES

[1] C. Bechinger, R. Di Leonardo, H. Löwen, C. Reichhardt, G. Volpe, and G. Volpe, Rev. Mod. Phys. **88**, 045006 (2016).
[2] M. C. Marchetti, J. F. Joanny, S. Ramaswamy, T. B. Liverpool, J. Prost, M. Rao, and R. A. Simha, Rev. Mod. Phys. **85**, 1143 (2013).
[3] J. Elgeti, R. G. Winkler, and G. Gompper, Rep. Prog. Phys. **78**, 056601 (2015).
[4] J. Arlt, V. A. Martinez, A. Dawson, T. Pilizota, and W. C. K. Poon, Nat. Commun. **9**, 768 (2018).
[5] G. Frangipane, D. Dell'Arciprete, S. Petracchini, C. Maggi, F. Saglimbeni, S. Bianchi, G. Vizsnyiczai, M. L. Bernardini, and R. Di Leonardo, Elife **7**, e36608 (2018).
[6] J. Yan, M. Han, J. Zhang, C. Xu, E. Luijten, and S. Granick, Nat. Mater. **15**, 1095 (2016).
[7] S. Ni, E. Marini, I. Buttinoni, H. Wolf, and L. Isa, Soft Matter **13**, 4252 (2017).
[8] M. Driscoll, B. Delmotte, M. Youssef, S. Sacanna, A. Donev, and P. Chaikin, Nat. Phys. **13**, 375 (2017).
[9] F. Ginot, I. Theurkauff, F. Detcheverry, C. Ybert, and C. Cottin-Bizonne, Nat. Commun. **9**, 696 (2018).
[10] U. Khadka, V. Holubec, H. Yang, and F. Cichos, Nat. Commun. **9**, 3864 (2018).
[11] R. L. Stoop and P. Tierno, Commun. Phys. **1**, 68 (2018).
[12] R. Alert and X. Trepat, Annu. Rev. Condens. Matter Phys. **11**, 77 (2020).
[13] I. D. Couzin, J. Krause, R. James, G. D. Ruxton, and N. R. Franks, J. Theor. Biol. **218**, 1 (2002).
[14] A. V. Zampetaki, B. Liebchen, A. V. Ivlev, and H. Löwen, Proc. Natl. Acad. Sci. U. S. A. **118**, e2111142118 (2021).
[15] A. Cavagna, I. Giardina, and T. S. Grigera, Phys. Rep. **728**, 1 (2018).
[16] A. Perna, G. Grégoire, and R. P. Mann, Mov. Ecol. **2**, 22 (2014).
[17] G. Gompper, R. G. Winkler, T. Speck, A. Solon, C. Nardini, F. Peruani, H. Löwen, R. Golestanian, U. B. Kaupp, L. Alvarez *et al.*, J. Phys.: Condens. Matter **32**, 193001 (2020).
[18] É. Fodor and M. Cristina Marchetti, Physica A **504**, 106 (2018).
[19] J. O'Byrne, Y. Kafri, J. Tailleur, and F. van Wijland, Nat. Rev. Phys. (published online 2022).
[20] I. Buttinoni, J. Bialké, F. Kümmel, H. Löwen, C. Bechinger, and T. Speck, Phys. Rev. Lett. **110**, 238301 (2013).
[21] Y. Fily and M. C. Marchetti, Phys. Rev. Lett. **108**, 235702 (2012).
[22] J. Stenhammar, D. Marenduzzo, R. J. Allen, and M. E. Cates, Soft Matter **10**, 1489 (2014).
[23] J. Bialké, J. T. Siebert, H. Löwen, and T. Speck, Phys. Rev. Lett. **115**, 098301 (2015).
[24] A. P. Solon, J. Stenhammar, R. Wittkowski, M. Kardar, Y. Kafri, M. E. Cates, and J. Tailleur, Phys. Rev. Lett. **114**, 198301 (2015).
[25] I. Petrelli, P. Digregorio, L. F. Cugliandolo, G. Gonnella, and A. Suma, Eur. Phys. J. E **41**, 128 (2018).
[26] L. Caprini, U. M. B. Marconi, C. Maggi, M. Paoluzzi, and A. Puglisi, Phys. Rev. Res. **2**, 023321 (2020).
[27] L. Caprini, U. Marini Bettolo Marconi, A. Puglisi, and A. Vulpiani, J. Chem. Phys. **150**, 024902 (2019).
[28] L. Dabelow, S. Bo, and R. Eichhorn, Phys. Rev. X **9**, 021009 (2019).
[29] L. Berthier, E. Flenner, and G. Szamel, J. Chem. Phys. **150**, 200901 (2019).
[30] R. Wittmann, J. M. Brader, A. Sharma, and U. M. B. Marconi, Phys. Rev. E **97**, 012601 (2018).
[31] Y. Fily, J. Chem. Phys. **150**, 174906 (2019).
[32] D. Mandal, K. Klymko, and M. R. DeWeese, Phys. Rev. Lett. **119**, 258001 (2017).
[33] É. Fodor, C. Nardini, M. E. Cates, J. Tailleur, P. Visco, and F. van Wijland, Phys. Rev. Lett. **117**, 038103 (2016).
[34] D. Martin, J. O'Byrne, M. E. Cates, É. Fodor, C. Nardini, J. Tailleur, and F. van Wijland, Phys. Rev. E **103**, 032607 (2021).
[35] C. Maggi, U. M. B. Marconi, N. Gnan, and R. Di Leonardo, Sci. Rep. **5**, 10742 (2015).
[36] G. Szamel, Phys. Rev. E **90**, 012111 (2014).
[37] C. Maggi, M. Paoluzzi, N. Pellicciotta, A. Lepore, L. Angelani, and R. Di Leonardo, Phys. Rev. Lett. **113**, 238303 (2014).
[38] C. Maggi, M. Paoluzzi, L. Angelani, and R. Di Leonardo, Sci. Rep. **7**, 17588 (2017).
[39] S. Chaki and R. Chakrabarti, Physica A **530**, 121574 (2019).
[40] K. Goswami, Physica A **566**, 125609 (2021).
[41] L. Caprini and U. Marini Bettolo Marconi, Soft Matter **14**, 9044 (2018).
[42] S. Das, G. Gompper, and R. G. Winkler, New J. Phys. **20**, 015001 (2018).
[43] L. Caprini and U. Marini Bettolo Marconi, Soft Matter **15**, 2627 (2019).
[44] J. Palacci, S. Sacanna, A. P. Steinberg, D. J. Pine, and P. M. Chaikin, Science **339**, 936 (2013).
[45] B. M. Mognetti, A. Šarić, S. Angioletti-Uberti, A. Cacciuto, C. Valeriani, and D. Frenkel, Phys. Rev. Lett. **111**, 245702 (2013).
[46] S. Paliwal, J. Rodenburg, R. van Roij, and M. Dijkstra, New J. Phys. **20**, 015003 (2018).
[47] M. N. Van Der Linden, L. C. Alexander, D. G. A. L. Aarts, and O. Dauchot, Phys. Rev. Lett. **123**, 098001 (2019).
[48] X.-q. Shi, G. Fausti, H. Chaté, C. Nardini, and A. Solon, Phys. Rev. Lett. **125**, 168001 (2020).
[49] F. Turci and N. B. Wilding, Phys. Rev. Lett. **126**, 038002 (2021).
[50] L. Caprini, U. M. B. Marconi, and A. Puglisi, Phys. Rev. Lett. **124**, 078001 (2020).
[51] C. Maggi, M. Paoluzzi, A. Crisanti, E. Zaccarelli, and N. Gnan, Soft Matter **17**, 3807 (2021).
[52] G. Szamel and E. Flenner, Europhys. Lett. **133**, 60002 (2021).
[53] L. Caprini and U. M. B. Marconi, Phys. Rev. Res. **2**, 033518 (2020).
[54] L. Caprini and U. Marini Bettolo Marconi, Soft Matter **17**, 4109 (2021).
[55] G. Szamel, E. Flenner, and L. Berthier, Phys. Rev. E **91**, 062304 (2015).
[56] E. Flenner, G. Szamel, and L. Berthier, Soft Matter **12**, 7136 (2016).
[57] S. C. Takatori, R. De Dier, J. Vermant, and J. F. Brady, Nat. Commun. **7**, 10694 (2016).
[58] K. Malakar, A. Das, A. Kundu, K. V. Kumar, and A. Dhar, Phys. Rev. E **101**, 022610 (2020).
[59] W. Yan and J. F. Brady, J. Fluid Mech. **785**, R1 (2015).
[60] Y. Fily, A. Baskaran, and M. F. Hagan, Eur. Phys. J. E **40**, 61 (2017).
[61] R. Wittmann, F. Smallenburg, and J. M. Brader, J. Chem. Phys. **150**, 174908 (2019).
[62] L. Caprini and U. Marini Bettolo Marconi, J. Chem. Phys. **154**, 024902 (2021).
[63] G. H. P. Nguyen, R. Wittmann, and H. Löwen, J. Phys.: Condens. Matter **34**, 035101 (2021).
[64] T. F. F. Farage, P. Krinninger, and J. M. Brader, Phys. Rev. E **91**, 042310 (2015).
[65] U. Marini Bettolo Marconi, C. Maggi, and S. Melchionna, Soft Matter **12**, 5727 (2016).
[66] U. M. B. Marconi, N. Gnan, M. Paoluzzi, C. Maggi, and R. Di Leonardo, Sci. Rep. **6**, 23297 (2016).
[67] R. Wittmann and J. M. Brader, Europhys. Lett. **114**, 68004 (2016).

Published under an exclusive license by AIP Publishing

The Journal of Chemical Physics COMMUNICATION scitation.org/journal/jcp

[68] R. Wittmann, C. Maggi, A. Sharma, A. Scacchi, J. M. Brader, and U. Marini Bettolo Marconi, J. Stat. Mech.: Theory Exp. **2017**, 113207.
[69] L. Caprini, E. Hernández-García, C. López, and U. Marini Bettolo Marconi, Sci. Rep. **9**, 16687 (2019).
[70] B. ten Hagen, S. van Teeffelen, and H. Löwen, J. Phys.: Condens. Matter **23**, 194119 (2011).
[71] F. J. Sevilla and M. Sandoval, Phys. Rev. E **91**, 052150 (2015).
[72] L. Dabelow, S. Bo, and R. Eichhorn, J. Stat. Mech.: Theory Exp. **2021**, 033216.
[73] L. Caprini, U. Marini Bettolo Marconi, and A. Puglisi, Sci. Rep. **9**, 1386 (2019).
[74] A. Pototsky and H. Stark, Europhys. Lett. **98**, 50004 (2012).
[75] M. Hennes, K. Wolff, and H. Stark, Phys. Rev. Lett. **112**, 238104 (2014).
[76] S. Rana, M. Samsuzzaman, and A. Saha, Soft Matter **15**, 8865 (2019).
[77] U. Basu, S. N. Majumdar, A. Rosso, and G. Schehr, Phys. Rev. E **100**, 062116 (2019).
[78] I. Santra, U. Basu, and S. Sabhapandit, Soft Matter **17**, 10108 (2021).
[79] O. Dauchot and V. Démery, Phys. Rev. Lett. **122**, 068002 (2019).
[80] Y. Wu, A. D. Kaiser, Y. Jiang, and M. S. Alber, Proc. Natl. Acad. Sci. U. S. A. **106**, 1222 (2009).
[81] M. Theves, J. Taktikos, V. Zaburdaev, H. Stark, and C. Beta, Biophys. J. **105**, 1915 (2013).
[82] E. Perez Ipiña, S. Otte, R. Pontier-Bres, D. Czerucka, and F. Peruani, Nat. Phys. **15**, 610 (2019).
[83] S. Otte, E. P. Ipiña, R. Pontier-Bres, D. Czerucka, and F. Peruani, Nat. Commun. **12**, 1990 (2021).
[84] S. Bazazi, P. Romanczuk, S. Thomas, L. Schimansky-Geier, J. J. Hale, G. A. Miller, G. A. Sword, S. J. Simpson, and I. D. Couzin, Proc. R. Soc. B **278**, 356 (2011).
[85] H. L. Devereux, C. R. Twomey, M. S. Turner, and S. Thutupalli, J. R. Soc., Interface **18**, 20210114 (2021).
[86] V. Mwaffo, S. Butail, and M. Porfiri, Sci. Rep. **7**, 39877 (2017).
[87] D. A. Burbano-L and M. Porfiri, J. Theor. Biol. **485**, 110054 (2020).
[88] F. Peruani and L. G. Morelli, Phys. Rev. Lett. **99**, 010602 (2007).
[89] P. Romanczuk and L. Schimansky-Geier, Phys. Rev. Lett. **106**, 230601 (2011).
[90] D. Breoni, M. Schmiedeberg, and H. Löwen, Phys. Rev. E **102**, 062604 (2020).
[91] A. Shee and D. Chaudhuri, arXiv:2112.13415v1 (2021).
[92] A. Ghosh and A. J. Spakowitz, Phys. Rev. E **105**, 014415 (2022).
[93] J. Tailleur and M. E. Cates, Phys. Rev. Lett. **100**, 218103 (2008).
[94] A. P. Solon, M. E. Cates, and J. Tailleur, Eur. Phys. J.: Spec. Top. **224**, 1231 (2015).
[95] L. Angelani, J. Phys. A: Math. Theor. **50**, 325601 (2017).
[96] G. Gradenigo and S. N. Majumdar, J. Stat. Mech.: Theory Exp. **2019**, 053206.
[97] F. Kümmel, B. Ten Hagen, R. Wittkowski, I. Buttinoni, R. Eichhorn, G. Volpe, H. Löwen, and C. Bechinger, Phys. Rev. Lett. **110**, 198302 (2013).
[98] H. Löwen, Eur. Phys. J.: Spec. Top. **225**, 2319 (2016).
[99] D. Banerjee, A. Souslov, A. G. Abanov, and V. Vitelli, Nat. Commun. **8**, 1573 (2017).
[100] C. Kurzthaler and T. Franosch, Soft Matter **13**, 6396 (2017).
[101] G.-J. Liao and S. H. L. Klapp, Soft Matter **14**, 7873 (2018).
[102] C. Reichhardt and C. J. O. Reichhardt, J. Chem. Phys. **150**, 064905 (2019).
[103] C. Lozano, B. Ten Hagen, H. Löwen, and C. Bechinger, Nat. Commun. **7**, 12828 (2016).
[104] J. Stenhammar, R. Wittkowski, D. Marenduzzo, and M. E. Cates, Sci. Adv. **2**, e1501850 (2016).
[105] A. Sharma and J. M. Brader, Phys. Rev. E **96**, 032604 (2017).
[106] G. Vizsnyiczai, G. Frangipane, C. Maggi, F. Saglimbeni, S. Bianchi, and R. Di Leonardo, Nat. Commun. **8**, 15974 (2017).
[107] N. A. Söker, S. Auschra, V. Holubec, K. Kroy, and F. Cichos, Phys. Rev. Lett. **126**, 228001 (2021).
[108] L. Caprini, U. M. B. Marconi, R. Wittmann, and H. Löwen, Soft Matter (published online 2021).
[109] S. C. Takatori and J. F. Brady, Phys. Rev. Fluids **2**, 094305 (2017).
[110] H. Löwen, J. Chem. Phys. **152**, 040901 (2020).
[111] L. L. Gutierrez-Martinez and M. Sandoval, J. Chem. Phys. **153**, 044906 (2020).
[112] C. Dai, I. R. Bruss, and S. C. Glotzer, Soft Matter **16**, 2847 (2020).
[113] J. Su, H. Jiang, and Z. Hou, New J. Phys. **23**, 013005 (2021).
[114] C. Scholz, S. Jahanshahi, A. Ldov, and H. Löwen, Nat. Commun. **9**, 5156 (2018).
[115] A. R. Sprenger, S. Jahanshahi, A. V. Ivlev, and H. Löwen, Phys. Rev. E **103**, 042601 (2021).

Published under an exclusive license by AIP Publishing

P7 Dynamics of active particles with translational and rotational inertia

The following manuscript was submitted to a peer-reviewed scientific journal and is currently under review. Reproduced from

A. R. Sprenger, L. Caprini, H. Löwen, and R. Wittmann,
Dynamics of active particles with translational and rotational inertia,
(under review) (2023) [294].

Digital Object Identifier (DOI): doi.org/10.48550/arXiv.2301.01865

Statement of contribution

A.R.S. developed the theoretical results and prepared the figures. A.R.S., L.C., and R.W. wrote the manuscript. All authors discussed the results, edited the text, and finalized the manuscript.

Copyright and license notice

©The Author(s), 2023.
This is an Open Access article, distributed under the terms of the Creative Commons Attribution licence (http://creativecommons.org/licenses/by/4.0/), which permits unrestricted re-use, distribution, and reproduction in any medium, provided the original work is properly cited

Dynamics of active particles with translational and rotational inertia

Alexander R. Sprenger,[1,2,*] Lorenzo Caprini,[1,†] Hartmut Löwen,[1] and René Wittmann[1]

[1] *Institut für Theoretische Physik II: Weiche Materie, Heinrich-Heine-Universität Düsseldorf, D-40225 Düsseldorf, Germany*
[2] *Institut für Physik, Otto-von-Guericke-Universität Magdeburg, Universitätsplatz 2, D-39106 Magdeburg, Germany*

Inertial effects affecting both the translational and rotational dynamics are inherent to a broad range of active systems at the macroscopic scale. Thus, there is a pivotal need for proper models in the framework of active matter to correctly reproduce experimental results, hopefully achieving theoretical insights. For this purpose, we propose an inertial version of the active Ornstein-Uhlenbeck particle (AOUP) model accounting for particle mass (translational inertia) as well as its moment of inertia (rotational inertia) and derive the full expression for its steady-state properties. The inertial AOUP dynamics introduced in this paper is designed to capture the basic features of the well-established inertial active Brownian particle (ABP) model, i.e., the persistence time of the active motion and the long-time diffusion coefficient. For a small or moderate rotational inertia, these two models predict similar dynamics at all timescales and, in general, our inertial AOUP model consistently yields the same trend upon changing the moment of inertia for various dynamical correlation functions.

I. INTRODUCTION

Active motion can be observed at both microscopic and macroscopic scales [1–3], with typical examples ranging from birds, fish and insects to colloids and bacteria or cell monolayers. A common feature of such active systems is the capability to convert energy from the environment to produce directed motion [3, 4], which allows them to swim, move or fly in their environment. As a consequence, their dynamics qualitatively differs from that of "passive" Brownian particles, originally introduced to describe the random motion of pollen grains in water solution [5] and extensively employed to model colloidal particles. While the (overdamped) passive motion of passive colloids is characterized by random (Brownian) trajectories, showing a pure diffusive behavior, active motion generally gives rise to persistent single-particle trajectories [3, 6]: an active particle typically moves persistently in one spatial direction with a typical velocity, known as the swim velocity, and only after a typical time, known as persistence time, randomizes its direction of motion.

These features have been identified as the basic ingredients to build coarse-grained models in the framework of stochastic processes, able to capture the essential behavior of this class of active systems. Among them, the famous model of active Brownian particles (ABPs) [7–15] introduces the "activity" as a time-dependent force of constant magnitude with a stochastic evolution of its direction. It is commonly used due to its simplicity while it also presents an accurate representation of active colloids [16–20] subject to both translational and rotational Brownian motion. Recently, an alternative model, known as active Ornstein-Uhlenbeck particles (AOUPs) [21–25], has been introduced, firstly, to describe the motion of a passive colloid in a bath formed by active bacteria [26–29], and, secondly, to further simplify the ABP dynamics in terms of Gaussian correlations [30–32], which allows to obtain exact analytical predictions [33–36] or devise approximate theories [37–39]. The two models show consistent results, being both able to reproduce the typical non-equilibrium phase coexistence of active particles, known as motility-induced phase separation (MIPS) [14, 16, 30, 40–45], as well as the accumulation or wetting at boundaries or generic obstacles [46–50]. Beyond the qualitative level, the results of the two models have been compared in several cases of interest [32, 51, 52], and, recently, their relation has been comprehensively investigated in Ref. [53].

Both ABPs and AOUPs have been originally developed to model the overdamped dynamics of microscopic active particles. However, also macroscopic active "particles" are rather common in the animal world, such as birds [54], fish [55] and insects [56, 57], as well as in the inanimate world, such as walking droplets [58], flying whirling fruits [59] and active granular particles [60–66]. The recent significant increase of interest in these systems generates the need to develop manageable generalized theoretical descriptions including inertial effects [67].

The first, and most obvious, step to model inertial active systems, is to account for a larger particle's mass or, equivalently, a smaller translational friction coefficient. Such inertial forces are easily included in an underdamped description for the translational motion of ABPs [68–75] and AOUPs [76–81] to obtain fully consistent results for dynamical observables like the mean-squared displacement [82, 83], which reveals a mass-independent long-time diffusive behavior of the single particle. Moreover, these theoretical models have been employed to evaluate the effect of inertia on the collective phenomena typical of active matter. It was found that (translational) inertia reduces MIPS [71, 84–86], hinders the crystallization [87, 88], promotes hexatic ordering [89]

* alexander.sprenger@hhu.de
† lorenzo.caprini@gssi.it

in homogeneous phases and, in general, reduces the spatial velocity correlations characterizing dense active systems [90–92] both the liquid and solid state.

The second, and arguably the more critical, step is to include the effect of a non-vanishing moment of inertia affecting the rotational motion. This ingredient is fundamentally relevant in granular experiments to reproduce the inertial delay, i.e., the temporal delay between the active force and particle velocity observed for a single active granular particle [93]. To model such a generic inertial active particle not only the overdamped translational equation of motion but also the stochastic process describing the dynamics of the active velocity (or active force) itself needs to be modified. Again, this can be quite naturally achieved by a second extension of the ABP dynamics through including inertia on the rotational velocity [93–98]. Using this inertial ABP (or active Langevin) model, it has been found that the long-time dynamics are strongly affected by a nonzero moment of inertia. Successively, the effect of rotational inertia in systems of interacting particles has been investigated and identified as a strategy to promote collective phenomena [99, 100]. Finally, rotational inertia has been recently considered also in macroscopic descriptions, such as active phase crystal model [101, 102], to investigate sound waves in active matter.

Despite the success of AOUPs for describing overdamped active particles or active particles with translational inertia, a comprehensive inertial AOUP model, i.e., a Gaussian process for the active velocity also accounting for rotational inertia, has not been properly introduced. While such an achievement would be helpful in view of making further theoretical progress, this challenge is complicated by the intrinsic coupling between the angular dynamics and those of the modulus of the active velocity [53], preventing conformance with inertial ABPs. A first attempt to do so has been introduced in Ref. [103] by mapping rotational inertia onto effective parameters of the AOUP model.

In this paper, we propose a generalization of the inertial active Ornstein-Uhlenbeck particle (AOUP) model incorporating the characteristic time scales of active particles with both translational and rotational inertia. As illustrated in Fig. 1, this ensures that, in analogy to the inertial ABP, the decay of the autocorrelation function of the self-propulsion vector takes longer that the single-exponential decay for zero moment of inertia [93]. As a result, both models consistently predict persistent trajectories, which also show inertial delay [93, 97]. However, the velocity distribution of the inertial AOUP has, by construction, a Gaussian shape at variance with the bimodal shape of the inertial ABP [96].

The paper is structured as follows. We first provide in Sec. II a rundown of the inertial ABP model and discuss briefly the effect of rotational inertia on the persistence time of the active motion. Then, in Sec. III, we extend the inertial AOUP to account for rotational inertia. Subsequently, in Sec. IV we discuss the dynamical

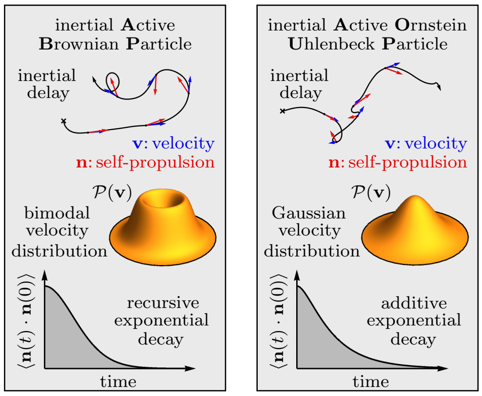

Figure 1. Schematic comparison of two models for active particles displaying both translational and rotational inertia. The left panel shows an inertial active Brownian particle (ABP) [97], while the right panel shows an inertial active Ornstein-Uhlenbeck particle (AOUP), introduced here through Eqs. (1) and (11). **Top:** both models display persistent trajectories with inertial delay (the particle velocity $\mathbf{v}(t)$ lags behind the self-propulsion vector $\mathbf{n}(t)$). **Middle:** the overall velocity distribution $\mathcal{P}(\mathbf{v})$ of the inertial AOUP has the advantageous Gaussian form, while that of the inertial ABP is bimodal. **Bottom:** The autocorrelation functions $\langle \mathbf{n}(t)\cdot\mathbf{n}(0)\rangle$ of the self-propulsion vector have a different form, contrast the recursive exponential decay (Eq. (5)) with the additive exponential decay (Eq. (14)), but each model incorporates three characteristic time scales of inertial active motion, see Eq. (3) or also Eq. (16a).

predictions for the time-dependent orientational correlation, velocity autocorrelation, delay function, as well as the mean and mean-square displacement. To validate the inertial AOUP model introduced in this paper, we compare the results for appropriately identified parameters to those of the inertial ABP. Finally, we present a conclusive discussion in Sec. V.

II. INERTIAL ABP MODEL

We consider an inertial self-propelled particle in two spatial dimensions, characterized by its mass m and moment of inertia J. The particle dynamics is described by stochastic evolution for the center-of-mass velocity $\mathbf{v} = \dot{\mathbf{r}}$ (with $\mathbf{r}$ being the center-of-mass position) and the angular velocity $\omega = \dot{\phi}$ (with ϕ being the orientational angle of the particle). The translational motion is governed by Newton's second law of motion

$$\dot{\mathbf{r}} = \mathbf{v}\,, \tag{1a}$$

$$m\,\dot{\mathbf{v}} = -\gamma\,\mathbf{v} - \boldsymbol{\nabla}U(\mathbf{r}) + \gamma\sqrt{2D_t}\boldsymbol{\xi} + \gamma v_0\mathbf{n}\,, \tag{1b}$$

where the acceleration term $m\,\dot{\mathbf{v}}$ accounts for translational inertia. The total force on the right-hand-side of Eq. (1b) is given by the sum of the friction force $-\gamma\mathbf{v}$, proportional to the translational frictions coefficient γ, the external force $-\boldsymbol{\nabla}U(\mathbf{r})$ with the potential $U(\mathbf{r})$, and the thermal force $\gamma\sqrt{2D_t}\boldsymbol{\xi}$, whose intensity is given by the translational diffusion coefficient D_t and distributed like a zero-mean unit variance Gaussian white noise $\boldsymbol{\xi}$. Finally, the active force $\gamma v_0\mathbf{n}$ couples via the orientation vector, $\mathbf{n} = (\cos\phi, \sin\phi)$, the translational motion to a rotational degree of freedom. In the ABP model the modulus of the active force is constant and sets the self-propulsion speed v_0.

In a similar manner, the rotational motion

$$\dot{\phi} = \omega\,, \tag{2a}$$

$$J\,\dot{\omega} + \gamma_{\rm r}\,\omega = \gamma_{\rm r}\sqrt{2D_{\rm r}}\eta\,, \tag{2b}$$

involves a friction torque $-\gamma_{\rm r}\omega$ with the rotational friction coefficient $\gamma_{\rm r}$ and a stochastic torque $\gamma_{\rm r}\sqrt{2D_{\rm r}}\eta$, where the effective rotational diffusion coefficient $D_{\rm r}$ quantifies the rotational noise strength and the Gaussian noise η has zero-mean and unit variance. Here, the angular acceleration term $J\,\dot{\omega}$ accounts for rotational inertia. Overall, the inertial ABP is characterized by three typical times

$$\tau := \frac{1}{D_{\rm r}}\,, \quad \tau_J := \frac{J}{\gamma_{\rm r}}\,, \quad \tau_m := \frac{m}{\gamma}\,, \tag{3}$$

representing rotational diffusion, translational memory and rotational memory, respectively. In what follows, we use τ as the unit time.

By taking a closer look at Eq. (2b), we see that the angular velocity ω is described by an Ornstein-Uhlenbeck process such that

$$\langle\omega(t)\,\omega(0)\rangle = \frac{1}{\tau\tau_J}e^{-t/\tau_J}\,. \tag{4}$$

Thus, the time scale τ_J, entering in Eq. (4), introduces memory in the angular velocity, such that the orientational correlation function

$$\langle\mathbf{n}(t)\cdot\mathbf{n}(0)\rangle = e^{-(t/\tau - \tau_J/\tau(1-e^{-t/\tau_J}))} \tag{5}$$

exhibits a *recursive* exponential decay (see footnote [104] for a clarification of the use of the term "recursive"), instead of the single-exponential decay in the absence of rotational inertia, $\tau_J \to 0$. In particular, this orientational correlation decays quadratically for short times,

$$\langle\mathbf{n}(t)\cdot\mathbf{n}(0)\rangle = 1 - t^2/(2\tau\tau_J) + \mathcal{O}\left(t^3\right), \tag{6}$$

and the overdamped result $\tau_{\rm p} = \tau$ for the characteristic persistence time $\tau_{\rm p} = \int_0^\infty\langle\mathbf{n}(t)\cdot\mathbf{n}(0)\rangle{\rm d}t$ generalizes to

$$\tau_{\rm p} = \tau_J\,e^{\tau_J/\tau}\,(\tau_J/\tau)^{-\tau_J/\tau}\,\Gamma(\tau_J/\tau, 0, \tau_J/\tau)\,, \tag{7}$$

where $\Gamma(x, z_0, z_1) = \int_{z_0}^{z_1} t^{x-1}e^{-t}\,dt$ is the incomplete gamma function.

In general, the persistence time $\tau_{\rm p}$ increases when τ is increased. Compared to the overdamped case, this increase is more significant when the typical time τ_J (or the moment of inertia) is increased. Therefore, it is apparent that inertial effects hinder the particle's ability of changing the direction of its self-propulsion vector in response to an applied torque. Further results for an inertial ABP are contained in Appendix A. It should be noted that, due to the implicit dependence of most quantities on τ_J, such as $\tau_{\rm p}$ in Eq. (7), a comprehensive analytical picture is impaired. Explicit analytical insight can be obtained in the small-rotational-inertia limit.

A. ABP for small rotational inertia

Neglecting rotational inertia, $\tau_J \to 0$, the rotational dynamics of the inertial ABP coincides with the usual ones, expected for overdamped ABP. In this limit, the angular velocity ω converges onto a zero-mean δ-correlated Gaussian white noise with

$$\langle\omega(t)\omega(t')\rangle \sim \frac{2}{\tau}\delta(t-t') \tag{8}$$

as a result of the asymptotic limit of Eq. (4). Secondly, expanding Eq. (5) in powers of τ_J, the autocorrelation of the orientational vector, $\mathbf{n}$, reads

$$\langle\mathbf{n}(t)\cdot\mathbf{n}(0)\rangle = e^{-t/\tau}\Big(1 + \tau_J/\tau + \mathcal{O}\left(\tau_J^2\right)\Big) \tag{9a}$$

$$= e^{-t/\tau}\Big(1 + \tau_J/\tau(1 - e^{-t/\tau_J}) + \mathcal{O}\left(\tau_J^2\right)\Big)\,, \tag{9b}$$

where the second equality conveniently retains τ_J as a typical exponential decay time. From Eq. (9), we can naturally identify the persistence time, $\tau_{\rm p}$, as the inverse of the rotational diffusion coefficient, τ, in the overdamped limit $\tau_J \to 0$. This can be explicitly verified by expanding Eq. (7) in powers of τ_J, such that

$$\tau_{\rm p} = \tau + \tau_J - \frac{\tau_J^2}{2\tau} + \mathcal{O}\left(\tau_J^3\right)\,, \tag{10}$$

and then considering the limit $\tau_J \to 0$.

III. FULLY INERTIAL AOUP MODEL

Despite the simplicity and intuitive nature of the ABP model, obtaining analytical results that go beyond the potential-free particle is not an easy task [105], even more so, in the presence of rotational inertia. The AOUP model, initially proposed in overdamped systems (without inertia) represents an alternative and simplified model to the ABP which is obtained by replacing the orientation vector $\mathbf{n}$ in Eq. (1b) by an Ornstein-Uhlenbeck process with correlation time τ and unit variance. This simple approach works well because the autocorrelation $\langle\mathbf{n}(t)\cdot\mathbf{n}(0)\rangle$ of both an (overdamped) ABP and AOUP has the same exponential shape decaying with a typical correlation time, that coincides with the common persistence time. To get consistent results, it is merely required to ensure that $\tau \equiv 1/D_\mathrm{r}$ describing the AOUP dynamics represents the inverse rotational diffusion coefficient of the ABP in two dimensions [32], as we imply here through Eq. (3). In the AOUP case, the whole stochastic process modeling the active self-propulsion vector $\mathbf{n}$ is Gaussian, thus offering a simplified platform to derive analytical results in the presence of interactions and external potentials [53].

The inclusion of translational inertia in the AOUP model has been proposed and investigated [78, 79], and, in general, does not present any additional conceptual or technical difficulties compared to the ABP model. This is because translational inertia does not affect the dynamics of the active force, i.e., the orientational angle ϕ in the ABP case or the Ornstein-Uhlenbeck process for the self-propulsion vector $\mathbf{n}$ (see below) in the AOUP case. In the presence of rotational inertia, pursuing a similar strategy of deriving a Gaussian approximation to the ABP dynamics is not straightforward because of the intricate structure of Eq. (5), which does no longer posses a single-exponential shape as in the overdamped case, Eq. (9a). Intuitively, a minimal description of rotational inertia requires (i) an additional time scale, τ_J, and (ii) an additional scaling factor, τ_J/τ, both related to the moment of inertia, which affects the angular velocity autocorrelation.

To generalize the AOUP model to the presence of rotational inertia, we introduce an additional colored noise $\boldsymbol{\chi}$ in the dynamics of the self-propulsion vector $\mathbf{n}$, characterized by its own rotational memory time τ_χ and the noise strength D_χ/τ_χ^2, so that $\mathbf{n}$ evolves as

$$\dot{\mathbf{n}} = -\frac{\mathbf{n}}{\tau} + \sqrt{\frac{1}{\tau}}\boldsymbol{\chi}, \tag{11a}$$

$$\dot{\boldsymbol{\chi}} = -\frac{\boldsymbol{\chi}}{\tau_\chi} + \frac{\sqrt{2D_\chi}}{\tau_\chi}\boldsymbol{\zeta}\,. \tag{11b}$$

This model ensures that Eq. (11a) formally coincides with the overdamped AOUP model, i.e., when the auxiliary process $\boldsymbol{\chi}$ is a white noise. Here, the additional Ornstein-Uhlembeck process for $\boldsymbol{\chi}$, evolving according to Eq. (11b), prescribes a more general colored noise. As a consequence, the rotational AOUP model is not only characterized by one typical time τ (which in overdamped systems coincides with the persistence time), but also by an additional time τ_χ and the inertial diffusivity D_χ. The latter can be conveniently determined as

$$D_\chi = \frac{\tau + \tau_\chi}{2\tau} \tag{12}$$

from the condition

$$\langle \mathbf{n}(0)\cdot\mathbf{n}(0)\rangle = 1\,, \tag{13}$$

ensuring the unitary normalization of $\mathbf{n}(t)$ (which is a unit vector in the ABP case) to set the velocity scale by v_0 without ambiguity [53].

The standard AOUP model in the overdamped limit is naturally achieved by requiring $\tau_\chi \to 0$ and $D_\chi \to 1/2$ such that Eq. (11b) reduces to a white noise with zero average and unit variance. Moreover, the linearity of Eq. (11) allows us to analytically derive the autocorrelation function

$$\langle \mathbf{n}(t)\cdot\mathbf{n}(0)\rangle = \frac{2D_\chi\tau}{\tau^2-\tau_\chi^2}\left(\tau\, e^{-t/\tau} - \tau_\chi\, e^{-t/\tau_\chi}\right) \tag{14}$$

of the self-propulsion vector $\mathbf{n}$, which is characterized by an *additive* exponential decay (see footnote [104] for a clarification of the use of the term "additive"), i.e., the superposition of two exponential functions with the correlation times τ and τ_χ. Comparing this result to the expansion in Eq. (9b) for the inertial ABP, we deduce that the structure of Eq. (14) with two different decay times constitutes the minimal ingredient to account for rotational inertia. In the rest of this work, we validate the inertial AOUP model by establishing a suitable relation between the parameters τ_χ and D_χ in and those, τ and τ_J, of the inertial ABP model to quantify the impact of rotational inertia through Eq. (11).

A. Relation to inertial ABP model

Comparing the full predictions of the two models for the autocorrelation function given by Eq. (5) and Eq. (14), it becomes apparent that, at variance with the overdamped limit ($\tau_\chi \to 0$ or $\tau_J \to 0$), the shape of $\langle \mathbf{n}(t)\cdot\mathbf{n}(0)\rangle$ does not coincide, see also Fig. 1. To provide a coherent scheme for identifying the rotational memory time τ_χ of our inertial AOUP model, we impose here, in addition to Eq. (13), the second natural condition

$$\int_0^\infty \langle \mathbf{n}(t)\cdot\mathbf{n}(0)\rangle\,\mathrm{d}t = \tau_\mathrm{p} \tag{15}$$

satisfied by the inertial ABP model, which enforces that both models have the same autocorrelation time and, thus, predict the same long-time diffusion behavior. Thus we can identify the parameters of both models according to

$$\tau_\chi = \tau_\mathrm{p} - \tau = \tau_J + \mathcal{O}\left(\tau_J^2\right)\,, \tag{16a}$$

$$D_\chi = \frac{\tau_\mathrm{p}}{2\tau} = \frac{1}{2} + \frac{\tau_J}{2\tau} + \mathcal{O}\left(\tau_J^2\right)\,, \tag{16b}$$

where the provided small-τ_J expansions are apparent from Eq. (10).

To understand the meaning of the new inertial parameters τ_χ and D_χ of our generalized AOUP model, their values are shown in Fig. 2 as a function of the rotational memory time τ_J of the inertial ABP. It can be seen that both parameters τ_χ and D_χ are increasing functions of τ_J. They scale as $\sim\sqrt{\tau_J/\tau}$ for $\tau_J/\tau \gg 1$, as can be deduced from the function τ_p given by Eq. (7). Moreover, the limit of vanishing rotational inertia, $\tau_J \to 0$, is consistent with

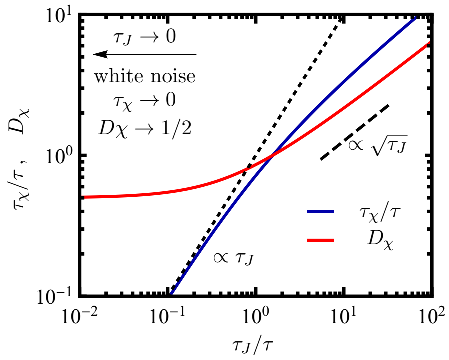

Figure 2. Additional parameters of the inertial AOUP model, τ_χ/τ (blue curve) and D_χ (red curve), related to the inertial ABP model through Eq. (16) as a function of the normalized rotational memory time τ_J of the inertial ABP. Dashed black lines indicate the scaling $\sim \sqrt{\tau_J}$ occurring for large τ_J while for $\tau_J \to 0$ the limiting values $D_\chi \to 1/2$ and $\tau_\chi \to 0$ are approached and τ_χ scales as $\sim \tau_J$ (dotted black line).

the overdamped AOUP, since according to Eq. (10) the persistence time τ_p reduces to τ, such that we observe the limits $\tau_\chi \to 0$ and $D_\chi \to 1/2$. As a consequence, Eq. (11a) reduces in the overdamped limit to a standard Ornstein-Uhlenbeck process with the white noise $\boldsymbol{\chi} = \boldsymbol{\zeta}$, employed to describe active particles without rotational inertia. Further aspects of the small-rotational-inertia limit are discussed in Sec. III C. In the opposite limit, $\tau_J \to \infty$, the inertial AOUP persistently moves along a straight line, which is consistent with the inertial ABP. Thus our model accurately includes both limits of vanishing and infinite rotational inertia.

B. Probability densities for inertial AOUPs

One of the main advantages of the inertial AOUP model, defined by Eqs. (1) and (11), is that the stationary probability density $\mathcal{P}(\mathbf{v}, \mathbf{n}, \boldsymbol{\chi})$ can be explicitly derived via its correlation matrix. We list these results in Appendix B. Here, we discuss the reduced probability $\mathcal{P}(\mathbf{v}, \mathbf{n})$ to find a given velocity $\mathbf{v}$ and self-propulsion $\mathbf{n}$ which is obtained via integration of the full probability density with respect to the auxiliary process $\boldsymbol{\chi}$. The distribution $\mathcal{P}(\mathbf{v}, \mathbf{n})$ can be expressed as

$$\mathcal{P}(\mathbf{v}, \mathbf{n}) = \mathcal{P}(\mathbf{v}|\mathbf{n})\mathcal{P}(\mathbf{n}), \tag{17}$$

where $\mathcal{P}(\mathbf{n})$ is the marginal probability density of the self-propulsion vector $\mathbf{n}$ with unit-variance, thus

$$\mathcal{P}(\mathbf{n}) \propto \exp\left(-\mathbf{n}^2\right), \tag{18}$$

and $\mathcal{P}(\mathbf{v}|\mathbf{n})$ defines the conditional probability to find a particle at a velocity $\mathbf{v}$ with prescribed $\mathbf{n}$. Using the time scales τ and τ_m from Eq. (3) and the rotational memory time τ_χ of the inertial AOUP, we have

$$\mathcal{P}(\mathbf{v}|\mathbf{n}) \propto \exp\left(-\frac{\left(\mathbf{v} - \langle \mathbf{v}|\mathbf{n}\rangle\right)^2}{\sigma(\mathbf{v}|\mathbf{n})}\right), \tag{19a}$$

$$\langle \mathbf{v}|\mathbf{n}\rangle = \frac{v_0}{\tau - \tau_\chi}\left(\frac{\tau^2}{\tau + \tau_m} - \frac{\tau_\chi^2}{\tau_\chi + \tau_m}\right)\mathbf{n}, \tag{19b}$$

$$\sigma(\mathbf{v}|\mathbf{n}) = \frac{2D_t}{\tau_m} + \frac{v_0^2 \tau_m^2 (\tau\tau_m + \tau_m\tau_\chi + \tau\tau_\chi)}{(\tau + \tau_m)^2(\tau_\chi + \tau_m)^2}, \tag{19c}$$

where $\mathcal{P}(\mathbf{v}|\mathbf{n})$ is centered around the conditional average $\langle \mathbf{v}|\mathbf{n}\rangle$ of $\mathbf{v}$ at given $\mathbf{n}$ with its corresponding conditional variance $\sigma(\mathbf{v}|\mathbf{n})$.

By integrating the distribution $\mathcal{P}(\mathbf{v}|\mathbf{n})$ in Eq. (17) over $\mathbf{n}$, we derive the velocity distribution of a system of ideal inertial AOUPs

$$\mathcal{P}(\mathbf{v}) \propto \exp\left(-\frac{\mathbf{v}^2}{\langle \mathbf{v}^2\rangle}\right), \tag{20a}$$

$$\langle \mathbf{v}^2\rangle = \frac{2D_t}{\tau_m} + \frac{v_0^2}{\tau - \tau_\chi}\left(\frac{\tau^2}{\tau + \tau_m} - \frac{\tau_\chi^2}{\tau_\chi + \tau_m}\right), \tag{20b}$$

with the mean-square velocity $\langle \mathbf{v}\rangle^2$. Such a distribution has a typical Boltzmann-like shape as illustrated in Fig. 1, with an effective temperature determined by the swim velocity v_0 and the three typical time scales τ, τ_m, and τ_χ.

C. AOUP for small rotational inertia

In the absence of rotational inertia, the inertial AOUP model converges onto the standard AOUP model employed to describe overdamped active particles or active particles with translational inertia only. This is evident by taking the overdamped limit in Eq. (11b), i.e., considering $\tau_\chi \to 0$. The nature of the Ornstein-Uhlenbeck process $\boldsymbol{\chi}$ allows us to derive the steady-state autocorrelation

$$\langle \boldsymbol{\chi}(t) \cdot \boldsymbol{\chi}(0)\rangle = 2\frac{D_\chi}{\tau_\chi} e^{-t/\tau_\chi} = \frac{\tau + \tau_J}{\tau\tau_J} e^{-t/\tau_J} + \mathcal{O}\left(\tau_J^2\right), \tag{21}$$

where, in the last equality, we have used Eqs. (16) holding at first order in τ_J. This shape links the correlator of $\boldsymbol{\chi}$ to the correlator, Eq. (4), of the angular velocity ω in the inertial ABP model. This confirms our identification of the additional degree of freedom $\boldsymbol{\chi}$ in the inertial AOUP model as the key dynamical variable able to capture the effects of rotational inertia. To see this, we further note that, in Cartesian coordinates, the dynamics of the self-propulsion vector $\mathbf{n}$ can be expressed as $\dot{\mathbf{n}} = \mathbf{n} \times \mathbf{z}\,\omega$, where $\mathbf{z}$ is the unit vector perpendicular to the two-dimensional plane of motion [97]. Similarly to the overdamped case [53], the AOUP approximation can then be imagined as replacing this term by an Orstein-Uhlenbeck process.

In the same spirit, the autocorrelation (14) of the self-propulsion vector $\mathbf{n}$ can be expanded with the help of Eq. (16) as

$$\langle \mathbf{n}(t) \cdot \mathbf{n}(0) \rangle = \frac{1}{\tau - \tau_J} \left(\tau \, e^{-t/\tau} - \tau_J \, e^{-t/\tau_J} \right) + \mathcal{O}\left(\tau_J^2\right) . \tag{22}$$

By additionally setting $\tau \gg \tau_J$ for small moment of inertia, we recover Eq. (9b). Thus, our model goes beyond a naive mapping of this small-rotational-inertia limit.

In addition, the probability distribution $\mathcal{P}(\mathbf{v}|\mathbf{n})$ in Eq. (19) converges to the one found in Ref. [78] without rotational inertia. By expanding for small τ_J, mean and variance of the Gaussian distribution reads

$$\langle \mathbf{v}|\mathbf{n} \rangle = \frac{v_0 \tau}{\tau + \tau_m} \mathbf{n} + \frac{v_0 \tau_J}{\tau + \tau_m} \mathbf{n} + \mathcal{O}\left(\tau_J^2\right) , \tag{23a}$$

$$\sigma(\mathbf{v}|\mathbf{n}) = \frac{2D_t}{\tau_m} + \frac{v_0^2 \tau_m \tau}{(\tau + \tau_m)^2} - \frac{v_0^2 (\tau - \tau_m) \tau_J}{(\tau + \tau_m)^2} + \mathcal{O}\left(\tau_J^2\right) , \tag{23b}$$

where we have neglected order τ_J^2. The zero-order result in Eq. (23) coincides with the variance calculated in Ref. [78], while the first correction in τ_J decreases the velocity variance if $\tau > \tau_J$ (long-persistent regime) and increases the variance in the opposite limit.

IV. COMPARISON BETWEEN INERTIAL ABP AND INERTIAL AOUP

The inertial AOUP model introduced in Sec. III defines a purely Gaussian process which in general significantly simplifies the theoretical analysis compared to the inertial ABP model, specified in Sec. II. However, at variance with the overdamped case, there is no one-to-one identification of the parameters in these two models, since the shape of the autocorrelations, Eqs. (5) and (14), does not coincide. Therefore, a careful comparison between the inertial ABP and inertial AOUP is needed. To this end, we evaluate in the following several observables for different values of the rotational memory time τ_J of the inertial ABP which sets the corresponding rotational memory time τ_χ of the inertial AOUP through Eqs. (16a) and (7). We thus explore all regimes where the rotational inertia plays a marginal ($\tau_J \ll \tau$), intermediate ($\tau_J \approx \tau$) and relevant ($\tau_J \gg \tau$) role. In particular, we compare the autocorrelation of the self-propulsion vector, velocity correlations and the cross correlation between self-propulsion vector and velocity, known as delay function. Finally, we consider the mean-square displacement and the long-time diffusion coefficient. The implicit analytic reference results for the inertial ABP model are listed in Appendix A.

A. Orientational correlation function

Having established in Sec. III C that both inertial ABP and AOUP models yield the same autocorrelation function $\langle \mathbf{n}(t) \cdot \mathbf{n}(0) \rangle$ of the self-propulsion vector $\mathbf{n}$ for small rotational inertia, we provide in Fig. 3 a comparison for different reduced moments of inertia τ_J/τ. As expected, for $\tau_J \ll \tau$ and $\tau_J \approx \tau$, a good agreement is obtained on all timescales (see the comparison between solid and dashed lines). However, for $\tau_J \gg \tau$, we observe small deviations between the two models. In particular, the inertial AOUP model predicts a faster early decay, which we understand from comparing the short-time expansion

$$\langle \mathbf{n}(t) \cdot \mathbf{n}(0) \rangle = 1 - \frac{t^2}{2\,\tau\tau_\chi} + \mathcal{O}\left(t^3\right) \tag{24}$$

to the ABP result in Eq. (6) and recognizing that $\tau_\chi \leq \tau_J$ (see Fig. 2). At later times, there is a crossover between $\tau_\chi \lesssim t \lesssim \tau_J$ as the autocorrelation of the inertial AOUP has a longer decay tail, which reflects the nature of the additive exponential decay, compared to the faster recursive exponential decay the of inertial ABP.

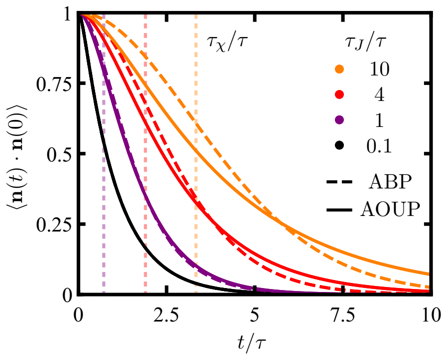

Figure 3. Orientational correlation $\langle \mathbf{n}(t) \cdot \mathbf{n}(0) \rangle$ as a function of time t/τ for different moments of inertia given through τ_J/τ (as labeled). Solid and dashed lines correspond to an AOUP and ABP, respectively. Vertical dotted lines indicate the rotational memory time τ_χ of the inertial AOUP.

B. Velocity correlation function

The velocity correlation of the inertial AOUP reads

$$\langle \mathbf{v}(t) \cdot \mathbf{v}(0) \rangle = \frac{2D_t}{\tau_m} e^{-t/\tau_m} + \frac{v_0}{2} \Big(\langle \mathbf{v}(t) \cdot \mathbf{n}(0) \rangle + \langle \mathbf{v}(0) \cdot \mathbf{n}(t) \rangle \Big), \tag{25}$$

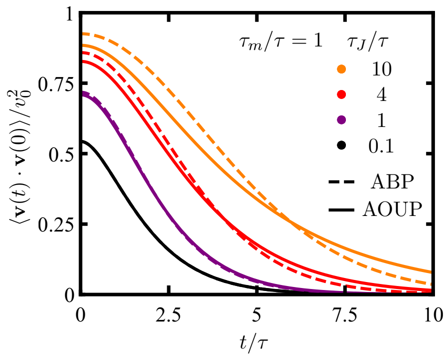

Figure 4. Velocity correlation function, $\langle \mathbf{v}(t)\cdot\mathbf{v}(0)\rangle$, as a function of time t/τ for a fixed mass m given through $\tau_m/\tau = 1$ different moments of inertia J given through τ_J/τ (as labeled). Solid and dashed lines correspond to an AOUP and ABP, respectively.

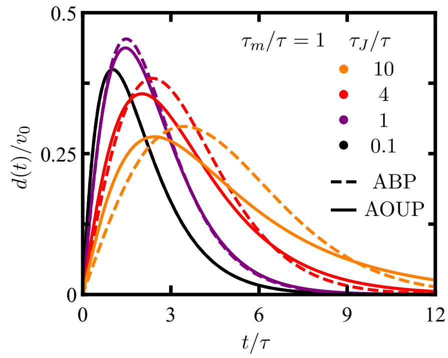

Figure 5. Delay function, $d(t)$, defined in Eq. (27), shown in the same style and for the same parameters as in Fig. (4).

with

$$\langle \mathbf{v}(t)\cdot\mathbf{n}(0)\rangle = \frac{v_0}{\tau-\tau_\chi}\left(\frac{\tau^2 e^{-t/\tau}}{\tau-\tau_m} - \frac{\tau_\chi^2 e^{-t/\tau_\chi}}{\tau_\chi-\tau_m}\right) + \frac{2v_0\tau_m^3(\tau+\tau_\chi)e^{-t/\tau_m}}{(\tau^2-\tau_m^2)(\tau_\chi^2-\tau_m^2)}, \tag{26a}$$

$$\langle \mathbf{v}(0)\cdot\mathbf{n}(t)\rangle = \frac{v_0}{\tau-\tau_\chi}\left(\frac{\tau^2 e^{-t/\tau}}{\tau+\tau_m} - \frac{\tau_\chi^2 e^{-t/\tau_\chi}}{\tau_\chi+\tau_m}\right). \tag{26b}$$

This result serves as a closed-form approximation for the inertial ABP result. As shown in Fig. 4, our model consistently predicts stronger velocity correlations for all times when the rotational inertia is increased. The small deviations for large moment of inertia and the crossover of the decay behavior are quite similar to those discussed in Sec. IV A for the orientational correlation function.

In addition, we observe in Fig. 4 an offset at $t = 0$ between the two models, i.e., they predict a distinct mean-square velocity $\langle \mathbf{v}^2\rangle \equiv \langle \mathbf{v}(0)\cdot\mathbf{v}(0)\rangle$. For the inertial AOUP, we recover the result for $\langle \mathbf{v}^2\rangle$ given by Eq. (20b). We can thus conclude that rotational inertia increases the translational kinetic temperature (which is proportional to $\langle \mathbf{v}^2\rangle$). Taking the limit $\tau_J \to \infty$ in Eq. (20b), we find that $\langle \mathbf{v}^2\rangle \to 2D_t/\tau_m + v_0^2$ reaches a plateau value which is the same as found for an inertial ABP.

C. Delay Function

Next we consider the delay function between the velocity and orientation of the inertial active particle, defined as [93, 97]

$$d(t) = \langle \mathbf{v}(t)\cdot\mathbf{n}(0)\rangle - \langle \mathbf{v}(0)\cdot\mathbf{n}(t)\rangle\,. \tag{27}$$

The two required correlation functions are given by Eq. (26) for the inertial AOUP. The inertial delay $d(t)$ has been introduced in Ref. [93] as one of the main dynamical effects characterizing ABP with inertia: the velocity $\mathbf{v}$ tends to lag behind the self-propulsion $\mathbf{n}$ at a typical delay time.

We see in Fig. 5 that our model also provides an accurate qualitative picture of effect of rotational inertia on the delay function, regarding both the maximal delay and the characteristic duration of this effect. Comparing the prediction to the inertial ABP, we find two crossover regimes for large moment of inertia: the inertial AOUP predicts a stronger delay at both short and long times.

Another benefit of our closed AOUP result is that the total inertial delay $d_{\text{tot}} := \int \mathrm{d}t\, d(t)$, i.e., the time integral of Eq. (27), can be determined in the compact form

$$d_{\text{tot}} = \frac{2v_0\tau_m(\tau\tau_\chi + \tau\tau_m + \tau_\chi\tau_m)}{(\tau+\tau_m)(\tau_\chi+\tau_m)}\,, \tag{28}$$

which immediately reveals that the delay effect is enhanced by increasing either of the relevant time scales of inertial active motion, given by Eq. (3).

D. Positional correlation functions

The conditional mean displacement for a given initial value $\mathbf{n}_0 = \mathbf{n}(0)$ of the self-propulsion vector can be calculated for an inertial AOUP as

$$\begin{aligned}\langle \Delta\mathbf{r}(t)|\mathbf{n}_0\rangle = &\langle \mathbf{v}|\mathbf{n}_0\rangle\tau_m\left(1-e^{-t/\tau_m}\right) + v_0\mathbf{n}_0\left(\tau+\tau_\chi\right)\\ &+ v_0\mathbf{n}_0\left(\frac{\tau_m e^{-t/\tau_m}(\tau\tau_m - \tau\tau_\chi + \tau_m\tau_\chi)}{(\tau-\tau_m)(\tau_m-\tau_\chi)}\right.\\ &\left. - \frac{\tau^3 e^{-t/\tau}}{(\tau-\tau_m)(\tau-\tau_\chi)} - \frac{\tau_\chi^3 e^{-t/\tau_\chi}}{(\tau_\chi-\tau)(\tau_\chi-\tau_m)}\right),\end{aligned} \tag{29}$$

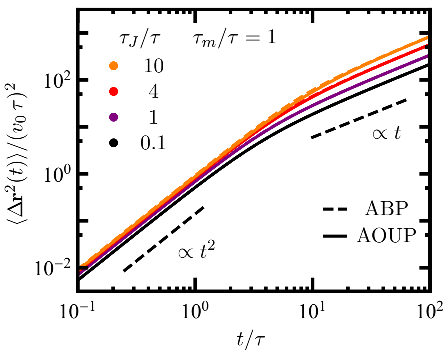

Figure 6. Mean-square displacement, $\langle \Delta \mathbf{r}^2(t) \rangle$, shown in the same style (mind the logarithmic scales) and for the same parameters as in Fig. (4). The curves for the two models cannot be distinguished here.

where we have used the initial condition $\boldsymbol{\chi}_0 = \langle \boldsymbol{\chi} | \mathbf{n}_0 \rangle = \mathbf{n}_0/\sqrt{\tau}$ for the auxiliary process $\boldsymbol{\chi}$ (see Eq. (B12b)) and the initial velocity $\langle \mathbf{v} | \mathbf{n}_0 \rangle$ follows from Eq. (19b). For $t \to \infty$ we find the persistence length

$$L_\mathrm{p} = \langle \mathbf{v} | \mathbf{n}_0 \rangle \tau_m + v_0 \mathbf{n}_0 (\tau + \tau_\chi) \,, \tag{30}$$

which has the same form as that of an inertial ABP.

Moreover, the mean-square displacement MSD(t) can be expressed as

$$\begin{aligned} \langle \Delta \mathbf{r}^2(t) \rangle =& 4D_L t + 2\big(\langle \mathbf{v}(t) \cdot \mathbf{v}(0) \rangle - \langle \mathbf{v}^2 \rangle\big)\tau_m^2 \\ & - \frac{2v_0^2}{\tau - \tau_\chi}\Big(\tau^3(1 - e^{-t/\tau}) - \tau_\chi^3(1 - e^{-t/\tau_\chi})\Big) \,, \end{aligned} \tag{31}$$

where the velocity correlation $\langle \mathbf{v}(t) \cdot \mathbf{v}(0) \rangle$ and the mean-square velocity $\langle \mathbf{v}^2 \rangle$ are given by Eq. (25) and Eq. (20b), respectively. The long-time diffusion coefficient

$$D_L = D_t + \frac{v_0^2}{2}(\tau + \tau_\chi) \tag{32}$$

is in full agreement with that of an inertial ABP. As shown in Fig. 6 the mean-square displacement MSD(t) of inertial AOUPs agrees fairly well with the ABP result also at intermediate times.

V. CONCLUSIONS

In this paper, we have generalized the inertial active Ornstein-Uhlenbeck particle (AOUP) model to account for translational and, in particular, for rotational inertia in two spatial dimensions. The inertial AOUP model introduced in this paper goes beyond mapping the rotational inertia onto an effective rotational diffusion coefficient [103] by incorporating a second characteristic time scale (in addition to the one related to the inverse rotational diffusion coefficient), which we have demonstrated to be the crucial ingredient for describing the proper long-time behavior. As such, our model matches both the small- and long-time regime with the inertial ABP model and thus represents a suitable alternative, which allows to determine closed analytical predictions for dynamical correlations. Indeed, the agreement between inertial ABP and AOUP models has been certified by comparing velocity correlations, the delay function and the mean-square displacement. For small or moderate moment of inertia, we have found similar predictions of these two models at all times, while small deviations only occur at intermediate times for large moment of inertia. In general, the effect of increasing rotational inertia is qualitatively captured well by the inertial AOUP model. In conclusion we have introduced and validated a Gaussian model to describe inertial active matter, which can be considered as an alternative to the inertial ABP model.

In analogy with the overdamped AOUP model, we expect that the inertial AOUP model presented here will offer an intriguing platform to provide analytic insight into various phenomena exhibited by active particles governed by both translational and rotational inertia. Most notably, future studies could focus on the generalization of effective-equilibrium theories with the inertial AOUP as a starting point. The extension of the unified colored noise approximation (UCNA) [33, 106–108] or Fox approach [38, 39, 109, 110] will helpful to understand the behavior of inertial active particles in the presence of interactions.

While, recently, it was shown that rotational inertia is able to promote phase separation [99] in purely repulsive systems, further interesting questions remain to be addressed at the collective level. For example, the effect of rotational inertia on the (continuous or discontinuous) nature of MIPS [85] or on the kinetic temperature difference between high- and low-density phases [71] is still unexplored. More generally, it would interesting to shed light on the effect of inertia on the recent micro-phase separation observed in field theories [111, 112] and overdamped particle-based simulations of repulsive ABPs [12, 43] or dumbbells [113]. To this end, it will be insightful to apply effective interactions [32, 48] or hydrodynamics [92, 114] and mean-field methods [115], to obtain theoretical predictions that take advantage of the intrinsic simplicity of the inertial AOUP model.

Appendix A: Results for an inertial ABP

For reference, we summarize here the essential analytic results of the inertial ABP model. Using methods of stochastic integration, we obtain the orientational correlation function in the steady state as

$$\langle \mathbf{n}(t) \cdot \mathbf{n}(0) \rangle = e^{-D_r\left(t - \tau_J(1 - e^{-t/\tau_J})\right)} . \tag{A1}$$

A characteristic orientational persistence time τ_p can be determined as

$$\tau_\mathrm{p} = \int_0^\infty \langle \mathbf{n}(t)\cdot\mathbf{n}(0)\rangle \mathrm{d}t = \tau_J e^{\mathcal{J}} \mathcal{J}^{-\mathcal{J}}\,\Gamma(\mathcal{J},0,\mathcal{J}) \quad \text{(A2)}$$

with the reduced moment of inertia $\mathcal{J} := \tau_J/\tau$.

Similarly, the translational velocity correlation function can be computed as

$$\langle \mathbf{v}(t)\cdot\mathbf{v}(0)\rangle = \frac{2D_t}{\tau_m}\,e^{-t/\tau_m} + \frac{v_0}{2}\big(\langle \mathbf{v}(t)\cdot\mathbf{n}(0)\rangle + \langle \mathbf{v}(0)\cdot\mathbf{n}(t)\rangle\big), \quad \text{(A3)}$$

as well as the delay function

$$d(t) = \langle \mathbf{v}(t)\cdot\mathbf{n}(0)\rangle - \langle \mathbf{v}(0)\cdot\mathbf{n}(t)\rangle \quad \text{(A4)}$$

with

$$\begin{aligned}\langle \mathbf{v}(t)\cdot\mathbf{n}(0)\rangle =& v_0\frac{\tau_J}{\tau_m}e^{\mathcal{J}}\Big(\mathcal{J}^{-\Omega_-}\Gamma(\Omega_-,\mathcal{J}e^{-t/\tau_J},\mathcal{J})\\ &+\mathcal{J}^{-\Omega_+}\Gamma(\Omega_+,0,\mathcal{J})\Big)e^{-t/\tau_m}, \quad \text{(A5)}\\ \langle \mathbf{v}(0)\cdot\mathbf{n}(t)\rangle =& v_0\frac{\tau_J}{\tau_m}e^{\mathcal{J}}\mathcal{J}^{-\Omega_+}\Gamma(\Omega_+,0,\mathcal{J}e^{-t/\tau_J})e^{t/\tau_m} \quad \text{(A6)}\end{aligned}$$

and $\Omega_\pm = \tau_J/\tau \pm \tau_J/\tau_m$.

Next, we address the mean displacement $\langle \Delta\mathbf{r}(t)|\mathbf{n}_0\rangle$ at prescribed initial orientation $\mathbf{n}_0$, which reads

$$\begin{aligned}\langle \Delta\mathbf{r}(t)|\mathbf{n}_0\rangle =& \langle \mathbf{v}|\mathbf{n}_0\rangle\tau_m\Big(1-e^{-t/\tau_m}\Big) \quad \text{(A7)}\\ &+\frac{v_0}{D_r}\mathcal{J}e^{\mathcal{J}}\Big(\mathcal{J}^{-\mathcal{J}}\Gamma(\mathcal{J},\mathcal{J}e^{-t/\tau_J},\mathcal{J})\\ &+\mathcal{J}^{-\Omega_-}\Gamma(\Omega_-,\mathcal{J}e^{-t/\tau_J},\mathcal{J})e^{-t/\tau_m}\Big)\hat{\mathbf{n}}_0\end{aligned}$$

with the mean initial velocity

$$\langle \mathbf{v}|\mathbf{n}_0\rangle = v_0\frac{\tau_J}{\tau_m}e^{\Omega}\Omega^{-\Omega_+}\Gamma(\Omega_+,0,\mathcal{J})\hat{\mathbf{n}}_0 \quad \text{(A8)}$$

at given $\mathbf{n}_0$. Thus, the long-time limit of Eq. (A7) yields the persistence length

$$L_\mathrm{p} = \langle \mathbf{v}|\mathbf{n}_0\rangle\tau_m + v_0\mathbf{n}_0\tau_\mathrm{p}\,, \quad \text{(A9)}$$

which has the same form as Eq. (30), while the required expression for $\langle \mathbf{v}|\mathbf{n}_0\rangle$ differs.

Last, the mean-square-displacement (MSD) is given by

$$\begin{aligned}\langle \Delta\mathbf{r}^2(t)\rangle =& 4D_Lt + 2\big(\langle \mathbf{v}(t)\cdot\mathbf{v}(0)\rangle - \langle \mathbf{v}^2\rangle\big)\tau_m^2 \quad \text{(A10)}\\ &+2v_0^2\tau_J^2\frac{e^{\mathcal{J}}}{\mathcal{J}^2}\Bigg({}_2F_2\left[\begin{matrix}\mathcal{J},\ \mathcal{J}\\ \mathcal{J}+1,\ \mathcal{J}+1\end{matrix};-\mathcal{J}\right]\\ &-{}_2F_2\left[\begin{matrix}\mathcal{J},\ \mathcal{J}\\ \mathcal{J}+1,\ \mathcal{J}+1\end{matrix};-\mathcal{J}e^{-t/\tau_J}\right]e^{-t/\tau}\Bigg)\end{aligned}$$

with the long-time diffusion coefficient

$$D_L = D_t + \frac{v_0^2}{2}\tau_\mathrm{p} \quad \text{(A11)}$$

and the generalized hypergeometric function ${}_pF_q$.

Appendix B: Stationary probability distribution for the inertial AOUP model

In this Appendix, we derive the stationary probability distribution $\mathcal{P}(\mathbf{v},\mathbf{n},\boldsymbol{\chi})$ for the AOUP model with rotational and translational inertia. First, we note that Eqs. (1b), (11a) and (11b), can be written in the form

$$\dot{\mathbf{w}} = -\boldsymbol{\mathcal{A}}\,\mathbf{w} + \boldsymbol{\sigma}\,\boldsymbol{\eta}\,, \quad \text{(B1)}$$

where $\boldsymbol{\mathcal{A}}$ and $\boldsymbol{\sigma}$ are the drift and the noise matrices, respectively, $\mathbf{w}$ the vector of dynamical variables, and $\boldsymbol{\eta}$ a white noise vector with unit-variance. The stationary probability distribution of this system is a multivariate Gaussian of the form

$$\mathcal{P}(\mathbf{w}) \propto \exp\big(-\mathbf{w}^T\boldsymbol{\mathcal{C}}^{-1}\,\mathbf{w}\big)\,, \quad \text{(B2)}$$

where $\boldsymbol{\mathcal{C}}^{-1}$ is the inverse of the correlation matrix $\boldsymbol{\mathcal{C}}$ to be determined by solving the following matrix equation

$$\boldsymbol{\mathcal{A}}\boldsymbol{\mathcal{C}} + \boldsymbol{\mathcal{C}}\,\boldsymbol{\mathcal{A}}^T = \boldsymbol{\sigma}\boldsymbol{\sigma}^T\,. \quad \text{(B3)}$$

Here, $\boldsymbol{\mathcal{A}}^T$ and $\boldsymbol{\sigma}^T$ the transpose of drift and noise matrix, respectively.

Applying this general approach for $\mathbf{w} = (\mathbf{v},\mathbf{n},\boldsymbol{\chi})$, we obtain

$$\begin{aligned}\mathcal{P}(\mathbf{v},\mathbf{n},\boldsymbol{\chi}) \propto& \exp\left(-\frac{\mathbf{v}^2}{2}\mathcal{C}^{-1}_{\mathbf{vv}} - \frac{\mathbf{n}^2}{2}\mathcal{C}^{-1}_{\mathbf{nn}} - \frac{\boldsymbol{\chi}^2}{2}\mathcal{C}^{-1}_{\boldsymbol{\chi\chi}}\right)\\ &\times\exp\Big(-\mathbf{v}\cdot\mathbf{n}\,\mathcal{C}^{-1}_{\mathbf{vn}} - \mathbf{v}\cdot\boldsymbol{\chi}\,\mathcal{C}^{-1}_{\mathbf{v}\boldsymbol{\chi}} - \mathbf{n}\cdot\boldsymbol{\chi}\,\mathcal{C}^{-1}_{\mathbf{n}\boldsymbol{\chi}}\Big), \quad \text{(B4)}\end{aligned}$$

where

$$\mathcal{C}^{-1}_{\mathbf{vv}} = \left(\frac{D_t}{\tau_m} + \frac{v_0^2\tau_m^3(\tau+\tau_\chi)}{2(\tau+\tau_m)^2(\tau_\chi+\tau_m)^2}\right)^{-1}, \tag{B5a}$$

$$\mathcal{C}^{-1}_{\mathbf{nn}} = \frac{\tau+\tau_\chi}{\tau}\left(\frac{2D_t}{\tau_m} + v_0^2\frac{\tau_\chi^2\tau_m^2 + \tau^2(\tau_\chi+\tau_m)^2 + \tau\tau_m\tau_\chi(2\tau_m+3\tau_\chi)}{(\tau+\tau_m)(\tau+\tau_\chi)(\tau_\chi+\tau_m)^2}\right)\left(\frac{D_t}{\tau_m} + \frac{v_0^2\tau_m^3(\tau+\tau_\chi)}{2(\tau+\tau_m)^2(\tau_\chi+\tau_m)^2}\right)^{-1}, \tag{B5b}$$

$$\mathcal{C}^{-1}_{\boldsymbol{\chi\chi}} = 2\tau_\chi + \frac{v_0^2\tau\tau_\chi^2\tau_m^2}{(\tau+\tau_m)^2(\tau_\chi+\tau_m)^2}\left(\frac{D_t}{\tau_m} + \frac{v_0^2\tau_m^3(\tau+\tau_\chi)}{2(\tau+\tau_m)^2(\tau_\chi+\tau_m)^2}\right)^{-1}, \tag{B5c}$$

$$\mathcal{C}^{-1}_{\mathbf{vn}} = -\frac{v_0}{\tau+\tau_m}\left(\tau + \frac{2\tau_\chi\tau_m}{\tau_\chi+\tau_m}\right)\left(\frac{D_t}{\tau_m} + \frac{v_0^2\tau_m^3(\tau+\tau_\chi)}{2(\tau+\tau_m)^2(\tau_\chi+\tau_m)^2}\right)^{-1}, \tag{B5d}$$

$$\mathcal{C}^{-1}_{\mathbf{v}\boldsymbol{\chi}} = \frac{v_0\sqrt{\tau}\tau_\chi\tau_m}{(\tau+\tau_m)(\tau_\chi+\tau_m)}\left(\frac{D_t}{\tau_m} + \frac{v_0^2\tau_m^3(\tau+\tau_\chi)}{2(\tau+\tau_m)^2(\tau_\chi+\tau_m)^2}\right)^{-1}, \tag{B5e}$$

$$\mathcal{C}^{-1}_{\mathbf{n}\boldsymbol{\chi}} = -\frac{\tau_\chi}{\sqrt{\tau}}\left(\frac{2D_t}{\tau_m} + \frac{v_0^2\tau_m}{(\tau+\tau_m)(\tau_\chi+\tau_m)}\left(\tau + \frac{\tau_\chi\tau_m}{\tau_\chi+\tau_m}\right)\right)\left(\frac{D_t}{\tau_m} + \frac{v_0^2\tau_m^3(\tau+\tau_\chi)}{2(\tau+\tau_m)^2(\tau_\chi+\tau_m)^2}\right)^{-1}. \tag{B5f}$$

The stationary probability distribution $\mathcal{P}(\mathbf{v},\mathbf{n},\boldsymbol{\chi})$ (Eq. (B4)) can be rewritten as

$$\mathcal{P}(\mathbf{v},\mathbf{n},\boldsymbol{\chi}) = \mathcal{P}(\mathbf{v}|\mathbf{n},\boldsymbol{\chi})\mathcal{P}(\mathbf{n},\boldsymbol{\chi})\,, \tag{B6}$$

where $\mathcal{P}(\mathbf{n},\boldsymbol{\chi})$ is the reduced probability describing the active self-propulsion and the $\mathcal{P}(\mathbf{v}|\mathbf{n},\boldsymbol{\chi})$ defines the conditional probability to find a particle at a velocity $\mathbf{v}$ with prescribed $\mathbf{n}$ and $\boldsymbol{\chi}$

$$\mathcal{P}(\mathbf{v}|\mathbf{n},\boldsymbol{\chi}) \propto \exp\left(-\frac{\big(\mathbf{v}-\langle\mathbf{v}|\mathbf{n},\boldsymbol{\chi}\rangle\big)^2}{\sigma(\mathbf{v}|\mathbf{n},\boldsymbol{\chi})}\right), \tag{B7a}$$

$$\langle\mathbf{v}|\mathbf{n},\boldsymbol{\chi}\rangle = \frac{v_0(\tau\tau_m + 2\tau_m\tau_\chi + \tau\tau_\chi)}{(\tau+\tau_m)(\tau_\chi+\tau_m)}\,\mathbf{n} - \frac{v_0\sqrt{\tau}\tau_m\tau_\chi}{(\tau+\tau_m)(\tau_\chi+\tau_m)}\,\boldsymbol{\chi}, \tag{B7b}$$

$$\sigma(\mathbf{v}|\mathbf{n},\boldsymbol{\chi}) = \frac{2D_t}{\tau_m} + \frac{v_0^2\tau_m^3(\tau+\tau_\chi)}{(\tau+\tau_m)^2(\tau_\chi+\tau_m)^2}\,. \tag{B7c}$$

The latter distribution fluctuates around the conditional average $\langle\mathbf{v}|\mathbf{n},\boldsymbol{\chi}\rangle$ of $\mathbf{v}$ at given $\mathbf{n}$ and $\boldsymbol{\chi}$ with its corresponding variance $\sigma(\mathbf{v}|\mathbf{n},\boldsymbol{\chi})$. Integration over the auxiliary process $\boldsymbol{\chi}$ yields the results stated and discussed in Sec. III B

In a similar way, the reduced probability $\mathcal{P}(\mathbf{n},\boldsymbol{\chi})$ can be expressed as

$$\mathcal{P}(\mathbf{n},\boldsymbol{\chi}) = \mathcal{P}(\mathbf{n}|\boldsymbol{\chi})\mathcal{P}(\boldsymbol{\chi}) \tag{B8}$$

with

$$\mathcal{P}(\mathbf{n}|\boldsymbol{\chi}) \propto \exp\left(-\frac{\big(\mathbf{n}-\langle\mathbf{n}|\boldsymbol{\chi}\rangle\big)^2}{\sigma(\mathbf{n}|\boldsymbol{\chi})}\right), \tag{B9a}$$

$$\langle\mathbf{n}|\boldsymbol{\chi}\rangle = \frac{\sqrt{\tau}\tau_\chi}{\tau+\tau_\chi}\boldsymbol{\chi}, \tag{B9b}$$

$$\sigma(\mathbf{n}|\boldsymbol{\chi}) = \frac{\tau}{\tau+\tau_\chi} \tag{B9c}$$

and

$$\mathcal{P}(\boldsymbol{\chi}) \propto \exp\left(-\frac{\boldsymbol{\chi}^2}{\langle\boldsymbol{\chi}^2\rangle}\right), \tag{B10a}$$

$$\langle\boldsymbol{\chi}^2\rangle = \frac{\tau+\tau_\chi}{\tau\tau_\chi}\,, \tag{B10b}$$

or alternatively

$$\mathcal{P}(\mathbf{n},\boldsymbol{\chi}) = \mathcal{P}(\boldsymbol{\chi}|\mathbf{n})\mathcal{P}(\mathbf{n}) \tag{B11}$$

with

$$\mathcal{P}(\boldsymbol{\chi}|\mathbf{n}) \propto \exp\left(-\frac{\big(\boldsymbol{\chi}-\langle\boldsymbol{\chi}|\mathbf{n}\rangle\big)^2}{\sigma(\boldsymbol{\chi}|\mathbf{n})}\right), \tag{B12a}$$

$$\langle\boldsymbol{\chi}|\mathbf{n}\rangle = \mathbf{n}/\sqrt{\tau}, \tag{B12b}$$

$$\sigma(\boldsymbol{\chi}|\mathbf{n}) = 1/\tau_\chi \tag{B12c}$$

and

$$\mathcal{P}(\mathbf{n}) \propto \exp\big(-\mathbf{n}^2\big)\,. \tag{B13}$$

The distribution $\mathcal{P}(\mathbf{v},\mathbf{n})$ (see Eq.(17)) can be derived via integration of the full probability density $\mathcal{P}(\mathbf{v},\mathbf{n},\boldsymbol{\chi})$ (see Eq.(B4)) with respect to $\boldsymbol{\chi}$.

ACKNOWLEDGMENTS

LC acknowledges support from the Alexander Von Humboldt foundation, while HL and RW acknowledge support by the Deutsche Forschungsgemeinschaft (DFG) through the SPP 2265, under grant numbers LO 418/25-1 (HL) and WI 5527/1-1 (RW).

[1] M. C. Marchetti, J. F. Joanny, S. Ramaswamy, T. B. Liverpool, J. Prost, M. Rao, and R. A. Simha, Reviews of Modern Physics **85**, 1143 (2013).
[2] J. Elgeti, R. G. Winkler, and G. Gompper, Reports on Progress in Physics **78**, 056601 (2015).
[3] C. Bechinger, R. Di Leonardo, H. Löwen, C. Reichhardt, G. Volpe, and G. Volpe, Reviews of Modern Physics **88**, 045006 (2016).
[4] G. Gompper, R. G. Winkler, T. Speck, A. Solon, C. Nardini, F. Peruani, H. Löwen, R. Golestanian, U. B. Kaupp, L. Alvarez, *et al.*, Journal of Physics: Condensed Matter **32**, 193001 (2020).
[5] C. W. Gardiner *et al.*, *Handbook of stochastic methods*, Vol. 3 (springer Berlin, 1985).
[6] M. R. Shaebani, A. Wysocki, R. G. Winkler, G. Gompper, and H. Rieger, Nature Reviews Physics **2**, 181–199 (2020).
[7] B. ten Hagen, S. van Teeffelen, and H. Löwen, Journal of Physics: Condensed Matter **23**, 194119 (2011).
[8] F. J. Sevilla and M. Sandoval, Physical Review E **91**, 052150 (2015).
[9] A. P. Solon, J. Stenhammar, R. Wittkowski, M. Kardar, Y. Kafri, M. E. Cates, and J. Tailleur, Physical Review Letters **114**, 198301 (2015).
[10] I. Petrelli, P. Digregorio, L. F. Cugliandolo, G. Gonnella, and A. Suma, The European Physical Journal E **41**, 128 (2018).
[11] L. Caprini, U. M. B. Marconi, C. Maggi, M. Paoluzzi, and A. Puglisi, Physical Review Research **2**, 023321 (2020).
[12] X.-q. Shi, G. Fausti, H. Chaté, C. Nardini, and A. Solon, Physical Review Letters **125**, 168001 (2020).
[13] J. R. Gomez-Solano and F. J. Sevilla, Journal of Statistical Mechanics: Theory and Experiment **2020**, 063213 (2020).
[14] J. Martin-Roca, R. Martinez, L. C. Alexander, A. L. Diez, D. G. Aarts, F. Alarcon, J. Ramírez, and C. Valeriani, The Journal of Chemical Physics **154**, 164901 (2021).
[15] A. R. Sprenger, C. Bair, and H. Löwen, Physical Review E **105**, 044610 (2022).
[16] I. Buttinoni, J. Bialké, F. Kümmel, H. Löwen, C. Bechinger, and T. Speck, Physical Review Letters **110**, 238301 (2013).
[17] J. Palacci, S. Sacanna, A. P. Steinberg, D. J. Pine, and P. M. Chaikin, Science **339**, 936 (2013).
[18] I. S. Aranson, Physics-Uspekhi **56**, 79 (2013).
[19] S. C. Takatori, R. De Dier, J. Vermant, and J. F. Brady, Nature Communications **7**, 10694 (2016).
[20] A. Zöttl and H. Stark, Journal of Physics: Condensed Matter **28**, 253001 (2016).
[21] D. Martin, J. O'Byrne, M. E. Cates, É. Fodor, C. Nardini, J. Tailleur, and F. van Wijland, Physical Review E **103**, 032607 (2021).
[22] L. Berthier, E. Flenner, and G. Szamel, The Journal of Chemical Physics **150**, 200901 (2019).
[23] L. Dabelow, S. Bo, and R. Eichhorn, Physical Review X **9**, 021009 (2019).
[24] F. J. Sevilla, R. F. Rodríguez, and J. R. Gomez-Solano, Physical Review E **100**, 032123 (2019).
[25] E. Woillez, Y. Kafri, and V. Lecomte, Journal of Statistical Mechanics: Theory and Experiment **2020**, 063204 (2020).
[26] X.-L. Wu and A. Libchaber, Physical Review Letters **84**, 3017 (2000).
[27] C. Maggi, M. Paoluzzi, N. Pellicciotta, A. Lepore, L. Angelani, and R. Di Leonardo, Physical Review Letters **113**, 238303 (2014).
[28] C. Maggi, M. Paoluzzi, L. Angelani, and R. Di Leonardo, Scientific Reports **7**, 17588 (2017).
[29] C. Maes, Physical Review Letters **125**, 208001 (2020).
[30] Y. Fily and M. C. Marchetti, Physical Review Letter **108**, 235702 (2012).
[31] G. Szamel, Physical Review E **90**, 012111 (2014).
[32] T. F. Farage, P. Krinninger, and J. M. Brader, Physical Review E **91**, 042310 (2015).
[33] C. Maggi, U. M. B. Marconi, N. Gnan, and R. Di Leonardo, Scientific Reports **5**, 10742 (2015).
[34] É. Fodor, C. Nardini, M. E. Cates, J. Tailleur, P. Visco, and F. van Wijland, Physical Review Letters **117**, 038103 (2016).
[35] D. Martin and T. A. de Pirey, Journal of Statistical Mechanics: Theory and Experiment **2021**, 043205 (2021).
[36] L. Caprini, A. Puglisi, and A. Sarracino, Symmetry **13**, 81 (2021).
[37] U. M. B. Marconi, N. Gnan, M. Paoluzzi, C. Maggi, and R. Di Leonardo, Scientific Reports **6**, 23297 (2016).
[38] A. Sharma, R. Wittmann, and J. M. Brader, Physical Review E **95**, 012115 (2017).
[39] R. Wittmann, C. Maggi, A. Sharma, A. Scacchi, J. M. Brader, and U. M. B. Marconi, Journal of Statistical Mechanics: Theory and Experiment **2017**, 113207 (2017).
[40] T. Speck, J. Bialké, A. M. Menzel, and H. Löwen, Physical Review Letters **112**, 218304 (2014).
[41] P. Digregorio, D. Levis, A. Suma, L. F. Cugliandolo, G. Gonnella, and I. Pagonabarraga, Physical Review Letters **121**, 098003 (2018).
[42] M. E. Cates and J. Tailleur, Annual Review of Condensed Matter Physics **6**, 219 (2015).
[43] C. B. Caporusso, P. Digregorio, D. Levis, L. F. Cugliandolo, and G. Gonnella, Physical Review Letters **125**, 178004 (2020).
[44] L. Caprini, U. M. B. Marconi, and A. Puglisi, Physical Review Letters **124**, 078001 (2020).
[45] Y.-E. Keta, R. L. Jack, and L. Berthier, Physical Review Letters **129**, 048002 (2022).
[46] G. Li and J. X. Tang, Physical Review Letters **103**, 078101 (2009).
[47] R. Ni, M. A. C. Stuart, and P. G. Bolhuis, Physical Review Letters **114**, 018302 (2015).
[48] R. Wittmann and J. M. Brader, EPL (Europhysics Letters) **114**, 68004 (2016).
[49] R. Wittmann, F. Smallenburg, and J. M. Brader, The Journal of Chemical Physics **150**, 174908 (2019).
[50] F. Turci and N. B. Wilding, Physical Review Letters **127**, 238002 (2021).
[51] S. Das, G. Gompper, and R. G. Winkler, New Journal of Physics **20**, 015001 (2018).
[52] L. Caprini, E. Hernández-García, C. López, and U. M. B. Marconi, Scientific Reports **9**, 16687 (2019).

[53] L. Caprini, A. R. Sprenger, H. Löwen, and R. Wittmann, The Journal of Chemical Physics **156**, 071102 (2022).
[54] A. Cavagna and I. Giardina, Annual Review of Condensed Matter Physics **5**, 183 (2014).
[55] D. Pavlov, A. Kasumyan, *et al.*, Journal of Ichthyology **40**, S163 (2000).
[56] H. Mukundarajan, T. C. Bardon, D. H. Kim, and M. Prakash, Journal of Experimental Biology **219**, 752 (2016).
[57] O. Feinerman, I. Pinkoviezky, A. Gelblum, E. Fonio, and N. S. Gov, Nature Physics **14**, 683 (2018).
[58] R. N. Valani, A. C. Slim, and T. Simula, Physical Review Letters **123**, 024503 (2019).
[59] J. Rabault, R. A. Fauli, and A. Carlson, Physical Review Letters **122**, 024501 (2019).
[60] C. A. Weber, T. Hanke, J. Deseigne, S. Léonard, O. Dauchot, E. Frey, and H. Chaté, Physical Review Letters **110**, 208001 (2013).
[61] N. Koumakis, A. Gnoli, C. Maggi, A. Puglisi, and R. Di Leonardo, New Journal of Physics **18**, 113046 (2016).
[62] C. Scholz, M. Engel, and T. Pöschel, Nature Communications **9**, 931 (2018).
[63] O. Dauchot and V. Démery, Physical Review Letters **122**, 068002 (2019).
[64] M. Leoni, M. Paoluzzi, S. Eldeen, A. Estrada, L. Nguyen, M. Alexandrescu, K. Sherb, and W. W. Ahmed, Physical Review Research **2**, 043299 (2020).
[65] H. Soni, N. Kumar, J. Nambisan, R. K. Gupta, A. Sood, and S. Ramaswamy, Soft Matter **16**, 7210 (2020).
[66] P. Baconnier, D. Shohat, C. Hernandèz, C. Coulais, V. Démery, G. Düring, and O. Dauchot, Nature Physics **18**, 1234 (2022).
[67] H. Löwen, The Journal of Chemical Physics **152**, 040901 (2020).
[68] M. Joyeux and E. Bertin, Physical Review E **93**, 032605 (2016).
[69] B.-Q. Ai and F.-G. Li, Soft Matter **13**, 2536 (2017).
[70] S. Shankar and M. C. Marchetti, Physical Review E **98**, 020604 (2018).
[71] S. Mandal, B. Liebchen, and H. Löwen, Physical Review Letters **123**, 228001 (2019).
[72] C. G. Wagner, M. F. Hagan, and A. Baskaran, Physical Review E **100**, 042610 (2019).
[73] H. D. Vuijk, J.-U. Sommer, H. Merlitz, J. M. Brader, and A. Sharma, Physical Review Research **2**, 013320 (2020).
[74] V. Holubec and R. Marathe, Physical Review E **102**, 060101 (2020).
[75] J. M. Martins and R. Wittkowski, arXiv preprint arXiv:2206.01960 (2022).
[76] F. Cecconi, A. Puglisi, A. Sarracino, and A. Vulpiani, Journal of Physics: Condensed Matter **30**, 264002 (2018).
[77] J. S. Lee, J.-M. Park, and H. Park, Physical Review E **100**, 062132 (2019).
[78] L. Caprini and U. Marini Bettolo Marconi, The Journal of Chemical Physics **154**, 024902 (2021).
[79] G. H. P. Nguyen, R. Wittmann, and H. Löwen, Journal of Physics: Condensed Matter **34**, 035101 (2021).
[80] K. Goswami, Physical Review E **105**, 044123 (2022).
[81] D. Frydel, arXiv preprint arXiv:2211.02082 (2022).
[82] D. Breoni, M. Schmiedeberg, and H. Löwen, Physical Review E **102**, 062604 (2020).
[83] M. Feng and Z. Hou, The Journal of Chemical Physics (2022).
[84] C. Dai, I. R. Bruss, and S. C. Glotzer, Soft Matter **16**, 2847 (2020).
[85] J. Su, H. Jiang, and Z. Hou, New Journal of Physics **23**, 013005 (2021).
[86] A. K. Omar, K. Klymko, T. GrandPre, P. L. Geissler, and J. F. Brady, arXiv preprint arXiv:2108.10278 (2021).
[87] S. De Karmakar and R. Ganesh, Physical Review E **101**, 032121 (2020).
[88] J.-j. Liao, F.-j. Lin, and B.-q. Ai, Physica A: Statistical Mechanics and its Applications **582**, 126251 (2021).
[89] G. Negro, C. B. Caporusso, P. Digregorio, G. Gonnella, A. Lamura, and A. Suma, The European Physical Journal E **45**, 75 (2022).
[90] L. Caprini and U. M. B. Marconi, Soft Matter **17**, 4109 (2021).
[91] L. Caprini, C. Maggi, and U. Marini Bettolo Marconi, The Journal of Chemical Physics **154**, 244901 (2021).
[92] U. M. B. Marconi, L. Caprini, and A. Puglisi, New Journal of Physics **23**, 103024 (2021).
[93] C. Scholz, S. Jahanshahi, A. Ldov, and H. Löwen, Nature Communications **9**, 5156 (2018).
[94] E. Crosato, M. Prokopenko, and R. E. Spinney, Physical Review E **100**, 042613 (2019).
[95] L. L. Gutierrez-Martinez and M. Sandoval, The Journal of Chemical Physics **153**, 044906 (2020).
[96] P. Herrera and M. Sandoval, Physical Review E **103**, 012601 (2021).
[97] A. R. Sprenger, S. Jahanshahi, A. V. Ivlev, and H. Löwen, Physical Review E **103**, 042601 (2021).
[98] L. Hecht, S. Mandal, H. Löwen, and B. Liebchen, Physical Review Letters **129**, 178001 (2022).
[99] L. Caprini, R. K. Gupta, and H. Löwen, Physical Chemistry Chemical Physics **24**, 24910 (2022).
[100] S. De Karmakar, A. Chugh, and R. Ganesh, Scientific Reports **12**, 22563 (2022).
[101] M. Te Vrugt, J. Jeggle, and R. Wittkowski, New Journal of Physics **23**, 063023 (2021).
[102] D. Arold and M. Schmiedeberg, arXiv preprint arXiv:2001.07948 (2020).
[103] E. Lisin, O. Vaulina, I. Lisina, and O. Petrov, Physical Chemistry Chemical Physics (2022).
[104] The recursive exponential decay of the orientational correlation function of the ABP, Eq. (5), is sometimes also referred to as double-exponential decay. Here, we choose a different terminology to avoid confusion with the additive exponential decay of the orientational correlation function of the AOUP, Eq. (14), which one could also refer to as double-exponential decay.
[105] M. Caraglio and T. Franosch, Physical Review Letters **129**, 158001 (2022).
[106] P. Jung and P. Hänggi, Physical Review A **35**, 4464 (1987).
[107] P. Hänggi and P. Jung, Advances in Chemical Physics **89**, 239 (1995).
[108] L. Caprini, F. Cecconi, and U. Marini Bettolo Marconi, The Journal of Chemical Physics **155**, 234902 (2021).
[109] R. F. Fox, Physical Review A **33**, 467 (1986).
[110] R. F. Fox, Physical Review A **34**, 4525 (1986).

[111] E. Tjhung, C. Nardini, and M. E. Cates, Physical Review X **8**, 031080 (2018).
[112] G. Fausti, E. Tjhung, M. Cates, and C. Nardini, Physical Review Letters **127**, 068001 (2021).
[113] C. Tung, J. Harder, C. Valeriani, and A. Cacciuto, Soft Matter **12**, 555 (2016).
[114] A. K. Omar, H. Row, S. A. Mallory, and J. F. Brady, arXiv preprint arXiv:2211.12673 (2022).
[115] T. Speck, A. M. Menzel, J. Bialké, and H. Löwen, The Journal of Chemical Physics **142**, 224109 (2015).

P8 Towards an analytical description of active microswimmers in clean and in surfactant-covered drops

Reproduced from

A. R. Sprenger, V. A. Shaik, A. M. Ardekani, M. Lisicki, A. J. T. M. Mathijssen, F. Guzmán-Lastra, H. Löwen, A. M. Menzel, and A. Daddi-Moussa-Ider,
Towards an analytical description of active microswimmers in clean and in surfactant-covered drops,
Eur. Phys. J. E **43**, 58 (2020),
published by *EDP Sciences, Società Italiana di Fisica and Springer Berlin Heidelberg* [295].

Digital Object Identifier (DOI): doi.org/10.1140/epje/i2020-11980-9

Statement of contribution

A.D.M.I. conceived the study and prepared the figures. A.R.S. and A.D.M.I. carried out the analytical calculations. V.A.S., M.L., and A.D.M.I. drafted the manuscript. All authors discussed and interpreted the results, edited the text, and finalized the manuscript.

Copyright and license notice

©The Author(s), 2020.
This is an Open Access article, distributed under the terms of the Creative Commons Attribution licence (http://creativecommons.org/licenses/by/4.0/), which permits unrestricted re-use, distribution, and reproduction in any medium, provided the original work is properly cited

Eur. Phys. J. E (2020) **43**: 58
DOI 10.1140/epje/i2020-11980-9

THE EUROPEAN PHYSICAL JOURNAL E

Regular Article

Towards an analytical description of active microswimmers in clean and in surfactant-covered drops*

Alexander R. Sprenger[1,a], Vaseem A. Shaik[2], Arezoo M. Ardekani[2], Maciej Lisicki[3], Arnold J.T.M. Mathijssen[4,5], Francisca Guzmán-Lastra[6], Hartmut Löwen[1], Andreas M. Menzel[7], and Abdallah Daddi-Moussa-Ider[1,b]

[1] Institut für Theoretische Physik II: Weiche Materie, Heinrich-Heine-Universität Düsseldorf, Universitätsstraße 1, D-40225 Düsseldorf, Germany
[2] School of Mechanical Engineering, Purdue University, West Lafayette, IN 47907, USA
[3] Institute of Theoretical Physics, Faculty of Physics, University of Warsaw, Pasteura 5, 02-093 Warsaw, Poland
[4] Department of Bioengineering, Stanford University, 443 Via Ortega, Stanford, CA 94305, USA
[5] Department of Physics and Astronomy, University of Pennsylvania, 209 South 33rd Street, Philadelphia, PA 19104, USA
[6] Centro de Investigación DAiTA Lab, Facultad de Estudios Interdisciplinarios, Universidad Mayor, Av. Manuel Montt 367, Providencia, Santiago de Chile, Chile
[7] Institut für Physik, Otto-von-Guericke-Universität Magdeburg, Universitätsplatz 2, 39106 Magdeburg, Germany

Received 29 May 2020 / Received in final form 3 August 2020 / Accepted 10 August 2020
Published online: 11 September 2020
© The Author(s) 2020. This article is published with open access at Springerlink.com

Abstract. Geometric confinements are frequently encountered in the biological world and strongly affect the stability, topology, and transport properties of active suspensions in viscous flow. Based on a far-field analytical model, the low-Reynolds-number locomotion of a self-propelled microswimmer moving inside a clean viscous drop or a drop covered with a homogeneously distributed surfactant, is theoretically examined. The interfacial viscous stresses induced by the surfactant are described by the well-established Boussinesq-Scriven constitutive rheological model. Moreover, the active agent is represented by a force dipole and the resulting fluid-mediated hydrodynamic couplings between the swimmer and the confining drop are investigated. We find that the presence of the surfactant significantly alters the dynamics of the encapsulated swimmer by enhancing its reorientation. Exact solutions for the velocity images for the Stokeslet and dipolar flow singularities inside the drop are introduced and expressed in terms of infinite series of harmonic components. Our results offer useful insights into guiding principles for the control of confined active matter systems and support the objective of utilizing synthetic microswimmers to drive drops for targeted drug delivery applications.

1 Introduction

Controlled locomotion of nano- and micro-scale objects in viscous media is of considerable importance in many areas of engineering and science [1]. Synthetic nano- and micro-motors hold significant promise for future biotechnological and medical applications such as precise assembly of materials [2–8], non-invasive microsurgery [9–11], targeted drug delivery [12–16], and biosensing [17]. Over the last few decades, there has been a rapidly mounting interest among researchers in understanding and unveiling the physics of self-propelled active particles and microswimmers, see refs. [18–28] for recent reviews. Various intriguing effects of collective behavior are displayed and fascinating self-organized spatiotemporal patterns are created by the mutual interaction of many active agents. Notable examples include the formation of propagating density waves [29–31], the emergence of mesoscale turbulence [32–39], the motility-induced phase separation [40–48], and lane formation [49–55].

In many biologically and technologically relevant situations, actively swimming biological microorganisms and artificial self-driven particles are present. Typically, they function and survive in confined environments which are known to strongly affect their swimming and propulsion behavior as well as the transport properties in viscous media. Examples include *Bacillus subtilis* in soil [56, 57], *Escherichia coli* in intestines [58, 59], pathogenic bacteria in microvasculature [60], and spermatozoa navigation through the mammalian female reproductive tract [61–63].

* Contribution to the Topical Issue "Motile Active Matter" edited by Gerhard Gompper, Clemens Bechinger, Roland G. Winkler, Holger Stark.

[a] e-mail: sprenger@thphy.uni-duesseldorf.de
[b] e-mail: ider@thphy.uni-duesseldorf.de

Geometric confinement caused by a plane rigid or fluid interface affects the dynamics of microswimmers by altering their speed and orientation with respect to the interface [64–90] and changing their swimming trajectories from straight lines in a bulk fluid to circular shapes near interfaces [91–96]. Studies of the dynamics of microswimmers in a microchannel bounded by two interfaces [97–101] or immersed in a thin liquid film [102–104] or spherical cavity [105] revealed complex evolution scenarios of microswimmers in the presence of narrow confinement [106].

Curved boundaries strongly affect the stability and topology of active suspensions under confinement and drive self-organization in a wide class of active matter systems [107–109]. For instance, a dense aqueous suspension of *Bacillus subtilis* confined inside a viscous drop self-organizes into a stable spiral vortex surrounded by a counter-rotating boundary layer of motile cells [107, 110]. In addition, a sessile drop containing photocatalytic particles exhibits a transition to a collective behavior leading to self-organized flow patterns [111]. Under the effect of an external magnetic field, swimming magnetotactic bacteria confined into water-in-oil drops can self-assemble into a rotary motor that exerts a net torque on the surrounding oil phase [112, 113]. In microfluidic systems, synthetic microswimmers, such as artificial bacterial flagella, are frequently used to drive drops in the context of targeted drug delivery systems [114, 115]. Along these lines, nontrivial dynamics of a particle-encapsulating drop in shear flow were revealed [116]. To understand the self-organization or the energy transport from the swimmer scale to the system scale or to develop efficient and reliable drug delivery systems, we need to unravel the physics underlying the dynamics of a motile microorganism encapsulated inside drop. This is the focus of the present work, concentrating on clean drops or those covered by a surfactant.

The swimming dynamics in the vicinity of a rigid spherical obstacle [117–119], a clean or a surfactant-covered drop [120–122] have been investigated theoretically. It has been demonstrated that a swimming organism reorients itself and gets scattered from the obstacle or gets trapped or captured by it if the size of the obstacle is large enough and the settling/rising speed of the microorganism is small enough. Near a viscous drop, the surfactant increases the trapping capability [120] and can even break the kinematic reversibility associated with the inertialess realm of swimming microorganisms [123]. In contrast to that, the presence of a surfactant near a planar interface was found not to change the reorientation dynamics [74] but to change the swimming speed [124] in addition to the circling direction [74].

In the theoretical investigation of locomotion under confinement, swimming microorganisms are commonly approximated by microswimmer models, frequently using a far-field representation based on higher-order flow singularities [18]. Well-established model microswimmers include Taylor's swimming sheet [125–129] and the spherical squirmer [130–143]. The former is a good representation of the tail of human spermatozoa and *Caenorhabditis elegans* while the latter is believed to describe well the behavior of *Paramecium*, *Opalina*, and *Volvox*. Linked spheres that are able to propel forward when the mutual distance between the spheres is varied in a nonreciprocal fashion constitute another class of model microswimmers [144–151]. Moreover, various minimal model microswimmers have been proposed to model swimming agents with rigid bodies and flexible propelling appendages [152–159]. Many of the organisms are approximately neutrally buoyant, so they hardly experience any gravitational force or torque. This implies that the action of a swimming organism in far-field representation can conveniently be described by a force dipole and higher-order singularities to investigate its motion under confinement. The accuracy of this simple far-field analysis was verified by comparison with other theoretical and fully resolved computer simulations [70, 103, 160]. In particular, the far-field analysis was shown to predict and reproduce experimental and numerical observations [66, 74, 104, 118]. This motivates us to employ the far-field representation to examine the swimming behavior inside a clean or surfactant-covered viscous drop.

Theoretically, one of the first studies of low-Reynolds-number locomotion inside a drop considered a spherical squirmer encapsulated inside a drop of a comparable size immersed in an otherwise quiescent viscous medium [161, 162]. The analytical theory was complemented and supplemented by numerical implementations based on a boundary element method [163]. It was reported that the drop can be propelled by the encaged swimmer, and in some situations the swimmer-drop composite remains in a stable co-swimming state so that the swimmer and drop maintain a concentric configuration and move with the same velocity [161]. Meanwhile, the presence of a surfactant on the surface of the drop was found to increase or decrease the squirmer or drop velocities depending on the precise location of the swimmer inside the confining drop [123]. In the presence of a shear flow, it was demonstrated that the activity of a squirmer inside a drop can significantly enhance or reduce the deformation of the drop depending on the orientation of the swimmer [164]. More recently, the dynamics of a drop driven by an internal active device composed of a three-point-force moving on a prescribed track was examined [165, 166].

The dynamics of a squirmer inside a drop is not analytically tractable for arbitrary positions and orientations of the swimmer. Therefore, recourse to numerical techniques is generally necessary to obtain a complete understanding of the low-Reynolds-number locomotion [161]. However, when keeping all details, these methods are not easily extensible to the case of multiple swimmers. To deal with these limitations, the swimming organism can be modeled in the far-field limit under confinement using the classical method of images [167, 168]. The latter has the advantage of being easily extensible to the case of a drop containing many active and hydrodynamically interacting organisms in the dilute suspension limit. In this context, an image system for a point force bounded by a rigid spherical container has previously been reported [169–176]. Nevertheless, image systems for force dipoles or higher-order singularities bounded by a spherical fluid interface possibly covered by a surfactant are still missing.

In the present contribution, we derive the image solution for a point force (Stokeslet) and dipole singularities inside a spherical drop, both with a clean surface, or covered by a surfactant. We model the interfacial viscous stresses at the surfactant-covered drop boundary by the well-established Boussinesq-Scriven rheological constitutive model [177]. Our approach is based on the method originally introduced by Fuentes *et al.* [178,179], who derived the solution for a Stokeslet acting outside a clean viscous drop. An analogous approach was employed by some of us to derive the Stokeslet solution near [180,181] or inside [182,183] a spherical elastic object, and outside a surfactant-covered drop [184]. We find that the presence of the surfactant alters the swimming behavior of the encaged microswimmer by enhancing its rate of rotation.

We organize the remainder of the paper as follows. In sect. 2, we derive the solution for the viscous flow field induced by an axisymmetric or transverse Stokeslet acting inside a clean and a surfactant-covered drop. We then use this flow field in sect. 3 to obtain the corresponding image solution for a force-dipole singularity of arbitrary location and orientation within the spherical drop. In sect. 4, we derive the induced translational and rotational velocities resulting from hydrodynamic couplings in the present geometry. Finally, concluding remarks are contained in sect. 5 and technical details are shifted to appendices A and B.

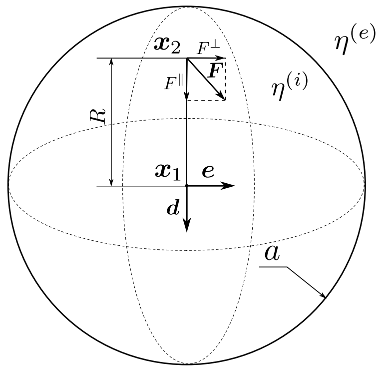

Fig. 1. Schematic illustration of the system setup. A point-force singularity of strength $\boldsymbol{F}$ is acting at the position $\boldsymbol{x}_2$ inside a spherical viscous drop of radius a. The origin of the system of coordinates coincides with the center of the drop $\boldsymbol{x}_1$. We denote the distance between the origin and the position of the singularity as R. The viscosities inside and outside the drop are designated as $\eta^{(i)}$ and $\eta^{(e)}$, respectively. For an arbitrary orientation, the point force is decomposed into an axisymmetric component $F^{\parallel}$ directed along the unit vector $\boldsymbol{d}$ and an transverse component $F^{\perp}$ pointing along the unit vector $\boldsymbol{e}$. Without loss of generality, the point force is taken to be located on the z-axis, with components along z and x directions, where $\boldsymbol{d} = -\hat{\boldsymbol{z}}$ and $\boldsymbol{e} = \hat{\boldsymbol{x}}$.

2 Monopole singularity

We derive the solution of the viscous incompressible flow induced by a point-force singularity of strength $\boldsymbol{F}$ acting at position $\boldsymbol{x}_2$ inside a viscous drop of radius a. The origin of the system of coordinates is located at position $\boldsymbol{x}_1$, the center of the viscous drop. We denote by $\boldsymbol{r} = \boldsymbol{x} - \boldsymbol{x}_1$ the position vector and by $r := |\boldsymbol{r}|$ the radial distance from the origin. Moreover, we refer by $\eta^{(i)}$ and $\eta^{(e)}$ to the dynamic viscosities of the Newtonian fluids inside and outside the drop, respectively. Next, we define the unit vector $\boldsymbol{d} = (\boldsymbol{x}_1 - \boldsymbol{x}_2)/R$ with $R = |\boldsymbol{x}_1 - \boldsymbol{x}_2|$ denoting the distance between the singularity position and the origin. In addition, we define the unit vector $\boldsymbol{e}$ orthogonal to $\boldsymbol{d}$ so that the force $\boldsymbol{F}$ can be decomposed into an axisymmetric component $F^{\parallel}\boldsymbol{d}$ and a transverse component $F^{\perp}\boldsymbol{e}$. See fig. 1 for an illustration of the system setup.

In the remainder of this article, we rescale all lengths by the radius a of the drop. We will denote by superscripts (i) and (e) quantities referring to the inside and outside of the drop, respectively. The problem of finding the incompressible hydrodynamic flow is thus equivalent to solving the singularly forced Stokes equations [185] for the fluid inside the drop

$$\eta^{(i)}\boldsymbol{\nabla}^2\boldsymbol{v}^{(i)} - \boldsymbol{\nabla}p^{(i)} + \boldsymbol{F}\delta\left(\boldsymbol{x} - \boldsymbol{x}_2\right) = \boldsymbol{0}, \tag{1a}$$

$$\boldsymbol{\nabla}\cdot\boldsymbol{v}^{(i)} = 0 \tag{1b}$$

for $r < 1$, and the homogeneous Stokes equations for the fluid outside the drop

$$\eta^{(e)}\boldsymbol{\nabla}^2\boldsymbol{v}^{(e)} - \boldsymbol{\nabla}p^{(e)} = \boldsymbol{0}, \tag{2a}$$

$$\boldsymbol{\nabla}\cdot\boldsymbol{v}^{(e)} = 0 \tag{2b}$$

for $r > 1$, wherein $\boldsymbol{v}^{(q)}$ and $p^{(q)}, q \in \{i, e\}$, denote the corresponding fluid-velocity and pressure fields, respectively. We focus on the small-deformation regime concerning the shape of the drop so that deviations from sphericity are assumed to be negligible. Moreover, we first assume the drop to be stationary. This implies that it is held fixed in space, for instance by means of optical tweezers [186]. Accordingly, the radial component of the fluid-velocity field at the surface of the stationary drop is assumed to vanish in the frame of reference associated with the viscous drop.

Under these assumptions, eqs. (1) and (2) are subject to the regularity conditions

$$|\boldsymbol{v}^{(i)}| < \infty \quad \text{for } r \to 0,\ \boldsymbol{v}^{(e)} \to \boldsymbol{0} \text{ as } r \to \infty, \tag{3}$$

in addition to the boundary conditions imposed at the surface of the stationary drop at $r = 1$,

$$v_r^{(i)} = v_r^{(e)} = 0, \tag{4a}$$

$$\boldsymbol{v}_{\mathrm{S}} := \boldsymbol{\Pi}\cdot\boldsymbol{v}^{(i)} = \boldsymbol{\Pi}\cdot\boldsymbol{v}^{(e)}, \tag{4b}$$

where $\boldsymbol{\Pi} = \boldsymbol{1} - \boldsymbol{e}_r\boldsymbol{e}_r$ is the projection operator, with $\boldsymbol{1}$ denoting the identity tensor, and $\boldsymbol{v}_{\mathrm{S}}$ is the tangential velocity. Equation (4a) represents the kinematic condition stating that the drop remains undeformed whereas eq. (4b) stands for the natural continuity of the tangential velocities across the surface of the drop.

On the one hand, for a clean drop, *i.e.*, without surfactant, shear elasticity, or bending rigidity, the tangential hydrodynamic stresses across the surface of the drop are continuous [187]. Then,

$$\boldsymbol{\Pi} \cdot \left(\boldsymbol{T}^{(i)} - \boldsymbol{T}^{(e)} \right) = \boldsymbol{0}, \tag{5}$$

where $\boldsymbol{T}^{(q)} = \boldsymbol{\sigma}^{(q)} \cdot \boldsymbol{e}_r$ with $\boldsymbol{\sigma}^{(q)}$, $q \in \{i, e\}$, denoting the hydrodynamic viscous stress tensor.

On the other hand, to model the surfactant-covered drop, we use the boundary conditions [184]

$$\boldsymbol{\nabla}_{\mathrm{S}} \cdot \boldsymbol{v}_{\mathrm{S}} = 0, \tag{6a}$$

$$\boldsymbol{\Pi} \cdot \left(\boldsymbol{T}^{(i)} - \boldsymbol{T}^{(e)} \right) = \boldsymbol{\nabla}_{\mathrm{S}} \gamma + \boldsymbol{\nabla}_{\mathrm{S}} \cdot \boldsymbol{\tau}_{\mathrm{S}}, \tag{6b}$$

where γ denotes the interfacial tension, $\boldsymbol{\nabla}_{\mathrm{S}} = \boldsymbol{\Pi} \cdot \boldsymbol{\nabla}$ is the surface gradient operator, and $\boldsymbol{\tau}_{\mathrm{S}}$ is the interfacial viscous stress tensor. Using the Boussinesq-Scriven constitutive law we have [184]

$$\boldsymbol{\nabla}_{\mathrm{S}} \cdot \boldsymbol{\tau}_{\mathrm{S}} = \eta_{\mathrm{S}} \left(\frac{2\boldsymbol{v}_{\mathrm{S}}}{r^2} + \frac{1}{r \sin\theta} \frac{\partial \varpi}{\partial \phi} \, \boldsymbol{e}_\theta - \frac{1}{r} \frac{\partial \varpi}{\partial \theta} \, \boldsymbol{e}_\phi \right), \tag{7}$$

wherein θ and ϕ, respectively, denote the polar and azimuthal angles in the system of spherical coordinates attached to the center of the drop, η_{S} denotes the interfacial shear viscosity, which we assume to be constant, and

$$\varpi = \frac{1}{r \sin\theta} \left(\frac{\partial v_\theta}{\partial \phi} - \frac{\partial}{\partial \theta} \left(v_\phi \sin\theta \right) \right). \tag{8}$$

Equation (6a) represents the transport equation for an insoluble, non-diffusing, incompressible, and homogeneously distributed surfactant [184, 188], which may be rewritten as

$$\frac{\partial v_{\mathrm{S}\phi}}{\partial \phi} + \frac{\partial}{\partial \theta} \left(v_{\mathrm{S}\theta} \sin\theta \right) = 0. \tag{9}$$

We note that the tangential components of the viscous stress vector are expressed in the usual way as

$$T_\theta^{(q)} = \eta^{(q)} \left(\frac{\partial v_\theta^{(q)}}{\partial r} + \frac{1}{r} \left(\frac{\partial v_r^{(q)}}{\partial \theta} - v_\theta^{(q)} \right) \right), \tag{10a}$$

$$T_\phi^{(q)} = \eta^{(q)} \left(\frac{\partial v_\phi^{(q)}}{\partial r} + \frac{1}{r} \left(\frac{1}{\sin\theta} \frac{\partial v_r^{(q)}}{\partial \phi} - v_\phi^{(q)} \right) \right), \tag{10b}$$

for $q \in \{i, e\}$.

To solve the Stokes equations (1) and (2), we write the solution for the fluid flow inside the drop as a sum of two contributions

$$\boldsymbol{v}^{(i)} = \boldsymbol{v}^{\mathrm{S}} + \boldsymbol{v}^*, \tag{11}$$

wherein $\boldsymbol{v}^{\mathrm{S}}$ denotes the velocity field induced by a point-force singularity in an unbounded bulk medium of viscosity $\eta^{(i)}$, *i.e.*, in the case of an infinitely extended drop, and $\boldsymbol{v}^*$ is the auxiliary solution (also known as the image or reflected flow field) that is required to satisfy the above regularity and boundary conditions.

We now sketch briefly the main steps of the resolution procedure. First, the fluid velocity induced by the free-space Stokeslet $\boldsymbol{v}^{\mathrm{S}}$ for an infinitely large drop is expressed in terms of harmonic functions based at $\boldsymbol{x}_2$, which are subsequently transformed into harmonics based at $\boldsymbol{x}_1$ by means of the Legendre expansion [189]. Second, the image solution $\boldsymbol{v}^*$ as well as the flow field outside the cavity $\boldsymbol{v}^{(e)}$ are, respectively, expressed in terms of interior and exterior harmonics based at $\boldsymbol{x}_1$. To this end, we make use of Lamb's general solution of Stokes flows in a spherical domain [190–192]. Finally, the unknown series expansion coefficients associated with each fluid domain are determined by satisfying the boundary conditions prescribed at the surface of the drop.

Thanks to the linearity of the Stokes equations, the Green's function for a point force directed along an arbitrary direction in space can be obtained by linear superposition of the solutions for the axisymmetric and transverse problems [171]. In the following, we detail the derivation of the solution for these two problems independently.

2.1 Axisymmetric Stokeslet

The velocity field induced by a free-space Stokeslet located at $\boldsymbol{x}_2$ is expressed in terms of the Oseen tensor as

$$\boldsymbol{v}^{\mathrm{S}} = \boldsymbol{\mathcal{G}}(\boldsymbol{x}-\boldsymbol{x}_2) \cdot \boldsymbol{F} = \frac{1}{8\pi\eta^{(i)}} \left(\frac{\boldsymbol{1}}{s} + \boldsymbol{s} \boldsymbol{\nabla}_2 \left(\frac{1}{s} \right) \right) \cdot \boldsymbol{F}, \tag{12}$$

where $\boldsymbol{s} = \boldsymbol{x} - \boldsymbol{x}_2$, $s = |\boldsymbol{s}|$, and $\boldsymbol{\nabla}_2 = \partial / \partial \boldsymbol{x}_2$ stands for the partial derivative with respect to the singularity position. The details of derivation have previously been reported by some of us in ref. [182], and will thus be omitted here. As shown there, the free-space Stokeslet for an axisymmetric point force $\boldsymbol{F} = F^\parallel \boldsymbol{d}$ can be expanded in terms of an infinite series of harmonics centered at $\boldsymbol{x}_1$ via the Legendre expansion as

$$8\pi\eta^{(i)} \boldsymbol{v}^{\mathrm{S}} = F^\parallel \sum_{n=1}^{\infty} \left(\alpha_n \boldsymbol{\nabla} \varphi_n - \frac{2(n+1)}{2n-1} \, \boldsymbol{r} \varphi_n \right) R^{n-1}, \tag{13}$$

wherein

$$\alpha_n = \frac{n-2}{2n-1} \, r^2 - \frac{n}{2n+3} \, R^2, \tag{14}$$

and φ_n are harmonics of degree n, that are related to the Legendre polynomials of degree n via [193]

$$\varphi_n(r, \theta) = \frac{(\boldsymbol{d} \cdot \boldsymbol{\nabla})^n}{n!} \frac{1}{r} = r^{-(n+1)} \, P_n(\cos\theta). \tag{15}$$

In addition, the image solution inside the drop can readily be determined from Lamb's general solution [191, 194], and can conveniently be expressed in terms of *interior* harmonics based at $\boldsymbol{x}_1$ as [182]

$$8\pi\eta^{(i)} \boldsymbol{v}^* = F^\parallel \sum_{n=1}^{\infty} \left(A_n^\parallel \boldsymbol{S}_n^{(1)} + B_n^\parallel \boldsymbol{S}_n^{(2)} \right), \tag{16}$$

where we have defined the vector functions

$$\boldsymbol{S}_n^{(1)} = \frac{1}{2} \big((n+3) r^2 \, \boldsymbol{\nabla} \varphi_n + (n+1)(2n+3) \boldsymbol{r} \varphi_n \big) r^{2n+1}, \tag{17a}$$

$$\boldsymbol{S}_n^{(2)} = \big(r^2 \boldsymbol{\nabla} \varphi_n + (2n+1) \boldsymbol{r} \varphi_n \big) r^{2n-1}. \tag{17b}$$

The total flow field inside the drop is obtained by summing both contributions stated by eqs. (13) and (16), while the series coefficients $A_n^{\parallel}$ and $B_n^{\parallel}$ remain to be determined.

Next, the solution of the flow problem outside the drop can likewise be obtained using Lamb's general solution, and can be expressed in terms of *exterior* harmonics based at $\boldsymbol{x}_1$ as [182]

$$8\pi\eta^{(i)}\boldsymbol{v}^{(e)} = F^{\parallel} \sum_{n=1}^{\infty} \left(a_n^{\parallel} \boldsymbol{\Phi} + b_n^{\parallel} \boldsymbol{\nabla}\varphi_n \right), \tag{18}$$

where

$$\boldsymbol{\Phi} = (n+1)\, \boldsymbol{r}\varphi_n - \frac{n-2}{2}\, r^2\, \boldsymbol{\nabla}\varphi_n. \tag{19}$$

It is worth noting that, for the ease of matching the boundary conditions at the surface of the drop, we have chosen to rescale the exterior velocity field given by eq. (18) by $8\pi\eta^{(i)}$ rather than by $8\pi\eta^{(e)}$.

Having expressed the velocity field on both sides of the drop in terms of harmonics based at the origin, we next determine the unknown series coefficients $\{A_n^{\parallel}, B_n^{\parallel}\}$ and $\{a_n^{\parallel}, b_n^{\parallel}\}$. By applying the boundary conditions prescribed at the surface of the drop, given by eqs. (4) and (5) for a clean drop, and by eqs. (4) and (6) for a surfactant-covered drop, and using the fact that $\boldsymbol{\nabla}\varphi_n$ and $\boldsymbol{r}\varphi_n$ form a set of orthogonal vector harmonics, we obtain a system of linear equations. Its solution yields the expressions of the series coefficients associated with the solution of the flow field inside and outside the drop. Further details of derivation are shifted to appendix A. For a clean drop, the coefficients are given by

$$A_n^{\parallel} = \left(\Lambda - 1 + \left(\frac{2n+1}{2n+3} - \Lambda \right) R^2 \right) R^{n-1}, \tag{20a}$$

$$B_n^{\parallel} = \frac{n+1}{2} \left(\frac{2n+1}{2n-1} - \Lambda + (\Lambda - 1)\, R^2 \right) R^{n-1}, \tag{20b}$$

$$a_n^{\parallel} = \Lambda \left(1 - R^2 \right) R^{n-1}, \tag{20c}$$

$$b_n^{\parallel} = \frac{\Lambda n}{2} \left(1 - R^2 \right) R^{n-1}, \tag{20d}$$

where we have defined for convenience the dimensionless number $\Lambda = \lambda/(1+\lambda)$ with $\lambda = \eta^{(i)}/\eta^{(e)}$ denoting the viscosity contrast. Accordingly, Λ vanishes in the rigid-cavity limit (*e.g.* water drop in extremely viscous oil) and approaches one for drops with a large viscosity compared to the external medium (*e.g.* water drop in air).

For a surfactant-covered drop, it follows from eq. (9) that the surface velocity vanishes in the axisymmetric case. Accordingly, the solution of the axisymmetric flow problem for a Stokeslet acting inside a viscous drop covered with a non-diffusing, insoluble, and incompressible layer of surfactant is identical to that inside a rigid spherical cavity ($\Lambda = 0$). Specifically,

$$A_n^{\parallel} = \left(\frac{2n+1}{2n+3}\, R^2 - 1 \right) R^{n-1}, \tag{21a}$$

$$B_n^{\parallel} = \frac{n+1}{2} \left(\frac{2n+1}{2n-1} - R^2 \right) R^{n-1}, \tag{21b}$$

$$a_n^{\parallel} = b_n^{\parallel} = 0. \tag{21c}$$

It is worth mentioning that analogous behavior has been found for a Stokeslet acting near a planar interface covered with surfactant [195] and for a Stokeslet acting outside a surfactant-covered drop [184].

2.2 Transverse Stokeslet

We proceed in an analogous way as in the axisymmetric case and express the velocity field on both sides of the drop in terms of harmonics based at $\boldsymbol{x}_1$. As demonstrated in detail in ref. [183], the free-space Stokeslet solution for a transverse point force $\boldsymbol{F} = F^{\perp}\boldsymbol{e}$ acting at the position $\boldsymbol{x}_2$ can be written via Legendre expansion as an infinite series as

$$8\pi\eta^{(i)}\boldsymbol{v}^{\mathrm{S}} = F^{\perp} \sum_{n=1}^{\infty} \left(\beta_n \boldsymbol{\nabla}\psi_{n-1} - \frac{2R^n}{n+1}\, \boldsymbol{\gamma}_{n-1} + \boldsymbol{\tau}_n \right), \tag{22}$$

where

$$\beta_n = \left(\frac{n-2}{n(2n-1)}\, r^2 - \frac{nR^2}{(n+2)(2n+3)} \right) R^{n-1}, \tag{23a}$$

$$\boldsymbol{\tau}_n = -\frac{2(n+1)R^{n-1}}{n(2n-1)}\, \boldsymbol{r}\psi_{n-1}, \tag{23b}$$

and where we have defined the harmonics $\psi_n = (\boldsymbol{e}\cdot\boldsymbol{\nabla})\varphi_n$ and $\boldsymbol{\gamma}_n = \boldsymbol{t} \times \boldsymbol{\nabla}\varphi_n$, with the unit vector $\boldsymbol{t} = \boldsymbol{e} \times \boldsymbol{d}$. By construction, $\psi_n = \boldsymbol{\gamma}_n \cdot \boldsymbol{d}$. In contrast to the simple axisymmetric case for which only two orthogonal vector harmonics are needed as basis function for the expansion of the flow field, the transverse situation requires three vector harmonics that we chose here for convenience to be $\boldsymbol{\nabla}\psi_n$, $\boldsymbol{r}\psi_n$, and $\boldsymbol{\gamma}_n$.

In addition, the image solution inside the drop can likewise be obtained using Lamb's general solution and be expressed in terms of *interior* harmonics as [183]

$$8\pi\eta^{(i)}\boldsymbol{v}^{*} = F^{\perp} \sum_{n=1}^{\infty} \left(A_n^{\perp}\boldsymbol{Q}_n^{(1)} + B_n^{\perp}\boldsymbol{Q}_n^{(2)} + C_n^{\perp}\boldsymbol{Q}_n^{(3)} \right), \tag{24}$$

where we have defined the vector functions

$$\boldsymbol{Q}_n^{(1)} = \left(\frac{n+3}{2n}\, r^2 \boldsymbol{\nabla}\psi_{n-1} + \frac{(n+1)(2n+3)}{2n}\, \boldsymbol{r}\psi_{n-1} \right) r^{2n+1}, \tag{25a}$$

$$\boldsymbol{Q}_n^{(2)} = \frac{1}{n} \left(r^2\, \boldsymbol{\nabla}\psi_{n-1} + (2n+1)\, \boldsymbol{r}\psi_{n-1} \right) r^{2n-1}, \tag{25b}$$

$$\boldsymbol{Q}_n^{(3)} = \left(\boldsymbol{\gamma}_{n-1} + \frac{2n-1}{r^2}\, (\boldsymbol{t} \times \boldsymbol{r})\varphi_{n-1} \right) r^{2n-1}. \tag{25c}$$

Finally, the solution of the flow problem outside the spherical drop can be expressed in terms of *exterior* harmonics as [183]

$$8\pi\eta^{(i)}\boldsymbol{v}^{(e)} = F^{\perp}\sum_{n=1}^{\infty}\left(a_n^{\perp}\left(\frac{n-2}{2(n+1)}\,r^2\boldsymbol{\nabla}\psi_{n-1}-\boldsymbol{r}\psi_{n-1}\right)\right.$$
$$\left.-\frac{b_n^{\perp}}{n+1}\,\boldsymbol{\nabla}\psi_{n-1}+c_n^{\perp}\boldsymbol{\gamma}_{n-1}\right), \tag{26}$$

where, again, we have chosen, for the sake of convenience, to rescale the exterior flow field by $8\pi\eta^{(i)}$ rather than by $8\pi\eta^{(e)}$.

For a clean drop, solving for the series coefficients $\{A_n^{\perp}, B_n^{\perp}, C_n^{\perp}\}$ and $\{a_n^{\perp}, b_n^{\perp}, c_n^{\perp}\}$ associated with the flow fields inside and outside the drop, respectively, yields

$$A_n^{\perp} = \left(\Lambda - 1 + \frac{n+3}{n+1}\left(\frac{2n+1}{2n+3}-\Lambda\right)R^2\right)R^{n-1}, \tag{27a}$$
$$B_n^{\perp} = \left((n+1)k_n - \frac{n+3}{2}(1-\Lambda)R^2\right)R^{n-1}, \tag{27b}$$
$$C_n^{\perp} = \frac{2n(1-2\Lambda)R^{n-2}}{(n-2)(3\Lambda-n)}, \tag{27c}$$
$$a_n^{\perp} = \frac{\Lambda}{n}((n+3)R^2-n-1)R^{n-1}, \tag{27d}$$
$$b_n^{\perp} = \Lambda\left(\left(g_{n+1}+\frac{n+3}{2}\right)R^2-\frac{n+1}{2}\right)R^{n-1}, \tag{27e}$$
$$c_n^{\perp} = \Lambda g_n\,R^n, \tag{27f}$$

where we have defined

$$k_n = \frac{2(1-2\Lambda)}{(n-1)(3\Lambda-n-1)}+\frac{2n+1}{2(2n-1)}-\frac{\Lambda}{2}, \tag{28a}$$
$$g_n = \frac{2(2n+1)}{(n+1)(3\Lambda-n-2)}. \tag{28b}$$

For a surfactant-covered drop, the corresponding coefficients are given by

$$A_n^{\perp} = \left(\frac{(n+3)(2n+1)}{(n+1)(2n+3)}\,R^2-1\right)R^{n-1}, \tag{29a}$$
$$B_n^{\perp} = \frac{1}{2}\left(\frac{(n+1)j_n}{(n-1)(2n-1)h_n}-(n+3)R^2\right)R^{n-1}, \tag{29b}$$
$$C_n^{\perp} = \frac{2n(\lambda+3w-1-wn)R^{n-2}}{(n-2)(wn^2+(1+\lambda-3w)n-3\lambda)}, \tag{29c}$$
$$a_n^{\perp} = 0, \tag{29d}$$
$$b_n^{\perp} = -\frac{2\lambda(2n+3)R^{n+1}}{(n+2)(wn^2+(1+\lambda+3w)n+3)}, \tag{29e}$$
$$c_n^{\perp} = b_{n-1}^{\perp}, \tag{29f}$$

where we have defined

$$w = \frac{\eta_{\mathrm{S}}}{\eta^{(e)}} \tag{30}$$

as an inverse length parameter. In addition,

$$j_n = 2wn^4+(2+2\lambda-3w)\,n^3+(1-5\lambda-12w)\,n^2$$
$$+(9\lambda+23w-10)\,n+3-2\lambda-6w, \tag{31a}$$
$$h_n = wn^2+(1+\lambda-w)\,n+1-2\lambda-2w. \tag{31b}$$

For further details of derivation, we refer to appendix A. Notably, the series coefficients $A_n^{\perp}$ and $a_n^{\perp}$ for a surfactant-covered drop are equal to those for a rigid spherical cavity ($\Lambda = 0$). We note that the rigid cavity limit is recovered for all the other series coefficients by taking the limits $\lambda \to 0$ (or alternatively $\Lambda \to 0$).

In the limit $w \to \infty$, the fluid flow outside the cavity is described by the only non-vanishing coefficient $c_1^{\perp} = -\lambda R$.

2.3 Solution for a freely moving drop

So far, we have assumed that the fluid velocity normal to the interface of the drop vanishes that the drop remains at rest. This implies that in general an external force has to be exerted on the drop to maintain it at its present location. The additionally applied force is equal in magnitude but different in sign when compared to the hydrodynamic force exerted by the Stokeslets on the stationary drop. Accordingly, the solution of the flow problem for a freely moving drop can be obtained by accounting for the Stokeslet solution derived above and adding a flow field induced by a drop subject to an external force that just balances the force applied previously to maintain the drop in position.

For a Stokeslet acting inside a stationary drop, the hydrodynamic force against the flow of the outside fluid is obtained by integrating the traction vector on the *outer* surface of the drop as [196]

$$\boldsymbol{F}_{\mathrm{Drop}}^{\mathrm{S}} = \int_0^{2\pi}\int_0^{\pi}\boldsymbol{T}^{(e)}\sin\theta\,\mathrm{d}\theta\,\mathrm{d}\phi, \tag{32}$$

which after calculation leads to

$$\boldsymbol{F}_{\mathrm{Drop}}^{\mathrm{S}} = \lambda^{-1}\left(a_1^{\parallel}F^{\parallel}\,\boldsymbol{d}-\frac{a_1^{\perp}}{4}\,F^{\perp}\,\boldsymbol{e}\right). \tag{33}$$

This force is necessary to be imposed on the surface of the drop to maintain it in position, which ensures the surface condition in eq. (4a). For a rigid cavity the flow field outside the cavity vanishes, $a_1^{\parallel} = a_1^{\perp} = 0$, and thus the cavity does not experience any force. Upon substitution of the two series coefficients $a_1^{\parallel}$ and $a_1^{\perp}$, we obtain for a clean drop

$$\boldsymbol{F}_{\mathrm{Drop}}^{\mathrm{S}} = \frac{1-\Lambda}{2}((1-R^2)F^{\parallel}\,\boldsymbol{d}+(1-2R^2)F^{\perp}\,\boldsymbol{e}). \tag{34}$$

The resulting translational velocity can then be obtained as $\boldsymbol{V}_{\mathrm{Drop}}^{\mathrm{S}} = \mu\boldsymbol{F}_{\mathrm{Drop}}^{\mathrm{S}}$, with $\mu = 1/(2\pi(2+\Lambda)\eta^{(e)})$ denoting the translational hydrodynamic mobility of a clean drop. We find

$$\boldsymbol{V}_{\mathrm{Drop}}^{\mathrm{S}} = \frac{(1-\Lambda)((1-R^2)F^{\parallel}\,\boldsymbol{d}+(1-2R^2)F^{\perp}\,\boldsymbol{e})}{4\pi(2+\Lambda)\eta^{(e)}}. \tag{35}$$

The axisymmetric flow field induced by a drop translating with a constant velocity $V\boldsymbol{d}$ is known as the

Hadamard-Rybczynski solution and can be found in classic fluid mechanics textbooks. It is given in the frame of the drop by [196] (Chapt. 7, p. 482)

$$v_r^{(e)} = -V\left(1 - \frac{2+\Lambda}{2r} + \frac{\Lambda}{2r^3}\right)\cos\theta, \tag{36a}$$

$$v_\theta^{(e)} = V\left(-1 + \frac{2+\Lambda}{4r} + \frac{\Lambda}{4r^3}\right)\sin\theta, \tag{36b}$$

for the outer fluid, and by

$$v_r^{(i)} = \frac{V}{2}\left(1-\Lambda\right)\left(1-r^2\right)\cos\theta, \tag{37a}$$

$$v_\theta^{(i)} = \frac{V}{2}\left(1-\Lambda\right)\left(1-2r^2\right)\sin\theta, \tag{37b}$$

for the inner fluid. Consequently, the total flow field induced by a Stokeslet acting inside a freely movable drop is obtained by superimposing the flow field resulting from a Stokeslet acting inside a stationary drop and the flow field induced by a drop translated with a constant velocity $-\boldsymbol{V}^{\mathrm{S}}_{\mathrm{Drop}}$. That is, we impose a flow field that is in principle resulting from a force $-\boldsymbol{F}^{\mathrm{S}}_{\mathrm{Drop}}$ added to cancel the force $\boldsymbol{F}^{\mathrm{S}}_{\mathrm{Drop}}$ that we had effectively imposed before to keep the drop in position and thus to satisfy eq. (4a).

For a surfactant-covered drop, we have shown that $a_1^{\parallel} = a_1^{\perp} = 0$. Thus for a rigid cavity and a surfactant-covered drop the total net force transmitted to the drop vanishes. This similarity can be motivated as follows. Any flow past a spherical surface, irrespective of boundary conditions on the surface, can be decomposed into a surface solenoidal and a surface irrotational flow field on the spherical surface [184]. The surface irrotational flow field is torque-free and it exerts a force and a stresslet on the particle, whereas the surface solenoidal flow field is force-free and stresslet-free and it exerts a torque on the particle. For a viscous drop (both clean and surfactant-covered), the surface solenoidal flow field is additionally torque-free [197]. For a drop covered with an incompressible surfactant of zero surface diffusivity, the surface irrotational flow field is the same as that of a rigid spherical cavity [184]. For this reason, the force and stresslet experienced by a surfactant-covered drop are the same as those experienced by a rigid spherical cavity, regardless of the specific value of the viscosity contrast λ and surface to external bulk viscosity ratio w.

The resulting flow fields can now be computed for an arbitrary position and viscosity ratio. As an illustration, in fig. 2, we draw on the left-hand side the streamlines and the magnitude of the flow field created by a point force inside a stiff spherical cavity (for $\Lambda = 0$), which coincides with the well-known image solution [170]. On the right-hand side, we depict the case of $\Lambda = 1/2$ for a freely moving drop in the absence of the surfactant. Here, the flow inside the drop induces motion of the exterior fluid. The magnitude of the flow velocity fields is shown on a logarithmic scale. In particular, the case of stiff confinement (left column) leads to a faster decay of the velocity magnitude due to an increased dissipation at the boundary. For the radially oriented Stokeslet, the patterns retain rotational symmetry about the Stokeslet direction. Accordingly, the flow field inside the drop consists of toroidal eddies owing to the axisymmetric nature of the flow [198]. In contrast to that, a single vortex is created inside the drop for the transverse point force.

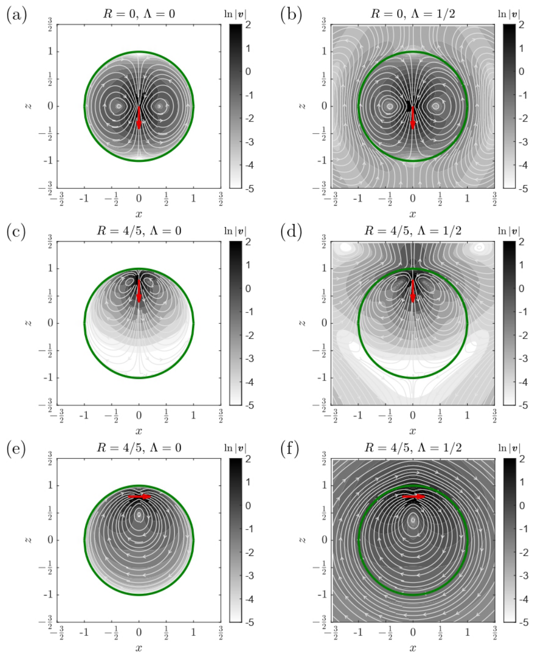

Fig. 2. Streamlines and contour plots of the flow field induced by an axisymmetric ((a)–(d)) and transverse Stokeslet ((e) and (f)) inside a clean freely moving drop for different values of R and Λ. The Stokeslet singularity is represented by a red one-headed arrow. In the left column, $\Lambda = 0$ corresponds to a rigid spherical cavity, while the right column of $\Lambda = 1/2$ allows flow fields to be induced in the outer fluid by the presence of a point force inside the drop. The velocity magnitude is scaled by $1/(8\pi\eta^{(i)})$. To indicate the magnitude of the flow field, shading is used on a logarithmic scale.

In fig. 3, we include the effect of the surfactant by examining two non-zero values of Λ and w. The non-vanishing surfactant shear viscosity does not change qualitatively the shape of the streamlines inside the drop. However, the outer fluid shows concentric circular streamlines similar to those resulting from the uniform rotation of a rigid body. For a fixed viscosity contrast, we observe a weak dependence of the velocity magnitude on the parameter w, whereas the topology and structure of the flow field remain nearly invariant in the investigated parameter regime.

Having derived the image solution for a point-force singularity acting inside a spherical viscous drop, we next make use of this solution to derive the corresponding image for a force dipole singularity.

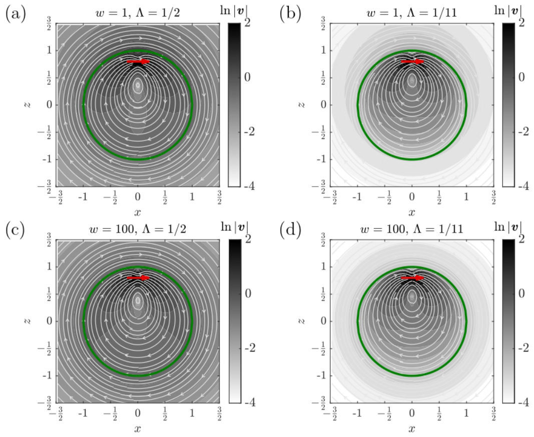

Fig. 3. Streamlines and contour plots of the flow field induced by a transverse Stokeslet inside a surfactant-covered drop for $R = 4/5$ and two different values for Λ and w. The transverse Stokeslet is represented by a red one-headed arrow. The inner flow field resembles that of a clean drop whereas the outer flow field consists of circular streamlines. Here, the velocity magnitude is scaled by $1/(8\pi\eta^{(i)})$.

3 Dipole singularity

In the following, we denote by $\boldsymbol{q} := \boldsymbol{F}/|\boldsymbol{F}|$ the unit vector pointing along the direction of the force. Additionally, we define the Green's function associated with the $\boldsymbol{q}$-directed Stokeslet acting at the position $\boldsymbol{x}_2$ of an unbounded fluid medium as

$$\boldsymbol{G}(\boldsymbol{q}) = 8\pi\eta^{(i)}\, \boldsymbol{\mathcal{G}}(\boldsymbol{x} - \boldsymbol{x}_2) \cdot \boldsymbol{q}. \tag{38}$$

In the far-field limit, the force monopole decays with inverse distance from the singularity position. For an arbitrary orientation of the Stokeslet, the unit vector $\boldsymbol{q}$ can be projected along the axisymmetric and transverse directions as

$$\boldsymbol{q} = \sin\delta\, \boldsymbol{d} + \cos\delta\, \boldsymbol{e}. \tag{39}$$

The flow field induced by force- and torque-free swimming microorganisms can be written as a multipole expansion of the solution of the Stokes equations [199]. To leading order, this flow field appears as induced by a force dipole, which exhibits a decay with inverse distance squared and thus faster than flows induced by force monopoles. Higher-order singularities associated with Stokes flows can be obtained by differentiations of the Stokeslet solution.

We define the free-space flow field caused by a force dipole as

$$\boldsymbol{G}_\mathrm{D}(\boldsymbol{q}, \boldsymbol{p}) = (\boldsymbol{p} \cdot \boldsymbol{\nabla})\, \boldsymbol{G}(\boldsymbol{q}), \tag{40}$$

where $\boldsymbol{p}$ is a unit vector along which the gradient operator is exerted. In an unbounded fluid medium, *i.e.*, for an infinitely large radius of the drop, the self-generated flow induced by an active force-dipole model microswimmer oriented along the direction of the unit vector $\boldsymbol{q}$ is expressed as $\boldsymbol{v}_\mathrm{D} = -\alpha\, \boldsymbol{G}_\mathrm{D}(\boldsymbol{q}, \boldsymbol{q})$. Accordingly,

$$\boldsymbol{v}_\mathrm{D} = -\alpha\, (\boldsymbol{q} \cdot \boldsymbol{\nabla})\, (\sin\delta\, \boldsymbol{G}(\boldsymbol{d}) + \cos\delta\, \boldsymbol{G}(\boldsymbol{e}))\,, \tag{41}$$

where α sets the strength of the force dipole. Then, for a general orientation, the force dipole can be written as a linear combination of axisymmetric and transverse force dipole singularities as

$$\begin{aligned}\boldsymbol{G}_\mathrm{D}(\boldsymbol{q}, \boldsymbol{q}) &= \boldsymbol{G}_\mathrm{D}(\boldsymbol{d}, \boldsymbol{d})\, \sin^2\delta + \boldsymbol{G}_\mathrm{D}(\boldsymbol{e}, \boldsymbol{e})\, \cos^2\delta \\ &\quad + \underbrace{\frac{1}{2}(\boldsymbol{G}_\mathrm{D}(\boldsymbol{e}, \boldsymbol{d}) + \boldsymbol{G}_\mathrm{D}(\boldsymbol{d}, \boldsymbol{e}))}_{\boldsymbol{G}_\mathrm{SS}(\boldsymbol{e}, \boldsymbol{d})} \sin(2\delta),\end{aligned} \tag{42}$$

where $\boldsymbol{G}_\mathrm{SS}(\boldsymbol{e}, \boldsymbol{d}) = \boldsymbol{G}_\mathrm{SS}(\boldsymbol{d}, \boldsymbol{e})$ stands for the symmetric part of the Green's function associated with the force dipole, which is commonly termed the stresslet [200].

We now summarize the main mathematical operations required for the calculation of each of the image flow fields resulting for eq. (42). Denoting by $\mathbb{I}\{\boldsymbol{v}\}$ the image solution for a given flow field $\boldsymbol{v}$, it can be shown that [178,179,184]

$$\mathbb{I}\{\boldsymbol{G}_\mathrm{D}(\boldsymbol{d}, \boldsymbol{d})\} = -\,(\boldsymbol{d} \cdot \boldsymbol{\nabla}_2)\, \mathbb{I}\{\boldsymbol{G}(\boldsymbol{d})\}, \tag{43a}$$

$$\mathbb{I}\{\boldsymbol{G}_\mathrm{D}(\boldsymbol{e}, \boldsymbol{e})\} = -\,(\boldsymbol{e} \cdot \boldsymbol{\nabla}_2)\, \mathbb{I}\{\boldsymbol{G}(\boldsymbol{e})\} + R^{-1}\, \mathbb{I}\{\boldsymbol{G}(\boldsymbol{d})\}, \tag{43b}$$

$$\mathbb{I}\{\boldsymbol{G}_\mathrm{D}(\boldsymbol{e}, \boldsymbol{d})\} = -\,(\boldsymbol{d} \cdot \boldsymbol{\nabla}_2)\, \mathbb{I}\{\boldsymbol{G}(\boldsymbol{e})\}, \tag{43c}$$

$$\mathbb{I}\{\boldsymbol{G}_\mathrm{D}(\boldsymbol{d}, \boldsymbol{e})\} = -\,(\boldsymbol{e} \cdot \boldsymbol{\nabla}_2)\, \mathbb{I}\{\boldsymbol{G}(\boldsymbol{d})\} - R^{-1}\, \mathbb{I}\{\boldsymbol{G}(\boldsymbol{e})\}. \tag{43d}$$

Here, we have made use of the relations $(\boldsymbol{e} \cdot \boldsymbol{\nabla}_2)R = 0$, $(\boldsymbol{e} \cdot \boldsymbol{\nabla}_2)\boldsymbol{d} = -(1/R)\boldsymbol{e}$, and $(\boldsymbol{e} \cdot \boldsymbol{\nabla}_2)\boldsymbol{e} = (1/R)\boldsymbol{d}$.

By noting that $\boldsymbol{d} \cdot \boldsymbol{\nabla}_2 = -\partial/\partial R$, it follows from eqs. (16) and (43a) that the image solution for the axisymmetric force dipole can be expressed as

$$\mathbb{I}\{\boldsymbol{G}_\mathrm{D}(\boldsymbol{d}, \boldsymbol{d})\} = \sum_{n=1}^{\infty} \left(\frac{\partial A_n^\parallel}{\partial R}\, \boldsymbol{S}_n^{(1)} + \frac{\partial B_n^\parallel}{\partial R}\, \boldsymbol{S}_n^{(2)} \right), \tag{44}$$

where the vector functions $\boldsymbol{S}_n^{(j)}$ $(j \in \{1, 2\})$ involve the harmonics $\boldsymbol{\nabla}\varphi_n$ and $\boldsymbol{r}\varphi_n$, and have previously been defined by eqs. (17).

In addition, it follows from eqs. (24) and (43c) that

$$\mathbb{I}\{\boldsymbol{G}_\mathrm{D}(\boldsymbol{e}, \boldsymbol{d})\} = \sum_{n=1}^{\infty} \left(\frac{\partial A_n^\perp}{\partial R} \boldsymbol{Q}_n^{(1)} + \frac{\partial B_n^\perp}{\partial R} \boldsymbol{Q}_n^{(2)} + \frac{\partial C_n^\perp}{\partial R} \boldsymbol{Q}_n^{(3)} \right), \tag{45}$$

where the vector functions $\boldsymbol{Q}_n^{(j)}$ $(j \in \{1, 2, 3\})$ involve the harmonics $\boldsymbol{\nabla}\psi_{n-1}, \boldsymbol{r}\psi_{n-1}$, and $\boldsymbol{\gamma}_{n-1}$, see the definitions in eqs. (25).

Involving the relation

$$(\boldsymbol{e} \cdot \boldsymbol{\nabla}_2)\, \varphi_n = -R^{-1}\, (\boldsymbol{e} \cdot \boldsymbol{\nabla})\, \varphi_{n-1} = -R^{-1}\, \psi_{n-1}, \tag{46}$$

we readily obtain

$$(\boldsymbol{e} \cdot \boldsymbol{\nabla}_2)\, \mathbb{I}\{\boldsymbol{G}(\boldsymbol{d})\} = -\frac{1}{R} \sum_{n=1}^{\infty} n \Big(A_n^\parallel \boldsymbol{Q}_n^{(1)} + B_n^\parallel \boldsymbol{Q}_n^{(2)} \Big). \tag{47}$$

Combining results, the image of the stresslet field can be cast in the final form

$$\mathbb{I}\{\boldsymbol{G}_{\mathrm{SS}}(\boldsymbol{d},\boldsymbol{e})\} = \sum_{n=1}^{\infty} \left(\hat{A}_n \boldsymbol{Q}_n^{(1)} + \hat{B}_n \boldsymbol{Q}_n^{(2)} + \hat{C}_n \boldsymbol{Q}_n^{(3)} \right), \tag{48}$$

where the series coefficients are given by

$$\hat{A}_n = \frac{1}{2} \left(\frac{n}{R} A_n^{\parallel} + R \frac{\partial}{\partial R} \left(\frac{A_n^{\perp}}{R} \right) \right), \tag{49a}$$

$$\hat{B}_n = \frac{1}{2} \left(\frac{n}{R} B_n^{\parallel} + R \frac{\partial}{\partial R} \left(\frac{B_n^{\perp}}{R} \right) \right), \tag{49b}$$

$$\hat{C}_n = \frac{R}{2} \frac{\partial}{\partial R} \left(\frac{C_n^{\perp}}{R} \right). \tag{49c}$$

Next, by making use of the relation

$$\begin{aligned} (\boldsymbol{e} \cdot \boldsymbol{\nabla}_2)\, \psi_{n-1} &= R^{-1} \big((\boldsymbol{d} \cdot \boldsymbol{\nabla})\, \varphi_{n-1} - (\boldsymbol{e} \cdot \boldsymbol{\nabla})\, \psi_{n-2} \big) \\ &= R^{-1} \left(n\varphi_n - \xi_{n-2} \right), \end{aligned} \tag{50a}$$

together with $\xi_n := (\boldsymbol{e} \cdot \boldsymbol{\nabla})\psi_n$, we readily obtain

$$(\boldsymbol{e} \cdot \boldsymbol{\nabla}_2)\, \mathbb{I}\{\boldsymbol{G}(\boldsymbol{e})\} = \sum_{n=1}^{\infty} \frac{1}{R} \left(A_n^{\perp} \boldsymbol{W}_n^{(1)} + B_n^{\perp} \boldsymbol{W}_n^{(2)} + C_n^{\perp} \boldsymbol{W}_n^{(3)} \right), \tag{51}$$

where we have defined the vector functions

$$\boldsymbol{W}_n^{(1)} = \boldsymbol{S}_n^{(1)} - \frac{1}{2n} \big((n+3)\, r^2 \boldsymbol{\nabla} \xi_{n-2} + \rho_n\, \boldsymbol{r}\, \xi_{n-2} \big) r^{2n+1},$$

$$\boldsymbol{W}_n^{(2)} = \boldsymbol{S}_n^{(2)} - \frac{1}{n} \big(r^2\, \boldsymbol{\nabla} \xi_{n-2} + (2n+1)\, \boldsymbol{r}\, \xi_{n-2} \big) r^{2n-1},$$

$$\boldsymbol{W}_n^{(3)} = - \left(\boldsymbol{t} \times \boldsymbol{\nabla} \psi_{n-2} + \frac{2n-1}{r^2} (\boldsymbol{t} \times \boldsymbol{r}) \psi_{n-2} \right) r^{2n-1},$$

together with $\rho_n = (n+1)(2n+3)$.

Having derived the image flow field for a force dipole singularity acting inside a stationary drop, we next determine the external force that is needed to maintain the drop in position, which corresponds to the condition of vanishing normal velocity at the interface imposed by eq. (4a).

The hydrodynamic force against the outside fluid flow in the presence of the force dipole can again be obtained by integrating the hydrodynamic traction vector on the *outer* surface as [196]

$$\boldsymbol{F}_{\mathrm{Drop}}^{\mathrm{D}} = \int_0^{2\pi} \int_0^{\pi} \boldsymbol{T}_{\mathrm{D}}^{(e)} \sin\theta \,\mathrm{d}\theta \,\mathrm{d}\phi, \tag{53}$$

which leads to

$$\boldsymbol{F}_{\mathrm{Drop}}^{\mathrm{D}} = -\alpha\pi\eta^{(e)} \left(2 f_{\parallel} \boldsymbol{d} + f_{\perp} \boldsymbol{e} \right), \tag{54}$$

together with the definitions

$$f_{\parallel} = \frac{2a_1^{\parallel} + a_1^{\perp}}{R} \cos^2\delta - 2 \frac{\partial a_1^{\parallel}}{\partial R} \sin^2\delta, \tag{55a}$$

$$f_{\perp} = \left(\frac{2a_1^{\parallel} + a_1^{\perp}}{R} - \frac{\partial a_1^{\perp}}{\partial R} \right) \sin(2\delta). \tag{55b}$$

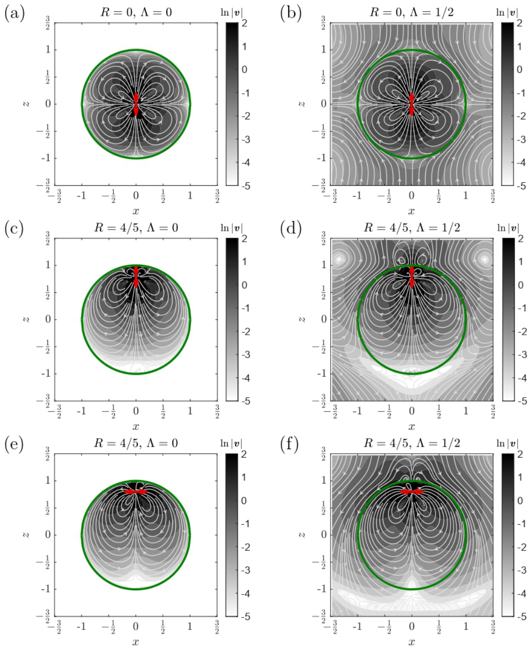

Fig. 4. Streamlines and contour plots of the flow field induced by an axisymmetric ((a)–(d)) and transverse force dipole (e)-(f) inside a clean drop for different positions R, orientations, and values of Λ. Similarly to the case of a point force, see fig. 2, for the effectively stiff spherical cavity (left column), we observe by construction a quick decay of the flow field towards the boundary of the drop. In the case of equal viscosity inside and outside the drop (right column), we find additional recirculation zones appearing close to the surface of the freely moving drop.

Upon substitution of the series coefficients, we readily obtain for a clean viscous drop

$$\boldsymbol{F}_{\mathrm{Drop}}^{\mathrm{D}} = -2\alpha\pi\eta^{(e)} R\Lambda ((3 - \cos(2\delta))\boldsymbol{d} - 3\sin(2\delta)\boldsymbol{e}). \tag{56}$$

Again, the induced translational velocity of a freely moving drop subject to this net force follows as $\boldsymbol{V}_{\mathrm{Drop}}^{\mathrm{D}} = \mu \boldsymbol{F}_{\mathrm{Drop}}^{\mathrm{D}}$ and can thus be expressed as

$$\boldsymbol{V}_{\mathrm{Drop}}^{\mathrm{D}} = -\frac{\alpha R \Lambda}{2 + \Lambda} ((3 - \cos(2\delta))\boldsymbol{d} - 3\sin(2\delta)\boldsymbol{e}). \tag{57}$$

Altogether, the total flow field resulting from a force-dipole acting inside a freely moving drop is obtained by superimposing the dipolar flow field inside a stationary drop derived above and the flow field induced by a drop translating with velocity $-\boldsymbol{V}_{\mathrm{Drop}}^{\mathrm{D}}$ provided by the Hadamard-Rybczynski solution (cf. eqs. (36) and (37)). Again, for a rigid cavity and a surfactant-covered drop the total hydrodynamic force vanishes because $a_1^{\parallel} = a_1^{\perp} = 0$.

In analogy to the flow fields caused by a Stokeslet presented above, we now illustrate the flow induced by a force dipole. Figure 4 shows corresponding results for a stiff

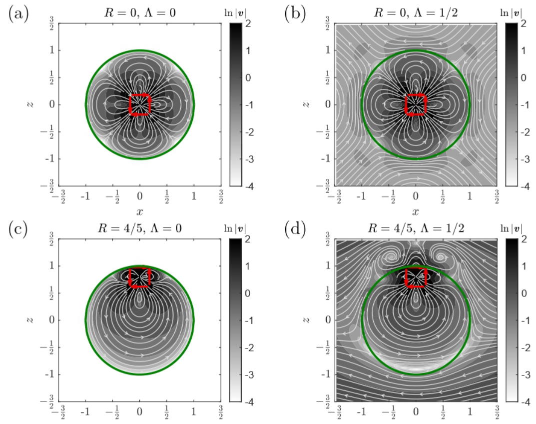

Fig. 5. Streamlines and contour plots of the flow field induced inside a clean drop by a stresslet placed at the origin ((a) and (b)) or off-center ((c) and (d)) for two different values of the viscosity contrast, corresponding to an effectively stiff boundary ($\Lambda = 0$) and to an equal viscosity of the inner and outer fluids for a freely moving drop. The flow far away from the drop, retains the same geometric signature as the generating stresslet.

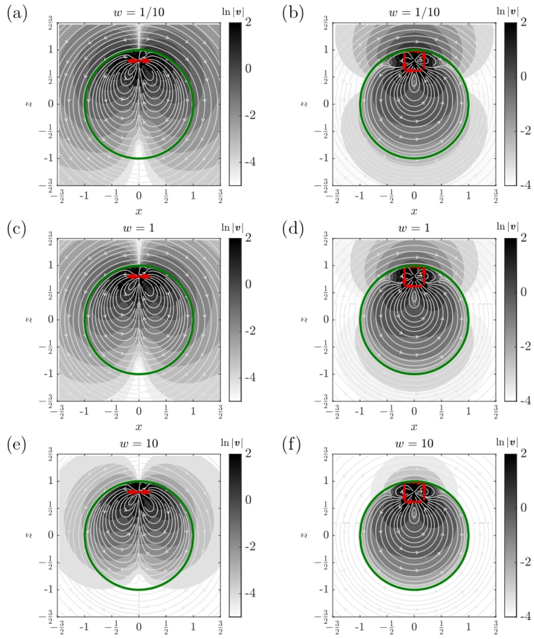

Fig. 6. Streamlines and contour plots of the flow field induced by a force dipole ((a), (c), and (e)) and a stresslet ((b), (d), and (f)) for $R = 4/5$, $\Lambda = 1/2$, and three different values of w when the surface of the drop contains a surfactant. The structure of the streamlines is qualitatively different from that of a clean drop.

spherical confinement of $\Lambda = 0$ (left column) and for the case of $\Lambda = 1/2$ (right column) for a clean freely moving drop in the absence of a surfactant. By varying the position of the force dipole inside the drop, we can control the additional recirculation zones appearing in the exterior fluid. The flow fields generally lose the axial symmetry, except for when the dipole is oriented radially. Similarly, in fig. 5, we present related results caused by a pure stresslet.

Adding a surfactant significantly changes the observed dynamics. In fig. 6, we present the flow fields caused by a dipole (left column) and a stresslet (right column) for various values of w. Increasing the shear viscosity of the surfactant leads to a "stiffening" that drastically reduces the effect of the singularity on the exterior flow. The exterior region consists of circular streamlines similar to those induced by rigid-body rotation.

4 Swimmer dynamics

We now analyze the effect of the drop on the dynamics of an active swimming microorganism encapsulated on the inside. To this end, we decompose in the usual way the generated flow field into a bulk contribution given by eq. (41) in addition to the correction due to the presence of the confining drop. For a clean drop, an additional contribution has to be considered to account for the free motion of the drop.

Here, we model the swimming microorganism as a prolate spheroidal particle of aspect ratio σ. The latter is defined as the ratio of major to minor semi-axes of the spheroid. For instance, the aspect ratio of the bacterium *Bacillus subtilis* [201] has been measured experimentally to be about $\sigma = 4$.

The induced translational and rotational velocities resulting from the fluid-mediated hydrodynamic interactions between the microswimmer and the surface of the drop are provided by Faxén's laws as [103, 199, 202, 203]

$$\boldsymbol{v}^{\mathrm{HI}} = \boldsymbol{v}_{\mathrm{D}}^{*}(\boldsymbol{x})\Big|_{\boldsymbol{x}=\boldsymbol{x}_2}, \tag{58a}$$

$$\boldsymbol{\Omega}^{\mathrm{HI}} = \frac{1}{2}\,\boldsymbol{\nabla}\times\boldsymbol{v}_{\mathrm{D}}^{*}(\boldsymbol{x})\Big|_{\boldsymbol{x}=\boldsymbol{x}_2} + \Gamma\boldsymbol{q}\times\boldsymbol{E}_{\mathrm{D}}^{*}(\boldsymbol{x})\Big|_{\boldsymbol{x}=\boldsymbol{x}_2}\cdot\boldsymbol{q}, \tag{58b}$$

where we have restricted these expressions to the leading order in the swimmer size. Here, $\boldsymbol{v}_{\mathrm{D}}^{*}$ denotes the image dipole flow field inside a freely moving drop. In addition, $\boldsymbol{E}_{\mathrm{D}}^{*} = (\boldsymbol{\nabla}\boldsymbol{v}_{\mathrm{D}}^{*} + (\boldsymbol{\nabla}\boldsymbol{v}_{\mathrm{D}}^{*})^{\top})/2$ denotes the symmetric rate-of-strain tensor associated with the image force dipole, and $\top$ represents the transposition operation. In addition, $\Gamma = (\sigma^2 - 1)/(\sigma^2 + 1) \in [0, 1)$ is a shape factor, where $\Gamma = 0$ holds for a spherical particle and $\Gamma \to 1$ for a needle-like particle of a significantly pronounced aspect ratio.

Then, the induced translational velocity of the swimmer can be written as

$$\boldsymbol{v}^{\mathrm{HI}} = -\alpha\big((V_1 + V_2\cos(2\delta))\boldsymbol{d} + V_3\sin(2\delta)\,\boldsymbol{e}\big), \tag{59}$$

$$\Omega_1 = \omega_1 + \frac{3}{4}\sum_{n=1}^{\infty} \frac{(n^2-1)(2\Lambda^2-4\Lambda+2+n)}{n+2-3\Lambda}\, R^{2n-2}, \tag{65a}$$

$$\Omega_2 = \omega_2 + \frac{3(3\Lambda-1)}{32} - \frac{3}{32}\sum_{n=1}^{\infty} \frac{(n-2)(2(1+\Lambda)n^2+(6\Lambda^2-13\Lambda+3)n-(1-\Lambda)(2+3\Lambda))}{n+2-3\Lambda}\, R^{2n-2}, \tag{65b}$$

$$\Omega_3 = \omega_3 + \frac{3(3\Lambda-1)}{32} + \frac{3}{32}\sum_{n=1}^{\infty} \frac{2(3-\Lambda)n^3+(2\Lambda-1)(5\Lambda-9)n^2-(1-\Lambda)((\Lambda+8)n+2(2-\Lambda))}{n+2-3\Lambda}\, R^{2n-2}, \tag{65c}$$

$$\Omega_1 = \sum_{n=1}^{\infty} \frac{3wn^4+(3+5\lambda+3w)n^3+(6-2\lambda-9w)n^2-(3+5\lambda+3w)n-6+2\lambda+6w}{4(wn^2+(1+\lambda+w)n+2-\lambda-2w)}\, R^{2n-2}, \tag{66a}$$

$$\Omega_2 = -\frac{3}{32} - \frac{3}{32}\sum_{n=1}^{\infty} \frac{2wn^4+(2+6\lambda-3w)n^3-(1+17\lambda+7w)n^2+(9\lambda+12w-8)n+4+2\lambda-4w}{wn^2+(1+\lambda+w)n+2-\lambda-2w}\, R^{2n-2}, \tag{66b}$$

$$\Omega_3 = -\frac{3}{32} + \sum_{n=1}^{\infty} \frac{18wn^4+(18+22\lambda+9w)n^3+(27-21\lambda-51w)n^2-(24+3\lambda-12w)n-12+2\lambda+12w}{32(wn^2+(1+\lambda+w)n+2-\lambda-2w)}\, R^{2n-2}. \tag{66c}$$

---

where for a clean drop

$$V_1 = v_1 - \frac{(3-\Lambda)R}{4(1-R^2)^2}\,, \tag{60a}$$

$$V_2 = v_2 + \frac{3(3-\Lambda)R}{4(1-R^2)^2}\,, \tag{60b}$$

$$V_3 = v_3 + \sum_{n=1}^{\infty} \frac{3(1-\Lambda)(2n+1)(\Lambda-n-2)}{4(n+2-3\Lambda)}\, R^{2n-1}, \tag{60c}$$

where

$$-v_1 = 3v_2 = 3LR(1-R^2), \quad v_3 = 3LR(1-2R^2) \tag{61}$$

are additional contributions required to account for the free motion of the drop, with

$$L = \frac{\Lambda(1-\Lambda)}{2(2+\Lambda)}\,. \tag{62}$$

For a surfactant-covered drop, we obtain

$$V_1 = -\frac{V_2}{3} = -\frac{3R}{4(1-R^2)^2}, \tag{63a}$$

$$V_3 = \sum_{n=1}^{\infty} \frac{u_n}{s_n}\, R^{2n-1}, \tag{63b}$$

where we have defined

$$u_n = -(2n+1)\big(3wn^2+(3+\lambda+3w)n+6-\lambda-6w\big),$$
$$s_n = 4\big(wn^2+(1+\lambda+w)n+2-\lambda-2w\big).$$

The induced rotational velocity due to hydrodynamic interactions with the surface of the drop can be cast in the form

$$\boldsymbol{\Omega}^{\mathrm{HI}} = -\alpha\big(\Omega_1 + \Gamma\big(\Omega_2\cos(2\delta)+\Omega_3\big)\big)\sin(2\delta)\boldsymbol{t}, \tag{64}$$

where, again, $\boldsymbol{t} = \boldsymbol{e} \times \boldsymbol{d}$. For a clean drop, we find

see eqs. (65) *above*

where $\omega_1 = -15R^2L/2$, $\omega_2 = -9R^2L/2$, and $\omega_3 = 6R^2L$ are contributions accounting for the free motion of the drop. For a surfactant-covered drop, we obtain

see eqs. (66) *above*

In particular, the induced translational and rotational swimming velocities inside a rigid spherical cavity are recovered when taking in eqs. (65) and (66) the limit $\lambda \to 0$.

It is worth noting that the infinite series appearing in eq. (60c) providing the velocity V_3 for a clean drop can be expressed in terms of Hurwitz-Lerch transcendent and Gauss hypergeometric functions [193]. However, the sum representation is more convenient for computational purposes. For a clean drop, for $\Lambda = 0$ (corresponding to the rigid-cavity limit), for $\Lambda = 1/2$ (corresponding to equal viscosities of the inner and outer fluids), and for $\Lambda = 1$ (corresponding to an infinitely small outer viscosity), the infinite sum can be expressed in terms of polynomial fractions as summarized in table 1. For the sake of clarity, we summarize in table 2 the basic operations that have been used to calculate the translational and rotational velocities stated by eqs. (59) and (64), respectively. In appendix B, we discuss the convergence properties of these series functions and estimate the number of terms required for their evaluation up to a given precision.

The addition of a surfactant increases the complexity of the solution. The magnitudes of the velocities V_1 and V_2 for a surfactant-covered drop given by eq. (63a) are independent of Λ and are generally larger than those for a clean drop given by eqs. (60). In fig. 7, we present the Λ-dependence of the components V_3 and Ω_i, $i \in \{1,2,3\}$, for different values of the surface viscosity ratio w. The induced translational swimming velocity V_3 and the rotation rates increase monotonically from the rigid-cavity limit

Table 1. Expressions of the infinite sums for a clean drop, given in eqs. (60) and (65) in terms of polynomial fractions for $\Lambda = 0$ (rigid-cavity limit), $\Lambda = 1/2$ (equal viscosities of the inner and outer fluids), and $\Lambda = 1$ (infinitely small outer viscosity).

Λ	$V_3 - v_3$	$\Omega_1 - \omega_1$	$\Omega_2 - \omega_2$	$\Omega_3 - \omega_3$
0	$-\frac{3}{4}\frac{R(3-R^2)}{(1-R^2)^2}$	$\frac{3}{4}\frac{R^2(3-R^2)}{(1-R^2)^3}$	$-\frac{3}{32}\frac{R^4(5-R^2)}{(1-R^2)^3}$	$\frac{3}{32}\frac{R^2(16-5R^2+R^4)}{(1-R^2)^3}$
$\frac{1}{2}$	$-\frac{3}{8}\frac{R(5-3R^2)}{(1-R^2)^2}$	$\frac{3}{4}\frac{R^2(3-R^2)}{(1-R^2)^3}$	$-\frac{3}{64}\frac{R^4(11+R^2)}{(1-R^2)^3}$	$\frac{3}{64}\frac{R^2(24-3R^2-R^4)}{(1-R^2)^3}$
1	0	$\frac{2}{(1-R^2)^3}$	$-\frac{3}{8}\frac{R^4(3-R^2)}{(1-R^2)^3}$	$\frac{3}{8}\frac{R^2(4-3R^2+R^4)}{(1-R^2)^3}$

Table 2. Summary of the basic operations required for the calculations of the translational and rotational velocities given by eqs. (59) and (64), respectively, for a surfactant-free, clean drop.

$\boldsymbol{f}$	$\boldsymbol{f}\vert_{\boldsymbol{x}=\boldsymbol{x}_2}$	$\boldsymbol{\nabla}\times\boldsymbol{f}\vert_{\boldsymbol{x}=\boldsymbol{x}_2}$	$\boldsymbol{q}\times\frac{1}{2}(\boldsymbol{\nabla f}+(\boldsymbol{\nabla f})^\top)\vert_{\boldsymbol{x}=\boldsymbol{x}_2}\cdot\boldsymbol{q}$
$\boldsymbol{S}_n^{(1)}$	$-\frac{1}{2}n(n+1)R^{n+1}\,\boldsymbol{d}$	$\boldsymbol{0}$	$\frac{3}{8}n(n+1)^2R^n\sin(2\delta)\boldsymbol{t}$
$\boldsymbol{S}_n^{(2)}$	$-nR^{n-1}\,\boldsymbol{d}$	$\boldsymbol{0}$	$\frac{3}{4}n(n-1)R^{n-2}\sin(2\delta)\boldsymbol{t}$
$\boldsymbol{Q}_n^{(1)}$	$-\frac{1}{4}(n+1)(n+3)R^{n+1}\,\boldsymbol{e}$	$-\frac{1}{2}(n+1)(2n+3)R^n\,\boldsymbol{t}$	$\frac{1}{4}n(n+1)(n+2)R^n\cos(2\delta)\boldsymbol{t}$
$\boldsymbol{Q}_n^{(2)}$	$-\frac{1}{2}(n+1)R^{n-1}\,\boldsymbol{e}$	$\boldsymbol{0}$	$\frac{1}{2}(n^2-1)R^{n-2}\cos(2\delta)\boldsymbol{t}$
$\boldsymbol{Q}_n^{(3)}$	$(n-1)R^{n-2}\,\boldsymbol{e}$	$\frac{1}{2}(n-1)(n-2)R^{n-3}\,\boldsymbol{t}$	$-\frac{3}{4}(n-1)(n-2)R^{n-3}\cos(2\delta)\boldsymbol{t}$
$\boldsymbol{W}_n^{(1)}$	$-\frac{1}{4}n(n+1)^2R^{n+1}\,\boldsymbol{d}$	$\boldsymbol{0}$	$\frac{1}{32}(n+1)(7n^3+16n^2+7n-6)R^n\sin(2\delta)\boldsymbol{t}$
$\boldsymbol{W}_n^{(2)}$	$-\frac{1}{2}n(n+1)R^{n-1}\,\boldsymbol{d}$	$\boldsymbol{0}$	$\frac{1}{16}(n^2-1)(7n+2)R^{n-2}\sin(2\delta)\boldsymbol{t}$
$\boldsymbol{W}_n^{(3)}$	$\frac{1}{2}n(n-1)R^{n-2}\,\boldsymbol{d}$	$\boldsymbol{0}$	$-\frac{1}{2}n(n-1)(n-2)R^{n-3}\sin(2\delta)\boldsymbol{t}$

($\Lambda = 0$) to the infinitely large viscosity contrast ($\Lambda = 1$). The presence of a surfactant strongly alters the dynamics of the encapsulated swimmer by enhancing its reorientation when compared to the situation of a clean drop.

Finally, we exploit our results to estimate the velocity and rotation rates for real biological microswimmers confined by the spherical drop. As an example, we chose the bacterium *E. coli*, which provides a frequently studied example system to unravel the physics of microswimmers [204–206]. We recall that throughout the article, we have rescaled all length by the radius a of the drop. In the following, we use the subscript "ph" to denote non-scaled quantities in physical units, which implies $\alpha_{\mathrm{ph}} = a^3\alpha$, $\boldsymbol{v}_{\mathrm{ph}}^{\mathrm{HI}} = a\,\boldsymbol{v}^{\mathrm{HI}}$, and $\boldsymbol{\Omega}_{\mathrm{ph}}^{\mathrm{HI}} = \boldsymbol{\Omega}^{\mathrm{HI}}$. The functions V_i and Ω_i, $i \in \{1,2,3\}$, are dimensionless quantities.

In a bulk Newtonian fluid of dynamic viscosity $\eta = 10^{-3}\,\mathrm{Pa\cdot s}$, *E. coli* bacteria swim with an average velocity of $v_0 \approx 20\,\mu\mathrm{m/s}$. By approximating the flagella thrust forces as $f \approx 0.5\,\mathrm{pN}$ [207, 208] and the inter-dipole distance as $\ell \approx 1\,\mu\mathrm{m}$ [209], the resulting force dipolar coefficient is estimated as $\alpha_{\mathrm{ph}} = f\ell/(8\pi\eta) \approx 20\,\mu\mathrm{m}^3/\mathrm{s}$. Rescaling the induced translational velocity by v_0 and the rotation rate by v_0/a, it follows from eqs. (59) and (64) that

$$\frac{|\boldsymbol{v}_{\mathrm{ph}}^{\mathrm{HI}}|}{v_0} = \Xi\Big(\big(V_1 + V_2\cos(2\delta)\big)^2 + V_3^2\sin^2(2\delta)\Big)^{\frac{1}{2}}, \quad (67a)$$

$$\frac{|\boldsymbol{\Omega}_{\mathrm{ph}}^{\mathrm{HI}}|}{v_0/a} = \Xi\Big|\big(\Omega_1 + \Gamma(\Omega_2\cos(2\delta) + \Omega_3)\big)\sin(2\delta)\Big|, \quad (67b)$$

where $\Xi := \alpha_{\mathrm{ph}}/(a^2v_0) = 10^{-4}$.

In fig. 8, we present the variation of the magnitude of the rescaled swimming velocities as stated by eqs. (67) *versus* the parameter Λ for various values of the surface to external bulk viscosity ratio w. Here, we consider a spherical viscous drop of radius $a = 0.1\,\mathrm{mm}$. To limit the parameter space, we assume that the bacterium has an orientation angle $\delta = \pi/4$ and an aspect ratio $\sigma = 2$ ($\Gamma = 3/5$) [209]. Compared to a microswimmer in a clean drop, we observe that the presence of a surfactant enhances the magnitude of the induced translational velocity as well as the rotation rate. For increasing w, the magnitude of the induced translational velocity approaches the maximal value found

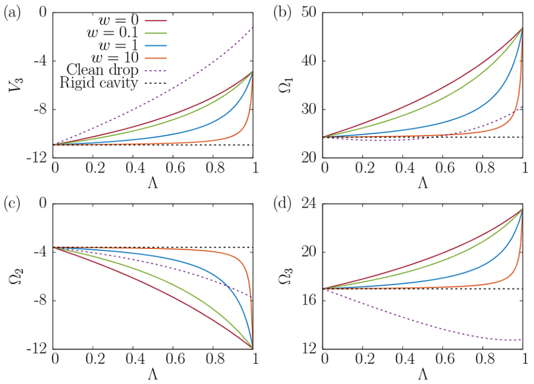

Fig. 7. Variation of the component V_3 of the induced swimming velocity (a) and Ω_i, $i \in \{1, 2, 3\}$, associated with the rotational swimming velocity ((b)–(d)) inside a clean drop (magenta dashed line) and surfactant-covered drops (solid lines) for various values of scaled interfacial viscosity w. The presence of a surfactant strongly alters the observed dynamics, particularly by enhancing reorientation. Here, we set $R = 4/5$.

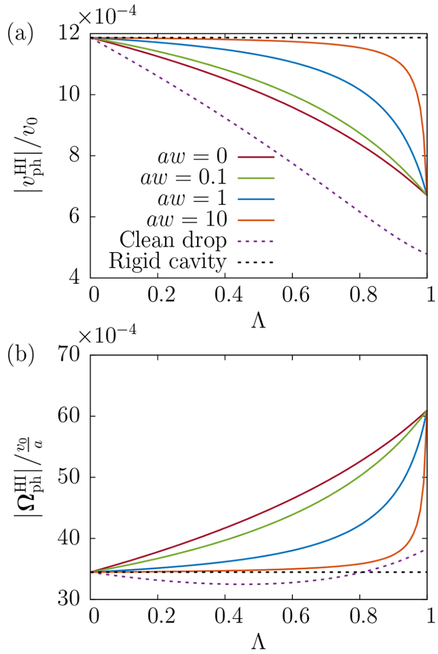

Fig. 8. Variations of the magnitude of the induced translational (a) and rotational (b) velocities for an *E. coli* bacterium of aspect ratio $\sigma = 2$. Here, we set $R = 4/5$ and $\delta = \pi/4$. For the other parameters, see main text.

for a swimmer inside a rigid cavity. Whether the induced translational velocity impedes or supports the translation of the microswimmer depends, in the end, on the orientation angle δ. In contrast to that, the effect of the surfactant on the rotation rate is weakened with increasing w and is the most severe in the case of vanishing shear viscosity (*i.e.*, $w = 0$), for which particularly the incompressibility of the surfactant on the surface of the drop distinguishes the situation from that of a clean drop. Since $|\boldsymbol{v}_{\mathrm{ph}}^{\mathrm{HI}}| \sim a^{-2}$ and $|\boldsymbol{\Omega}_{\mathrm{ph}}^{\mathrm{HI}}| \sim a^{-3}$, the confinement effect on the induced swimming velocities and rotation rates becomes more important upon decreasing the size of the drop.

5 Conclusions

Stokes flows in complex and confined geometries have significant relevance for a variety of applications in industrial and biological systems. In this context, drops of particular importance, because a number of microfluidic realizations exploits their potential for trapping active or passive particles and biological material, including proteins, biopolymers, and microswimmers. Understanding the dynamics inside these micro-containers requires an adequate description of the flow generated by the enclosed matter.

In this contribution, we have developed analytical expressions for the lowest-order flow singularities, namely the Stokeslet and force dipole, enclosed inside a liquid drop surrounded by a fluid environment. We have explored the flow structure for arbitrary viscosity contrast between the spherical drop and the suspending fluid. First, we have provided our results both for the case when the drop is clean, and thus tangential stresses are continuous across the boundary. Second, we have analyzed the effect of the presence of a homogeneously distributed, incompressible surfactant on the surface of the drop on the resulting flow fields. To model the surfactant, we have employed the Boussinesq-Scriven constitutive law, with the surfactant characterized by an interfacial shear viscosity. Using spherical harmonic expansion techniques, we have been able to determine the flow fields in each case and present them for a varying interior/exterior fluid viscosity ratio and also for different values of the surfactant shear viscosity.

Having derived the image flows in each case, we have further discussed the effective forces exerted on the surface of the drop due to the presence of the enclosed point singularities. On our way, this was necessary to render the drop moving freely. Next, we have focused our discussion on the case of drops with entrapped microswimmers and found the resulting translational and rotational velocities of force- and torque-free swimmers inside such spherical confinements. To this end, we have used the Faxén relations and modeled the swimmer as a prolate spheroid. We have found that the presence of the surfactant tends to enhance the rotation rate of the encapsulated swimmer.

The results derived in this paper constitute a step towards understanding the complex dynamics resulting from hydrodynamic interactions in a confined and complex environment. The minimal model proposed here for the interpretation of any experimentally observed motion of active or passive particles can be directly employed to describe the dynamics observed in flows both internal and external to the drop, *e.g.* in colloidal suspension of microdrops and microfluidic diagnostic devices.

Open Access funding enabled and organized by Projekt DEAL. We would like to thank B. Ubbo Felderhof and Shubhadeep Mandal for various stimulating discussions. HL and AMM gratefully acknowledge support from the Deutsche Forschungsgemeinschaft (DFG) through the priority program SPP 1726 on microswimmers, Grant Nos. LO 418/16 and ME 3571/2. ADMI thanks the DFG for support through the project DA 2107/1-1. AMA acknowledges support from National Science Foundation (CBET-1700961). VAS acknowledges support from Bisland Dissertation Fellowship. AJTMM acknowledges funding from the Human Frontier Science Program (fellowship LT001670/2017), and the United States Department of Agriculture (USDA-NIFA AFRI grant 2019-06706). FGL acknowledges Millennium Nucleus Physics of Active Matter of ANID (Agencia Nacional de Investigación y Desarrollo).

Author contribution statement

ADMI conceived the study and prepared the figures. ARS and ADMI carried out the analytical calculations. VAS, ML, and ADMI drafted the manuscript. All authors discussed and interpreted the results, edited the text, and finalized the manuscript.

Publisher's Note The EPJ Publishers remain neutral with regard to jurisdictional claims in published maps and institutional affiliations.

Appendix A. Determination of the series coefficients

In this appendix, we provide the resulting equations for the boundary conditions stated by eqs. (4) and (5) for clean drop and by eqs. (4) and (6) for a surfactant-covered drop.

Appendix A.1. Axisymmetric Stokeslet

As already mentioned, the solution of the axisymmetric flow field induced by a point force inside a surfactant-covered drop is identical to that inside a rigid cavity for which $\lambda \to 0$ (or alternatively $\Lambda \to 0$). Thus, in the axisymmetric case, we will provide in the following the resulting equations for the boundary conditions for a clean viscous drop only.

By applying the boundary conditions of vanishing radial velocity at the surface of the drop, given by eq. (4a), and using the fact that $\boldsymbol{\nabla}\varphi_n$ and $\boldsymbol{r}\varphi_n$ form a set of independent vector harmonics, we find

$$\begin{aligned} &\frac{n(n+1)}{2}\, A_n^{\parallel} + nB_n^{\parallel} = \frac{n(n+1)}{2n-1}\, R^{n-1} - \frac{n(n+1)}{2n+3}\, R^{n+1}, \\ &\frac{n(n+1)}{2}\, a_n^{\parallel} - (n+1)b_n^{\parallel} = 0. \end{aligned} \tag{A.1}$$

In addition, the continuity of the tangential components of the velocity and stress vector fields, respectively given by eqs. (4b) and (5), leads to two additional equations

$$-\frac{n+3}{2}\, A_n^{\parallel} - B_n^{\parallel} - \frac{n-2}{2}\, a_n^{\parallel} + b_n^{\parallel} = \frac{n-2}{2n-1}\, R^{n-1} - \frac{n}{2n+3}\, R^{n+1}, \tag{A.2a}$$

$$\frac{n(n+3)}{2} A_n^{\parallel} + (n-2)B_n^{\parallel} - \frac{(n+1)(n-2)}{2\lambda} a_n^{\parallel} + \frac{n+3}{\lambda} b_n^{\parallel} = \frac{(n+1)(n-2)}{2n-1}\, R^{n-1} - \frac{n(n+3)}{2n+3}\, R^{n+1}. \tag{A.2b}$$

Equations (A.1) and (A.2) form a linear system of equations, amenable to resolution using the standard substitution technique. From here, we obtain the expressions of the series coefficients $\{A_n^{\parallel}, B_n^{\parallel}\}$ and $\{a_n^{\parallel}, b_n^{\parallel}\}$ associated with the solution for the flow field inside and outside the drop, respectively, see eqs. (20) of the main text.

Appendix A.2. Transverse Stokeslet

Applying the boundary condition of vanishing radial velocity field at the surface of the drop, as given by eq. (4a), yields

$$\begin{aligned} &\frac{n+1}{2}\, A_n^{\perp} + B_n^{\perp} - C_{n+1}^{\perp} = \frac{n+1}{2n-1}\, R^{n-1} - \frac{n+3}{2n+3}\, R^{n+1}, \\ &-\frac{n}{2}\, a_n^{\perp} + b_n^{\perp} - c_{n+1}^{\perp} = 0. \end{aligned} \tag{A.3}$$

In addition, the continuity of the tangential components of the velocity vector field, as given by eq. (4b), implies

$$\frac{n+1}{n+2}\, C_{p+3}^{\perp} + c_{n+1}^{\perp} = -\frac{2R^{n+1}}{n+2}, \tag{A.4a}$$

$$\frac{n+3}{2n} A_n^{\perp} + \frac{B_n^{\perp}}{n} - \frac{C_{n+1}^{\perp}}{n} + \frac{C_{n+3}^{\perp}}{n+2} - \frac{(n-2)a_n^{\perp}}{2(n+1)} + \frac{b_n^{\perp}}{n+1} = \left(-\frac{n-2}{n(2n-1)} + \frac{nR^2}{(n+2)(2n+3)}\right) R^{n-1}. \tag{A.4b}$$

On the one hand, for a clean drop, the continuity of the tangential hydrodynamic stresses stated by eq. (5) yields

$$\frac{n(n+1)}{n+2}\, C_{n+3}^{\perp} - \frac{n+3}{\lambda}\, c_{n+1}^{\perp} = \frac{2(n+3)}{n+2}\, R^{n+1}, \tag{A.5a}$$

$$\frac{n+3}{2}\, A_n^{\perp} + \frac{n-2}{n}(B_n^{\perp} - C_{n+1}^{\perp}) + \frac{nC_{n+3}^{\perp}}{n+2} + \frac{n-2}{2\lambda}\, a_n^{\perp} - \frac{n+3}{\lambda(n+1)}\, b_n^{\perp} = \left(\frac{(n+1)(n-2)}{n(2n-1)} - \frac{n(n+3)R^2}{(2n+3)(n+2)}\right) R^{n-1}. \tag{A.5b}$$

Next we solve eqs. (A.3) through (A.5) for the series coefficients $\{A_n^{\perp}, B_n^{\perp}, C_n^{\perp}\}$ and $\{a_n^{\perp}, b_n^{\perp}, c_n^{\perp}\}$ associated with the flow fields inside and outside the drop, respectively. Explicit expressions of these coefficients are given in eq. (27).

On the other hand, for a surfactant-covered drop, eqs. (6) representing the incompressibility of the in-plane surfactant flow and the discontinuity of the tangential hydrodynamic stresses, lead to

$$\left(\frac{n}{2}-1\right) a_n^\perp - b_n^\perp + c_{n+1}^\perp = 0, \tag{A.6a}$$

$$n(n+1)(wn+\lambda+3w)C_{n+3} - (n+2)(n+3)c_{n+1} = 2(n+3)(\lambda - wn)R^{n+1}. \tag{A.6b}$$

It is worth noting that eq. (A.6b) is obtained upon operating $\boldsymbol{e}_r \cdot \boldsymbol{\nabla}_\mathrm{S} \times$ on both sides of eq. (6b) to eliminate the term $\boldsymbol{\nabla}_\mathrm{S}\gamma$.

The expressions of the series coefficients follow forthwith upon solving the linear system of equations composed of eqs. (4a), (A.4), and (A.6) to yield the expressions given by eqs. (29) of the main body of the paper.

Appendix B. Convergence and estimation of the number of terms required for the evaluation of infinite series functions

In this appendix, we discuss the convergence of the series functions for the induced translational and rotational swimming velocities given by eqs. (60c) and (65) for a clean drop, and by eqs. (63b) and (66) for a surfactant-covered drop.

Let us denote by v_{3n} the general term of the infinite series for V_3 given for a clean drop eq. (60c), *i.e.*, $V_3 = \sum_{n=1}^\infty v_{3n}$. To test the convergence of the series, we define in the usual way the ratio $L = \lim_{n\to\infty} |v_{3n+1}/v_{3n}| = R^2 < 1$ in rescaled units of length. Therefore, the series is absolutely convergent [210]. Then, for $n \sim \infty$, we have the leading-order asymptotic behavior

$$v_{3n} = -\frac{3}{4}(1-\Lambda)(2n+1+4\Lambda)R^{2n-1} + \mathcal{O}\left(\frac{R^{2n}}{n}\right). \tag{B.1}$$

To compute the infinite series at a given desired precision, we define the truncation error as

$$\mathcal{E}\{V_3\} := \left|\sum_{n=N+1}^{\infty} v_{3n}\right| \simeq \frac{3(1-\Lambda)N}{2(1-R^2)}\, R^{1+2N}. \tag{B.2}$$

The number of terms required to achieve a certain precision ε can readily be obtained by solving numerically the inequality $\mathcal{E}(V_3) < \varepsilon$.

For a surfactant-covered drop, it can be shown that

$$\mathcal{E}\{V_3\} \simeq \frac{3N}{2(1-R^2)}\, R^{1+2N}. \tag{B.3}$$

We proceed analogously for the series functions for the rotational velocity given for a clean drop by eq. (65). Here, we obtain

$$\mathcal{E}\{\Omega_1\} \simeq \frac{3N^2}{4(1-R^2)}\, R^{2N}, \tag{B.4a}$$

$$\mathcal{E}\{\Omega_2\} \simeq \frac{3(1+\Lambda)N^2}{16(1-R^2)}\, R^{2N}, \tag{B.4b}$$

$$\mathcal{E}\{\Omega_3\} \simeq \frac{3(3-\Lambda)N^2}{16(1-R^2)}\, R^{2N}. \tag{B.4c}$$

Similarly, for a surfactant-covered drop, we obtain

$$\mathcal{E}\{\Omega_1\} \simeq 4\mathcal{E}\{\Omega_2\} \simeq \frac{4}{3}\,\mathcal{E}\{\Omega_3\} \simeq \frac{3N^2}{4(1-R^2)}\, R^{2N}. \tag{B.5}$$

For instance, for $R = 4/5$ about 30–40 terms are required for $\varepsilon = 10^{-3}$ whereas about 40–50 terms are required for $\varepsilon = 10^{-6}$. The number of required terms increases quickly as $R \to 1$.

Open Access This is an open access article distributed under the terms of the Creative Commons Attribution License (http://creativecommons.org/licenses/by/4.0), which permits unrestricted use, distribution, and reproduction in any medium, provided the original work is properly cited.

References

1. G. Gompper, R.G. Winkler, T. Speck, A. Solon, C. Nardini, F. Peruani, H. Löwen, R. Golestanian, U.B. Kaupp, L. Alvarez *et al.*, J. Phys.: Condens. Matter **32**, 193001 (2020).
2. J. Palacci, S. Sacanna, A.P. Steinberg, D.J. Pine, P.M. Chaikin, Science **339**, 936 (2013).
3. S. Sacanna, M. Korpics, K. Rodriguez, L. Colón-Meléndez, S.H. Kim, D.J. Pine, G.R. Yi, Nat. Commun. **4**, 1688 (2013).
4. N. Chronis, L.P. Lee, J. Microelectromech. Syst. **14**, 857 (2005).
5. M. Junkin, S. Ling Leung, S. Whitman, C.C. Gregorio, P.K. Wong, J. Cell Sci. **124**, 4213 (2011).
6. E. Diller, M. Sitti, Adv. Funct. Mater. **24**, 4397 (2014).
7. D. Ahmed, M. Lu, A. Nourhani, P.E. Lammert, Z. Stratton, H.S. Muddana, V.H. Crespi, T.J. Huang, Sci. Rep. **5**, 9744 (2015).
8. F. Schmidt, B. Liebchen, H. Löwen, G. Volpe, J. Chem. Phys. **150**, 094905 (2019).
9. D. Kagan, M.J. Benchimol, J.C. Claussen, E. Chuluun-Erdene, S. Esener, J. Wang, Angew. Chem. Int. Ed. **51**, 7519 (2012).
10. D. Walker, B.T. Käsdorf, H.H. Jeong, O. Lieleg, P. Fischer, Sci. Adv. **1**, e1500501 (2015).
11. B.J. Nelson, I.K. Kaliakatsos, J.J. Abbott, Annu. Rev. Biomed. Eng. **12**, 55 (2010).
12. F. Qiu, S. Fujita, R. Mhanna, L. Zhang, B.R. Simona, B.J. Nelson, Adv. Funct. Mater. **25**, 1666 (2015).
13. B.W. Park, J. Zhuang, O. Yasa, M. Sitti, ACS Nano **11**, 8910 (2017).
14. B. Mostaghaci, O. Yasa, J. Zhuang, M. Sitti, Adv. Sci. **4**, 1700058 (2017).

15. D. Gourevich, O. Dogadkin, A. Volovick, L. Wang, J. Gnaim, S. Cochran, A. Melzer, J. Control. Release **170**, 316 (2013).
16. U. Kei Cheang, K. Lee, A.A. Julius, M.J. Kim, Appl. Phys. Lett. **105**, 083705 (2014).
17. J. Wang, M.S. Lin, Anal. Chem. **60**, 1545 (1988).
18. E. Lauga, T.R. Powers, Rep. Prog. Phys. **72**, 096601 (2009).
19. M.C. Marchetti, J.F. Joanny, S. Ramaswamy, T.B. Liverpool, J. Prost, M. Rao, R.A. Simha, Rev. Mod. Phys. **85**, 1143 (2013).
20. J. Elgeti, R.G. Winkler, G. Gompper, Rep. Prog. Phys. **78**, 056601 (2015).
21. A.M. Menzel, Phys. Rep. **554**, 1 (2015).
22. C. Bechinger, R. Di Leonardo, H. Löwen, C. Reichhardt, G. Volpe, G. Volpe, Rev. Mod. Phys. **88**, 045006 (2016).
23. A. Zöttl, H. Stark, J. Phys.: Condens. Matter **28**, 253001 (2016).
24. E. Lauga, Annu. Rev. Fluid Mech. **48**, 105 (2016).
25. P. Illien, R. Golestanian, A. Sen, Chem. Soc. Rev. **46**, 5508 (2017).
26. N. Desai, A.M. Ardekani, Soft Matter **13**, 6033 (2017).
27. K.K. Dey, Angew. Chem. Int. Ed. **58**, 2208 (2019).
28. M.R. Shaebani, A. Wysocki, R.G. Winkler, G. Gompper, H. Rieger, Nat. Rev. Phys. **2**, 181 (2020).
29. G. Grégoire, H. Chaté, Phys. Rev. Lett. **92**, 025702 (2004).
30. S. Mishra, A. Baskaran, M.C. Marchetti, Phys. Rev. E **81**, 061916 (2010).
31. A.M. Menzel, Phys. Rev. E **85**, 021912 (2012).
32. H.H. Wensink, H. Löwen, J. Phys.: Condens. Matter **24**, 464130 (2012).
33. H.H. Wensink, J. Dunkel, S. Heidenreich, K. Drescher, R.E. Goldstein, H. Löwen, J.M. Yeomans, Proc. Natl. Acad. Sci. U.S.A. **109**, 14308 (2012).
34. J. Dunkel, S. Heidenreich, K. Drescher, H.H. Wensink, M. Bär, R.E. Goldstein, Phys. Rev. Lett. **110**, 228102 (2013).
35. R. Großmann, P. Romanczuk, M. Bär, L. Schimansky-Geier, Phys. Rev. Lett. **113**, 258104 (2014).
36. A. Kaiser, A. Peshkov, A. Sokolov, B. ten Hagen, H. Löwen, I.S. Aranson, Phys. Rev. Lett. **112**, 158101 (2014).
37. S. Heidenreich, S.H.L. Klapp, M. Bär, J. Phys.: Conf. Ser. **490**, 012126 (2014).
38. S. Heidenreich, J. Dunkel, S.H.L. Klapp, M. Bär, Phys. Rev. E **94**, 020601 (2016).
39. A. Doostmohammadi, T.N. Shendruk, K. Thijssen, J.M. Yeomans, Nat. Commun. **8**, 15326 (2017).
40. M.E. Cates, J. Tailleur, Annu. Rev. Condens. Matter Phys. **6**, 219 (2015).
41. M.E. Cates, J. Tailleur, EPL **101**, 20010 (2013).
42. J. Tailleur, M.E. Cates, Phys. Rev. Lett. **100**, 218103 (2008).
43. I. Buttinoni, J. Bialké, F. Kümmel, H. Löwen, C. Bechinger, T. Speck, Phys. Rev. Lett. **110**, 238301 (2013).
44. T. Speck, J. Bialké, A.M. Menzel, H. Löwen, Phys. Rev. Lett. **112**, 218304 (2014).
45. T. Speck, A.M. Menzel, J. Bialké, H. Löwen, J. Chem. Phys. **142**, 224109 (2015).
46. P. Digregorio, D. Levis, A. Suma, L.F. Cugliandolo, G. Gonnella, I. Pagonabarraga, Phys. Rev. Lett. **121**, 098003 (2018).
47. S. Mandal, B. Liebchen, H. Löwen, Phys. Rev. Lett. **123**, 228001 (2019).
48. L. Caprini, U.M.B. Marconi, A. Puglisi, Phys. Rev. Lett. **124**, 078001 (2020).
49. A. Menzel, J. Phys.: Condens. Matter **25**, 505103 (2013).
50. F. Kogler, S.H.L. Klapp, EPL **110**, 10004 (2015).
51. P. Romanczuk, H. Chaté, L. Chen, S. Ngo, J. Toner, New J. Phys. **18**, 063015 (2016).
52. A.M. Menzel, New J. Phys. **18**, 071001 (2016).
53. C. Reichhardt, C.J.O. Reichhardt, Soft Matter **14**, 490 (2018).
54. C.W. Wächtler, F. Kogler, S.H.L. Klapp, Phys. Rev. E **94**, 052603 (2016).
55. S.H.L. Klapp, Curr. Opin. Colloid Interface Sci. **21**, 76 (2016).
56. A.M. Earl, R. Losick, R. Kolter, Trends Microbiol. **16**, 269 (2008).
57. M. Pantastico-Caldas, K.E. Duncan, C.A. Istock, J.A. Bell, Ecology **73**, 1888 (1992).
58. H.W. Moon, R.E. Isaacson, J. Pohlenz, Am. J. Clin. Nutr. **32**, 119 (1979).
59. C. Palmela, C. Chevarin, Z. Xu, J. Torres, G. Sevrin, R. Hirten, N. Barnich, S.C. Ng, J.F. Colombel, Gut **67**, 574 (2018).
60. T.J. Moriarty, M.U. Norman, P. Colarusso, T. Bankhead, P. Kubes, G. Chaconas, PLoS Pathog. **4**, e1000090 (2008).
61. S.S. Suarez, A.A. Pacey, Hum. Reprod. Update **12**, 23 (2006).
62. V. Kantsler, J. Dunkel, M. Blayney, R.E. Goldstein, eLife **3**, e02403 (2014).
63. R. Nosrati, A. Driouchi, C.M. Yip, D. Sinton, Nat. Commun. **6**, 8703 (2015).
64. A.J. Reynolds, J. Fluid Mech. **23**, 241 (1965).
65. D.F. Katz, J. Fluid Mech. **64**, 33 (1974).
66. A.P. Berke, L. Turner, H.C. Berg, E. Lauga, Phys. Rev. Lett. **101**, 038102 (2008).
67. J. Elgeti, G. Gompper, EPL **85**, 38002 (2009).
68. G. Li, J.X. Tang, Phys. Rev. Lett. **103**, 078101 (2009).
69. I. Llopis, I. Pagonabarraga, J. Non-Newton. Fluid Mech. **165**, 946 (2010).
70. S.E. Spagnolie, E. Lauga, J. Fluid Mech. **700**, 105 (2012).
71. K. Ishimoto, E.A. Gaffney, Phys. Rev. E **88**, 062702 (2013).
72. K. Ishimoto, E.A. Gaffney, J. Theor. Biol. **360**, 187 (2014).
73. G.J. Li, A.M. Ardekani, Phys. Rev. E **90**, 013010 (2014).
74. D. Lopez, E. Lauga, Phys. Fluids **26**, 071902 (2014).
75. W.E. Uspal, M.N. Popescu, S. Dietrich, M. Tasinkevych, Soft Matter **11**, 434 (2015).
76. Y. Ibrahim, T.B. Liverpool, EPL **111**, 48008 (2015).
77. K. Schaar, A. Zöttl, H. Stark, Phys. Rev. Lett. **115**, 038101 (2015).
78. S. Das, A. Garg, A.I. Campbell, J. Howse, A. Sen, D. Velegol, R. Golestanian, S.J. Ebbens, Nat. Commun. **6**, 8999 (2015).
79. J. Elgeti, G. Gompper, Eur. Phys. J. ST **225**, 2333 (2016).
80. A. Mozaffari, N. Sharifi-Mood, J. Koplik, C. Maldarelli, Phys. Fluids **28**, 053107 (2016).
81. J. Simmchen, J. Katuri, W.E. Uspal, M.N. Popescu, M. Tasinkevych, S. Sánchez, Nat. Commun. **7**, 10598 (2016).
82. J.S. Lintuvuori, A.T. Brown, K. Stratford, D. Marenduzzo, Soft Matter **12**, 7959 (2016).

83. E. Lushi, V. Kantsler, R.E. Goldstein, Phys. Rev. E **96**, 023102 (2017).
84. K. Ishimoto, Phys. Rev. E **96**, 043103 (2017).
85. S. Yazdi, A. Borhan, Phys. Fluids **29**, 093104 (2017).
86. F. Rühle, J. Blaschke, J.-T. Kuhr, H. Stark, New J. Phys. **20**, 025003 (2018).
87. A. Mozaffari, N. Sharifi-Mood, J. Koplik, C. Maldarelli, Phys. Rev. Fluids **3**, 014104 (2018).
88. Z. Shen, A. Würger, J.S. Lintuvuori, Eur. Phys. J. E **41**, 39 (2018).
89. M. Mirzakhanloo, M.R. Alam, Phys. Rev. E **98**, 012603 (2018).
90. A. Ahmadzadegan, S. Wang, P.P. Vlachos, A.M. Ardekani, Phys. Rev. E **100**, 062605 (2019).
91. E. Lauga, W.R. DiLuzio, G.M. Whitesides, H.A. Stone, Biophys. J. **90**, 400 (2006).
92. R. Di Leonardo, D. Dell'Arciprete, L. Angelani, V. Iebba, Phys. Rev. Lett. **106**, 038101 (2011).
93. J. Hu, A. Wysocki, R.G. Winkler, G. Gompper, Sci. Rep. **5**, 9586 (2015).
94. A. Daddi-Moussa-Ider, M. Lisicki, C. Hoell, H. Löwen, J. Chem. Phys. **148**, 134904 (2018).
95. A. Daddi-Moussa-Ider, M. Lisicki, S. Gekle, A.M. Menzel, H. Löwen, J. Chem. Phys. **149**, 014901 (2018).
96. S.M. Mousavi, G. Gompper, R.G. Winkler, Soft Matter **16**, 4866 (2020).
97. A. Bilbao, E. Wajnryb, S.A. Vanapalli, J. Bławzdziewicz, Phys. Fluids **25**, 081902 (2013).
98. H. Wu, M. Thiébaud, W.-F. Hu, A. Farutin, S. Rafai, M.C. Lai, P. Peyla, C. Misbah, Phys. Rev. E **92**, 050701 (2015).
99. H. Wu, A. Farutin, W.F. Hu, M. Thiébaud, S. Rafaï, P. Peyla, M.C. Lai, C. Misbah, Soft Matter **12**, 7470 (2016).
100. A. Daddi-Moussa-Ider, M. Lisicki, A.J.T.M. Mathijssen, C. Hoell, S. Goh, Bławzdziewicz, A.M. Menzel, H. Löwen, J. Phys.: Condens. Matter **30**, 254004 (2018).
101. S. Dalal, A. Farutin, C. Misbah, Soft Matter **16**, 1599 (2020).
102. T. Brotto, J.-B. Caussin, E. Lauga, D. Bartolo, Phys. Rev. Lett. **110**, 038101 (2013).
103. A.J.T.M. Mathijssen, A. Doostmohammadi, J.M. Yeomans, T.N. Shendruk, J. Fluid Mech. **806**, 35 (2016).
104. N. Desai, A.M. Ardekani, Soft Matter **16**, 1731 (2020).
105. S. Das, A. Cacciuto, J. Chem. Phys. **151**, 244904 (2019).
106. P. Malgaretti, G. Oshanin, J. Talbot, J. Phys.: Condens. Matter **31**, 270201 (2019).
107. H. Wioland, F.G. Woodhouse, J. Dunkel, J.O. Kessler, R.E. Goldstein, Phys. Rev. Lett. **110**, 268102 (2013).
108. M. Theillard, R. Alonso-Matilla, D. Saintillan, Soft Matter **13**, 363 (2017).
109. T. Gao, M.D. Betterton, A.-S. Jhang, M.J. Shelley, Phys. Rev. Fluids **2**, 093302 (2017).
110. E. Lushi, H. Wioland, R.E. Goldstein, Proc. Natl. Acad. Sci. U.S.A. **111**, 9733 (2014).
111. D.P. Singh, A. Domínguez, U. Choudhury, S.N. Kottapalli, M.N. Popescu, S. Dietrich, P. Fischer, Nat. Commun. **11**, 2210 (2020).
112. B. Vincenti, G. Ramos, M.L. Cordero, C. Douarche, R. Soto, E. Clement, Nat. Commun. **10**, 5082 (2019).
113. G. Ramos, M.L. Cordero, R. Soto, Soft Matter **16**, 1359 (2020).
114. T. Mirkovic, N.S. Zacharia, G.D. Scholes, G.A. Ozin, ACS Nano **4**, 1782 (2010).
115. Y. Ding, F. Qiu, X. Casadevall i Solvas, F.W.Y. Chiu, B.J. Nelson, A. DeMello, Micromachines **7**, 25 (2016).
116. L. Zhu, F. Gallaire, Phys. Rev. Lett. **119**, 064502 (2017).
117. D. Takagi, J. Palacci, A.B. Braunschweig, M.J. Shelley, J. Zhang, Soft Matter **10**, 1784 (2014).
118. S.E. Spagnolie, G.R. Moreno-Flores, D. Bartolo, E. Lauga, Soft Matter **11**, 3396 (2015).
119. H. Jashnsaz, M. Al Juboori, C. Weistuch, N. Miller, T. Nguyen, V. Meyerhoff, B. McCoy, S. Perkins, R. Wallgren, B.D. Ray, K. Tsekouras, G.G. Anderson, S. Pressé, Biophys. J. **112**, 1282 (2017).
120. N. Desai, V.A. Shaik, A.M. Ardekani, Soft Matter **14**, 264 (2018).
121. N. Desai, A.M. Ardekani, Phys. Rev. E **98**, 012419 (2018).
122. N. Desai, V.A. Shaik, A.M. Ardekani, Front. Microbiol. **10**, 289 (2019).
123. V.A. Shaik, V. Vasani, A.M. Ardekani, J. Fluid Mech. **851**, 187 (2018).
124. V.A. Shaik, A.M. Ardekani, Phys. Rev. E **99**, 033101 (2019).
125. G.I. Taylor, Proc. R. Soc. Lond. A **209**, 447 (1951).
126. G.J. Elfring, E. Lauga, Phys. Rev. Lett. **103**, 088101 (2009).
127. M. Sauzade, G.J. Elfring, E. Lauga, Physica D **240**, 1567 (2011).
128. M. Dasgupta, B. Liu, H.C. Fu, M. Berhanu, K.S. Breuer, T.R. Powers, A. Kudrolli, Phys. Rev. E **87**, 013015 (2013).
129. T.D. Montenegro-Johnson, E. Lauga, Phys. Rev. E **89**, 060701 (2014).
130. M.J. Lighthill, Commun. Pure Appl. Math. **5**, 109 (1952).
131. J.R. Blake, J. Fluid Mech. **46**, 199 (1971).
132. O.S. Pak, E. Lauga, J. Eng. Math. **88**, 1 (2014).
133. I.O. Götze, G. Gompper, Phys. Rev. E **82**, 041921 (2010).
134. S. Thutupalli, R. Seemann, S. Herminghaus, New J. Phys. **13**, 073021 (2011).
135. L. Zhu, E. Lauga, L. Brandt, Phys. Fluids **24**, 051902 (2012).
136. L. Zhu, E. Lauga, L. Brandt, J. Fluid Mech. **726**, 285 (2013).
137. A. Zöttl, H. Stark, Phys. Rev. Lett. **112**, 118101 (2014).
138. J.S. Lintuvuori, A. Würger, K. Stratford, Phys. Rev. Lett. **119**, 068001 (2017).
139. J.-T. Kuhr, J. Blaschke, F. Rühle, H. Stark, Soft Matter **13**, 7548 (2017).
140. A. Zöttl, H. Stark, Eur. Phys. J. E **41**, 61 (2018).
141. M. Kuron, P. Stärk, C. Burkard, J. De Graaf, C. Holm, J. Chem. Phys. **150**, 144110 (2019).
142. J.-T. Kuhr, F. Rühle, H. Stark, Soft Matter **15**, 5685 (2019).
143. A. Zöttl, Chinese Phys. B (2020).
144. A. Najafi, R. Golestanian, Phys. Rev. E **69**, 062901 (2004).
145. R. Golestanian, A. Ajdari, Phys. Rev. E **77**, 036308 (2008).
146. R. Golestanian, Eur. Phys. J. E **25**, 1 (2008).
147. B. Liebchen, P. Monderkamp, B. ten Hagen, H. Löwen, Phys. Rev. Lett. **120**, 208002 (2018).
148. G.P. Alexander, C.M. Pooley, J.M. Yeomans, J. Phys.: Condens. Matter **21**, 204108 (2009).
149. S. Ziegler, M. Hubert, N. Vandewalle, J. Harting, A.-S. Smith, New J. Phys. **21**, 113017 (2019).

150. A. Sukhov, S. Ziegler, Q. Xie, O. Trosman, J. Pande, G. Grosjean, M. Hubert, N. Vandewalle, A.-S. Smith, J. Harting, J. Chem. Phys. **151**, 124707 (2019).
151. B. Nasouri, A. Vilfan, R. Golestanian, Phys. Rev. Fluids **4**, 073101 (2019).
152. A.M. Menzel, A. Saha, C. Hoell, H. Löwen, J. Chem. Phys. **144**, 024115 (2016).
153. C. Hoell, H. Löwen, A.M. Menzel, New J. Phys. **19**, 125004 (2017).
154. T.C. Adhyapak, S. Jabbari-Farouji, Phys. Rev. E **96**, 052608 (2017).
155. T.C. Adhyapak, S. Jabbari-Farouji, J. Chem. Phys. **149**, 144110 (2018).
156. C. Hoell, H. Löwen, A.M. Menzel, J. Chem. Phys. **149**, 144902 (2018).
157. A. Daddi-Moussa-Ider, A.M. Menzel, Phys. Rev. Fluids **3**, 094102 (2018).
158. A. Daddi-Moussa-Ider, M. Lisicki, H. Löwen, A.M. Menzel, Phys. Fluids **32**, 021902 (2020).
159. C. Hoell, H. Löwen, A.M. Menzel, J. Chem. Phys. **151**, 064902 (2019).
160. V.A. Shaik, A.M. Ardekani, J. Fluid Mech. **824**, 42 (2017).
161. S.Y. Reigh, L. Zhu, F. Gallaire, E. Lauga, Soft Matter **13**, 3161 (2017).
162. S.Y. Reigh, E. Lauga, Phys. Rev. Fluids **2**, 093101 (2017).
163. C. Pozrikidis, *Boundary Integral and Singularity Methods for Linearized Viscous Flow* (Cambridge University Press, Cambridge, UK, 1992).
164. C. K.V.S., S. Thampi, J. Phys. D: Appl. Phys. **53**, 314001 (2020).
165. L. Rückert, A. Zippelius, R. Kree, *Trajectories of a droplet driven by an internal active device* (2019) arXiv:1902.01159.
166. R. Kree, L. Rückert, A. Zippelius, *Dynamics of a droplet driven by an internal active device* arXiv:2004.10045 (2020).
167. J.R. Blake, Math. Proc. Camb. Philos. Soc. **70**, 303 (1971).
168. J.W. Swan, J.F. Brady, Phys. Fluids **19**, 113306 (2007).
169. R. Usha, S.D. Nigam, Fluid Dyn. Res. **11**, 75 (1993).
170. C. Maul, S. Kim, Phys. Fluids **6**, 2221 (1994).
171. C. Maul, S. Kim, J. Eng. Math. **30**, 119 (1996).
172. H. Hasimoto, Phys. Fluids **9**, 1838 (1997).
173. A. Sellier, Comput. Model. Eng. Sci. **25**, 165 (2008).
174. B.U. Felderhof, A. Sellier, J. Chem. Phys. **136**, 054703 (2012).
175. C. Aponte-Rivera, R.N. Zia, Phys. Rev. Fluids **1**, 023301 (2016).
176. C.A. Aponte Rivera, *Spherically confined colloidal suspensions of hydrodynamically interacting particles: A model for intracellular transport* PhD Thesis, Cornell University, USA (2017).
177. D.A. Edwards, H. Brenner, D.T. Wasan, *Interfacial Transport Processes and Rheology* (Elsevier Butterworth-Heinemann, Oxford, UK, 1991).
178. Y.O. Fuentes, S. Kim, D.J. Jeffrey, Phys. Fluids **31**, 2445 (1988).
179. Y.O. Fuentes, S. Kim, D.J. Jeffrey, Phys. Fluids A **1**, 61 (1989).
180. A. Daddi-Moussa-Ider, S. Gekle, Phys. Rev. E **95**, 013108 (2017).
181. A. Daddi-Moussa-Ider, M. Lisicki, S. Gekle, Phys. Rev. E **95**, 053117 (2017).
182. A. Daddi-Moussa-Ider, H. Löwen, S. Gekle, Eur. Phys. J. E **41**, 104 (2018).
183. C. Hoell, H. Löwen, A.M. Menzel, A. Daddi-Moussa-Ider, Eur. Phys. J. E **42**, 89 (2019).
184. V.A. Shaik, A.M. Ardekani, Phys. Rev. Fluids **2**, 113606 (2017).
185. S. Kim, S.J. Karrila, *Microhydrodynamics: Principles and Selected Applications* (Courier Corporation, New York, USA, 2013).
186. K.C. Neuman, S.M. Block, Rev. Sci. Instrum. **75**, 2787 (2004).
187. B.U. Felderhof, R.B. Jones, Physicochem. Hydrodyn. **11**, 507 (1989).
188. H.A. Stone, Phys. Fluids A: Fluid Dyn. **2**, 111 (1990).
189. L.C. Andrews, *Special Functions of Mathematics for Engineers*, Vol. **49** (SPIE Press, Bellingham, Washington, USA, 1998).
190. H. Lamb, *Hydrodynamics* (Cambridge University Press, Cambridge, UK, 1932).
191. R.G. Cox, J. Fluid Mech. **37**, 601 (1969).
192. J. Happel, H. Brenner, *Low Reynolds Number Hydrodynamics: With Special Applications to Particulate Media* (Springer Netherlands, Martinus Nijhoff Publishers, The Hague, 2012).
193. M. Abramowitz, I.A. Stegun, *Handbook of Mathematical Functions*, Vol. **5** (Dover, New York, 1972).
194. C. Misbah, Phys. Rev. Lett. **96**, 028104 (2006).
195. J. Bławzdziewicz, V. Cristini, M. Loewenberg, Phys. Fluids **11**, 251 (1999).
196. L.G. Leal, *Advanced Transport Phenomena: Fluid Mechanics and Convective Transport Processes*, Vol. **7** (Cambridge University Press, Cambridge, UK, 2007).
197. P.C.-H. Chan, L.G. Leal, J. Fluid Mech. **82**, 549 (1977).
198. H.K. Moffatt, J. Fluid Mech. **18**, 1 (1964).
199. S.E. Spagnolie, E. Lauga, J. Fluid Mech. **700**, 105 (2012).
200. D. Lopez, E. Lauga, Phys. Fluids **26**, 400 (2014).
201. S.D. Ryan, L. Berlyand, B.M. Haines, D.A. Karpeev, Multiscale Model. Simul. **11**, 1176 (2013).
202. S.E. Spagnolie, G.R. Moreno-Flores, D. Bartolo, E. Lauga, Soft Matter **11**, 3396 (2015).
203. A. Daddi-Moussa-Ider, C. Kurzthaler, C. Hoell, A. Zöttl, M. Mirzakhanloo, M.-R. Alam, A.M. Menzel, H. Löwen, S. Gekle, Phys. Rev. E **100**, 032610 (2019).
204. H.C. Berg, R.A. Anderson, Nature **245**, 380 (1973).
205. H.C. Berg, *E. coli in Motion* (Springer-Verlag New York, Inc., NY, USA, 2008).
206. J. Schwarz-Linek, J. Arlt, A. Jepson, A. Dawson, T. Vissers, D. Miroli, T. Pilizota, V.A. Martinez, W.C.K. Poon, Colloid Surf. B **137**, 2 (2016).
207. S. Chattopadhyay, R. Moldovan, C. Yeung, X.L. Wu, Proc. Natl. Acad. Sci. U.S.A. **103**, 13712 (2006).
208. N.C. Darnton, L. Turner, S. Rojevsky, H.C. Berg, J. Bacteriol. **189**, 1756 (2007).
209. A.P. Berke, L. Turner, H.C. Berg, E. Lauga, Phys. Rev. Lett. **101**, 038102 (2008).
210. G.B. Folland, *Real Analysis: Modern Techniques and Their Applications*, Vol. **40** (John Wiley & Sons, New York, USA, 1999).

P9 Axisymmetric Stokes flow due to a point-force singularity acting between two coaxially positioned rigid no-slip disks

Reproduced from

A. Daddi-Moussa-Ider, A. R. Sprenger, Y. Amarouchene, T. Salez, C. Schönecker, T. Richter, H. Löwen, and A. M. Menzel,
Axisymmetric Stokes flow due to a point-force singularity acting between two coaxially positioned rigid no-slip disks,
J. Fluid Mech. **904**, A34 (2020),
published by *Cambridge University Press* [296].

Digital Object Identifier (DOI): doi.org/10.1017/jfm.2020.706

Statement of contribution

A.D.M.I. conceived the study and prepared the figures. A.R.S. and A.D.M.I. carried out the analytical calculations. T.R. performed the numerical simulations. A.D.M.I. drafted the manuscript. All authors discussed and interpreted the results, edited the text, and finalized the manuscript.

Copyright and license notice

©The Author(s), 2020.
This is an Open Access article, distributed under the terms of the Creative Commons Attribution licence (http://creativecommons.org/licenses/by/4.0/), which permits unrestricted re-use, distribution, and reproduction in any medium, provided the original work is properly cited

J. Fluid Mech. (2020), *vol*. 904, A34. © The Author(s), 2020. **904** A34-1
Published by Cambridge University Press
This is an Open Access article, distributed under the terms of the Creative Commons Attribution licence (http://creativecommons.org/licenses/by/4.0/), which permits unrestricted re-use, distribution, and reproduction in any medium, provided the original work is properly cited.
doi:10.1017/jfm.2020.706

Axisymmetric Stokes flow due to a point-force singularity acting between two coaxially positioned rigid no-slip disks

Abdallah Daddi-Moussa-Ider[1,†], Alexander R. Sprenger[1], Yacine Amarouchene[2], Thomas Salez[2,3], Clarissa Schönecker[4,5], Thomas Richter[6], Hartmut Löwen[1] and Andreas M. Menzel[1,7]

[1]Institut für Theoretische Physik II: Weiche Materie, Heinrich-Heine-Universität Düsseldorf, 40225 Düsseldorf, Germany

[2]Univ. Bordeaux, CNRS, LOMA, UMR 5798, 33405 Talence, France

[3]Global Station for Soft Matter, Global Institution for Collaborative Research and Education, Hokkaido University, Sapporo, Hokkaido 060-0808, Japan

[4]Technische Universität Kaiserslautern, 67663 Kaiserslautern, Germany

[5]Max-Planck-Institut für Polymerforschung, 55218 Mainz, Germany

[6]Institut für Analysis und Numerik, Otto-von-Guericke-Universität Magdeburg, Universitätsplatz 2, 39106 Magdeburg, Germany

[7]Institut für Physik, Otto-von-Guericke-Universität Magdeburg, Universitätsplatz 2, 39106 Magdeburg, Germany

(Received 26 March 2020; revised 8 June 2020; accepted 14 August 2020)

We investigate theoretically, on the basis of the steady Stokes equations for a viscous incompressible fluid, the flow induced by a stokeslet located on the centre axis of two coaxially positioned rigid disks. The stokeslet is directed along the centre axis. No-slip boundary conditions are assumed to hold at the surfaces of the disks. We perform the calculation of the associated Green's function in large parts analytically, reducing the spatial evaluation of the flow field to one-dimensional integrations amenable to numerical treatment. To this end, we formulate the solution of the hydrodynamic problem for the viscous flow surrounding the two disks as a mixed boundary-value problem, which we then reduce to a system of four dual integral equations. We show the existence of viscous toroidal eddies arising in the fluid domain bounded by the two disks, manifested in the plane containing the centre axis through adjacent counter-rotating eddies. Additionally, we probe the effect of the confining disks on the slow dynamics of a point-like particle by evaluating the hydrodynamic mobility function associated with axial motion. Thereupon, we assess the appropriateness of the commonly employed superposition approximation and discuss its validity and applicability as a function of the geometrical properties of the system. Additionally, we complement our semi-analytical approach by finite-element computer simulations, which reveals a good agreement. Our results may find applications

† Email address for correspondence: abdallah.daddi.moussa.ider@uni-duesseldorf.de

Downloaded from https://www.cambridge.org/core. Universitaets und Landesbibliothek Duesseldorf, on 09 Mar 2022 at 15:29:48, subject to the Cambridge Core terms of use, available at https://www.cambridge.org/core/terms. https://doi.org/10.1017/jfm.2020.706

in guiding the design of microparticle-based sensing devices and electrokinetic transport in small-scale capacitors.

Key words: colloids, Navier–Stokes equations

1. Introduction

Manipulating colloidal particles suspended in viscous media is a challenging task and is of paramount importance in various fields of engineering and natural sciences. Frequently, taking into account the fluid-mediated hydrodynamic interactions between particles moving through a liquid is essential to predict the behaviour of colloidal suspensions and polymer solutions (Probstein 2005; Mewis & Wagner 2012). Recent advances in micro- and nanofluidic technologies have permitted the fabrication and manufacturing of channels with well-defined geometries and characteristic dimensions ranging from the micro- to the nanoscale. A deep understanding of the nature of the mutual interactions between particles and their confining interfaces is of crucial importance in guiding the design of devices and tools for an optimal nanoscale control of biological macromolecules. Notable examples include single-molecule manipulation (Turner *et al.* 1998; Campbell *et al.* 2004), DNA mapping for genomic applications (Reisner *et al.* 2005; Riehn *et al.* 2005; Persson & Tegenfeldt 2010), DNA separation and sorting (Doyle *et al.* 2002; Cross, Strychalski & Craighead 2007; Xia, Yan & Hou 2012), and rheological probing of complex structures using atomic force microscopy cantilevers (François *et al.* 2008, 2009; Dufour *et al.* 2012; Darwiche *et al.* 2013).

At these small scales, fluid flows are governed by low-Reynolds-number hydrodynamics, where viscous effects dominate over inertial effects (Kim & Karrila 2013). Solutions for fluid flows due to point forces, or stokeslets, acting close to confining boundaries have been tabulated for various types of geometries, as summarised in the classic textbook by Happel & Brenner (1983). The study of the fluid-mediated hydrodynamic interactions in a channel confinement has received significant attention from many researchers over the past couple of years. In the following, we provide a survey of the current state of the art and summarise the relevant literature on this subject.

The first attempt to address the motion of a spherical particle confined between two infinitely extended no-slip walls dates back to Faxén (1921), who calculated in his PhD dissertation the hydrodynamic mobility parallel to the walls. These calculations were performed when the particle is located in the quarter-plane or mid-plane between the two confining walls (Happel & Brenner 1983). Later, Oseen (1928) suggested that the hydrodynamic mobility between two walls could approximately be obtained by superposition of the contributions resulting from each single wall. A modified coherent superposition approximation was further suggested by Benesch, Yiacoumi & Tsouris (2003), providing the diffusion coefficients of a Brownian sphere in confining channels. These predictions were found to match more accurately the existing experimental data reported in the literature.

Exact solutions for a point-force singularity acting at an arbitrary position between two walls were first obtained using the image technique in a seminal article by Liron & Mochon (1976). It was noted that the effect of the second wall becomes important when the distance separating the particle from the closest wall is larger than approximately one-tenth of the channel width (Brenner 1999). Using this solution, Liron (1978) further investigated the fluid transport problem of cilia between two parallel plates.

Downloaded from https://www.cambridge.org/core. Universitaets und Landesbibliothek Duesseldorf, on 09 Mar 2022 at 15:29:48, subject to the Cambridge Core terms of use, available at https://www.cambridge.org/core/terms. https://doi.org/10.1017/jfm.2020.706

Downloaded from https://www.cambridge.org/core. Universitaets und Landesbibliothek Duesseldorf, on 09 Mar 2022 at 15:29:48, subject to the Cambridge Core terms of use, available at https://www.cambridge.org/core/terms. https://doi.org/10.1017/jfm.2020.706

A joint analytical–numerical approach (Ganatos, Pfeffer & Weinbaum 1980*a*; Ganatos, Weinbaum & Pfeffer 1980*b*) as well as a multipole expansion technique (Swan & Brady 2010) were presented to address the motion of an extended particle confined between two hard walls. Bhattacharya & Bławzdziewicz (2002) constructed the image system for the flow field produced by a force multipole in a space bounded by two parallel walls using the image representation for Stokes flow. In addition, compressibility effects were examined by Felderhof (2006, 2010*a*,*b*). In this context, Hackborn (1990) investigated the asymmetric Stokes flow between two parallel planes due to a rotlet singularity, the axis of which is parallel to the boundary planes. Further, Ozarkar & Sangani (2008) prescribed an analytical approach using the image-system technique for determining the Stokes flow around particles in a thin film bounded by a wall and a gas–liquid interface. More recently, Daddi-Moussa-Ider, Guckenberger & Gekle (2016) provided the frequency-dependent hydrodynamic mobility functions between two planar elastic interfaces endowed with resistance towards shear and bending deformation modes.

Experimentally, Dufresne, Altman & Grier (2001) reported direct imaging measurements of a colloidal particle diffusing between two parallel surfaces, finding a good agreement with the superposition approximation suggested by Oseen. In addition, video microscopy (Faucheux & Libchaber 1994) combined with optical tweezers (Lin, Yu & Rice 2000; Tränkle, Ruh & Rohrbach 2016) as well as dynamic light scattering (Lobry & Ostrowsky 1996) have also allowed for good agreement with available theoretical predictions. Further experimental investigations have focused on DNA conformation and diffusion in slit-like confinements (Balducci *et al.* 2006; Stein *et al.* 2006; Strychalski, Levy & Craighead 2008; Tang *et al.* 2010; Graham 2011; Dai *et al.* 2013; Jones, van der Maarel & Doyle 2013).

Concerning collective properties, the behaviour of suspensions in a channel bounded by two planar walls has received a lot of attention. For instance, Bhattacharya, Bławzdziewicz & Wajnryb (2005) examined the fluid-mediated hydrodynamic interactions in a suspension of spherical particles confined between two parallel planar walls under creeping-flow conditions. In addition, Bhattacharya (2008) considered the collective motion of a two-dimensional periodic array of colloidal particles in a slit pore. Using a novel accelerated Stokesian-dynamics algorithm, Baron, Bławzdziewicz & Wajnryb (2008) performed fully resolved computer simulations to investigate the collective motion of linear trains and regular square arrays of particles suspended in a viscous fluid bounded by two parallel plates. Further, Bławzdziewicz & Wajnryb (2008) analysed the far-field response to external forcing of a suspension of particles in a channel. Swan & Brady (2011) presented a numerical method for computing the hydrodynamic forces exerted on particles in a suspension confined between two parallel walls. Furthermore, Saintillan, Shaqfeh & Darve (2006) employed Brownian dynamics simulations to investigate the effect of chain flexibility on the cross-streamline migration of short polymers in a pressure-driven flow between two flat plates. The latter numerical study confirmed the existence of a shear-induced migration towards the channel centreline away from the confining solid boundaries.

The hydrodynamic problem of particles freely moving between plane-parallel walls in the presence of an incident flow has been further considered in still more details. Under an external flow, Uspal, Eral & Doyle (2013) showed how shape and geometric confinement of rigid microparticles can conveniently be tailored for self-steering. Jones (2004) made use of a two-dimensional Fourier-transform technique to obtain an analytic expression of the Green tensor for the Stokes equations with an incident Poiseuille flow. In addition, he provided the elements of the resistance and mobility tensors in this slit-like geometry. Bhattacharya, Bławzdziewicz & Wajnryb (2006) introduced a novel numerical algorithm

Downloaded from https://www.cambridge.org/core. Universitaets und Landesbibliothek Duesseldorf, on 09 Mar 2022 at 15:29:48, subject to the Cambridge Core terms of use, available at https://www.cambridge.org/core/terms. https://doi.org/10.1017/jfm.2020.706

based on transformations between Cartesian and spherical representations of Stokes flow to account for an incident Poiseuille flow. Staben, Zinchenko & Davis (2003) presented a novel boundary-integral algorithm for the motion of a particle between two parallel planar walls in Poiseuille flow. The boundary-integral method formulated in their work allowed the effects of the confining walls to be directly incorporated into the stress tensor, without requiring discretisation of the two walls. In this context, Griggs, Zinchenko & Davis (2007) and Janssen & Anderson (2007, 2008) employed boundary-integral methods to examine the motion of a deformable drop between two parallel walls in Poiseuille flow, where lateral migration towards the channel centre is observed.

Geometric confinement significantly alters the behaviour of swimming micro-organisms and can affect the motility of self-propelling active particles in a pronounced way (Lauga & Powers 2009; Menzel 2013, 2015; Bechinger *et al.* 2016; Lauga 2016; Zöttl & Stark 2016; Ostapenko *et al.* 2018; Gompper *et al.* 2020; Shaebani *et al.* 2020). Surface-related effects on microswimmers can lead to crucial implications for biofilm formation and microbial activity. In a channel bounded by two walls, Bilbao *et al.* (2013) studied the locomotion of a model nematode, finding that the swimming organism tends to swim faster and navigate more effectively under confinement. Furthermore, Wu *et al.* (2015, 2016) investigated the effect of confinement on the swimming behaviour of a model eukaryotic cell undergoing amoeboid motion. There, the swimmer has been modelled as an inextensible membrane deploying local active force. It has been found that confinement can strongly alter the swimming gait. In addition, Brotto *et al.* (2013) described theoretically the dynamics of self-propelling active particles in rigidly confined thin liquid films. They demonstrated that, due to hydrodynamic friction with the nearby rigid walls, confined microswimmers not only reorient themselves in response to flow gradients but also can show reorientation in uniform flows. In this context, Mathijssen *et al.* (2016) investigated theoretically the hydrodynamics of self-propelling microswimmers in a thin film. Daddi-Moussa-Ider *et al.* (2018) examined the behaviour of a three-sphere microswimmer in a channel bounded by two walls, where different swimming states have been observed. More recently, amoeboid swimming in a compliant channel was numerically investigated (Dalal, Farutin & Misbah 2020).

In all of the above-mentioned studies, the confining channel was assumed to be of infinite extent or periodically replicated along the lateral directions. Instead, here we consider the hydrodynamic problem for a point force acting near two coaxially positioned disks of finite radius. In many biologically and industrially relevant applications, finite-size effects become crucial for an accurate and reliable description of transport processes ranging from the microscale to the nanoscale. Prime examples include the ionic transport and electrokinetics in small-scale capacitors (Marini Bettolo Marconi & Melchionna 2012; Thakore & Hickman 2015; Babel, Eikerling & Löwen 2018; Asta *et al.* 2019), electrochemomechanical energy conversion in microfluidic channels (Daiguji *et al.* 2004), and the rheology of droplets, capsules or cells in constricted/structured microchannels (Park & Dimitrakopoulos 2013; Le Goff *et al.* 2017; Trégouët *et al.* 2018, 2019), where boundary effects may play a pivotal role.

In this paper, we take a step towards addressing this context by presenting an analytical theory for the viscous flow resulting from a stokeslet singularity acting along the centre axis of two coaxially positioned disks of no-slip surfaces. We formulate the hydrodynamic problem as a mixed boundary-value problem, which we then transform into a system of dual integral equations. Along this path, we show that the solution of the flow field in the fluid region bounded by the two disks exhibits viscous toroidal eddies. In addition to that, we derive expressions for the hydrodynamics mobility functions and discuss the applicability and limitations of the superposition approximation. Moreover, we support

Downloaded from https://www.cambridge.org/core. Universitaets und Landesbibliothek Duesseldorf, on 09 Mar 2022 at 15:29:48, subject to the Cambridge Core terms of use, available at https://www.cambridge.org/core/terms. https://doi.org/10.1017/jfm.2020.706

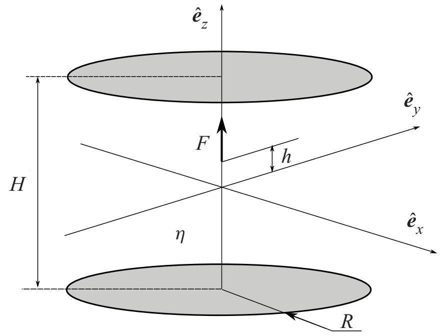

FIGURE 1. Schematic of the system. The surrounding viscous Newtonian fluid is set into motion through the action of a point-force singularity located on the symmetry axis of two coaxially positioned disks.

our semi-analytical results by numerical simulations using a finite-element method (FEM), which leads to a good agreement.

The remainder of this paper is organised as follows. In § 2, we formulate the problem mathematically and derive the corresponding system of dual integral equations, from which the solution for the hydrodynamic flow fields can be obtained. We then make use of this solution in § 3 to yield an integral expression of the mobility function of a point-like particle slowly translating along the axis of the disks. Concluding remarks and outlooks are contained in § 4. In appendix A, we detail the analytical derivation of the kernel functions arising in the resulting integral equations.

2. Mathematical formulation

We examine the axisymmetric flow induced by a stokeslet singularity acting on the axis of symmetry of two coaxially positioned circular disks of equal radius R. Moreover, we suppose that the disks are located within the planes $z = -H/2$ and $z = H/2$, with H denoting the separation distance between the disks. Their centres are positioned on the z axis. In addition, we assume that the surrounding viscous fluid is Newtonian, of constant dynamic viscosity η, and that the flow is incompressible.

2.1. *Governing equations*

In low-Reynolds-number hydrodynamics, the fluid dynamics is governed by the Stokes equations (Happel & Brenner 1983)

$$\nabla \cdot \boldsymbol{v} = 0, \tag{2.1a}$$

$$\nabla \cdot \boldsymbol{\sigma} + F\delta(\boldsymbol{r} - \boldsymbol{r}_0)\,\hat{\boldsymbol{e}}_z = \boldsymbol{0}, \tag{2.1b}$$

where $\boldsymbol{v}$ and $\boldsymbol{\sigma}$ denote, respectively, the fluid velocity field and the hydrodynamic stress tensor. For a Newtonian fluid, the latter is given by $\boldsymbol{\sigma} = -p\boldsymbol{I} + 2\eta\boldsymbol{E}$, where p is the pressure field and $\boldsymbol{E} = (\nabla\boldsymbol{v} + (\nabla\boldsymbol{v})^{\mathrm{T}})/2$ is the rate-of-strain tensor, with the superscript T denoting a transpose. In addition, δ stands for the Dirac delta function, and F is the amplitude of a stationary point force acting on the fluid at position $\boldsymbol{r}_0 = h\hat{\boldsymbol{e}}_z$, where $-H/2 < h < H/2$, with $\hat{\boldsymbol{e}}_z$ denoting the unit vector along the z direction. See figure 1 for an illustration of the system set-up. In the remainder of this paper, we scale all the lengths involved in the problem by the separation H of the two disks.

Downloaded from https://www.cambridge.org/core. Universitaets und Landesbibliothek Duesseldorf, on 09 Mar 2022 at 15:29:48, subject to the Cambridge Core terms of use, available at https://www.cambridge.org/core/terms. https://doi.org/10.1017/jfm.2020.706

We designate by the subscript 1 the variables and parameters in the fluid region underneath the plane containing the lower disk, for which $z \leq -1/2$, by the subscript 2 the fluid domain bounded by the planes $z = -1/2$ and $z = 1/2$, and by the subscript 3 the region above the plane containing the upper disk, for which $z \geq 1/2$. Since the system is axisymmetric, all field variables are thus functions of the radial and axial coordinates only. Accordingly, the Stokes equations (2.1) can be projected onto the cylindrical coordinate system as

$$\frac{v_r}{r} + \frac{\partial v_r}{\partial r} + \frac{\partial v_z}{\partial z} = 0, \tag{2.2a}$$

$$-\frac{\partial p}{\partial r} + \eta \left(\Delta v_r - \frac{v_r}{r^2} \right) = 0, \tag{2.2b}$$

$$-\frac{\partial p}{\partial z} + \eta \Delta v_z + F\delta(\boldsymbol{r} - \boldsymbol{r}_0) = 0, \tag{2.2c}$$

wherein v_r and v_z denote the radial and axial fluid velocities, respectively, and Δ is the Laplace operator given by

$$\Delta := \frac{\partial^2}{\partial r^2} + \frac{1}{r}\frac{\partial}{\partial r} + \frac{\partial^2}{\partial z^2}. \tag{2.3}$$

We note that the three-dimensional Dirac delta function is expressed in axisymmetric cylindrical coordinates as $\delta(\boldsymbol{r} - \boldsymbol{r}_0) = (\pi r)^{-1}\delta(r)\delta(z-h)$ (Bracewell 1999).

In an unbounded viscous fluid, i.e. in the absence of the disks, the solution of equations (2.2) is given by the Oseen tensor, commonly denominated as the free-space Green function (Kim & Karrila 2013)

$$v_r^S = \frac{F}{8\pi\eta}\frac{r(z-h)}{\rho^3}, \quad v_z^S = \frac{F}{8\pi\eta}\left(\frac{2}{\rho} - \frac{r^2}{\rho^3}\right), \tag{2.4a,b}$$

with the distance from the position of the point force $\rho = (r^2 + (z-h)^2)^{1/2}$. The corresponding pressure field reads

$$p^S = \frac{F}{4\pi}\frac{z-h}{\rho^3}. \tag{2.5}$$

In the presence of the confining disks, the solution of the flow problem can be expressed as a superposition of the solution in an unbounded fluid, given above by (2.4*a*,*b*) and (2.5), and a complementary solution, the sum of the two solutions being required to satisfy the underlying regularity and boundary conditions. Then

$$\boldsymbol{v} = \boldsymbol{v}^S + \boldsymbol{v}^*, \quad p = p^S + p^*, \tag{2.6a,b}$$

wherein $\boldsymbol{v}^*$ and p^* stand for the complementary solutions (also referred to as the image solution (Blake 1971)) for the velocity and pressure fields, respectively.

For an axisymmetric Stokes flow, the general solution can be expressed in terms of two harmonic functions ϕ and ψ as (Imai 1973; Kim 1983)

$$v_r^* = z\frac{\partial \phi}{\partial r} + \frac{\partial \psi}{\partial r}, \quad v_z^* = z\frac{\partial \phi}{\partial z} - \phi + \frac{\partial \psi}{\partial z}, \quad p^* = 2\eta\frac{\partial \phi}{\partial z}, \tag{2.7a–c}$$

with

$$\Delta\phi = 0, \quad \Delta\psi = 0. \tag{2.8a,b}$$

Downloaded from https://www.cambridge.org/core. Universitaets und Landesbibliothek Duesseldorf, on 09 Mar 2022 at 15:29:48, subject to the Cambridge Core terms of use, available at https://www.cambridge.org/core/terms. https://doi.org/10.1017/jfm.2020.706

In each of the three fluid domains introduced above, the solution of Laplace's equations (2.8*a*,*b*) can be expressed in terms of Fourier–Bessel integrals as

$$\phi_i = \frac{F}{8\pi\eta} \int_0^\infty \left(A_i^+(\lambda)\mathrm{e}^{\lambda z} + A_i^-(\lambda)\mathrm{e}^{-\lambda z}\right) J_0(\lambda r)\,\mathrm{d}\lambda, \tag{2.9a}$$

$$\psi_i = \frac{F}{8\pi\eta} \int_0^\infty \left(B_i^+(\lambda)\mathrm{e}^{\lambda z} + B_i^-(\lambda)\mathrm{e}^{-\lambda z}\right) J_0(\lambda r)\,\mathrm{d}\lambda, \tag{2.9b}$$

for $i \in \{1, 2, 3\}$, with λ denoting the wavenumber and J_k the kth-order Bessel function of the first kind (Abramowitz & Stegun 1972). In addition, $A_i^\pm$ and $B_i^\pm$ are wavenumber-dependent unknown coefficients, to be determined from the regularity and boundary conditions. Then, the components of the image velocity and pressure fields are given by

$$v_{r\,i}^* = -\frac{F}{8\pi\eta} \int_0^\infty \lambda\left((zA_i^+ + B_i^+)\mathrm{e}^{\lambda z} + (zA_i^- + B_i^-)\mathrm{e}^{-\lambda z}\right) J_1(\lambda r)\,\mathrm{d}\lambda, \tag{2.10a}$$

$$v_{z\,i}^* = -\frac{F}{8\pi\eta} \int_0^\infty \left(E_i^+\mathrm{e}^{\lambda z} + E_i^-\mathrm{e}^{-\lambda z}\right) J_0(\lambda r)\,\mathrm{d}\lambda, \tag{2.10b}$$

$$p_i^* = \frac{F}{4\pi} \int_0^\infty \lambda\left(A_i^+\mathrm{e}^{\lambda z} - A_i^-\mathrm{e}^{-\lambda z}\right) J_0(\lambda r)\,\mathrm{d}\lambda, \tag{2.10c}$$

for $i \in \{1, 2, 3\}$, where we have defined the abbreviations $E_i^\pm = (1 \mp \lambda z)A_i^\pm \mp \lambda B_i^\pm$.

2.2. *Boundary conditions and dual integral equations*

As regularity conditions, for the image field we require the velocity and pressure far away from the singularity location to vanish as $\rho \to \infty$. This implies that $A_1^- = B_1^- = A_3^+ = B_3^+ = 0$. In what follows, to simplify notation, we drop the plus sign in the fluid domain underneath the lower disk to denote $A_1 = A_1^+$ and $B_1 = B_1^+$, and we drop the minus sign in the fluid domain above the upper disk to denote $A_3 = A_3^-$ and $B_3 = B_3^-$.

The boundary conditions consist of requiring (*a*) the natural continuity of the total fluid velocity field at the interfaces between the fluid domains, (*b*) vanishing total velocities at the surfaces of the disks (the no-slip and no-permeability boundary condition Lauga, Brenner & Stone 2007), and (*c*) continuity of the total viscous-stress vectors at the interfaces between the fluid domains outside the regions occupied by the disks. Mathematically, these conditions can be expressed as

$$(\boldsymbol{v}_1 - \boldsymbol{v}_2)|_{z=-1/2} = (\boldsymbol{v}_2 - \boldsymbol{v}_3)|_{z=1/2} = \boldsymbol{0} \quad (r > 0), \tag{2.11a}$$

$$\boldsymbol{v}_1|_{z=-1/2} = \boldsymbol{v}_2|_{z=\pm 1/2} = \boldsymbol{v}_3|_{z=1/2} = \boldsymbol{0} \quad (r < R), \tag{2.11b}$$

$$(\boldsymbol{\sigma}_2 - \boldsymbol{\sigma}_1)\boldsymbol{\cdot}\hat{\boldsymbol{e}}_z|_{z=-1/2} = (\boldsymbol{\sigma}_3 - \boldsymbol{\sigma}_2)\boldsymbol{\cdot}\hat{\boldsymbol{e}}_z|_{z=1/2} = \boldsymbol{0} \quad (r > R), \tag{2.11c}$$

where the components of the stress vector are expressed in cylindrical coordinates for an axisymmetric flow field by

$$\boldsymbol{\sigma}_i\boldsymbol{\cdot}\hat{\boldsymbol{e}}_z = \eta\left(\frac{\partial v_{ri}}{\partial z} + \frac{\partial v_{zi}}{\partial r}\right)\hat{\boldsymbol{e}}_r + \left(-p_i + 2\eta\,\frac{\partial v_{zi}}{\partial z}\right)\hat{\boldsymbol{e}}_z, \quad i \in \{1, 2, 3\}. \tag{2.12}$$

Applying the continuity of the radial components of the fluid velocity at the surfaces occupied by the two disks yields the expressions of the wavenumber-dependent

Downloaded from https://www.cambridge.org/core. Universitaets und Landesbibliothek Duesseldorf, on 09 Mar 2022 at 15:29:48, subject to the Cambridge Core terms of use, available at https://www.cambridge.org/core/terms. https://doi.org/10.1017/jfm.2020.706

coefficients associated with the intermediate fluid domain bounded by the two disks as functions of those in the lower and upper fluid domains. Defining $\boldsymbol{X}_2 = (A_2^-, B_2^-, A_2^+, B_2^+)^{\mathrm{T}}$ and $\boldsymbol{X}_{13} = (A_1, B_1, A_3, B_3)^{\mathrm{T}}$, we obtain

$$\boldsymbol{X}_2 = \boldsymbol{Q} \boldsymbol{\cdot} \boldsymbol{X}_{13}, \tag{2.13}$$

where the matrix $\boldsymbol{Q}$ is given by

$$\boldsymbol{Q} = \left(s^2 - \lambda^2\right)^{-1} \begin{pmatrix} \frac{1}{2}\,(s + \lambda c) & -\lambda s & -\frac{1}{2}\,\phi^+ & -\lambda^2 \\ \frac{1}{4}\lambda s & \frac{1}{2}\,(s - \lambda c) & -\frac{1}{4}\lambda^2 & -\frac{1}{2}\,\phi^- \\ -\frac{1}{2}\,\phi^+ & \lambda^2 & \frac{1}{2}\,(s + \lambda c) & \lambda s \\ \frac{1}{4}\lambda^2 & -\frac{1}{2}\,\phi^- & -\frac{1}{4}\lambda s & \frac{1}{2}\,(s - \lambda c) \end{pmatrix}. \tag{2.14}$$

Here, we have defined for convenience the abbreviations $s = \sinh(\lambda)$ and $c = \cosh(\lambda)$. In addition, $\phi^{\pm} = \lambda(\lambda \pm 1) + s\mathrm{e}^{-\lambda}$.

On the one hand, by addressing the no-slip velocity boundary conditions at the surfaces of the disks prescribed by (2.11*b*) and projecting the resulting equations onto the radial and tangential directions, four integral equations on the *inner* domain are obtained:

$$\int_0^\infty \lambda\left(\tfrac{1}{2}A_1 - B_1\right)\mathrm{e}^{-(\lambda/2)} J_1(\lambda r)\,\mathrm{d}\lambda = \psi_1^+(r) \quad (r < R), \tag{2.15a}$$

$$\int_0^\infty \lambda\left(\tfrac{1}{2}A_3 + B_3\right)\mathrm{e}^{-(\lambda/2)} J_1(\lambda r)\,\mathrm{d}\lambda = \psi_1^-(r) \quad (r < R), \tag{2.15b}$$

$$\int_0^\infty \left(A_1 + \lambda\left(\tfrac{1}{2}A_1 - B_1\right)\right)\mathrm{e}^{-(\lambda/2)} J_0(\lambda r)\,\mathrm{d}\lambda = \psi_2^+(r) \quad (r < R), \tag{2.15c}$$

$$\int_0^\infty \left(A_3 + \lambda\left(\tfrac{1}{2}A_3 + B_3\right)\right)\mathrm{e}^{-(\lambda/2)} J_0(\lambda r)\,\mathrm{d}\lambda = \psi_2^-(r) \quad (r < R). \tag{2.15d}$$

Here the terms appearing on the right-hand sides in these equations are radial functions resulting from the evaluation of the terms associated with the flow velocity field induced by the free-space stokeslet at the surfaces of the coaxially positioned disks. They are explicitly given by

$$\psi_1^{\pm}(r) = \frac{\pm r\left(h \pm \frac{1}{2}\right)}{\left(r^2 + \left(h \pm \frac{1}{2}\right)^2\right)^{3/2}}, \quad \psi_2^{\pm}(r) = \frac{r^2 + 2\left(h \pm \frac{1}{2}\right)^2}{\left(r^2 + \left(h \pm \frac{1}{2}\right)^2\right)^{3/2}}. \tag{2.16a,b}$$

On the other hand, four integral equations on the *outer* domain are obtained by addressing the continuity of the hydrodynamic stress vector at $z = \pm 1/2$ prescribed by (2.11*c*). They can be cast in the form

$$\int_0^\infty g_i(\lambda) J_1(\lambda r)\,\mathrm{d}\lambda = 0 \quad (r > R), \quad i \in \{1, 3\}, \tag{2.17a}$$

$$\int_0^\infty g_i(\lambda) J_0(\lambda r)\,\mathrm{d}\lambda = 0 \quad (r > R), \quad i \in \{2, 4\}, \tag{2.17b}$$

Downloaded from https://www.cambridge.org/core. Universitaets und Landesbibliothek Duesseldorf, on 09 Mar 2022 at 15:29:48, subject to the Cambridge Core terms of use, available at https://www.cambridge.org/core/terms. https://doi.org/10.1017/jfm.2020.706

where we have defined the wavenumber-dependent quantities

$$g_1(\lambda) = \lambda^2 \left(\left(\tfrac{1}{2}A_2^- - B_2^- \right) e^{\lambda/2} + \left(\tfrac{1}{2}\left(A_1 - A_2^+\right) + B_2^+ - B_1 \right) e^{-(\lambda/2)} \right), \tag{2.18a}$$

$$g_3(\lambda) = \lambda^2 \left(\left(\tfrac{1}{2}A_2^+ + B_2^+ \right) e^{\lambda/2} + \left(\tfrac{1}{2}\left(A_3 - A_2^-\right) + B_3 - B_2^- \right) e^{-(\lambda/2)} \right), \tag{2.18b}$$

$$g_2(\lambda) = C^- e^{\lambda/2} + \lambda \left(\left(1 + \tfrac{1}{2}\lambda\right) \left(A_1 - A_2^+\right) + \lambda \left(B_2^+ - B_1\right) \right) e^{-(\lambda/2)}, \tag{2.18c}$$

$$g_4(\lambda) = C^+ e^{\lambda/2} + \lambda \left(\left(1 + \tfrac{1}{2}\lambda\right) \left(A_3 - A_2^-\right) + \lambda \left(B_3 - B_2^-\right) \right) e^{-(\lambda/2)}, \tag{2.18d}$$

wherein $C^\pm = \lambda((1-\lambda/2)A_2^\pm \mp \lambda B_2^\pm)$.

Inserting (2.13) and (2.14), equations (2.15)–(2.18) form a system of four dual integral equations (Tricomi 1985) for the unknown wavenumber-dependent coefficients regrouped in $\boldsymbol{X}_{13}$. A solution of such types of dual integral equations with Bessel kernels can be obtained by the methods prescribed by Sneddon (1960, 1966) and Copson (1961). A similar procedure has recently been employed by some of us to address the axisymmetric flow induced by a stokeslet near a circular elastic membrane (Daddi-Moussa-Ider, Kaoui & Löwen 2019), and the asymmetric flow field near a finite-sized rigid disk (Daddi-Moussa-Ider *et al.* 2020). Once $\boldsymbol{X}_{13}$ is determined from solving the dual integral equations derived above, the remaining wavenumber-dependent coefficients expressed by $\boldsymbol{X}_2$ follow forthwith from (2.13) and (2.14).

The core idea of our solution approach consists of expressing the solution of (2.17) as definite integrals of the forms

$$g_i(\lambda) = 2\lambda^{1/2} \int_0^R f_i(t) J_{3/2}(\lambda t)\, dt, \quad i \in \{1, 3\}, \tag{2.19a}$$

and

$$g_i(\lambda) = 2\lambda^{1/2} \int_0^R f_i(t) J_{1/2}(\lambda t)\, dt, \quad i \in \{2, 4\}, \tag{2.19b}$$

where $f_i : [0, R] \to \mathbb{R}$, for $i \in \{1, 2, 3, 4\}$, are unknown functions to be determined. Accordingly, the integral equations in the outer domain boundaries are automatically satisfied upon making use of the following identity, which holds for any positive integer p (Abramowitz & Stegun 1972),

$$\int_0^\infty \lambda^{1/2} J_p(\lambda r) J_{p+1/2}(\lambda t)\, d\lambda = 0 \quad (0 < t < r). \tag{2.20}$$

By solving (2.18) for the coefficients A_1, B_1, A_3 and B_3 upon making use of (2.13) and (2.14), equation (2.15) can be rewritten as

$$\int_0^\infty (2\lambda)^{-1} \left(g_1(\lambda) + (\lambda - 1)\, e^{-\lambda} g_3(\lambda) + \lambda e^{-\lambda} g_4(\lambda) \right) J_1(\lambda r)\, d\lambda = \psi_1^+(r), \tag{2.21a}$$

$$\int_0^\infty (2\lambda)^{-1} \left((\lambda - 1)\, e^{-\lambda} g_1(\lambda) + \lambda e^{-\lambda} g_2(\lambda) + g_3(\lambda) \right) J_1(\lambda r)\, d\lambda = \psi_1^-(r), \tag{2.21b}$$

$$\int_0^\infty (2\lambda)^{-1} \left(g_2(\lambda) + \lambda e^{-\lambda} g_3(\lambda) + (\lambda + 1)\, e^{-\lambda} g_4(\lambda) \right) J_0(\lambda r)\, d\lambda = \psi_2^+(r), \tag{2.21c}$$

$$\int_0^\infty (2\lambda)^{-1} \left(\lambda e^{-\lambda} g_1(\lambda) + (\lambda + 1)\, e^{-\lambda} g_2(\lambda) + g_4(\lambda) \right) J_0(\lambda r)\, d\lambda = \psi_2^-(r). \tag{2.21d}$$

Downloaded from https://www.cambridge.org/core. Universitaets und Landesbibliothek Duesseldorf, on 09 Mar 2022 at 15:29:48, subject to the Cambridge Core terms of use, available at https://www.cambridge.org/core/terms. https://doi.org/10.1017/jfm.2020.706

Next, by substituting (2.19) into (2.21) and interchanging the order of the integrations with respect to the variables t and λ, the equations associated with the inner problem can be expressed in the following final forms:

$$\int_0^R (L_5(r,t)f_1(t) + L_4(r,t)f_3(t) + L_1(r,t)f_4(t))\,\mathrm{d}t = \psi_1^+(r), \tag{2.22a}$$

$$\int_0^R (L_4(r,t)f_1(t) + L_1(r,t)f_2(t) + L_5(r,t)f_3(t))\,\mathrm{d}t = \psi_1^-(r), \tag{2.22b}$$

$$\int_0^R (L_6(r,t)f_2(t) + L_3(r,t)f_3(t) + L_2(r,t)f_4(t))\,\mathrm{d}t = \psi_2^+(r), \tag{2.22c}$$

$$\int_0^R (L_3(r,t)f_1(t) + L_2(r,t)f_2(t) + L_6(r,t)f_4(t))\,\mathrm{d}t = \psi_2^-(r), \tag{2.22d}$$

where the kernels $L_i : [0, R]^2 \to \mathbb{R}$, for $i \in \{1, 2, 3, 4\}$, are complex mathematical functions that are defined and provided in appendix A.

Equations (2.22) form a system of four Fredholm integral equations of the first kind (Smithies 1958; Polyanin & Manzhirov 1998) for the unknown functions $f_i(t)$, $i \in \{1, 2, 3, 4\}$. Owing to the complicated nature of the kernel functions, we make recourse to numerical solutions.

2.3. *Numerical solution of the integral equations and comparison with FEM simulations*

We now summarise the main steps involved in the numerical computations of the flow field. First, the integration over the intervals $[0, R]$ in (2.22) are partitioned into N subintervals and each integral is approximated by the standard middle Riemann sum (Davis & Rabinowitz 2007). The four resulting equations are evaluated at N values of t_j that are uniformly distributed over the interval $[0, R]$ such that $t_j = (j - 1/2)(R/N)$, with $j = 1, \ldots, N$. Secondly, the discrete values of $f_i(t_j)$, with $i \in \{1, 2, 3, 4\}$, are obtained by solving the resulting linear system of $4N$ equations. Thirdly, the four integrals in (2.19) are converted into well-behaved definite integrals over $[0, \pi/2]$ by using the change of variable $\lambda = \tan u$ and thus $\mathrm{d}\lambda = \mathrm{d}u/\cos^2 u$. Thereupon, the resulting integrals are also approximated by the middle Riemann sum, and the wavenumber-dependent functions $g_i(\lambda_k = \tan u_k)$, $k = 1, \ldots, M$, are evaluated at discrete values of u_k such that $u_k = (k - 1/2)(\pi/2)/M$. Fourthly, the values of $\boldsymbol{X}_2$ at each discrete point λ_k are readily obtained by inverting the linear system of four equations given by (2.18). In addition, it follows from (2.13) that $\boldsymbol{X}_{13} = \boldsymbol{Q}^{-1} \boldsymbol{\cdot} \boldsymbol{X}_2$. Finally, the image flow fields are obtained from (2.10) by approximating, again, the integrals by the middle Riemann sum.

Even though the approach employed here may seem cumbersome at first glance, it has the advantage of being amenable to straightforward implementation. Unlike many direct numerical simulation techniques, which generally require discretisation of the entire three-dimensional fluid domain, or of at least an effectively two-dimensional domain when the axial symmetry is exploited, the integral formulation presented in this work reduces the solution of the flow problem to a set of one-dimensional integrals. Besides, the present semi-analytical approach might serve as a motivation for various theoretical investigations of related problems that could possibly pave the way towards real engineering applications.

In figure 2, we present a log–log plot of the variations of the discretisation error (Roy 2010) associated with the numerical computation of the amplitude of the image velocity

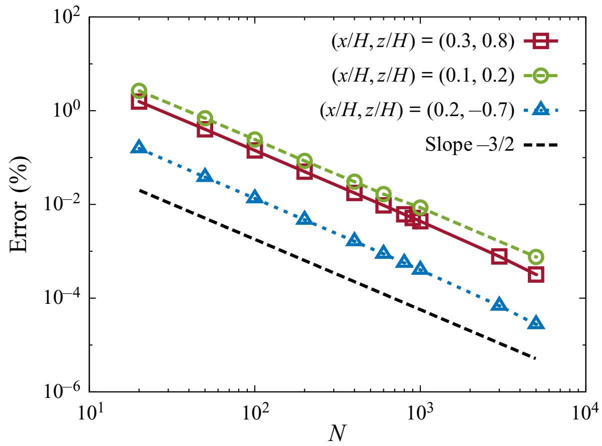

FIGURE 2. Log–log plot of the relative discretisation error occurring in the computation of the amplitude of the image velocity field versus the number of discretisation points, evaluated at various positions within the fluid domain. Here, we set $R = H$, $h/H = 0.3$ and $M = 10N$. The errors are estimated relative to the corresponding values computed using a finer grid spacing with $N = 15\,000$ and $M = 150\,000$.

field versus the number of discrete points used in the numerical integration of (2.22) while keeping $M = 10N$ in the discretisation of (2.19) and (2.10). The error is estimated relative to the numerical solution on a finer gird size for $N = 15\,000$ and $M = 150\,000$ at three different points of the fluid domain. We observe that the error decays approximately algebraically as $N^{-3/2}$ over the whole range of considered values of N and lies well below 10^{-3} % for $N \geq 5000$. We have checked that a similar behaviour is also found when varying the position of the stokeslet or the evaluation point within the fluid domain.

To validate our semi-analytical solution, we perform direct numerical simulations for the same geometry as well. We use a piecewise-quadratic finite-element discretisation of the Stokes problem stated by (2.2) in cylindrical coordinates. Since such an equal-order discretisation does not satisfy the inf-sup condition, we add stabilisation terms of local projection type (Becker & Braack 2001). The numerical domain is artificially limited to $(0, R) \times (-Z, Z)$ with $R, Z \in \mathbb{R}$ being sufficiently large numbers so as to avoid spurious feedback to the region of interest close to the plates. In addition, the Dirac delta function forcing the flow is represented exactly in the variational formulation by means of

$$\int_0^R \int_{-Z}^{Z} r\delta(\boldsymbol{r} - \boldsymbol{r}_0)\phi_z(\boldsymbol{r})\,\mathrm{d}r\,\mathrm{d}z = \phi_z(\boldsymbol{r}_0), \tag{2.23}$$

where ϕ_z is the test function corresponding to the vertical direction. Numerically, the singularity calls for very fine mesh resolution close to $\boldsymbol{r}_0$ and in proximity to the coaxially positioned plates, which we accomplish by local mesh adaptivity (Braack & Richter 2006). Further details on the discretisation method and the solution of the resulting linear systems of equations can be found in Richter (2017).

In figure 3, we represent the graphs of the resulting streamlines as well as contour plots of the total velocity field resulting from a stokeslet singularity axisymmetrically acting at various positions along the axis of two coaxially disposed disks of unit radius. Here, we set the numbers of discrete points to $N = 15\,000$ and $M = 150\,000$ in our numerical evaluation of the analytical description. The magnitude of the scaled velocity field is

Downloaded from https://www.cambridge.org/core. Universitaets und Landesbibliothek Duesseldorf, on 09 Mar 2022 at 15:29:48, subject to the Cambridge Core terms of use, available at https://www.cambridge.org/core/terms. https://doi.org/10.1017/jfm.2020.706

Downloaded from https://www.cambridge.org/core. Universitaets und Landesbibliothek Duesseldorf, on 09 Mar 2022 at 15:29:48, subject to the Cambridge Core terms of use, available at https://www.cambridge.org/core/terms. https://doi.org/10.1017/jfm.2020.706

shown on a logarithmic scale in order to better appreciate the difference in magnitude between the different fluid regions. In each panel, we depict on the left-hand side the results obtained via our semi-analytical approach derived in the present work. On the right-hand side in each panel, we include the corresponding flow fields determined via the FEM simulations. Good agreement between the two solution procedures is obtained over the whole fluid domain, demonstrating the robustness and applicability of our semi-analytical approach. Most noticeably, we observe the existence of adjacent counter-rotating eddies, the axis of rotation of which is directed along the azimuthal direction. Accordingly, the resulting flow field in the inner region consists of toroidal eddies on account of the axisymmetric nature of the flow (Moffatt 1964). In contrast to that, descending streamlines are obtained in the outer region. For infinitely large disks, analogous toroidal structures have previously been identified and proven to decay exponentially with distance from the singularity position (Liron & Blake 1981). Moreover, we remark that the overall magnitude of the flow field becomes less important as the point force gets closer to a confining plate. This behaviour is accompanied by a notable increase of the asymmetry of the counter-rotating eddies.

Having derived the solution of the flow problem due to an axisymmetric stokeslet acting near two finite-sized coaxially positioned disks, we next employ our formalism to recover the solution earlier obtained by Liron & Mochon (1976) for a stokeslet acting between two parallel planar walls of infinite extent along the transverse direction.

2.4. *Solution for $R \to \infty$*

For infinitely large disks, the integral equations (2.21) in the inner domain become defined for the whole axis of positive real numbers. Accordingly, the solution for the unknown functions $g_i(\lambda)$, for $i \in \{1, 2, 3, 4\}$, can be obtained using inverse Hankel transforms. By making use of the orthogonality property of Bessel functions (Abramowitz & Stegun 1972)

$$\int_0^\infty rJ_\nu(\lambda r)J_\nu(\lambda' r)\,\mathrm{d}r = \lambda^{-1}\delta(\lambda - \lambda'), \tag{2.24}$$

we readily obtain

$$\boldsymbol{H}\boldsymbol{\cdot}\boldsymbol{g} = \hat{\boldsymbol{\psi}}, \tag{2.25}$$

where we have defined the unknown vector $\boldsymbol{g} = (g_1, g_2, g_3, g_4)^{\mathrm{T}}$, the wavenumber-dependent matrix

$$\boldsymbol{H} = \begin{pmatrix} \mathrm{e}^\lambda & 0 & \lambda - 1 & \lambda \\ \lambda - 1 & \lambda & \mathrm{e}^\lambda & 0 \\ 0 & \mathrm{e}^\lambda & \lambda & \lambda + 1 \\ \lambda & \lambda + 1 & 0 & \mathrm{e}^\lambda \end{pmatrix}, \tag{2.26}$$

and where $\hat{\boldsymbol{\psi}} = (\hat{\psi}_1^+, \hat{\psi}_1^-, \hat{\psi}_2^+, \hat{\psi}_2^-)^{\mathrm{T}}$ gathers the inverse Hankel transforms of the previously introduced auxiliary functions defined by (2.16*a*,*b*). Specifically, we have

$$\hat{\psi}_1^\pm(\lambda) = \int_0^\infty r\psi_1^\pm(r)J_1(\lambda r)\,\mathrm{d}r = (\tfrac{1}{2} \pm h)\exp(-\lambda(\tfrac{1}{2} \pm h)), \tag{2.27a}$$

$$\hat{\psi}_2^\pm(\lambda) = \int_0^\infty r\psi_2^\pm(r)J_0(\lambda r)\,\mathrm{d}r = \left(\frac{1}{\lambda} + \frac{1}{2} \pm h\right)\exp\left(-\lambda\left(\frac{1}{2} \pm h\right)\right), \tag{2.27b}$$

Downloaded from https://www.cambridge.org/core. Universitaets und Landesbibliothek Duesseldorf, on 09 Mar 2022 at 15:29:48, subject to the Cambridge Core terms of use, available at https://www.cambridge.org/core/terms. https://doi.org/10.1017/jfm.2020.706

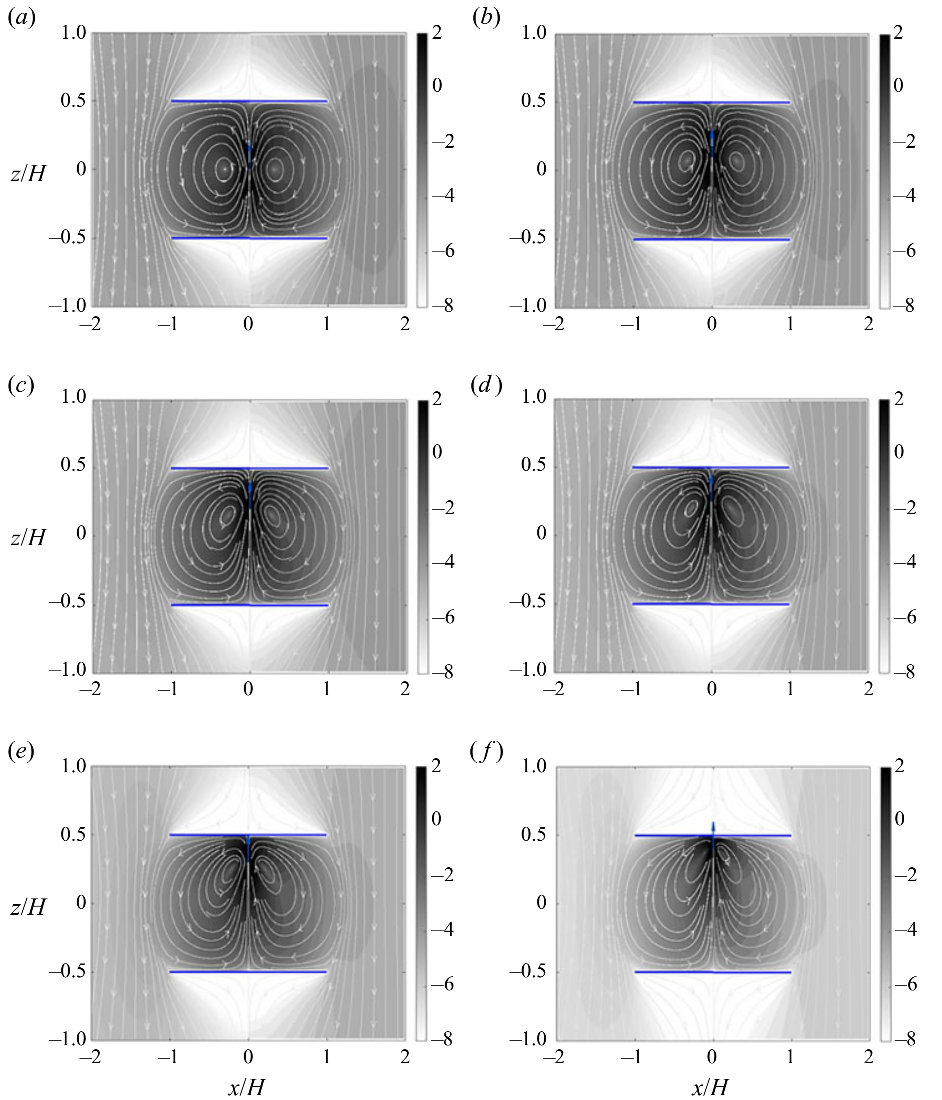

FIGURE 3. Streamlines and contour plots of the flow field induced by a point-force singularity acting inside two coaxially positioned disks of no-slip surfaces and of rescaled unit radius for various values of the vertical distance h/H. In each panel, the flow velocity field obtained using the present semi-analytical approach is displayed in the left domain corresponding to $x \leq 0$, while the solution obtained using FEM simulations is presented in the right domain corresponding to $x \geq 0$ for the same set of parameters. Here, we have defined the scaled flow velocity as $\boldsymbol{V} = \boldsymbol{v}/(F/(8\pi\eta))$. (*a*) $h/H = 0$, (*b*) $h/H = 0.1$, (*c*) $h/H = 0.2$, (*d*) $h/H = 0.25$, (*e*) $h/H = 0.3$, (*f*) $h/H = 0.4$.

for $|h| < 1/2$. Solving the linear system of equations given by (2.25) and (2.26) for the unknown vector function $\boldsymbol{g}$ upon making use of (2.13), (2.14) and (2.18) leads to

$$\boldsymbol{X}_{13} = (\mathrm{e}^{-\lambda h}, -h\mathrm{e}^{-\lambda h}, \mathrm{e}^{\lambda h}, -h\mathrm{e}^{\lambda h})^{\mathrm{T}}. \tag{2.28}$$

Accordingly, the total velocity and pressure fields in the lower and upper regions vanish in the limit $R \to \infty$. The corresponding solution in the intermediate fluid domain can readily be obtained by invoking (2.13) and (2.14).

3. Hydrodynamic mobility

Our calculation of the flow field presented in the previous section can be employed in order to probe the effect of the two hard disks on the hydrodynamic drag acting on an enclosed point-like particle axially moving along the coaxially positioned axis. This effect is commonly quantified by the hydrodynamic mobility function, which relates the velocity of a particle to the net force exerted on its surface (Leal 1980; Swan & Brady 2007; Daddi-Moussa-Ider & Gekle 2016, 2017, 2018; Driscoll & Delmotte 2019). In a bulk Newtonian fluid of constant dynamic viscosity η, the mobility function μ of a spherical particle of radius a is given by the familiar Stokes law (Stokes 1851), which states that in this case the mobility is $\mu_0 = 1/(6\pi\eta a)$. In the presence of the confining disks, the leading-order correction to the particle mobility for an axisymmetric motion along the axis is obtained by evaluating the image flow field at the particle position as

$$\Delta\mu = F^{-1} \lim_{(r,z)\to(0,h)} v_{z\,2}^{*}(r,z). \tag{3.1}$$

Evaluating the limit in the latter equation and scaling by the bulk mobility, the scaled correction to the particle mobility is obtained as

$$\frac{\Delta\mu}{\mu_0} = -ka, \tag{3.2}$$

where

$$k = \tfrac{3}{4} \int_0^\infty \left(\left((1-\lambda h)\, A_2^+ - \lambda B_2^+ \right) \mathrm{e}^{\lambda h} + \left((1+\lambda h)\, A_2^- + \lambda B_2^- \right) \mathrm{e}^{-\lambda h} \right) \mathrm{d}\lambda \tag{3.3}$$

is a positive dimensionless number commonly denominated as the correction factor of the Stokes steady mobility (Happel & Brenner 1983). Unfortunately, an analytical evaluation of this infinite integral is not auspicious. Therefore, we make recourse to a numerical evaluation.

For infinitely large disks, i.e. as $R \to \infty$, the correction factor k in (3.2) can conveniently be cast into the simple integral form

$$k_\infty = \tfrac{3}{8} \int_0^\infty W(\lambda) \left(\sinh^2 \lambda - \lambda^2 \right)^{-1} \mathrm{d}\lambda, \tag{3.4}$$

where we have defined the wavenumber-dependent function

$$W(\lambda) = \Gamma_+ + \Gamma_- + \gamma_+ + \gamma_- + \mathrm{e}^{-2\lambda} - \beta_+\beta_-\lambda^3 - 2\lambda^2 - 2\lambda - 1, \tag{3.5}$$

with

$$\beta_\pm = 1 \pm 2h, \quad \Gamma_\pm = (1 + \tfrac{1}{2}\lambda^2\beta_\pm^2) \sinh(\lambda\beta_\mp), \quad \gamma_\pm = \lambda\beta_\pm \cosh(\lambda\beta_\mp). \tag{3.6a–c}$$

This result is found to be in full agreement with the expression obtained by Swan & Brady (2010), who used a two-dimensional Fourier transform technique.

Downloaded from https://www.cambridge.org/core. Universitaets und Landesbibliothek Duesseldorf, on 09 Mar 2022 at 15:29:48, subject to the Cambridge Core terms of use, available at https://www.cambridge.org/core/terms. https://doi.org/10.1017/jfm.2020.706

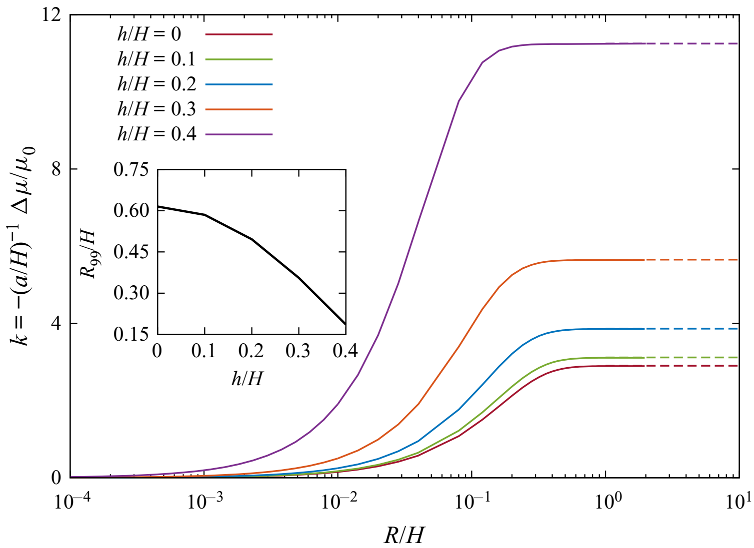

FIGURE 4. Variations of the correction factor of the hydrodynamic mobility as defined by (3.3) versus R/H for various values of h/H. Horizontal dashed lines correspond to the correction factor near two infinitely large disks as given by (3.4). Inset: Evolution of R_{99}/H versus h/H, where R_{99} is defined such that $k(R_{99}/H) = 0.99k_\infty$, for which the correction factor near infinitely large disks is almost recovered.

In figure 4, we present a linear–logarithmic plot of the correction factor of the mobility function versus the radius of the disks for various values of the singularity position. Results are obtained by integrating (3.3) numerically. We observe that the curves follow a sigmoid-logistic-like phenomenology, implying that the correction factor increases significantly in the range of small radii before it reaches a saturation value. The latter corresponds to the correction factor predicted near two infinitely large disks given by (3.4).

Next, in order to quantify the effect of finite disk size on the correction to the hydrodynamic mobility, we customarily define the radius R_{99} for which the mobility near infinitely large disks is essentially reached, such that $k(R_{99}) = 0.99k_\infty$. In the inset of figure 4, we display the variations of R_{99} versus h based on the data presented in the main plot. We observe that R_{99} reaches a maximum value of approximately 0.62 at the mid-plane of the channel before it monotonically decreases with h. This observation suggests that, to a good approximation, the mobility near two infinitely large disks can adequately be used to estimate the mobility at an arbitrary position along the axis provided that the ratio of radius to channel height is above 0.62. Hence, accounting for the finite-size effect here becomes crucial only for values below this threshold.

Finally, we comment on the applicability of the often-used approximation originally suggested by Oseen (1928) to predict the particle mobility between two boundaries by superimposing separately the leading-order effects of each boundary. Accordingly,

$$\frac{\Delta\mu_{Sup}}{\mu_0} = -k_{Sup}a, \quad k_{Sup} = -a^{-1}\left(\left.\frac{\Delta\mu_{Disk}}{\mu_0}\right|_{b=1/2-h} + \left.\frac{\Delta\mu_{Disk}}{\mu_0}\right|_{b=1/2+h}\right), \tag{3.7a,b}$$

where the leading-order correction to the mobility function for axisymmetric motion normal to one rigid circular disk has previously been obtained by Kim (1983) and is

Downloaded from https://www.cambridge.org/core. Universitaets und Landesbibliothek Duesseldorf, on 09 Mar 2022 at 15:29:48, subject to the Cambridge Core terms of use, available at https://www.cambridge.org/core/terms. https://doi.org/10.1017/jfm.2020.706

Downloaded from https://www.cambridge.org/core. Universitaets und Landesbibliothek Duesseldorf, on 09 Mar 2022 at 15:29:48, subject to the Cambridge Core terms of use, available at https://www.cambridge.org/core/terms. https://doi.org/10.1017/jfm.2020.706

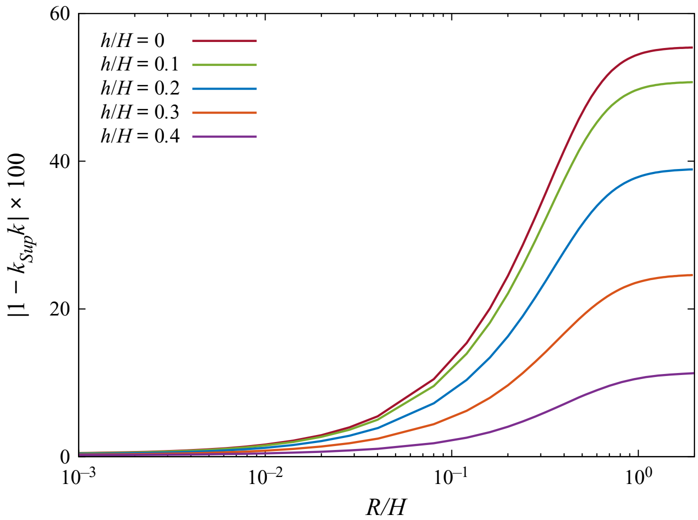

FIGURE 5. Percentage relative error between the correction factor of the Stokes steady mobility as obtained from the superposition approximation given by (3.7*a*,*b*) and the exact expression given by (3.3).

expressed by

$$\frac{\Delta\mu_{Disk}}{\mu_0} = -\frac{3}{4\pi}\left(\frac{3+5\xi^2}{(1+\xi^2)^2} + \frac{3}{\xi}\arctan\left(\frac{1}{\xi}\right)\right)\frac{a}{R}, \tag{3.8}$$

wherein $\xi = b/R$ is a dimensionless parameter with b denoting the distance between the particle and the centre of the disk. This solution was obtained by formulating the flow problem in terms of a mixed boundary-value problem and solving the resulting dual integral equations using an approach analogous to that employed in the present work. Notably, for $\xi \to 0$ we recover the familiar correction to the hydrodynamic mobility near an infinitely extended plane solid wall of no-slip boundary condition at its surface, namely $\Delta\mu_{Disk}/\mu_0 = -9a/(8b)$, as originally obtained by Lorentz using the reciprocal theorem more than a century ago (Lorentz 1907; Lee, Chadwick & Leal 1979).

We now assess the accuracy of the superposition approximation stated by (3.7*a*,*b*) by direct comparison with the exact prediction given by (3.3). In figure 5, we plot the variations of the percentage relative error between the correction factors k_{Sup} and k versus the radius of the disks R for various values of the particle position h. In the range of small values of R, the relative error amounts to small values, typically smaller than 10 % for $R < 0.1$. Upon increasing R, the relative error gradually increases in a logistic-like manner, before it saturates on a plateau value as R gets larger. The maximum error is obtained for the particle located on the mid-plane between the two disks for $h = 0$ and is found to be approximately 55 % in the limit of infinite disk radius. Therefore, the superposition approximation cannot be applied properly in this case. Nonetheless, as the particle position gets closer to either disk, the maximum error notably decreases to amount to only approximately 12 % for $h = 0.4$. Consequently, the superposition approximation can frequently be utilised in this range of values to predict the hydrodynamic mobility for axisymmetric motion along the axis of the disks.

Downloaded from https://www.cambridge.org/core. Universitaets und Landesbibliothek Duesseldorf, on 09 Mar 2022 at 15:29:48, subject to the Cambridge Core terms of use, available at https://www.cambridge.org/core/terms. https://doi.org/10.1017/jfm.2020.706

4. Conclusions

To summarise, we have examined the axisymmetric Stokes flow resulting from a stokeslet singularity acting on the axis of two coaxially positioned circular disks of equal radius. We have formulated the solution for the viscous incompressible flow field as a mixed boundary-value problem, which we have then reduced to a system of dual integral equations for four unknown wavenumber-dependent functions. Most importantly, we have shown the existence of viscous toroidal eddies in the fluid region bounded by the two plates. In the limit of infinitely large disks, we have successfully recovered the classic solution by Liron & Mochon (1976) for a stokeslet acting normal to two parallel planar walls.

Additionally, we have provided an integral expression of the hydrodynamic mobility function quantifying the effect of the confining plates on the motion of a point-like particle moving along the axis of the coaxially positioned disks. Furthermore, we have demonstrated that accounting for the finite-size effect of the disks becomes essential only below a threshold value of the ratio of radius to channel height. Beyond this value, the mobility near two infinitely large disks can appropriately be employed. Finally, we have tested the validity and robustness of Oseen's approximation that postulates that the particle mobility between two boundaries could approximately be predicted by superimposing the contributions from each boundary independently. We have found that this simplistic approximation works quite well as the particle gets closer to either boundary but severely breaks down when the particle is located in the mid-plane between the two disks.

The analytical approach in the present paper is based on the assumption of flow axisymmetry. The Stokes flow induced by a stokeslet directed along an arbitrary direction in the presence of two coaxially positioned disks would be worth investigating in a future study. We conjecture that this solution might be obtained by making use of the Green and Neumann functions supplemented by the edge function, following the approach by Miyazaki (1984). This solution can then be employed to evaluate the translational and rotational mobility functions of particles located at arbitrary positions between the two disks. Alternatively, the problem can possibly be approached differently by means of multipole expansion methods involving the expression of the relevant hydrodynamic fields using oblate spheroidal coordinates (Lee & Leal 1980). This approach has been widely employed in the context of micromechanics of heterogeneous composite materials and fracture analysis (Kushch & Sangani 2000; Kushch 2013). In principle, our calculations can be extended to account for higher-order correction factors in the aspect ratio between the radius of the disks and the distance between the particle and the bounding plates (Swan & Brady 2010), but this would require a very challenging effort.

For applications requiring the precise manipulation of single molecules at the nanoscale level, the no-slip boundary condition may need to be lifted. In this context, the effect of partial slip at the surfaces of the disks is commonly characterised by assuming that the velocity components of the fluid tangent to the surfaces of the disks is proportional to the rate of strain at the surfaces (Lauga & Squires 2005; Lasne *et al.* 2008). This is an interesting aspect that could be included in our formalism and represents a worthwhile extension of the problem for future studies. We hope that our study will prove useful to researchers as well as practitioners working on particulate flow problems involving finitely sized boundaries, and pave the way towards better design and control of various processes in micro- and nanofluidic systems.

Acknowledgements

A.D.M.I., H.L. and A.M.M. gratefully acknowledge support from the DFG (Deutsche Forschungsgemeinschaft) through the projects DA 2107/1-1, LO 418/16-3 and ME 3571/2-2.

Declaration of interests

The authors report no conflict of interest.

Appendix A. Analytical expressions for the kernel functions

In this appendix, we provide technical details regarding the analytical derivation of the kernel functions appearing in the system of Fredholm integral equations of the first kind given by (2.22) of the main body of the paper.

The kernel functions can be expressed as infinite integrals over the wavenumber λ as

$$L_1(r,t) = \int_0^\infty \lambda^{1/2} \mathrm{e}^{-\lambda} J_1(\lambda r) J_{1/2}(\lambda t)\, \mathrm{d}\lambda, \tag{A 1a}$$

$$L_2(r,t) = \int_0^\infty \left(\lambda^{1/2} + \lambda^{-1/2}\right) \mathrm{e}^{-\lambda} J_0(\lambda r) J_{1/2}(\lambda t)\, \mathrm{d}\lambda, \tag{A 1b}$$

$$L_3(r,t) = \int_0^\infty \lambda^{1/2} \mathrm{e}^{-\lambda} J_0(\lambda r) J_{3/2}(\lambda t)\, \mathrm{d}\lambda, \tag{A 1c}$$

$$L_4(r,t) = \int_0^\infty \left(\lambda^{1/2} - \lambda^{-1/2}\right) \mathrm{e}^{-\lambda} J_1(\lambda r) J_{3/2}(\lambda t)\, \mathrm{d}\lambda, \tag{A 1d}$$

$$L_5(r,t) = \int_0^\infty \lambda^{-1/2} J_1(\lambda r) J_{3/2}(\lambda t)\, \mathrm{d}\lambda, \tag{A 1e}$$

$$L_6(r,t) = \int_0^\infty \lambda^{-1/2} J_0(\lambda r) J_{1/2}(\lambda t)\, \mathrm{d}\lambda, \tag{A 1f}$$

where $(r,t) \in [0,R]^2$. It can be shown that the first four integrals can conveniently be expressed in closed mathematical forms as

$$L_1(r,t) = \left(\frac{2}{\pi t}\right)^{1/2} \frac{1}{r}\, \mathrm{Im}(\xi_+ \delta_+), \tag{A 2a}$$

$$L_2(r,t) = \left(\frac{2}{\pi t}\right)^{1/2} \left(\mathrm{Re}(\Lambda) + \mathrm{Im}(\delta_-)\right), \tag{A 2b}$$

$$L_3(r,t) = \left(\frac{2}{\pi t}\right)^{1/2} \mathrm{Re}(\Lambda t^{-1} - \delta_-), \tag{A 2c}$$

$$L_4(r,t) = \left(\frac{2}{\pi t}\right)^{1/2} \left(\mathrm{Re}(\chi_1) + \mathrm{Im}(\chi_2)\right), \tag{A 2d}$$

Downloaded from https://www.cambridge.org/core. Universitaets und Landesbibliothek Duesseldorf, on 09 Mar 2022 at 15:29:48, subject to the Cambridge Core terms of use, available at https://www.cambridge.org/core/terms. https://doi.org/10.1017/jfm.2020.706

Downloaded from https://www.cambridge.org/core. Universitaets und Landesbibliothek Duesseldorf, on 09 Mar 2022 at 15:29:48, subject to the Cambridge Core terms of use, available at https://www.cambridge.org/core/terms. https://doi.org/10.1017/jfm.2020.706

where we have defined the abbreviations

$$\xi_{\pm} = 1 \pm \mathrm{i}t, \quad \delta_{\pm} = \left(r^2 + \xi_{\pm}^2\right)^{-1/2}, \quad \Lambda = \arcsin\left(\frac{t+\mathrm{i}}{r}\right), \quad \sigma = \frac{r}{\xi_- + \delta_-^{-1}}, \tag{A 3a}$$

$$\alpha = \frac{t}{r}, \quad \chi_1 = \delta_-\left(\frac{r}{2}\left(1+\sigma^2\right) + \frac{\xi_-}{r}\right) - \frac{\Lambda}{2\alpha}, \quad \chi_2 = \frac{1}{rt\delta_-} + \frac{\delta_-}{8\alpha}\left(\xi_- - r\sigma^3\right). \tag{A 3b}$$

In addition, the integrals L_5 and L_6 have analytical forms and can be calculated directly from standard integration tables or software algebra systems such as Mathematica (Wolfram 1999) as

$$L_5(r,t) = \frac{1}{2}\left(\frac{\pi}{2t}\right)^{1/2}\alpha^{-1}H(t-r) + \left(\frac{1}{2\pi t}\right)^{1/2}\left(\alpha^{-1}\arcsin(\alpha) - (1-\alpha^2)^{1/2}\right)H(r-t), \tag{A 4a}$$

$$L_6(r,t) = \left(\frac{\pi}{2t}\right)^{1/2}H(t-r) + \left(\frac{2}{\pi t}\right)^{1/2}\arcsin(\alpha)H(r-t), \tag{A 4b}$$

where $H(\cdot)$ denotes the Heaviside step function.

In the following, we will show how the integrals given by (A 1) can be evaluated analytically. The core idea of our approach consists of expressing these integrals in the form of Laplace transforms of Bessel functions of the first kind (Spiegel 1965; Widder 2015),

$$\mathcal{L}\left\{J_k(z)\right\}(p) = (1+p^2)^{-1/2}\left(p + (1+p^2)^{1/2}\right)^{-k}, \tag{A 5}$$

and using the recurrence relation (Abramowitz & Stegun 1972)

$$\frac{2k}{z}J_k(z) = J_{k-1}(z) + J_{k+1}(z). \tag{A 6}$$

In addition, we will employ the following identities providing closed-form expressions for the Bessel functions of the first kind of half-integer order in terms of the standard trigonometric functions,

$$J_{1/2}(z) = \left(\frac{2}{\pi z}\right)^{1/2}\sin(z), \tag{A 7a}$$

$$J_{-1/2}(z) = \left(\frac{2}{\pi z}\right)^{1/2}\cos(z). \tag{A 7b}$$

A.1. *Evaluation of the integral L_1*

By making use of the identity given by (A 7*a*), the integral L_1 stated by (A 1*a*) can be expressed as

$$L_1(r,t) = \left(\frac{2}{\pi t}\right)^{1/2}\int_0^\infty \mathrm{e}^{-\lambda}J_1(\lambda r)\sin(\lambda t)\,\mathrm{d}\lambda. \tag{A 8}$$

Using the change of variable $x = \lambda r$ and Euler's representation of the sine function, the latter integral can be expressed as

$$L_1(r,t) = \left(\frac{2}{\pi t}\right)^{1/2}\frac{1}{r}\,\mathrm{Im}\left(\int_0^\infty \exp\left(-\frac{x}{r}(1-\mathrm{i}t)\right)J_1(x)\,\mathrm{d}x\right). \tag{A 9}$$

Downloaded from https://www.cambridge.org/core. Universitaets und Landesbibliothek Duesseldorf, on 09 Mar 2022 at 15:29:48, subject to the Cambridge Core terms of use, available at https://www.cambridge.org/core/terms. https://doi.org/10.1017/jfm.2020.706

This leads to (A 2*a*) after making use of the Laplace transform given by (A 5) for $k = 1$ and $p = (1 - \mathrm{i}t)/r$. We note that $\mathrm{Im}(z) = -\mathrm{Im}(\bar{z})$ for $z \in \mathbb{C}$, where $\bar{z}$ denotes the complex conjugate of z.

A.2. *Evaluation of the integral L_2*

We next consider the integral defined by (A 1*b*), which can conveniently be decomposed into two parts as

$$L_2(r,t) = L_{2,1}(r,t) + L_{2,2}(r,t), \tag{A 10}$$

where

$$L_{2,1}(r,t) = \left(\frac{2}{\pi t}\right)^{1/2} \int_0^\infty \mathrm{e}^{-\lambda} J_0(\lambda r)\sin(\lambda t)\,\mathrm{d}\lambda, \tag{A 11a}$$

$$L_{2,2}(r,t) = \left(\frac{2}{\pi t}\right)^{1/2} \int_0^t \mathrm{d}u \int_0^\infty \mathrm{e}^{-\lambda} J_0(\lambda r)\cos(\lambda u)\,\mathrm{d}\lambda. \tag{A 11b}$$

Here, we have made use of (A 7*a*) together with the integral representation

$$\sin(\lambda t) = \lambda \int_0^t \cos(\lambda u)\,\mathrm{d}u. \tag{A 12}$$

Using Euler's relation together with (A 5) for $k = 0$, (A 11) can be evaluated as

$$L_{2,1}(r,t) = \left(\frac{2}{\pi t}\right)^{1/2} \mathrm{Im}\left(\left(r^2 + (1-\mathrm{i}t)^2\right)^{-1/2}\right), \tag{A 13a}$$

$$L_{2,2}(r,t) = \left(\frac{2}{\pi t}\right)^{1/2} \mathrm{Re}\left(\int_0^t \left(r^2 + (1-\mathrm{i}u)^2\right)^{-1/2} \mathrm{d}u\right). \tag{A 13b}$$

The definite integral in (A 13*b*) can be evaluated as

$$L_{2,2}(r,t) = \left(\frac{2}{\pi t}\right)^{1/2} \mathrm{Re}\left(\arcsin\left(\frac{t+\mathrm{i}}{r}\right)\right). \tag{A 14}$$

Equation (A 2*b*) follows forthwith after collecting terms.

It is worth mentioning that, for a given complex number $z = x + \mathrm{i}y$, the arcsine function is defined when $\pm x \notin (1, \infty)$ as (Abramowitz & Stegun 1972)

$$\arcsin(z) = \arcsin(\alpha_-) + \mathrm{i}\,\mathrm{sign}(y)\ln\left(\alpha_+ + \left(\alpha_+^2 - 1\right)^{1/2}\right), \tag{A 15}$$

where

$$\alpha_\pm = \tfrac{1}{2}((x+1)^2 + y^2)^{1/2} \pm \tfrac{1}{2}((x-1)^2 + y^2)^{1/2}. \tag{A 16}$$

Downloaded from https://www.cambridge.org/core. Universitaets und Landesbibliothek Duesseldorf, on 09 Mar 2022 at 15:29:48, subject to the Cambridge Core terms of use, available at https://www.cambridge.org/core/terms. https://doi.org/10.1017/jfm.2020.706

A.3. *Evaluation of the integral L_3*

Analogously, the integral L_3 defined by (A 1*c*) can be decomposed into two parts as

$$L_3(r, t) = L_{3,1}(r, t) - L_{3,2}(r, t), \tag{A 17}$$

upon using the recurrence relation stated by (A 6) and setting $k = 1/2$ together with the identities given by (A 7). Here, we have defined $L_{3,1}(r, t) = t^{-1} L_{2,2}(r, t)$ and

$$L_{3,2}(r, t) = \left(\frac{2}{\pi t}\right)^{1/2} \int_0^\infty \mathrm{e}^{-\lambda} J_0(\lambda r) \cos(\lambda t)\, \mathrm{d}\lambda, \tag{A 18}$$

which can readily be evaluated as (A 11*a*) but this time by taking the real part. This leads to (A 2*c*) upon collecting terms.

A.4. *Evaluation of the integral L_4*

Finally, upon using (A 6) for $k = 1/2$ and the identities given by (A 7), the integral L_4 can be decomposed into four parts:

$$L_4(r, t) = L_{4,1} + L_{4,2} - (L_{4,3} + L_{4,4}), \tag{A 19}$$

where we have defined

$$L_{4,1}(r, t) = \left(\frac{2}{\pi t}\right)^{1/2} t^{-1} \int_0^\infty \lambda^{-1} \mathrm{e}^{-\lambda} J_1(\lambda r) \sin(\lambda t)\, \mathrm{d}\lambda, \tag{A 20a}$$

$$L_{4,2}(r, t) = \left(\frac{2}{\pi t}\right)^{1/2} \int_0^\infty \lambda^{-1} \mathrm{e}^{-\lambda} J_1(\lambda r) \cos(\lambda t)\, \mathrm{d}\lambda, \tag{A 20b}$$

$$L_{4,3}(r, t) = \left(\frac{2}{\pi t}\right)^{1/2} \int_0^\infty \mathrm{e}^{-\lambda} J_1(\lambda r) \cos(\lambda t)\, \mathrm{d}\lambda, \tag{A 20c}$$

$$L_{4,4}(r, t) = \left(\frac{2}{\pi t}\right)^{1/2} t^{-1} \int_0^\infty \lambda^{-2} \mathrm{e}^{-\lambda} J_1(\lambda r) \sin(\lambda t)\, \mathrm{d}\lambda. \tag{A 20d}$$

In the following, we will make use when appropriate of the shorthand notation defined in (A 3*a*). By using the integral representation of the sine function given by (A 12), the first integral can be expressed as

$$L_{4,1}(r, t) = \left(\frac{2}{\pi t}\right)^{1/2} t^{-1} \int_0^t \mathrm{d}u \int_0^\infty \mathrm{e}^{-\lambda} J_1(\lambda r) \cos(\lambda u)\, \mathrm{d}\lambda. \tag{A 21}$$

Similarly, the evaluation of the indefinite integral over λ can be performed using the Laplace transform of the Bessel function given by (A 5) to obtain

$$L_{4,1}(r, t) = \left(\frac{2}{\pi t}\right)^{1/2} (tr)^{-1}\, \mathrm{Re}\left(\int_0^t \left(1 - (1 - \mathrm{i}u)\left(r^2 + (1 - \mathrm{i}u)^2\right)^{-1/2}\right) \mathrm{d}u \right). \tag{A 22}$$

The definite integral in the latter equation can then be evaluated and cast in the final simplified form

$$L_{4,1}(r, t) = \left(\frac{2}{\pi t}\right)^{1/2} r^{-1} \left(1 + t^{-1}\, \mathrm{Im}(\delta_-^{-1})\right). \tag{A 23}$$

Next, the evaluation of the second integral is straightforward after expressing the first-order Bessel function as a function of the zeroth- and second-order Bessel functions using the recurrence relation given by (A 6) for $k = 1$ to obtain

$$L_{4,2}(r,t) = r(2\pi t)^{-1/2} \int_0^\infty \mathrm{e}^{-\lambda} \left(J_0(\lambda r) + J_2(\lambda r)\right) \cos(\lambda t)\, \mathrm{d}\lambda, \tag{A 24}$$

which can readily be evaluated as

$$L_{4,2}(r,t) = r(2\pi t)^{-1/2} \operatorname{Re}\left(\delta_- \left(1 + \sigma^2\right)\right). \tag{A 25}$$

The third integral can be deduced from the calculation of $L_1(r,t)$ given by (A 9), this time by taking the real part to obtain

$$L_{4,3} = \left(\frac{2}{\pi t}\right)^{1/2} r^{-1} \operatorname{Re}(1 - \xi_- \delta_-). \tag{A 26}$$

Lastly, the fourth integral can be decomposed into two parts as

$$L_{4,4}(r,t) = L_{4,4,1}(r,t) + L_{4,4,2}(r,t), \tag{A 27}$$

where $L_{4,4,1}(r,t) = (2\alpha)^{-1} L_{2,2}(r,t)$ and

$$L_{4,4,2}(r,t) = (2\pi t)^{-1/2} \frac{r}{t} \int_0^\infty \lambda^{-1} \mathrm{e}^{-\lambda} J_2(\lambda r) \sin(\lambda t)\, \mathrm{d}\lambda. \tag{A 28}$$

This integral can be handled using the recurrence formula given by (A 6) to obtain

$$L_{4,4,2}(r,t) = (2\pi t)^{-1/2} \frac{r^2}{4t} \int_0^\infty \mathrm{e}^{-\lambda} \left(J_1(\lambda r) + J_3(\lambda r)\right) \sin(\lambda t)\, \mathrm{d}\lambda. \tag{A 29}$$

The latter integral can be calculated and cast in the final simplified form

$$L_{4,4,2}(r,t) = (2\pi t)^{-1/2} (4\alpha)^{-1} \left(r \operatorname{Im}(\delta_- \sigma^3) - \operatorname{Im}(\xi_- \delta_-)\right). \tag{A 30}$$

By collecting terms, (A 2*d*) is readily obtained.

REFERENCES

Abramowitz, M. & Stegun, I. A. 1972 *Handbook of Mathematical Functions*. Dover.

Asta, A. J., Palaia, I., Trizac, E., Levesque, M. & Rotenberg, B. 2019 Lattice Boltzmann electrokinetics simulation of nanocapacitors. *J. Chem. Phys.* **151** (11), 114104.

Babel, S., Eikerling, M. & Löwen, H. 2018 Impedance resonance in narrow confinement. *J. Phys. Chem.* C **122** (38), 21724–21734.

Balducci, A., Mao, P., Han, J. & Doyle, P. S. 2006 Double-stranded DNA diffusion in slitlike nanochannels. *Macromolecules* **39** (18), 6273–6281.

Baron, M., Bławzdziewicz, J. & Wajnryb, E. 2008 Hydrodynamic crystals: collective dynamics of regular arrays of spherical particles in a parallel-wall channel. *Phys. Rev. Lett.* **100** (17), 174502.

Bechinger, C., Di Leonardo, R., Löwen, H., Reichhardt, C., Volpe, G. & Volpe, G. 2016 Active particles in complex and crowded environments. *Rev. Mod. Phys.* **88** (4), 045006.

Becker, R. & Braack, M. 2001 A finite element pressure gradient stabilization for the Stokes equations based on local projections. *Calcolo* **38** (4), 173–199.

Benesch, T., Yiacoumi, S. & Tsouris, C. 2003 Brownian motion in confinement. *Phys. Rev.* E **68** (2), 021401.

Bhattacharya, S. 2008 Cooperative motion of spheres arranged in periodic grids between two parallel walls. *J. Chem. Phys.* **128** (7), 074709.

Downloaded from https://www.cambridge.org/core. Universitaets und Landesbibliothek Duesseldorf, on 09 Mar 2022 at 15:29:48, subject to the Cambridge Core terms of use, available at https://www.cambridge.org/core/terms. https://doi.org/10.1017/jfm.2020.706

BHATTACHARYA, S. & BŁAWZDZIEWICZ, J. 2002 Image system for Stokes-flow singularity between two parallel planar walls. *J. Math. Phys.* **43** (11), 5720–5731.

BHATTACHARYA, S., BŁAWZDZIEWICZ, J. & WAJNRYB, E. 2005 Hydrodynamic interactions of spherical particles in suspensions confined between two planar walls. *J. Fluid Mech.* **541**, 263–292.

BHATTACHARYA, S., BŁAWZDZIEWICZ, J. & WAJNRYB, E. 2006 Hydrodynamic interactions of spherical particles in Poiseuille flow between two parallel walls. *Phys. Fluids* **18** (5), 053301.

BILBAO, A., WAJNRYB, E., VANAPALLI, S. A. & BŁAWZDZIEWICZ, J. 2013 Nematode locomotion in unconfined and confined fluids. *Phys. Fluids* **25** (8), 081902.

BLAKE, J. R. 1971 A note on the image system for a Stokeslet in a no-slip boundary. *Math. Proc. Camb. Phil. Soc.* **70** (02), 303–310.

BŁAWZDZIEWICZ, J. & WAJNRYB, E. 2008 An analysis of the far-field response to external forcing of a suspension in the Stokes flow in a parallel-wall channel. *Phys. Fluids* **20** (9), 093303.

BRAACK, M. & RICHTER, T. 2006 Solutions of 3D Navier–Stokes benchmark problems with adaptive finite elements. *Comput. Fluids* **35** (4), 372–392.

BRACEWELL, R. 1999 *The Fourier Transform and Its Applications*. McGraw-Hill.

BRENNER, M. P. 1999 Screening mechanisms in sedimentation. *Phys. Fluids* **11** (4), 754–772.

BROTTO, T., CAUSSIN, J.-B., LAUGA, E. & BARTOLO, D. 2013 Hydrodynamics of confined active fluids. *Phys. Rev. Lett.* **110** (3), 038101.

CAMPBELL, L. C., WILKINSON, M. J., MANZ, A., CAMILLERI, P. & HUMPHREYS, C. J. 2004 Electrophoretic manipulation of single DNA molecules in nanofabricated capillaries. *Lab Chip* **4** (3), 225–229.

COPSON, E. T. 1961 On certain dual integral equations. *Glasgow Math. J.* **5** (1), 21–24.

CROSS, J. D., STRYCHALSKI, E. A. & CRAIGHEAD, H. G. 2007 Size-dependent DNA mobility in nanochannels. *J. Appl. Phys.* **102** (2), 024701.

DADDI-MOUSSA-IDER, A. & GEKLE, S. 2016 Hydrodynamic interaction between particles near elastic interfaces. *J. Chem. Phys.* **145** (1), 014905.

DADDI-MOUSSA-IDER, A. & GEKLE, S. 2017 Hydrodynamic mobility of a solid particle near a spherical elastic membrane: axisymmetric motion. *Phys. Rev.* E **95**, 013108.

DADDI-MOUSSA-IDER, A. & GEKLE, S. 2018 Brownian motion near an elastic cell membrane: a theoretical study. *Eur. Phys. J.* E **41** (2), 19.

DADDI-MOUSSA-IDER, A., GUCKENBERGER, A. & GEKLE, S. 2016 Particle mobility between two planar elastic membranes: Brownian motion and membrane deformation. *Phys. Fluids* **28** (7), 071903.

DADDI-MOUSSA-IDER, A., KAOUI, B. & LÖWEN, H. 2019 Axisymmetric flow due to a Stokeslet near a finite-sized elastic membrane. *J. Phys. Soc. Japan* **88** (5), 054401.

DADDI-MOUSSA-IDER, A., LISICKI, M., LÖWEN, H. & MENZEL, A. M. 2020 Dynamics of a microswimmer–microplatelet composite. *Phys. Fluids* **32** (2), 021902.

DADDI-MOUSSA-IDER, A., LISICKI, M., MATHIJSSEN, A. J. T. M., HOELL, C., GOH, S., BŁAWZDZIEWICZ, J., MENZEL, A. M. & LÖWEN, H. 2018 State diagram of a three-sphere microswimmer in a channel. *J. Phys.: Condens. Matter* **30** (25), 254004.

DAI, L., TREE, D. R., VAN DER MAAREL, J. R. C., DORFMAN, K. D. & DOYLE, P. S. 2013 Revisiting blob theory for DNA diffusivity in slitlike confinement. *Phys. Rev. Lett.* **110**, 168105.

DAIGUJI, H., YANG, P., SZERI, A. J. & MAJUMDAR, A. 2004 Electrochemomechanical energy conversion in nanofluidic channels. *Nano Lett.* **4** (12), 2315–2321.

DALAL, S., FARUTIN, A. & MISBAH, C. 2020 Amoeboid swimming in compliant channel. *Soft Matt.* **16**, 1599–1613.

DARWICHE, A., INGREMEAU, F., AMAROUCHENE, Y., MAALI, A., DUFOUR, I. & KELLAY, H. 2013 Rheology of polymer solutions using colloidal-probe atomic force microscopy. *Phys. Rev.* E **87** (6), 062601.

DAVIS, P. J. & RABINOWITZ, P. 2007 *Methods of Numerical Integration*. Courier Corporation.

DOYLE, P. S., BIBETTE, J., BANCAUD, A. & VIOVY, J.-L. 2002 Self-assembled magnetic matrices for DNA separation chips. *Science* **295** (5563), 2237–2237.

DRISCOLL, M. & DELMOTTE, B. 2019 Leveraging collective effects in externally driven colloidal suspensions: experiments and simulations. *Curr. Opin. Colloid Interface Sci.* **40**, 42–57.

Downloaded from https://www.cambridge.org/core. Universitaets und Landesbibliothek Duesseldorf, on 09 Mar 2022 at 15:29:48, subject to the Cambridge Core terms of use, available at https://www.cambridge.org/core/terms. https://doi.org/10.1017/jfm.2020.706

Downloaded from https://www.cambridge.org/core. Universitaets und Landesbibliothek Duesseldorf, on 09 Mar 2022 at 15:29:48, subject to the Cambridge Core terms of use, available at https://www.cambridge.org/core/terms. https://doi.org/10.1017/jfm.2020.706

DUFOUR, I., MAALI, A., AMAROUCHENE, Y., AYELA, C., CAILLARD, B., DARWICHE, A., GUIRARDEL, M., KELLAY, H., LEMAIRE, E., MATHIEU, F., *et al.* 2012 The microcantilever: a versatile tool for measuring the rheological properties of complex fluids. *J. Sens.* **2012**, 719898.

DUFRESNE, E. R., ALTMAN, D. & GRIER, D. G. 2001 Brownian dynamics of a sphere between parallel walls. *Europhys. Lett.* **53** (2), 264.

FAUCHEUX, L. P. & LIBCHABER, A. J. 1994 Confined Brownian motion. *Phys. Rev.* E **49**, 5158–5163.

FAXÉN, H. 1921 Einwirkung der Gefässwände auf den Widerstand gegen die Bewegung einer kleinen Kugel in einer zähen Flüssigkeit. PhD thesis, Uppsala University, Uppsala, Sweden.

FELDERHOF, B. U. 2006 Diffusion and velocity relaxation of a Brownian particle immersed in a viscous compressible fluid confined between two parallel plane walls. *J. Chem. Phys.* **124** (5), 054111.

FELDERHOF, B. U. 2010*a* Echoing in a viscous compressible fluid confined between two parallel plane walls. *J. Fluid Mech.* **656**, 223–230.

FELDERHOF, B. U. 2010*b* Loss of momentum in a viscous compressible fluid due to no-slip boundary condition at one or two planar walls. *J. Chem. Phys.* **133** (7), 074707.

FRANÇOIS, N., AMAROUCHENE, Y., LOUNIS, B. & KELLAY, H. 2009 Polymer conformations and hysteretic stresses in nonstationary flows of polymer solutions. *Europhys. Lett.* **86** (3), 34002.

FRANÇOIS, N., LASNE, D., AMAROUCHENE, Y., LOUNIS, B. & KELLAY, H. 2008 Drag enhancement with polymers. *Phys. Rev. Lett.* **100** (1), 018302.

GANATOS, P., PFEFFER, R. & WEINBAUM, S. 1980*a* A strong interaction theory for the creeping motion of a sphere between plane parallel boundaries. Part 2. Parallel motion. *J. Fluid Mech.* **99**, 755–783.

GANATOS, P., WEINBAUM, S. & PFEFFER, R. 1980*b* A strong interaction theory for the creeping motion of a sphere between plane parallel boundaries. Part 1. Perpendicular motion. *J. Fluid Mech.* **99**, 739–753.

GOMPPER, G., WINKLER, R. G., SPECK, T., SOLON, A., NARDINI, C., PERUANI, F., LÖWEN, H., GOLESTANIAN, R., KAUPP, U. B., ALVAREZ, L., *et al.* 2020 The 2020 motile active matter roadmap. *J. Phys.: Condens. Matter* **32** (19), 193001.

GRAHAM, M. D. 2011 Fluid dynamics of dissolved polymer molecules in confined geometries. *Annu. Rev. Fluid Mech.* **43**, 273–298.

GRIGGS, A. J., ZINCHENKO, A. Z. & DAVIS, R. H. 2007 Low-Reynolds-number motion of a deformable drop between two parallel plane walls. *Intl J. Multiphase Flow* **33** (2), 182–206.

HACKBORN, W. W. 1990 Asymmetric Stokes flow between parallel planes due to a rotlet. *J. Fluid Mech.* **218**, 531–546.

HAPPEL, J. & BRENNER, H. 1983 *Low Reynolds Number Hydrodynamics: With Special Applications to Particulate Media*. Springer, Martinus Nijhoff Publishers, The Hague.

IMAI, I. 1973 *Fluid Dynamics (Ryūtai Rikigaku)*. Syokabo Publishing. [in Japanese].

JANSSEN, P. J. A. & ANDERSON, P. D. 2007 Boundary-integral method for drop deformation between parallel plates. *Phys. Fluids* **19** (4), 043602.

JANSSEN, P. J. A. & ANDERSON, P. D. 2008 A boundary-integral model for drop deformation between two parallel plates with non-unit viscosity ratio drops. *J. Comp. Phys.* **227** (20), 8807–8819.

JONES, R. B. 2004 Spherical particle in Poiseuille flow between planar walls. *J. Chem. Phys.* **121** (1), 483–500.

JONES, J. J., VAN DER MAAREL, J. R. C. & DOYLE, P. S. 2013 Intrachain dynamics of large dsDNA confined to slitlike channels. *Phys. Rev. Lett.* **110** (6), 068101.

KIM, M. U. 1983 Axisymmetric Stokes flow due to a point force near a circular disk. *J. Phys. Soc. Japan* **52** (2), 449–455.

KIM, S. & KARRILA, S. J. 2013 *Microhydrodynamics: Principles and Selected Applications*. Courier Corporation.

KUSHCH, V. I. 2013 *Micromechanics of Composites: Multipole Expansion Approach*. Butterworth-Heinemann.

KUSHCH, V. I. & SANGANI, A. S. 2000 Conductivity of a composite containing uniformly oriented penny–shaped cracks or perfectly conducting discs. *Proc. R. Soc. Lond.* A **456** (1995), 683–699.

LASNE, D., MAALI, A., AMAROUCHENE, Y., COGNET, L., LOUNIS, B. & KELLAY, H. 2008 Velocity profiles of water flowing past solid glass surfaces using fluorescent nanoparticles and molecules as velocity probes. *Phys. Rev. Lett.* **100** (21), 214502.

LAUGA, E. 2016 Bacterial hydrodynamics. *Annu. Rev. Fluid Mech.* **48**, 105–130.

LAUGA, E., BRENNER, M. & STONE, H. 2007 Microfluidics: the no-slip boundary condition. In *Springer Handbook of Experimental Fluid Mechanics* (ed. C. Tropea, A. Yarin & J. F. Foss), pp. 1219–1240. Springer.

LAUGA, E. & POWERS, T. R. 2009 The hydrodynamics of swimming microorganisms. *Rep. Prog. Phys.* **72** (9), 096601.

LAUGA, E. & SQUIRES, T. M. 2005 Brownian motion near a partial-slip boundary: a local probe of the no-slip condition. *Phys. Fluids* **17** (10), 103102.

LE GOFF, A., KAOUI, B., KURZAWA, G., HASZON, B. & SALSAC, A.-V. 2017 Squeezing bio-capsules into a constriction: deformation till break-up. *Soft Matt.* **13** (41), 7644–7648.

LEAL, L. G. 1980 Particle motions in a viscous fluid. *Annu. Rev. Fluid Mech.* **12** (1), 435–476.

LEE, S. H., CHADWICK, R. S. & LEAL, L. G. 1979 Motion of a sphere in the presence of a plane interface. Part 1. An approximate solution by generalization of the method of Lorentz. *J. Fluid Mech.* **93**, 705–726.

LEE, S. H. & LEAL, L. G. 1980 Motion of a sphere in the presence of a plane interface. Part 2. An exact solution in bipolar co-ordinates. *J. Fluid Mech.* **98**, 193–224.

LIN, B., YU, J. & RICE, S. A. 2000 Direct measurements of constrained Brownian motion of an isolated sphere between two walls. *Phys. Rev.* E **62**, 3909–3919.

LIRON, N. 1978 Fluid transport by cilia between parallel plates. *J. Fluid Mech.* **86** (4), 705–726.

LIRON, N. & BLAKE, J. R. 1981 Existence of viscous eddies near boundaries. *J. Fluid Mech.* **107**, 109–129.

LIRON, N. & MOCHON, S. 1976 Stokes flow for a Stokeslet between two parallel flat plates. *J. Engng Maths* **10** (4), 287–303.

LOBRY, L. & OSTROWSKY, N. 1996 Diffusion of Brownian particles trapped between two walls: theory and dynamic-light-scattering measurements. *Phys. Rev.* B **53**, 12050–12056.

LORENTZ, H. A. 1907 Ein allgemeiner Satz, die Bewegung einer reibenden Flüssigkeit betreffend, nebst einigen Anwendungen desselben. *Abh. Theor. Phys.* **1**, 23.

MARINI BETTOLO MARCONI, U. & MELCHIONNA, S. 2012 Charge transport in nanochannels: a molecular theory. *Langmuir* **28** (38), 13727–13740.

MATHIJSSEN, A. J. T. M., DOOSTMOHAMMADI, A., YEOMANS, J. M. & SHENDRUK, T. N. 2016 Hydrodynamics of microswimmers in films. *J. Fluid Mech.* **806**, 35–70.

MENZEL, A. M. 2013 Unidirectional laning and migrating cluster crystals in confined self-propelled particle systems. *J. Phys.: Condens. Matter* **25** (50), 505103.

MENZEL, A. M. 2015 Tuned, driven, and active soft matter. *Phys. Rep.* **554**, 1–45.

MEWIS, J. & WAGNER, N. J. 2012 *Colloidal Suspension Rheology*. Cambridge University Press.

MIYAZAKI, T. 1984 The effect of a circular disk on the motion of a small particle in a viscous fluid. *J. Phys. Soc. Japan* **53** (3), 1017–1025.

MOFFATT, H. K. 1964 Viscous and resistive eddies near a sharp corner. *J. Fluid Mech.* **18** (1), 1–18.

OSEEN, C. W. 1928 *Neuere Methoden und Ergebnisse in der Hydrodynamik*. Leipzig, Akademische Verlagsgesellschaft, M. B. H.

OSTAPENKO, T., SCHWARZENDAHL, F. J., BÖDDEKER, T. J., KREIS, C. T., CAMMANN, J., MAZZA, M. G. & BÄUMCHEN, O. 2018 Curvature-guided motility of microalgae in geometric confinement. *Phys. Rev. Lett.* **120**, 068002.

OZARKAR, S. S. & SANGANI, A. S. 2008 A method for determining Stokes flow around particles near a wall or in a thin film bounded by a wall and a gas-liquid interface. *Phys. Fluids* **20** (6), 063301.

PARK, S.-Y. & DIMITRAKOPOULOS, P. 2013 Transient dynamics of an elastic capsule in a microfluidic constriction. *Soft Matt.* **9** (37), 8844–8855.

PERSSON, F. & TEGENFELDT, J. O. 2010 DNA in nanochannels-directly visualizing genomic information. *Chem. Soc. Rev.* **39** (3), 985–999.

POLYANIN, A. D. & MANZHIROV, A. V. 1998 *Handbook of Integral Equations*. CRC Press.

PROBSTEIN, R. F. 2005 *Physicochemical Hydrodynamics: An Introduction*. John Wiley & Sons.

REISNER, W., MORTON, K. J., RIEHN, R., WANG, Y. M., YU, Z., ROSEN, M., STURM, J. C., CHOU, S. Y., FREY, E. & AUSTIN, R. H. 2005 Statics and dynamics of single DNA molecules confined in nanochannels. *Phys. Rev. Lett.* **94** (19), 196101.

Downloaded from https://www.cambridge.org/core. Universitaets und Landesbibliothek Duesseldorf, on 09 Mar 2022 at 15:29:48, subject to the Cambridge Core terms of use, available at https://www.cambridge.org/core/terms. https://doi.org/10.1017/jfm.2020.706

Downloaded from https://www.cambridge.org/core. Universitaets und Landesbibliothek Duesseldorf, on 09 Mar 2022 at 15:29:48, subject to the Cambridge Core terms of use, available at https://www.cambridge.org/core/terms. https://doi.org/10.1017/jfm.2020.706

RICHTER, T. 2017 *Fluid-structure Interactions: Models, Analysis and Finite Elements*. Lecture Notes in Computational Science and Engineering, vol. 118. Springer.

RIEHN, R., LU, M., WANG, Y.-M., LIM, S. F., COX, E. C. & AUSTIN, R. H. 2005 Restriction mapping in nanofluidic devices. *Proc. Natl Acad. Sci. USA* **102** (29), 10012–10016.

ROY, C. J. 2010 Review of discretization error estimators in scientific computing. In *48th AIAA Aerospace Sciences Meeting Including the New Horizons Forum and Aerospace Exposition, Orlando, Florida*, p. 126.

SAINTILLAN, D., SHAQFEH, E. S. G. & DARVE, E. 2006 Effect of flexibility on the shear-induced migration of short-chain polymers in parabolic channel flow. *J. Fluid Mech.* **557**, 297–306.

SHAEBANI, M. R., WYSOCKI, A., WINKLER, R. G., GOMPPER, G. & RIEGER, H. 2020 Computational models for active matter. *Nat. Rev. Phys.* **2**, 181–199.

SMITHIES, F. 1958 *Integral Equations*. Cambridge University Press.

SNEDDON, I. N. 1960 The elementary solution of dual integral equations. *Glasgow Math. J.* **4** (3), 108–110.

SNEDDON, I. N. 1966 *Mixed Boundary Value Problems in Potential Theory*. North-Holland.

SPIEGEL, M. R. 1965 *Laplace Transforms*. McGraw-Hill.

STABEN, M. E., ZINCHENKO, A. Z. & DAVIS, R. H. 2003 Motion of a particle between two parallel plane walls in low-Reynolds-number Poiseuille flow. *Phys. Fluids* **15** (6), 1711–1733.

STEIN, D., VAN DER HEYDEN, F. H. J., KOOPMANS, W. J. A. & DEKKER, C. 2006 Pressure-driven transport of confined DNA polymers in fluidic channels. *Proc. Natl Acad. Sci. USA* **103** (43), 15853–15858.

STOKES, G. G. 1851 On the effect of the internal friction of fluids on the motion of pendulums. *Trans. Camb. Phil. Soc.* **9**, 8.

STRYCHALSKI, E. A., LEVY, S. L. & CRAIGHEAD, H. G. 2008 Diffusion of DNA in nanoslits. *Macromolecules* **41** (20), 7716–7721.

SWAN, J. W. & BRADY, J. F. 2007 Simulation of hydrodynamically interacting particles near a no-slip boundary. *Phys. Fluids* **19** (11), 113306.

SWAN, J. W. & BRADY, J. F. 2010 Particle motion between parallel walls: hydrodynamics and simulation. *Phys. Fluids* **22** (10), 103301.

SWAN, J. W. & BRADY, J. F. 2011 The hydrodynamics of confined dispersions. *J. Fluid Mech.* **687**, 254–299.

TANG, J., LEVY, S. L., TRAHAN, D. W., JONES, J. J., CRAIGHEAD, H. G. & DOYLE, P. S. 2010 Revisiting the conformation and dynamics of DNA in slitlike confinement. *Macromolecules* **43** (17), 7368–7377.

THAKORE, V. & HICKMAN, J. J. 2015 Charge relaxation dynamics of an electrolytic nanocapacitor. *J. Phys. Chem.* C **119** (4), 2121–2132.

TRÄNKLE, B., RUH, D. & ROHRBACH, A. 2016 Interaction dynamics of two diffusing particles: contact times and influence of nearby surfaces. *Soft Matt.* **12** (10), 2729–2736.

TRÉGOUËT, C., SALEZ, T., MONTEUX, C. & REYSSAT, M. 2018 Transient deformation of a droplet near a microfluidic constriction: a quantitative analysis. *Phys. Rev. Fluids* **3** (5), 053603.

TRÉGOUËT, C., SALEZ, T., MONTEUX, C. & REYSSAT, M. 2019 Microfluidic probing of the complex interfacial rheology of multilayer capsules. *Soft Matt.* **15** (13), 2782–2790.

TRICOMI, F. G. 1985 *Integral Equations*. Courier Corporation.

TURNER, S. W., PEREZ, A. M., LOPEZ, A. & CRAIGHEAD, H. G. 1998 Monolithic nanofluid sieving structures for DNA manipulation. *J. Vac. Sci. Technol.* B **16** (6), 3835–3840.

USPAL, W. E., ERAL, H. B. & DOYLE, P. S. 2013 Engineering particle trajectories in microfluidic flows using particle shape. *Nat. Commun.* **4**, 2666.

WIDDER, D. V. 2015 *Laplace Transform (PMS-6)*. Princeton University Press.

WOLFRAM, S. 1999 The MATHEMATICA® Book, Version 4. Cambridge University Press.

WU, H., FARUTIN, A., HU, W.-F., THIÉBAUD, M., RAFAÏ, S., PEYLA, P., LAI, M.-C. & MISBAH, C. 2016 Amoeboid swimming in a channel. *Soft Matt.* **12** (36), 7470–7484.

WU, H., THIÉBAUD, M., HU, W.-F., FARUTIN, A., RAFAI, S., LAI, M.-C., PEYLA, P. & MISBAH, C. 2015 Amoeboid motion in confined geometry. *Phys. Rev.* E **92** (5), 050701.

XIA, D., YAN, J. & HOU, S. 2012 Fabrication of nanofluidic biochips with nanochannels for applications in DNA analysis. *Small* **8** (18), 2787–2801.

ZÖTTL, A. & STARK, H. 2016 Emergent behavior in active colloids. *J. Phys.: Condens. Matter* **28** (25), 253001.

P10 Steady azimuthal flow field induced by a rotating sphere near a rigid disk or inside a gap between two coaxially positioned rigid disks

Reproduced from

A. Daddi-Moussa-Ider, A. R. Sprenger, T. Richter, H. Löwen, and A. M. Menzel, *Steady azimuthal flow field induced by a rotating sphere near a rigid disk or inside a gap between two coaxially positioned rigid disks*, Phys. Fluids **33**, 082011 (2021), with the permission of *AIP Publishing* [297].

Digital Object Identifier (DOI): doi.org/10.1063/5.0062688

Statement of contribution

A.D.M.I. conceived the study and prepared the figures. A.R.S. and A.D.M.I. carried out the analytical calculations. T.R. performed the numerical simulations. A.D.M.I. drafted the manuscript. All authors discussed and interpreted the results, edited the text, and finalized the manuscript.

Copyright and license notice

©AIP Publishing LLC.
AIP Publishing permits authors to reprint the Version of Record (VOR) in their theses or dissertations. It is understood and agreed that the thesis or dissertation may be made available electronically on the university's site or in its repository and that copies may be offered for sale on demand.

Physics of Fluids ARTICLE scitation.org/journal/phf

Steady azimuthal flow field induced by a rotating sphere near a rigid disk or inside a gap between two coaxially positioned rigid disks

Cite as: Phys. Fluids **33**, 082011 (2021); doi: 10.1063/5.0062688
Submitted: 7 July 2021 · Accepted: 6 August 2021 ·
Published Online: 20 August 2021

View Online Export Citation CrossMark

Abdallah Daddi-Moussa-Ider,[1,2,a)] Alexander R. Sprenger,[1] Thomas Richter,[3] Hartmut Löwen,[1] and Andreas M. Menzel[4]

AFFILIATIONS

[1]Institut für Theoretische Physik II: Weiche Materie, Heinrich-Heine-Universität Düsseldorf, Universitätsstraße 1, D-40225 Düsseldorf, Germany
[2]Abteilung Physik lebender Materie, Max-Planck-Institut für Dynamik und Selbstorganisation, Am Faßberg 17, D-37077 Göttingen, Germany
[3]Institut für Analysis und Numerik, Otto-von-Guericke-Universität Magdeburg, Universitätsplatz 2, D-39106 Magdeburg, Germany
[4]Institut für Physik, Otto-von-Guericke-Universität Magdeburg, Universitätsplatz 2, D-39106 Magdeburg, Germany

[a)]Author to whom correspondence should be addressed: ider@ds.mpg.de

ABSTRACT

Geometric confinements play an important role in many physical and biological processes and significantly affect the rheology and behavior of colloidal suspensions at low Reynolds numbers. On the basis of the linear Stokes equations, we investigate theoretically and computationally the viscous azimuthal flow induced by the slow rotation of a small spherical particle located in the vicinity of a rigid no-slip disk or inside a gap between two coaxially positioned rigid no-slip disks of the same radius. We formulate the solution of the hydrodynamic problem as a mixed-boundary-value problem in the whole fluid domain, which we subsequently transform into a system of dual integral equations. Near a stationary disk, we show that the resulting integral equation can be reduced into an elementary Abel integral equation that admits a unique analytical solution. Between two coaxially positioned stationary disks, we demonstrate that the flow problem can be transformed into a system of two Fredholm integral equations of the first kind. The latter are solved by means of numerical approaches. Using our solution, we further investigate the effect of the disks on the slow rotational motion of a colloidal particle and provide expressions of the hydrodynamic mobility as a function of the system geometry. We compare our results with corresponding finite-element simulations and observe very good agreement.

Published under an exclusive license by AIP Publishing. https://doi.org/10.1063/5.0062688

I. INTRODUCTION

Hydrodynamic interactions in viscous flows are ubiquitous in nature and find numerous applications in various industrial and environmental processes. Simultaneously, confinements play a pivotal role in a wide range of biological and biotechnological processes, including the dynamics of polymer solutions and melts in microfluidic devices,[1–4] DNA translocation through pores,[5,6] transport and rheology of red blood cell suspensions in microcirculation,[7–12] colloidal gelation,[13] biofilm formation in microchannels,[14–17] and swimming behavior of active self-propelled agents in viscous media.[18–23]

Fluid flows at small length scales are characterized by low Reynolds numbers, where the viscous forces typically dominate the inertial forces. Under such conditions, the fluid dynamics can well be described by the linear Stokes equations.[24] Over the past few decades, there has been mounting interest in the theoretical and experimental characterization of the behavior of hydrodynamically interacting particles near confining interfaces.[25] These include, for instance, a flat rigid wall,[26–35] a planar surface with partial slip,[29] a flat interface separating two immiscible fluids,[36–39] an interface covered with a surfactant,[40,41] a rough boundary characterized by random surface textures,[42] or a soft deformable membrane possessing elastic and bending properties.[43–57] Thanks to the advent of new particle tracking and measurement techniques, the field has benefited from important recent advances in the characterization of the behavior of colloidal particles near confinement at small scales.[58–62]

Published under an exclusive license by AIP Publishing

Physics of Fluids ARTICLE scitation.org/journal/phf

From a chronological standpoint, one of the first attempts to address the creeping flow induced by a spherical particle confined between two infinitely extended planar walls dates back to Faxén.[63] One century ago, Faxén provided in his doctoral dissertation a few approximate analytical expressions of the hydrodynamic mobility function for parallel translational motion in a channel bounded by two flat plates. Later, using the method of images, Liron and Mochon[64] obtained in a pioneering work an exact solution of the Stokes flow induced by a point-force singularity acting between two parallel no-slip walls. The problem of fluid motion in a channel bounded by two no-slip walls has further been addressed using the multipole expansion technique[65,66] and a strong interaction theory.[67,68]

In the present article, we proceed a step further by examining the low-Reynolds-number flow induced by a point-like particle rotating near a rigid finite-sized no-slip disk or between two coaxially positioned rigid finite-sized no-slip disks of the same radius. Mathematically, we model the situation using a rotlet (also called a point-torque or point-couple) singularity acting on the surrounding fluid medium. We formulate the flow problem at hand as a mixed-boundary-value problem which we subsequently transform into a system of dual integral equations on the domain boundary. For their solution, we employ conventional procedures outlined by Sneddon and Copson so as to express the solutions of the flow problems in terms of convergent definite integrals. Moreover, we quantify the effect of the confining finite-sized disks on the rotational motion by calculating the effect on the corresponding hydrodynamic mobility function.

The remainder of this article is organized as follows. In Sec. II, we derive the solution of the hydrodynamic equations for a rotlet singularity acting near a fixed no-slip disk. We show that the induced velocity field can be presented in a compact analytical form in terms of a definite one-dimensional integral. Afterwards, we obtain in Sec. III a semi-analytical solution of the flow problem inside a gap between two coaxially positioned rigid no-slip disks. We demonstrate that the solution can be reduced into a system of two Fredholm equations of the first kind that can be solved by means of standard numerical approaches. Finally, concluding remarks are contained in Sec. IV. Technical aspects and simulation details regarding the finite-element method we employ to compare our theory with are shifted to the Appendixes.

II. SOLUTION NEAR A SINGLE DISK

A. Problem formulation

First, we examine the low-Reynolds-number dynamics of a point-like particle undergoing rotational motion near one fixed finite-sized disk of radius R. We assume a no-slip boundary condition to hold at the surface of the disk. In addition, we suppose that the disk is located within the plane $z = 0$ and that the center of the disk coincides with the origin of our coordinate frame; see Fig. 1 for an illustration of the system setup. In addition, we assume that the fluid is incompressible and Newtonian with constant shear viscosity η.

At low Reynolds numbers, the fluid dynamics is thus governed by the steady Stokes equations,[69]

$$\eta \boldsymbol{\nabla}^2 \boldsymbol{v} - \boldsymbol{\nabla} p + \boldsymbol{F}_{\mathrm{B}} = \boldsymbol{0}, \quad \boldsymbol{\nabla} \cdot \boldsymbol{v} = 0, \tag{1}$$

wherein $\boldsymbol{v}$ and p denote the hydrodynamic velocity and pressure fields, respectively. In addition, $\boldsymbol{F}_{\mathrm{B}}$ represents an arbitrary bulk force density acting on the fluid at position $\boldsymbol{r}_0 = h\boldsymbol{e}_z$ with $\boldsymbol{e}_z$ denoting the unit

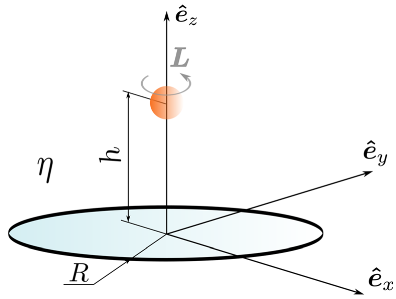

FIG. 1. Graphical illustration of the system setup. A point-like particle undergoing slow rotational motion near a rigid no-slip disk of radius R sets the fluid into motion. The center of the particle is located at a distance h above the center of the disk, while the surrounding viscous fluid medium is characterized by a dynamic shear viscosity η. $\boldsymbol{L} = L\hat{\boldsymbol{e}}_z$ sets the torque acting via the particle at the particle position on the fluid.

vector directed along the z direction. The torque $\boldsymbol{L}$ on the particle is transmitted to the fluid and linked to the surface force density $\boldsymbol{F}$ acting on the fluid via the surface of the spherical particle

$$\boldsymbol{L} = \oint_A (\boldsymbol{r} - \boldsymbol{r}_0) \times \boldsymbol{F} \, \mathrm{d}S, \tag{2}$$

with A denoting the surface area of the tiny particle. In the point-particle approximation, the asymmetric dipolar term in the multipole expansion is associated with the flow field induced by a rotlet singularity of strength $\boldsymbol{L}$ acting above the disk at position $\boldsymbol{r}_0$. Here, we consider the case in which the point torque is directed along the axis of symmetry of the disk and set $\boldsymbol{L} = L\boldsymbol{e}_z$.

In an unbounded (infinite) fluid medium, the flow field induced by a rotlet singularity is given by

$$\boldsymbol{v}^\infty(\boldsymbol{r}) = \frac{1}{8\pi\eta} \frac{\boldsymbol{L} \times \boldsymbol{s}}{s^3}, \tag{3}$$

wherein $\boldsymbol{s} = \boldsymbol{r} - \boldsymbol{r}_0$ and $s = |\boldsymbol{s}|$ is the distance from the singularity position. Using cylindrical coordinates (r, ϕ, z), the azimuthal component of the flow velocity field induced by a free-space rotlet oriented along the z direction reads

$$v_\phi^\infty(r, z) = \frac{Kr}{\left(r^2 + (z-h)^2\right)^{\frac{3}{2}}}, \tag{4}$$

where we have defined, for convenience, the abbreviation $K = L/(8\pi\eta)$ of dimension $(\text{length})^3\,(\text{time})^{-1}$.

The solution of the flow problem in the presence of the confining disk can generally be expressed as a linear superposition of the solution in an unbounded fluid medium, given by Eq. (4), and a complementary solution that is required to satisfy the underlying regularity and boundary conditions for the total induced flow field. Specifically,

$$v_\phi = v_\phi^\infty + v_\phi^*, \tag{5}$$

with v_ϕ^* standing for the complementary solution for the azimuthal flow velocity, also sometimes called the image solution.[70]

Published under an exclusive license by AIP Publishing

Physics of Fluids ARTICLE scitation.org/journal/phf

The solution of the homogeneous equations governing the fluid motion can be expressed in our case in terms of a single harmonic function as $v_\phi^* = -\partial\Omega/\partial r$ [cf. Ref. 69, Eq. (3–3.58), or Ref. 71, Eq. (5), and references therein for the expression of the complete solution] with Ω satisfying the Laplace equation $\boldsymbol{\nabla}^2\Omega = 0$. Then, the harmonic function Ω can be written in the general form in terms of a Fourier–Bessel integral of the form

$$\Omega(r,z) = K\int_0^\infty \omega(\lambda)J_0(\lambda r)e^{-\lambda|z|}\,\mathrm{d}\lambda, \tag{6}$$

wherein $\omega(\lambda)$ is an unknown wavenumber-dependent function to be subsequently determined from the prescribed boundary conditions. In addition, J_ν denotes the Bessel function[72] of the first kind of order ν. The image solution for the azimuthal component of the velocity field is then obtained as

$$v_\phi^*(r,z) = K\int_0^\infty \lambda\omega(\lambda)J_1(\lambda r)e^{-\lambda|z|}\,\mathrm{d}\lambda. \tag{7}$$

Evidently, the solution form given by Eq. (7) satisfies the natural continuity of the azimuthal velocity field at the plane $z=0$. We note that the rotlet singularity does not induce a pressure gradient and that the radial and axial components of the fluid velocity vanish. Therefore, the solution of the flow problem reduces to the search for the azimuthal component of the velocity field only.

B. Boundary conditions and dual integral equations

We require no-slip boundary conditions on the surface of the disk and assume the continuity of the azimuthal component of the normal stress vector on the plane $z=0$ outside the disk. Specifically,

$$v_\phi^\infty + v_\phi^*|_{z=0} = 0 \quad \text{for} \quad r < R, \tag{8a}$$

$$\eta\left.\frac{\partial v_\phi^*}{\partial z}\right|_{z=0^+} - \eta\left.\frac{\partial v_\phi^*}{\partial z}\right|_{z=0^-} = 0 \quad \text{for} \quad r > R. \tag{8b}$$

By inserting the expressions of the free-space and image fields given by Eqs. (4) and (7), respectively, into Eq. (8), we obtain the mixed-boundary-value problem on the inner and outer domain boundaries. Specifically,

$$\int_0^\infty \lambda\omega(\lambda)J_1(\lambda r)\,\mathrm{d}\lambda = f(r) \quad (r<R), \tag{9a}$$

$$\int_0^\infty \lambda^2\omega(\lambda)J_1(\lambda r)\,\mathrm{d}\lambda = 0 \quad (r>R), \tag{9b}$$

with the radial function

$$f(r) = -\frac{r}{(r^2+h^2)^{\frac{3}{2}}}, \tag{10}$$

stemming from the free-space rotlet field.

The solution of the type of dual integral equations stated by Eq. (9) can generally be obtained using the theory of Mellin transforms.[73,74] We will follow in the present article a different route based on the analytical approach outlined by Sneddon[75] and Copson.[76] In the sequel, we will show that the present dual integral equations problem with Bessel function kernels can conveniently be reduced to an elementary Abel integral equation that may readily be inverted. This solution strategy has previously been employed to examine the low-Reynolds-number flow induced by nonrotational force singularities near a finite-sized elastic disk possessing shear and bending properties,[77,78] the flow field near a no-slip disk,[79,80] or the axisymmetric flow due to a Stokeslet acting between two coaxially positioned rigid no-slip disks.[81]

We search a solution for the unknown wavenumber-dependent function $\omega(\lambda)$ of the integral form

$$\omega(\lambda) = \lambda^{-\frac{1}{2}}\int_0^R \hat{\omega}(t)J_{\frac{1}{2}}(\lambda t)\,\mathrm{d}t, \tag{11}$$

wherein $\hat{\omega}(t)$, with $t\in[0,R]$, is an unknown function later to be determined. We will show in the sequel that the equation for the outer problem (9b) is indeed satisfied using this form of solution.

First, it can readily be checked that Eq. (11) can further be expressed in the form

$$\omega(\lambda) = \lambda^{-\frac{3}{2}}\int_0^R \hat{\omega}(t)\,t^{-\frac{3}{2}}\frac{\mathrm{d}}{\mathrm{d}t}\left(t^{\frac{3}{2}}J_{\frac{3}{2}}(\lambda t)\right)\mathrm{d}t. \tag{12}$$

By defining

$$\hat{F}(t) = t^{\frac{3}{2}}\frac{\mathrm{d}}{\mathrm{d}t}\left(t^{-\frac{3}{2}}\hat{\omega}(t)\right), \tag{13}$$

and assuming that $t^{\frac{3}{2}}\hat{\omega}(t)\to 0$ as $t\to 0^+$, Eq. (12) can be rewritten upon integration by parts as

$$\omega(\lambda) = \lambda^{-\frac{3}{2}}\left(\hat{\omega}(R)J_{\frac{3}{2}}(\lambda R) - \int_0^R \hat{F}(t)J_{\frac{3}{2}}(\lambda t)\,\mathrm{d}t\right). \tag{14}$$

Then, by substituting the modified form of solution given by Eq. (14) into Eq. (9b), the integral equation for the outer problem can be expressed as

$$\mathcal{K}_+(r,R)\,\hat{\omega}(R) - \int_0^R \mathcal{K}_+(r,t)\hat{F}(t)\,\mathrm{d}t = 0 \quad (r>R). \tag{15}$$

In this context, we define the kernel functions

$$\mathcal{K}_\pm(r,t) = \int_0^\infty \lambda^{\frac{1}{2}}J_{1\pm\frac{1}{2}}(\lambda t)J_1(\lambda r)\,\mathrm{d}\lambda. \tag{16}$$

It turned out that the latter improper (infinite) integral can be evaluated analytically as

$$\mathcal{K}_+(r,t) = \left(\frac{2}{\pi t}\right)^{\frac{1}{2}}\frac{r}{t}\frac{\Theta(t-r)}{(t^2-r^2)^{\frac{1}{2}}}, \tag{17}$$

with $\Theta(\cdot)$ denoting the Heaviside step function (or the unit step function). Since $r>R$, it can readily be perceived that the transformed integral equation for the outer problem stated by Eq. (15) is trivially satisfied.

Thereafter, substituting Eq. (11) into the integral equation for the inner problem given by Eq. (9a) yields

$$\int_0^R \mathcal{K}_-(r,t)\,\hat{\omega}(t)\,\mathrm{d}t = f(r) \quad (r<R). \tag{18}$$

By noting that

Published under an exclusive license by AIP Publishing

Physics of Fluids ARTICLE scitation.org/journal/phf

$$\mathcal{K}_-(r,t) = \left(\frac{2t}{\pi}\right)^{\frac{1}{2}} \frac{1}{r} \frac{\Theta(r-t)}{(r^2-t^2)^{\frac{1}{2}}}. \tag{19}$$

Equation (18) can subsequently be rewritten in a much simplified form as

$$\int_0^r \frac{t^{\frac{1}{2}}\hat{\omega}(t)}{(r^2-t^2)^{\frac{1}{2}}}\,\mathrm{d}t = \left(\frac{\pi}{2}\right)^{\frac{1}{2}} rf(r) \quad (r<R). \tag{20}$$

Equation (20) is a classical Abel integral equation which constitutes a special form of the linear Volterra equation of the first kind having a weakly singular kernel.[82–84] It admits a unique solution if and only if $f(r)$ is a continuously differentiable function.[85–87] Its solution is formally given in an integral form as (cf. Appendix A for further details)

$$\hat{\omega}(t) = \left(\frac{2}{\pi t}\right)^{\frac{1}{2}} \frac{\mathrm{d}}{\mathrm{d}t}\int_0^t \frac{v^2 f(v)\,\mathrm{d}v}{(t^2-v^2)^{\frac{1}{2}}}. \tag{21}$$

Inserting the expression of $f(r)$ stated by Eq. (10) into Eq. (21) and performing the resulting integration yields

$$\hat{\omega}(t) = -2\left(\frac{2t}{\pi}\right)^{\frac{1}{2}} \frac{ht}{(t^2+h^2)^2}. \tag{22}$$

Evidently, the condition $t^{\frac{3}{2}}\hat{\omega}(t) \to 0$ as $t \to 0^+$ assumed above upon integrating by parts is well satisfied.

Next, by substituting Eq. (22) into Eq. (11) upon noting that

$$J_{\frac{1}{2}}(\lambda t) = \left(\frac{2}{\pi}\right)^{\frac{1}{2}} (\lambda t)^{-\frac{1}{2}} \sin(\lambda t), \tag{23}$$

the unknown wavenumber-dependent function $\omega(\lambda)$ can be written in a compact integral form as

$$\omega(\lambda) = -\frac{4h}{\pi\lambda}\int_0^R \frac{t\sin(\lambda t)\,\mathrm{d}t}{(t^2+h^2)^2}. \tag{24}$$

The latter integral can be expressed in a general way in terms of hyperbolic functions and trigonometric integrals. However, choosing the integral form is more convenient for later treatment. In particular, it follows that $\omega(\lambda) = -e^{-\lambda h}$ as $R \to \infty$. Finally, by inserting Eq. (24) into Eq. (7) and interchanging the order of integration with respect to the variables λ and t, the solution for the image azimuthal velocity field follows as

$$v_\phi^*(r,z) = -\frac{4Kh}{\pi}\int_0^R \frac{t\,\mathcal{Q}(r,z,t)\,\mathrm{d}t}{(t^2+h^2)^2}, \tag{25}$$

where we have defined the kernel function

$$\mathcal{Q}(r,z,t) = \int_0^\infty J_1(\lambda r)\sin(\lambda t)\,e^{-\lambda|z|}\,\mathrm{d}\lambda. \tag{26}$$

To obtain an analytical expression for $\mathcal{Q}$, we proceed by making use of Euler's formula in complex analysis[88] and write $\sin(\lambda t) = \mathrm{Im}\{e^{i\lambda t}\}$, with Im denoting the imaginary part of the argument. By using the change of variable $u = \lambda r$, Eq. (26) can be rewritten in the form

$$\mathcal{Q}(r,z,t) = \frac{1}{r}\mathrm{Im}\left\{\int_0^\infty J_1(u)\,e^{-su}\,\mathrm{d}u\right\}, \tag{27}$$

with $s = (|z|-it)/r$. By invoking the Laplace transform[89] of $J_1(u)$ given as $1 - s(1+s^2)^{-\frac{1}{2}}$, Eq. (27) can then be evaluated as

$$\mathcal{Q}(r,z,t) = -\frac{1}{r}\mathrm{Im}\left\{\frac{|z|-it}{\left(r^2+(|z|-it)^2\right)^{\frac{1}{2}}}\right\}. \tag{28}$$

The latter can further be cast in the final form as

$$\mathcal{Q}(r,z,t) = \frac{2^{\frac{1}{2}}}{2rU}\left(t(U+V)^{\frac{1}{2}} - |z|(U-V)^{\frac{1}{2}}\right), \tag{29}$$

where we have defined

$$U = \left(\left(\rho^2+t^2\right)^2 - 4r^2t^2\right)^{\frac{1}{2}}, \quad V = \rho^2 - t^2, \tag{30}$$

where $\rho^2 = r^2 + z^2$. It can be shown that $\mathcal{Q}$ is always well defined except when $U=0$, for which $z=0$ and $t=r$. In this case, $\mathcal{Q}(r,z,t) \sim (r-t)^{-\frac{1}{2}}\Theta(r-t)$. We note that $Q(r,z,t) \to 0$ as $r \to 0$.

An analytical integration of Eq. (25) is delicate, if not downright impossible. Therefore, recourse to numerical procedures is necessary. To this end, we approximate the integral by a standard middle Riemann sum using the partition $t_1, \ldots, t_N$, where $t_i = (i-1/2)\delta$, with $i = 1, \ldots, N$ and $\delta = R/N$. Here, N denotes the number of discretization points. Throughout this work, we consistently set $N = 10\,000$.

In Fig. 2, we show contour plots of the scaled azimuthal flow velocity induced by a rotlet singularity positioned at different distances along the axis of the disk. The analytical predictions [(a), (b), and (c)] are in good agreement with the results from finite-element simulations [(d), (e), and (f); see Appendix B for technical details regarding the simulation method].

The magnitude of the scaled velocity field is shown on a logarithmic scale to emphasize the difference between the different regions. Similarly, as in the bulk, the flow velocity is decaying faster along the z direction (or axis of rotation) compared to the radial direction. However, near the disk, the azimuthal flow velocity becomes asymmetric with respect to the rotlet position, and for $z<0$ the total flow field almost vanishes completely. Last, we remark that the overall magnitude of the flow field reduces as the rotlet gets closer to the disk.

C. Exact solution for $R \to \infty$

The solution for a rotlet oriented normal to a hard wall can be obtained using the image system technique noted by Blake.[70] For completeness, we here derive this solution in a different way using our formalism. For an infinitely large disk located at $z=0$, the integral equations (9a) for the inner domain hold for all positive r, and thus we can directly apply a Hankel transform[90] on both sides of this equation. Here, we make use of the orthogonality property of Bessel functions,[72]

$$\int_0^\infty rJ_\nu(\lambda r)J_\nu(\lambda' r)\,\mathrm{d}r = \lambda^{-1}\delta(\lambda-\lambda'), \tag{31}$$

and obtain the solution for

Physics of Fluids ARTICLE scitation.org/journal/phf

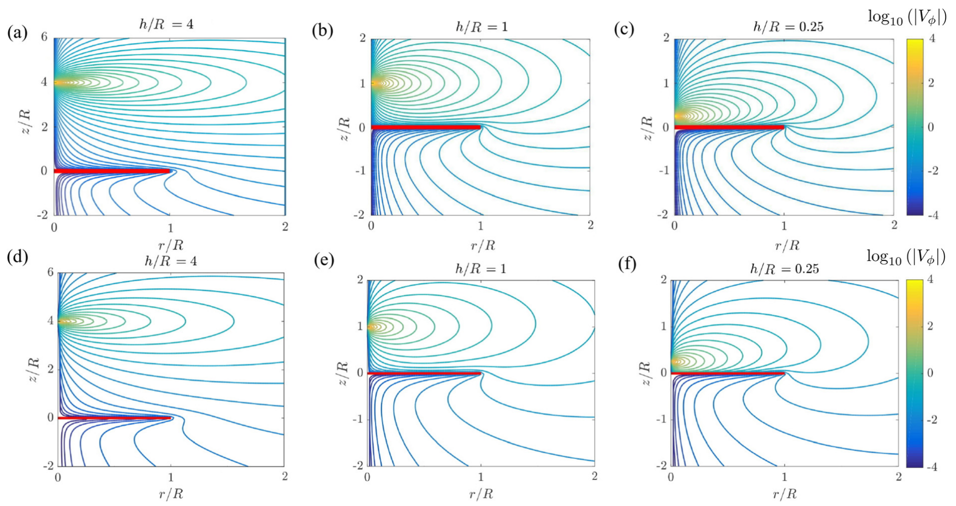

FIG. 2. Contour plot of the amplitude of the scaled azimuthal flow velocity as obtained theoretically [first row, (a), (b), and (c)] and using finite-element simulations [second row, (d), (e), and (f)]. The flows are induced by a rotlet singularity positioned at $h/R = 4$ [(a) and (d)], $h/R = 1$ [(b) and (e)] and $h/R = 0.25$ [(c) and (f)] on the axis of a no-slip disk of radius R (red). The scaled azimuthal velocity is defined as $V_\phi = v_\phi/(L/(8\pi\eta R^2))$. The results are presented on a decimal logarithmic scale.

$$\omega(\lambda) = \int_0^\infty r f(r) J_1(\lambda r)\, \mathrm{d}r = -e^{-\lambda h}. \tag{32}$$

Inserting the latter result into Eq. (7) yields

$$v^*_{\phi\mathrm{Blake}}(r,z) = -\frac{Kr}{\left(r^2 + (|z|+h)^2\right)^{\frac{3}{2}}}. \tag{33}$$

The image solution for the azimuthal component in the limit $R \to \infty$ can alternatively be calculated analytically from Eq. (25). Consequently, the total flow field vanishes underneath the disk, i.e., for $z < 0$.

Figure 3 shows the variation of the percentage relative error in the flow velocity field as obtained using Blake's solution given by Eq. (33) in comparison with the exact solution derived in the present work for a finite-sized disk given in an integral form by Eq. (25). Here, the flow field is evaluated at five different axial distances z/h, while keeping the radial position $r/R = 0.2$. We observe that the error is vanishingly small for $h \ll R$ and increases monotonically as the ratio h/R gets larger. In addition, the error amounts to small values in the fluid domain close to the singularity position in which the flow velocity is primarily determined by the infinite-space rotlet. Upon increasing z/h, the maximum percentage relative error (MPRE) increases and it was found to be as high as approximately 55% for $z/h = 10$ and $h/R = 10^2$. We have systematically checked that the MPRE is, in general, less sensitive to variations in the radial position.

D. Hydrodynamic rotational mobility

Having derived the solution of the flow problem for a point-torque singularity acting near a finite-sized disk, we next investigate how the presence of the nearby disk affects the rotational mobility. For this purpose, we think of the rotlet generated by a small colloidal particle of radius a. By restricting ourselves to the situation in which $a \ll h$, the leading-order correction to the particle rotational mobility can be obtained by evaluating the image angular velocity of the fluid,

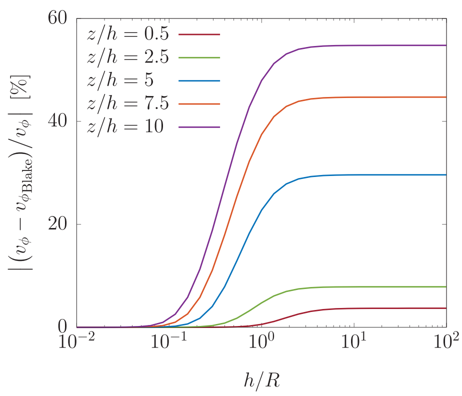

FIG. 3. Percentage relative error in the flow field as obtained using Blake's solution for an infinitely extended disk in comparison with the exact solution for a disk of finite size, as a function of increasing vertical distance h/R of the rotlet from the disk. The flow field is evaluated at five different values of z/h while keeping $r/R = 0.2$.

Published under an exclusive license by AIP Publishing

Physics of Fluids ARTICLE scitation.org/journal/phf

$\frac{1}{2}\,\nabla\times v^*$, at the singularity position.[30] In a scaled form, it can be presented as

$$\frac{\Delta\mu}{\mu_0}=\frac{a^3}{K}\lim_{(r,z)\to(0,h)}\frac{1}{2r}\frac{\partial}{\partial r}\left(rv^*_\phi\right), \tag{34}$$

wherein $\mu_0=(8\pi\eta a^3)^{-1}$ is the bulk rotational mobility, i.e., in the absence of the disk.

Following the notation employed in our previous considerations,[77–79] we define the positive dimensionless number k_1 to be the scaled correction factor to the mobility near a no-slip disk as

$$k_1=-\frac{\Delta\mu}{\mu_0}\Big/\left(\frac{a}{h}\right)^3, \tag{35}$$

and substituting Eq. (7) expressing the image azimuthal velocity into Eq. (34), we obtain

$$k_1=-\frac{h^3}{2}\int_0^\infty \lambda^2\omega(\lambda)e^{-\lambda h}\,\mathrm{d}\lambda. \tag{36}$$

Next, by inserting the expression of $\omega(\lambda)$ stated by Eq. (24) into Eq. (36) and using the changes of variables $u=\lambda h$ and $v=t/R$, the scaled correction factor can be presented as an integral over the interval $[0,1]$ as

$$k_1(\xi)=\frac{2}{\pi}\,\xi^2\int_0^1\frac{v\,G(v,\xi)\,\mathrm{d}v}{\left(v^2+\xi^2\right)^2}, \tag{37}$$

with the dimensionless number $\xi=h/R$. Here,

$$G(v,\xi)=\int_0^\infty u\sin\left(\frac{uv}{\xi}\right)e^{-u}\,\mathrm{d}u=\frac{2v\xi^3}{\left(v^2+\xi^2\right)^2}. \tag{38}$$

Finally, evaluating the definite integral in Eq. (37) yields the expression of the scaled correction factor as

$$k_1(\xi)=\frac{1}{8}-\frac{1}{4\pi}\left(\arctan\xi+\frac{\xi\left(\xi^2-3\right)\left(1+3\xi^2\right)}{3\left(1+\xi^2\right)^3}\right). \tag{39}$$

In particular, for $\xi\ll 1$ (or $h\ll R$), we obtain

$$k_1(\xi)=\frac{1}{8}-\frac{4}{5\pi}\,\xi^5+\mathcal{O}\left(\xi^7\right). \tag{40}$$

Notably, the familiar correction factor $k_1=1/8$ near an infinitely extended hard wall is recovered in the limit $\xi\to 0$. For $\xi\gg 1$, we get

$$k_1(\xi)=\frac{4}{3\pi}\,\xi^{-3}+\mathcal{O}\left(\xi^{-5}\right). \tag{41}$$

Interestingly, the correction factor takes a particularly simple expression when $\xi=\sqrt{3}$, for which $k_1=1/24$.

In Fig. 4, we present the variation of the scaled correction factor given by Eq. (39) as a function of the dimensionless number $\xi=h/R$. We observe that the scaled correction factor is a monotonically decaying function of ξ. On a semilogarithmic scale (main plot), the curve exhibits an inverse logistic-like (sigmoid) evolution between two plateau values. The scaled correction factor undergoes a cubic decay with ξ while vanishing in the limit $\xi\to\infty$.

Recapitulating, we have presented a dual integral equation approach to determine the solution of the hydrodynamic equations for a point-torque singularity acting near a rigid disk. In the following, we will employ a similar technique to obtain the corresponding solution of the flow problem in the presence of two coaxially positioned rigid disks.

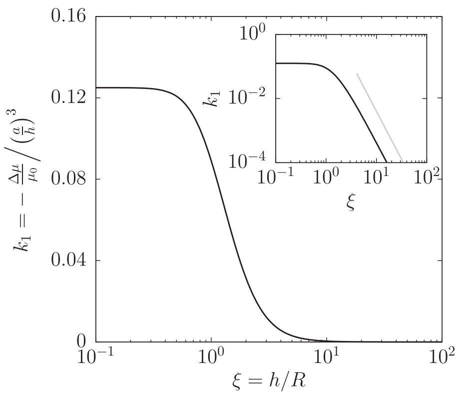

FIG. 4. Scaled correction factor k_1 to the rotational hydrodynamic mobility near a rigid no-slip disk, Eq. (39), vs the dimensionless number $\xi=h/R$ plotted on a semilogarithmic scale. The same curve is shown in the inset on a log–log scale, where the scaling law ξ^{-3} is displayed in the range $\xi\gg 1$ (gray).

III. SOLUTION FOR TWO COAXIALLY POSITIONED DISKS

A. Problem formulation

We now assume that two parallel coaxially positioned rigid disks are located within the planes at $z=-H/2$ and $z=H/2$, where H represents the distance separating the two disks. The z axis passes through the centers of the coaxially positioned disks. We suppose that the rotlet is acting between the disks at position $\boldsymbol{r}_0=h\boldsymbol{e}_z$, where $-H/2<h<H/2$; see Fig. 5 for a graphical illustration of the setup.

To find a solution to the flow problem, we partition the fluid medium into three distinct parts. We label by the superscript 1 the flow velocity field in the fluid domain beneath the plane $z=-H/2$ containing the lower disk, subscript 2 the fluid region delimited by the planes at $z=-H/2$ and $z=H/2$, and we designate by the subscript 3 the fluid domain above the plane $z=H/2$ containing the top disk. In the remainder of this article, we choose, for convenience, to scale all lengths by the gap width H.

We now express the solution for the azimuthal velocity field in each region of the fluid domain as

$$v^*_{\phi 1}=K\int_0^\infty A(\lambda)e^{\lambda z}J_1(\lambda r)\,\mathrm{d}\lambda, \tag{42a}$$

$$v^*_{\phi 2}=K\int_0^\infty \left(B(\lambda)e^{-\lambda z}+C(\lambda)e^{\lambda z}\right)J_1(\lambda r)\,\mathrm{d}\lambda, \tag{42b}$$

$$v^*_{\phi 3}=K\int_0^\infty D(\lambda)e^{-\lambda z}J_1(\lambda r)\,\mathrm{d}\lambda, \tag{42c}$$

where $A(\lambda)$, $B(\lambda)$, $C(\lambda)$, and $D(\lambda)$ are unknown functions to be determined from the underlying boundary conditions. It can readily

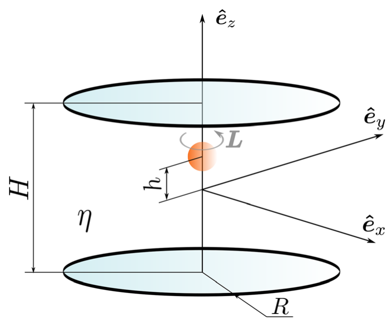

FIG. 5. Slow rotational motion of a point-like particle confined between two coaxially positioned rigid no-slip disks of identical radius R. The confining disks are located within the planes $z = \pm H/2$ with H denoting the separation distance between the parallel disks. The particle is located at a distance h from the origin of the system of coordinates on the axis of the disks.

be checked that the regularity condition of a finite velocity field is inherently satisfied in the whole domain.

B. Boundary conditions and dual integral equations

Requiring the natural continuity of the velocity field at the planes $z = \pm 1/2$ yields the expressions of the functions associated with the intermediate fluid domain in terms of those related to the lower and upper domains. Specifically,

$$B(\lambda) = \frac{1}{2}\left(A(\lambda) - D(\lambda)e^{-\lambda}\right)\operatorname{csch}(\lambda), \tag{43a}$$

$$C(\lambda) = \frac{1}{2}\left(D(\lambda) - A(\lambda)e^{-\lambda}\right)\operatorname{csch}(\lambda), \tag{43b}$$

with csch denoting the hyperbolic cosecant function, defined as $\operatorname{csch}(\lambda) = 1/\sinh\lambda = 2/(e^{\lambda} - e^{-\lambda})$.

By imposing the no-slip boundary condition at the surfaces of the two disks, we obtain the equations for the inner problem for $r < R$ as

$$\int_0^\infty A(\lambda)e^{-\frac{\lambda}{2}}J_1(\lambda r)\,\mathrm{d}\lambda = \psi_+(r), \tag{44a}$$

$$\int_0^\infty D(\lambda)e^{-\frac{\lambda}{2}}J_1(\lambda r)\,\mathrm{d}\lambda = \psi_-(r), \tag{44b}$$

where we have defined the radially symmetric functions

$$\psi_\pm(r) = -\frac{r}{\left(r^2 + \left(h \pm \frac{1}{2}\right)^2\right)^{\frac{3}{2}}}. \tag{45}$$

In addition, the continuity of the azimuthal stress vector outside the regions containing the disk yields the equations for the outer problem for $r > R$. Specifically,

$$\int_0^\infty \lambda\left(A(\lambda)e^{\frac{\lambda}{2}} - D(\lambda)e^{-\frac{\lambda}{2}}\right)\operatorname{csch}(\lambda)J_1(\lambda r)\,\mathrm{d}\lambda = 0, \tag{46a}$$

$$\int_0^\infty \lambda\left(A(\lambda)e^{-\frac{\lambda}{2}} - D(\lambda)e^{\frac{\lambda}{2}}\right)\operatorname{csch}(\lambda)J_1(\lambda r)\,\mathrm{d}\lambda = 0. \tag{46b}$$

Equations (44) and (46) constitute a system of dual integral equations for the unknown functions $A(\lambda)$ and $D(\lambda)$. For its solution, we employ the standard solution approach outlined by Sneddon[75] and Copson[76] and set

$$\frac{1}{2}\left(A(\lambda)e^{\frac{\lambda}{2}} - D(\lambda)e^{-\frac{\lambda}{2}}\right)\operatorname{csch}(\lambda) = \lambda^{\frac{1}{2}}f_1(\lambda), \tag{47a}$$

$$\frac{1}{2}\left(A(\lambda)e^{-\frac{\lambda}{2}} - D(\lambda)e^{\frac{\lambda}{2}}\right)\operatorname{csch}(\lambda) = \lambda^{\frac{1}{2}}f_2(\lambda), \tag{47b}$$

where

$$f_i(\lambda) = \int_0^R \hat{f}_i(t)J_{\frac{1}{2}}(\lambda t)\,\mathrm{d}t, \tag{48}$$

with $\hat{f}_i(t), i \in \{1, 2\}$ are two unknown functions defined on the interval $[0, R]$ to be subsequently determined. In this way, the equations for the outer problem are automatically satisfied following the same reasoning in Sec. II. Solving Eq. (47) for $A(\lambda)$ and $D(\lambda)$ yields

$$A(\lambda) = \lambda^{\frac{1}{2}}\left(f_1(\lambda)e^{\frac{\lambda}{2}} - f_2(\lambda)e^{-\frac{\lambda}{2}}\right), \tag{49a}$$

$$D(\lambda) = \lambda^{\frac{1}{2}}\left(f_1(\lambda)e^{-\frac{\lambda}{2}} - f_2(\lambda)e^{\frac{\lambda}{2}}\right). \tag{49b}$$

Upon substitution of Eq. (49) into Eq. (44), the inner problem can be expressed in the form

$$\int_0^R \left(\mathcal{K}_-(r,t)\hat{f}_1(t) - \mathcal{S}(r,t)\hat{f}_2(t)\right)\mathrm{d}t = \psi_+(r), \tag{50a}$$

$$\int_0^R \left(\mathcal{S}(r,t)\hat{f}_1(t) - \mathcal{K}_-(r,t)\hat{f}_2(t)\right)\mathrm{d}t = \psi_-(r). \tag{50b}$$

Here, we have defined the kernel function

$$\mathcal{S}(r,t) = \left(\frac{2}{\pi t}\right)^{\frac{1}{2}}\mathcal{Q}(r,1,t), \tag{51}$$

where $\mathcal{Q}$ has been defined earlier by Eq. (27). We note that the expression of the kernel function $\mathcal{K}_-$ has previously been given by Eq. (19) and can further be expressed in term of $\mathcal{Q}$ as

$$\mathcal{K}_-(r,t) = \left(\frac{2}{\pi t}\right)^{\frac{1}{2}}\mathcal{Q}(r,0,t). \tag{52}$$

Equation (50) represent a system of Fredholm integral equations of the first kind.[91] Due to the complicated expressions of their kernel functions, exact analytical expressions for the unknown functions $\hat{f}_1(t)$ and $\hat{f}_2(t)$ are far from trivial. Following a computational approach, we partition the integration intervals $[0, R]$ into N subintervals, approximating the integrals by the standard middle Riemann sum. We then evaluate the two resulting equations at N discrete values of r that are distributed uniformly over the interval $[0, R]$. Inverting the resulting linear system of $2N$ independent equations, we obtain accurate values of $\hat{f}_1(t)$ and $\hat{f}_2(t)$ at each discretization point.

Inserting the expressions of $A(\lambda)$ and $D(\lambda)$ stated by Eq. (49) into Eq. (42), the image solution for the azimuthal flow field everywhere in the fluid domain can be cast in the final compact form

Published under an exclusive license by AIP Publishing

Physics of Fluids ARTICLE scitation.org/journal/phf

$$v_\phi^*(r,z) = K \int_0^R \left(\frac{2}{\pi t}\right)^{\frac{1}{2}} \hat{g}(r,z,t)\,\mathrm{d}t, \tag{53}$$

wherein

$$\hat{g}(r,z,t) = \mathcal{Q}\left(r, z+\frac{1}{2}, t\right)\hat{f}_1(t) - \mathcal{Q}\left(r, z-\frac{1}{2}, t\right)\hat{f}_2(t).$$

Notably, the system of Fredholm integral equations stated by Eq. (50) is recovered when enforcing the no-slip condition at $z = \pm 1/2$.

Likewise, the definite integral given by Eq. (53) can be discretized via the middle Riemann sum to yield an approximate solution for the image velocity field at any point (r, z) in the entire fluid domain.

Figure 6 shows the contour plots of the amplitude of the scaled azimuthal flow velocity for different positions on the axis of two coaxial disks, as obtained analytically and by means of finite-element simulations. Again, the flow velocity is the highest in the near vicinity of the rotlet and decays faster along the z direction compared to the radial direction. Moreover, the magnitude is substantially smaller above and below the disks. As the rotlet approaches one side of the confining disks, the overall magnitude of the flow field becomes reduced and the structure becomes more asymmetric. Good agreement is obtained between the semi-analytical theory and the finite-element simulations.

C. Solution for $R \to \infty$

For completeness, we additionally address by our approach the solution for the flow field in a gap bounded by two infinitely extended planar walls located at $z = \pm 1/2$. To this end, a Hankel transform is applied on both sides of Eq. (44). We obtain

$$A(\lambda) = \lambda e^{\frac{\lambda}{2}} \bar{\psi}^+(\lambda) = -\lambda e^{-\lambda h}, \tag{54a}$$

$$D(\lambda) = \lambda e^{\frac{\lambda}{2}} \bar{\psi}^-(\lambda) = -\lambda e^{\lambda h}, \tag{54b}$$

with

$$\bar{\psi}^\pm(\lambda) = \int_0^\infty r\psi^\pm(r) J_1(\lambda r)\,\mathrm{d}r = -e^{-\lambda(\frac{1}{2}\pm h)}, \tag{55}$$

for $|h| < 1/2$. Then, it follows from Eq. (43) that the wavenumber-dependent function associated with the fluid domain bounded by the planes $z = \pm 1/2$ is given by

$$B(\lambda) = -\frac{\lambda}{2}\left(e^{-\lambda h} - e^{-\lambda(1-h)}\right)\operatorname{csch}(\lambda), \tag{56a}$$

$$C(\lambda) = -\frac{\lambda}{2}\left(e^{\lambda h} - e^{-\lambda(1+h)}\right)\operatorname{csch}(\lambda). \tag{56b}$$

Finally, the corresponding solution of the image flow field can be obtained by inserting Eqs. (54) and (56) into Eq. (42). As expected, the total velocity in the lower and upper regions vanishes in the limit $R \to \infty$. Figure 7 illustrates exemplary contour plots of the azimuthal flow field induced by a rotlet acting between two infinitely extended no-slip walls for three different positions of the singularity.

D. Hydrodynamic rotational mobility

The scaled correction to the particle rotational mobility in the point-particle approximation can be obtained from the image velocity field via Eq. (34). Between two coaxially positioned disks, we alternatively choose to define the scaled correction factor as

$$k_2 = -\frac{\Delta\mu}{\mu_0} \Big/ a^3. \tag{57}$$

Then, it follows from Eq. (53) that the scaled correction to leading order can conveniently be expressed as

$$k_2 = \frac{1}{2}\left(\frac{2}{\pi}\right)^{\frac{1}{2}} \int_0^R t^{-\frac{1}{2}}\left(\chi_-(t)\hat{f}_2(t) - \chi_+(t)\hat{f}_1(t)\right)\mathrm{d}t, \tag{58}$$

where we have defined

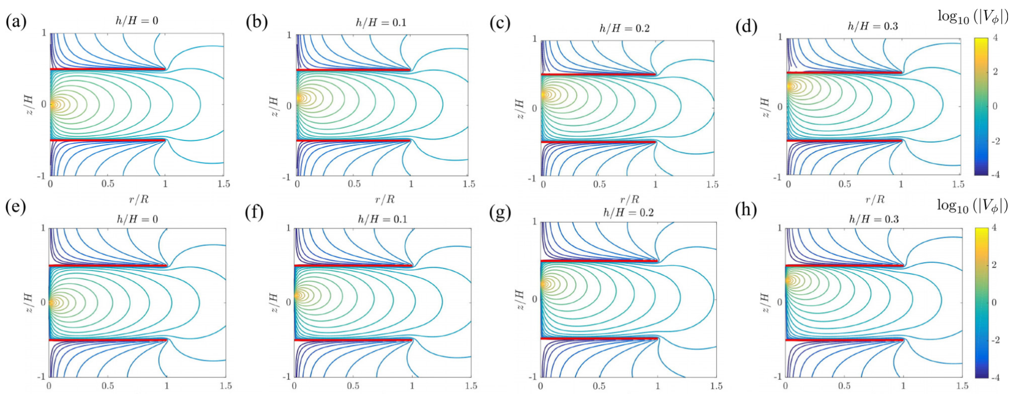

FIG. 6. Contour plots of the amplitude of the scaled azimuthal velocity as obtained semi-analytically [first row, (a)–(d)] and by means of finite-element simulations [second row, (e)–(h)]. The results are shown for a rotlet acting at $h/H = 0$ [(a) and (e)], $h/H = 0.1$ [(b) and (f)], $h/H = 0.2$ [(c) and (g)], and $h/H = 0.3$ [(d) and (h)] on the axis of two coaxially positioned no-slip disks of radius $R = H$ (red). Here, the scaled azimuthal velocity is defined as $V_\phi = v_\phi/(L/(8\pi\eta R^2))$, and the results are presented on a decimal logarithmic scale.

Physics of Fluids ARTICLE scitation.org/journal/phf

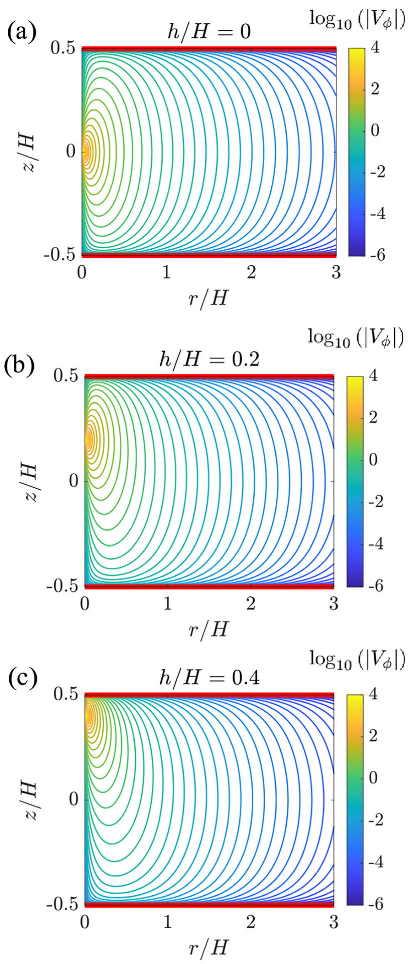

FIG. 7. Contour plots of the amplitude of the scaled azimuthal velocity induced by a rotlet singularity acting between two infinitely extended no-slip walls. Again, the scaled azimuthal velocity is defined as $V_\phi = v_\phi/(L/(8\pi\eta R^2))$.

$$\chi_\pm(t) = \operatorname{Im}\left\{ \left(\frac{1}{2} \pm h - it \right)^{-2} \right\}. \tag{59}$$

Again, an approximate evaluation of the definite integral given by Eq. (58) can be performed by numerical discretization via the standard middle Riemann sum.

In the limit of an infinitely extended channel $R \to \infty$, we obtain

$$k_2 = \frac{1}{2}\int_0^\infty \lambda^2 \operatorname{csch}(\lambda)\left(\cosh(2\lambda h) - e^{-\lambda}\right) \mathrm{d}\lambda. \tag{60}$$

Using computer algebra systems such as Mathematica,[92] the latter can further be expressed as

$$k_2 = \frac{1}{8}\left(\zeta\left(3, \frac{1}{2} + h\right) + \zeta\left(3, \frac{1}{2} - h\right) - 2\zeta(3) \right), \tag{61}$$

wherein

$$\zeta(s,t) = \sum_{n>m\geq 1} n^{-s} m^{-t}, \tag{62}$$

denotes the double zeta functions with $s > 1$ and $t \geq 0$. Moreover, $\zeta(s)$ is the Riemann zeta function with $s > 1$ defined as $\zeta(s) = \sum_{n\geq 1} n^{-s}$. In particular, $\zeta(3)$ is an irrational number known as Apéry's constant.[93] We quote the famous identity derived by Euler $\zeta(3) = \zeta(2,1)$. In the mid-plane of the channel, the correction factor reaches its minimum value $k_2(h=0) = \frac{3}{2}\zeta(3) \approx 1.8031$. Performing a Taylor expansion near the upper wall around $h = 1/2$, we obtain

$$k_2 = \frac{1}{8}\epsilon^{-3} + \frac{3}{2}\zeta(5)\epsilon^2 + \mathcal{O}(\epsilon^4), \tag{63}$$

where $\epsilon = \frac{1}{2} - h$.

In Fig. 8, we present on a log–log scale the variation of the scaled correction factor to the rotational hydrodynamic mobility given by Eq. (58) vs the scaled radius of the coaxially positioned rigid disks for various values of the singularity position within the gap between the two disks. The correction factor increases monotonically upon increasing the size of the disks because the rotational motion of the confined particle becomes more restricted. In the limit of infinitely large disks, the correction factor asymptotically tends to the value given by Eq. (61).

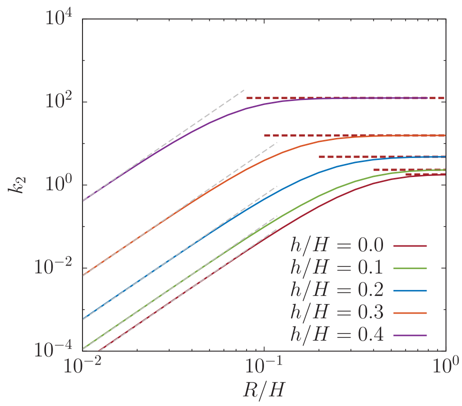

FIG. 8. Scaled correction factor stated by Eq. (61) vs R/H for various singularity positions along the axis of two coaxially positioned rigid no-slip disks. Horizontal dashed lines correspond to the scaled correction factors inside an infinitely extended channel. The lines shown in gray displays the scaling law $k_2 \sim (R/H)^3$ in the range of small values of $R \ll H$ (cf. Appendix C for the derivation of this scaling relation).

Published under an exclusive license by AIP Publishing

Physics of Fluids ARTICLE scitation.org/journal/phf

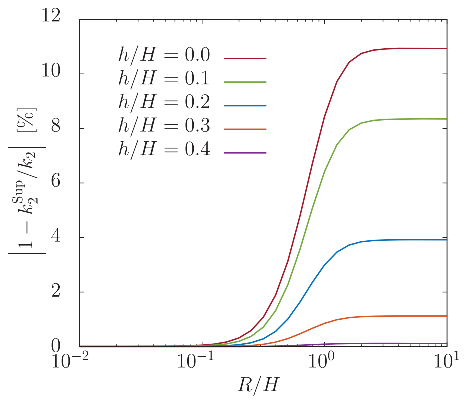

FIG. 9. Percentage relative error of the scaled correction factor of the rotational hydrodynamic mobility between two coaxially positioned rigid no-slip disks as obtained using the simplistic superposition approximation stated by Eq. (64) in comparison with the exact formula given by Eq. (58).

1. Superposition approximation

In the presence of two sufficiently separated confining boundaries, the correction to the hydrodynamic mobility can sometimes be approximated by superimposing the individual contributions arising from each boundary.[94–100] This superposition approximation has originally been introduced by Oseen[101] to estimate the translational hydrodynamic mobility in a channel bounded by two plates. In this approach, the scaled correction factor can be approximated by

$$k_2^{\mathrm{Sup}} = R^{-3}\left(\xi_-^{-3}k_1(\xi_-) + \xi_+^{-3}k_1(\xi_+)\right), \tag{64}$$

wherein $\xi_\pm = \left(\frac{1}{2} \pm h\right)/R$ with k_1 representing the scaled correction factor near a single disk given by Eq. (39). In particular, near the upper wall, a Taylor expansion around $h = 1/2$ leads to

$$k_2^{\mathrm{Sup}} = \frac{1}{8}\,\epsilon^{-3} + k_1(R^{-1}) + \mathcal{O}(\epsilon). \tag{65}$$

Figure 9 displays the evolution of the percentage relative error committed by using Oseen's superposition approximation. We observe that the error increases monotonically with the system size and reaches its maximum value in the limit $R \to \infty$. In particular, the error attains its extreme value in the mid-plane of the channel for $h = 0$, where the MPRE amounts to about 11%. The latter value is remarkably lower than the one previously obtained for axisymmetric translational motion along the axis of two coaxially positioned rigid no-slip disks[81] for which the MPRE was found to be as high as 55% in the mid-plane. Consequently, the superposition approximation can be employed to estimate the rotational mobility between two confining disks without significantly compromising the accuracy of the prediction.

IV. CONCLUSIONS

To summarize, we have presented an analytical and semi-analytical theory to quantify the low-Reynolds-number flow induced by a point-torque singularity acting near a single disk or between two coaxially positioned rigid disks, respectively, satisfying no-slip boundary conditions on the surfaces of the disks. The rotlet is assumed to be located on the axis of symmetry of the disks with the torque directed along that axis. We have formulated the solution of the hydrodynamic equations as mixed-boundary-value problems, which we subsequently reduced into systems of dual integral equations with Bessel-function kernels. On the one hand, we have demonstrated that, near a single disk, the resulting integral equation can appropriately be transformed into a classical Abel integral equation that admits a unique solution. On the other hand, we have shown that, between two coaxially positioned disks, a system of two Fredholm integral equations of the first kind arises. For its solution, we have approximated the integral by standard middle Riemann sums reducing the dual integral equations into a linear system of equations amenable to immediate inversion using standard numerical approaches.

Moreover, we have made use of the derived solution of the flow problems to probe the effect of confinement on the rotational hydrodynamic mobility of a small colloidal particle through which the torque is exerted on the fluid. More importantly, we have assessed the accuracy and reliability of Oseen's superposition approximation, which is commonly employed to predict the rotational mobility in confined geometries. We have found that the maximum percentage relative error of Oseen's approximation is only about 11% in the mid-plane of the channel, suggesting that this simplistic approximation could generally be employed to estimate the rotational mobility between two finite-sized disks.

The systems addressed in the present study may find useful applications in various biologically and technologically relevant processes. On the one hand, the solution of the flow problem for a rotlet singularity acting near a finite-sized disk may be employed in the context of micromixing, as a small-scale analog to a magnetic stir bar mixer driven by an external rotating magnetic field. On the other hand, the solution inside a gap bounded by two coaxially positioned disks may prove to be useful, for instance, in the modeling of ionic transport in small-scale capacitors.

The present results may be extended to further explore the rotational motion of a spherical particle of finite size, with a radius comparable to the radii of the confining disks. For that purpose, the solution of the flow problem could, in principle, be formulated in bipolar coordinates. Another possible extension of the present work could be to address the general problem of rotational motion near one or two no-slip disks for arbitrary positioning of the singularity and arbitrary orientation of the torque. These steps could be the subject of possible future investigations.

ACKNOWLEDGMENTS

A.D.M.I. and H.L. gratefully acknowledge support from the DFG (Deutsche Forschungsgemeinschaft) through the projects DA 2107/1-1 and LO 418/23-1. A.M.M. thanks the DFG for support through the Heisenberg Grant No. ME 3571/4-1.

APPENDIX A: SOLUTION OF THE INTEGRAL EQUATION (20)

In this Appendix, we show that the solution of the resulting integral equation (20) can be cast in the form of solution of a

Published under an exclusive license by AIP Publishing

classical Abel integral equation. The general form of an Abel integral equation can be presented as[102]

$$\int_0^x \frac{\phi(s)}{(x-s)^{\frac{1}{2}}}\,\mathrm{d}s = g(x), \tag{A1}$$

the solution of which is given by

$$\phi(x) = \frac{1}{\pi}\frac{\mathrm{d}}{\mathrm{d}x}\int_0^x \frac{g(u)}{(x-u)^{\frac{1}{2}}}\,\mathrm{d}u. \tag{A2}$$

Using the changes of variables $s = t^2$ and $x = r^2$, Eq. (20) can be written as

$$\int_0^x \frac{s^{-\frac{1}{4}}\hat{\omega}(s^{\frac{1}{2}})}{(x-s)^{\frac{1}{2}}}\,\mathrm{d}s = (2\pi)^{\frac{1}{2}}x^{\frac{1}{2}}f(x^{\frac{1}{2}}). \tag{A3}$$

By identification with Eq. (A1), we get $\phi(s) = s^{-\frac{1}{4}}\hat{\omega}(s^{\frac{1}{2}})$ and $g(x) = (2\pi)^{\frac{1}{2}}x^{\frac{1}{2}}f(x^{\frac{1}{2}})$. Using the solution form given by Eq. (A2), we then obtain

$$x^{-\frac{1}{4}}\hat{\omega}(x^{\frac{1}{2}}) = \left(\frac{2}{\pi}\right)^{\frac{1}{2}}\frac{\mathrm{d}}{\mathrm{d}x}\int_0^x \frac{u^{\frac{1}{2}}f(u^{\frac{1}{2}})}{(x-u)^{\frac{1}{2}}}\,\mathrm{d}u. \tag{A4}$$

Next, applying the change of variable $r = x^{\frac{1}{2}}$, the latter equation can readily be expressed as

$$\hat{\omega}(r) = \frac{1}{2}\left(\frac{2}{\pi r}\right)^{\frac{1}{2}}\frac{\mathrm{d}}{\mathrm{d}r}\int_0^{r^2} \frac{u^{\frac{1}{2}}f(u^{\frac{1}{2}})}{(r^2-u)^{\frac{1}{2}}}\,\mathrm{d}u. \tag{A5}$$

Finally, the change of variable $v = u^{\frac{1}{2}}$ yields

$$\hat{\omega}(r) = \left(\frac{2}{\pi r}\right)^{\frac{1}{2}}\frac{\mathrm{d}}{\mathrm{d}r}\int_0^r \frac{v^2 f(v)}{(r^2-v^2)^{\frac{1}{2}}}\,\mathrm{d}v, \tag{A6}$$

which exactly corresponds to Eq. (21) rewriting $r = t$.

APPENDIX B: COMPARISON WITH NUMERICAL CALCULATIONS USING THE FINITE-ELEMENT METHOD

To confirm our analytical solutions, we perform numerical simulations using the finite-element method. Formulated in cylindrical coordinates, $\boldsymbol{v} = (v_r, v_\theta, v_z)$, we can take advantage of the fact that the solution is constant in angular direction, $\partial_\theta \boldsymbol{v} = \boldsymbol{0}$. This reduces the problem to a two-dimensional equation formulated in the r/z-plane for the angular component v_θ only. Since there is also no coupling to the pressure field, the problem reduces to a scalar one. In the following, we illustrate our approach for the two-disk geometry and denote by

$$\begin{aligned}\Omega = {} & ((0, R_{max}) \times (-Z_{max}, Z_{max}))\backslash \\ & ((0,R)\times\{H/2\}\cup(0,R)\times\{-H/2\}),\end{aligned} \tag{B1}$$

the numerical domain, artificially restricted to $0 < r < R_{max}$ and $-Z_{max} < z < Z_{max}$. To limit the impact of the artificial outer boundaries, we set $R_{max} = Z_{max} = 6.625$. We could not identify a significant effect by further extending these limits.

The variational formulation of the problem is then given by[103]

$$\int_\Omega \eta r\left(\frac{\partial v_\theta}{\partial r}\frac{\partial\phi}{\partial r} + \frac{\partial v_\theta}{\partial z}\frac{\partial\phi}{\partial z} + \frac{1}{r}v_\theta\phi\right)\mathrm{d}r\,\mathrm{d}z = F(\phi), \tag{B2}$$

$\forall\phi \in H_0^1(\Omega; D)$, where we denote by $H_0^1(\Omega; D)$ the space of square integrable functions with weak derivatives that are zero on the two disks $D = (0,R)\times\{-H/2\}\cup(0,R)\times\{H/2\}$. On the right-hand side of Eq. (B2), the problem is driven by a Dirac form as

$$F(\phi) = \phi(\boldsymbol{r}_h), \tag{B3}$$

centered in a point close to the z-axis $\boldsymbol{r}_h = (r_0, z_h)$, $z_h = 1/128$.

The equation is discretized with quadratic finite-elements using piecewise quadratic elements on a quadrilateral mesh[104] featuring about 1 750 000 unknowns. All computations are performed in the finite-element software library Gascoigne 3D.[105]

APPENDIX C: MOBILITY BETWEEN TWO DISKS IN THE LIMIT $R \ll 1$

In the range of small values of $R \ll 1$, we attempt to find an approximate expression of the scaled correction factor. For $t \ll 1$, it follows from Eqs. (19) and (51) that $\mathcal{K}_-(t) \sim t^{\frac{1}{2}}$ and $\mathcal{S}(t) \sim t^{-\frac{1}{2}}$, respectively. Therefore, to ensure the convergence of the system of integral equations (50) at the lower limit $t = 0$, we require that the unknown functions $\hat{f}_1(t)$ and $\hat{f}_2(t)$ scale (at least) as $t^{\frac{1}{2}}$ as $t \to 0$.

We now use the ansatz $\hat{f}_1(t) = \alpha_1 t^{\frac{1}{2}}$ and $\hat{f}_2(t) = \alpha_2 t^{\frac{1}{2}}$, where α_1 and α_2 are two real numbers to be subsequently determined. Inserting these expressions into Eq. (50) evaluated at $r = \beta R$, with $\beta \in (0,1)$, performing analytically the integration, expanding the resulting expressions into Taylor series of R, and solving for α_1 and α_2 yield

$$\alpha_1 = -\left(\frac{\pi}{2}\right)^{\frac{1}{2}}\frac{\beta R}{\left(\frac{1}{2}+h\right)^3}, \quad \alpha_2 = \left(\frac{\pi}{2}\right)^{\frac{1}{2}}\frac{\beta R}{\left(\frac{1}{2}-h\right)^3}. \tag{C1}$$

Next, by substituting the above expressions of $\hat{f}_1(t)$ and $\hat{f}_2(t)$ into Eq. (58), evaluating the integral analytically and performing a series expansion about $R = 0$, we obtain

$$k_2 \simeq \frac{R^2}{2}\left(\frac{2}{\pi}\right)^{\frac{1}{2}}\left(\frac{\alpha_2}{\left(\frac{1}{2}-h\right)^3} - \frac{\alpha_1}{\left(\frac{1}{2}+h\right)^3}\right). \tag{C2}$$

Finally, by inserting the expressions of α_1 and α_2 stated by Eq. (C1) into Eq. (C2), the correction factor in the range $R \ll 1$ can be obtained as

$$k_2 \simeq \frac{\beta R^3}{2}\left(\left(\frac{1}{2}-h\right)^{-6} + \left(\frac{1}{2}+h\right)^{-6}\right). \tag{C3}$$

By setting $\beta = 5/6$, the latter approximate expression is found to be in good agreement with the numerical results.

DATA AVAILABILITY

The data that support the findings of this study are available from the corresponding author upon reasonable request.

Published under an exclusive license by AIP Publishing

Physics of Fluids ARTICLE scitation.org/journal/phf

REFERENCES

[1] Y. Zhou, K.-W. Hsiao, K. E. Regan, D. Kong, G. B. McKenna, R. M. Robertson-Anderson, and C. M. Schroeder, "Effect of molecular architecture on ring polymer dynamics in semidilute linear polymer solutions," Nat. Commun. **10**, 1753 (2019).

[2] M. Müller, C. Pastorino, and J. Servantie, "Hydrodynamic boundary condition of polymer melts at simple and complex surfaces," Comput. Phys. Commun. **180**, 600–604 (2009).

[3] J. H. Piette, C. Saengow, and A. J. Giacomin, "Hydrodynamic interaction for rigid dumbbell suspensions in steady shear flow," Phys. Fluids **31**, 053103 (2019).

[4] M. A. Kanso, L. Jbara, A. J. Giacomin, C. Saengow, and P. H. Gilbert, "Order in polymeric liquids under oscillatory shear flow," Phys. Fluids **31**, 033103 (2019).

[5] A. J. Storm, C. Storm, J. Chen, H. Zandbergen, J.-F. Joanny, and C. Dekker, "Fast DNA translocation through a solid-state nanopore," Nano Lett. **5**, 1193–1197 (2005).

[6] A. Izmitli, D. C. Schwartz, M. D. Graham, and J. J. de Pablo, "The effect of hydrodynamic interactions on the dynamics of DNA translocation through pores," J. Chem. Phys. **128**, 085102 (2008).

[7] T. Secomb, R. Skalak, N. Özkaya, and J. Gross, "Flow of axisymmetric red blood cells in narrow capillaries," J. Fluid Mech. **163**, 405–423 (1986).

[8] C. Pozrikidis, "Axisymmetric motion of a file of red blood cells through capillaries," Phys. Fluids **17**, 031503 (2005).

[9] J. L. McWhirter, H. Noguchi, and G. Gompper, "Flow-induced clustering and alignment of vesicles and red blood cells in microcapillaries," Proc. Natl. Acad. Sci. U. S. A. **106**, 6039 (2009).

[10] J. B. Freund, "Numerical simulation of flowing blood cells," Annu. Rev. Fluid Mech. **46**, 67–95 (2014).

[11] T. W. Secomb, "Blood flow in the microcirculation," Annu. Rev. Fluid Mech. **49**, 443–461 (2017).

[12] D. Barthès-Biesel, "Motion and deformation of elastic capsules and vesicles in flow," Annu. Rev. Fluid Mech. **48**, 25–52 (2016).

[13] A. Furukawa and H. Tanaka, "Key role of hydrodynamic interactions in colloidal gelation," Phys. Rev. Lett. **104**, 245702 (2010).

[14] R. Rusconi, S. Lecuyer, L. Guglielmini, and H. A. Stone, "Laminar flow around corners triggers the formation of biofilm streamers," J. R. Soc. Interface **7**, 1293–1299 (2010).

[15] R. Rusconi, S. Lecuyer, N. Autrusson, L. Guglielmini, and H. A. Stone, "Secondary flow as a mechanism for the formation of biofilm streamers," Biophys. J. **100**, 1392–1399 (2011).

[16] K. Drescher, Y. Shen, B. L. Bassler, and H. A. Stone, "Biofilm streamers cause catastrophic disruption of flow with consequences for environmental and medical systems," Proc. Natl. Acad. Sci. U.S.A. **110**, 4345–4350 (2013).

[17] M. K. Kim, K. Drescher, O. S. Pak, B. L. Bassler, and H. A. Stone, "Filaments in curved streamlines: Rapid formation of staphylococcus aureus biofilm streamers," New J. Phys. **16**, 065024 (2014).

[18] A. P. Berke, L. Turner, H. C. Berg, and E. Lauga, "Hydrodynamic attraction of swimming microorganisms by surfaces," Phys. Rev. Lett. **101**, 038102 (2008).

[19] S. Yazdi and A. Borhan, "Effect of a planar interface on time-averaged locomotion of a spherical squirmer in a viscoelastic fluid," Phys. Fluids **29**, 093104 (2017).

[20] S. Bianchi, F. Saglimbeni, and R. D. Leonardo, "Holographic imaging reveals the mechanism of wall entrapment in swimming bacteria," Phys. Rev. X **7**, 011010 (2017).

[21] S. Y. Reigh, L. Zhu, F. Gallaire, and E. Lauga, "Swimming with a cage: Low-Reynolds-number locomotion inside a droplet," Soft Matter **13**, 3161–3173 (2017).

[22] A. Daddi-Moussa-Ider, M. Lisicki, C. Hoell, and H. Löwen, "Swimming trajectories of a three-sphere microswimmer near a wall," J. Chem. Phys. **148**, 134904 (2018).

[23] A. Dhar, P. S. Burada, and G. P. R. Sekhar, "Hydrodynamics of active particles confined in a periodically tapered channel," Phys. Fluids **32**, 102005 (2020).

[24] S. Kim and S. J. Karrila, *Microhydrodynamics: Principles and Selected Applications* (Courier Corporation, New York, 2013).

[25] H. Diamant, "Hydrodynamic interaction in confined geometries," J. Phys. Soc. Jpn. **78**, 041002 (2009).

[26] G. D. M. MacKay and S. G. Mason, "Approach of a solid sphere to a rigid plane interface," J. Colloid Sci. **16**, 632–635 (1961).

[27] T. Gotoh and Y. Kaneda, "Effect of an infinite plane wall on the motion of a spherical Brownian particle," J. Chem. Phys. **76**, 3193–3197 (1982).

[28] B. Cichocki and R. B. Jones, "Image representation of a spherical particle near a hard wall," Physica A **258**, 273–302 (1998).

[29] E. Lauga and T. M. Squires, "Brownian motion near a partial-slip boundary: A local probe of the no-slip condition," Phys. Fluids **17**, 103102 (2005).

[30] J. W. Swan and J. F. Brady, "Simulation of hydrodynamically interacting particles near a no-slip boundary," Phys. Fluids **19**, 113306 (2007).

[31] T. Franosch and S. Jeney, "Persistent correlation of constrained colloidal motion," Phys. Rev. E **79**, 031402 (2009).

[32] B. U. Felderhof, "Hydrodynamic force on a particle oscillating in a viscous fluid near a wall with dynamic partial-slip boundary condition," Phys. Rev. E **85**, 046303 (2012).

[33] M. De Corato, F. Greco, G. Davino, and P. L. Maffettone, "Hydrodynamics and Brownian motions of a spheroid near a rigid wall," J. Chem. Phys. **142**, 194901 (2015).

[34] K. Huang and I. Szlufarska, "Effect of interfaces on the nearby Brownian motion," Nat. Commun. **6**, 8558 (2015).

[35] B. Rallabandi, S. Hilgenfeldt, and H. A. Stone, "Hydrodynamic force on a sphere normal to an obstacle due to a non-uniform flow," J. Fluid Mech. **818**, 407–434 (2017).

[36] S. H. Lee, R. S. Chadwick, and L. G. Leal, "Motion of a sphere in the presence of a plane interface. Part 1. An approximate solution by generalization of the method of Lorentz," J. Fluid Mech. **93**, 705–726 (1979).

[37] C. Berdan II and L. G. Leal, "Motion of a sphere in the presence of a deformable interface: I. Perturbation of the interface from flat: The effects on drag and torque," J. Colloid Interface Sci. **87**, 62–80 (1982).

[38] J. Bławzdziewicz, M. L. Ekiel-Jeżewska, and E. Wajnryb, "Hydrodynamic coupling of spherical particles to a planar fluid-fluid interface: Theoretical analysis," J. Chem. Phys. **133**, 114703 (2010).

[39] J. Bławzdziewicz, M. L. Ekiel-Jeżewska, and E. Wajnryb, "Motion of a spherical particle near a planar fluid-fluid interface: The effect of surface incompressibility," J. Chem. Phys. **133**, 114702 (2010).

[40] J. Bławzdziewicz, V. Cristini, and M. Loewenberg, "Stokes flow in the presence of a planar interface covered with incompressible surfactant," Phys. Fluids **11**, 251–258 (1999).

[41] J. Blawzdziewicz, E. Wajnryb, and M. Loewenberg, "Hydrodynamic interactions and collision efficiencies of spherical drops covered with an incompressible surfactant film," J. Fluid Mech. **395**, 29–59 (1999).

[42] C. Kurzthaler, L. Zhu, A. A. Pahlavan, and H. A. Stone, "Particle motion nearby rough surfaces," Phys. Rev. Fluids **5**, 082101 (2020).

[43] B. U. Felderhof, "Effect of surface tension and surface elasticity of a fluid-fluid interface on the motion of a particle immersed near the interface," J. Chem. Phys. **125**, 144718 (2006).

[44] T. Bickel, "Brownian motion near a liquid-like membrane," Eur. Phys. J. E **20**, 379–385 (2006).

[45] T. Bickel, "Hindered mobility of a particle near a soft interface," Phys. Rev. E **75**, 041403 (2007).

[46] T. Boatwright, M. Dennin, R. Shlomovitz, A. A. Evans, and A. J. Levine, "Probing interfacial dynamics and mechanics using submerged particle microrheology. II. Experiment," Phys. Fluids **26**, 071904 (2014).

[47] A. Daddi-Moussa-Ider, A. Guckenberger, and S. Gekle, "Long-lived anomalous thermal diffusion induced by elastic cell membranes on nearby particles," Phys. Rev. E **93**, 012612 (2016).

[48] A. Daddi-Moussa-Ider and S. Gekle, "Hydrodynamic interaction between particles near elastic interfaces," J. Chem. Phys. **145**, 014905 (2016).

[49] F. Jünger, F. Kohler, A. Meinel, T. Meyer, R. Nitschke, B. Erhard, and A. Rohrbach, "Measuring local viscosities near plasma membranes of living cells with photonic force microscopy," Biophys. J. **109**, 869–882 (2015).

[50] T. Salez and L. Mahadevan, "Elastohydrodynamics of a sliding, spinning and sedimenting cylinder near a soft wall," J. Fluid Mech. **779**, 181–196 (2015).

[51] A. Daddi-Moussa-Ider, M. Lisicki, and S. Gekle, "Mobility of an axisymmetric particle near an elastic interface," J. Fluid Mech. **811**, 210–233 (2017).

Published under an exclusive license by AIP Publishing

Physics of Fluids ARTICLE scitation.org/journal/phf

[52]A. Daddi-Moussa-Ider, M. Lisicki, and S. Gekle, "Hydrodynamic mobility of a sphere moving on the centerline of an elastic tube," Phys. Fluids **29**, 111901 (2017).

[53]A. Daddi-Moussa-Ider and S. Gekle, "Brownian motion near an elastic cell membrane: A theoretical study," Eur. Phys. J. E **41**, 19 (2018).

[54]B. Rallabandi, N. Oppenheimer, M. Y. B. Zion, and H. A. Stone, "Membrane-induced hydroelastic migration of a particle surfing its own wave," Nat. Phys. **14**, 1211–1215 (2018).

[55]A. Daddi-Moussa-Ider, B. Rallabandi, S. Gekle, and H. A. Stone, "Reciprocal theorem for the prediction of the normal force induced on a particle translating parallel to an elastic membrane," Phys. Rev. Fluids **3**, 084101 (2018).

[56]A. Daddi-Moussa-Ider, M. Lisicki, S. Gekle, A. M. Menzel, and H. Löwen, "Hydrodynamic coupling and rotational mobilities nearby planar elastic membranes," J. Chem. Phys. **149**, 014901 (2018).

[57]C. Hoell, H. Löwen, A. M. Menzel, and A. Daddi-Moussa-Ider, "Creeping motion of a solid particle inside a spherical elastic cavity: II. Asymmetric motion," Eur. Phys. J. E **42**, 89 (2019).

[58]L. Lobry and N. Ostrowsky, "Diffusion of Brownian particles trapped between two walls: Theory and dynamic-light-scattering measurements," Phys. Rev. B **53**, 12050–12056 (1996).

[59]M. D. Graham, "Fluid dynamics of dissolved polymer molecules in confined geometries," Annu. Rev. Fluid Mech. **43**, 273–298 (2011).

[60]L. P. Faucheux and A. J. Libchaber, "Confined Brownian motion," Phys. Rev. E **49**, 5158–5163 (1994).

[61]B. Lin, J. Yu, and S. A. Rice, "Direct measurements of constrained Brownian motion of an isolated sphere between two walls," Phys. Rev. E **62**, 3909–3919 (2000).

[62]B. Tränkle, D. Ruh, and A. Rohrbach, "Interaction dynamics of two diffusing particles: Contact times and influence of nearby surfaces," Soft Matter **12**, 2729–2736 (2016).

[63]H. Faxén, "Einwirkung der Gefässwände auf den Widerstand gegen die Bewegung einer kleinen Kugel in einer zähen Flüssigkeit," Ph.D. thesis (Uppsala University, Uppsala, Sweden, 1921).

[64]N. Liron and S. Mochon, "Stokes flow for a stokeslet between two parallel flat plates," J. Eng. Math. **10**, 287–303 (1976).

[65]S. Bhattacharya and J. Blawzdziewicz, "Image system for Stokes-flow singularity between two parallel planar walls," J. Math. Phys. **43**, 5720–5731 (2002).

[66]J. W. Swan and J. F. Brady, "Particle motion between parallel walls: Hydrodynamics and simulation," Phys. Fluids **22**, 103301 (2010).

[67]P. Ganatos, S. Weinbaum, and R. Pfeffer, "A strong interaction theory for the creeping motion of a sphere between plane parallel boundaries. Part 1. Perpendicular motion," J. Fluid Mech. **99**, 739–753 (1980).

[68]P. Ganatos, R. Pfeffer, and S. Weinbaum, "A strong interaction theory for the creeping motion of a sphere between plane parallel boundaries. Part 2. Parallel motion," J. Fluid Mech. **99**, 755–783 (1980).

[69]J. Happel and H. Brenner, *Low Reynolds Number Hydrodynamics: With Special Applications to Particulate Media* (Springer/Martinus Nijhoff Publishers, The Hague, 2012).

[70]J. R. Blake, "A note on the image system for a stokeslet in a no-slip boundary," Math. Proc. Cambridge Philos. Soc. **70**, 303–310 (1971).

[71]R. Shail and B. A. Packham, "Some asymmetric Stokes-flow problems," J. Eng. Math. **21**, 331 (1987).

[72]M. Abramowitz and I. A. Stegun, *Handbook of Mathematical Functions* (Dover, New York, 1972), Vol. 5.

[73]C. J. Tranter, *Integral Transforms in Mathematical Physics* (Wiley, New York, 1951).

[74]E. C. Titchmarsh, *Introduction to the Theory of Fourier Integrals* (Clarendon Press, Oxford, 1948).

[75]I. N. Sneddon, "The elementary solution of dual integral equations," Glasgow Math. J. **4**, 108–110 (1960).

[76]E. T. Copson, "On certain dual integral equations," Glasgow Math. J. **5**, 21–24 (1961).

[77]A. Daddi-Moussa-Ider, B. Kaoui, and H. Löwen, "Axisymmetric flow due to a stokeslet near a finite-sized elastic membrane," J. Phys. Soc. Jpn. **88**, 054401 (2019).

[78]A. Daddi-Moussa-Ider, "Asymmetric Stokes flow induced by a transverse point force acting near a finite-sized elastic membrane," J. Phys. Soc. Jpn. **89**, 124401 (2020).

[79]A. Daddi-Moussa-Ider, M. Lisicki, H. Löwen, and A. M. Menzel, "Dynamics of a microswimmer–microplatelet composite," Phys. Fluids **32**, 021902 (2020).

[80]M. U. Kim, "Axisymmetric Stokes flow due to a point force near a circular disk," J. Phys. Soc. Jpn. **52**, 449–455 (1983).

[81]A. Daddi-Moussa-Ider, A. R. Sprenger, Y. Amarouchene, T. Salez, C. Schönecker, T. Richter, H. Löwen, and A. M. Menzel, "Axisymmetric Stokes flow due to a point-force singularity acting between two coaxially positioned rigid no-slip disks," J. Fluid Mech. **904**, A34 (2020).

[82]T. Carleman, "Zur Theorie der linearen Integralgleichungen," Math. Z. **9**, 196–217 (1921).

[83]F. Smithies, *Integral Equations* (Cambridge University Press, Cambridge, UK, 1958), Vol. 172.

[84]R. S. Anderssen, F. R. De Hoog, and M. A. Lukas, *The Application and Numerical Solution of Integral Equations* (Kluwer Academic Publishers, Dordrecht, The Netherlands, 1980), Vol. 6.

[85]E. T. Whittaker and G. N. Watson, *A Course of Modern Analysis* (Cambridge University Press, Cambridge, UK, 1996).

[86]T. Carleman, "Über die Abelsche Integralgleichung mit konstanten Integrationsgrenzen," Math. Z. **15**, 111–120 (1922).

[87]J. D. Tamarkin, "On integrable solutions of Abel's integral equation," Ann. Math. **31**, 219–229 (1930).

[88]L. V. Ahlfors, *Complex Analysis: An Introduction to the Theory of Analytic Functions of One Complex Variable* (McGraw-Hill, New York, 1966), Vol. 2.

[89]D. V. Widder, *Laplace Transform (PMS-6)* (Princeton University Press, New Jersey, 2015).

[90]R. Piessens, *The Hankel Transform* (CRC Press Second, Boca Raton, Florida, 2000), Vol. 2.

[91]F. G. Tricomi, *Integral Equations* (Courier Corporation, Mineola, New York, 1985), Vol. 5.

[92]S. Wolfram, *Mathematica: A System for Doing Mathematics by Computer* (Addison Wesley Longman Publishing Co., Inc., Boston, 1991).

[93]A. Van der Poorten and R. Apéry, "A proof that Euler missed… Apéry proof of the irrationality of $\zeta(3)$," Math. Intell. **1**, 195–203 (1979).

[94]E. R. Dufresne, D. Altman, and D. G. Grier, "Brownian dynamics of a sphere between parallel walls," Europhys. Lett. **53**, 264 (2001).

[95]T. Benesch, S. Yiacoumi, and C. Tsouris, "Brownian motion in confinement," Phys. Rev. E **68**, 021401 (2003).

[96]M. Polin, D. G. Grier, and S. R. Quake, "Anomalous vibrational dispersion in holographically trapped colloidal arrays," Phys. Rev. Lett. **96**, 088101 (2006).

[97]A. Daddi-Moussa-Ider, A. Guckenberger, and S. Gekle, "Particle mobility between two planar elastic membranes: Brownian motion and membrane deformation," Phys. Fluids **28**, 071903 (2016).

[98]A. J. T. M. Mathijssen, A. Doostmohammadi, J. M. Yeomans, and T. N. Shendruk, "Hydrodynamics of micro-swimmers in films," J. Fluid Mech. **806**, 35–70 (2016).

[99]A. Daddi-Moussa-Ider, M. Lisicki, A. J. T. M. Mathijssen, C. Hoell, S. Goh, J. Bławzdziewicz, A. M. Menzel, and H. Löwen, "State diagram of a three-sphere microswimmer in a channel," J. Phys.: Condes. Matter **30**, 254004 (2018).

[100]A. Daddi-Moussa-Ider, H. Löwen, and B. Liebchen, "Hydrodynamics can determine the optimal route for microswimmer navigation," Commun. Phys. **4**, 15 (2021).

[101]C. W. Oseen, *Neuere Methoden und Ergebnisse in der Hydrodynamik* (Akademische Verlagsgesellschaft mbH, Leipzig, Germany, 1927).

[102]H. Hochstadt, *Integral Equations* (John Wiley & Sons, Inc., Canada, 2011), Vol. 91.

[103]H. von Wahl, T. Richter, S. Frei, and T. Hagemeier, "Falling balls in a viscous fluid with contact: Comparing numerical simulations with experimental data," Phys. Fluids **33**, 033304 (2021).

[104]T. Richter, *Fluid-Structure Interactions. Models, Analysis and Finite Elements*, Lecture Notes in Computational Science and Engineering Vol. 118 (Springer, 2017).

[105]See R. Becker, M. Braack, D. Meidner, T. Richter, and B. Vexler, www.gascoigne.de for "The finite element toolkit Gascoigne3D" (2020).

Published under an exclusive license by AIP Publishing

Chapter 4

Conclusion

This dissertation explored a wide range of problems in active matter physics. Ranging from effects of memory – be it caused by its particle inertia or by the viscoelastic response of the dispersion medium in the case of non-Newtonian fluids – to complex orientation-dependent propulsion strategies. Using among others the theory of active Brownian motion, we characterized the stochastic dynamics of self-propelled particles in terms of averaged quantities and dynamic correlation functions. It is crucial to understand how the physical properties of the particle and its environment affect its individual dynamics before examining more complex collective behavior. In the following, we provide concise summaries of the findings from each contribution constituting this dissertation:

First, in **P1**, we introduced a new method to impose complex anisotropic motility behavior on ABPs: Using a feedback scheme, we programmed the propulsion velocity of magnetic dumbells as a function of the particles' orientation. Accompanying, we developed a theoretical framework that explains the dynamic features of the particles entirely by deriving an analytic expression for the n-th translational moment for arbitrary orientation-dependent motility. We studied the motion on short, intermediate, and long time scales and found fair agreement between our theoretical predictions and experimental data.

Next, in **P2**, we studied a self-propelled colloid in a viscoelastic medium using generalized Langevin equations. In the model, the temporal properties of the dispersion medium are incorporated in memory kernels for translation and rotation. For arbitrary memory, we presented analytical solutions for several dynamic correlations and evaluated them explicitly in the prominent case of a Maxwell fluid. This model provides a simple framework to interpret particle trajectories in complex environments and starting point for further research adding external potential, inertia, and many-particle interactions.

The motion of self-propelled colloids in viscoelastic media shares considerable similarities with mesoscopic active particles subject to inertial effects. From increased orientational correlation (i.e., higher persistence) to delay between self-propulsion or velocity and the particles' orientation. In **P3**, we studied the behavior of mesoscopic active particles, both small enough to experience fluctuations and large enough to display inertial effects. In particular, we accounted for the case of time-dependent inertia and discussed various specific setups - including a Langevin-rocket model. The optimal strategy of a Langevin-rocket for achieving maximal reach undergoes a discontinuous change from a complete, extended mass ejection over time to an instantaneous ejection of a mass fraction as rotational noise increases. Experiments on macroscopic robots, living particles, or self-propelled mesoscopic objects in low-viscosity media, such as complex plasma, can be used to test our results.

Subsequently, in **P4**, we investigated a macroscopic system comprising self-propelled vibrated granular particles on a striated substrate that exhibits orientation-dependent motility. From the theoretical side, we combined aspects from **P1** and **P3**: proposing an extension of the active Brownian motion model that incorporates inertial effects and orientation-dependent motility. The persistence length, time, and long-time diffusion are important control-parameter for collective phenomena and can be predicted by our model. Thus, our model can be used to optimize driving parameters for navigation in anisotropic environments and provides a baseline for future research on swarms of self-propelled particles.

Both the experimental investigation in **P1** and **P4** relied on the measurement of physical properties like the self-propulsion velocity or the rotational diffusion coefficient. In **P5**, we compared different fitting methods to extract those parameters by using the theoretical expression for the mean-squared displacement (MSD) of an ABP. We address heteroscedasticity and the effect of hidden correlations when using overlapping displacements. We recommend using bootstrapping to construct confidence intervals and avoiding the truncated form of the MSD equation. Generally, we found that log transforming the data before fitting works better than other methods and is easy to use. However, our results only apply to ideal, non-interacting ABP models and do not account for factors such as torque, anisotropic shape, or experimental errors, which should be considered with care in experimental design and data analysis.

In the next two contributions, we examined the active Ornstein-Uhlenbeck particle (AOUP) model, also commonly employed to depict the stochastic behavior of self-propelled particles. Although the ABP model is arguably the more prominent, the AOUP model has significant similarities while being mathematically more accessible. To clarify similarities and differences, we propose, in **P6**, the Parental Active Model (PAM) that incorporates both models and interpolates between them. The ABP and AOUP model share the same defining features of active matter, like an exponential orientation correlation and a shared velocity scale. The characterizing difference between them is the distribution of the self-propulsion velocity, which can be changed by adjusting one parameter within the PAM: going from Gaussian-distributed for AOUPs to a ring-shaped distribution for ABPs. However, both ABPs and AOUPs are idealized, and PAM provides a more realistic approach as it includes fluctuations in both velocity modulus and direction.

Advancing in **P7**, we extended the AOUP model to include both translational and rotational inertia. Our inertial AOUP model goes beyond previous models by incorporating a second timescale and accurately matching both small- and long-time regimes with the inertial active Brownian particle (ABP) model. We compared velocity correlations, delay function, and mean-square displacement to confirm the agreement between the two models. The effect of increasing rotational inertia is well captured by the inertial AOUP model, making it a suitable alternative for analytical predictions of dynamical correlations. This Gaussian model of inertial active matter offers a platform for future studies and a potential starting point for effective equilibrium theories and colored noise approximations.

In the last part of this thesis, we studied hydrodynamic flow fields in the vicinity of boundaries and their induced hydrodynamic interaction on active and passive particles nearby. In **P8**, we derived analytic expressions for the flow field induced by a Stokeslet and force dipole singularity inside a liquid drop surrounded by fluid. We explored the flow structure with and without homogeneously distributed surfactant on the surface and calculated the effective force exerted on the viscous drop. Our results also include the hydrodynamic correction to translational and rotational velocities of microswimmers moving inside. This theoretical description advances our understanding of hydrodynamic interactions in complex environments and provides a minimal model for interpreting the motion of active or passive particles in colloidal suspensions and microfluidic diagnostic devices.

In **P9** and **P10**, we studied the Stokes flow from an axisymmetric stokeslet and rotlet singularity between two equal-radius circular disks, respectively. In both cases, we transformed the solution of the flow field into integral equations and used standard numerical approaches to solve them. Our semi-analytic solutions exhibit excellent conformity with corresponding finite-element simulations. We also provided an expression for the translational and rotational mobility that quantifies the effect of the confining plates on a small particle axially moving or rotating. These systems could have applications in micromixing and the design of microparticle-based sensors.

References

[1] M. C. Marchetti, J. F. Joanny, S. Ramaswamy, T. B. Liverpool, J. Prost, M. Rao, and R. A. Simha, *Hydrodynamics of soft active matter*, Rev. Mod. Phys. **85**, (2013).

[2] C. Bechinger, R. Di Leonardo, H. Löwen, C. Reichhardt, G. Volpe, and G. Volpe, *Active particles in complex and crowded environments*, Rev. Mod. Phys. **88**, 045006 (2016).

[3] G. Gompper, R. G. Winkler, T. Speck, A. Solon, C. Nardini, F. Peruani, H. Löwen, R. Golestanian, U. B. Kaupp, L. Alvarez, T. Kiorboe, E. Lauga, W. C. K. Poon, A. DeSimone, S. Muiños-Landin, A. Fischer, N. A. Söker, F. Cichos, K. Raymond, P. Gaspard, M. Ripoll, F. Sagues, A. Doostmohammadi, J. M. Yeomans, I. S. Aranson, C. Bechinger, H. Stark, C. K. Hemelrijk, F. J. Nedelec, T. Sarkar, T. Aryaksama, M. Lacroix, G. Duclos, V. Yashunsky, P. Silberzan, M. Arroyo, and S. Kale, *The 2020 motile active matter roadmap*, J. Phys.: Condens. Matter **32**, 193001 (2020).

[4] P. Romanczuk, M. Bär, W. Ebeling, B. Lindner, and L. Schimansky-Geier, *Active brownian particles from individual to collective stochastic dynamics*, Eur. Phys. J. Spec. Top. **202**, 1 (2012).

[5] É. Fodor and M. C. Marchetti, *The statistical physics of active matter: From self-catalytic colloids to living cells*, Physica A **504**, 106 (2018).

[6] A. Kudrolli, G. Lumay, D. Volfson, and L. S. Tsimring, *Swarming and swirling in self-propelled polar granular rods*, Phys. Rev. Lett. **100**, 058001 (2008).

[7] C. Scholz, S. Jahanshahi, A. Ldov, and H. Löwen, *Inertial delay of self-propelled particles*, Nat. Commun. **9**, 5156 (2018).

[8] L. Giomi, N. Hawley-Weld, and L. Mahadevan, *Swarming, swirling and stasis in sequestered bristle-bots*, Proc. Royal Soc. A **469**, 20120637 (2013).

[9] O. Feinerman, I. Pinkoviezky, A. Gelblum, E. Fonio, and N. S. Gov, *The physics of cooperative transport in groups of ants*, Nat. Phys. **14**, 683 (2018).

[10] S. Bazazi, P. Romanczuk, S. Thomas, L. Schimansky-Geier, J. J. Hale, G. A. Miller, G. A. Sword, S. J. Simpson, and I. D. Couzin, *Nutritional state and collective motion: from individuals to mass migration*, Proc. R. Soc. B: Biol. Sci. **278**, 356 (2011).

[11] H. L. Devereux, C. R. Twomey, M. S. Turner, and S. Thutupalli, *Whirligig beetles as corralled active brownian particles*, J. R. Soc. Interface **18**, 20210114 (2021).

[12] I. D. Couzin, J. Krause, R. James, G. D. Ruxton, and N. R. Franks, *Collective memory and spatial sorting in animal groups*, J. Theor. Biol. **218**, 1 (2002).

[13] A. Perna, G. Grégoire, and R. P. Mann, *On the duality between interaction responses and mutual positions in flocking and schooling*, Mov. Ecol. **2**, 1 (2014).

[14] A. Cavagna, I. Giardina, and T. S. Grigera, *The physics of flocking: Correlation as a compass from experiments to theory*, Phys. Rep. **728**, 1 (2018).

[15] A. V. Zampetaki, B. Liebchen, A. V. Ivlev, and H. Löwen, *Collective self-optimization of communicating active particles*, Proc. Natl. Acad. Sci. U.S.A. **118**, e2111142118 (2021).

[16] J. M. Yeomans, D. O. Pushkin, and H. Shum, *An introduction to the hydrodynamics of swimming microorganisms*, Eur. Phys. J.: Spec. Top. **223**, (2014).

[17] A. M. Menzel, *Tuned, driven, and active soft matter*, Phys. Rep. **554**, (2015).

[18] J. Elgeti, R. G. Winkler, and G. Gompper, *Physics of microswimmers–single particle motion and collective behavior: a review*, Rep. Prog. Phys. **78**, 056601 (2015).

[19] A. Callegari and G. Volpe, *Flowing Matter* (Springer International Publishing, 2019).

[20] J. Yan, M. Han, J. Zhang, C. Xu, E. Luijten, and S. Granick, *Reconfiguring active particles by electrostatic imbalance*, Nat. Mater. **15**, 1095 (2016).

[21] S. Ni, E. Marini, I. Buttinoni, H. Wolf, and L. Isa, *Hybrid colloidal microswimmers through sequential capillary assembly*, Soft Matter **13**, 4252 (2017).

[22] M. Driscoll, B. Delmotte, M. Youssef, S. Sacanna, A. Donev, and P. Chaikin, *Unstable fronts and motile structures formed by microrollers*, Nat. Phys. **13**, 375 (2017).

[23] F. Ginot, I. Theurkauff, F. Detcheverry, C. Ybert, and C. Cottin-Bizonne, *Aggregation-fragmentation and individual dynamics of active clusters*, Nat. Commun. **9**, 696 (2018).

[24] U. Khadka, V. Holubec, H. Yang, and F. Cichos, *Active particles bound by information flows*, Nat. Commun. **9**, 3864 (2018).

[25] S. Thutupalli, R. Seemann, and S. Herminghaus, *Swarming behavior of simple model squirmers*, New J. Phys. **13**, 073021 (2011).

[26] S. Herminghaus, C. C. Maass, C. Krüger, S. Thutupalli, L. Goehring, and C. Bahr, *Interfacial mechanisms in active emulsions*, Soft Matter **10**, 7008 (2014).

[27] R. Seemann, J.-B. Fleury, and C. C. Maass, *Self-propelled droplets*, Eur. Phys. J.: Spec. Top. **225**, (2016).

[28] J. Arlt, V. A. Martinez, A. Dawson, T. Pilizota, and W. C. K. Poon, *Painting with light-powered bacteria*, Nat. Commun. **9**, 768 (2018).

[29] G. Frangipane, D. Dell'Arciprete, S. Petracchini, C. Maggi, F. Saglimbeni, S. Bianchi, G. Vizsnyiczai, M. L. Bernardini, and R. Di Leonardo, *Dynamic density shaping of photokinetic e. coli*, Elife **7**, e36608 (2018).

[30] R. Jeanneret, M. Contino, and M. Polin, *A brief introduction to the model microswimmer Chlamydomonas reinhardtii*, Eur. Phys. J. Spec. Top. **225**, (2016).

[31] R. Alert and X. Trepat, *Physical Models of Collective Cell Migration*, Annu. Rev. Condens. **11**, 77 (2020).

[32] A. Einstein, *Über die von der molekularkinetischen Theorie der Wärme geforderte Bewegung von in ruhenden Flüssigkeiten suspendierten Teilchen*, Ann. Phys. **322**, 549 (1905).

[33] A. Einstein, *Zur Theorie der Brownschen Bewegung*, Ann. Phys. **324**, 371 (1906).

[34] R. Brown, *XXVII. A brief account of microscopical observations made in the months of june, july and august 1827, on the particles contained in the pollen of plants; and on the general existence of active molecules in organic and inorganic bodies*, Philos. Mag. **4**, 161 (1828).

[35] R. Brown, *XXIV. Additional remarks on active molecules*, Philos. Mag. **6**, 161 (1829).

[36] M. von Smoluchowski, *Zur kinetischen Theorie der Brownschen Molekularbewegung und der Suspensionen*, Ann. Phys. **326**, 756 (1906).

[37] M. von Smoluchowski, *Über Brownsche Molekularbewegung unter Einwirkung äußerer Kräfte und deren Zusammenhang mit der verallgemeinerten Diffusionsgleichung*, Ann. Phys. **353**, 1103 (1916).

[38] A. D. Fokker, *Over Brown'sche bewegingen in het stralingsveld: en waarschijnlijkheids-beschouwingen in de stralingstheorie* (Joh. Enschedé en Zonen, Haarlem, 1913).

[39] A. D. Fokker, *Sur les mouvements browniens dans le champ du rayonnement noir*, Arch. Néerlandaises Sci. Exactes **4**, 269 (1918).

[40] M. Planck, *An essay on statistical dynamics and its amplification in the quantum theory*, Sitz. Ber. Preuss. Akad. Wiss **325**, 324 (1917).

[41] P. Langevin, *Sur la théorie du mouvement brownien*, C. R. Acad. Sci. **146**, 530 (1908).

[42] K. Przibram, *Über die ungeordnete Bewegung niederer Tiere*, Pflügers Arch. Gesamte Physiol. Menschen Tiere **153**, 401 (1913).

[43] K. Przibram, *Über die ungeordnete Bewegung niederer Tiere. II*, Archiv für Entwicklungsmechanik der Organismen **43**, 20 (1917).

[44] R. Fürth, *Die Brownsche Bewegung bei Berücksichtigung einer Persistenz der Bewegungsrichtung. mit Anwendungen auf die Bewegung lebender Infusorien*, Z. Phys. **2**, 244 (1920).

[45] L. S. Ornstein, *On the Brownian motion*, Proc. Ser. B Phys. Sci. (1919).

[46] G. E. Uhlenbeck and L. S. Ornstein, *On the theory of the Brownian motion*, Phys. Rev. **36**, 823 (1930).

[47] H. C. Berg and D. A. Brown, *Chemotaxis in Escherichia coli analysed by Three-dimensional Tracking*, Nature **239**, 500 (1972).

[48] P. S. Lovely and F. Dahlquist, *Statistical measures of bacterial motility and chemotaxis*, J. theor. Biol. **50**, 477 (1975).

[49] E. M. Purcell, *Life at low Reynolds number*, Am. J. Phys. **45**, 3 (1977).

[50] M. J. Schnitzer, *Theory of continuum random walks and application to chemotaxis*, Phys. Rev. E **48**, 2553 (1993).

[51] H. C. Berg, *Random walks in biology* (Princeton University Press, 1993).

[52] H. C. Berg, *E. coli in motion* (Springer New York, NY, 2004).

[53] J. Tailleur and M. E. Cates, *Statistical mechanics of interacting run-and-tumble bacteria*, Phys. Rev. Lett. **100**, 218103 (2008).

[54] T. Vicsek, A. Czirók, E. Ben-Jacob, I. Cohen, and O. Shochet, *Novel type of phase transition in a system of self-driven particles*, Phys. Rev. Lett. **75**, 1226 (1995).

[55] J. Toner and Y. Tu, *Long-range order in a two-dimensional dynamical* XY *model: How birds fly together*, Phys. Rev. Lett. **75**, 4326 (1995).

[56] J. Toner and Y. Tu, *Flocks, herds, and schools: A quantitative theory of flocking*, Phys. Rev. E **58**, 4828 (1998).

[57] R. Golestanian, T. B. Liverpool, and A. Ajdari, *Designing phoretic micro- and nano-swimmers*, New J. Phys. **9**, 126 (2007).

[58] P. Illien, R. Golestanian, and A. Sen, *'Fuelled' motion: phoretic motility and collective behaviour of active colloids*, Chem. Soc. Rev. **46**, 5508 (2017).

[59] W. Wang, L. A. Castro, M. Hoyos, and T. E. Mallouk, *Autonomous motion of metallic microrods propelled by ultrasound*, ACS Nano **6**, 6122 (2012).

[60] J. Voß and R. Wittkowski, *Acoustically propelled nano- and microcones: fast forward and backward motion*, Nanoscale Adv. **4**, 281 (2021).

[61] A. Bricard, J.-B. Caussin, N. Desreumaux, O. Dauchot, and D. Bartolo, *Emergence of macroscopic directed motion in populations of motile colloids*, Nature **503**, 95 (2013).

[62] A. Morin, N. Desreumaux, J.-B. Caussin, and D. Bartolo, *Distortion and destruction of colloidal flocks in disordered environments*, Nat. Phys. **13**, 63 (2017).

[63] A. Kaiser, A. Snezhko, and I. S. Aranson, *Flocking ferromagnetic colloids*, Sci. Adv. **3**, e1601469 (2017).

[64] M. A. Fernandez-Rodriguez, F. Grillo, L. Alvarez, M. Rathlef, I. Buttinoni, G. Volpe, and L. Isa, *Feedback-controlled active brownian colloids with space-dependent rotational dynamics*, Nat. Commun. **11**, 4223 (2020).

[65] L. Alvarez, M. A. Fernandez-Rodriguez, A. Alegria, S. Arrese-Igor, K. Zhao, M. Kröger, and L. Isa, *Reconfigurable artificial microswimmers with internal feedback*, Nat. Commun. **12**, 4762 (2021).

[66] W. F. Paxton, K. C. Kistler, C. C. Olmeda, A. Sen, S. K. St. Angelo, Y. Cao, T. E. Mallouk, P. E. Lammert, and V. H. Crespi, *Catalytic nanomotors: autonomous movement of striped nanorods*, J. Am. Chem. Soc. **126**, 13424 (2004).

[67] J. R. Howse, R. A. L. Jones, A. J. Ryan, T. Gough, R. Vafabakhsh, and R. Golestanian, *Self-motile colloidal particles: From directed propulsion to random walk*, Phys. Rev. Lett. **99**, 048102 (2007).

[68] S. van Teeffelen and H. Löwen, *Dynamics of a brownian circle swimmer*, Phys. Rev. E **78**, 020101 (2008).

[69] B. Hagen, S. van Teeffelen, and H. Löwen, *Non–gaussian behaviour of a self-propelled particle on a substrate*, Condens Matter Phys. **12**, 725 (2009).

[70] B. ten Hagen, S. van Teeffelen, and H. Löwen, *Brownian motion of a self-propelled particle*, J. Phys. Condens. Matter **23**, 194119 (2011).

[71] Y. Fily and M. C. Marchetti, *Athermal phase separation of self-propelled particles with no alignment*, Phys. Rev. Lett. **108**, 235702 (2012).

[72] I. Buttinoni, J. Bialké, F. Kümmel, H. Löwen, C. Bechinger, and T. Speck, *Dynamical clustering and phase separation in suspensions of self-propelled colloidal particles*, Phys. Rev. Lett. **110**, 238301 (2013).

[73] J. Bialké, J. T. Siebert, H. Löwen, and T. Speck, *Negative interfacial tension in phase-separated active brownian particles*, Phys. Rev. Lett. **115**, 098301 (2015).

[74] M. E. Cates and J. Tailleur, *Motility-Induced Phase Separation*, Annu. Rev. Condens. Matter Phys. **6**, 219 (2015).

[75] R. Kubo, M. Toda, and N. Hashitsume. *Statistical Mechanics of Linear Response*, pages 146–202. Springer, Berlin, Heidelberg, Berlin, Heidelberg, (1985).

[76] H. Risken, *The Fokker-Planck Equation: Methods of Solution and Applications* (Springer Berlin, Heidelberg, 1996).

[77] B. ten Hagen, R. Wittkowski, D. Takagi, F. Kümmel, C. Bechinger, and H. Löwen, *Can the self-propulsion of anisotropic microswimmers be described by using forces and torques?*, J. Phys. Condens. Matter **27**, 194110 (2015).

[78] G. S. Chirikjian, *Stochastic Models, Information Theory, and Lie Groups, Volume 1: Classical Results and Geometric Methods* (Birkhäuser Boston, MA, 2009).

[79] J. Bickmann and R. Wittkowski, *Predictive local field theory for interacting active Brownian spheres in two spatial dimensions*, J. Phys. Condens. **32**, 214001 (2020).

[80] M. te Vrugt, J. Bickmann, and R. Wittkowski, *How to derive a predictive field theory for active brownian particles: a step-by-step tutorial*, J. Phys. Condens. (2023).

[81] F. A. Lavergne, H. Wendehenne, T. Bäuerle, and C. Bechinger, *Group formation and cohesion of active particles with visual perception-dependent motility*, Science **364**, 70 (2019).

[82] H. H. Wensink, J. Dunkel, S. Heidenreich, K. Drescher, R. E. Goldstein, H. Löwen, and J. M. Yeomans, *Meso-scale turbulence in living fluids*, Proc. Natl. Acad. Sci. U.S.A. **109**, 14308 (2012).

[83] J. Dunkel, S. Heidenreich, K. Drescher, H. H. Wensink, M. Bär, and R. E. Goldstein, *Fluid dynamics of bacterial turbulence*, Phys. Rev. Lett. **110**, 228102 (2013).

[84] A. Doostmohammadi, T. N. Shendruk, K. Thijssen, and J. M. Yeomans, *Onset of meso-scale turbulence in active nematics*, Nat. Commun. **8**, 15326 (2017).

[85] C. B. Caporusso, P. Digregorio, D. Levis, L. F. Cugliandolo, and G. Gonnella, *Motility-induced microphase and macrophase separation in a two-dimensional active brownian particle system*, Phys. Rev. Lett. **125**, 178004 (2020).

[86] S. Henkes, Y. Fily, and M. C. Marchetti, *Active jamming: Self-propelled soft particles at high density*, Phys. Rev. E **84**, 040301 (2011).

[87] C. Reichhardt and C. J. Olson Reichhardt, *Active matter transport and jamming on disordered landscapes*, Phys. Rev. E **90**, 012701 (2014).

[88] R. L. Stoop and P. Tierno, *Clogging and jamming of colloidal monolayers driven across disordered landscapes*, Commun. Phys. **1**, 68 (2018).

[89] S. Henkes, K. Kostanjevec, J. M. Collinson, R. Sknepnek, and E. Bertin, *Dense active matter model of motion patterns in confluent cell monolayers*, Nat. Commun. **11**, 1405 (2020).

[90] É. Fodor, C. Nardini, M. E. Cates, J. Tailleur, P. Visco, and F. van Wijland, *How far from equilibrium is active matter?*, Phys. Rev. Lett. **117**, 038103 (2016).

[91] D. Mandal, K. Klymko, and M. R. DeWeese, *Entropy production and fluctuation theorems for active matter*, Phys. Rev. Lett. **119**, 258001 (2017).

[92] P. Pietzonka and U. Seifert, *Entropy production of active particles and for particles in active baths*, J. Phys. A Math. Gen. **51**, 01LT01 (2018).

[93] L. Dabelow, S. Bo, and R. Eichhorn, *Irreversibility in active matter systems: Fluctuation theorem and mutual information*, Phys. Rev. X **9**, 021009 (2019).

[94] J. O'Byrne, Y. Kafri, J. Tailleur, and F. van Wijland, *Time irreversibility in active matter, from micro to macro*, Nat. Rev. Phys. **4**, 167 (2022).

[95] L. F. Cugliandolo, *The effective temperature*, J. Phys. A: Math. Theor. **44**, 483001 (2011).

[96] A. P. Solon, Y. Fily, A. Baskaran, M. E. Cates, Y. Kafri, M. Kardar, and J. Tailleur, *Pressure is not a state function for generic active fluids*, Nat. Phys. **11**, 673 (2015).

[97] G. Szamel, *Self-propelled particle in an external potential: Existence of an effective temperature*, Phys. Rev. E **90**, 012111 (2014).

[98] C. Maggi, U. M. B. Marconi, N. Gnan, and R. Di Leonardo, *Multidimensional stationary probability distribution for interacting active particles*, Sci. Rep. **5**, 10742 (2015).

[99] C. Maggi, M. Paoluzzi, N. Pellicciotta, A. Lepore, L. Angelani, and R. Di Leonardo, *Generalized energy equipartition in harmonic oscillators driven by active baths*, Phys. Rev. Lett. **113**, 238303 (2014).

[100] C. Maggi, M. Paoluzzi, L. Angelani, and R. Di Leonardo, *Memory-less response and violation of the fluctuation-dissipation theorem in colloids suspended in an active bath*, Sci. Rep. **7**, 17588 (2017).

[101] S. Chaki and R. Chakrabarti, *Effects of active fluctuations on energetics of a colloidal particle: Superdiffusion, dissipation and entropy production*, Physica A **530**, 121574 (2019).

[102] K. Goswami, *Work fluctuations in a generalized gaussian active bath*, Physica A **566**, 125609 (2021).

[103] X. Zheng, B. ten Hagen, A. Kaiser, M. Wu, H. Cui, Z. Silber-Li, and H. Löwen, *Non-gaussian statistics for the motion of self-propelled janus particles: Experiment versus theory*, Phys. Rev. E **88**, 032304 (2013).

[104] L. Caprini, U. Marini Bettolo Marconi, A. Puglisi, and A. Vulpiani, *Active escape dynamics: The effect of persistence on barrier crossing*, J. Chem. Phys. **150**, 024902 (2019).

[105] R. Wittmann, J. M. Brader, A. Sharma, and U. M. B. Marconi, *Effective equilibrium states in mixtures of active particles driven by colored noise*, Phys. Rev. E **97**, 012601 (2018).

[106] L. Berthier, E. Flenner, and G. Szamel, *Glassy dynamics in dense systems of active particles*, J. Chem. Phys. **150**, 200901 (2019).

[107] Y. Fily, *Self-propelled particle in a nonconvex external potential: Persistent limit in one dimension*, J. Chem. Phys. **150**, 174906 (2019).

[108] D. Martin, J. O'Byrne, M. E. Cates, É. Fodor, C. Nardini, J. Tailleur, and F. van Wijland, *Statistical mechanics of active ornstein-uhlenbeck particles*, Phys. Rev. E **103**, 032607 (2021).

[109] L. Caprini and U. M. B. Marconi, *Active particles under confinement and effective force generation among surfaces*, Soft Matter **14**, 9044 (2018).

[110] S. Das, G. Gompper, and R. G. Winkler, *Confined active brownian particles: theoretical description of propulsion-induced accumulation*, New J. Phys. **20**, 015001 (2018).

[111] J. Palacci, S. Sacanna, A. P. Steinberg, D. J. Pine, and P. M. Chaikin, *Living crystals of light-activated colloidal surfers*, Science **339**, 936 (2013).

[112] B. M. Mognetti, A. Šarić, S. Angioletti-Uberti, A. Cacciuto, C. Valeriani, and D. Frenkel, *Living clusters and crystals from low-density suspensions of active colloids*, Phys. Rev. Lett. **111**, 245702 (2013).

[113] L. Caprini, U. M. B. Marconi, C. Maggi, M. Paoluzzi, and A. Puglisi, *Hidden velocity ordering in dense suspensions of self-propelled disks*, Phys. Rev. Res. **2**, 023321 (2020).

[114] G. Szamel and E. Flenner, *Long-ranged velocity correlations in dense systems of self-propelled particles*, EPL **133**, 60002 (2021).

[115] G. Szamel, E. Flenner, and L. Berthier, *Glassy dynamics of athermal self-propelled particles: Computer simulations and a nonequilibrium microscopic theory*, Phys. Rev. E **91**, 062304 (2015).

[116] E. Flenner, G. Szamel, and L. Berthier, *The nonequilibrium glassy dynamics of self-propelled particles*, Soft matter **12**, 7136 (2016).

[117] A. Pototsky and H. Stark, *Active Brownian particles in two-dimensional traps*, EPL **98**, 50004 (2012).

[118] D. Klotsa, *As above, so below, and also in between: mesoscale active matter in fluids*, Soft Matter **15**, 8946 (2019).

[119] H. Löwen, *Inertial effects of self-propelled particles: From active brownian to active langevin motion*, J. Chem. Phys. **152**, 040901 (2020).

[120] R. Wittkowski and H. Löwen, *Self-propelled brownian spinning top: Dynamics of a biaxial swimmer at low reynolds numbers*, Phys. Rev. E **85**, 021406 (2012).

[121] D. J. Kraft, R. Wittkowski, B. ten Hagen, K. V. Edmond, D. J. Pine, and H. Löwen, *Brownian motion and the hydrodynamic friction tensor for colloidal particles of complex shape*, Phys. Rev. E **88**, 050301 (2013).

[122] D. Takagi, A. B. Braunschweig, J. Zhang, and M. J. Shelley, *Dispersion of self-propelled rods undergoing fluctuation-driven flips*, Phys. Rev. Lett. **110**, 038301 (2013).

[123] C. Kurzthaler and T. Franosch, *Intermediate scattering function of an anisotropic brownian circle swimmer*, Soft Matter **13**, 6396 (2017).

[124] F. Kümmel, B. ten Hagen, R. Wittkowski, I. Buttinoni, R. Eichhorn, G. Volpe, H. Löwen, and C. Bechinger, *Circular motion of asymmetric self-propelling particles*, Phys. Rev. Lett. **110**, 198302 (2013).

[125] N. A. Marine, P. M. Wheat, J. Ault, and J. D. Posner, *Diffusive behaviors of circle-swimming motors*, Phys. Rev. E **87**, 052305 (2013).

[126] A. P. Berke, L. Turner, H. C. Berg, and E. Lauga, *Hydrodynamic attraction of swimming microorganisms by surfaces*, Phys. Rev. Lett. **101**, (2008).

[127] J. Elgeti, U. B. Kaupp, and G. Gompper, *Hydrodynamics of sperm cells near surfaces*, Biophys. J. **99**, (2010).

[128] B. Liebchen and D. Levis, *Collective behavior of chiral active matter: Pattern formation and enhanced flocking*, Phys. Rev. Lett. **119**, 058002 (2017).

[129] B. Liebchen and D. Levis, *Chiral active matter*, EPL **139**, 67001 (2022).

[130] C. Scholz, M. Engel, and T. Pöschel, *Rotating robots move collectively and self-organize*, Nat. Commun. **9**, 931 (2018).

[131] C. Scholz, A. Ldov, T. Pöschel, M. Engel, and H. Löwen, *Surfactants and rotelles in active chiral fluids*, Sci. Adv. **7**, eabf8998 (2021).

[132] S. Jahanshahi, H. Löwen, and B. ten Hagen, *Brownian motion of a circle swimmer in a harmonic trap*, Phys. Rev. E **95**, 022606 (2017).

[133] K. Malakar, A. Das, A. Kundu, K. V. Kumar, and A. Dhar, *Steady state of an active brownian particle in a two-dimensional harmonic trap*, Phys. Rev. E **101**, 022610 (2020).

[134] L. Caprini, U. Marini Bettolo Marconi, A. Puglisi, and A. Vulpiani, *Active escape dynamics: The effect of persistence on barrier crossing*, J. Chem. Phys. **150**, 024902 (2019).

[135] D. Breoni, M. Schmiedeberg, and H. Löwen, *Active brownian and inertial particles in disordered environments: Short-time expansion of the mean-square displacement*, Phys. Rev. E **102**, 062604 (2020).

[136] S. C. Takatori, R. de Dier, J. Vermant, and J. F. Brady, *Acoustic trapping of active matter*, Nat. Commun. **7**, 10694 (2016).

[137] O. Dauchot and V. Démery, *Dynamics of a self-propelled particle in a harmonic trap*, Phys. Rev. Lett. **122**, 068002 (2019).

[138] F. Schmidt, H. Šípová-Jungová, M. Käll, A. Würger, and G. Volpe, *Non-equilibrium properties of an active nanoparticle in a harmonic potential*, Nat. Commun. **12**, 1902 (2021).

[139] I. Buttinoni, L. Caprini, L. Alvarez, F. J. Schwarzendahl, and H. Löwen, *Active colloids in harmonic optical potentials*, EPL **140**, 27001 (2022).

[140] L. Angelani, A. Costanzo, and R. Di Leonardo, *Active ratchets*, EPL **96**, 68002 (2011).

[141] C. J. O. Reichhardt and C. Reichhardt, *Ratchet Effects in Active Matter Systems*, Annu. Rev. Condens. Matter Phys. **8**, 51 (2017).

[142] B.-Q. Ai and F.-G. Li, *Transport of underdamped active particles in ratchet potentials*, Soft Matter **13**, 2536 (2017).

[143] C. Lozano, B. Ten Hagen, H. Löwen, and C. Bechinger, *Phototaxis of synthetic microswimmers in optical landscapes*, Nat. Commun. **7**, 12828 (2016).

[144] J. R. Gomez-Solano, S. Samin, C. Lozano, P. Ruedas-Batuecas, R. van Roij, and C. Bechinger, *Tuning the motility and directionality of self-propelled colloids*, Sci. Rep. **7**, 14891 (2017).

[145] F. Schmidt, B. Liebchen, H. Löwen, and G. Volpe, *Light-controlled assembly of active colloidal molecules*, J. Chem. Phys. **150**, 094905 (2019).

[146] C. Maggi, F. Saglimbeni, M. Dipalo, F. de Angelis, and R. di Leonardo, *Micromotors with asymmetric shape that efficiently convert light into work by thermocapillary effects*, Nat. Commun. **6**, 7855 (2015).

[147] G. Vizsnyiczai, G. Frangipane, C. Maggi, F. Saglimbeni, S. Bianchi, and R. di Leonardo, *Light controlled 3D micromotors powered by bacteria*, Nat. Commun. **8**, 15974 (2017).

[148] J. Stenhammar, R. Wittkowski, D. Marenduzzo, and M. E. Cates, *Light-induced self-assembly of active rectification devices*, Sci. Adv. **2**, e1501850 (2016).

[149] N. Koumakis, A. T. Brown, J. Arlt, S. E. Griffiths, V. A. Martinez, and W. C. K. Poon, *Dynamic optical rectification and delivery of active particles*, Soft Matter **15**, 7026 (2019).

[150] C. Lozano, B. Liebchen, B. ten Hagen, C. Bechinger, and H. Löwen, *Propagating density spikes in light-powered motility-ratchets*, Soft Matter **15**, 5185 (2019).

[151] A. P. Bregulla, H. Yang, and F. Cichos, *Stochastic localization of microswimmers by photon nudging*, ACS Nano **8**, 6542 (2014).

[152] N. A. Söker, S. Auschra, V. Holubec, K. Kroy, and F. Cichos, *How activity landscapes polarize microswimmers without alignment forces*, Phys. Rev. Lett. **126**, 228001 (2021).

[153] P. K. Ghosh, Y. Li, F. Marchesoni, and F. Nori, *Pseudochemotactic drifts of artificial microswimmers*, Phys. Rev. E **92**, 012114 (2015).

[154] A. Sharma and J. M. Brader, *Brownian systems with spatially inhomogeneous activity*, Phys. Rev. E **96**, 032604 (2017).

[155] L. Caprini, U. Marini Bettolo Marconi, R. Wittmann, and H. Löwen, *Dynamics of active particles with space-dependent swim velocity*, Soft Matter **18**, 1412 (2022).

[156] L. Caprini, U. M. B. Marconi, R. Wittmann, and H. Löwen, *Active particles driven by competing spatially dependent self-propulsion and external force*, SciPost Phys. **13**, 065 (2022).

[157] S. Babel, B. ten Hagen, and H. Löwen, *Swimming path statistics of an active Brownian particle with time-dependent self-propulsion*, J. Stat. Mech.: Theory Exp. **2014**, P02011 (2014).

[158] G. Volpe and G. Volpe, *The topography of the environment alters the optimal search strategy for active particles*, Proc. Natl. Acad. Sci. U.S.A. **114**, 11350 (2017).

[159] F. Cichos, K. Gustavsson, B. Mehlig, and G. Volpe, *Machine learning for active matter*, Nat. Mach. Intell. **2**, 94 (2020).

[160] A. Daddi-Moussa-Ider, H. Löwen, and B. Liebchen, *Hydrodynamics can determine the optimal route for microswimmer navigation*, Commun. Phys. **4**, 15 (2021).

[161] P. A. Monderkamp, F. J. Schwarzendahl, M. A. Klatt, and H. Löwen, *Active particles using reinforcement learning to navigate in complex motility landscapes*, Mach. Learn.: Sci. Technol. **3**, 045024 (2022).

[162] M. Gassner, S. Goh, G. Gompper, and R. G. Winkler, *Noisy pursuit by a self-steering active particle in confinement*, EPL **142**, 21002 (2023).

[163] J. A. Cohen and R. Golestanian, *Emergent cometlike swarming of optically driven thermally active colloids*, Phys. Rev. Lett. **112**, 068302 (2014).

[164] W. E. Uspal, *Theory of light-activated catalytic Janus particles*, J. Chem. Phys. **150**, 114903 (2019).

[165] J. Voß and R. Wittkowski, *Orientation-dependent propulsion of triangular nano- and microparticles by a traveling ultrasound wave*, ACS Nano **16**, 3604 (2022).

[166] S. Bröker, J. Bickmann, M. te Vrugt, M. E. Cates, and R. Wittkowski, *Orientation-dependent propulsion of active Brownian spheres: from self-advection to programmable cluster shapes*, arXiv:2210.13357 (2022).

[167] B. Liu, T. R. Powers, and K. S. Breuer, *Force-free swimming of a model helical flagellum in viscoelastic fluids*, Proceedings of the National Academy of Sciences U.S.A. **108**, 19516 (2011).

[168] J. Schwarz-Linek, C. Valeriani, A. Cacciuto, M. E. Cates, D. Marenduzzo, A. N. Morozov, and W. C. K. Poon, *Phase separation and rotor self-assembly in active particle suspensions*, Proceedings of the National Academy of Sciences U.S.A. **109**, 4052 (2012).

[169] F. Höfling and T. Franosch, *Anomalous transport in the crowded world of biological cells*, Rep. Prog. Phys. **76**, 046602 (2013).

[170] T. Qiu, T.-C. Lee, A. G. Mark, K. I. Morozov, R. Münster, O. Mierka, S. Turek, A. M. Leshansky, and P. Fischer, *Swimming by reciprocal motion at low reynolds number*, Nat. Commun. **5**, 5119 (2014).

[171] E. E. Riley and E. Lauga, *Enhanced active swimming in viscoelastic fluids*, EPL **108**, 34003 (2014).

[172] T. Annable, R. Buscall, R. Ettelaie, and D. Whittlestone, *The rheology of solutions of associating polymers: Comparison of experimental behavior with transient network theory*, J. Rheol. **37**, 695 (1993).

[173] J. Sprakel, J. van der Gucht, M. A. Cohen Stuart, and N. A. M. Besseling, *Brownian particles in transient polymer networks*, Phys. Rev. E **77**, 061502 (2008).

[174] A. Zöttl and J. M. Yeomans, *Enhanced bacterial swimming speeds in macromolecular polymer solutions*, Nat. Phys. **15**, 554–558 (2019).

[175] S. Liu, S. Shankar, M. C. Marchetti, and Y. Wu, *Viscoelastic control of spatiotemporal order in bacterial active matter*, Nature **590**, 80–84 (2021).

[176] F. Cardinaux, L. Cipelletti, F. Scheffold, and P. Schurtenberger, *Microrheology of giant-micelle solutions*, EPL **57**, 738 (2002).

[177] J. Galvan-Miyoshi, J. Delgado, and R. Castillo, *Diffusing wave spectroscopy in Maxwellian fluids*, Eur. Phys. J. E **26**, 369 (2008).

[178] M. S. Krieger, S. E. Spagnolie, and T. R. Powers, *Locomotion and transport in a hexatic liquid crystal*, Phys. Rev. E **90**, 052503 (2014).

[179] B. van der Meer, L. Filion, and M. Dijkstra, *Fabricating large two-dimensional single colloidal crystals by doping with active particles*, Soft Matter **12**, 3406 (2016).

[180] S. Zhou, A. Sokolov, O. D. Lavrentovich, and I. S. Aranson, *Living liquid crystals*, Proceedings of the National Academy of Sciences U.S.A. **111**, 1265 (2014).

[181] M. S. Krieger, S. E. Spagnolie, and T. Powers, *Microscale locomotion in a nematic liquid crystal*, Soft Matter **11**, 9115 (2015).

[182] C. Wilhelm, F. Gazeau, and J.-C. Bacri, *Rotational magnetic endosome microrheology: Viscoelastic architecture inside living cells*, Phys. Rev. E **67**, 061908 (2003).

[183] É. Fodor, M. Guo, N. S. Gov, P. Visco, D. A. Weitz, and F. van Wijland, *Activity-driven fluctuations in living cells*, EPL **110**, 48005 (2015).

[184] J. F. Berret, *Local viscoelasticity of living cells measured by rotational magnetic spectroscopy*, Nat. Commun. **7**, 10134 (2016).

[185] M. Grimm, S. Jeney, and T. Franosch, *Brownian motion in a Maxwell fluid*, Soft Matter **7**, 2076 (2011).

[186] Y. L. Raikher, V. V. Rusakov, and R. Perzynski, *Brownian motion in a viscoelastic medium modelled by a Jeffreys fluid*, Soft Matter **9**, 10857 (2013).

[187] P. K. Ghosh, Y. Li, G. Marchegiani, and F. Marchesoni, *Communication: Memory effects and active brownian diffusion*, J. Chem. Phys. **143**, 211101 (2015).

[188] F. J. Sevilla, R. F. Rodríguez, and J. R. Gomez-Solano, *Generalized ornstein-uhlenbeck model for active motion*, Phys. Rev. E **100**, 032123 (2019).

[189] N. Narinder, C. Bechinger, and J. R. Gomez-Solano, *Memory-induced transition from a persistent random walk to circular motion for achiral microswimmers*, Phys. Rev. Lett. **121**, 078003 (2018).

[190] J. R. Gomez-Solano, A. Blokhuis, and C. Bechinger, *Dynamics of self-propelled janus particles in viscoelastic fluids*, Phys. Rev. Lett. **116**, 138301 (2016).

[191] B. Liebchen and H. Löwen, *Synthetic chemotaxis and collective behavior in active matter*, Acc. Chem. Res. **51**, 2982 (2018).

[192] C. Jin, C. Krüger, and C. C. Maass, *Chemotaxis and autochemotaxis of self-propelling droplet swimmers*, Proc. Natl. Acad. Sci. U.S.A. **114**, 5089 (2017).

[193] W. T. Kranz, A. Gelimson, K. Zhao, G. C. L. Wong, and R. Golestanian, *Effective dynamics of microorganisms that interact with their own trail*, Phys. Rev. Lett. **117**, 038101 (2016).

[194] A. Sengupta, S. van Teeffelen, and H. Löwen, *Dynamics of a microorganism moving by chemotaxis in its own secretion*, Phys. Rev. E **80**, 031122 (2009).

[195] E. F. Keller and L. A. Segel, *Model for chemotaxis*, J. Theor. Biol. **30**, 225 (1971).

[196] S. Saha, R. Golestanian, and S. Ramaswamy, *Clusters, asters, and collective oscillations in chemotactic colloids*, Phys. Rev. E **89**, 062316 (2014).

[197] O. Pohl and H. Stark, *Dynamic clustering and chemotactic collapse of self-phoretic active particles*, Phys. Rev. Lett. **112**, 238303 (2014).

[198] B. Liebchen, D. Marenduzzo, and M. E. Cates, *Phoretic interactions generically induce dynamic clusters and wave patterns in active colloids*, Phys. Rev. Lett. **118**, 268001 (2017).

[199] J. Grauer, H. Löwen, A. Be'er, and B. Liebchen, *Swarm Hunting and Cluster Ejections in Chemically Communicating Active Mixtures*, Sci. Rep. **10**, 5594 (2020).

[200] J. Grauer, F. Schmidt, J. Pineda, B. Midtvedt, H. Löwen, G. Volpe, and B. Liebchen, *Active droploids*, Nat. Commun. **12**, 6005 (2021).

[201] S. I. Krasheninnikov, A. Y. Pigarov, R. D. Smirnov, and T. K. Soboleva, *Theoretical aspects of dust in fusion devices*, Contrib. to Plasma Phys. **50**, 410 (2010).

[202] V. Nosenko, A. V. Ivlev, and G. E. Morfill, *Laser-induced rocket force on a microparticle in a complex (dusty) plasma*, Phys. Plasmas **17**, 123705 (2010).

[203] G. E. Morfill and A. V. Ivlev, *Complex plasmas: An interdisciplinary research field*, Rev. Mod. Phys. **81**, 1353 (2009).

[204] A. V. Ivlev, J. Bartnick, M. Heinen, C.-R. Du, V. Nosenko, and H. Löwen, *Statistical mechanics where newton's third law is broken*, Phys. Rev. X **5**, 011035 (2015).

[205] V. Nosenko, F. Luoni, A. Kaouk, M. Rubin-Zuzic, and H. Thomas, *Active janus particles in a complex plasma*, Phys. Rev. Research **2**, 033226 (2020).

[206] M. Sandoval, *Pressure and diffusion of active matter with inertia*, Phys. Rev. E **101**, 012606 (2020).

[207] L. L. Gutierrez-Martinez and M. Sandoval, *Inertial effects on trapped active matter*, J. Chem. Phys. **153**, 044906 (2020).

[208] P. Herrera and M. Sandoval, *Maxwell-boltzmann velocity distribution for noninteracting active matter*, Phys. Rev. E **103**, 012601 (2021).

[209] J. Deseigne, O. Dauchot, and H. Chaté, *Collective motion of vibrated polar disks*, Phys. Rev. Lett. **105**, 098001 (2010).

[210] A. Suma, G. Gonnella, D. Marenduzzo, and E. Orlandini, *Motility-induced phase separation in an active dumbbell fluid*, EPL **108**, 56004 (2014).

[211] I. Petrelli, P. Digregorio, L. F. Cugliandolo, G. Gonnella, and A. Suma, *Active dumbbells: Dynamics and morphology in the coexisting region*, Eur. Phys. J. E **41**, 128 (2018).

[212] C. A. Weber, T. Hanke, J. Deseigne, S. Léonard, O. Dauchot, E. Frey, and H. Chaté, *Long-range ordering of vibrated polar disks*, Phys. Rev. Lett. **110**, 208001 (2013).

[213] G. Briand, M. Schindler, and O. Dauchot, *Spontaneously flowing crystal of self-propelled particles*, Phys. Rev. Lett. **120**, 208001 (2018).

[214] D. Arold and M. Schmiedeberg, *Mean field approach of dynamical pattern formation in underdamped active matter with short-ranged alignment and distant anti-alignment interactions*, J. Phys. Condens. **32**, 315403 (2020).

[215] Y. Kuroda, H. Matsuyama, T. Kawasaki, and K. Miyazaki, *Anomalous fluctuations in homogeneous fluid phase of active brownian particles*, Phys. Rev. Res. **5**, 013077 (2023).

[216] S. Mandal, B. Liebchen, and H. Löwen, *Motility-induced temperature difference in coexisting phases*, Phys. Rev. Lett. **123**, 228001 (2019).

[217] I. Petrelli, L. F. Cugliandolo, G. Gonnella, and A. Suma, *Effective temperatures in inhomogeneous passive and active bidimensional brownian particle systems*, Phys. Rev. E **102**, 012609 (2020).

[218] A. R. Plastino and J. C. Muzzio, *On the Use and Abuse of Newton's Second Law for Variable Mass Problems*, Celest. Mech. Dyn. Astron. **53**, 227 (1992).

[219] W. T. Thomson, *Equations of motion for the variable mass system*, AIAA Journal **4**, 766 (1966).

[220] R. A. Rankin and L. Rosenhead, *The mathematical theory of the motion of rotated and unrotated rockets*, Philos. Trans. R. Soc. A **241**, 457 (1949).

[221] A. S. Bodrova, A. V. Chechkin, A. G. Cherstvy, H. Safdari, I. M. Sokolov, and R. Metzler, *Underdamped scaled brownian motion: (non-)existence of the overdamped limit in anomalous diffusion*, Sci. Rep. **6**, 30520 (2016).

[222] L. D. Landau and E. M. Lifshitz, *Fluid Mechanics* (Pergamon Press, 1987).

[223] L. Euler, *Principes généraux du mouvement des fluides*, Mémoires de l'académie des sciences de Berlin (1757).

[224] C. L. M. H. Navier, *Mémoire sur les lois du mouvement des fluides*, Mémoires de l'Académie Royale des Sciences de l'Institut de France **6**, 389 (1822).

[225] G. G. Stokes, *On the theories of internal friction of fluids in motion*, Soc., UK **8**, 287 (1845).

[226] O. Reynolds, *An Experimental Investigation of the Circumstances Which Determine Whether the Motion of Water Shall Be Direct or Sinuous, and of the Law of Resistance in Parallel Channels*, Philos. Trans. Royal Soc. **174**, 935 (1883).

[227] C. Oseen, *Über die stokes' sche formel und eine verwandte aufgabe in der hydromechanik*, Arkiv för Mathematik, Astronomi o. Fysik **6**, 1 (1910).

[228] H. K. Versteeg and W. Malalasekera, *An introduction to computational fluid dynamics: the finite volume method* (Pearson Education, 1995).

[229] H. A. Stone, *A simple derivation of the time-dependent convective-diffusion equation for surfactant transport along a deforming interface*, Phys. Fluids A **2**, 111 (1990).

[230] D. A. Edwards, H. Brenner, and D. T. Wasan, *Interfacial transport processes and rheology* (Elsevier Butterworth-Heinemann, Oxford, UK, 1991).

[231] J. Bławzdziewicz, V. Cristini, and M. Loewenberg, *Stokes flow in the presence of a planar interface covered with incompressible surfactant*, Phys. Fluids **11**, 251 (1999).

[232] J. D. Jackson, *Classical electrodynamics* (John Wiley and Sons, New York, 1998).

[233] J. Happel and H. Brenner, *Low Reynolds number hydrodynamics: with special applications to particulate media* (Springer, Den Haag, 1983).

[234] J. R. Blake, *A note on the image system for a stokeslet in a no-slip boundary*, Math. Proc. Camb. Philos. Soc. **70**, 303 (1971).

[235] Y. O. Fuentes, S. Kim, and D. J. Jeffrey, *Mobility functions for two unequal viscous drops in Stokes flow. I. Axisymmetric motions*, Phys. Fluids **31**, 2445 (1988).

[236] Y. O. Fuentes, S. Kim, and D. J. Jeffrey, *Mobility functions for two unequal viscous drops in Stokes flow. II. Asymmetric motions*, Phys. Fluids A **1**, 61 (1989).

[237] A. Daddi-Moussa-Ider and S. Gekle, *Hydrodynamic mobility of a solid particle near a spherical elastic membrane: Axisymmetric motion*, Phys. Rev. E **95**, 013108 (2017).

[238] A. Daddi-Moussa-Ider, M. Lisicki, and S. Gekle, *Hydrodynamic mobility of a solid particle near a spherical elastic membrane. ii. asymmetric motion*, Phys. Rev. E **95**, 053117 (2017).

[239] A. Daddi-Moussa-Ider, H. Löwen, and S. Gekle, *Creeping motion of a solid particle inside a spherical elastic cavity*, Eur. Phys. J. E **41**, 104 (2018).

[240] C. Hoell, H. Löwen, A. M. Menzel, and A. Daddi-Moussa-Ider, *Creeping motion of a solid particle inside a spherical elastic cavity: Ii. asymmetric motion*, Eur. Phys. J. E **42**, 89 (2019).

[241] V. A. Shaik and A. M. Ardekani, *Point force singularities outside a drop covered with an incompressible surfactant: Image systems and their applications*, Phys. Rev. Fluids **2**, (2017).

[242] M.-U. Kim, *Axisymmetric Stokes Flow Due to a Point Force near a Circular Disk*, J. Phys. Soc. Jpn. **52**, 449 (1983).

[243] A. Daddi-Moussa-Ider, *Stokeslet parallèle entre deux disques rigides antidérapants positionnés de manière coaxiale : une approche aux équations intégrales duales*, LHB **108**, 2016023 (2022).

[244] Y. Sowa and R. M. Berry, *Bacterial flagellar motor*, Q. Rev. Biophys. **41**, 103–132 (2008).

[245] L. Alvarez, B. M. Friedrich, G. Gompper, and U. B. Kaupp, *The computational sperm cell*, Trends Cell Biol. **24**, 198 (2014).

[246] G. S. Klindt and B. M. Friedrich, *Flagellar swimmers oscillate between pusher- and puller-type swimming*, Phys. Rev. E **92**, 063019 (2015).

[247] R. Dreyfus, J. Baudry, M. L. Roper, M. Fermigier, H. A. Stone, and J. Bibette, *Microscopic artificial swimmers*, Nature **437**, 862 (2005).

[248] A. Najafi and R. Golestanian, *Simple swimmer at low reynolds number: Three linked spheres*, Phys. Rev. E **69**, 062901 (2004).

[249] M. J. Lighthill, *On the squirming motion of nearly spherical deformable bodies through liquids at very small reynolds numbers*, Commun. Pure Appl. Math. **5**, 109 (1952).

[250] J. R. Blake, *A spherical envelope approach to ciliary propulsion*, J. Fluid Mech. **46**, 199 (1971).

[251] S. E. Spagnolie and E. Lauga, *Hydrodynamics of self-propulsion near a boundary: predictions and accuracy of far-field approximations*, J. Fluid Mech. **700**, (2012).

[252] A. M. Menzel, A. Saha, C. Hoell, and H. Löwen, *Dynamical density functional theory for microswimmers*, J. Chem. Phys. **144**, 024115 (2016).

[253] C. Hoell, H. Löwen, and A. M. Menzel, *Dynamical density functional theory for circle swimmers*, New J. Phys. **19**, 125004 (2017).

[254] K. Drescher, J. Dunkel, L. H. Cisneros, S. Ganguly, and R. E. Goldstein, *Fluid dynamics and noise in bacterial cell-cell and cell-surface scattering*, Proc. Natl. Acad. Sci. U.S.A. **108**, 10940 (2011).

[255] J. Hu, M. Yang, G. Gompper, and R. G. Winkler, *Modelling the mechanics and hydrodynamics of swimming e. coli*, Soft Matter **11**, (2015).

[256] K. Drescher, R. E. Goldstein, N. Michel, M. Polin, and I. Tuval, *Direct measurement of the flow field around swimming microorganisms*, Phys. Rev. Lett. **105**, 168101 (2010).

[257] R. E. Goldstein, *Green algae as model organisms for biological fluid dynamics*, Annu. Rev. Fluid Mech. **47**, (2015).

[258] L. G. Leal, *Particle Motions in a Viscous Fluid*, Annu. Rev. Fluid Mech. **12**, 435 (1980).

[259] J. W. Swan and J. F. Brady, *Simulation of hydrodynamically interacting particles near a no-slip boundary*, Phys. Fluids **19**, 113306 (2007).

[260] G. G. Stokes, *On the Effect of the Internal Friction of Fluids on the Motion of Pendulums*, Trans. Camb. Phil. Soc. **9**, 8 (1851).

[261] C. W. Oseen, *Neuere methoden und ergebnisse in der hydrodynamik* (Akademische Verlagsgesellschaft, Leipzig, 1927).

[262] R. Di Leonardo, D. Dell'Arciprete, L. Angelani, and V. Iebba, *Swimming with an image*, Phys. Rev. Lett. **106**, 038101 (2011).

[263] A. J. T. M. Mathijssen, N. Figueroa-Morales, G. Junot, É. Clément, A. Lindner, and A. Zöttl, *Oscillatory surface rheotaxis of swimming E. coli bacteria*, Nat. Commun. **10**, 3434 (2019).

[264] G. Junot, T. Darnige, A. Lindner, V. A. Martinez, J. Arlt, A. Dawson, W. C. K. Poon, H. Auradou, and E. Clément, *Run-to-tumble variability controls the surface residence times of e. coli bacteria*, Phys. Rev. Lett. **128**, 248101 (2022).

[265] V. Kantsler, J. Dunkel, M. Polin, and R. E. Goldstein, *Ciliary contact interactions dominate surface scattering of swimming eukaryotes*, Proc. Natl. Acad. Sci. U.S.A. **110**, (2013).

[266] G. J. Li and A. M. Ardekani, *Hydrodynamic interaction of microswimmers near a wall*, Phys. Rev. E **90**, (2014).

[267] A. J. T. M. Mathijssen, T. N. Shendruk, J. M. Yeomans, and A. Doostmohammadi, *Upstream swimming in microbiological flows*, Phys. Rev. Lett. **116**, (2016).

[268] P. Malgaretti and H. Stark, *Model microswimmers in channels with varying cross section*, J. Chem. Phys. **146**, (2017).

[269] A. Choudhary and H. Stark, *On the cross-streamline lift of microswimmers in viscoelastic flows*, Soft Matter **18**, (2022).

[270] D. Takagi, J. Palacci, A. B. Braunschweig, M. J. Shelley, and J. Zhang, *Hydrodynamic capture of microswimmers into sphere-bound orbits*, Soft Matter **10**, (2014).

[271] O. Sipos, K. Nagy, R. D. Leonardo, and P. Galajda, *Hydrodynamic trapping of swimming bacteria by convex walls*, Phys. Rev. Lett. **114**, (2015).

[272] A. Kaiser, H. H. Wensink, and H. Löwen, *How to capture active particles*, Phys. Rev. Lett. **108**, (2012).

[273] H. Wioland, F. G. Woodhouse, J. Dunkel, J. O. Kessler, and R. E. Goldstein, *Confinement stabilizes a bacterial suspension into a spiral vortex*, Phys. Rev. Lett. **110**, 268102 (2013).

[274] M. Theillard, R. Alonso-Matilla, and D. Saintillan, *Geometric control of active collective motion*, Soft Matter **13**, 363 (2017).

[275] T. Gao, M. D. Betterton, A.-S. Jhang, and M. J. Shelley, *Analytical structure, dynamics, and coarse graining of a kinetic model of an active fluid*, Phys. Rev. Fluids **2**, 093302 (2017).

[276] T. Ostapenko, F. J. Schwarzendahl, T. J. Böddeker, C. T. Kreis, J. Cammann, M. G. Mazza, and O. Bäumchen, *Curvature-guided motility of microalgae in geometric confinement*, Phys. Rev. Lett. **120**, 068002 (2018).

[277] J. Cammann, F. J. Schwarzendahl, T. Ostapenko, D. Lavrentovich, O. Bäumchen, and M. G. Mazza, *Emergent probability fluxes in confined microbial navigation*, Proc. Natl. Acad. Sci. U.S.A. **118**, (2021).

[278] B. Vincenti, G. Ramos, M. L. Cordero, C. Douarche, R. Soto, and E. Clement, *Magnetotactic bacteria in a droplet self-assemble into a rotary motor*, Nat. Commun. **10**, 5082 (2019).

[279] G. Ramos, M. L. Cordero, and R. Soto, *Bacteria driving droplets*, Soft Matter **16**, 1359 (2020).

[280] J. Dhont, *An Introduction to Dynamics of Colloids* (Elsevier Science, 1996).

[281] H. Brenner, *The stokes resistance of an arbitrary particle*, Chem. Eng. Sci. **18**, 1 (1963).

[282] P. Mazur and W. van Saarloos, *Many-sphere hydrodynamic interactions and mobilities in a suspension*, Phys. A: Stat. Mech. **115**, 21 (1982).

[283] A. A. Evans, T. Ishikawa, T. Yamaguchi, and E. Lauga, *Orientational order in concentrated suspensions of spherical microswimmers*, Phys. Fluids **23**, 111702 (2011).

[284] F. Alarcón and I. Pagonabarraga, *Spontaneous aggregation and global polar ordering in squirmer suspensions*, J. Mol. Liq. **185**, 56 (2013).

[285] A. Zöttl and H. Stark, *Hydrodynamics determines collective motion and phase behavior of active colloids in quasi-two-dimensional confinement*, Phys. Rev. Lett. **112**, (2014).

[286] F. J. Schwarzendahl and M. G. Mazza, *Maximum in density heterogeneities of active swimmers*, Soft Matter **14**, 4666 (2018).

[287] A. J. T. M. Mathijssen, F. Guzmán-Lastra, A. Kaiser, and H. Löwen, *Nutrient transport driven by microbial active carpets*, Phys. Rev. Lett. **121**, 248101 (2018).

[288] F. Guzmán-Lastra, H. Löwen, and A. J. T. M. Mathijssen, *Active carpets drive non-equilibrium diffusion and enhanced molecular fluxes*, Nat. Commun. **12**, (2021).

[289] A. R. Sprenger, M. A. Fernandez-Rodriguez, L. Alvarez, L. Isa, R. Wittkowski, and H. Löwen, *Active Brownian motion with orientation-dependent motility: Theory and experiments*, Langmuir **36**, 7066 (2020).

[290] A. R. Sprenger, C. Bair, and H. Löwen, *Active brownian motion with memory delay induced by a viscoelastic medium*, Phys. Rev. E **105**, 044610 (2022).

[291] A. R. Sprenger, S. Jahanshahi, A. V. Ivlev, and H. Löwen, *Time-dependent inertia of self-propelled particles: The Langevin rocket*, Phys. Rev. E **103**, 042601 (2021).

[292] M. R. Bailey, A. R. Sprenger, F. Grillo, H. Löwen, and L. Isa, *Fitting an active brownian particle's mean-squared displacement with improved parameter estimation*, Phys. Rev. E **106**, L052602 (2022).

[293] L. Caprini, A. R. Sprenger, H. Löwen, and R. Wittmann, *The parental active model: A unifying stochastic description of self-propulsion*, J. Chem. Phys. **156**, 071102 (2022).

[294] A. R. Sprenger, L. Caprini, H. Löwen, and R. Wittmann, *Dynamics of active particles with translational and rotational inertia*, arXiv:2301.01865 (2023).

[295] A. R. Sprenger, V. A. Shaik, A. M. Ardekani, M. Lisicki, A. J. T. M. Mathijssen, F. Guzmán-Lastra, H. Löwen, A. M. Menzel, and A. Daddi-Moussa-Ider, *Towards an analytical description of active microswimmers in clean and in surfactant-covered drops*, Eur. Phys. J. E **43**, (2020).

[296] A. Daddi-Moussa-Ider, A. R. Sprenger, Y. Amarouchene, T. Salez, C. Schönecker, T. Richter, H. Löwen, and A. M. Menzel, *Axisymmetric Stokes flow due to a point-force singularity acting between two coaxially positioned rigid no-slip disks*, J. Fluid Mech. **904**, (2020).

[297] A. Daddi-Moussa-Ider, A. R. Sprenger, T. Richter, H. Löwen, and A. M. Menzel, *Steady azimuthal flow field induced by a rotating sphere near a rigid disk or inside a gap between two coaxially positioned rigid disks*, Phys. Fluids **33**, 082011 (2021).

Eidesstattliche Versicherung

Ich versichere an Eides Statt, dass die Dissertation von mir selbständig und ohne unzulässige fremde Hilfe unter Beachtung der „Grundsätze zur Sicherung guter wissenschaftlicher Praxis an der Heinrich-Heine-Universität Düsseldorf“ erstellt worden ist. Die aus fremden Quellen direkt oder indirekt übernommenen Inhalte wurden als solche kenntlich gemacht.

Düsseldorf, ____________________   _________________________